

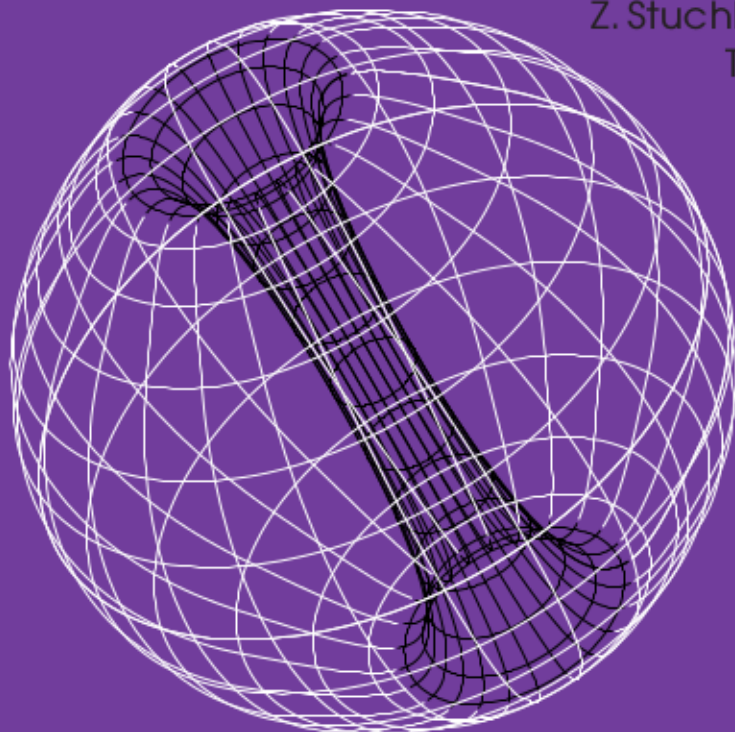
---

Proceedings of

# RAGtime 14-16: Workshops on black holes and neutron stars

18-22 September / 15-18 July/  
11-19 October '12/'13/'14  
Opava, Prague, Czech Republic

Editors:  
Z. Stuchlík, G. Török,  
T. Pecháček





SILESIAIAN UNIVERSITY IN OPAVA

Publications of the Institute of Physics No. 7



Proceedings of RAGtime 14–16:  
Workshops on black holes and neutron stars  
18–22 Sept./15–18 July/11–19 Oct. '12/'13/'14  
Opava, Prague, Czech Republic

Z. Stuchlík, G. Török and T. Pecháček, editors

Opava, Prague 2014

Editorial Board: Prof. Dr. Marek Abramowicz  
Prof. John Miller, D. Phil. (Oxon)  
Prof. Włodzimierz Kluźniak, Ph.D.  
Prof. RNDr. Vladimír Karas, DrSc.  
Prof. RNDr. Zdeněk Stuchlík, CSc.  
RNDr. Gabriel Török, Ph.D.  
RNDr. Michal Dovčiak, Ph.D.  
Mgr. Michal Bursa, Ph.D.  
RNDr. Jiří Horák, Ph.D.  
Mgr. Tomáš Pecháček, Ph.D.

Editorial assistant: Mgr. Pavlína Adámková

Annotation: In this Proceedings, the talks presented during workshops *RAGtime 14–16: Workshops on black holes and neutron stars, Opava, Prague, 18–22 Sept./15–18 July/11–19 Oct. '12/'13/'14* are collected.

Copyright © 2014 Silesian University in Opava

## PREFACE

Since 1999, the RAGtime meetings have been organized by the Relativistic Astrophysics Group (RAG) at the Institute of Physics, the Faculty of Philosophy and Science of the Silesian University in Opava in order to provide opportunities for discussing the recent advances and developments in the field of relativistic astrophysics. During the past sixteen years, RAGtime has grown from a small workshop to become a regular international conference that brings together collaborators of the Opava's research group who are coming from EU, USA, China and Japan. It has also provided a starting point for many new collaborations. Among the involved institutions are the Astronomical Institute of the Academy of Sciences of the Czech Republic, the Faculty of Mathematics and Physics of the Charles University in Prague, the International School for Advanced Studies and the Abdus Salam International Centre for Theoretical Physics in Trieste, the Institute of Astrophysics at the University of Oxford, the Department of Astrophysics of the University in Gothenburg, the Institute of Astronomy of the Polish Academy of Sciences, the Massachusetts Institute of Technology, the Harvard University, the Cornell University, the Hiroshima University, the Fudan University, and the Xiamen University.

Concordantly, the scope of the topics discussed at the meetings has widened considerably in recent years. New results have been presented at the conference from different areas, such as the alternative theories of gravitation and their astrophysical implications, physics of plasma and magnetic fields in the presence of a strong gravity and X-ray variability modelling connected, but not limited, to the proposed ESA X-ray missions ATHENA and LOFT. However, the main focus of the meeting remains on the general physical phenomena connected to accretion processes onto black holes and neutron stars and the internal structure of neutron stars and quark stars.

The RAGtime workshops and conferences have always provided an important and unique opportunity for undergraduate and graduate students of the Silesian University to meet and discuss problems with the world's leading astrophysicists. Among the regular guests are Marek Abramowicz, John Miller, Włodzimierz Kluźniak, and Vladimír Karas, Jeff McClintock, Shoji Kato, Ron Remillard, Didier Barret, Luciano Rezzolla, Yasufumi Kojima, Wen Fei Yu.

We would like to thank all the authors for a careful preparation of their contributions. This publication has been made possible through the support provided in the framework of the project "Supporting Integration with the International Theoretical and Observational Research Network in Relativistic Astrophysics of Compact Objects", CZ.1.07/2.3.00/20.0071. The project is co-financed by the European Social fund and state budget of the Czech Republic.

Opava, Prague, December 2014

Z. Stuchlík, G. Török and T. Pecháček  
editors

## CONTENTS

<i>K. Adámek and M. Bursa</i> Simulating Compton Scattering using Monte Carlo method: COSMOC library . . . . .	1
<i>M. Blaschke, Z. Stuchlík and P. Slaný</i> Some Aspects of Brany Kerr Spacetimes Relevant to Accretion Processes . . . . .	11
<i>V. V. Breus, I. L. Andronov, P. Dubovský, Y. Kim, L. L. Chinarova, J. Park, J.-N. Yoon, K. Petřík, S. Zola, S. V. Kolesnikov, K. A. Antonyuk, A. R. Baransky, P. Beringer, T. Hegedüs, J. W. Robertson and I. Kudzej</i> Rotational Evolution of the Magnetic White Dwarfs in Intermediate Polars . . . . .	19
<i>M. Bursa and K. Adámek</i> Compton scattering in strong gravity . . . . .	31
<i>M. Bursa, J. Horák and G. Karssen</i> Polarization vector transport in Kerr geometry . . . . .	39
<i>M. Dovčiak, J. Svoboda, R. Goosmann, V. Karas, G. Matt and V. Sochora</i> An XSPEC model to explore spectral features from black-hole sources – II. The relativistic iron line in the lamp-post geometry . . . . .	51
<i>F. Ficek, M. Rutkowski and W. Kluźniak</i> Evolutionary tracks of millisecond pulsars with low-mass companions . . . . .	83
<i>L. Giussani, W. Kluźniak and B. Mishra</i> Frequency spectrum of axisymmetric horizontal oscillations in accretion disks . . . . .	93
<i>K. Goluchová and Z. Stuchlík</i> Embedding diagrams of Bardeen geometry . . . . .	99
<i>J. Hamerský and V. Karas</i> Triggered oscillations and destruction of magnetized relativistic tori in 2D . . . . .	107
<i>J. Juryšek</i> Regularity of pulsar glitches . . . . .	115
<i>V. Karas and M. A. Abramowicz</i> Modified Newtonian potentials for particles and fluids in permanent rotation around black holes . . . . .	121
<i>V. Karas, M. Dovčiak, D. Kunneriath, W. Yu and W. Zhang</i> Tidal disruption events from a nuclear star cluster as possible origin of transient relativistic spectral lines near SMBH . . . . .	129
<i>V. Karas, L. Šubr, D. Kunneriath and M. Zajaček</i> Effects of environmental drag onto a fast-moving magnetic compact star near a supermassive black hole . . . . .	137
<i>S. Khanna, Z. Strzelecka, B. Mishra and W. Kluźniak</i> Eigenmodes of trapped horizontal oscillations in accretion disks . . . . .	145

<i>M. Kološ, Z. Stuchlík and A. Tursunov</i> Oscillations of electric current-carrying string loop near a Schwarzschild black hole immersed in an asymptotically uniform magnetic field . . . . .	159
<i>V. Marchenko, O. Kobzar, O. Sushchov and B. Hnatyk</i> Centaurus A as a source of ultra high energy cosmic rays . . . . .	171
<i>J. C. Miller and I. Musco</i> Causal horizons and some topics concerning structure formation . . . . .	181
<i>B. Mishra and B. Vaidya</i> Geometrically thin accretion disk around Maclaurin spheroids . . . . .	193
<i>V. Parthasarathy and W. Kluźniak</i> Numerical simulation of thin disc with PLUTO . . . . .	205
<i>J. Schee, P. Adámková and Z. Stuchlík</i> Radiating perfect fluid tori in static braneworld spacetime: frequency shift map of torus image . . . . .	213
<i>P. Slaný, J. Kovář, Z. Stuchlík and V. Karas</i> Equilibria of charged dust tori in a dipole magnetic field: hydrodynamic approach . . . . .	221
<i>E. Šrámková and G. Török</i> Black hole spin inferred from disc oscillation models of high-frequency quasi-periodic oscillations . . . . .	229
<i>Z. Stuchlík and M. Blaschke</i> Braneworld naked singularities . . . . .	237
<i>Z. Stuchlík and M. Kološ</i> HF QPOs in the neutron star binary system XTE J1701-462 fitted by the model of oscillating string loops . . . . .	243
<i>M. G. Tkachenko and I. L. Andronov</i> Determination of Characteristics of Eclipsing Binaries with Spots: Phenomenological vs Physical Models . . . . .	257
<i>G. Török, K. Goluchová, M. Urbanec, E. Šrámková, K. Adámek, G. Urbancová, T. Pecháček, P. Bakala, Z. Stuchlík, J. Horák and J. Juryšek</i> Confronting models of twin peak quasi-periodic oscillations: Mass and spin estimates fixed by neutron star equation of state . . . . .	269
<i>G. Török, K. Goluchová, J. Horák, E. Šrámková, M. Urbanec, T. Pecháček and P. Bakala</i> Twin peak quasi-periodic oscillations as signature of oscillating cusp torus . . . . .	283
<i>M. Wielgus and M. Abramowicz</i> Stress-energy tensor of a radiating sphere inclosing black hole . . . . .	293
<i>M. Wiśniewicz, D. Gondek-Rosińska, W. Kluźniak and N. Stergioulas</i> Unusual behaviour of epicyclic frequencies around rapidly rotating compact stars . . . . .	299

<i>L. Xue, W. Kluźniak, A. Sądowski, J.-F. Lu and M. Abramowicz</i> High frequency oscillations of a slim disk undergoing a limit-cycle outburst . . . . .	305
<i>W. Yan, F. H. Vincent, M. A. Abramowicz, A. A. Zdziarski and O. Straub</i> The Komissarov Model of Sgr A* . . . . .	311

# Simulating Compton Scattering using Monte Carlo method: COSMOC library

Karel Adámek<sup>1</sup> and Michal Bursa<sup>2</sup>

<sup>1</sup>Institute of Physics, Faculty of Philosophy and Science, Silesian University in Opava,  
Bezručovo nám. 13, CZ-74601 Opava, Czech Republic

<sup>2</sup>Astronomical Institute, Academy of Sciences of the Czech Republic,  
Boční II 1401/1a, CZ-14131 Prague, Czech Republic

## ABSTRACT

In the following article we present properties and functionality of the COSMOC library designed to exploit basic features of Compton scattering process and its computational modelling. Basic physics of Compton scattering is pointed out, accompanied by various procedures accessible by user. The COSMOC library uses Monte Carlo method to perform single photon scattering. Special care is given to emphasize use of proper random number generator for Monte Carlo method.

**Keywords:** Monte Carlo – Compton scattering – C++

## 1 INTRODUCTION

Scattering of photons on free charged particle is called Compton scattering. It was first observed in year 1923 by Arthur H. Compton when he was examining scattering of X-ray photons on stationary electrons. The Compton scattering was found to be useful in many areas of science and astrophysics is no exception. Its influence can be found in spectra produced by many astrophysical objects and phenomena. This is especially true in low densities of matter where Compton scattering is dominating in comparison with other types of scatterings. By scattering on non-relativistic electrons the photons can only lose energy on the other hand scattering by relativistic electrons can result in increased energy of the scattered photons. Even moderately energetic electrons can contribute to the resulting spectra by multiple scatterings of photons, this behaviour is called comptonization.

The Compton scattering is suspected to be responsible for power law shaped spectra emitted by many astrophysical objects. Scattering of synchrotron photons is considered in explaining non-thermal (power law) parts of the spectra of sources like blazars or radio quasars. The comptonization has considerable effect in X-ray emission in hard (low) and soft (high) spectral states of black-hole binaries.

Effects of the Compton scattering on observed spectra can be more easily simulated by Monte Carlo method. One of the first Monte Carlo simulations of the Compton scattering and its effect on observed spectra is work by (Pozdnyakov et al., 1983). Full relativistic treatment of the Compton scattering was recently done by (Dolence et al., 2009) or

(Schnittman and Krolik, 2013). Polarisation was also introduced into Compton scattering codes, for more details see works by (McNamara et al., 2008) or (Krawczynski, 2012). Aim of our code is to calculate Compton scattering in Kerr space-time with help of Monte Carlo method. The code is in form of C library.

This library is concerned only with Compton scattering on free electrons and does not consider any modifications needed for scatterings on bounded electrons. It is also limited to gases which can be approximated by equation of state for ideal gas. It also does not consider polarization. Polarization should be first candidate for improvements of the library in the future. The COSMOC library was written using GSL 1.16. The GSL is an abbreviation of GNU Scientific Library and it is a numerical library for C and C++. It provides wide variety of numerical methods for scientific purposes.

## 2 COMPTON SCATTERING

### 2.1 Compton Scattering

The Compton scattering is an inelastic scattering process, where photon is scattered by free charged particle, usually electron. Since the scattering is inelastic photon loses energy in favour of the scattering particle. The differential cross-section is described by the Klein–Nishina formula (Rybicki and Lightman, 1985)

$$\frac{d\sigma}{d\Omega} = \frac{1}{2} r_0^2 \frac{\epsilon_f^2}{\epsilon_i^2} \left( \frac{\epsilon_i}{\epsilon_f} + \frac{\epsilon_f}{\epsilon_i} - \sin^2(\theta) \right), \quad (1)$$

where  $r_0$  is classical electron radius,  $\epsilon_i$  is the energy of the incident photon and  $\epsilon_f$  is the energy of the scattered photon. This equation also gives probability distribution function  $\text{pdf}_C(\theta)$  for scattering angle  $\theta$  of the Compton scattering.

The energy of the scattered photon is given by following relationship (Rybicki and Lightman, 1985)

$$\epsilon_f = \frac{\epsilon_i}{1 + \frac{\epsilon_i}{m_e c^2} (1 - \cos(\theta))}. \quad (2)$$

The total cross-section is an integral of differential cross-section (1) over spatial angle  $\Omega$  and it is given by

$$\sigma = \int \frac{d\sigma}{d\Omega} d\Omega = \int_0^{2\pi} d\varphi \int_0^\pi d\theta \frac{d\sigma}{d\Omega} \sin(\theta). \quad (3)$$

After we perform integration we arrive at (Rybicki and Lightman, 1985)

$$\sigma = \sigma_T \frac{3}{4} \left[ \frac{1+x}{x^3} \left( \frac{2x(1+x)}{1+2x} - \ln(1+2x) \right) + \frac{1}{2x} \ln(1+2x) - \frac{1+3x}{(1+2x)^2} \right], \quad (4)$$

where  $x = \epsilon_i / (m_e c^2)$  and  $\sigma_T = (8\pi/3)r_0^2$  is Thomson total cross-section.

To obtain cumulative distribution function  $\text{cdf}_C(\theta)$  we must integrate Eq. (1) over scattering angle  $\theta$ , where  $\epsilon_f$  is given by Eq. (2). This gives

$$\begin{aligned} \text{cdf}_C(\theta) = & \frac{r_0^2}{4x^2} \left[ 2\theta - \frac{2B \arctan(-\sqrt{1+2x} \tan(\theta/2))}{\sqrt{(1+2x)^5}} \right] + \\ & + \frac{r_0^2}{4x^2} \left[ \frac{x^3 \sin(\theta)}{(1+2x)(1+x(1-\cos(\theta)))^2} \right] + \frac{r_0^2}{4x^2} \left[ \frac{x(3x^3+11x^2+8x+2)\sin(\theta)}{(1+2x)^2(1+x(1-\cos(\theta)))} \right], \end{aligned} \quad (5)$$

where  $B = 11x^4 + 4x^3 - 12x^2 - 10x - 2$ .

### Implementation in the code

The implementation of Compton scattering consists of following subroutines. Equation (1) can be invoked by calling function `CM_diffcr`, total cross-section Eq. (4) is returned by function `CM_totcr`. To obtain values of the  $\text{cdf}_C(\theta)$  for different values of scattering angle  $\theta$  one must call function `CM_EDiE_cdf`. These functions are used by procedure for generating random numbers with Klein–Nishina distribution `Random_num_icdf_bisection_CM_EDiE`. This function implements bisection to search for value of the inverse  $\text{cdf}_C(\theta)$  and produces one random number per call.

## 2.2 Thomson Scattering

The Thomson scattering is a special case of Compton scattering, it is an approximation of the Compton scattering for low photon energies. This approximation can be used as long as incident photon energies  $\epsilon_i \ll 511 \text{ keV}$  (electron rest energy). The differences in probability distribution functions  $\text{pdf}_C(\theta)$  for distinct photon energies are shown in the Figure 1. Since energy of the incident photon is much smaller than electron rest energy  $\epsilon_i \ll m_e c^2$  we can neglect denominator in Eq. (2) and get

$$\epsilon_f = \epsilon_i, \quad (6)$$

which means that photon energy  $\epsilon_i$  is not changed by the scattering. Using this approximation we can simplify the differential cross-section given by the Klein–Nishina Eq. (1) to (Rybicki and Lightman, 1985)

$$\frac{d\sigma}{d\Omega} = \frac{1}{2} r_0^2 (1 - \cos^2(\theta)), \quad (7)$$

and the total cross-section is then reduced to

$$\sigma_T = \frac{8\pi}{3} r_0^2. \quad (8)$$

The  $\text{cdf}_{\text{TH}}(\theta)$  can be obtained by integration of the Eq. (7) and it has form

$$\text{cdf}_{\text{TH}}(\theta) = \frac{1}{8} r_0^2 (6\theta + \sin(2\theta)). \quad (9)$$

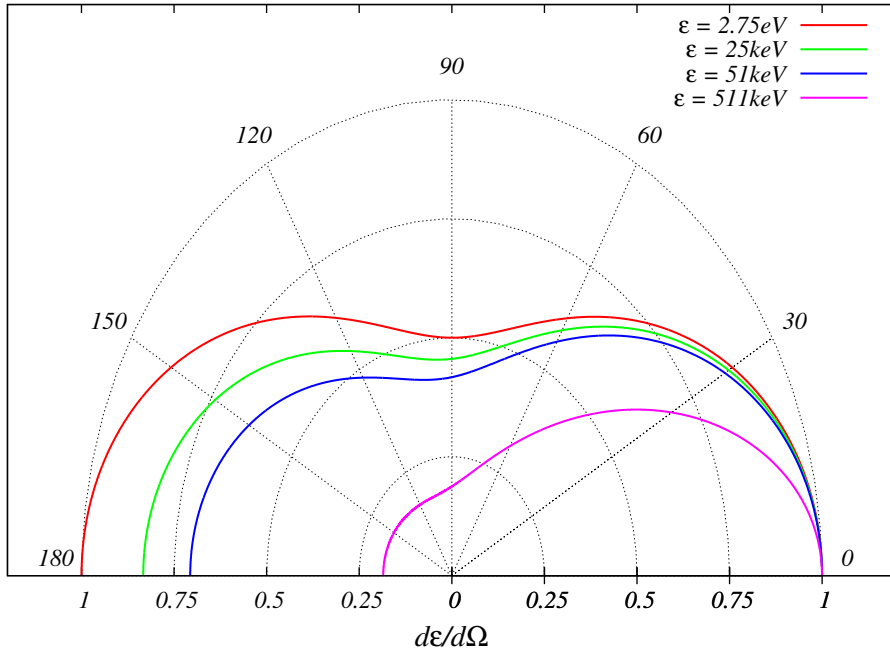


**Figure 1.** Differential cross-section  $d\epsilon/d\Omega$  of Compton scattering for low energy photons as it depends on scattering angle. The cross-sections are normalized. Chosen photon energies demonstrate deviation of  $d\epsilon/d\Omega$  with increasing photon energy. Differential cross-section for photons with energy above  $\epsilon = 51$  keV starts to deviate from Thomson limit (photons with  $\epsilon = 2.75$  eV).

### *Implementation in the code*

As with Compton scattering the library contains similar functions for Thomson approximation. To get differential cross-section (7) call of function `TH_diffcr` is appropriate. Thomson total cross-section is stored at variable `TH_totcr` since it is independent on incident photon energy. To get the value of the  $\text{cdf}_{\text{TH}}(\theta)$  one must call the function `TH_cdf_value`. However since we do not have direct expression for inverse  $\text{cdf}_{\text{TH}}(\theta)$ , the Thomson approximation is not useful in a sense of performance. In other words using Thomson approximation for evaluation of low energy photons we would not gain any increase in performance.

### **2.3 Inverse Compton Scattering**

If we restrict ourselves just to scattering particle at rest we are confined to Compton scattering frame where photons can only loose energy. To increase energy of the scattered photons we need to take into account motion of the scattering particle as well. Since we are able to calculate Compton scattering only in the frame where the scattering particle is at rest we must transform photon's momentum by Lorentz transformation into this rest frame first. This transformation involves two effects: The first effect is relativistic aberration or beaming

effect. This effect changes the angle  $\alpha$  between scattering particle's velocity and incident photon direction. This transformation reads (Rybicki and Lightman, 1985)

$$\cos(\bar{\alpha}) = \frac{\cos(\alpha) + \beta}{1 + \beta \cos(\alpha)}, \quad (10)$$

where  $\beta = |v_e|/c$  and  $|v_e|$  is electron velocity. This effect is applied to both incident and radiated photons.

The second phenomenon is the Doppler effect which modifies photon frequency thus causes increase or decrease of its energy as measured by observer comoving with electron. The energy of the interacting photon is transformed as follows (Rybicki and Lightman, 1985)

$$\bar{\epsilon}_i = \epsilon_i \gamma (1 - \beta \cos(\alpha)), \quad (11)$$

where again  $\beta = |v_e|/c$ . This transformation must be performed before as well as after scattering took place.

### 3 ELECTRON VELOCITY

#### 3.1 Maxwell–Boltzmann Distribution

Maxwell–Boltzmann distribution gives distribution of velocities of particles of ideal gas. We assume point-like, non-relativistic particles with negligible inter-particle forces. Many gases in astrophysics behave as ideal gas or they are similar to it. In Compton scattering scheme we are mostly dealing with rarefied real gasses. For these, at ordinary temperatures, the Maxwell–Boltzmann distribution is a good approximation.

The probability of particle having magnitude of velocity  $v$  within a gas with temperature  $T$  is given as (Bradt, 2014)

$$\text{pdf}_{\text{MB}}(v) = \sqrt{\left(\frac{m}{2\pi kT}\right)^3} 4\pi v^2 \exp\left(-\frac{mv^2}{2kT}\right), \quad (12)$$

where  $k$  is Boltzmann constant  $k = 8.61 \times 10^{-5}$  eV/K and  $m$  is mass of the gas particle (in this case electrons  $m_e = 9.11 \times 10^{-31}$  kg). To acquire cumulative distribution function  $\text{cdf}_{\text{MB}}(v)$  we must integrate (12)

$$\text{cdf}_{\text{MB}}(v) = \text{erf}\left(\sqrt{\frac{mv^2}{2kT}}\right) - \sqrt{\frac{2mv^2}{\pi kT}} \exp\left(\frac{mv^2}{2kT}\right), \quad (13)$$

where  $\text{erf}(x)$  is Error function.

#### *Implementation in the code*

Maxwell–Boltzmann distribution is implemented in these routines: `MB_pdf` returns value of  $\text{pdf}_{\text{MB}}(v)$  Eq. (12), `MB_cdf` gives  $\text{cdf}_{\text{MB}}(v)$  Eq. (13). The function for random electron

speed is called `Random_num_icdf_bisection_MB` and it returns electron speed sampled from Maxwell–Boltzmann distribution. To evaluate  $\text{cdf}_{\text{MB}}(v)$  we are using GSL library implementation of Error function  $\text{erf}(x)$  by calling `gsl_sf_erf()`.

If the temperatures throughout the simulation do not exceed  $T_{\text{B}} = 2 \times 10^8$  K the Maxwell–Boltzmann distribution can be used reasonably well. However if the temperature  $T > T_{\text{B}}$  we recommend using Maxwell–Jüttner distribution for whole computation.

### 3.2 Maxwell–Jüttner Distribution

The Maxwell–Jüttner distribution is a generalization of the Maxwell–Boltzmann distribution for ideal non-interacting gas. For low temperatures  $T$  and in limit of small velocities this distribution becomes identical with the Maxwell–Boltzmann distribution.

Probability distribution for  $\gamma$  of the electrons within the gas with temperature  $T$  such that  $kT$  approaches or exceeds  $mc^2$  is given by (Kershaw et al., 1986)

$$f(\gamma) = \frac{\gamma^2 \beta}{\tau K_2(1/\tau)} \exp -\frac{\gamma}{\tau}, \quad (14)$$

where  $\beta = v/c$ ,  $\tau = kT/mc^2$ ,  $K_2$  is Bessel function of the second kind and  $c$  is speed of light.

Integral through all velocities must be

$$\int_{-\infty}^{\infty} f(\gamma) = 1. \quad (15)$$

Behaviour of the distribution for low temperatures can be seen in the Fig. 2.

#### *Implementation in the code*

In the code we implement the distribution using logarithmic expression  $\ln f(\gamma)$ . This is advantageous because we can express Bessel function  $K_2$  in its logarithmic form thus reducing possible errors due to round-off error. For calculating Bessel function we are using GSL library by calling function `gsl_sf_bessel_lnKnu()`. After we got value  $\ln f(\gamma)$  we return  $\exp(\ln f(\gamma))$ .

#### **Random number with Maxwell–Jüttner distribution**

Implementation of random number generation, which produces random numbers with Maxwell–Jüttner distribution is similar to the technique described in Section 4.2. There is slight modification of the binary search starting position which is determined by the function `get_points_MJ()`. This function returns approximation of the peak of the distribution and end point of the distribution (which is a point where  $f(\gamma) < 10^{-30}$ ). The aim is to decrease searching time and number of evaluations of the  $\text{cdf}(x)$  (which involves integrals) by setting middle point to the peak thus near most probable random value.

## Cut-off Temperature

From the Fig. 2 we can see that for temperatures  $T < 2 \times 10^8$  K the distribution has its maximum very near  $\gamma = 1$ . Thus no relativistic effects are noticeable. Putting cut off temperature to  $T_{\text{cut}} = 2 \times 10^8$  K is reasonable.

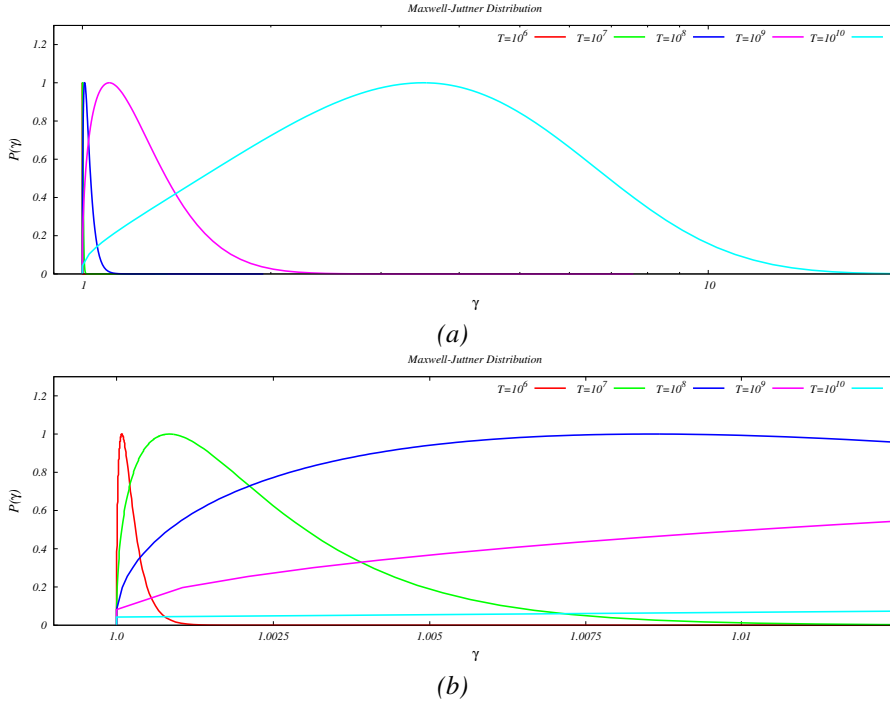


**Figure 2.** Maxwell–Jüttner distribution for different temperatures. Probability  $P(\gamma)$  is normalized to unity.

## 4 NUMERICAL METHODS

Our simulation, in current state, is intended to follow single photons by using Monte Carlo method. The Monte Carlo method heavily depends on random numbers and thus good random number generator is needed for accurate results.

### 4.1 Random Number Generators

On computer using algorithms it is very hard if not impossible to get truly random unbiased, uncorrelated random numbers with uniform distributions in multiple dimensions. When using computer we are using a pseudo-random numbers produced by the pseudo-random number generators like `rand` in standard C. However some generators are better than others. The ‘good’ random number generator should pass number of theoretical and empirical tests. More can be found in (L’Ecuyer and Simard, 2007).

For our Monte Carlo simulation we choose to use GSL library random number generator MT19937. This generator has unusually long period of  $P = 2^{19937} - 1$  numbers. This algorithm has been developed with special attention to the most significant bits. This property makes it especially well suited for Monte Carlo simulations (Matsumoto and Nishimura, 1998). With performance comparable to the standard C `rand` it is ideal pseudo-random number generator for our needs. It also performed well in tests conducted by (L'Ecuyer and Simard, 2007).

## 4.2 Random Numbers with Distribution

Standard random number generator produces uniformly distributed random numbers in range  $(0, 1)$ . To obtain random numbers with desired custom distribution we must project this range onto some other which is defined by  $\text{cdf}(x)$ . For this projection we need to find an inverse cumulative distribution function  $\text{cdf}(x)^{-1}$  of our custom distribution. To check if our custom distribution of random numbers does agree with  $\text{cdf}(x)$  we have used Kolmogorov–Smirnov test for random number distribution (Wall and Jenkins, 2003).

### *Inverse cdf method*

Assuming we have probability density function  $\text{pdf}(x)$  with property

$$\int_{-\infty}^{\infty} \text{pdf}(x') dx' = 1, \quad (16)$$

we can construct cumulative distribution function  $\text{cdf}(x)$  given as

$$\text{cdf}(x) = \int_{-\infty}^x \text{pdf}(x') dx'. \quad (17)$$

Taking into consideration the Eq. (16) we can see that  $\text{cdf}(x) \in [0, 1]$ . To generate random numbers with distribution given by  $\text{pdf}(x)$  we need to construct inverse cumulative distribution function  $\text{cdf}(x)^{-1}$  and project generated random numbers in interval  $(0, 1)$  by the  $\text{cdf}(x)^{-1}$  to get random number with desired custom distribution. If we cannot find  $\text{cdf}^{-1}(x)$  then we have to find appropriate function value by using root-finding algorithm. Since  $\text{cdf}(x)$  is strictly increasing in the interval  $(0, 1)$  we can apply bisection to find the value of the  $\text{cdf}^{-1}(x)$ .

## 5 IMPLEMENTATION

### 5.1 Structures and constants

The COSMOC library uses these classes:

- `kn_par` class is directly used by user and it holds all variables connected with the scattering of the photon. For example it holds energy of the incident photon `kn_par::nu_i`, energy of the scattered photon `kn_par::nu_f`, scattering angles `kn_par::theta_f` and `kn_par::phi_f`. These are variables most likely to be accessed by the user.
- `prop`, `approx` and `Max_dis_int` are internal classes and user does not need to interact with them.

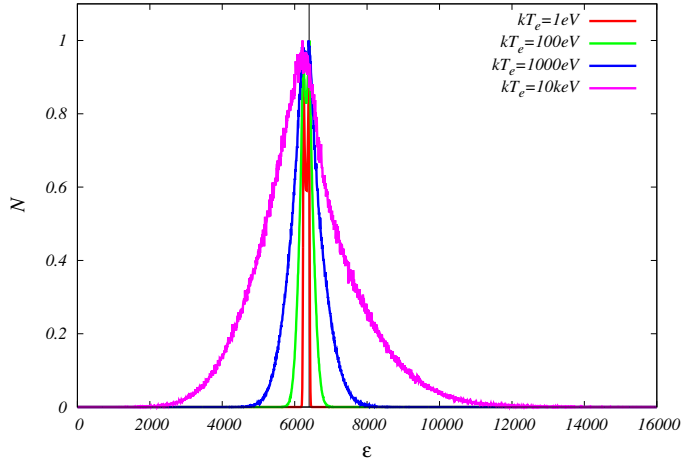


**Figure 3.** Broadening of iron spectral line with initial energy  $\nu = 6400$  eV. On x axis we see energy of the scattered photon, y axis shows normalized count. The scattering is performed on electrons with different temperatures, where  $k$  is Boltzmann constant and  $T_e$  is electron temperature. Temperatures are distinguished by different colours.

## 5.2 Scattering

The whole process of scattering is performed by function `scatter_EDiE`, which then makes use of other internal functions of COSMOC library. These internal functions are accessible by user. Whole library as of now has a form of includable `.h` and `.cpp` file and it is not en-capsuled into a class. The declaration of function `scatter` is following:

```
void scatter_EDiE(
    kn_par *par – information about incident photon,
    double eT – temperature of the gas,
    approx *mj_app – internal class which must be initiated at the beginning of the code,
    int mj_size – size of mj_app,
    gsl_rng *rnd – GSL library handle for random numbers
    gsl_integration_workspace *w – GSL library handle for integration,
    int force_relativistic=0 – optional switch to force relativistic treatment
).
```

The procedure `scatter_EDiE` works in three modes, which mode is triggered depends on temperature of the gas. For temperatures  $T > 2.0 \times 10^8$  K the relativistic treatment is used. This includes beaming effect Eq. (10) and Doppler effect Eq. (11). For electron velocities the Maxwell–Jüttner distribution is used.

The second mode is for temperatures  $300 \text{ K} < T < 2.0 \times 10^8 \text{ K}$ . In this mode Maxwell–Boltzmann distribution is used and only Doppler effect is taken into account.

Last mode is for stationary electrons for temperatures below  $T = 300 \text{ K}$ , where only Compton scattering without any additional effects is performed.

The effect of Doppler shift can be seen on spectral line broadening, which is shown in the Fig. 3. The figure shows broadening of iron  $\nu = 6.4 \text{ keV}$  spectral line.

**SUMMARY**

The COSMOC library simulates Compton scattering by following single photon by Monte Carlo method. It includes Compton as well as inverse Compton scattering. We have implemented Maxwell–Boltzmann distribution of electron velocities and its relativistic version the Maxwell–Jüttner distribution. The random number generator used is MT19937. The accuracy of generated distribution (Klein–Nishina, Maxwell–Boltzmann, Maxwell–Jüttner) were tested by using Kolmogorov–Smirnov test. The functions in COSMOC library can also be used separately.

**ACKNOWLEDGEMENTS**

This work has been supported by OPVK project CZ.1.07/2.3.00/20.0071.

**REFERENCES**

- Bradt, H. (2014), *Astrophysics Processes: The Physics of Astronomical Phenomena*, Cambridge University Press.
- Dolence, J. C., Gammie, C. F., Mościbrodzka, M. and Leung, P. K. (2009), grmonty: A Monte Carlo Code for Relativistic Radiative Transport, *The Astrophysical Journal Supplement*, **184**, pp. 387–397, arXiv: 0909.0708.
- Kershaw, D. S., Prasad, M. K. and Beason, J. D. (1986), A simple and fast method for computing the relativistic Compton Scattering Kernel for radiative transfer, *Journal of Quantitative Spectroscopy and Radiative Transfer*, **36**, pp. 273–282.
- Krawczynski, H. (2012), Tests of General Relativity in the Strong-gravity Regime Based on X-Ray Spectropolarimetric Observations of Black Holes in X-Ray Binaries, *The Astrophysical Journal*, **754**, 133, arXiv: 1205.7063.
- L’Ecuyer, P. and Simard, R. (2007), TestU01: A C Library for Empirical Testing of Random Number Generators, *ACM Transactions on Mathematical Software*, **33**(4).
- Matsumoto, M. and Nishimura, T. (1998), Mersenne Twister: A 623-dimensionally equidistributed uniform pseudorandom number generator, *ACM Transactions on Modeling and Computer Simulation*, **8**(1), pp. 3–30.
- McNamara, A. L., Kuncic, Z. and Wu, K. (2008), X-ray polarization signatures of Compton scattering in magnetic cataclysmic variables, *Monthly Notices of the Royal Astronomical Society*, **386**, pp. 2167–2172, arXiv: 0803.0350.
- Pozdnyakov, L. A., Sobol, I. M. and Syunyaev, R. A. (1983), Comptonization and the shaping of X-ray source spectra - Monte Carlo calculations, *Astrophysics and Space Physics Reviews*, **2**, pp. 189–331.
- Rybicki, G. B. and Lightman, A. P. (1985), *Radiative Processes in Astrophysics*, Wiley-VCH.
- Schnittman, J. D. and Krolik, J. H. (2013), A Monte Carlo Code for Relativistic Radiation Transport around Kerr Black Holes, *The Astrophysical Journal*, **777**, 11, arXiv: 1302.3214.
- Wall, J. V. and Jenkins, C. R. (2003), *Practical Statistics for Astronomers*, Cambridge University Press.

# Some Aspects of Brany Kerr Spacetimes Relevant to Accretion Processes

Martin Blaschke,<sup>a</sup> Zdeněk Stuchlík<sup>b</sup> and Petr Slaný<sup>c</sup>

Institute of Physics, Faculty of Philosophy & Science, Silesian University in Opava,  
Bezručovo nám. 13, CZ-746 01 Opava, Czech Republic

<sup>a</sup>Martin.Blaschke@fpf.slu.cz

<sup>b</sup>Zdenek.Stuchlik@fpf.slu.cz

<sup>c</sup>Petr.Slany@fpf.slu.cz

## ABSTRACT

We consider equatorial motion of test particles around a rotating Kerr naked singularity in the Randall–Sundrum braneworld scenario and its implications for the properties of Keplerian accretion disks. We demonstrate existence of some unexpected phenomena related to properties of spacetimes having positive braneworld tidal charges. This new phenomenon can be an interesting explanation for extremely high energy cosmic radiation.

**Keywords:** Randall Sundrum – Brane-world

## 1 INTRODUCTION

In recent years, one of the promising approaches to the higher-dimensional gravity theories seems to be the string theory and particularly M-theory (Hořava and Witten, 1996; Hořava and Witten, 1996). This new idea is describing gravity as a truly higher-dimensional interaction becoming effectively 4D at low enough energies. Also these theories inspired so called braneworld models, in which the observable universe is a 3-brane on which the standard-model fields are confined, while gravity enters the extra spatial dimensions (Arkani-Hamed et al., 1998). The braneworld models provide an elegant solution to the hierarchy problem of the electroweak and quantum gravity scales, as these scales could become to be of the same order (TeV) due to large scale extra dimensions (Arkani-Hamed et al., 1998). Future collider experiments can test the braneworld models quite well, including even the hypothetical mini black hole production (Dimopoulos and Landsberg, 2001). The braneworld models could be tested observationally since they predict relevant astrophysically important properties of black holes. Gravity can be localized near the brane even with a non-compact, infinite size extra dimension with the warped spacetime satisfying the 5D Einstein equations as shown by Randall and Sundrum (1999). The rotating brany black hole spacetimes are represented by the Kerr-Newman geometry (without an electromagnetic field). The standard studies of black hole and naked-singularity geodetical motion (Stuchlík, 1981; Stuchlík and Calvani, 1991; Stuchlík and Hledík, 2000) can thus be fully applied for brane-world black holes and naked singularities with positive tidal charge.

## 2 ORBITAL MOTION IN THE BRANEWORLD KERR SPACETIMES

Using standard Boyer–Lindquist coordinates  $(t, r, \theta, \varphi)$  and geometric units ( $c = G = 1$ ), we can write the line element of a rotating (Kerr) black hole or naked singularity on the 3D-brane in the form

$$ds^2 = - \left( 1 - \frac{2Mr - b}{\Sigma} \right) dt^2 - \frac{2a(2Mr - b)}{\Sigma} \sin^2\theta dt d\varphi + \frac{\Sigma}{\Delta} dr^2 + \Sigma d\theta^2 + \left( r^2 + a^2 + \frac{2Mr - b}{\Sigma} a^2 \sin^2\theta \right) \sin^2\theta d\varphi^2, \quad (1)$$

where

$$\Delta = r^2 - 2Mr + a^2 + b, \quad (2)$$

$$\Sigma = r^2 + a^2 \cos^2\theta, \quad (3)$$

$M$  and  $a = J/M$  are the mass parameter and the specific angular momentum of the background, and the braneworld parameter  $b$ , called the “tidal charge”, represents the imprint of non-local (tidal) gravitational effects of the bulk space (Aliev and Gümrükçüoğlu, 2005). The physical “ring” singularity of the braneworld rotating black holes (and naked singularities) is located at  $r = 0$  and  $\theta = \pi/2$ , as in the Kerr spacetimes.

The form of the metric (1) is the same as that of the standard Kerr–Newman solution of the 4D Einstein–Maxwell equations, with the tidal charge  $b$  being replaced by the squared electric charge  $Q^2$  (Misner et al., 1973). The following discussion can then be separated into these cases:

- a)  $b = 0$  in which we are dealing just with the standard Kerr metric.
- b)  $b > 0$  in which we are dealing with the standard Kerr–Newmann metric.
- c)  $b < 0$  where we are in the domain of new physics.

In the brany K-N spacetimes the geodetic motion is also relevant to charged test particles.

## 3 EFFECTIVE POTENTIAL AND RADIAL FUNCTION

The radial function  $R(r)$  of the geodesic motion is defined by:

$$R(r) \equiv -\text{sign}(m) + \frac{E^2 g_{\varphi\varphi} + 2ELg_{t\varphi} + L^2 g_{tt}}{g_{t\varphi}^2 - g_{tt}g_{\varphi\varphi}}, \quad (4)$$

and the effective potential of the brany Kerr spacetimes takes the form:

$$V_{\text{Eff}}(r, a, b, L) = \frac{-aL(b - 2r) \pm r\sqrt{\Delta}\sqrt{L^2 r^2 + r^4 + a^2(r^2 + 2r - b)}}{r^4 + a^2(r^2 + 2r - b)}, \quad (5)$$

where  $L$  is the specific angular momentum as measured by an observer at infinity,  $E$  is the specific energy and  $m$  is the mass of the test particle. Circular motion is discussed in Stuchlík and Kotrlóvá (2009).

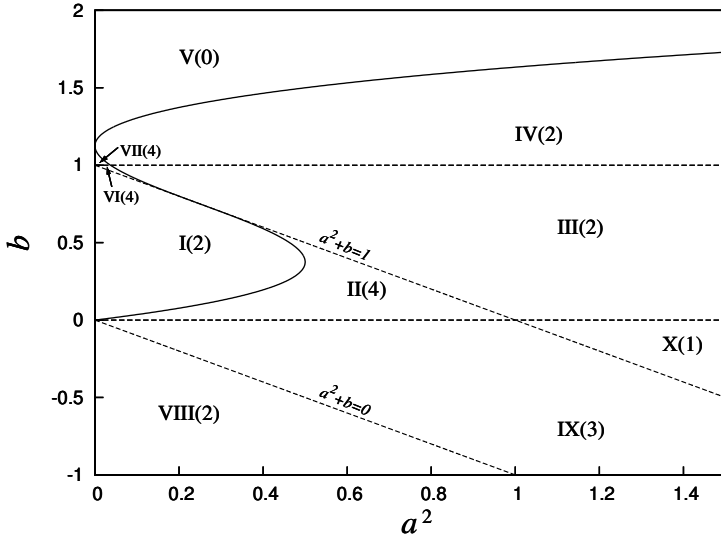


**Figure 1.** Brany Kerr black holes and naked singularities are divided into ten classes according to the properties of circular photon orbits. The corresponding regions of the  $b-a^2$  plane are denoted by I–X; the number in parentheses gives the number of circular photon orbits in the respective class. See also Stuchlík (1981); Balek et al. (1989).

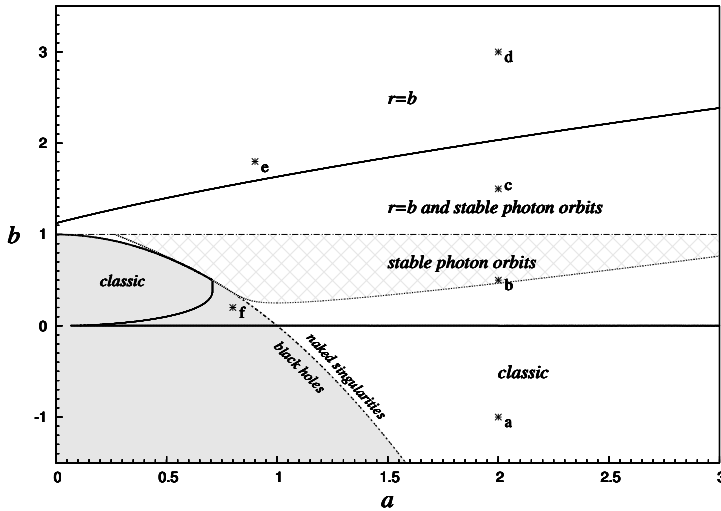


**Figure 2.** Classification of accretion disks with respect to parameters  $a$  and  $b$ . *Classic*: stands for those combinations of  $a$  and  $b$  where the ISCO coincides with the marginally stable orbit. *Stable photon orbit*: the ISCO for particles coincides with the stable circular photon orbit (the efficiency of accretion can then theoretically tend to infinity). *Stable photon orbit and  $r = b$* : the ISCO is located at  $r = b$  and the effective potential has a minimum for all positive values of  $L$  (this minimum is always higher than  $r = b$  and is unimportant for accretion processes). *Region  $r = b$* : the ISCO is located at  $r = b$ . The depicted star points correspond to chosen examples given in Fig. 3.

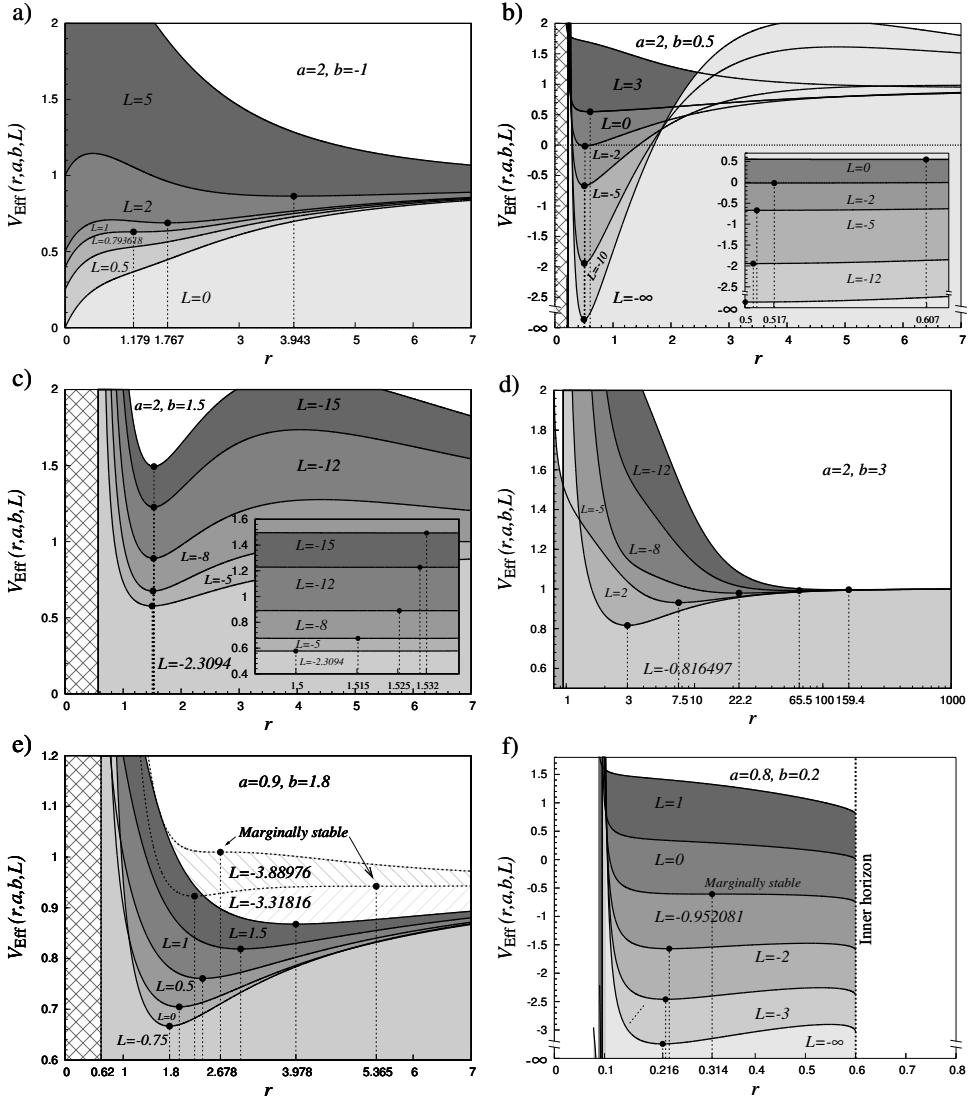


**Figure 3.** Examples of the effective potential from each region.

## 4 PHOTONS

In the case of photon orbits in the equatorial plane, the radial function  $R(r)$  is determined by Eq. (4) with  $m$  set to zero (Schee and Stuchlík, 2009a,b):

$$\frac{R(r)}{E^2} = \frac{[r^2 - a(\lambda - a)]^2 - \Delta(\lambda - a)^2}{r^2 \Delta}, \quad (6)$$

where the impact parameter is defined by  $\lambda = L/E$ .

The photon orbits depend only on the impact parameter  $\lambda$ . The character of the photon motion is given by the number of circular orbits. We can distinguish ten cases of the brany Kerr spacetimes (Fig. 1).

## 5 EFFECTIVENESS OF ACCRETION

We discuss here some properties of thin Keplerian accretion disks. We will focus on disks orbiting naked singularities. The circular orbits can exist from infinity down to the radius of the limiting circular photon orbit, determined by the condition

$$r^2 - 3r + 2b \pm 2a\sqrt{r-b} = 0. \quad (7)$$

At this point  $E$  goes to  $\pm\infty$  and  $L$  goes to  $\pm\infty$ , but the impact parameter  $\lambda = L/E$  remains finite.

The loci of the stable circular orbits are given by the condition

$$\frac{\partial^2 R}{\partial r^2} \leq 0, \quad (8)$$

where the case of equality corresponds to the  $r$  coordinates of the marginally stable circular orbits  $r_{\text{ms}}$ . This procedure of finding the marginally stable orbit as an inflexion point of the effective potential given by the condition (8), is what we will be calling a “standard treatment”. We obtain<sup>1</sup>

$$r(6r - r^2 - 9b + 3a^2) + 4b(b - a^2) \mp 8a(r - b)^{3/2} = 0. \quad (9)$$

This standard treatment works perfectly for the black holes, but as we shall demonstrate, does not work as well for counter-rotating disks around naked singularities.

The innermost stable circular orbit (ISCO) does not always correspond to the marginally stable orbit defined by Eq. (9).<sup>2</sup> This is demonstrated in Fig. (3, e) where we have depicted the effective potentials  $V_{\text{Eff}}(r, a, b, L)$ . We can clearly see that sometimes the marginally stable orbit defined by Eq. (9) is not the innermost stable circular orbit. The ISCOs are actually located at  $r = b$ . The reason for this is that there can be a stable circular orbit at  $r = b$ , but not at  $r < b$ . This makes it possible to have an ISCO which is not an inflexion point of the radial function (4), which is the reason why the “standard treatment” (8) has to be treated very carefully. Of course, for accretion processes, the marginally stable circular orbits, i.e. the stable orbits with lowest energy, are relevant as the orbiting matter loses energy (and angular momentum) during accretion.

In the Figure 2 we have shown the classification of parameter space spanned by spin  $a$  and tidal charge  $b$ . This parameter space is divided into several areas according to following physical properties:

- (1) existence of stable circular orbits in spacetime,

<sup>1</sup> Formally the same results, relevant for Kerr–Newman spacetime, can be found in Aliev and Galtsov (1981).

<sup>2</sup> In some of the naked-singularity spacetimes (Reisner–Nordström, Kehagias–Sfetsos), two marginally stable orbits (ISCO and OSCO) can appear, (Pugliese et al., 2013; Stuchlík et al., 2014; Stuchlík and Schee, 2014; Vieira et al., 2014). However, this is not the case for the Kerr spacetimes (Stuchlík, 1980). See also Favata (2011).

(2) existence of ISCO at  $r = b$  which is different than marginally stable orbit found by classic treatment,

(3) existence of ISCO which is identical with marginally stable orbit found by classic treatment.

Most interesting situation in Fig. 2 is lightly shaded area, where there are no present any ISCO's or marginally stable orbits. All orbits are stable up to a photon circular orbit, what is new phenomenon which can theoretically leads to unbound effectiveness of accretion.

## 6 CONCLUSIONS

We have shown an interesting new behaviour of the effective potential with regard to the stable circular photon orbits. These stable orbits can exist in the case of naked singularities in the Randall–Sundrum II brane-world scenario and in the case of classical Kerr–Newman naked singularities with quite a large amount of charge. This new phenomenon can be an interesting explanation for extremely high energy cosmic radiation.

## ACKNOWLEDGEMENTS

Presented work was supported by EU grant Synergy CZ.1.07./2.3.00/20.0071, the internal student grant SGS/23/2013 of the Silesian University and astrophysics supported by the Czech Science Foundation Grant No. 14-37086G and the Albert Einstein Centre for gravitation.

## REFERENCES

- Aliev, A. N. and Galtsov, D. V. (1981), Radiation from relativistic particles in nongeodesic motion in a strong gravitational field, *General Relativity and Gravitation*, **13**, pp. 899–912.
- Aliev, A. N. and Gümrükçüoğlu, A. E. (2005), Charged rotating black holes on a 3-brane, *Phys. Rev. D*, **71**(10), p. 104027, arXiv: hep-th/0502223.
- Arkani-Hamed, N., Dimopoulos, S. and Dvali, G. (1998), The hierarchy problem and new dimensions at a millimeter, *Physics Letters B*, **429**, pp. 263–272, arXiv: hep-ph/9803315.
- Balek, V., Bicak, J. and Stuchlík, Z. (1989), The motion of the charged particles in the field of rotating charged black holes and naked singularities. II - The motion in the equatorial plane, *Bulletin of the Astronomical Institutes of Czechoslovakia*, **40**, pp. 133–165.
- Dimopoulos, S. and Landsberg, G. (2001), Black Holes at the Large Hadron Collider, *Physical Review Letters*, **87**(16), 161602, arXiv: hep-ph/0106295.
- Favata, M. (2011), Conservative corrections to the innermost stable circular orbit (ISCO) of a Kerr black hole: A new gauge-invariant post-Newtonian ISCO condition, and the ISCO shift due to test-particle spin and the gravitational self-force, *Phys. Rev. D*, **83**, p. 024028, arXiv: 1010.2553.
- Hořava, P. and Witten, E. (1996), Eleven-dimensional supergravity on a manifold with boundary, *Nuclear Physics B*, **475**, pp. 94–114, arXiv: hep-th/9603142.
- Hořava, P. and Witten, E. (1996), Heterotic and Type I string dynamics from eleven dimensions, *Nuclear Physics B*, **460**, pp. 506–524, arXiv: hep-th/9510209.

- Misner, C. W., Thorne, K. S. and Wheeler, J. A. (1973), *Gravitation*, W. H. Freeman and Co, New York, San Francisco.
- Pugliese, D., Quevedo, H. and Ruffini, R. (2013), Equatorial circular orbits of neutral test particles in the Kerr-Newman spacetime, *Phys. Rev. D*, **88**(2), 024042, arXiv: 1303.6250.
- Randall, L. and Sundrum, R. (1999), An Alternative to Compactification, *Physical Review Letters*, **83**, pp. 4690–4693, arXiv: hep-th/9906064.
- Schee, J. and Stuchlík, Z. (2009a), Optical Phenomena in the Field of Braneworld Kerr Black Holes, *International Journal of Modern Physics D*, **18**, pp. 983–1024, arXiv: 0810.4445.
- Schee, J. and Stuchlík, Z. (2009b), Profiles of emission lines generated by rings orbiting braneworld Kerr black holes, *General Relativity and Gravitation*, **41**, pp. 1795–1818, arXiv: 0812.3017.
- Stuchlík, Z. (1980), Equatorial circular orbits and the motion of the shell of dust in the field of a rotating naked singularity, *Bulletin of the Astronomical Institutes of Czechoslovakia*, **31**, pp. 129–144.
- Stuchlík, Z. (1981), The radial motion of photons in Kerr metric, *Bulletin of the Astronomical Institutes of Czechoslovakia*, **32**, pp. 40–52.
- Stuchlík, Z. and Calvani, M. (1991), Null geodesics in black hole metrics with non-zero cosmological constant, *General Relativity and Gravitation*, **23**, pp. 507–519.
- Stuchlík, Z. and Hledík, S. (2000), Equatorial photon motion in the Kerr-Newman spacetimes with a non-zero cosmological constant, *Classical and Quantum Gravity*, **17**, pp. 4541–4576, arXiv: 0803.2539.
- Stuchlík, Z. and Kotrlová, A. (2009), Orbital resonances in discs around braneworld Kerr black holes, *General Relativity and Gravitation*, **41**, pp. 1305–1343, arXiv: 0812.5066.
- Stuchlík, Z. and Schee, J. (2014), Optical effects related to Keplerian discs orbiting Kehagias-Sfetsos naked singularities, *ArXiv e-prints*, arXiv: 1402.2891.
- Stuchlík, Z., Schee, J. and Abdujabbarov, A. (2014), Ultra-high-energy collisions of particles in the field of near-extreme Kehagias-Sfetsos naked singularities and their appearance to distant observers, *Phys. Rev. D*, **89**(10), 104048.
- Vieira, R. S. S., Schee, J., Kluźniak, W., Stuchlík, Z. and Abramowicz, M. (2014), Circular geodesics of naked singularities in the Kehagias-Sfetsos metric of Hořava's gravity, *Phys. Rev. D*, **90**(2), 024035, arXiv: 1311.5820.



# Rotational Evolution of the Magnetic White Dwarfs in Intermediate Polars

V. V. Breus,<sup>1,a</sup> I. L. Andronov,<sup>1,b</sup> P. Dubovský,<sup>2</sup> Yonggi Kim,<sup>3,4</sup>  
L. L. Chinarova,<sup>5</sup> Jiwon Park,<sup>3,4</sup> Joh-Na Yoon,<sup>3,4</sup> Yong-Hee Kim,<sup>4</sup>  
K. Petřík,<sup>6</sup> S. Zola,<sup>7,8</sup> S. V. Kolesnikov,<sup>5</sup> K. A. Antonyuk,<sup>9</sup>  
A. R. Baransky,<sup>10</sup> P. Beringer,<sup>11</sup> T. Hegedüs,<sup>11</sup>  
J. W. Robertson<sup>12</sup> and I. Kudzej<sup>2</sup>

<sup>1</sup> Department “High and Applied Mathematics”, Odessa National Maritime University, Odessa, Ukraine

<sup>2</sup> Vihorlat Astronomical Observatory, Humenne, Slovakia

<sup>3</sup> University Observatory, Chungbuk National University, Cheongju, Korea

<sup>4</sup> Department of Astronomy and Space Science, Chungbuk National University, Cheongju, Korea

<sup>5</sup> Astronomical Observatory, Odessa National University, Odessa, Ukraine

<sup>6</sup> Astronomical Observatory and Planetarium, Hlohovec, Slovakia

<sup>7</sup> Astronomical Observatory of the Jagiellonian university, Krakow, Poland

<sup>8</sup> Mt. Suhora Observatory, Pedagogical University, Krakow, Poland

<sup>9</sup> Crimean Astrophysical Observatory, Nauchny, Ukraine

<sup>10</sup> Astronomical Observatory of Taras Shevshenko National University, Kiev, Ukraine

<sup>11</sup> Baja Astronomical Observatory, Baja, Hungary

<sup>12</sup> Arkansas Tech University, Russellville, USA

<sup>a</sup> [vitaly.breus@gmail.com](mailto:vitaly.breus@gmail.com)

<sup>b</sup> [il-a@mail.ru](mailto:il-a@mail.ru)

## ABSTRACT

We provide the results of the long-term multicolour photometric monitoring of selected intermediate polars MU Cam, V405 Aur, FO Aqr, EX Hya, V1323 Her, V2306 Cyg, obtained at different observatories. We analysed variability of the spin period of the white dwarf using our observations and previously published spin maxima timings. We found that some of these stars show spin-up, some show spin-down, sometimes we see no spin period variability and sometimes we may see more complicated changes of the spin periods. For some binary systems we studied also orbital period variations.

**Keywords:** cataclysmic variables – close binaries – white dwarfs – period variability

## 1 INTRODUCTION

Intermediate polars, often called DQ Her star, are interacting binary systems with strong magnetic fields (Patterson, 1994; Warner, 1997; Hellier, 2001). Gravity of the white dwarf leads to the gravitational capture of the part of the substance of the secondary component

near the inner Lagrange points. Due to the Coriolis force, plasma flux deviates from the center line and forms an accretion disk around a white dwarf. A strong magnetic field destroys the inner part of the disk and leads to the formation of two accretion columns, which are one of the brightest sources of radiation in a wide spectral range from x-ray to infrared. The cyclotron radiation is characterized by the presence of polarization. The matter forms a shock wave heats up and settles on the surface of the white dwarf. Rare outbursts are possible (e.g. DO Dra (Andronov et al., 2008)). Intermediate polars were often classified as nova-like stars with relatively small changes in average per night light.

Usually intermediate polars show two kinds of optical variability which are caused by different physical processes. The orbital period is usually 3–7 hours. The spin variability is caused by the rotation of the white dwarf with one or two accretion columns with the period range from few to dozens of minutes. So, the light curve is a superposition of two different periodic variations and some aperiodic processes like flickering, outbursts, changes from high to low luminosity state etc. But, in case of V1323 Her we may see no orbital variability, suggesting a low orbit inclination (Andronov et al., 2011) and in case of V709 Cas we may see no spin variability because the object is faint, spin period is very short and time resolution is not sufficient (Hric et al., 2014).

Some of selected intermediate polars exhibit a statistically significant dependence of the color index on the spin phase, indicating a variable distribution of energy in the spectrum and necessity of multicolour observations rather than mono-filter or unfiltered ones. During our monitoring we obtained mainly time series with alternatively changing V and R color filters.

## 2 DATA PROCESSING

The CCD frames were processed using C-MuniPack software. In some cases (too few stars in the field, not enough to match frames automatically) we used the program Winfits written by V. P. Goranskij. The final time series were obtained using the program MCV (Andronov and Baklanov, 2004) taking into account multiple comparison stars (Kim et al., 2004), the same software was used for periodogram analysis. For our objects we analysed all available photometric data, including long CCD series published in AAVSO database.

To determine extrema timings we used trigonometric polynomial approximation. We choose 2-periodic variability model for smoothing

$$m(t) = m_0 - r_1 \cos(\omega_1(t - T_{01})) - r_2 \cos(\omega_2(t - T_{02})), \quad (1)$$

where  $m(t)$  – is the smoothed value of brightness at time  $t$ ,  $m_0$  – average brightness on theoretical curve (generally different from the sample mean (Andronov, 2003),  $\omega_j = 2\pi/P_j$ ,  $r_j$  – semi-amplitude,  $T_{0j}$  is the epoch for maxima of brightness of photometric wave with number  $j$  and period  $P_j$ . We calculated only one moment per set of observations (i.e. per night) because the accuracy estimate is much better then for individual extrema. This method is optimal for approximation of observations of intermediate polars and is often used in case of spin + orbital variability, e.g. EX Hya (Andronov and Breus, 2013), MU Cam (Kim et al., 2005). For objects that show variability with one period we used regular trigonometric polynomial approximation. This way we determined spin maxima and orbital minima timings.

To study period variations we used O-C analysis. Generally we calculated two O-C diagrams: for spin maxima and for orbital minima timings. Along with moments determined using our own data we used all published ones. Contrary to a classical representation of the “O-C diagram” as a dependence of the timings from an ephemeris, i.e.

$$O - C = T - (T_0 + P \cdot E) \quad (2)$$

on the cycle number  $E$ , we have used phases instead, i.e.  $\phi = (O - C)/P$ . For a correct ephemeris, the phases should be concentrated near the zero value. For some objects we detected cycle miscounts caused by gaps in regular observations and not enough-precisely determined values of the periods. After correction of it, we smoothed O-C diagram with a polynomial with statistically-optimal degree. Using coefficients of these polynomials after many years of monitoring, it is possible to determine the value of the period more precisely and (in some cases) detect second derivatives of the period, e.g. acceleration of the spin period of the white dwarf. Sometimes the period increase was turned to a period decrease (FO Aqr). These changes may be interpreted by a model of precession of a rapidly rotating white dwarf (Andronov 2005), which predicts chaotic variability of the spin period at time scales of decades.

### 3 MU CAMELOPARDALIS

The X-Ray source 1RXS J062518.2+733433 was classified as an Intermediate polar (Araujo-Betancor et al., 2003; Staude et al., 2003). Later, results of 7 nights of CCD-photometry obtained using 1.8m telescope in Korea were published (Kim et al., 2005): ephemeris of the orbital minima

$$\text{BJD} = 2453023.6159(42) + 0.1966431(33) \cdot (E - 1735) \quad (3)$$

and improved ephemeris for spin maxima

$$\text{BJD} = 2452893.78477(10) + 0.01374116815(17) \cdot (E - 15382) . \quad (4)$$

Hereafter in brackets we provide a statistical error estimate in units of a last digit.

After this publication, photometric monitoring of the system was continued in Korea (Chungbuk National University Observatory), Slovakia (Astronomical observatory and planetarium in Hlohovec and Vihorlat observatory in Kolonica, 2007–2014) and Poland (Jagiellonian university observatory, Krakow, 2013–2014). First we determined the value of orbital period of the system  $0^{\text{d}}.1968538 \pm 0.0000013$  and spin period  $0^{\text{d}}.01374$  which were close to published earlier values. By now we collected more then 300 spin maxima timings. We used two-periodic trigonometric polynomial fit. Dependence of phase on time is presented on the Fig. 1

As we see significant trends and phase shifts, we suggested period variability hypothesis. Taking into account results obtained for other intermediate polars, where phase variability was detected on the timescale of years or decades, this dependence should be smooth so we corrected cycle numbers for MU Cam and found parabolic dependence:

$$T(E) = 2454085.50721(14) + 0.0137409414(13) \cdot E - 1.520(13) \cdot 10^{-12} \cdot E^2 . \quad (5)$$

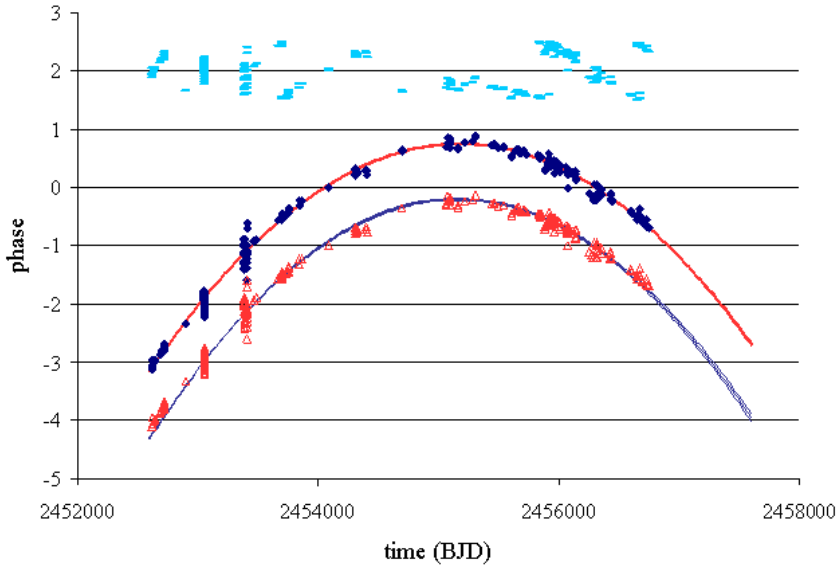


**Figure 1.** Dependence of phase of MU Cam spin maxima on time. Cycle count for constant period model (*top*) and variable period model (*middle and bottom*). Weighted (*red*) and non-weighted (*blue*) polynomial approximation are presented with corresponding error corridors.

The  $Q$  coefficient is 114 times higher of it's error estimate and is statistically significant. So we may see the decrease of the spin period of the white dwarf (the spin-up of the white dwarf). The characteristic time of the spin-up is  $\tau = 170 \pm 1.5$  thousand years. If we will take into account individual error estimates of maxima timings (i.e. weighted polynomial fit) we got slightly different parameters:

$$T(E) = 2454085.50766(25) + 0.0137409545(16) \cdot E - 1.635(23) \cdot 10^{-12} \cdot E^2. \quad (6)$$

Here the  $Q$  coefficient is only 70 times higher of it's error estimate but still is statistically significant. The characteristic time of the spin-up is  $\tau = 158.1 \pm 2.2$  thousand years. This value is 30 times smaller then 4.71 million years observed for the intermediate polar EX Hya (Andronov and Breus, 2013), but only 2 times smaller then 290 thousand years for BG CMi (Kim et al., 2004)

#### 4 V405 AURIGAE

The intermediate polar V405 Aur was discovered as an optical counterpart of the soft ROSAT source 1RXS J055800.7+535358 (Haberl et al., 1994). The soft X-Ray flux was changing with a period of 272.74 s, which was supposed to be a spin period of the white dwarf. The presence of optical pulsations at a period of  $272.785 \pm 0.003$  s was reported (Ashoka et al., 1995).

Later two independent announcements (Allan et al., 1995; Skillman, 1996) were made that the spin period of the white dwarf in V405 Aur is twice longer (545.45 s). It was justified by detection of circular polarization with a period of  $P = 0.006301 \pm 0.000055$  d ( $544.4 \pm 4.8$ ) s and semi-amplitude of  $1.80 \pm 0.16$  percent (Shakhovskoj and Kolesnikov, 1997).

The O-C analysis of the maxima timings obtained in 1994–2007 and second-order polynomial fit to the timings were published (Piirola et al., 2008):

$$T_{\max} = \text{HJD} \sim 2449681.46389(5) + 0.0063131474(4)E + 4(4) \cdot 10^{-16}E^2. \quad (7)$$

The quadratic term is formally positive (corresponding to a period increase) it is not statistically significant.

We analysed photometric CCD observations obtained using different telescopes in Slovakia (Kolonica and Hlohovec), Hungary (Baja), Ukraine (Crimea), USA (Arkansas Tech University Observatory) and got 93 spin maxima timings (Breus et al., 2013). The O-C diagram for historical timings (Piirola et al., 2008), maxima timings published later and our own ones was analysed. Contrary to a suggestion of Piirola et al., the points for the recent years show a distinct period decrease. We considered 4 models of period variations, the most probable were the 3-rd order weighted fit to the phases of maxima:

$$T_{\max} = \text{HJD} 2452867.07807(2) + 0.006313147760(131) \cdot (E - E_0) - 502(237) \times 10^{-18}(E - E_0)^2 - 239(80) \times 10^{-23}(E - E_0)^3. \quad (8)$$

It corresponds to all observations better than quadratic one and fits most recent observations showing a negative trend (see Fig. 2). Also we checked a hypothesis of periodic change of O-C. We calculated the periodogram using the approximation combining a 1-st order trigonometric and a 1-st order algebraic polynomials. The maximum peak at the periodogram corresponds to a period of  $2268^{\text{d}} = 6.2$  yr. The corresponding fit is

$$\phi = -0.00049(219) + 0.0000002(14) \times (T - 2452881) + 0.0315(32) \cos(2\pi \cdot (T - 2452389)/2268). \quad (9)$$

As these periodic variations are statistically significant (at a level of semi-amplitude of  $9.7\sigma$ ), we suggested a third body orbiting the inner binary system with a period of  $\approx 6.2$  yr, with a distance of the center of masses to the binary of  $(5.15 \pm 0.53) \times 10^9$  meters). The corresponding mass function is  $F(M) \approx 0.09 M_{\odot}$ , so a third body may be a low-mass red dwarf (Breus et al., 2013). But, the latest observations show us continuation of period decrease, thus we should confirm it by new observations and return to the 3-rd order polynomial fit.

## 5 FO AQUARI

The intermediate polar FO Aqr is known for many years. Observations were obtained in Slovakia (Vihorlat Astronomical Observatory) and Hungary (Baja Astronomical Observatory). Periodogram analysis revealed that the photometric period of the system is

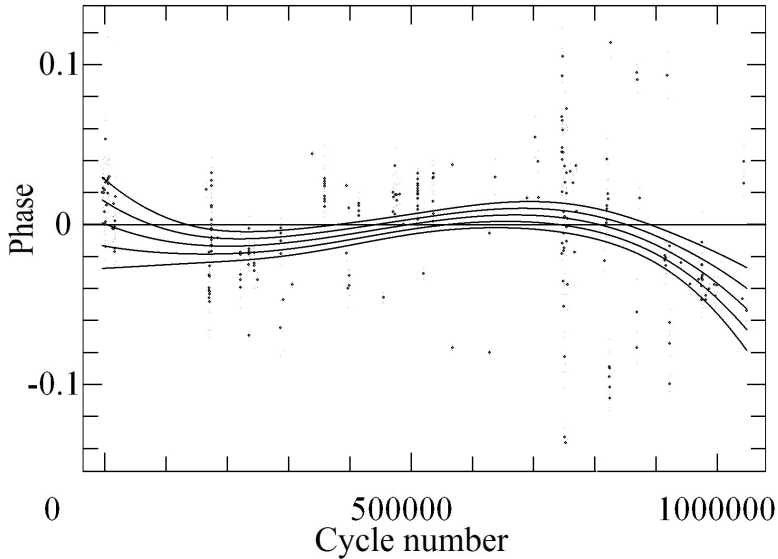


**Figure 2.** Dependence of phases of maxima timings of V405 Aur on cycle number of the spin period: *circles* – original observations, *line* – an approximation using 3-rd order polynomial fit with corresponding  $\pm 1\sigma$  and  $\pm 2\sigma$  error corridors.

$0^{\text{d}}.014312(5)$  that was a daily alias of the spin period of the white dwarf published before. So we concluded that the period during our observations was  $0^{\text{d}}.014521(3)$  with an initial epoch for the maximum brightness of 2455068.72430(36) (Breus et al., 2012). The previous published values of the spin period were  $0^{\text{d}}.01451905$  (Patterson et al., 1998) and  $0^{\text{d}}.01451718$  (Williams, 2003) so, the spin period is significantly shorter than earlier.

We collected spin maxima timings for more than 30 years and carried out the O-C analysis (see Fig. 3). At the beginning the observations were regular and no cycle miscount was done. Later on, there was a gap for almost 6 years after which we have started our own monitoring. So, we have 2 branches on the O-C diagram, which are separated with a gap and there is no published timings or time series which could help in filling this gap with points to restore the correct cycle numbering. This shows a very high importance of regular studies of such short period objects. Opposite to other objects, period variations of FO Aqr are complicated. From 1981 to 1987, the white dwarf showed a spin-down, then it changed to a spin-up.

## 6 EX HYDRAE

The intermediate polar EX Hya is another “old” variable star, according to the SAO/NASA Astrophysics Data System (ADS) the first publication on it was in 1957. We observed this object using remotely-controlled telescopes TOA150 (15cm) and BigMak (35cm) at the Tzec Maun observatories (<http://tzecmaun.org/>) in 2010–2011. For the O-C analysis we used as moments of maxima of our own and published patrol observations, as published moments. In total we used 452 moment of maxima, that cover 49 years.

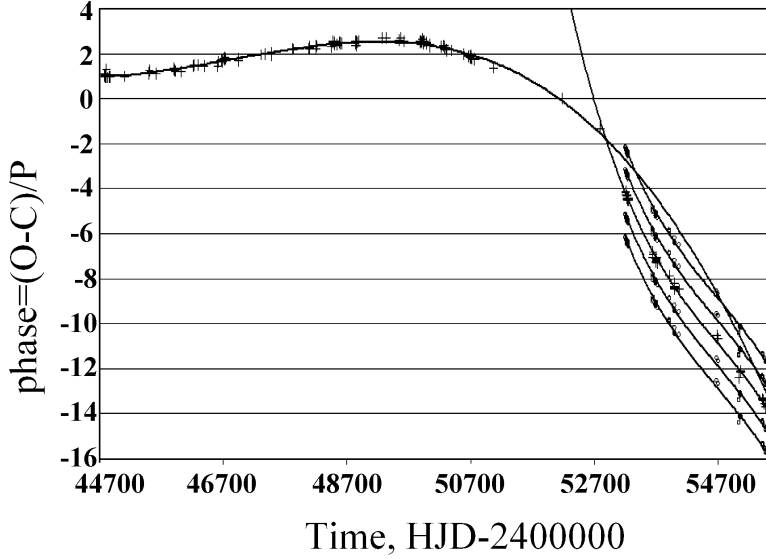


**Figure 3.** Dependence of phase of FO Aqr spin maxima on time with 2 branches – based on own and compiled observations. Best fit 3-rd order polynomials are shown for different cycle difference between the branches.

As a result of previous analysis (Mauche et al., 2009) the ephemeris was published:

$$T(E) = 2437699.8917(6) + 0.046546484(9) \cdot E - 7.3(4) \times 10^{-13} \cdot E^2 + 2.2(6) \times 10^{-19} \cdot E^3. \quad (10)$$

Authors suggested the presence of a statistically significant cubic coefficient  $Q_3$ . Using the program MCV we determined the statistically optimal degree of the polynomial for O-C approximation and it was equal to two. So, analysed timings do not confirm the assumption of the presence of a statistically significant cubic term in ephemeris by Mauche (Mauche et al., 2009). O-C diagram and it's  $\pm 1\sigma$  and  $\pm 2\sigma$  error corridors are shown on Fig. 4.

We obtained the ephemeris for spin maxima

$$T_{\max} = 2437699.89079(59) + 0.0465464808(69) \cdot E - 6.3(2) \times 10^{-13} \cdot E^2. \quad (11)$$

The  $Q$  coefficient corresponds to the characteristic time of the spin-up of  $\tau = 4.67(14) \times 10^6$  years.

## 7 V1323 HERCULIS

The intermediate polar V1323 Her (previously known as RXS J180340.0+401214) was regularly observed in Slovakia (Kolonica and Hlohovec) and Korea (Chungbuk National University Observatory). The light curve shows that the orbital variability is almost absent,

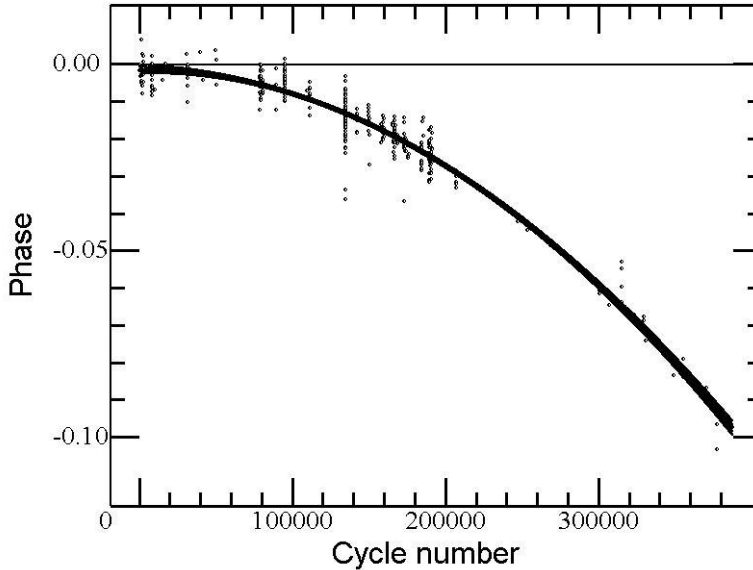


**Figure 4.** O-C diagram for spin maxima of the EX Hya, calculated for the values of the initial epoch  $T_0 = 2437699.8920$  (Vogt et al., 1980) and the period  $P_0 = 0^{\text{d}}.046546484$  (Mauche et al., 2009).

no eclipses were found, suggesting a low orbit inclination (less than 70 degrees). The photometric wave is originated due to a spin rotation of the white dwarf, during which the viewing conditions of the accretion columns are continuously changing. So the variability seems to be due to the geometric conditions (changing of the angle between stream and beam of view in the rotation), rather than for the physical ones (instability of the accretion column – that really is present, but not periodic). One hump shape at the phase light curve argues for a high inclination of the magnetic axis in this system, so we see mainly an upper accretion column.

From periodogram analysis of our first observations in 2007 we obtained the value of the spin period of  $1520.4509 \pm 0.0022$  seconds (25.34 minutes). It had 30 times better accuracy than published earlier value because of more time series obtained during longer time interval were used. Later on, the O-C analysis (see Fig. 5) showed the necessity of improvement of this value. However, due to a published epoch of minimum instead of maximum (Teichgraber et al., 2007), previous attempt to fit all timings (Andronov et al., 2011) were not successive. So, we determined a new linear ephemeris for the spin maxima:

$$T_{\text{max}} = 2454604.04449(14) + 0.017596986(3) \cdot E . \quad (12)$$

We checked quadratic polynomial approximation. The coefficient  $Q = (9 \pm 5) \times 10^{-14}$  formally corresponds to characteristic time scale of period variations of  $\tau = (4.6 \pm 2.5) \times 10^6$  years, but the parameter is equal to 1.9 of its error estimate and thus is not statistically significant (Andronov et al., 2012). So, we conclude that contrary to other intermediate polars, no spin period variations were detected in V1323 Her.

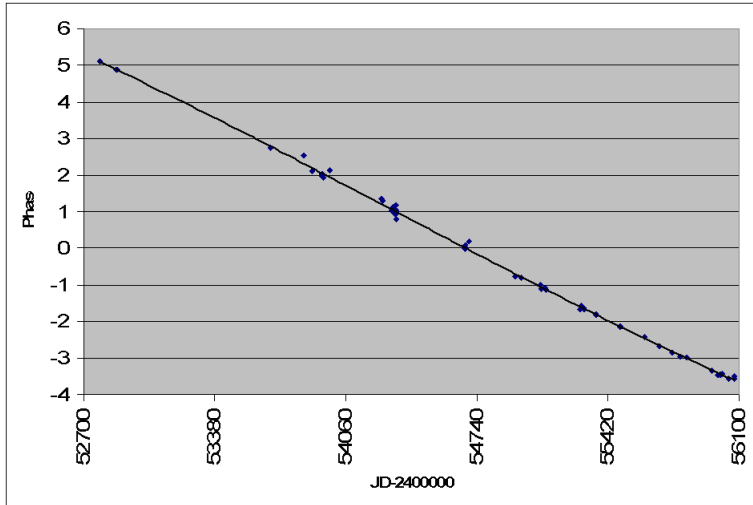


Figure 5. O-C diagram of the V1323 Her for the spin maxima timings.

## 8 V2306 CYG

The pulsating X-ray source 1WGAJ1958.2+3232 was discovered using ROSAT observations (Israel et al., 1998). From the spectroscopy and photometry an orbital period of 4 h 36 m and the pulsation period of 733 s were found (Zharikov et al., 2001). Later on, orbital period 5.387 h was reported (Norton et al., 2002), corresponding to the  $-1$  day alias of the previous value (Zharikov et al., 2001). Just after it, Zharikov et al. repeated the analysis using own photometric and spectroscopic data along with the data by A. Norton and confirmed their previously found orbital period of 4 h 35 m (Zharikov et al., 2002). The star was named as V2306 Cyg in 2003. For V2306 Cyg, we obtained large dataset with the timespan of 4 years mainly in Hlohovec and Krakow observatories, between 2010 and 2014. Additionally, we analysed all 14 CCD time series from the AAVSO data archive. Extrema timings were determined. Unfortunately, short timespan and high error estimates does not allow us to find spin period variations. We used linear fit to the O-C which shows that the spin period is  $0^{\text{d}}.008487557(9)$  instead of  $0^{\text{d}}.00848$ . At the same time, periodogram analysis shows different peaks, including the published values of the orbital period and its aliases, and many of these peaks are even higher. We built O-C diagram for the orbital minima timings (see Fig. 6) and found a few cycles per year miscount, which gave us the linear trend on the O-C. So, we can conclude that the correct orbital period may be  $0.2232685(24)$  days or  $0.181545(3)$  days, which are daily aliases of each other and are close to (Norton et al., 2002; Zharikov et al., 2002) respectively.

## 9 CONCLUSIONS

Period variations are frequently observed in intermediate polars and are typically detectable at a time scale of decades. Some objects do not show a statistically significant period change (e.g. V1323 Her (Andronov et al., 2012) and V2306 Cyg), some show a period

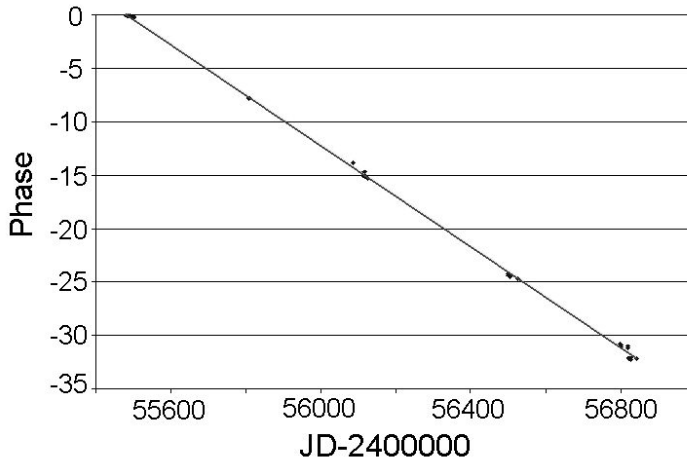


**Figure 6.** O-C diagram of the V2306 Cyg orbital minima timings.

decrease (e.g. MU Cam, EX Hya (Andronov and Breus, 2013), V405 Aur (Breus et al., 2013), BG CMi (Kim et al., 2004)), some show more complicated spin period variations (e.g. FO Aqr (Breus et al., 2012)). From theoretical expectations, the spin periods of the white dwarf should be equal to some equilibrium value, which is equal to period of “Kepler” rotation of the inner accretion disk at a distance of the magnetospheric radius (Warner, 1997; Hellier, 2001). Period variations may be caused by changes of the accretion rate due to modulation of the mass transfer caused by magnetic activity of the red secondary (Andronov and Shakun, 1990) fluctuations of the orbital separation (Andronov and Chinarova, 2002), or precession of the magnetic white dwarf (which will be present either with constant, or variable accretion rate), (Andronov, 2005). At time scales of decades, one may see only a part of the curve of cyclic variations. Thus apparently the “O-C” diagram may be not a “wave”, but a square (for smaller time intervals) or cubic parabola (for larger intervals).

## ACKNOWLEDGEMENTS

This work is part of the international project Inter-longitude astronomy and the national project The Ukrainian virtual Observatory.

## REFERENCES

- Allan, A., Horne, K. and Hilditch, R. W. (1995), RX J0558+53, *IAU Circ.*, **6154**, p. 2.
- Andronov, I. L. (2003), Multiperiodic versus noise variations: mathematical methods, in C. Sterken, editor, *Interplay of Periodic, Cyclic and Stochastic Variability in Selected Areas of the H-R Diagram*, volume 292 of *Astronomical Society of the Pacific Conference Series*, p. 391.
- Andronov, I. L. (2005), Spin-Up and Spin-Down of Magnetic White Dwarfs in Cataclysmic Variables: Theory vs Long-Term Monitoring, in D. Koester and S. Moehler, editors, *14th European Workshop on White Dwarfs*, volume 334 of *Astronomical Society of the Pacific Conference Series*, p. 447.
- Andronov, I. L. and Baklanov, A. v. (2004), *Astron. School Reports*, **5**, p. 264.

- Andronov, I. L. and Breus, V. V. (2013), Variability of the Rotation Period of the White Dwarf in the Magnetic Cataclysmic Binary System EX Hya, *Astrophysics*, **56**, pp. 518–530, arXiv: 1308.1805.
- Andronov, I. L., Breus, V. V. and Zola, S. (2012), Determination of Characteristics of Newly Discovered Eclipsing Binary 2MASS J18024395 +4003309 = Vsx J180243.9+400331, *Odessa Astronomical Publications*, **25**, p. 150, arXiv: 1212.6741.
- Andronov, I. L. and Chinarova, L. L. (2002), Third component in cataclysmic variables: Additional mechanism for accretion rate changes?, in B. T. Gänsicke, K. Beuermann and K. Reinsch, editors, *The Physics of Cataclysmic Variables and Related Objects*, volume 261 of *Astronomical Society of the Pacific Conference Series*, p. 47.
- Andronov, I. L., Chinarova, L. L., Han, W., Kim, Y. and Yoon, J.-N. (2008), Multiple timescales in cataclysmic binaries. The low-field magnetic dwarf nova DO Draconis, *Astronomy and Astrophysics*, **486**, pp. 855–865, arXiv: 0806.1995.
- Andronov, I. L., Kim, Y. K., Yoon, J.-N., Breus, V. V., Smecker-Hane, T. A., Chinarova, L. L. and Han, W. (2011), Two-Color CCD Photometry of the Intermediate Polar 1RXS J180340.0+401214, *Journal of Korean Astronomical Society*, **44**, pp. 89–96.
- Andronov, I. L. and Shakun, L. I. (1990), Alternating cycle durations in dwarf novae, *apss*, **169**, pp. 237–240.
- Araujo-Betancor, S., Gänsicke, B. T., Hagen, H.-J., Rodriguez-Gil, P. and Engels, D. (2003), 1RXS J062518.2+733433: A new intermediate polar, *Astronomy and Astrophysics*, **406**, pp. 213–219, arXiv: astro-ph/0305270.
- Ashoka, B. N., Marar, T. M. K., Seetha, S., Kasturirangan, K. and Bhattacharyya, J. C. (1995), Detection of optical pulsations from RX J0558.0+5353., *Astronomy and Astrophysics*, **297**, p. L83.
- Breus, V. V., Andronov, I. L., Dubovsky, P., Kolesnikov, S. V., Zhuzhulina, E. A., Hegedus, T., Beringer, P., Petrik, K., Robertson, J. W., Ryabov, A. V., Kudzej, I. and Shakhovskoy, N. M. (2013), Variability of the Spin Period of the White Dwarf in the Intermediate Polar V405 Aur: Low-Mass Third Body or Precession?, *Journal of Physical Studies*, **17**, iD: 3902.
- Breus, V. V., Andronov, I. L., Hegedus, T., Dubovsky, P. A. and Kudzej, I. (2012), Two-period variability of the intermediate polar FO Aqr, *Advances in Astronomy and Space Physics*, **2**, pp. 9–10.
- Haberl, F., Throstensen, J. R., Motch, C., Schwarzenberg-Czerny, A., Pakull, M., Sharnbrook, A. and Pietsch, W. (1994), Discovery of the new intermediate polar RX J0558.0+5353, *Astronomy and Astrophysics*, **291**, pp. 171–180.
- Hellier, C. (2001), *Cataclysmic Variable Stars*, Springer.
- Hric, L., Breus, V., Katysheva, N. A., Shugarov, S. Y. and Dubovský, P. (2014), The new period of the intermediate polar v709 cas, *Astronom. Nachr.*, **335**(4), pp. 362–366, ISSN 1521-3994, URL <http://dx.doi.org/10.1002/asna.201312044>.
- Israel, G. L., Angelini, L., Campana, S., Giommi, P., Stella, L. and White, N. E. (1998), The discovery of 12-min X-ray pulsations from 1WGA J1958.2+3232, *Monthly Notices Roy. Astronom. Soc.*, **298**, pp. 502–506, arXiv: astro-ph/9802119.
- Kim, Y., Andronov, I. L. and Jeon, Y.-B. (2004), CCD Photometry Using Multiple Comparison Stars, *Journal of Astronomy and Space Sciences*, **21**, pp. 191–200.
- Kim, Y.-G., Andronov, I. L., Park, S.-S., Chinarova, L. L., Baklanov, A. V. and Jeon, Y.-B. (2005), Two-Color VR CCD Photometry of the Intermediate Polar 1RXS J062518.2+733433, *Journal of Astronomy and Space Sciences*, **22**, pp. 197–210.
- Mauche, C. W., Brickhouse, N. S., Hoogerwerf, R., Luna, G. J. M., Mukai, K. and Sterken, C. (2009), Updated spin ephemeris for the cataclysmic variable EX Hydrae, *Information Bulletin on Variable Stars*, **5876**, p. 1, arXiv: 0902.1977.

- Norton, A. J., Quaintrell, H., Katajainen, S., Lehto, H. J., Mukai, K. and Negueruela, I. (2002), Pulsations and orbital modulation of the intermediate polar 1WGA J1958.2+3232, *Astronomy and Astrophysics*, **384**, pp. 195–205, arXiv: astro-ph/0201088.
- Patterson, J. (1994), The DQ Herculis stars, *Publications of the Astronomical Society of the Pacific*, **106**, pp. 209–238.
- Patterson, J., Kemp, J., Richman, H. R., Skillman, D. R., Vanmunster, T., Jensen, L., Buckley, D. A. H., O’Donoghue, D. and Kramer, R. (1998), Rapid Oscillations in Cataclysmic Variables. XIV. Orbital and Spin Ephemerides of FO Aquarii, *Publications of the Astronomical Society of the Pacific*, **110**, pp. 415–419.
- Pirola, V., Vornanen, T., Berdyugin, A. and Coyne, S. J., G. V. (2008), V405 Aurigae: A High Magnetic Field Intermediate Polar, *Astrophys. J.*, **684**, pp. 558–568, arXiv: 0805.4289.
- Shakhovskoj, N. M. and Kolesnikov, S. V. (1997), RX J0558.0+5353, *IAU Circ.*, **6760**, p. 2.
- Skillman, D. R. (1996), Photometry of the New DQ HER Star, RX J0558.0+5353, *Publications of the Astronomical Society of the Pacific*, **108**, p. 130.
- Staude, A., Schwöpe, A. D., Krumpe, M., Hambaryan, V. and Schwarz, R. (2003), 1RXS J062518.2+733433: A bright, soft intermediate polar, *Astronomy and Astrophysics*, **406**, pp. 253–257, arXiv: astro-ph/0304323.
- Teichgraber, C., Wood, M. A., Patterson, J., Monard, B., Rea, R. and Kemp, J. (2007), Updates on Two New Cataclysmic Variable Systems: 1RXS J173021.5-055933 and 1RXS J180340.0+401214, *Journal of the Southeastern Association for Research in Astronomy*, **1**, pp. 24–27.
- Vogt, N., Krzeminski, W. and Sterken, C. (1980), Periodic and secular variations in the lightcurve of dwarf nova EX Hydrae, *Astronomy and Astrophysics*, **85**, pp. 106–112.
- Warner, B. (1997), Book review: Cataclysmic variables stars, *Irish Astronomical Journal*, **24**, p. 85.
- Williams, G. (2003), CCD Photometry of the Intermediate Polars FO Aquarii and AO Piscium, *Publications of the Astronomical Society of the Pacific*, **115**, pp. 618–625.
- Zharikov, S. V., Tovmassian, G. H. and Echevarría, J. (2002), On the orbital period of the Intermediate Polar 1WGA J1958.2+3232, *Astronom. and Astrophys. Lett.*, **390**, pp. L23–L26, arXiv: astro-ph/0206303.
- Zharikov, S. V., Tovmassian, G. H., Echevarría, J. and Cárdenas, A. A. (2001), The orbital period of intermediate polar 1WGA J1958.2+3232, *Astronomy and Astrophysics*, **366**, pp. 834–839, arXiv: astro-ph/0009049.

# Compton scattering in strong gravity

Michal Bursa<sup>1,a</sup> and Karel Adámek<sup>2,b</sup>

<sup>1</sup>Astronomical Institute of the ASCR, Boční II 1401/1, 141 00 Praha 4, Czech Republic

<sup>2</sup>Institute of Physics, Faculty of Philosophy and Science, Silesian University in Opava,  
Bezručovo nám. 13, 746 01 Opava, Czech Republic

<sup>a</sup>bursa@astro.cas.cz

<sup>b</sup>karel.adamek@fpf.slu.cz

## ABSTRACT

We present a new numerical code for radiation transport in strong gravity regime that includes arbitrary emission and absorption mechanisms and also electron scattering. We give a brief description of the methods employed. A simple example of a possible use is presented that also illustrates the effect of light bending on the comptonized thermal spectra.

**Keywords:** Radiation transport – relativity – Compton scattering

## 1 INTRODUCTION

There has been a growing interest in radiation transport codes in astronomy since the pioneering paper of Shakura and Sunyaev (1973) and there already exists plentiful of such codes that treat the problem of high photon and electron energies with different level of accuracy. X-ray sources usually contain a compact object as their central engine and so not only special relativistic but also general relativistic effects have to be properly included in the accurate and physically realistic treatment of radiation transport. Such codes must necessarily employ the emitter-to-observer scheme, which is naturally more computationally expensive. This seem to be the main reason why such codes have been developed only quite recently. The most advanced codes have been presented by Dolence et al. (2009) and by Schnittman and Krolik (2013).

In this paper, we introduce our own code for general relativistic radiation transport that includes arbitrary emission and absorption mechanisms and also electron scattering while properly taking into account all GR effects. We demonstrate the capabilities of the code on a simplified model of an accretion disk and comptonizing corona. Such an example will help us to quantify the effect of gravitation light bending on resulting spectra of comptonized thermal radiation and so to stress and justify the importance of GR treatment.

## 2 PHOTON GEODESIC MOTION

Motion of photons in the Kerr spacetime can be solved for using several approaches. For instance, the geodesic equation can be numerically integrated to find a photon trajectory (e.g. Dovčiak et al., 2004), or one can proceed using Hamilton equations (e.g. Schnittman and Bertschinger, 2004) or one can write down the equation of motion and try to find a solution to it, which is possible in terms of elliptic integrals (e.g. Li et al., 2005).

Following Carter (1968), Bardeen et al. (1972) and Merloni et al. (1999), we can write down equations of motion for a photon in a separable form. In Boyer–Lindquist coordinates, where we employ a substitution of  $m = \cos \theta$ , they look like

$$\rho^2 \frac{dr}{d\lambda} = \pm \sqrt{R(r)}, \quad (1a)$$

$$\rho^2 \frac{d\theta}{d\lambda} = \pm \sqrt{M(m)}, \quad (1b)$$

$$\rho^2 \frac{d\varphi}{d\lambda} = -a + \frac{l}{1-m^2} + \frac{a}{\Delta}(r^2 + a^2 - al), \quad (1c)$$

$$\rho^2 \frac{dt}{d\lambda} = -a^2(1-m^2) + al + \frac{r^2 + a^2}{\Delta}(r^2 + a^2 - al), \quad (1d)$$

where

$$R = (r^2 + a^2 - al)^2 - \Delta((l-a)^2 + Q), \quad (2)$$

$$M = Q - \frac{l^2 m^2}{1-m^2} + a^2 m^2, \quad (3)$$

$$\Delta = r^2 - 2r + a^2, \quad (4)$$

$$\rho^2 = r^2 + a^2 m^2 \quad (5)$$

and  $q = Q/E_\infty^2$  is scaled Carter's constant,  $l = L_z/E_\infty$  is conserving angular momentum about the black hole  $z$ -axis.

With the help of above equation the photon trajectory can be directly calculated if we know the initial conditions, *i.e.* a point on the trajectory and the direction of the photon. As an example, we can think of a photon that has been emitted from the surface (photosphere) of an accretion disk. If photons are emitted isotropically, we can randomly choose the initial direction at a given place, calculate photon's 4-momentum and constants of motion and iterate numerically Eq. (1). We will describe the exact procedure in Section 5.

## 3 COMPTON SCATTERING

If photons have to propagate through a non-empty environment, they may encounter collisions with other particles. In astrophysics, the most relevant process of this type is a collision of a photon with a (quasi-)free particle, usually with an electron. Such a process is called Compton scattering after Arthur Holly Compton who observed it for the first time in 1923 while scattering X-ray photons on stationary electrons (Compton, 1923). This experiment played an important role in persuading physicists that light can behave as a stream of particle-like objects (quanta) whose energy is proportional to the frequency. Eventually, Compton earned Nobel Prize for his discovery five years later.

Often, the term Compton scattering is used to describe the original process in which an energetic electron scatters off an electron at rest. However, an opposite situation may happen as well: a lower energy photon is scattered to higher energy by a relativistic electron. This process is referred to as Inverse Compton scattering and it is of great importance in astrophysics. However, as basically both processes share the same mechanism, we are using the term Compton scattering for both throughout this paper.

The energy of the photon after the scattering event is different from its initial energy, because some of it is exchanged with the electron. The ratio of photon energy after and before the collision is

$$P(E_\gamma, \theta) = \frac{1}{1 + (E_\gamma/m_e c^2)(1 - \cos \theta)}, \quad (6)$$

where  $E_\gamma$  is the original photon energy before collision,  $m_e$  is mass of an electron and  $\cos \theta$  is the scattering angle, which itself is given by Klein–Nishina differential cross-section formula. For incident photon energies much lower than the electron rest energy,  $\epsilon \ll m_e c^2$ , the energy-dependent Klein–Nishina formula can be replaced by a simpler Thomson approximation

$$\frac{d\sigma}{d\Omega} = \frac{1}{2} r_0^2 (1 - \cos \theta), \quad (7)$$

which does not depend on the photon energy. We should keep in mind that the photon momentum must be Lorentz-transformed to the electron rest frame, so if we have a distribution of thermal electrons, there is a factor  $\gamma$  that modifies the photon's energy in the frame of the electron. Still, if we consider initial photons with energy  $\lesssim 1$  keV and  $\lesssim 10^8$  K electron temperature, Thomson approximation can be used safely.

#### 4 COMPGR

In this article, we are introducing a new code, COMPGR, that is capable of calculating effects of Compton scattering in the regime of strong gravity.

COMPGR combines two existing codes, a code for Compton scattering COSMOC (Adámek and Bursa, 2014) and a code for relativistic ray-tracing SIM5 (Bursa et al., 2004), in a readily usable package. COMPGR finds its use in situations where it is necessary to accurately compute comptonization effects on radiation in a close vicinity of a black hole, where strong gravitational light bending causes photons to follow curved geodesic trajectories.

The code generates photons according to the specified geometry and distribution and those are then propagated along geodesics based on their initial conditions. At each step of the trajectory, the total optical depth to scattering along the travelled path is increased by

$$d\tau = \kappa_{\text{es}} \rho dl \quad (8)$$

and the probability of scattering is evaluated as

$$P_{\text{SC}} = 1 - e^{-\tau}. \quad (9)$$

When the photon does scatter off an electron, we make a coordinate transformation from coordinate basis to fluid local rest frame (LRF). In LRF we determine the temperature of the fluid and corresponding electron energy distribution. This gives us particular electron velocity and direction and after transforming into the rest frame of the electron, we perform the scattering calculation. The electron velocity is taken from isotropic Maxwell–Jüttner distribution (Jüttner, 1911)

$$f_{\text{MJ}}(\gamma) = \frac{\gamma^2 \beta}{\theta_T K_2(1/\theta_T)} \exp(-\gamma/\theta_T), \quad (10)$$

where  $\gamma = (1 - v^2/c^2)^{-1/2}$ ,  $\theta_T = kT/m_e c^2$ , and  $K_2$  is modified Bessel function. After we determine new photon energy and direction, we make a back-transformation from electron rest frame to LRF and from LRF to the coordinate frame, we update photon momentum and constants of motion and the photon is followed along the new trajectory until it scatters again or until it either escapes sufficiently far or hits the black hole or is destroyed by some other means depending on the physical setup.

The code can also handle optically thin emission and absorption, such as bremsstrahlung or synchrotron. In the fluid rest frame, the radiation transport equation is

$$\frac{dI_\nu}{dl} = j_\nu - \alpha_\nu I_\nu, \quad (11)$$

where  $dl$  is the path element and  $I_\nu$ ,  $j_\nu$  and  $\alpha_\nu$  are respectively the specific intensity, emissivity and absorption of the fluid that are given by the specific radiation process. The emission and absorption processes are integrated along the photon path so that the intensity of a particular photon bundle is updated at each step.

## 5 EXAMPLE

We demonstrate the code on a simple example of a thin Shakura–Sunyaev-type accretion disk that is surrounded by a optically thin hot corona. We employ a very simple physical setup that shall demonstrate the effect of light bending on the scattered spectra.

In the case of an accretion disk surrounding a black hole the disk produces a thermal spectrum with typical energy of few kiloelectronvolts or less (depending on the mass of the black hole). The lower energy photons emitted from the disk surface are scattered to higher energies by relativistic electrons in the surrounding corona. This effect is believed to cause the power law component observed in X-ray spectra of accreting black holes.

In this numerical experiment, we use a non-rotating Schwarzschild black hole with an accretion disk around it. The disk has a standard inner edge at  $6M$  and we will use a power-law temperature profile  $T = T_0 r^{-3/4}$  for it (flux  $F(r) \sim r^{-3}$ ), where  $T_0$  is fixed at 3 keV.

In addition, there is a radial and spherically symmetric wind with constant temperature  $T_e = 10^8$  K, constant  $\dot{M}$  and constant radial velocity  $v_e = 0.1c$ . In our simplified setup, the wind originates from the black hole, but more realistically we can imagine a wind that is fed by the material from the disk. Density of the wind decreases with radius as

$$\rho = \frac{\dot{M}}{4\pi r^2 v_e}. \quad (12)$$

The total optical depth of the wind along the line of sight is

$$\tau = \int_{r_0}^{\infty} \rho \sigma_T dr, \quad (13)$$

which combined with the previous expression gives the density

$$\rho = \frac{r_0}{r^2} \frac{\tau}{\sigma_T} \quad (14)$$

simply as a function of radius and total optical depth.  $r_0$  is the radius of the wind base, that is of the black hole horizon in our case,  $r_0 = 2M$ . Photons are scattered in the wind, but we assume that after 10 such events the photon is lost (it is likely to be absorbed by an ion).

To illustrate the effect of light bending, we perform two simulations for each setup: one uses full GR with geodesic photon trajectories, in the second one we follow the photon path along straight lines in the original direction of emission while preserving other GR effects. True photon geodesic motion has been described in Section 2. In the simulation, where we assume straight photon paths, we replace Eq. (1) by its limit version for  $M = a = 0$  and we solve it. That way, we can follow the marked direction of emitted photon as it would go through a flat spherically symmetric space until the trajectory escapes far enough from the black hole, ends up in the black hole, ends up in the disk, or we encounter a scattering event in corona. No other changes are made and the scattering,  $g$ -factor evaluation, etc., still use standard Kerr metric and GR formalism, so we can say that the the eventual difference in results is solely due to photons taking bended or straight paths.

What can we expect? When the corona is not considered and photons travel from the disk to the observer freely without any scatterings, we expect the ‘flat’ spectrum to be identical to ‘GR’ spectrum at lower energies that are contributed by photons coming from cooler outer parts of the disk, where relativistic effects do not play much role. At higher energies, on the other hand, we expect the ‘flat’ spectrum to be slightly harder than the ‘GR’ spectrum simply because the photons come from the disk to the observer, who has a fixed inclination of  $60^\circ$ , on average at slightly more grazing angles than it is the case in GR, where light bending effect allows for escaping angles nearly parallel to the disk normal from parts of the disk. Larger emission angles mean larger Doppler boost and thus the spectrum should harden. The corresponding two spectra (‘GR’ and ‘flat’) are compared in Fig. 1, where the difference due to light bending can clearly be seen.

With corona present, we eventually expect the difference to go in the opposite direction – the ‘flat’ spectra should be softer as the corona becomes optically thicker. The density of the corona decreases with square of the distance from the black hole, so the largest scattering probability is very close to the black hole. If photons follow true GR geodesics they feel the ‘attractive force’ of the black hole’s gravity and the strongly bended trajectories cause photons to stay around the black hole longer then it is the case for ‘flat’ photons that do not feel such effect. Again, that acts mostly on the most on energetic photons coming from inner parts of the disk that have more chances to upscatter and harden the ‘GR’ spectra. Figure 2 shows how the spectrum evolves with increasing optical depth  $\tau = 1$ ,  $\tau = 5$  and  $\tau = 10$ . When the optical depth is too high and the corona is largely optically thick, the difference in the two spectra should diminish.

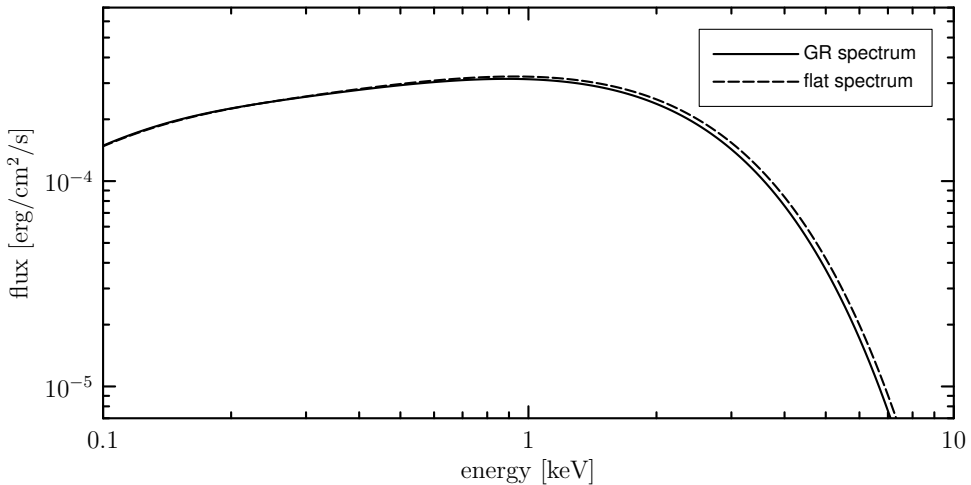


**Figure 1.** Observed spectra when no corona is assumed. Photons travel from the disk to the observer freely without any scatterings. Solid line represents the *true* spectrum with all GR effects taken account properly. Dashed line shows how would the spectrum look like if there was no relativistic light bending and photons were following straight lines as in a flat space (all other GR effects are preserved).

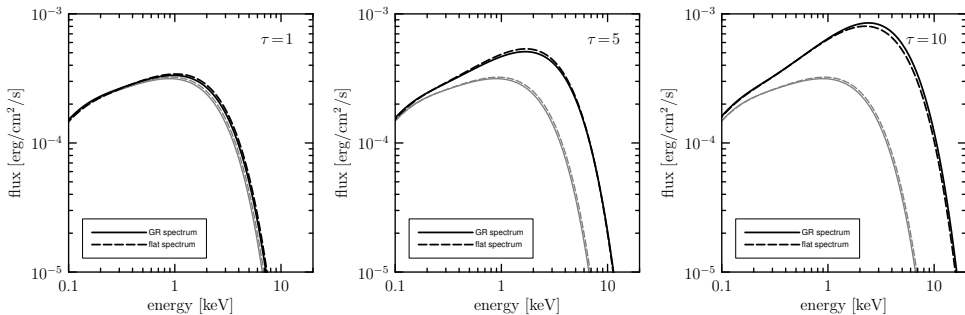


**Figure 2.** Observed spectra (*lines in bold black*) for total optical depths  $\tau = 1$  (*left*),  $\tau = 5$  (*middle*) and  $\tau = 10$  (*right*). Gray lines show the spectra from Fig. 1 without corona for reference. Corona temperature is  $10^8$  K and its density decreases with square of radius.

## 6 SUMMARY

We have presented a new numerical code, COMPGR along with some technical details behind its treatment of general relativistic radiation transport. Its capabilities include namely Compton scattering with proper treatment of geodesic photon propagation between collision events and as such it finds its use in setups involving scattering regions close to a black hole, where gravitational effects on light propagation play a strong role.

We have demonstrated the importance of GR effect on the simple example of scattering soft thermal photons in the radial wind of hot electrons. The results clearly justify the need for a proper GR treatment of radiation transport.

## ACKNOWLEDGEMENTS

This work has been supported by OPVK project CZ.1.07/2.2.00/28.0271 (MB, KA) and MŠMT project LH 14049 (MB).

## REFERENCES

- Adámek, K. and Bursa, M. (2014), Simulating Compton Scattering using Monte Carlo method: COSMOC library, in Z. Stuchlík, G. Török and T. Pecháček, editors, *Proceedings of RAGtime 14–16: Workshops on black holes and neutron stars, Opava, Prague, 18–22 September/15–18 July/11–19 October '12/'13/'14*, pp. 1–10, Silesian University in Opava, Opava, ISBN 978-80-7510-126-6, in this proceedings.
- Bardeen, J. M., Press, W. H. and Teukolsky, S. A. (1972), Rotating Black Holes: Locally Nonrotating Frames, Energy Extraction, and Scalar Synchrotron Radiation, *Astrophys. J.*, **178**, pp. 347–370.
- Bursa, M., Abramowicz, M. A., Karas, V. and Kluźniak, W. (2004), The Upper Kilohertz Quasi-periodic Oscillation: A Gravitationally Lensed Vertical Oscillation, *Astrophys. J. Lett.*, **617**, pp. L45–L48, arXiv: astro-ph/0406586.
- Carter, B. (1968), Global Structure of the Kerr Family of Gravitational Fields, *Physical Review*, **174**, pp. 1559–1571.
- Compton, A. H. (1923), A Quantum Theory of the Scattering of X-rays by Light Elements, *Physical Review*, **21**, pp. 483–502.
- Dolence, J. C., Gammie, C. F., Mościbrodzka, M. and Leung, P. K. (2009), grmonty: A Monte Carlo Code for Relativistic Radiative Transport, *Astrophys. J. Suppl.*, **184**, pp. 387–397, arXiv: 0909.0708.
- Dovčiak, M., Karas, V. and Yaqoob, T. (2004), An Extended Scheme for Fitting X-Ray Data with Accretion Disk Spectra in the Strong Gravity Regime, *Astrophys. J. Suppl.*, **153**, pp. 205–221, arXiv: astro-ph/0403541.
- Jüttner, F. (1911), Das Maxwellsche Gesetz der Geschwindigkeitsverteilung in der Relativtheorie, *Annalen der Physik*, **339**, pp. 856–882.
- Li, L.-X., Zimmerman, E. R., Narayan, R. and McClintock, J. E. (2005), Multitemperature Blackbody Spectrum of a Thin Accretion Disk around a Kerr Black Hole: Model Computations and Comparison with Observations, *Astrophys. J. Suppl.*, **157**, pp. 335–370, arXiv: astro-ph/0411583.
- Merloni, A., Vietri, M., Stella, L. and Bini, D. (1999), On gravitomagnetic precession around black holes, *Monthly Notices Roy. Astronom. Soc.*, **304**, pp. 155–159, arXiv: astro-ph/9811198.
- Schnittman, J. D. and Bertschinger, E. (2004), The Harmonic Structure of High-Frequency Quasi-periodic Oscillations in Accreting Black Holes, *Astrophys. J.*, **606**, pp. 1098–1111, arXiv: astro-ph/0309458.
- Schnittman, J. D. and Krolik, J. H. (2013), A Monte Carlo Code for Relativistic Radiation Transport around Kerr Black Holes, *Astrophys. J.*, **777**, 11, arXiv: 1302.3214.
- Shakura, N. I. and Sunyaev, R. A. (1973), Black holes in binary systems. Observational appearance., *Astronomy and Astrophysics*, **24**, pp. 337–355.



# Polarization vector transport in Kerr geometry

Michal Bursa,<sup>1,a</sup> Jiří Horák<sup>1</sup> and Grischa D. Karssen<sup>2</sup>

<sup>1</sup>Astronomical Institute of the ASCR, Boční II 1401/1, 141 00 Praha 4, Czech Republic

<sup>2</sup>I. Physikalisches Institut, Universität zu Köln, Zülpicher Str. 77, 50937 Köln, Germany

<sup>a</sup>bursa@astro.cas.cz

## ABSTRACT

In this paper we provide a set of practical formulae that are helpful in calculating the orientation of polarization vectors that are parallel transported from a region of strong gravitational field of a Kerr black hole to a distant observer.

**Keywords:** Polarization – black hole – electromagnetic radiation – synchrotron radiation

## 1 INTRODUCTION

Polarization of light is an important phenomenon in physics and astronomy makes no exception. When technology allowed astronomers to extend their view of the universe from optical to other spectral bands of electromagnetic spectrum, they also realized that electromagnetic waves carry some more information than just intensity and wavelength. It is the information about polarization of the waves. But it took time until detectors were build able to detect polarization properties of electromagnetic waves.

Polarization of solar radio emission was discovered already in 1939, but was published only in 1946 (Hey, 1946; Reber, 1946). It was followed by discovery of polarization of starlight by Hall (1949) and Hiltner (1949). Radio polarization of Crab nebula was detected in 1954 (Dombrowskii, 1954) and shortly after that Jupiter radiation belt polarization was reported in 1956 (Franklin and Burke, 1956). On the largest scale, polarization of radio galaxies and of the Milky Way was reported in 1962 (Wielebinski et al., 1962; Westerhout et al., 1962).

Highly polarized radiation of synchrotron origin is often observed from active galactic nuclei, where it originates from ejections of jets by super-massive black holes. A super-massive black hole, Sgr A\*, rests also in the center of our Galaxy and it is a source of compact non-thermal radio emission (Rogers et al., 1994), which is believed to originate from a synchrotron emitting region closely surrounding the black hole (Beckert and Duschl, 1997; Aitken et al., 2000). Near-infrared observations of Sgr A\* from past years revealed repeating simultaneous NIR and X-ray flares of partially polarized (in NIR) emission (e.g. Eckart et al. 2004) that may be produced by synchrotron self-Compton mechanism (Eckart et al., 2008).

Models that deal with an emission region that is closer than some  $\sim 30 r_g$  from the central black hole must take into account relativistic effects such as gravitational red-shift and lensing, beaming and light bending, and also the change of polarization angle. For the change of polarization angle, authors usually use the method described by Connors and Stark (1977) and Connors et al. (1980). In this paper, we present a derivation of a simple formula for the change of polarization angle of a linearly polarized synchrotron radiation during parallel transport along the photon path from the point of emission to infinity. The formula is still based on the approach of Connors, Stark and Piran, but hides the details of the parallel transport.

Throughout this paper we use geometrical units with  $G = c = M = 1$ . According to Misner et al. (1973), we denote 4-vectors either as  $X^\mu$  or with bold face as  $\mathbf{X}$  depending on whether we mean their components in a specific basis or we mean an invariant geometrical object independent of coordinate system, respectively. For scalar products of two 4-vectors  $\mathbf{A}$  and  $\mathbf{B}$  we use a simplified notation  $A^\mu B_\mu = A^\mu B^\nu g_{\mu\nu} = \mathbf{A} \cdot \mathbf{B} = (\mathbf{A} \mathbf{B})$ .

## 2 DESCRIPTION OF POLARIZED LIGHT

In the geometrical optics approximation, which is appropriate whenever the wavelength of an electromagnetic wave is much lower than both the typical radius of curvature of the spacetime and the typical length over which wave characteristics like amplitude or wavelength vary, three fundamental assumptions are made: (a) light rays are null geodesics, (b) the number of photons is conserved, and (c) the polarization vector is perpendicular to the rays and is parallel transported along the rays (Misner et al., 1973).

In Maxwell's theory, a monochromatic wave is described by the vector potential

$$\mathbf{A} = \Re \left\{ \mathbf{a} e^{i\theta} \right\}, \quad (1)$$

which satisfies the source-free wave equation  $\Delta \mathbf{A} = 0$  and the Lorentz gauge condition  $\nabla \cdot \mathbf{A} = 0$ . Here,  $\mathbf{a}$  is a slowly varying complex amplitude of the wave and  $\theta$  is a rapidly varying real phase that is proportional to the distance the wave has travelled and inversely proportional to its wavelength. In general, the amplitude vector  $\mathbf{a}$  consists of a main part, which is independent of the wavelength  $\lambda$ , plus eventually small corrections that depend on  $\lambda$  and that represent any deviations from pure geometrical optics due to finite wavelength (we will ignore those here).

When seeking for a solution of the wave equation with gauge condition, it is useful to introduce three quantities that describe the electromagnetic wave: wave vector  $\mathbf{k} = \nabla \theta$ , scalar amplitude of the wave  $a = (\mathbf{a} \cdot \bar{\mathbf{a}})^{1/2}$ , and polarization vector  $\mathbf{f} = \mathbf{a}/a$ . If we then insert the vector potential (1) into the Lorentz gauge condition, we get

$$0 = A_{;\mu}^\mu = \Re \left\{ \left[ i k_\mu a^\mu + a_{;\mu}^\mu \right] e^{i\theta} \right\} \quad (2)$$

from which we see that  $k_\mu a^\mu = 0$  or equivalently that

$$\mathbf{k} \cdot \mathbf{f} = 0, \quad (3)$$

meaning that the polarization vector is perpendicular to the wave vector. From the definition of  $\mathbf{f}$  we see that it also satisfies

$$\mathbf{f} \cdot \mathbf{f} = 1. \quad (4)$$

The polarization state of electromagnetic radiation can be described by a set of Stokes parameters  $[I, Q, U, V]$  proposed by Stokes (1852) or alternatively in terms of its total intensity  $I$ , (fractional) degree of polarization  $\delta$ , and the shape parameters of the polarization ellipse  $\psi$  and  $\chi$ .

Both descriptions use total intensity of radiation  $I$  as one parameter and the relation between the remaining three Stokes parameters and polarization ellipse parameters is

$$Q/I = \delta \cos 2\psi \cos 2\chi, \quad (5)$$

$$U/I = \delta \sin 2\psi \cos 2\chi, \quad (6)$$

$$V/I = \delta \sin 2\chi, \quad (7)$$

or inversely

$$\delta = \frac{(Q^2 + U^2 + V^2)^{1/2}}{I}, \quad (8)$$

$$\tan 2\psi = \frac{Q}{U}, \quad (9)$$

$$\sin 2\chi = \frac{V}{(Q^2 + U^2 + V^2)^{1/2}}, \quad (10)$$

where the factor of two before  $\psi$  reflects the rotational symmetry of the ellipse (rotation by  $180^\circ$ ) and the same factor before  $\chi$  reflects another symmetry of  $90^\circ$  rotation and swapping axes.

Stokes' description has the advantage over other ways that Stokes parameters can be expressed in units of spectral density  $I(\nu)$ , which is what is measured at the end, and that they can be added, which is useful when summing up contributions from many elements of the solid angle.

Most processes in astrophysics produce linearly or highly linearly polarized light. If we only focus on a case of linearly polarized wave ( $\chi = 0$ ), then the polarization ellipse degenerates into a line and instead of two parameters for its description we only need one, which is the polarization angle  $\psi$ . The relation between Stokes parameter and polarization ellipse parameters then simplifies into

$$Q/I = \delta \cos 2\psi, \quad (11)$$

$$U/I = \delta \sin 2\psi, \quad (12)$$

$$V/I = 0 \quad (13)$$

and

$$\delta = (Q^2 + U^2)^{1/2}/I, \quad (14)$$

$$\psi = \frac{1}{2} \tan^{-1} Q/U. \quad (15)$$

When we denote

$$f_X = Q/I, \quad f_Y = U/I, \quad (16)$$

then both  $f_X$  and  $f_Y$  range from  $-1$  to  $+1$  and can be viewed as components of a polarization vector  $\mathbf{f}$  relative to a chosen basis  $(\mathbf{X}, \mathbf{Y})$ , where  $\mathbf{X}$  and  $\mathbf{Y}$  are unit space-like vectors orthogonal to wave-vector  $\mathbf{k}$ . The choice of the polarization plane basis can be arbitrary.

The angle between one of the polarization basis vectors and the polarization vector then defines the polarization angle. While polarization degree is a Lorentz invariant, polarization angle is somewhat loosely defined as it depends on the orientation of an at-will chosen basis.

When a different basis  $(\mathbf{X}', \mathbf{Y}')$  is chosen, which is rotated against the original basis  $(\mathbf{X}, \mathbf{Y})$  by an angle  $\beta$ , the polarization vector  $(f_X, f_Y)$  changes to

$$\begin{pmatrix} f'_X \\ f'_Y \end{pmatrix} = \begin{pmatrix} \cos 2\beta & \sin 2\beta \\ -\sin 2\beta & \cos 2\beta \end{pmatrix} \begin{pmatrix} f_X \\ f_Y \end{pmatrix} = \begin{pmatrix} f_X \cos 2\beta + f_Y \sin 2\beta \\ -f_X \sin 2\beta + f_Y \cos 2\beta \end{pmatrix} \quad (17)$$

Assume that the original basis is conveniently chosen in such a way that one of its base vectors coincides with the polarization vector ( $\mathbf{X} = \mathbf{f}$ ,  $\mathbf{Y} \perp \mathbf{X}$ ). Then  $f_Y = 0$  and the above expression simplifies to

$$\mathbf{f}' = (f_X \cos 2\beta, -f_X \sin 2\beta), \quad (18)$$

which after applying some goniometric relations becomes

$$\begin{pmatrix} f'_X \\ f'_Y \end{pmatrix} = \begin{pmatrix} (\mathbf{f} \cdot \mathbf{X})^2 - (\mathbf{f} \cdot \mathbf{Y})^2 \\ 2(\mathbf{f} \cdot \mathbf{X})(\mathbf{f} \cdot \mathbf{Y}) \end{pmatrix} = \begin{pmatrix} f_X^2 - f_Y^2 \\ 2f_X f_Y \end{pmatrix}, \quad (19)$$

where  $f_X = \mathbf{f} \cdot \mathbf{X} = \cos \beta$  and  $f_Y = \mathbf{f} \cdot \mathbf{Y} = \cos(90^\circ - \beta) = \sin \beta$ .

Although we started from a special case of conveniently oriented polarization basis, due to its invariant form, the final expression (19) is valid generally.

### 3 PARALLEL TRANSPORT OF POLARIZATION VECTOR

Kerr spacetime has two obvious symmetries that arise from the fact that it does not depend on time and azimuthal coordinate. This enables one to find two corresponding Killing vectors associated with those differentiable symmetries that satisfy Killing equation  $\nabla_\mu K_\nu + \nabla_\nu K_\mu = 0$ . The Kerr solution also admits a hidden symmetry represented mathematically by the existence of a Killing tensor field  $K'_{\mu\nu}$  – a symmetric tensor field satisfying condition  $\nabla_{(\alpha} K'_{\mu\nu)} = 0$  (that the trace-free part of the symmetrization of  $\nabla K$  vanishes).

According to Noether's theorem (Noether, 1918), all spacetime symmetries are related to conserved quantities. Each Killing vector corresponds to a quantity that is conserved along geodesics, meaning that the product of the Killing vector and the geodesic tangent vector is

conserved along the geodesic so that  $d(K_\mu dx^\mu/d\lambda)/d\lambda = 0$ , where  $\lambda$  is an affine parameter of the geodesic. However, these two constants of motion would not be enough to solve non-equatorial geodesic motion. There exists a third constant of motion, Carter's constant  $Q$  (Carter, 1968), which is associated with Killing tensor ( $Q = K'_{\mu\nu} u^\mu u^\nu$ ). Physically, the three constants correspond to the conserved energy, the angular momentum with respect to the symmetric axis of the black hole, and the square of the total angular momentum along the geodesic (Bardeen et al., 1972; Wald, 1984) and enable to solve general geodesic motion in Kerr spacetime (Misner et al., 1973; Chandrasekhar, 1983) analytically.

In addition, Kerr spacetime, as well as other  $\{2, 2\}$  vacuum spacetimes, possess a conformal Killing spinor, which helps to determine parallel propagation of vectors that are perpendicular to geodesics, e.g. 'polarization vectors' (Walker and Penrose, 1970; Chandrasekhar, 1983). Walker and Penrose proved that if  $k^\mu(\lambda)$  is a null geodesic and  $f^\mu$  is a vector such that

$$k^\mu f_\mu = 0 \quad \text{and} \quad (20a)$$

$$f^\mu f_\mu = 1 \quad (20b)$$

(unit vector orthogonal to  $k^\mu$ ; c.f. Eqs. (3) and (4) and parallel propagated along  $k^\mu$ , then the quantity

$$K_{\text{WP}} = 2[\mathbf{k} \cdot \mathbf{l} \mathbf{f} \cdot \mathbf{n} - \mathbf{k} \cdot \mathbf{m} \mathbf{f} \cdot \bar{\mathbf{m}}] \Psi_2^{-1/3}, \quad (21)$$

is conserved along the geodesic, i.e.  $k^\mu \nabla_\mu K_{\text{WP}} = 0$ . Here  $l^\mu, n^\mu, m^\mu, \bar{m}^\mu$  are components of Newmann–Penrose orthonormal tetrad and  $\Psi_2$  is the only non-zero Weyl scalar representing the gravitational monopole of Kerr metric.

Since  $\Psi_2$  is a complex scalar, we can write  $K_{\text{WP}}$  in the form

$$K_{\text{WP}} = K_1 + i K_2 \quad (22)$$

and in Boyer–Lindquist coordinates (see e.g. Walker and Penrose 1970; Connors and Stark 1977; Chandrasekhar 1983; Li et al. 2009 for details) we find that

$$K_1 + i K_2 = (A - iB)(r - ia \cos \theta), \quad (23)$$

where

$$A = (k^t f^r - k^r f^t) + a \sin^2 \theta (k^r f^\phi - k^\phi f^r), \quad (24)$$

$$B = \left[ (r^2 + a^2)(k^\phi f^\theta - f^\phi k^\theta) + a(k^t f^\theta - k^\theta f^t) \right] \sin \theta. \quad (25)$$

If we evaluate  $K_{\text{WP}}$  at any given point, we can then solve the parallel transport of vector  $\mathbf{f}$  along the whole geodesic. Equation (23) is equivalent to two real equations plus we have the condition of orthogonality (20a) that does not follow from Walker–Penrose theorem and is an independent one. With these three equations we can fix three space-like components of vector  $\mathbf{f}$ . The time-like component of  $\mathbf{f}$  can be chosen arbitrarily at a fixed point, because  $\mathbf{f}$  is defined only up to an additive multiple of  $\mathbf{k}$ . This follows trivially from the fact that  $\mathbf{k}$

is a null vector and that for  $f' = f + \alpha k$  both conditions (20a) and (20b) are satisfied. The polarization vector can be thus written without loss of generality, e.g. as

$$f^\mu = (0, \cos \psi X^i + \sin \psi Y^i), \quad (26)$$

for some polarization basis characterized by space-like vectors  $(X, Y)$  orthogonal to  $k$ .

When the above choice of  $f^\mu$  is plugged into Eq. (23) and the set of equations is solved for a null geodesic that passes through a point  $(t, r, \theta, \phi)$ , it is possible to express the final polarization vector at infinity in terms of photon's constants of motions  $\lambda$  and  $Q$ . The relative change of polarization angle due to parallel transport is then (Connors et al., 1980)

$$\Delta\chi = \tan^{-1} \left( \frac{-S K_2 + T K_1}{-S K_1 - T K_2} \right), \quad (27)$$

where

$$S = \frac{\lambda}{\sin \theta_{\text{obs}}} - a \sin \theta_{\text{obs}} = -\alpha - a \sin \theta_{\text{obs}}, \quad (28)$$

$$T = \text{sgn}(k^\theta)_\infty (Q - \lambda^2 \cot^2 \theta_{\text{obs}} + a^2 \cos^2 \theta_{\text{obs}})^{1/2} = \beta \quad (29)$$

with  $a$ ,  $\alpha$ ,  $\beta$  and  $\theta_{\text{obs}}$  being respectively the black-hole spin, the horizontal and vertical impact parameters of the null geodesic on the observer's image plane and the observer's inclination angle.

## 4 APPLICATION TO SYNCHROTRON RADIATION

### 4.1 Synchrotron emission

When high-energy charged particles (especially electrons) move fast through magnetic fields while they move along magnetic field lines), synchrotron radiation is produced. Synchrotron radiation is like standard cyclotron radiation with the difference that the energetic particles have relativistic speeds and the observed frequency of radiation is affected by the Doppler effect and by the Lorentz factor  $\gamma$ . Another factor  $\gamma$  comes from the relativistic length contraction, which can put the radiation spectrum into the X-ray range. The radiated power is given by the relativistic Larmor formula while the force on the emitting electron is given by the Abraham–Lorentz–Dirac force.

Two main characteristics of astronomical synchrotron radiation include non-thermal power-law spectra and polarization. Following Rybicki and Lightman (1979), a power-law distribution of electrons  $n(E) dE \sim E^{-p} dE$  has the specific intensity distribution  $I(\nu) \sim \nu^{-s}$ , where  $s = (p - 1)/2$  is the spectral index and maximal degree of polarization

$$\delta = \frac{s + 1}{s + 5/3} = \frac{p + 1}{p + 7/3}. \quad (30)$$

The simplified model of local synchrotron emissivity (taking into account only the power-law part of the synchrotron spectrum) is then gives spectral density

$$I(\nu) = I_0 \left( \frac{\rho}{\rho_0} \right) \left( \frac{B}{B_0} \sin \vartheta \right)^{1+s} \nu^{-s}, \quad (31)$$

where  $\vartheta$  is the local angle between the magnetic field and the direction of emission and the relation is valid up to the critical frequency  $\nu_c$ .

## 4.2 Polarization vector for linearly polarized radiation

In this section we derive practical formulae for determining initial polarization vector  $\mathbf{f}$  at a point of emission.

Let us assume a packet of synchrotron radiation emitted from a certain place by electrons that pass this place moving along magnetic field lines of intensity  $\mathbf{B}$ . Photons from the packet that eventually reach an observer at infinity all have 4-momentum  $\mathbf{P}$ . The electrons have some local distribution of energies and velocities, but they are part of a fluid with bulk motion characterized by 4-velocity  $\mathbf{U}$ .

From the properties of synchrotron radiation we know that the radiation will be partially linearly polarized and that the direction of polarization will be perpendicular to the projection of magnetic field onto the polarization plane.

The polarization plane contains polarization vector  $\mathbf{f}$  (it is the plane in which electric and magnetic field vectors oscillate) and it is perpendicular to the direction of photon propagation. We can determine the polarization plane by constructing its normal vector  $\mathbf{Z}$  pointing in the direction of propagation of the wave. From the the concept of ideal magneto-hydrodynamics (perfectly conducting fluid) it follows that  $\mathbf{B}$  is a space vector ( $\mathbf{B} \cdot \mathbf{U} = 0$ ) and so  $\mathbf{Z}$  and  $\mathbf{f}$  must be space-vectors too.

Because the direction of propagation is given by photons' 4-momentum  $\mathbf{P}$ , we are looking for a unit vector in a form

$$\mathbf{Z} \sim \mathbf{P} + \alpha_1 \mathbf{U}, \quad (32)$$

that has to satisfy  $\mathbf{Z} \cdot \mathbf{Z} = 1$  (unit vector) and  $\mathbf{Z} \cdot \mathbf{U} = 0$  (space vector). It is easy to find that

$$\mathbf{Z} = \mathbf{U} + \frac{\mathbf{U}}{(U P)}. \quad (33)$$

Now, with the help of  $\mathbf{Z}$ , we can find a projection of magnetic field vector  $\mathbf{B}$  onto the polarization plane simply as

$$\mathbf{B}_\perp = \mathbf{B} - \alpha_2 \mathbf{Z}, \quad (34)$$

where  $\alpha_2 \mathbf{Z} = \mathbf{B}_\parallel$  stands for the component of  $\mathbf{B}$  parallel with the direction of propagation. The factor  $\alpha_2$  can be fixed from the condition  $\mathbf{B} \cdot \mathbf{P} = 0$  and so we have

$$\mathbf{B}_\perp = \mathbf{B} - \frac{(B P)}{(U P)} \mathbf{Z}. \quad (35)$$

Our polarization vector  $\mathbf{f}$  can be then chosen in the direction of  $\mathbf{B}_\perp$ .

$$\mathbf{f} = \frac{\mathbf{B}_\perp}{|\mathbf{B}_\perp|} = \frac{(U P) \mathbf{B} - (P B) \mathbf{Z}}{\left[ (U P)^2 B^2 - (P B)^2 \right]^{1/2}}. \quad (36)$$

## 4.3 Linear polarization at infinity

For a practical calculation of parallel transport of polarization vector, we are going to need to define a set of base vectors in the polarization plane.

We have free will in setting up the polarization plane basis and that can be done in a number of ways. Since one usually constructs an orthonormal basis that defines a local reference frame of the fluid (LRF), we may use that frame for construction of our polarization basis. Because LRF is a Cartesian frame by definition, we may choose a completely random vector  $\tilde{\mathbf{r}}$ , from which we derive two other vectors  $\mathbf{V}$  and  $\mathbf{W}$  that are both perpendicular to  $\mathbf{P}$  and they are also perpendicular one another.

$$\mathbf{V} = \tilde{\mathbf{r}} \times \mathbf{P} \quad \text{and} \quad \mathbf{W} = \mathbf{V} \times \mathbf{P}. \quad (37)$$

The choice of the initial random vector  $\tilde{\mathbf{r}}$  can be simply made as  $\tilde{\mathbf{r}}^{(a)} = (0, r_1, r_2, r_3)$  in LRF, where  $r_1, r_2, r_3$  are non-zero independent random numbers (the time component is zero for the vector to be a space vector). Due to the fact that scalar product of vectors is invariant, vectors  $\mathbf{V}$ ,  $\mathbf{W}$  and  $\mathbf{P}$  remain perpendicular in any frame of reference.

We must still make sure that the base vectors of our polarization plane are unit vectors and that they lie in the plane. For that reason we introduce another set of vectors  $\mathbf{X}$  and  $\mathbf{Y}$ , where

$$\mathbf{X} = \mathbf{V} + \alpha_3 \mathbf{P}, \quad (38a)$$

$$\mathbf{Y} = \mathbf{W} + \alpha_4 \mathbf{P} \quad (38b)$$

and we require that  $|\mathbf{X}| = |\mathbf{Y}| = 1$  and that  $\mathbf{X} \cdot \mathbf{U} = \mathbf{Y} \cdot \mathbf{U} = 0$ . The later condition allows us to fix  $\alpha_3$  and  $\alpha_4$  and we have

$$\mathbf{X} = \left( \mathbf{V} - \frac{(\mathbf{V} \mathbf{U})}{(\mathbf{P} \mathbf{U})} \mathbf{P} \right) \frac{1}{(\mathbf{V} \mathbf{V})^{1/2}}, \quad (39a)$$

$$\mathbf{Y} = \left( \mathbf{W} - \frac{(\mathbf{W} \mathbf{U})}{(\mathbf{P} \mathbf{U})} \mathbf{P} \right) \frac{1}{(\mathbf{W} \mathbf{W})^{1/2}}. \quad (39b)$$

These are the base vectors of our polarization plane. It is easy to verify that  $\mathbf{X} \cdot \mathbf{Y} = 0$ .

The last thing we need to do is to project polarization vector  $\mathbf{f}$  into our polarization plane basis:

$$f_X = \mathbf{f} \cdot \mathbf{X} = \frac{(\mathbf{U} \mathbf{P})(\mathbf{B} \mathbf{V}) - (\mathbf{B} \mathbf{P})(\mathbf{U} \mathbf{V})}{\left[ (\mathbf{U} \mathbf{P})\mathbf{B}^2 - (\mathbf{P} \mathbf{B})^2 \right]^{1/2} (\mathbf{V} \mathbf{V})^{1/2}}, \quad (40a)$$

$$f_Y = \mathbf{f} \cdot \mathbf{Y} = \frac{(\mathbf{U} \mathbf{P})(\mathbf{B} \mathbf{W}) - (\mathbf{B} \mathbf{P})(\mathbf{U} \mathbf{W})}{\left[ (\mathbf{U} \mathbf{P})\mathbf{B}^2 - (\mathbf{P} \mathbf{B})^2 \right]^{1/2} (\mathbf{W} \mathbf{W})^{1/2}}. \quad (40b)$$

Coming back to Eq. (16) and (19), we can express the angle between polarization plane and our polarization basis ( $\mathbf{X}$ ,  $\mathbf{Y}$ ) (the polarization angle) as

$$\chi = \frac{1}{2} \tan^{-1} \left( \frac{2f_X f_Y}{f_Y^2 - f_X^2} \right). \quad (41)$$

and its change due to strong gravity effects from Eq. (27) as

$$\Delta\chi = \tan^{-1} \left( \frac{-S K_2 + T K_1}{-S K_1 - T K_2} \right). \quad (42)$$

The final set of Stokes parameters for a single light-ray is then

$$I(\nu) = g^3 I_0(\nu/g), \quad (43a)$$

$$Q(\nu) = I(\nu) \delta \cos(2\chi + 2\Delta\chi), \quad (43b)$$

$$U(\nu) = I(\nu) \delta \sin(2\chi + 2\Delta\chi), \quad (43c)$$

$$V(\nu) = 0, \quad (43d)$$

where  $g$  is the relativistic red-shift factor relating the place of emission and infinity,  $\delta$  is the conserved polarization degree and  $I_0$  is the specific intensity of the emission (see Eqs. 30 and 31).

## 5 SUMMARY

We have presented a detailed description of the theory of parallel transport of polarized light in Kerr spacetime with an emphasis on the example of parallel transport of linearly polarized light.

In case of linear polarization induced by synchrotron radiation produced in a fluid with a magnetic field, we give useful and practical formulae for numerical computation of the observed polarization angle. The procedure can be summarized to a step-by-step guide of how to proceed:

(1) At a given point  $(t, r, \theta, \phi)$  evaluate the vector of magnetic field  $\mathbf{B}$ , 4-velocity  $\mathbf{U}$  of the fluid, and the photon 4-momentum vector  $\mathbf{P}$ .

(2) Set up an orthonormal tetrad for the local rest frame (LRF) based on  $\mathbf{U}$  and in LRF construct a random vector  $\tilde{\mathbf{r}}$  and from that two vectors  $\mathbf{V}$  and  $\mathbf{W}$  that are perpendicular to each other and to the direction of  $\mathbf{P}$  (Eq. 37).

(3) Calculate the necessary scalar products  $(\mathbf{U} \cdot \mathbf{P}, \mathbf{B} \cdot \mathbf{P}, \mathbf{B} \cdot \mathbf{B}$  and  $\mathbf{U} \cdot \mathbf{V}, \mathbf{U} \cdot \mathbf{W}, \mathbf{V} \cdot \mathbf{V}, \mathbf{W} \cdot \mathbf{W})$  and with the help of those evaluate the components  $f_X, f_Y$  of the polarization vector (Equation 40).

(4) Evaluate the polarization angle and its change due to parallel transport using Eqs. (41) and (42).

(5) Integrate the resulting Stokes parameters at the detector using Eq. (43).

## ACKNOWLEDGEMENTS

The present work was supported by the following projects: RVO:67985815 (MB,JH) and EC-FP7 StrongGravity 312789 (MB, GK). We thank Michal Dovčiak for useful discussion and comments during the work.

## REFERENCES

- Aitken, D. K., Greaves, J. S., Chrysostomou, A., Holland, W. S., Hough, J. H., Pierce-Price, D. and Richer, J. S. (2000), Detection of Polarized Millimeter and Submillimeter Emission from Sagittarius A\*, *Astrophys. J. Lett.*, **534**, pp. L173–L176.
- Bardeen, J. M., Press, W. H. and Teukolsky, S. A. (1972), Rotating Black Holes: Locally Nonrotating Frames, Energy Extraction, and Scalar Synchrotron Radiation, *Astrophys. J.*, **178**, pp. 347–370.
- Beckert, T. and Duschl, W. J. (1997), Synchrotron radiation from quasi-monoenergetic electrons. Modelling the spectrum of Sagittarius A(\*), *Astronomy and Astrophysics*, **328**, pp. 95–106, arXiv: astro-ph/9707162.
- Carter, B. (1968), Global Structure of the Kerr Family of Gravitational Fields, *Physical Review*, **174**, pp. 1559–1571.
- Chandrasekhar, S. (1983), *The Mathematical Theory of Black Holes*, International series of monographs on physics, Oxford, URL <http://books.google.cz/books?id=aj6ANAEACAAJ>.
- Connors, P. A. and Stark, R. F. (1977), Observable gravitational effects on polarised radiation coming from near a black hole, *Nature*, **269**, p. 128.
- Connors, P. A., Stark, R. F. and Piran, T. (1980), Polarization features of x-ray radiation emitted near black holes, *Astrophys. J.*, **235**, pp. 224–244.
- Dombrowskii, V. A. (1954), Optical polarisation of the Crab Nebula., *Doklady Akadademii Nauk SSSR*, **94**, p. 1021.
- Eckart, A., Baganoff, F. K., Morris, M., Bautz, M. W., Brandt, W. N., Garmire, G. P., Genzel, R., Ott, T., Ricker, G. R., Straubmeier, C., Viehmann, T., Schödel, R., Bower, G. C. and Goldston, J. E. (2004), First simultaneous NIR/X-ray detection of a flare from Sgr A\*, *Astronomy and Astrophysics*, **427**, pp. 1–11, arXiv: astro-ph/0403577.
- Eckart, A., Baganoff, F. K., Zamaninasab, M., Morris, M. R., Schödel, R., Meyer, L., Muzic, K., Bautz, M. W., Brandt, W. N., Garmire, G. P., Ricker, G. R., Kunneriath, D., Straubmeier, C., Duschl, W., Dovciak, M., Karas, V., Markoff, S., Najarro, F., Mauerhan, J., Moulataka, J. and Zensus, A. (2008), Polarized NIR and X-ray flares from Sagittarius A\*, *Astronomy and Astrophysics*, **479**, pp. 625–639, arXiv: 0712.3165.
- Franklin, K. L. and Burke, B. F. (1956), Radio observations of Jupiter., *Astronom. J.*, **61**, p. 177.
- Hall, J. S. (1949), Observations of the Polarized Light from Stars, *Science*, **109**, pp. 166–167.
- Hey, J. S. (1946), Solar radiations in the 4-6 metre radio wave-length band, *Nature*, **157**, pp. 47–48.
- Hiltner, W. A. (1949), Polarization of Radiation from Distant Stars by the Interstellar Medium, *Nature*, **163**, p. 283.
- Li, L.-X., Narayan, R. and McClintock, J. (2009), Inferring the Inclination of a Black Hole Accretion Disk from Observations of its Polarized Continuum Radiation, *Astrophys. J.*, **691**, pp. 847–865, arXiv: 0809.0866.
- Misner, C. W., Thorne, K. S. and Wheeler, J. A. (1973), *Gravitation*, Freeman, San Francisco.
- Noether, E. (1918), Invariante variationsprobleme, *Nachr. D. König. Gesellsch. D. Wiss. Zu Göttingen, Math-phys. Klasse*, p. 235.
- Reber, G. (1946), Solar Radiation at 480 Mc./sec., *Nature*, **158**, p. 945.
- Rogers, A. E. E., Doeleman, S., Wright, M. C. H., Bower, G. C., Backer, D. C., Padin, S., Philips, J. A., Emerson, D. T., Greenhill, L., Moran, J. M. and Kellermann, K. I. (1994), Small-scale structure and position of Sagittarius A(\*) from VLBI at 3 millimeter wavelength, *Astrophys. J. Lett.*, **434**, pp. L59–L62.
- Rybicki, G. and Lightman, A. (1979), *Radiative processes in astrophysics*, Wiley-Interscience publication, Wiley, ISBN 978-0471048152.

- Stokes, G. G. (1852), *Transactions of the Cambridge Philosophical Society*, **9**, p. 399.
- Wald, R. M. (1984), *General Relativity*, The University of Chicago Press.
- Walker, M. and Penrose, R. (1970), On quadratic first integrals of the geodesic equations for type {22} spacetimes, *Comm. Math. Phys.*, **18**, pp. 265–274.
- Westerhout, G., Seeger, C. L., Brouw, W. N. and Tinbergen, J. (1962), Polarization of the galactic 75-cm radiation, *Bulletin of the Astronomical Institutes of the Netherlands*, **16**, p. 187.
- Wielebinski, R., Shakeshaft, J. R. and Pauliny-Toth, I. I. K. (1962), A search for a linearly polarized component of the galactic radio emission at 408 Mc/s, *The Observatory*, **82**, pp. 158–164.



# An XSPEC model to explore spectral features from black-hole sources – II.

## The relativistic iron line in the lamp-post geometry

Michal Dovčiak,<sup>1,a</sup> Jiří Svoboda,<sup>1</sup> René W. Goosmann,<sup>2</sup>  
Vladimír Karas,<sup>1</sup> Giorgio Matt<sup>3</sup> and Vjačeslav Sochora<sup>1</sup>

<sup>1</sup>Astronomical Institute, Academy of Sciences of the Czech Republic, Boční II 1401,  
CZ -141 00 Prague, Czech Republic

<sup>2</sup>Observatoire Astronomique de Strasbourg, 11 rue de l'Université, F-67000 Strasbourg, France

<sup>3</sup>Dipartimento di Matematica e Fisica, Università degli Studi “Roma Tre”,  
Via della Vasca Navale 84, I-00146 Roma, Italy

<sup>a</sup>dovciak@asu.cas.cz

### ABSTRACT

In X-ray spectra of several active galactic nuclei and Galactic black hole binaries a broad relativistically smeared iron line is observed. This feature arises by fluorescence when the accretion disc is illuminated by hot corona above it. Due to central location of the corona the illumination and thus also the line emission decrease with radius. It was reported in the literature that this decrease is very steep in some of the sources, suggesting a highly compact corona.

We revisit the lamp-post setup in which the corona is positioned on the axis above the rotating black hole and investigate to what extent the steep emissivity can be explained by this scenario. We show the contributions of the relativistic effects to the disc illumination by the primary source – energy shift, light bending and aberration. The lamp-post radial illumination pattern is compared to the widely used radial broken power-law emissivity profile. We find that very steep emissivities require the primary illuminating source to be positioned very near the black hole horizon and/or the spectral power-law index of the primary emission to be very high. The broken power-law approximation of the illumination can be safely used when the primary source is located at larger heights. However, for low heights the lamp-post illumination considerably differs from this approximation.

We also show the variations of the iron line local flux over the disc due to the flux dependence on incident and emission angles. The former depends mainly on the height of the primary source while the latter depends on the inclination angle of the observer. Thus the strength of the line varies substantially across the disc. This effect may contribute to the observed steeper emissivity.<sup>1</sup>

**Keywords:** accretion, accretion discs – black hole physics – line: formation – line: profiles – relativistic processes – X-rays: galaxies – X-rays: binaries

---

<sup>1</sup> This paper summarises the work done for the workshop *Ragtime 12* held in 2010.

## 1 Introduction

The broad iron line in the X-ray spectra of active galactic nuclei (AGN) and Galactic X-ray binaries has been studied by various authors for more than two decades. The first mention of the relativistic broadening of spectral lines due to high orbital velocities of the accretion disc, where the iron  $K\alpha$  line arise by fluorescence, dates as far as 1989 when Fabian et al. studied the X-ray spectrum of Cygnus X-1 observed by EXOSAT in 1983. Since then the relativistically broadened line was discovered in systems with diverse masses: in AGN with central supermassive black holes (e.g. Risaliti et al., 2013), in X-ray binaries with the black hole of several solar masses (e.g. Miller et al., 2013) and even in systems with a neutron star (e.g. Cackett and Miller, 2013). Although the broad lines seem very well established, one should mention that there exist an alternative explanation of the phenomena – partially covering scenario proposed by Miller and Turner (2013). However, recent X-ray reverberation studies of AGN support the reflection scenario, see e.g. Fabian et al. (2013).

The shape of the observed line is determined by several factors: by the geometry of the illuminating and reflecting region, by the physical properties of the re-processing matter and by the properties of the central gravitating body. The shaping of line, mainly its broadening, by the black-hole gravitation acting on photons emitted in the inner accretion disc is used to measure the spin of the black hole. Actually, high energy redshift due to large gravity near the centre is completely responsible for the extreme width of the line. The other components can modify the overall line profile, yet, they are not able to change the width of the line by themselves. Still their contribution may be important in determining the spin value. This is caused by the particular shape of the relativistically broadened line – the line flux gradually decreases with the decreasing energy, thus the lower edge of the line is not easily pinpointed, its determination depends on how strong the line's red wing is and the contribution of the mentioned components may be important.

One of the inevitable components, that makes the formation of the fluorescent line possible, is the illuminating corona. Its geometry will affect the illumination of the disc and consequently also the emission of the line from different parts of the disc. This will eventually alter the overall line profile. Usually the corona is supposed to be either extended (e.g. Wilkins and Fabian, 2012) over large area above the disc or concentrated in a compact region (e.g. Fabian et al., 2011). In the first case the illumination of the disc is often assumed to be a broken power-law function of the radius, with more intensive illumination and resulting higher line emission in the inner parts of the disc. Sometimes the observed radial power-law near the black hole is quite steep (Wilkins and Fabian, 2011) and it was suggested (Svoboda et al., 2012) that it could be caused by the second possible scenario, i.e. sort of a lamp-post configuration, where the compact patch of the corona located above the black hole illuminates the accretion disc, sometimes referred to as an aborted jet scenario (Ghisellini et al., 2004) or a light bending model (Miniutti and Fabian, 2004). In this geometry, the illumination of the disc is due to a compact primary source and photon trajectories close to the centre are bent by strong gravity of the black hole. Consequently, the radial profile of the line emission takes a particular form that depends on the height of the lamp-post.

In this paper we compare the two radial profiles of the line emission – the broken power-law dependence and illumination in the lamp-post scenario. We concentrate mainly on the question if the observed steep radial decrease of the emissivity could be interpreted in terms of the lamp-post geometry. To this purpose we at first assume very simple local physics of the emission, particularly, the emission does not depend on incident and emission angles, and the flux in line is isotropic and proportional to the incident flux. Then, we also apply the emission directionality given by the numerical modelling of radiative transfer (using Monte Carlo multi-scattering code NOAR, see Dumont et al., 2000).

## **2 Relativistic lamp-post geometry**

The lamp-post geometry has been introduced to describe the observed emission from X-ray irradiated accretion discs by Matt et al. (1991) and Martocchia and Matt (1996). The model consists of an X-ray source (‘lamp’) producing the primary irradiation and representing an optically thin corona that is thought to extend above the optically thick medium of a standard accretion disc (Frank et al., 2002). This scheme has proved to be very popular in the context of accreting supermassive black holes in cores of AGN (Peterson, 1997). Location of the primary source on the black hole axis can be imagined, e.g. as a site of action where jets are initially accelerated (Biretta et al., 2002) or where the shocks in an aborted jet collide (Ghisellini et al., 2004). A down-scaled version of the model has been also invoked to describe microquasars (Mirabel and Rodríguez, 1998).

The lamp-post geometry (on or off-axis) has already been studied in various context by several authors – AGN variability was studied by (Miniutti and Fabian, 2004) and Niedźwiecki and Miyakawa (2010), the polarisation properties were investigated by Dovčiak et al. (2011) and the X-ray reverberation mapping by Emmanoulopoulos et al. (2014) and Cackett et al. (2014). Recently, Dauser et al. (2013) has studied disc reflection due to illumination by a jet, i.e. radially extended region moving along the axis.

Despite the fact that realistic corona must be a very complex, inhomogeneous and turbulent medium, the lamp-post model captures the main components of a typical AGN spectrum, and it allows us to search for the parameter values. In particular, the slope of the primary power-law continuum, and the skewed and redshifted profile of the broad iron line around 6–7 keV that has been interpreted in terms of relativistically smeared reflection spectrum.

It has been shown (Wilms et al., 2001) that a steep emissivity profile of  $\simeq 4.3$ – $5.0$  of the iron-line and reflection features are required in XMM-Newton observation of MCG -6-30-15. This has been interpreted in terms of highly central concentration of the irradiating flux, in a much more compact nuclear region than predicted by pure accretion disc models. Similarly steep emissivity profile has been reported in 1H0707-495 (Fabian et al., 2009) and IRAS13224-3809 (Ponti et al., 2009). In order to explain the unusually steep spectrum, Wilms et al. (2001) invoke some additional X-ray source that is presumably associated with the extraction of the black hole spin energy, perhaps via some kind of magnetic coupling (Blandford and Znajek, 1977).

The main aim of the present investigation is to verify whether the relativistic effects can produce the steep emissivity required by the mentioned observations. To this end we consider Kerr metric for the gravitation of a rotating black hole, and we allow for both prograde and retrograde rotation of the accretion disc with respect to the black hole spin.

A complex interplay of the energy shifts, aberration, boosting and light-bending effects acts on the primary as well as reflection components of the X-ray spectrum, especially when the source of irradiation is placed at a small height near above the horizon and if the black hole rotates rapidly, so that the inner edge of the disc is at a small radius. As a result of this interplay, it is not obvious at all whether the resulting emissivity comes out significantly steeper in comparison to the non-relativistic limit of an irradiated standard disc.

To study the radial emissivity we first turn our attention to the reflected line component. We assume the line flux to be proportional to the incident flux and the photons will be emitted isotropically in local frame co-rotating with the Keplerian disc, no matter what the incident and emission angles are. In this way we are going to study the effect of the relativistic lamp-post geometry only, separating it from the effects due to the dependence of the local physics on geometry of the incident and emission light rays.

In this approach the local line emission in the disc is proportional to the normalization of the power-law incident flux. We assume the primary emission to be isotropic in local frame and that it is a power law with the photon index  $\Gamma$ , i.e.  $f_1(E_1) = N_1 E_1^{-\Gamma}$ . Then the incident flux,  $f_i$ , is a power law with the same photon index but with a different normalization

$$f_i(E_i) = N_i(r) N_1 E_i^{-\Gamma}. \quad (1)$$

Here, the normalization  $N_i(r)$  is given by the curved geometry of the light rays and relativistic shift of the energy. It can be expressed in the following way (see e.g. Dovčiak, 2004)

$$N_i(r) = g_i^\Gamma \frac{d\Omega_1}{dS_i} = \frac{g_i^{\Gamma-1}}{U_1^t} \frac{d\Omega_1}{dS}. \quad (2)$$

The primary photons emitted by the lamp-post into the local solid angle  $d\Omega_1$  fall down onto the disc area measured in the frame co-moving with the disc  $dS_i = p_{i\mu} U^\mu dS = g_i U_1^t dS$ . These photons are shifted to the incident energy  $E_i$  from the emission energy  $E_1$  by the energy shift  $g_i = E_i/E_1 = p_{i\mu} U^\mu / p_{1\mu} U_1^\mu$  which is responsible for the factor of  $g_i^\Gamma$  in the above equation. We have denoted the four-momentum of the incident photons by  $p_i^\mu$ , the four-velocity of the static lamp-post by  $U_1^\mu = (U_1^t, 0, 0, 0)$  and the four-velocity of the disc by  $U^\mu$ . We assume the disc to be Keplerian above the marginally stable orbit and freely falling below it with the constant energy and momentum that the matter had at this orbit. The area element  $dS = r dr d\varphi$  is evaluated in Boyer–Lindquist coordinates.

The normalization of the incident flux,  $N_i$ , is a function of radius, and thus it determines the radial emission profile of the line flux. We can separate this function into several components

$$N_i(r) = \frac{1}{r} \frac{d\mu_n}{dr} \times \frac{g_i^{\Gamma-1}}{U_1^t} \times \frac{d\mu}{d\mu_n} \times \frac{d\mu_1}{d\mu}. \quad (3)$$

The first component is chosen in such a way that it represents exactly the Newtonian value of  $N_i(r)$

$$N_i^n(r) \equiv \frac{d\Omega_n}{dS} = \frac{1}{r} \frac{d\mu_n}{dr} = \frac{h}{(r^2 + h^2)^{3/2}}. \quad (4)$$

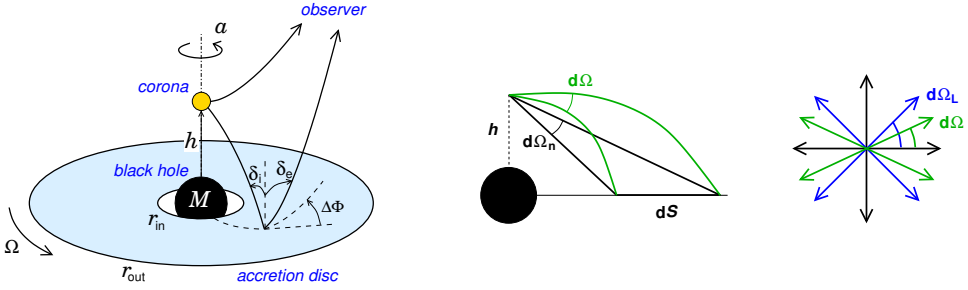


**Figure 1.** *Left:* The sketch of the lamp-post geometry. *Middle:* Due to the light bending the photons illuminating the same area of the disc are emitted by the primary source into different solid angles in the relativistic and the Newtonian cases. *Right:* The photons emitted isotropically in the rest frame of the primary source are beamed perpendicularly to the rotation axis because of the strong gravity near the black hole.

In the above, we have introduced the Newtonian angle of emission,  $\theta_n$ , as the angle under which the primary photon has to be emitted from the lamp-post at height  $h$  in the Newtonian non-curved space so that it falls down onto the disc at the radius  $r$  and  $\mu_n \equiv \cos \theta_n$ .

The second component,  $g_i(r)^{\Gamma-1}/U_1^i$ , is connected with the energy shift of the incident photons and it should be emphasized that it depends on the primary flux via the photon index  $\Gamma$ . For Keplerian discs in the Kerr space-time it can be expressed above the marginally stable orbit as

$$N_i^s(r) = \left( \frac{r^2 + a\sqrt{r}}{r\sqrt{r^2 - 3r + 2a\sqrt{r}}} \right)^{\Gamma-1} \left( 1 - \frac{2h}{h^2 + a^2} \right)^{\frac{\Gamma}{2}}. \quad (5)$$

The third component,

$$N_i^b(r) \equiv \frac{d\Omega}{d\Omega_n} = \frac{d\mu}{d\mu_n} = \frac{\sin \theta}{\sin \theta_n} \frac{d\theta}{d\theta_n}, \quad (6)$$

represents the effects of the light bending in the curved space-time. It compares the solid angle  $d\Omega$  in the Boyer–Lindquist coordinates with the Newtonian value, defined above, into which primary photons have to be emitted to illuminate the disc area  $dS$  at the disc radius  $r$ .

The fourth component represents the “gravitational aberration”. Due to the fact that the local observers on the axis measure the distances differently along the axis and perpendicular to it, the local isotropic emission will be beamed in Boyer–Lindquist coordinates in the direction perpendicular to the axis. We can express it by comparing the solid angle in local frame of the lamp-post with the solid angle in Boyer–Lindquist coordinates

$$N_i^a(r) = \frac{d\Omega_1}{d\Omega} = \frac{h}{\sqrt{\Delta_h}} \left[ 1 + \left( \frac{\Delta_h}{h^2} - 1 \right) \cos^2 \theta_1 \right]^{3/2}, \quad (7)$$

where  $\Delta_h \equiv h^2 - 2h + a^2$  and the photon’s local emission angle  $\theta_1$  is a function of the radius  $r$  at which such a photon strikes the disc. One can see that the solid angle  $d\Omega$  is amplified by the factor  $h^2/\Delta_h > 1$  along the axis ( $\theta_1 = 0^\circ$  or  $\theta_1 = 180^\circ$ ) and it is diminished by the factor  $\sqrt{\Delta_h}/h < 1$  in the direction perpendicular to the axis ( $\theta_1 = 90^\circ$ ).

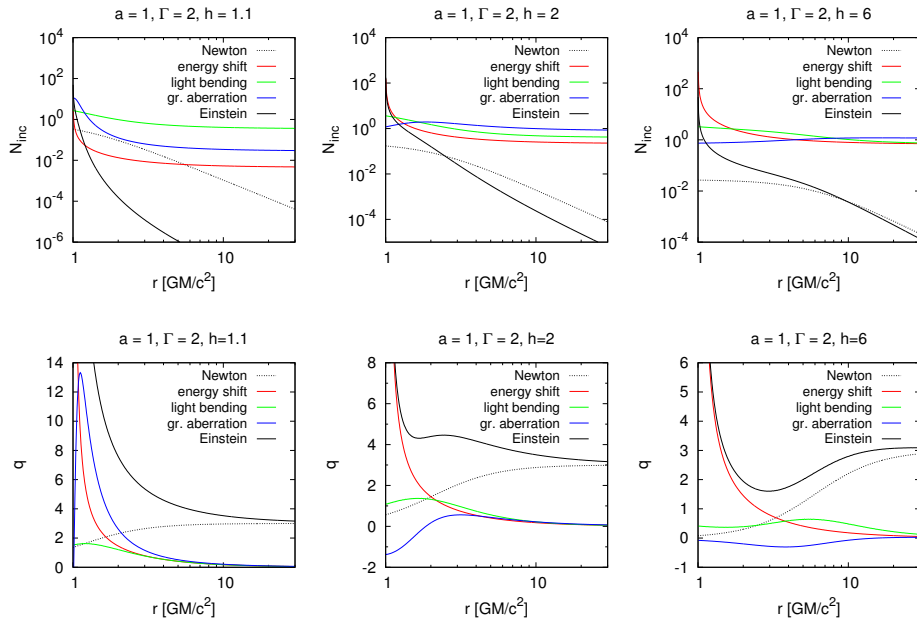


**Figure 2.** The radial profile of the incident flux  $N_i(r)$  (top) and its radial power-law index  $q(r)$  (bottom) in the relativistic lamp-post geometry with the illuminating primary source at heights  $h = 1.1, 2$  and  $6 \text{ GM}/c^2$  (from left to right). The primary flux is a power law with the index  $\Gamma = 2$  and the Kerr black hole rotates extremely with the spin  $a = J/M = 1 \text{ GM}/c$ . The contributions from the Newtonian, energy shift, light bending and gravitational aberration parts are shown. The solid black line (Einstein) depicts the overall incident flux and its radial power-law index.

On the top panels of Fig. 2 we show the radial profile of the function  $N_i(r)$  and its components for extremely rotating black hole and for several heights of the primary source. In Newtonian case the illumination of the disc is flat below the lamp-post and decreases with the radius with the third power far from the centre. The energy shift component is higher than unity for the radius lower than the height of the lamp-post (however, due to the Doppler shift and black hole spin the transition radius is somewhat shifted) and it is lower than unity above this radius. It is due to the fact that in the first case the photon falls closer to the black hole, gaining the energy, whereas in the second case it climbs out of the gravitational potential well, losing its energy. As a result, the shift gains very high values for small radii close to the horizon and quite low values far from the black hole if the height of the primary source is low.

The effect of light bending is stronger closer to the black hole. Thus the photon trajectory that is nearer to the black hole is more curved, the difference in bending of two close trajectories gets smaller farther away from the centre. This results in light bending component  $N_i^b(r)$  to be a decreasing function of radius.

Due to the fact that the gravitational aberration decreases the solid angle, which photons are emitted into, the most in the direction perpendicular to the axis, the incident flux will be amplified for those radii where the photons emitted in this direction strike the disc. That is

why the component  $N_i^a(r)$  first increases with the radius and then decreases. The maximum moves farther away from the black hole for higher lamp-post. For very low heights of the primary source, the photon trajectories emanating perpendicularly to the axis are bend so much that they do not strike the disc, rather they fall onto the horizon. In that case this component of the incident flux decreases with the radius.

To compare the relativistic lamp-post illumination with the broken power law one, we define the radial power-law index for the lamp-post geometry as the slope of the radial profile of  $N_i(r)$  in the log-log graph (i.e. slope of the graphs on top panels in Fig. 2). The definition reads

$$q(r) \equiv \frac{d \log N_i(r)}{d \log r} = -r \frac{d}{dr} \ln N_i(r). \quad (8)$$

The radial power-law index defined in this way clearly depends on the radius. The four components of the incident flux that has to be multiplied to give the overall illumination translate into four components of the power-law index  $q(r)$  that have to be added to give the overall relativistic radial power-law index. We show all four components of the index on bottom panels in Fig. 2.

The index  $q(r)$  for large radius is given by the Newtonian value,  $q(r \rightarrow \infty) = 3$ . For very low radii, close to the horizon, the energy shift component dictates the behaviour of the  $q(r)$ . Its influence extend farther for higher primary spectral power-law index. For very low heights, heights near above the black hole horizon, the component due to gravitational aberration adds also quite significantly to the index for low radius. For low lamp-post heights ( $h \lesssim 6 GM/c^2$ ), the light bending and gravitational aberration component may create local maxima in the radial power-law index, depending on the black hole spin and primary spectral power-law index  $\Gamma$ . More examples of the behaviour of the radial power-law index  $q(r)$  for different parameter values are shown in Fig. A2. Note, that if the line emission were proportional to the incident flux also below the marginally stable orbit (dotted lines in Fig. A2), the index  $q(r)$  for lower absolute value of the black hole spin, i.e. larger radius of the event horizon, would be larger. This is due to the energy shift component of the  $q(r)$ , which gains large values also at higher radii.

From Figures 2 and A2 it is evident that the relativistic lamp-post illumination is very different from the broken power law, which would be represented by two constant values in these figures. For comparison, we show the relativistic lamp-post emission together with a broken power law in Fig. A1. The graphs in this figure are renormalized in such a way that they do not intersect each other, here, we are interested in their shape only. The broken-power-law graphs (depicted by red) have Newtonian value of the index,  $q_{\text{out}} = 3$ , above the break radius,  $r_b$ . The break radius and index  $q$  below it were chosen by eye so that they approximately represent the relativistic lamp-post flux. We show their values in Tables A1–A4. One can see that the broken power law is close enough only in some radial regions whereas it fails for small radii near the horizon and region around the break radius. Although the difference between the two is large in these regions (note, that the graphs are in logarithmic scale), one still cannot jump to the conclusion that the broken power-law approximation would fail in fitting the spectra originated in the relativistic lamp-post geometry. The energy of the photons coming to the observer from regions close to the horizon is strongly shifted to very low values and the troublesome region near the break

radius may be small enough with respect to the whole disc to change the overall spectrum. Thus the spectra for the broken power-law emissivity and for relativistic lamp-post geometry might still be similar sufficiently.

From graphs in Fig. A1 one can see that the illumination profile would actually be much better approximated with a power-law with two breaks instead of one, especially for higher locations of the primary source. Comparisons between simple power-law and once or twice broken power-law are investigated by Wilkins and Fabian (2011).

### 3 The directionality of the local flux

The flux emitted by the primary source illuminates the disc and the incident photons are then re-processed in the orbiting material. They scatter on electrons, are absorbed by ions or neutral atoms or they can be created by the fluorescence when electrons in ions or neutral atoms change their state. Fluorescent spectral lines, line edges and Compton hump are typical features of such reflected X-ray spectra (Ross and Fabian, 2005; García et al., 2013). The most prominent spectral line in this energy band is that of iron (Fe  $K\alpha$  line doublet for neutral iron is at 6.4 keV) due to its large abundance and high fluorescence yield. The flux emitted locally in this line depends on number of absorbed photons that create the vacancies and fluorescent yield which characterises how fast these vacancies fill. If we assume that there is always enough photons that induce the fluorescence then the flux in the line is mainly dependent on the absorption. A vacancy at the K level of a neutral iron line is created when a photon with the energy above the iron K edge (at approx. 7.1 keV) is absorbed. The efficiency of the absorption quickly decreases with the energy, thus only photons up to a few keV above this edge are absorbed. This is due to the fact that the K-absorption cross-section of a photon with energy  $E$  above the K-absorption edge at 7.1 keV (measured in the local disc frame) decreases approximately as (Verner et al., 1993)  $1.9 (E/7.1 \text{ keV})^{-3.1} - 0.9 (E/7.1 \text{ keV})^{-4.1}$  and thus levels off to 1% of its initial value already at 37.4 keV. Since the primary spectrum assumed in our model extends to much higher energies, the flux in the line is simply proportional to the normalisation of the incident power-law spectrum. We generally assume that both cut-off energies of the primary spectrum lie outside the energy band where absorption occurs. We give two examples for extremely rotating Kerr black hole to show how well this assumption is fulfilled:

(1) The lower energy cut-off is shifted to higher energy when the primary source is very high above the disc. Then the incident photons gain the highest energy if they fall close to the horizon. For the lamp at height  $h = 100 \text{ GM}/c^2$  and incident radius at  $r_1 = 1.035 \text{ GM}/c^2$  the photon energy shift is  $g_1 = 67$ . Thus the lower energy cut-off at 0.1 keV would be shifted to 6.7 keV which is still below the Fe K edge. Note, that the emission below this region will have very low contribution to the overall spectral shape of the observed broadened line both due to small emission area and due to small value of the transfer function (that amplifies local flux when transferred to the observer at infinity),  $G < 0.1$  for inclination  $\theta_o = 70^\circ$  (and smaller for lower inclinations). The contribution from this region will be shifted by the factor  $g < 0.1$ , thus to energy  $E < 0.64 \text{ keV}$ .

(2) The high energy cut-off is shifted to lower energy when the primary source is very low above the black hole horizon. Then the incident photons lose the energy when they have to climb out of deep potential well, thus they lose more if they fall to the disc far away from

the horizon. For the lamp at height  $h = 1.3 \text{ GM}/c^2$  and incident radius at  $r_i = 1000 \text{ GM}/c^2$  the photon energy shift is  $g_i = 0.186$ . Thus the higher energy cut-off at 200 keV would be shifted to 37.2 keV which is still high enough above the Fe K edge. Note, that the emission above this region will have quite low contribution to the overall spectral shape of the observed broadened line due to radial decrease of the line emissivity as  $r^{-3}$ .

We have computed the reflection from a neutral disc in constant density slab approximation by the Monte Carlo code NOAR (Dumont et al., 2000). The line flux was then computed by subtracting the interpolated reflected continuum from the reflection spectra. The line flux includes also the Compton shoulder created by scattering of the fluorescent photons before they leave the disc. We approximate the line with a narrow box function with a width of 1 eV (simulating a delta function) that has the numerically computed flux. This speeds up the code without loss of precision since the relativistically broadened line does not depend on the exact shape of the locally narrow line. The local Fe  $K\alpha$  flux depends on incident and emission angles due to the fact that incident photon travels different distances in different layers during radiative transfer in the disc. On the other hand it does not depend on the azimuthal angle between incident and emitted light rays. We define the emission directionality function as the numerically computed flux in line per unit normalisation of the incident power-law flux

$$\mathcal{M}(\mu_i, \mu_e) \equiv \frac{dN}{dt dS^\perp d\Omega dE} = \frac{1}{2\pi \mu_e} \frac{\Delta N}{\Delta\mu_e \Delta E N_{\text{tot}}} \int_{E_0}^{E_c} E^{-\Gamma} dE, \quad (9)$$

where  $\Delta N$  is the number of photons emitted into the emission angle bin characterised by its cosine,  $\Delta\mu_e$ , i.e. into the whole azimuth of  $2\pi$ , hence the leading factor in the definition, and into energy bin  $\Delta E$ .  $N_{\text{tot}}$  is the total number of photons used in Monte Carlo computation and thus we multiply by the integrated energy dependence to normalise it as mentioned earlier, i.e. for incident power-law being exactly  $F_i(E) = E^{-\Gamma}$ . In the definition (9) there is one more factor of  $1/\mu_e$  due to the local flux being defined with respect to the area perpendicular to the emitted light ray while the reflected number of photons was computed per unit disc area. The sharp low,  $E_0$ , and high,  $E_c$ , energy cut-offs at 2 and 300 keV, respectively, were used in the computation. With this definition of emission directionality, the local line flux is defined as

$$F_{\text{loc}}(E) \equiv \mathcal{R}(r) \mathcal{M}(\mu_i, \mu_e) \delta(E - E_{\text{rest}}) \quad (10)$$

with  $E_{\text{rest}} = 6.4 \text{ keV}$  being the rest energy of the neutral Fe  $K\alpha$  line and radial dependence of the normalisation of the incident power-law as discussed in the previous section,  $\mathcal{R}(r) = N_1 N_i(r)$ , see Eq. (1).

We show the emission directionality function,  $\mathcal{M}(\mu_i, \mu_e)$ , in the bottom panel of Fig. 3 for the photon index of the primary radiation  $\Gamma = 2$ . To see which values this function may acquire we also show the values of cosines of incident and emission angles at the top panel of the same figure (maps of cosine of emission angles are also shown in Figs. B1, B4 and B7). One can see that more radiation is emitted when the incident angle is large (measured from the normal to the disc), i.e. when the photons arrive almost parallelly with the disc. The same applies for the angular dependence of emissivity which obeys limb brightening

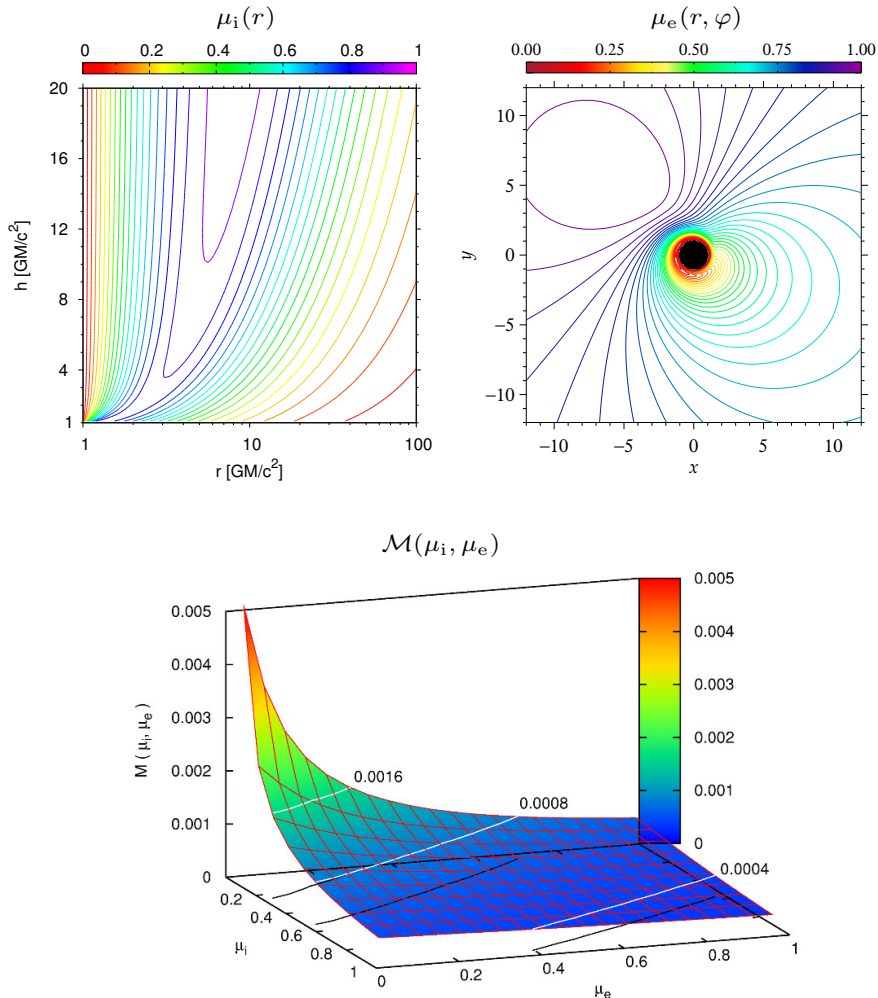


**Figure 3.** *Top left:* The radial dependence of the cosine of the incident angle,  $\mu_i$ , for different heights of the primary source and for the extremely rotating black hole with the spin  $a = 1 \text{ GM}/c$ . *Top right:* The dependence of the cosine of the emission angle,  $\mu_e$ , on the position on the disc. The spin of the black hole is  $a = 1 \text{ GM}/c$  and the inclination of the observer is  $\theta_o = 30^\circ$ . *Bottom:* The emission directionality function,  $\mathcal{M}(\mu_i, \mu_e)$ , is depicted for the photon index  $\Gamma = 2$ . Notice the high values it acquires for large incident and emission angles.

law. The brightening is, however, smaller than the limb brightening law derived by Haardt and Matt (1993), where  $\mathcal{M}(\mu_e) \sim \ln(1 + \mu_e^{-1})$ . Since both the incident as well as emission angles are very high close above the horizon due to aberration caused by high Keplerian velocity, the emission directionality will be highest in this region. We show the map of  $\mathcal{M}(\mu_i(r, \varphi), \mu_e(r, \varphi))$  in the equatorial plane for several values of black hole spin, observer

inclination and height of the primary source in Figs. B2, B5 and B8. One can already appreciate the importance of the limb brightening effect by comparing the values of this function with the values of energy shift,  $g$ , and transfer function (i.e. the amplification of the local emission due to relativistic effects),  $G$ , shown in Figs. B1, B4 and B7. Thus we can expect that the shape of the broad iron line may be substantially influenced by the emission directionality. Moreover, the dependence of the emission directionality on the radius through the radially dependent incident and emission angles might cause that the observed radial emissivity profile, characterised by the radial power-law index  $q$ , might be measured with a systematic error if wrong assumption on emission directionality is taken (Svoboda et al., 2014).

#### 4 The shape of the relativistic line in lamp-post geometry

In the previous two sections we have discussed the local line flux and its dependence on the disc illumination, that gave us the radial part of the local emission, and local re-processing in the disc, that determined the emission directionality. The final shape of the observed spectral line is influenced by the relativistic effects that change the spectral properties of the local emission when transferred to the observer at infinity. The local spectrum will be shifted in energy due to Doppler shift and gravitational redshift, and it will be amplified due to Doppler boosting, gravitational lensing, aberration and light bending (the last two influence the local emission angle i.e. change the projections of the emitting area). To get the observed shape of the line one has to integrate the local emission over the whole disc

$$F_{\text{obs}}(E) \equiv \frac{dN_{\text{obs}}}{dt d\Omega dE} = \int dS G F_{\text{loc}} \delta(E - g E_{\text{rest}}), \quad (11)$$

where  $G$  is the transfer function (see e.g. Cunningham, 1975; Dovčiak, 2004) characterising an amplification of the local line flux,  $F_{\text{loc}} = \mathcal{R}(r)\mathcal{M}(\mu_i, \mu_e)$ , which is shifted to the observed energy by the  $g$ -factor,  $g = E/E_{\text{rest}}$ . Note, that the  $\delta$ -function in this equation is in the observed energy while in the eq. (10) it was in the local energy. The transfer function for a photon number density flux is  $G = g^2 l \mu_e$ , where the lensing,  $l$ , characterises amplification due to focusing of the light rays (caused by light bending). As mentioned in the previous sections, each part that contributes to the overall shape of the observed line,  $\mathcal{R}(r)$ ,  $\mathcal{M}(\mu_i, \mu_e)$ ,  $G(r, \varphi)$  as well as the energy shift  $g(r, \varphi)$  are depicted in the Appendices A and B. Additionally we also show the overall map of the observed flux  $F_{\text{obs}}(r, \varphi) = G \mathcal{R}(r)\mathcal{M}(\mu_i, \mu_e)$  in the equatorial plane in Figs. B3, B6 and B9. Note, that in the Eq. (11) for each observed energy one integrates this function along the energy shift contour.

The shape of the relativistically broadened spectral line of iron for different assumptions on radial emissivity and emission directionality is shown in Fig. 4. One can see that the broken power-law emissivities result in quite a different line shape only for a very low locations of the corona when compared with a lamp-post illumination profile, in both cases an isotropic local emission being assumed. The differences might be very well explained by comparing the emissivity profiles in Fig. A1. The broken power-law emissivity underestimates the flux, the largest deficiency occurs in the region very close to the black hole,

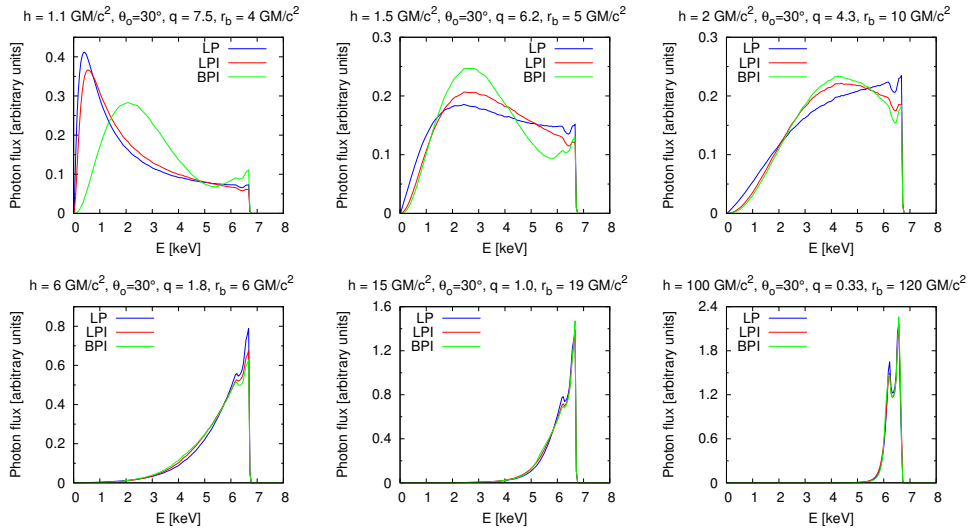


**Figure 4.** The comparison between the shape of the line in the lamp-post geometry with numerically computed angular directionality (*blue*) and with isotropic emission (*red*), and with the radial broken power-law emission with isotropic directionality (*green*). The height,  $h$ , the value of the inner radial power-law index,  $q$ , and the break radius,  $r_b$ , where it changes to  $q_{\text{out}} = 3$ , are shown at the top of each graph. The inclination of the observer is  $\theta_o = 30^\circ$ , the spin of the black hole is  $a = 1 \text{ GM}/c$  and the photon index of the primary source is  $\Gamma = 2$ .

where the gravitational redshift is large, and around the break radius,  $r_b$ . Note, that in Fig. 4 the line flux is in all cases normalised to unit total flux, so the spectral line for broken power-law radial profile is not below that one for the lamp-post geometry for all energies. One can see, however, that the line flux is much lower in two energy bands, one, where the energy shift is large with small values of g-factor,  $g \ll 1$ , (i.e. for low energies) and one when the g-factor is widely spread around unity (i.e. energies around iron line rest energy) that corresponds to the break radius region. Note, that the deficiency in the flux for low heights changes to an excess in flux for high heights of the primary source.

Further differences in the line shape arise when isotropic emission is compared with the numerically computed one given by the emission directionality function  $\mathcal{M}(\mu_i, \mu_e)$ . Again these differences are large only for low heights of the corona. The numerically computed directionality results in larger flux for low energies and energies around the rest energy of the line. This is mainly due the incident angle being very high both in the vicinity of the black hole as well as farther away from the centre (see the top left panel in Fig. 3) when the emission directionality function acquires higher values (see the bottom panel in the same figure).

To see how the shape of the relativistically broadened line depends on the height of the source, let's compare the line for three different spins and three different heights (Fig. 5). One immediately sees that the line is much narrower for higher heights even for the extreme Kerr black hole. This is due to the fact that the disc is illuminated much more homogeneously from higher lamps and since the area of the inner part of the disc, where

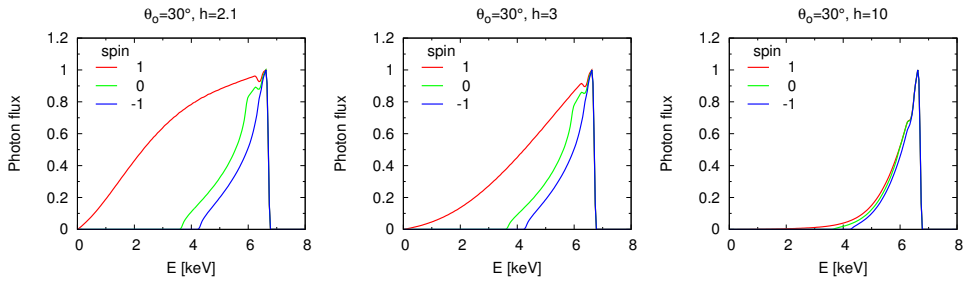


**Figure 5.** The comparison between the shape of the line in the lamp-post geometry for the Schwarzschild (*green*) and co-rotating (*red*) and counter-rotating (*blue*) extreme Kerr black holes for the primary source height,  $h = 2.1, 3$  and  $10 \text{ GM}/c^2$ . The inclination of the observer is  $\theta_o = 30^\circ$  and the photon index of the primary source is  $\Gamma = 2$ .

the red wing of the line arises, is very small compared to the area of the whole disc. Thus the shape of the line changes very little for different black hole spins if the corona is positioned more than  $10 \text{ GM}/c^2$  above the centre. Opposite is also true, i.e. if the black hole counter-rotates with an extreme spin, one would not be able to distinguish between different heights of the corona if the height is below approximately  $10 \text{ GM}/c^2$  above the centre. This is due to the fact that in this case the hole in the disc below marginally stable orbit ( $r_{\text{ms}} = 9 \text{ GM}/c^2$ ) is quite large and the disc illumination for small heights of the primary source changes mainly below this radius while it does not change that much above the inner edge of the disc.

## 5 Application to MCG-6-30-15

Using the computations from previous sections we have prepared a new XSPEC model for the relativistically broadened Iron line in the lamp-post geometry, see the Appendix C for more details. To find out what value of the height of the primary source one can expect in real observations where large spin have been observed in the past, we applied our new lamp-post model to the XMM-Newton spectrum of a nearby Seyfert 1 galaxy MCG-6-30-15. Very broad iron line was reported in this source by several authors (e.g. Fabian et al., 2002; Ballantyne et al., 2003; Vaughan and Fabian, 2003; Brenneman and Reynolds, 2006). We followed the analysis presented in Svoboda et al. (2009) and we employed the same model for the underlying X-ray continuum. However, we have used the new KYNRLPLI model instead of the KYRLINE (Dovčiak et al., 2004b) so that we replaced the broken power-law radial emissivity by the one that corresponds to the lamp-post geometry. In XSPEC syntax the overall model reads: PHABS\*(POWERLAW+ZGAUSS+ZGAUSS+KYNRLPLI). The best-fit parameter values and their errors are shown in the table in the right panel of Fig. 6. The parameters not shown in the table were frozen to their best-fit values from the previous model set-up. The reduced  $\chi^2$  value was 1.33. The contour plot of the primary source height versus the black hole spin is shown in the left panel of Fig. 6. The best-fit value for the height,  $h = 2.3 \text{ GM}/c^2$ , confirms our findings that if the primary source of power-law radiation is static, it has to be located very close to the black hole so that it illuminates the inner regions by large enough intensity to reveal the imprints of high spin in the observed spectrum.

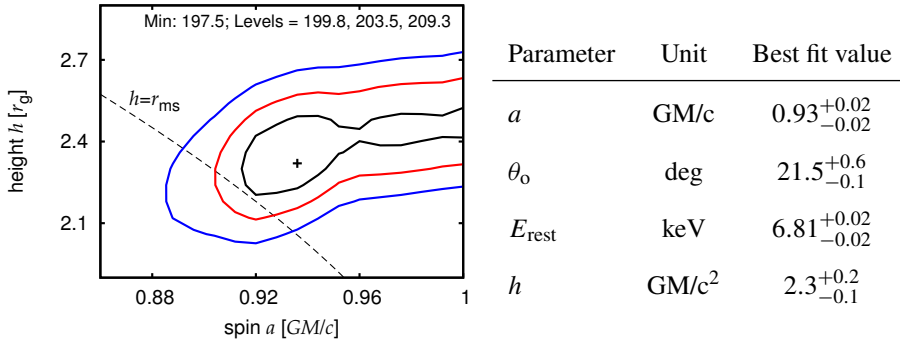


**Figure 6.** *Left:* The  $\chi^2$  contour graphs for the height,  $h$ , versus spin,  $a$ . Other parameters were kept frozen. *Right:* The best fit values and their errors for the parameters of the model.

## 6 Conclusions

In this paper we have compared two types of iron line radial emissivity profiles, the one governed by the illumination in the lamp-post geometry and the radial broken power-law emissivity. We find that

- for the primary source height  $h \gtrsim 3 \text{ GM}/c^2$  the lamp-post geometry is very well approximated with the broken power-law emissivity with the inner power-law index  $q_{\text{in}} \lesssim 4$  and the outer index  $q_{\text{out}} = 3$ ,
- a very high radial power-law index,  $q > 5$ , may be achieved in the lamp-post geometry only for very small heights,  $h \lesssim 2 \text{ GM}/c^2$ , and, the difference in the line shape in the lamp-post geometry and the broken power-law emissivity becomes large,
- very high  $q$  values originate very close to the central black hole, thus it can occur only in the case of a highly spinning black hole,
- high  $q$  values are mainly due to the gravitational redshift for the primary emission with the spectral index  $\Gamma > 1$  and due to the gravitational aberration for very small heights; the contribution of the light bending, as defined in this paper, is moderate.

Further we have investigated how the numerically computed emission directionality changes the profile of the iron line approximated by isotropic emission. We show that

- the emission from the disc where the incident and emission angles are large is greatly enhanced (limb brightening effect),
- the local emission directionality changes the shape of the broad line significantly, however, only for small heights,  $h \lesssim 10 \text{ GM}/c^2$ .

To summarise our modelling we conclude that in the lamp-post geometry with a corona approximated by a static isotropic point source a very broad iron line profile arises for highly spinning black holes only for the heights  $h \lesssim 5 \text{ GM}/c^2$ , while for the heights  $h \gtrsim 10 \text{ GM}/c^2$  the non-spinning and extremely spinning black holes are indistinguishable.

Similar conclusions were drawn by Dauser et al. (2013) for a moving elongated jet-like structure along the axis. Another interesting conclusion in their paper is that such a vertically extended region may be very well approximated by a point source at some

effective intermediate height. On the other hand, Wilkins and Fabian (2012) show that such steep emissivities may still be reached even if the corona is extended horizontally (as far as  $30 \text{ GM}/c^2$ ), provided it is very low above the disc (as low as  $2 \text{ GM}/c^2$ ). For a more detailed discussion on the prospects of spin determination using X-ray reflection we refer the reader to a recent paper by Fabian et al. (2014).

## ACKNOWLEDGEMENTS

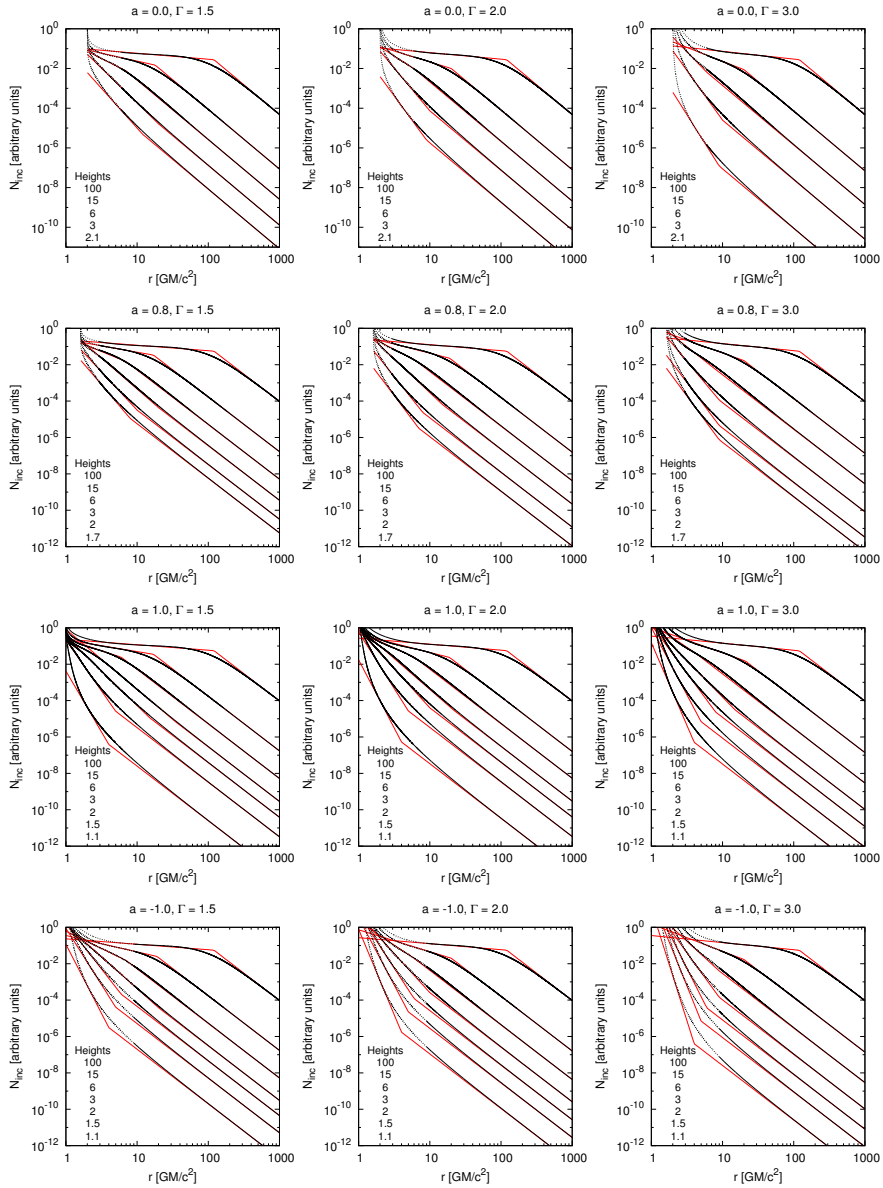
The research leading to these results has received funding from the European Union Seventh Framework Programme (FP7/2007-2013) under grant agreement n°312789. RG would like to thank French GdR PCHE and the CNRS-AV exchange programme for their support. JS acknowledges financial support from the grant 14-20970P of the Czech Science Foundation. GM acknowledges financial support from Agenzia Spaziale Italiana (ASI).

## REFERENCES

- Arnaud, K. A. (1996), XSPEC: The First Ten Years, in G. H. Jacoby and J. Barnes, editors, *Astronomical Data Analysis Software and Systems V, A.S.P. Conference Series*, volume 101, p. 17.
- Ballantyne, D. R., Vaughan, S. and Fabian, A. C. (2003), A two-component ionized reflection model of MCG–6-30-15, *Monthly Notices Roy. Astronom. Soc.*, **342**, p. 11.
- Biretta, J., Junor, W. and Livio, M. (2002), Evidence for initial jet formation by an accretion disk in the radio galaxy M87, *New Astronomy Reviews*, **46**, pp. 239–245.
- Blandford, R. D. and Znajek, R. L. (1977), Electromagnetic extraction of energy from Kerr black holes., *Monthly Notices Roy. Astronom. Soc.*, **179**, pp. 433–456.
- Brenneman, L. W. and Reynolds, C. S. (2006), Constraining Black Hole Spin Via X-ray Spectroscopy, *Astrophys. J.*, **652**, p. 42.
- Cackett, E. M. and Miller, J. M. (2013), Broad iron lines in neutrons stars: dynamical broadening or wind scattering?, *Astrophys. J.*, **777**, p. 5.
- Cackett, E. M., Zoghbi, A., Reynolds, C., Fabian, A. C., Kara, E., Uttley, P. and Wilkins, D. R. (2014), Modelling the broad Fe K reverberation in the AGN NGC 4151, *Monthly Notices Roy. Astronom. Soc.*, **438**, pp. 2980–2994.
- Cunningham, C. T. (1975), The effects of redshifts and focusing on the spectrum of an accretion disk around a Kerr black hole, *Astrophys. J.*, **202**, p. 788.
- Dauser, T., Garcia, J., Wilms, J., Bock, M., Brenneman, L. W., Falanga, M., Fukumura, K. and Reynolds, C. S. (2013), Irradiation of an accretion disc by a jet: general properties and implications for spin measurements of black holes, *Monthly Notices Roy. Astronom. Soc.*, **430**, pp. 1694–1708.
- Dovčiak, M. (2004), *Radiation of Accretion Discs in Strong Gravity*, PhD thesis, Charles University, Prague.
- Dovčiak, M., Karas, V., Martocchia, A., Matt, G. and Yaqoob, T. (2004a), An XSPEC model to explore spectral features from black-hole sources, in *Proceedings of RAGtime: Workshops on black holes and neutron stars*, volume 4/5, p. 35.
- Dovčiak, M., Karas, V. and Yaqoob, T. (2004b), An Extended Scheme for Fitting X-Ray Data with Accretion Disk Spectra in the Strong Gravity Regime, *Astrophys. J. Suppl.*, **153**, pp. 205–221.
- Dovčiak, M., Muleri, F., Goosmann, R. W., Karas, V. and Matt, G. (2011), Light bending scenario for accreting black holes in X-ray polarimetry, *Astrophys. J.*, **731**, p. 17.

- Dumont, A. M., Abrassart, A. and Collin, S. (2000), A code for optically thick and hot photoionized media, *Astronomy and Astrophysics*, **357**, p. 17.
- Emmanoulopoulos, D., Papadakis, I. E., Dovčiak, M. and McHardy, I. M. (2014), General relativistic modelling of the negative reverberation X-ray time delays in AGN, *Monthly Notices Roy. Astronom. Soc.*, **439**, pp. 3931–3950.
- Fabian, A. C., Kara, E., Walton, D. J., Wilkins, D. R., Ross, R. R., Lozanov, K., Uttley, P., Gallo, L. C., Zoghbi, A., Miniutti, G., Boller, T., Brandt, W. N., Cackett, E. M., Chiang, C.-Y., Dwelly, T., Malzac, J., Miller, J. M., Nardini, E., Ponti, G., Reis, R. C., Reynolds, C. S., Steiner, J., Tanaka, Y. and Young, A. J. (2013), Long XMM observation of the Narrow-Line Seyfert 1 galaxy IRAS13224-3809: rapid variability, high spin and a soft lag, *Monthly Notices Roy. Astronom. Soc.*, **429**, p. 7.
- Fabian, A. C., Parker, M. L., Wilkins, D. R., Miller, J. M., Kara, E., Reynolds, C. S. and Dauser, T. (2014), On the determination of the spin and disc truncation of accreting black holes using X-ray reflection, *Monthly Notices Roy. Astronom. Soc.*, **439**, pp. 2307–2313.
- Fabian, A. C., Rees, M. J., Stella, L. and White, N. E. (1989), X-ray fluorescence from the inner disc in Cygnus X-1, *Monthly Notices Roy. Astronom. Soc.*, **238**, pp. 729–736.
- Fabian, A. C., Vaughan, S., Nandra, K., Iwasawa, K., Ballantyne, D. R., Lee, J. C., De Rosa, A., Turner, A. and Young, A. J. (2002), A long hard look at MCG-6-30-15 with XMM-Newton, *Monthly Notices Roy. Astronom. Soc.*, **335**, p. 5.
- Fabian, A. C., Zoghbi, A., Ross, R. R., Uttley, P., Gallo, L. C., Brandt, W. N., Blustin, A. J., Boller, T., Caballero-García, M. D., Larsson, J., Miller, J. M., Miniutti, G., Ponti, G., Reis, R. C., Reynolds, C. S., Tanaka, Y. and Young, A. J. (2009), Broad line emission from iron K- and L-shell transitions in the active galaxy 1H 0707-495., *Nature*, **459**, pp. 540–2.
- Fabian, A. C., Zoghbi, A., Wilkins, D., Dwelly, T., Uttley, P., Schartel, N., Miniutti, G., Gallo, L., Grupe, D., Komossa, S. and Santos-Lleo, M. (2011), 1H0707-495 in 2011: An X-ray source within a gravitational radius of the event horizon, *Monthly Notices Roy. Astronom. Soc.*, **419**, p. 9.
- Frank, J., King, A. and Raine, D. J. (2002), *Accretion Power in Astrophysics*, UK: Cambridge University Press, Cambridge, third edition, ISBN 0521620538.
- García, J., Dauser, T., Reynolds, C. S., Kallman, T. R., McClintock, J. E., Wilms, J. and Eikmann, W. (2013), X-ray reflected spectra from accretion disk models. III. A complete grid of ionized reflection calculations, *Astrophys. J.*, **768**, p. 146.
- Ghisellini, G., Haardt, F. and Matt, G. (2004), Aborted jets and the X-ray emission of radio-quiet AGNs, *Astronomy and Astrophysics*, **413**, p. 11.
- Haardt, F. and Matt, G. (1993), X-ray polarization in the two-phase model for AGN and X-ray binaries, *Monthly Notices Roy. Astronom. Soc.*, **261**, pp. 346–352.
- Martocchia, A. and Matt, G. (1996), Iron K $\alpha$  line intensity from accretion discs around rotating black holes, *Monthly Notices Roy. Astronom. Soc.*, **282**, pp. L53–L57.
- Matt, G., Perola, G. C. and Piro, L. (1991), The iron line and high energy bump as X-ray signatures of cold matter in Seyfert 1 galaxies., *Astronomy and Astrophysics*, **247**, pp. 25–34.
- Miller, J. M., Parker, M. L., Fuerst, F., Bachetti, M., Harrison, F. A., Barret, D., Boggs, S. E., Chakrabarty, D., Christensen, F. E., Craig, W. W., Fabian, A. C., Grefenstette, B. W., Hailey, C. J., King, A. L., Stern, D. K., Tomsick, J. A., Walton, D. J. and Zhang, W. W. (2013), NuSTAR Spectroscopy of GRS 1915+105: Disk Reflection, Spin, and Connections to Jets, *Astrophys. J.*, **775**, p. L45.
- Miller, L. and Turner, T. J. (2013), The hard X-ray spectrum of NGC 1365: scattered light, not black hole spin, *Astrophys. J.*, **773**, p. L5.

- Miniutti, G. and Fabian, A. C. (2004), A light bending model for the X-ray temporal and spectral properties of accreting black holes, *Monthly Notices Roy. Astronom. Soc.*, **349**, pp. 1435–1448.
- Mirabel, I. F. and Rodríguez, L. F. (1998), Microquasars in our Galaxy, *Nature*, **392**, pp. 673–676.
- Niedźwiecki, A. and Miyakawa, T. (2010), General relativistic models of the X-ray spectral variability of MCG-6-30-15, *Astronomy and Astrophysics*, **509**, p. A22.
- Peterson, B. M. (1997), *An Introduction to Active Galactic Nuclei*, New York Cambridge University Press, Cambridge, ISBN 0521473489.
- Ponti, G., Gallo, L. C., Fabian, A. C., Miniutti, G., Zoghbi, A., Uttley, P., Ross, R. R., Vasudevan, R. V., Tanaka, Y. and Brandt, W. N. (2009), Relativistic disc reflection in the extreme NLS1 IRAS13224-3809, *Monthly Notices Roy. Astronom. Soc.*, **406**, pp. 2591–2604.
- Risaliti, G., Harrison, F. A., Madsen, K. K., Walton, D. J., Boggs, S. E., Christensen, F. E., Craig, W. W., Grefenstette, B. W., Hailey, C. J., Nardini, E., Stern, D. and Zhang, W. W. (2013), A rapidly spinning supermassive black hole at the centre of NGC 1365, *Nature*, **494**, p. 22.
- Ross, R. R. and Fabian, A. C. (2005), A comprehensive range of X-ray ionized reflection models, *Monthly Notices Roy. Astronom. Soc.*, **358**, p. 6.
- Svoboda, J., Dovčiak, M., Goosmann, R. and Karas, V. (2009), Role of emission angular directionality in spin determination of accreting black holes with a broad iron line, *Astronomy and Astrophysics*, **507**, pp. 1–17.
- Svoboda, J., Dovčiak, M., Goosmann, R. W., Jethwa, P., Karas, V., Miniutti, G. and Guainazzi, M. (2012), Origin of the X-ray disc-reflection steep radial emissivity, *Astronomy and Astrophysics*, **545**, p. 10.
- Svoboda, J., Dovčiak, M., Goosmann, R. W. and Karas, V. (2014), On the interplay between radial and angular reflection emissivity from the black hole accretion disc, in J. Bičák and T. Ledvinka, editors, *Relativity and Gravitation, Springer Proceedings in Physics*, volume 157 of *Springer Proceedings in Physics*, pp. 415–422, Springer International Publishing, Cham, ISBN 978-3-319-06760-5.
- Vaughan, S. and Fabian, A. C. (2003), A long, hard look at MCG-6-30-15 with XMM-Newton II: detailed EPIC analysis and modelling, *Monthly Notices Roy. Astronom. Soc.*, **348**, p. 25.
- Verner, D., Yakovlev, D., Band, I. and Trzhaskovskaya, M. (1993), Subshell Photoionization Cross Sections and Ionization Energies of Atoms and Ions from He to Zn, *Atomic Data and Nuclear Data Tables*, **55**, pp. 233–280.
- Wilkins, D. R. and Fabian, A. C. (2011), Determination of the X-ray reflection emissivity profile of 1H 0707-495, *Monthly Notices Roy. Astronom. Soc.*, **414**, p. 9.
- Wilkins, D. R. and Fabian, A. C. (2012), Understanding X-ray reflection emissivity profiles in AGN: locating the X-ray source, *Monthly Notices Roy. Astronom. Soc.*, **424**, pp. 1284–1296.
- Wilms, J., Reynolds, C. S., Begelman, M. C., Reeves, J., Molendi, S., Staubert, R. and Kendziorra, E. (2001), XMM-EPIC observation of MCG-6-30-15: Direct evidence for the extraction of energy from a spinning black hole?, *Monthly Notices Roy. Astronom. Soc.*, **328**, p. 6.

**A The radial illumination profile**

**Figure A1.** The radial profile of the incident flux,  $N_i(r)$ , defined in Eq. (2), for the photon index  $\Gamma = 1.5, 2$  and  $3$  (left to right) and the BH spin  $a = 0, 0.8, 1$  and  $-1 \text{ GM}/c$  (top to bottom). For better clarity, the results shown for different heights, as depicted in each panel, are renormalized so as not to cross. The red lines represent the approximating broken-power-law profiles with the outer slope set to  $-3$  (see the Tables A1–A4 for details).

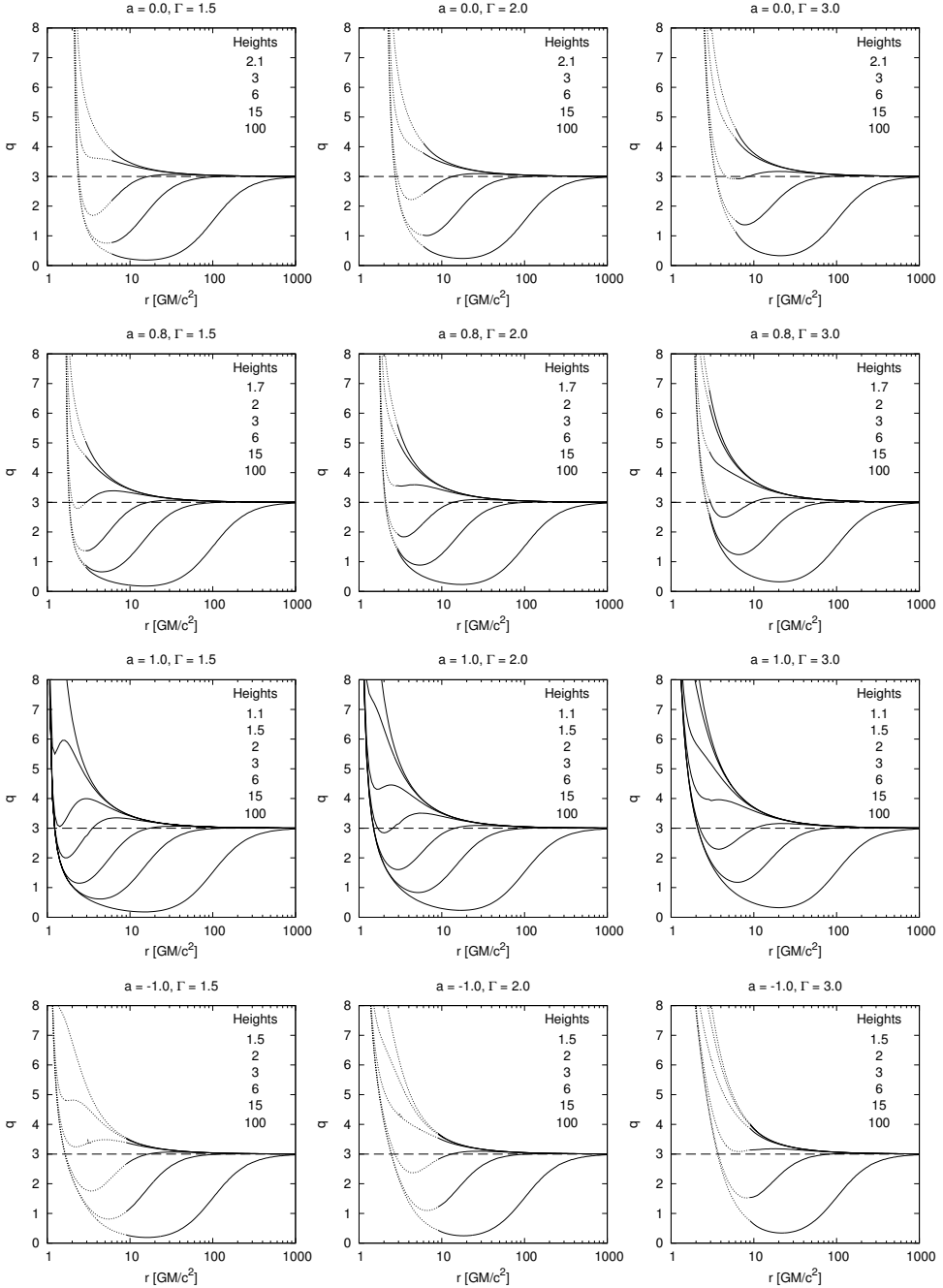


**Figure A2.** The radial dependence of the power-law index  $q(r)$ , defined in Eq. (8), for the photon index  $\Gamma = 1.5, 2$  and  $3$  (left to right) and the BH spin  $a = 0, 0.8, 1$  and  $-1 \text{ GM}/c$  (top to bottom). The results for different heights, as depicted on each panel, are shown by solid lines above and by dotted lines below the marginally stable orbit.

**Table A1.** The values of the inner slope for the broken power-law,  $q_i$ , and the break radius,  $r_b$ , for different height,  $h$ , (rows) and photon index,  $\Gamma$ , (columns) in the case of a non-rotating Schwarzschild black hole (with the spin  $a = 0$  GM/c, horizon  $r_h = 2$  GM/c<sup>2</sup> and marginally stable orbit  $r_{ms} = 6$  GM/c<sup>2</sup>). Both the height and the break radius are specified in units of GM/c<sup>2</sup>. These values correspond to the broken power-law dependences in the top panels in Fig. A1.

$a = 0$						
$\Gamma$	1.5		2		3	
$h$	$q_i$	$r_b$	$q_i$	$r_b$	$q_i$	$r_b$
100	0.3	120	0.33	120	0.39	120
15	0.8	18	1.1	20	1.4	20
6	1.8	7	2.3	6	3.7	6
3	3.5	20	4.3	10	5.0	10
2.1	4.0	12	4.9	9	5.7	9

**Table A2.** The same as in Table A1 but for the co-rotating Kerr black hole with the spin  $a = 0.8$  GM/c (horizon  $r_h = 1.6$  GM/c<sup>2</sup> and marginally stable orbit  $r_{ms} = 2.9$  GM/c<sup>2</sup>). These values correspond to the broken power-law dependences in the second row panels in Fig. A1.

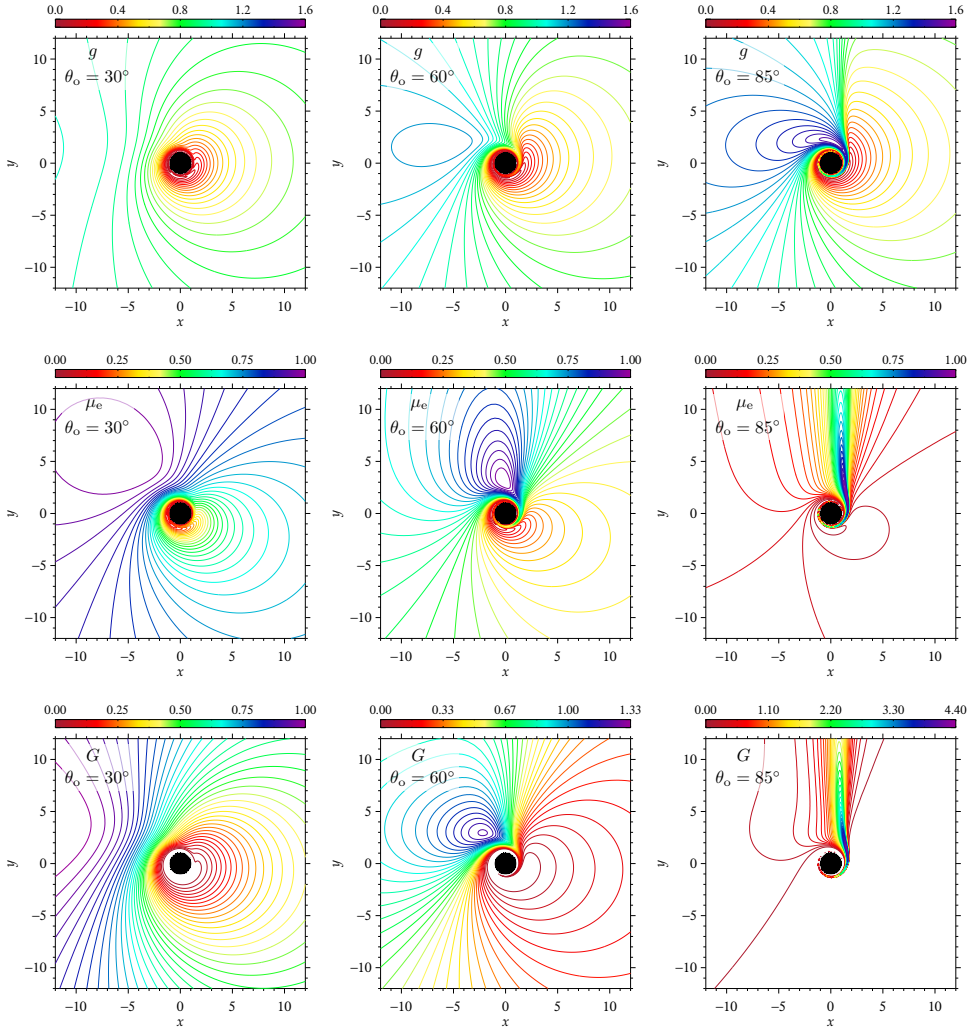
$a = 0.8$						
$\Gamma$	1.5		2		3	
$h$	$q_i$	$r_b$	$q_i$	$r_b$	$q_i$	$r_b$
100	0.3	120	0.33	120	0.39	120
15	0.7	17	1.0	19	1.4	20
6	1.6	7	2.0	6	3.1	8
3	3.4	20	3.7	15	4.7	9
2	4.2	10	4.9	8	5.2	9
1.7	4.6	8	5.2	7	5.3	9

**Table A3.** The same as in Table A1 but for the extreme co-rotating Kerr black hole (with the spin  $a = 1 \text{ GM}/c$ , horizon  $r_h = 1 \text{ GM}/c^2$  and marginally stable orbit  $r_{\text{ms}} = 1 \text{ GM}/c^2$ ). These values correspond to the broken power-law dependences in the third row panels in Fig. A1.

$a = 1$						
$\Gamma$	1.5		2		3	
$h$	$q_i$	$r_b$	$q_i$	$r_b$	$q_i$	$r_b$
100	0.3	120	0.33	120	0.39	120
15	0.65	17	1.0	19	1.4	21
6	1.3	6	1.8	6	2.6	4
3	3.3	35	3.4	22	4.0	15
2	3.8	15	4.3	10	5.3	8
1.5	5.6	5	6.2	5	7.4	5
1.1	6.7	4	7.5	4	9.1	4

**Table A4.** The same as in Table A1 but for the extreme counter-rotating Kerr black hole (with the spin  $a = -1 \text{ GM}/c$ , horizon  $r_h = 1 \text{ GM}/c^2$  and marginally stable orbit  $r_{\text{ms}} = 9 \text{ GM}/c^2$ ). These values correspond to the broken power-law dependences in the bottom panels in Fig. A1.

$a = -1$						
$\Gamma$	1.5		2		3	
$h$	$q_i$	$r_b$	$q_i$	$r_b$	$q_i$	$r_b$
100	0.3	120	0.33	120	0.39	120
15	0.9	19	1.2	20	1.5	20
6	1.9	7	2.6	6	3.6	9
3	3.5	20	4.3	10	5.4	9
2	5.0	6	6.0	6	7.8	6
1.5	6.2	5	7.4	5	9.7	5
1.1	7.6	4	9.4	4	12.4	4

**B Maps of the transfer function, emission directionality and observed flux**

**Figure B1.** The equatorial plane map of the energy shift,  $g$ , cosine of emission angle,  $\mu_e$ , and transfer function,  $G$ , (top to bottom) for the co-rotating Kerr black hole ( $a = 1 \text{ GM}/c$ ) and three inclination angles,  $\theta_o = 30^\circ$ ,  $60^\circ$  and  $85^\circ$  (left to right).

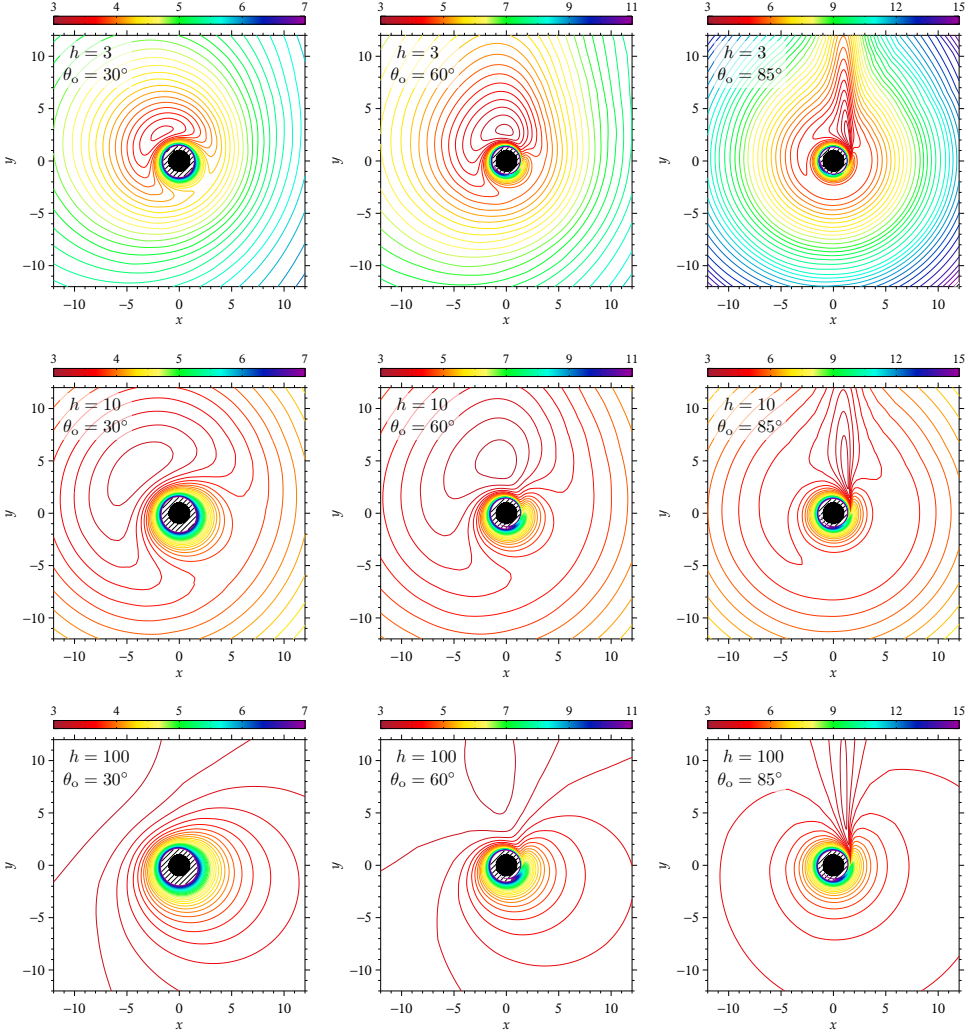


**Figure B2.** The equatorial plane map of the local flux emission directionality,  $\mathcal{M}(\mu_i, \mu_e)$ , for the co-rotating Kerr black hole ( $a = 1 \text{ GM}/c$ ) and three inclination angles,  $\theta_o = 30^\circ$ ,  $60^\circ$  and  $85^\circ$  (left to right), and three heights of the primary source,  $h = 3$ ,  $10$  and  $100 \text{ GM}/c^2$  (top to bottom).

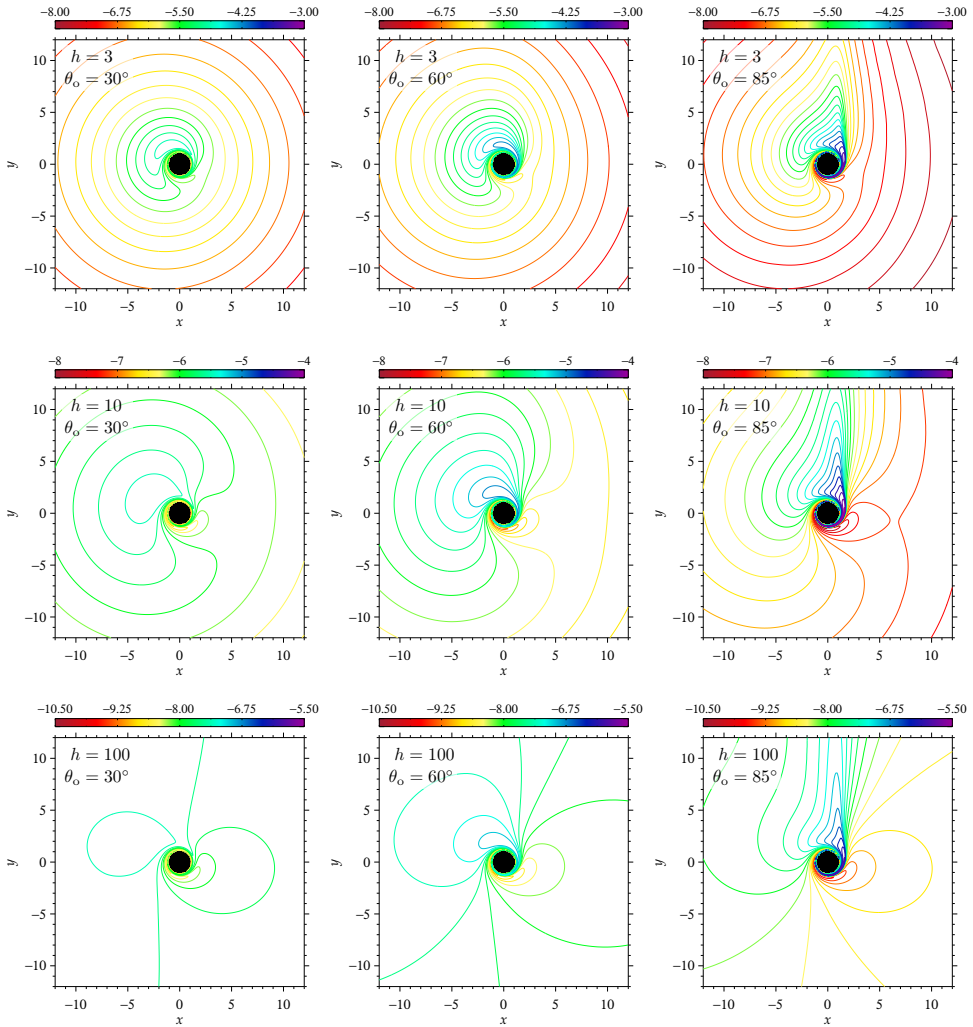


**Figure B3.** The equatorial plane map of the observed line flux,  $F_{\text{obs}}(r, \varphi)$ , for the co-rotating Kerr black hole ( $a = 1 \text{ GM}/c$ ) and three inclination angles,  $\theta_o = 30^\circ, 60^\circ$  and  $85^\circ$  (left to right), and three heights of the primary source,  $h = 3, 10$  and  $100 \text{ GM}/c^2$  (top to bottom).

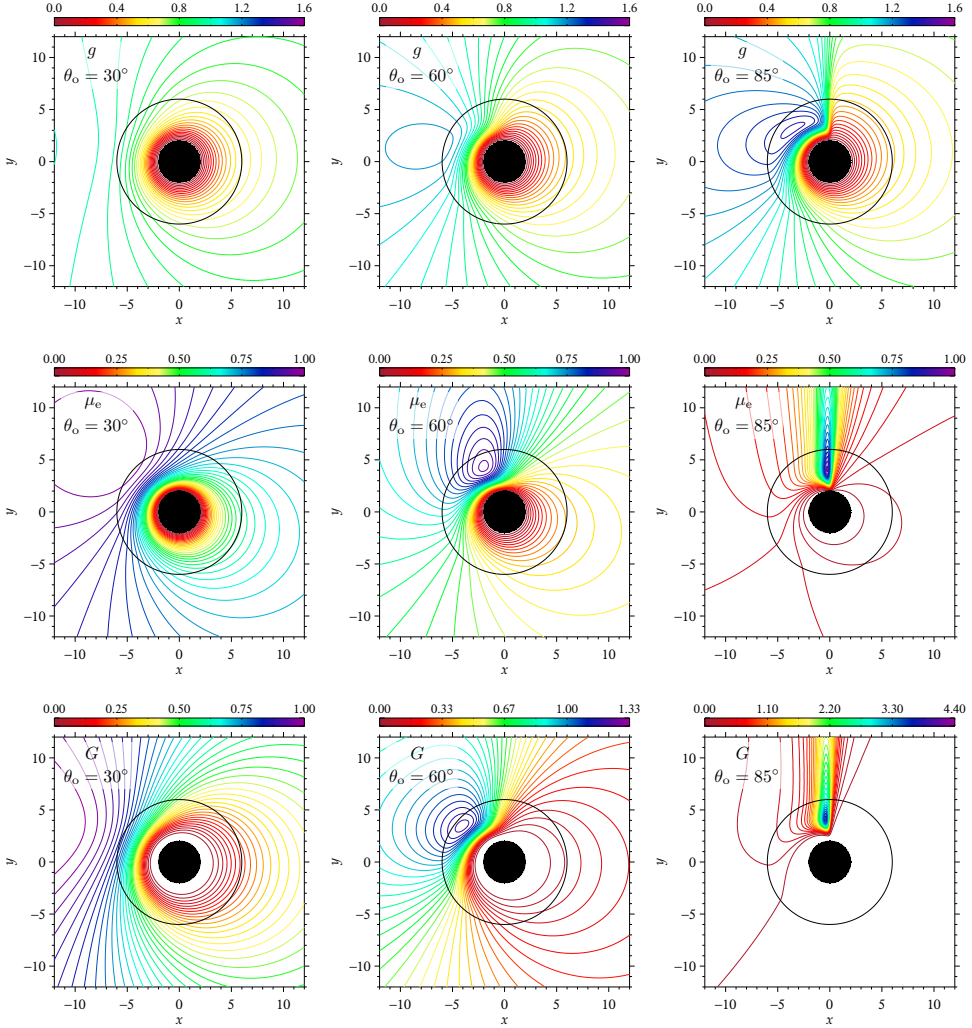


**Figure B4.** The equatorial plane map of the energy shift,  $g$ , cosine of emission angle,  $\mu_e$ , and transfer function,  $G$ , (top to bottom) for the Schwarzschild black hole ( $a = 0 \text{ GM}/c$ ) and three inclination angles,  $\theta_o = 30^\circ$ ,  $60^\circ$  and  $85^\circ$  (left to right). The marginally stable orbit at  $r_{\text{ms}} = 6 \text{ GM}/c^2$  is denoted by a black circle.

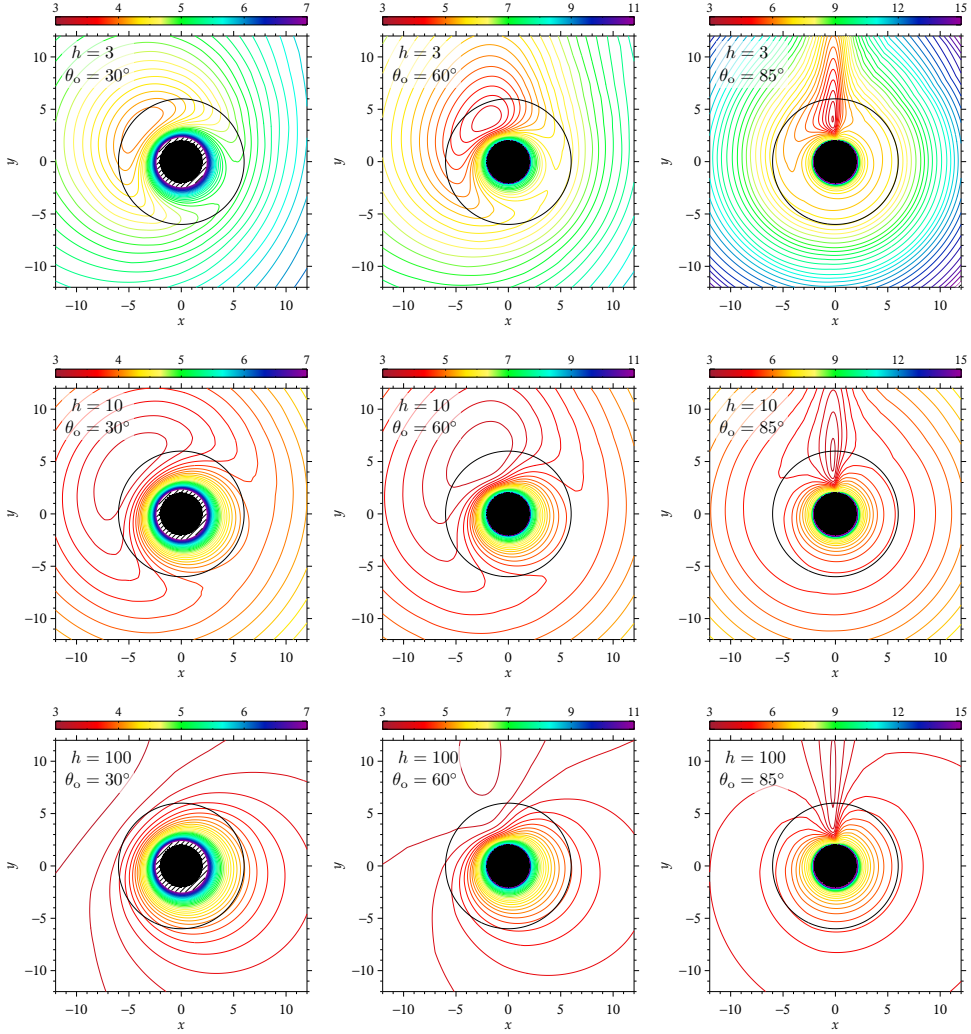


**Figure B5.** The equatorial plane map of the local flux emission directionality,  $\mathcal{M}(\mu_i, \mu_e)$ , for the Schwarzschild black hole ( $a = 0 \text{ GM}/c$ ) and three inclination angles,  $\theta_o = 30^\circ$ ,  $60^\circ$  and  $85^\circ$  (left to right), and three heights of the primary source,  $h = 3$ ,  $10$  and  $100 \text{ GM}/c^2$  (top to bottom). The marginally stable orbit at  $r_{\text{ms}} = 6 \text{ GM}/c^2$  is denoted by a black circle.

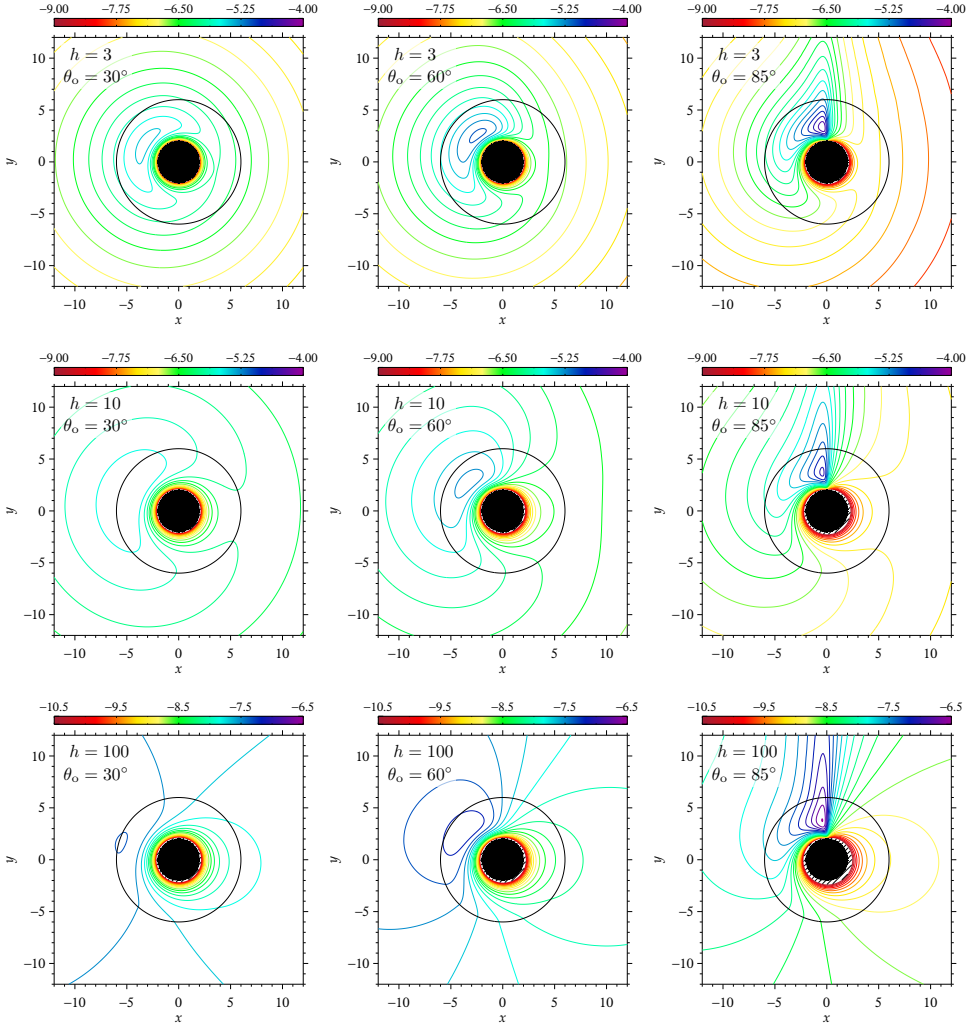


**Figure B6.** The equatorial plane map of the observed line flux,  $F_{\text{obs}}(r, \varphi)$ , for the Schwarzschild black hole ( $a = 0 \text{ GM}/c$ ) and three inclination angles,  $\theta_o = 30^\circ$ ,  $60^\circ$  and  $85^\circ$  (left to right), and three heights of the primary source,  $h = 3$ ,  $10$  and  $100 \text{ GM}/c^2$  (top to bottom). The marginally stable orbit at  $r_{\text{ms}} = 6 \text{ GM}/c^2$  is denoted by a black circle.

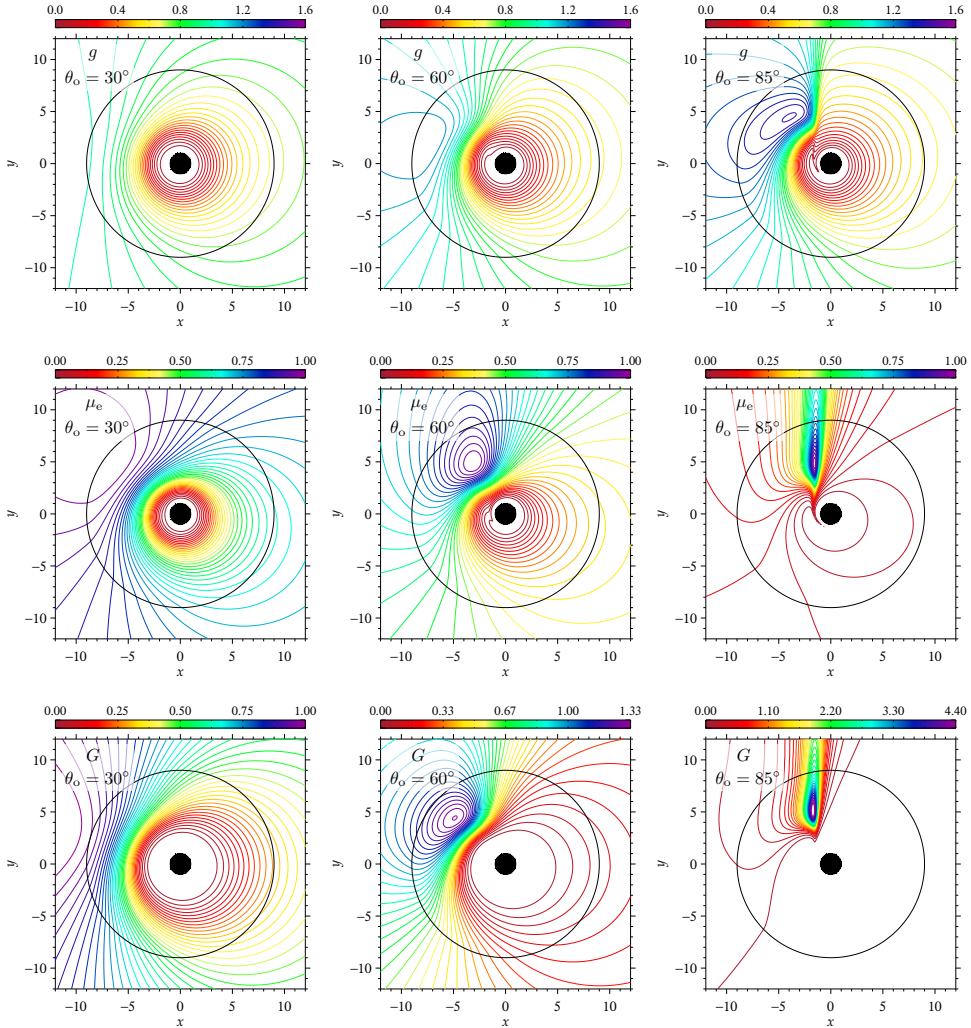


**Figure B7.** The equatorial plane map of the energy shift,  $g$ , cosine of emission angle,  $\mu_e$ , and transfer function,  $G$ , (top to bottom) for the counter-rotating Kerr black hole ( $a = -1 \text{ GM}/c$ ) and three inclination angles,  $\theta_o = 30^\circ$ ,  $60^\circ$  and  $85^\circ$  (left to right). The marginally stable orbit at  $r_{\text{ms}} = 9 \text{ GM}/c^2$  is denoted by a black circle.

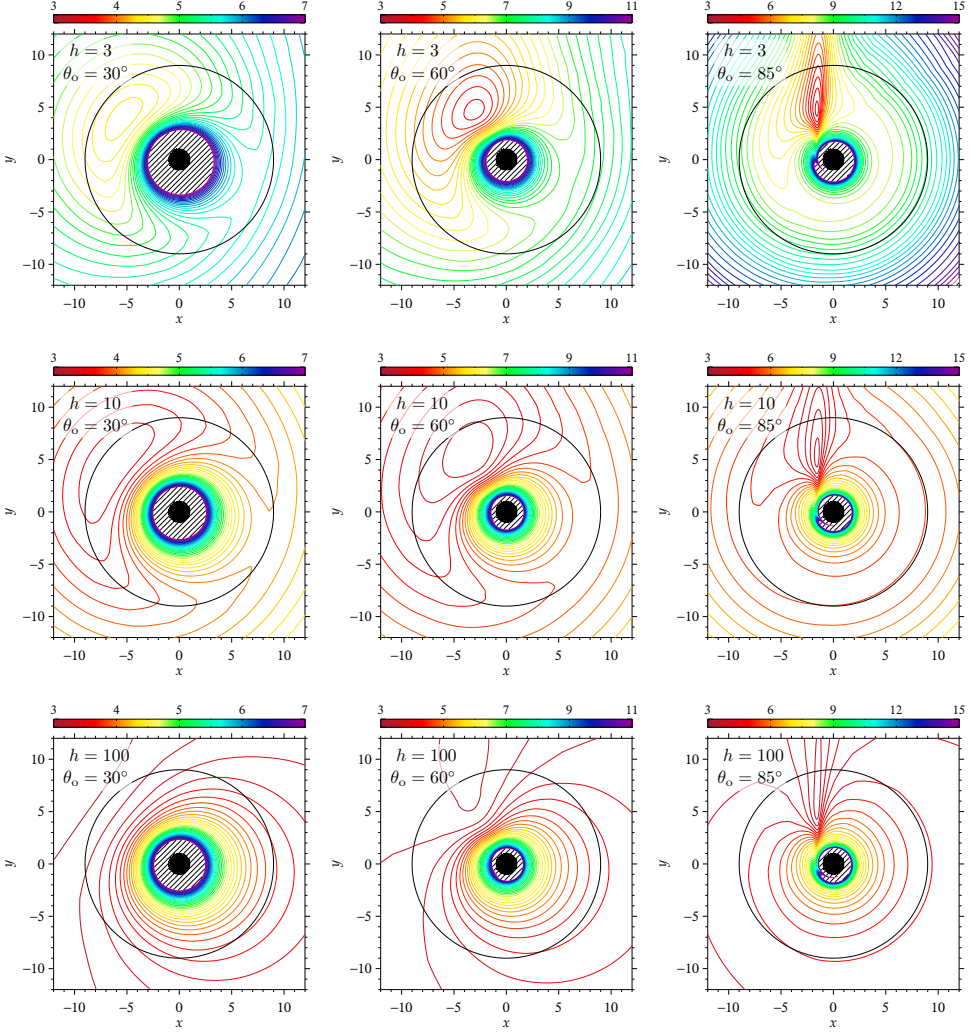


**Figure B8.** The equatorial plane map of the local flux emission directionality,  $\mathcal{M}(\mu_i, \mu_e)$ , for the counter-rotating Kerr black hole ( $a = -1 \text{ GM}/c$ ) and three inclination angles,  $\theta_o = 30^\circ$ ,  $60^\circ$  and  $85^\circ$  (left to right), and three heights of the primary source,  $h = 3$ ,  $10$  and  $100 \text{ GM}/c^2$  (top to bottom). The marginally stable orbit at  $r_{\text{ms}} = 9 \text{ GM}/c^2$  is denoted by a black circle.

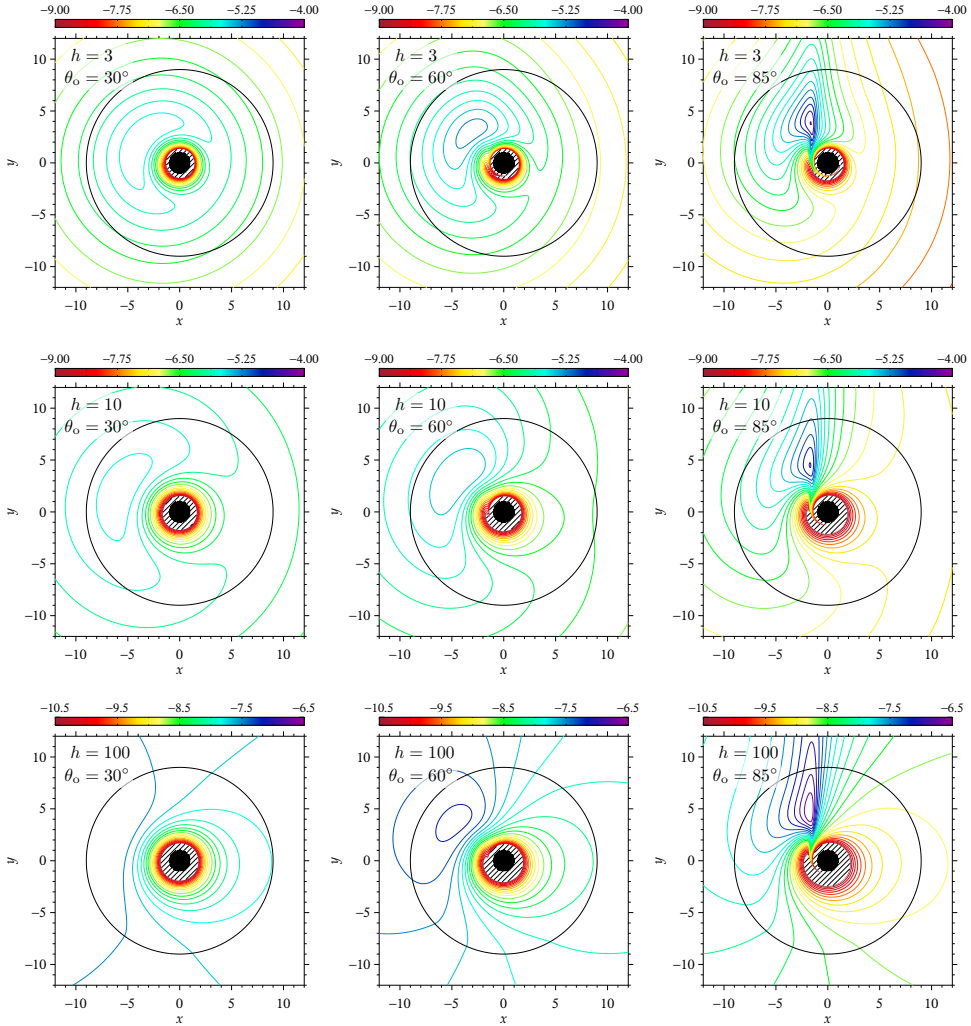


**Figure B9.** The equatorial plane map of the observed line flux,  $F_{\text{obs}}(r, \varphi)$ , for the counter-rotating Kerr black hole ( $a = -1 \text{ GM}/c$ ) and three inclination angles,  $\theta_o = 30^\circ$ ,  $60^\circ$  and  $85^\circ$  (left to right), and three heights of the primary source,  $h = 3$ ,  $10$  and  $100 \text{ GM}/c^2$  (top to bottom). The marginally stable orbit at  $r_{\text{ms}} = 9 \text{ GM}/c^2$  is denoted by a black circle.

### C The relativistic iron line model for the lamp-post geometry

To be able to use the lamp-post scheme with the data we have developed the model for XSPEC (Arnaud, 1996) – KYNRLPLI (KY Non-axisymmetric Relativistic Lamp-Post Line). This model is based on the non-axisymmetric version of the KY package of models (Dovčiak et al., 2004a,b; Dovčiak, 2004).

The model approximates the corona above the disc by a static isotropic point source located on the rotational axis at height,  $h$ , above the disc (measured from the centre of the black hole). Thus the radial emissivity profile is given by the illumination from such corona. All relativistic effects are taken into account all the way from the primary source to the disc and from the disc to the observer.

The local flux angular dependence,  $\mathcal{M}(\mu_i, \mu_e)$ , is computed with the Monte Carlo code NOAR (Dumont et al., 2000), see also Fig. 3 and Appendix B.

As is usual in non-axisymmetric KY models, it is possible to choose that the radiation comes only from a segment of the disc to simulate an emission from a spot. The inner and outer radius might be set either in physical units of  $\text{GM}/c^2$  or as a multiple of the marginally stable orbit,  $r_{\text{ms}}$ .

On the other hand we have added a possibility to obscure part of the disc by a circular cloud in the observer’s sky (i.e. farther away from the centre). The centre of the cloud is set in impact parameters,  $\alpha$  and  $\beta$ , where  $\alpha$  is positive for approaching side of the disc and  $\beta$  is positive above the black hole and negative below it (in the observer’s sky).

**Table C1.** Description of the KYNRLPLI parameters par1–par9.

param. number	param.	unit	possible values	description
par1	$a$	$\text{GM}/c$	–1–1	black hole angular momentum
par2	$\theta_o$	deg	0–89	observer inclination ( $0^\circ$ – pole, $90^\circ$ – disc)
par3	$r_{\text{in}}$	$\text{GM}/c^2$	1–1000	inner disc edge
par4	ms		0, 1, 2	changes definition of inner edge 0: $r_{\text{in}} = \text{par3}$ 1: $r_{\text{in}} = \text{par3}$ but if $\text{par3} < r_{\text{ms}}$ then $r_{\text{in}} = r_{\text{ms}}$ 2: $r_{\text{in}} = \text{par3} \times r_{\text{ms}}$ , $r_{\text{out}} = \text{par5} \times r_{\text{ms}}$
par5	$r_{\text{out}}$	$\text{GM}/c^2$	1–1000	outer disc edge
par6	$\varphi_o$	deg	–180–180	lower azimuth of the disc segment
par7	$\Delta\varphi$	deg	0–360	width of the disc segment
par8	$h$	$\text{GM}/c^2$	1–100	height (location) of the primary
par9	$\Gamma$		1.1–3	primary energy power-law index

The model can be used also for computing polarisation in a very simple toy model where all the local line polarisation in the disc is fully polarised perpendicularly to the disc.

**Table C2.** Description of the KYNRLPLI parameters par10–par20.

param. number	param.	unit	possible values	description
par10	$\alpha_c$	$\text{GM}/c^2$		$\alpha$ -position of the obscuring cloud
par11	$\beta_c$	$\text{GM}/c^2$		$\beta$ -position of the obscuring cloud
par12	$r_c$	$\text{GM}/c^2$		radius of the obscuring cloud
par13	zshift			overall Doppler shift
par14	ntable		80	defines fits file with tables
par15	$n_r$		1–10 <sup>4</sup>	number of radial grid points
par16	division		0, 1	type of step in radial integration (0 – equidistant, 1 – exponential)
par17	$n_\varphi$		1–2 × 10 <sup>4</sup>	number of azimuthal grid points
par18	smooth		0, 1	smooth the resulting spectrum (0 – no, 1 – yes)
par19	Stokes		0–6	output of the computation: 0: photon number density flux (Stokes parameter I/E) 1: Stokes parameter Q/E 2: Stokes parameter U/E 3: Stokes parameter V/E 4: degree of polarization 5: linear polarization angle, $\chi = \frac{1}{2} \text{atan} \frac{U}{Q}$ 6: circular polarization angle, $\psi = \frac{1}{2} \text{asin} \frac{V}{\sqrt{Q^2+U^2+V^2}}$
par 20	$n_{\text{threads}}$		1–100	number of computation threads

Due to the fact that the non-axisymmetric models integrate the emission over the disc and thus are slower, the model may be run in multiple threads to use all CPU cores available for computing. In this case the XSPEC may need to be run with a preloaded thread library (e.g. LD\_PRELOAD=libpthread.so.0 \$HEADAS/bin/xspec)

As usual for spectral line models inside XSPEC, also the KYNRLPLI model is normalised to the unit total photon flux.

The model parameters, their definitions and possible values are summarised in Tables C1 and C2.

# Evolutionary tracks of millisecond pulsars with low-mass companions

Filip Ficek<sup>1</sup>, Mieszko Rutkowski<sup>1</sup> and Włodek Kluźniak<sup>2</sup>

<sup>1</sup>Institute of Physics, Jagiellonian University, ul. Łojasiewicza 11, 30-348 Kraków, Poland

<sup>2</sup>Nicolaus Copernicus Astronomical Center, Bartycka 18, 00-716 Warszawa, Poland

## ABSTRACT

We consider the evolution of millisecond radio pulsars in binary systems with a main-sequence or evolved stellar companion. Evolution of non-accreting binary systems with “eclipsing” millisecond pulsars was described by Kluźniak, Czerny and Ray (1992) who predicted that systems like the one containing the Terzan 5 PSR 1744-24A will in the future become accreting low mass X-ray binaries (LMXBs), while PSR 1957+20 may evaporate its companion. The model presented in the current paper gives similar results for these two objects and allows to obtain diverse evolutionary tracks of millisecond pulsars with low mass companions (black widows). Our results suggest that the properties of many black widow systems can be explained by an ablation phase lasting a few hundred million years. Some of these sources may regain Roche lobe contact in a comparable time, and become LMXBs.

**Keywords:** millisecond pulsar – redback – black widow – binary evolution – ablation – LMXBs – gravitational waves

## 1 INTRODUCTION

Millisecond pulsars are probably intimately connected with LMXBs, as was realized soon after their discovery: it was suggested that millisecond pulsars have been spun up in LMXBs and will end their history in the radio pulsar phase (Radhakrishnan and Srinivasan, 1982; Alpar et al., 1982). However, with the discovery of the eclipsing pulsars it was realized that some millisecond pulsars currently ablating their companions may re-enter the LMXB phase in a later epoch (Bisnovatyi-Kogan, 1989; Ergma and Fedorova, 1991; Kluźniak et al., 1992). Recent discoveries of many ablating binary systems have led to a rekindling of these ideas, and to the necessity of explaining the evolutionary status of these black widows and redbacks, as they are called (e.g. Roberts et al., 2014).

We are presenting an evolutionary model describing a binary system composed of a pulsar and its stellar companion. The model includes effects like gravitational wave emission by the binary, ablation of the companion, and pulsar spindown. In general, part of the ablated matter may accrete onto the neutron star and another part may leave the system. The computed evolutionary tracks begin with the pulsar turn-on at the conclusion of the standard epoch of accretion in a semi-detached phase. Throughout most of the computed

evolutionary history, the separation between the pulsar and the companion star is large enough for the latter to be below its Roche lobe. Therefore the only mechanism of mass loss considered in our model is ablation by the pulsar wind.

## 2 MODEL DESCRIPTION

The period of a binary system including a pulsar of mass  $M$  and its companion of mass  $m$  is

$$P = \frac{2\pi J^3(M+m)}{G^2 M^3 m^3}, \quad (1)$$

where  $J$  denotes total orbital angular momentum. The rate of change of the companion mass  $m$  is assumed to be proportional to the spin-down flux

$$\dot{m} \propto \frac{\dot{E}}{4\pi d^2} m^a P^b, \quad (2)$$

where  $\dot{E}$  is the energy loss of the pulsar primary owing to its spindown,  $d$  is the separation between the primary and the secondary, and  $a, b$  are model dependent exponents. In the simple model assumed in Kluźniak et al. (1992)  $a = b = 0$ . However, in Brookshaw and Tavani (1995) one may find  $a = 1/6$  and  $b = -4/3$ . We will adopt the latter values. The change of mass of the primary is in principle connected with  $\dot{m}$  as  $\dot{M} = -\beta\dot{m}$ . The coefficient  $\beta$  describes how much of the mass lost by the companion is accreted by the neutron star, and how much is lost from the binary in a wind, thus  $0 \leq \beta \leq 1$  with 0 corresponding to no accretion and 1 to no wind. We will take  $\beta = 0$ .

The change of angular momentum [first term in Eq. (5)] is connected with two processes: emission of the gravitational waves (GW) and mass loss from system. We take the rate of angular momentum loss to gravitational waves to be described by (e.g. Shapiro and Teukolsky, 1983)

$$\dot{J}_{\text{GW}} = -\frac{256\pi^3}{5} \frac{G}{c^5} \frac{J^2}{P^3}. \quad (3)$$

If we assume that specific angular momentum carried away by a wind escaping from the system is  $j = \alpha M J / [m(m+M)]$ , we have

$$\dot{J}_{\dot{m}} = \alpha(1-\beta) \frac{M J}{(M+m)} \frac{\dot{m}}{m}. \quad (4)$$

Both Equations (3) and (4) contribute to the rate of change of the angular momentum:  $\dot{J} = \dot{J}_{\dot{m}} + \dot{J}_{\text{GW}}$ . By differentiating Eq. (1) with respect to time we get the rate of change of the period

$$\frac{\dot{P}}{P} = 3 \frac{\dot{J}}{J} - \frac{2M + 3m}{M + m} \frac{\dot{M}}{M} - \frac{3M + 2m}{M + m} \frac{\dot{m}}{m}, \quad (5)$$

$$\dot{m} = \gamma \frac{\dot{E} m^{1/6} P^{-4/3}}{4\pi d^2}, \quad (6)$$

$$\dot{M} = -\beta \dot{m}, \quad (7)$$

$$\frac{\dot{J}}{J} = \frac{\alpha(1 - \beta)M}{m + M} \frac{\dot{m}}{m} - \frac{256\pi^3 G J}{5c^5 P^3}. \quad (8)$$

Equations (5), (6), (7) and (8) constitute a system of first-order ordinary differential equations, which we proceed to solve with various assumptions and different initial conditions.

In the simple case of no accretion onto the primary star, negligible companion mass,  $m \ll M$ , and hence negligible gravitational wave emission, the equations reduce to (Kluźniak et al., 1992)

$$\frac{\dot{P}}{P} = 3(\alpha - 1) \frac{\dot{m}}{m}, \quad (9)$$

and can be easily integrated, yielding

$$P(m) \propto m^{3(\alpha-1)}. \quad (10)$$

With suitable initial conditions the evolutionary paths on the  $P$  vs.  $m$  plot described by this equation can be made to pass through the current positions of some of the known pulsars, e.g. PSR 1957-20 (see the Appendix, Fig. A1).

The source of the energy driving the ablation process is pulsar spindown. From the magnetic dipole formula (e.g. Shapiro and Teukolsky, 1983) we have

$$\dot{E} = -\frac{B^2 R^6 \Omega^4 \sin^2 \theta}{6c^3}, \quad (11)$$

where  $B$  denotes the surface magnetic field near the pole,  $\Omega$  is the pulsar spin rate (the pulsar period being  $P_0 = 2\pi/\Omega$ ),  $R$  is the pulsar radius and  $\theta$  denotes the angle between the magnetic and the rotation axes (for simplicity we take  $\sin^2 \theta = 1$  and  $R = 10$  km). On the other hand we have  $\dot{E} = I\Omega\dot{\Omega}$ , where  $I$  is the moment of inertia of the pulsar. These two equations provide

$$\Omega(t) = \frac{\Omega_0}{\sqrt{2t/\tau + 1}}, \quad (12)$$

where  $\Omega_0 = \Omega(0)$  is the initial angular velocity of the pulsar and  $\tau = -\Omega(0)/\dot{\Omega}(0)$  is the characteristic age of the pulsar (at time  $t=0$ ). Equations (11) and (12), are used in Eq. (6) to find  $\dot{m}$  as a function of time.

When the secondary star is sufficiently close to the pulsar that it fills the Roche lobe, accretion through the inner Lagrangian point starts. This situation is not described by our

model, although our tracks may bring the system to this point. When the radius of the companion is equal to Roche lobe radius, the relation between orbital period  $P$  and companion mass  $m$  is

$$P = 2\pi \sqrt{\frac{A^3}{B^3 G}} m^{(3n-1)/2}, \quad (13)$$

where  $B \approx 0.462$ . The values of  $n$  and  $A$  correspond to the radius of the companion through  $r = Am^n$ . For degenerate stars like white dwarfs,  $n = -1/3$ , and for a hydrogen white dwarf  $A = 2.82 \times 10^4 M_\odot^{1/3}$  km (Shapiro and Teukolsky, 1983), while from Hamada and Salpeter (1961) one obtains  $A = 8.80 \times 10^3 M_\odot^{1/3}$  km for a helium white dwarf. One may also obtain this coefficient for a carbon white dwarf, which is  $A = 8.72 \times 10^3 M_\odot^{1/3}$  km (Hamada and Salpeter, 1961), it is almost indistinguishable from the helium one. Lines corresponding to Eq. (13) indicate where the evolutionary track may terminate in a Roche-lobe overflowing LMXB, depending on the companion type (Fig. 1).

### 3 RESULTS OF NUMERICAL CALCULATIONS

Using Mathematica, we solved numerically the system of four differential equations, i.e. Eqs. (5), (6), (7) and (8) discussed above. We consider a model with no accretion ( $\beta = 0$ ), we assume  $\gamma = 2.5 \times 10^4 \text{ s}^{10/3} \text{ g}^{-1/6}$  (cf., Chen et al., 2013) and, following Kluźniak et al. (1992), we take  $\alpha = 0.86$ . For the initial point on the  $(m, P)$  plane we use one of two points on the track of Tauris and Savonije (1999), which describes the evolution of a LMXB with an evolved companion. For the PSR 1957+20 and B1744-74A (Terzan 5) tracks we use the starting point of Kluźniak et al. (1992), corresponding to the point at which magnetic braking is supposed to lose importance in the evolution of binaries with a main sequence companion. Current system parameters are taken from ATNF Database (2014); Manchester et al. (2005), and they can be found in Table 1, together with other data, for the six tracks which are presented in Fig. 1.

Derived times of evolution are  $t_{\text{ev}} \simeq 7 \times 10^8$  y for PSR 1957+20 and  $t_{\text{ev}} \simeq 5.5 \times 10^9$  y for Terzan 5. For PSR 1957+20, evolution is steady, whereas for Terzan 5 one can distinguish three stages of evolution. The first stage, when the evolution curve is nearly a straight line, lasts about  $4.5 \times 10^8$  y. The second one, when the evolution path “turns downwards” on the  $P$  vs  $m$  plot, lasts  $2.4 \times 10^9$  y. The last stage, when gravitational radiation is dominant, lasts  $2.6 \times 10^9$  y. Objects with convex evolution curves evolve comparably fast: e.g. for J1807-2459A the evolution time is  $t_{\text{ev}} \simeq 5.7 \times 10^8$  y. The values of  $t_{\text{ev}}$  in parentheses in Table 1 (for the Terzan 5 pulsar and J1023+0038) correspond to the time it will take for the system to regain the line of Roche-lobe contact starting from the present position.

### 4 EVOLUTIONARY TRACKS

Evolution of the system depends on the ratio between angular momentum losses caused by ablation and gravitational wave emission. There seem to be three types of tracks.

In the case where gravitational waves emission can be neglected (like in the PSR 1957-20 system) the track is well described by the formula of Eq. (10). The system very nearly

**Table 1.** System parameters

Quantity	<b>PSR 1957+20</b>		<b>B1744-74A/Terzan 5</b>	
	Initial	Present	Initial	Present
$P$ [hr]	2.9	9.2	3.0	1.82
$m$ [ $M_{\odot}$ ]	0.235	0.022	0.235	0.087
$M$ [ $M_{\odot}$ ]	1.7	1.7	1.4	1.4
$\dot{m}$ [g/s]	$-2.0 \times 10^{17}$	$-7.6 \times 10^{14}$	$-1.1 \times 10^{17}$	$-3.1 \times 10^{14}$
$P_0$ [ms]	0.92	1.60	1.95	11.56
$B$ [G]	$4.0 \times 10^8$		$1.3 \times 10^{9.0}$	
$\mu$ [ $G \times \text{cm}^3$ ]	$4.0 \times 10^{26}$		$1.3 \times 10^{27}$	
$t_{\text{ev}}$ [y]	$6.72 \times 10^8$		$5.52 \times 10^9$ ( $5.90 \times 10^9$ )	
Quantity	<b>J1807-2459A</b>		<b>J2241-5236</b>	
	Initial	Present	Initial	Present
$P$ [hr]	1.75	1.71	1.75	3.50
$m$ [ $M_{\odot}$ ]	0.115	0.009	0.115	0.012
$M$ [ $M_{\odot}$ ]	1.4	1.4	1.4	1.4
$\dot{m}$ [g/s]	$-4.5 \times 10^{15}$	$-2.6 \times 10^{15}$	$-1.4 \times 10^{16}$	$-1.1 \times 10^{15}$
$P_0$ [ms]	2.91	3.06	1.98	2.19
$B$ [G]	$2.9 \times 10^8$		$2.4 \times 10^8$	
$\mu$ [ $G \times \text{cm}^3$ ]	$2.9 \times 10^{26}$		$2.4 \times 10^{26}$	
$t_{\text{ev}}$ [y]	$5.60 \times 10^8$		$7.88 \times 10^8$	
Quantity	<b>J1311-3430</b>		<b>J1023+0038</b>	
	Initial	Present	Present	Predicted
$P$ [hr]	1.75	1.56	4.73	0.31
$m$ [ $M_{\odot}$ ]	0.115	0.008	0.136	0.061
$M$ [ $M_{\odot}$ ]	1.4	1.4	1.4	1.4
$\dot{m}$ [g/s]	$-3.6 \times 10^{15}$	$-3.0 \times 10^{15}$	$-2.2 \times 10^{16}$	LMXB
$P_0$ [ms]	2.48	3.56	1.67	11.09
$B$ [G]	$2.0 \times 10^8$		$7.9 \times 10^8$	
$\mu$ [ $G \times \text{cm}^3$ ]	$2.0 \times 10^{26}$		$7.9 \times 10^{26}$	
$t_{\text{ev}}$ [y]	$5.44 \times 10^8$		$(1.8 \times 10^{10})$	

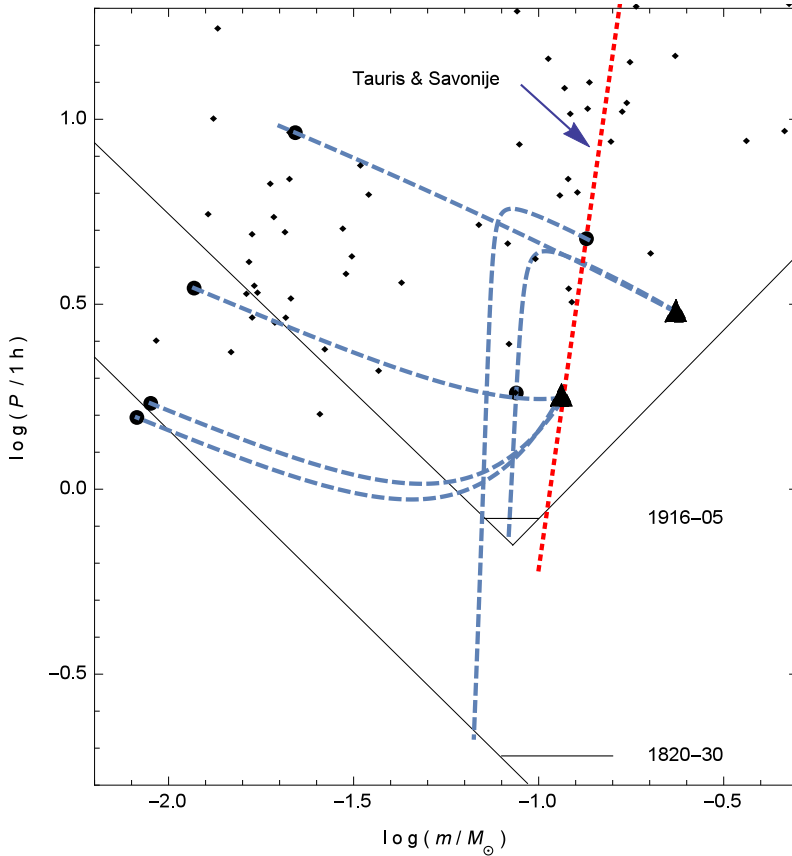


**Figure 1.** *Large dots* correspond to the present parameters of the observed pulsar systems for which the evolutionary tracks have been computed (*dashed blue lines*). *Small dots* are other objects taken from the ATNF Database (2014). *Solid lines* correspond to Roche lobe contact for a cold companion. The *short-dashed red line*, taken from Tauris and Savonije (1999), corresponds to LMXB evolution of a system with an evolved companion. Also shown (thin horizontal line segments) are the positions of two short-period LMXBs. The *filled triangles* mark plausible initial points of the evolutionary tracks.

follows a straight line on a  $\log P$  versus  $\log m$  plot. The slope of this line depends only on the parameter  $\alpha$ . The track may be deflected a little bit due to vestigial gravitational wave emission.

Another possible track passes through the Terzan 5 pulsar B1744-24A. In the initial phase of system evolution the track is similar to the one described in the previous paragraph. The difference is that at a certain moment, owing to pulsar spindown, gravitational wave emission starts to dominate over ablation. If, from that point on, mass loss were neglected (i.e. the evolution were driven by GW emission alone), the track would be a vertical line on the  $\log P$ – $\log m$  plot. In fact, a residual effect of ablation is still felt, and the track deviates slightly in the direction of lower companion mass (to the left in the figures).

Neglecting mass loss from and mass transfer in the system ( $\gamma = 0$  in Eq. (6)) one easily obtains the time elapsed in the evolution from binary period  $P_i$  to period  $P$ :

$$T = \frac{5c^5}{2048\pi^3 G J_i} (P^{8/3} P_i^{1/3} - P_i^3), \quad (14)$$

where  $J_i$  is the initial angular momentum (corresponding to  $P_i$ ). Time scales of evolution obtained from this equation are similar to the numerical values for the nearly vertical tracks in Fig. 1.

Tracks similar to those described above were already obtained by Kluźniak et al. (1992). They cover situations in the limit where one of the effects, ablation or GW emission, dominates over the other along each major segment of the trajectory (although, as remarked above in Section 3, PSR B1744-74A spends most of its evolutionary time in transition between two such states). It seems that systems with an evolved very low mass companion ( $m < 0.04M_\odot$ ) cannot evolve this way. For instance, obtaining a ‘‘Terzan-like’’ evolution track for these systems leads to evolution time amounting to several dozens of billion years. A third type of evolutionary track seems to be required.

We have found evolutionary tracks connecting the currently observed binary parameters of the pulsars J2241-5236, J1807-2459A and J1311-3430 with a plausible initial point and having reasonable time scales of evolution. These evolutionary tracks are characterized by angular momentum loss to both GW emission and ablation effects, and have a convex shape on a  $\log P$  versus  $\log m$  plot (Fig. 1). Eventually, the separation of the system components becomes large enough that GW emission loses importance, and the track becomes parallel to that of PSR 1957+20.

## 5 DISCUSSION

We have considered the evolution of millisecond radio pulsars with binary low-mass companions assuming simple formulae for the ablation rate of the companion by the pulsar wind. For the starting point of each evolutionary track that we considered we have taken a plausible moment of pulsar turn-on in an erstwhile LMXB, either along the standard evolutionary curve familiar from discussion of cataclysmic variables and the period gap, i.e. a binary with a main-sequence companion (Paczyński and Sienkiewicz, 1983), or along an evolutionary track with an evolved companion Tauris and Savonije (1999). Pulsar turn-on (or turn-off) in (potentially) accreting low mass binaries was discussed in Kluźniak et al. (1988).

We have reproduced the results of Kluźniak et al. (1992) who performed a similar study for the only two known eclipsing pulsars at the time (PSR 1957+20 and B1744-74A in Ter 5), and found that there are periods of their evolutionary history in the ablation phase when either one or the other of two major angular momentum loss mechanisms dominates (mass loss from the system or GW emission). We note that evolutionary tracks that we now find based on the Brookshaw and Tavani (1995) evaporation formula, Eq. (2), imply shorter initial pulsar periods than previously obtained, this can be seen from a comparison of the entries in Table 1 with the description of tracks (b) and (e) in the Appendix, Fig. A1.

We find that we are able to reproduce the current positions of typical millisecond radio pulsars with a low mass binary companion, typically this involves an ablation phase lasting several hundred years. However, we find that for the majority of the black widow pulsars known today the relative importance of the two considered angular momentum loss mechanisms is comparable in their evolutionary history, i.e. unlike in the case of PSR 1957+20 and B1744-74A, neither GW emission nor mass loss dominates the other over major portions of the evolutionary track in the period-mass diagram (Fig. 1).

We confirm the conclusion of Kluźniak et al. (1992), who predicted that some ms pulsars may become accreting LMXBs at the end of their evolution. Two of the tracks presented in this paper end very close to the line of Roche-lobe contact, in the current position of PSR J1807-2459A and PSR J1311-3430. These two pulsars seem to be close to the end of a  $5 \times 10^8$  y ablation phase.

We note that detailed binary evolutionary calculations, which included an ablation phase similar to the model considered here were presented recently in Chen et al. (2013).

## ACKNOWLEDGEMENTS

We thank Dr. Thomas Tauris, as well as the anonymous referee, for many detailed comments on the manuscript. This work was supported in part by NCN grant 2013/08/A/ST9/00795.

## REFERENCES

- Alpar, M. A., Cheng, A. F., Ruderman, M. A. and Shaham, J. (1982), A new class of radio pulsars, *Nature*, **300**, pp. 728–730.
- ATNF Database (2014), <http://www.atnf.csiro.au/research/pulsar/psrcat/>.
- Bisnovatyi-Kogan, A. S. (1989), Two Generations of Low-Mass X-Binaries and Recycled Radio Pulsars, *Astrofizika*, **31**, p. 567.
- Brookshaw, L. and Tavani, M. (1995), Outflow Hydrodynamics of Eclipsing Pulsar Binaries, *ASP Conference Series*, **72**, pp. 244–252.
- Chen, H.-L., Chen, X., Tauris, T. M. and Han, Z. (2013), Formation of Black Widows and Redbacks—Two Distinct Populations of Eclipsing Binary Millisecond Pulsars, *Astrophys. J.*, **775**, 27, arXiv: 1308.4107.
- Ergma, E. V. and Fedorova, A. V. (1991), An 11-ms pulsar in the globular cluster TER 5 - A possible test for determination of the progenitor of millisecond pulsars, *Pisma v Astronomicheskii Zhurnal*, **17**, pp. 433–439.
- Hamada, T. and Salpeter, E. (1961), Models for Zero-Temperature Stars, *Astrophys. J.*, **134**, pp. 683–698.
- Kluźniak, W., Czerny, M. and Ray, A. (1992), From Millisecond Pulsars to X-Ray Binaries, *NATO Advanced Research Workshop on X-Ray Binaries and the Formation of Binary and Millisecond Radio Pulsars*, pp. 425–436.
- Kluźniak, W., Ruderman, M., Shaham, J. and Tavani, M. (1988), Nature and evolution of the eclipsing millisecond binary pulsar PSR1957 + 20, *Nature*, **334**, pp. 225–227.
- Manchester, R. N., Hobbs, G. B., Teoh, A. and Hobbs, M. (2005), The Australia Telescope National Facility Pulsar Catalogue, *Astronom. J.*, **129**, pp. 1993–2006, arXiv: astro-ph/0412641.

- Paczyński, B. and Sienkiewicz, R. (1983), The minimum period and the gap in periods of cataclysmic binaries, *Astrophys. J.*, **268**, pp. 825–831.
- Radhakrishnan, V. and Srinivasan, G. (1982), On the origin of the recently discovered ultra-rapid pulsar, *Current Science*, **51**, pp. 1096–1099.
- Roberts, M. S. E., McLaughlin, M. A., Gentile, P., Aliu, E., Hessels, J. W. T., Ransom, S. M. and Ray, P. S. (2014), Intrabinary shock emission from “black widows” and “redbacks”, *Astronom. Nachr.*, **335**, pp. 313–317, arXiv: 1402.5507.
- Shapiro, S. and Teukolsky, S. (1983), *Black Holes, White Dwarfs and Neutron Stars: The Physics of Compact Objects*, Wiley, Weinheim.
- Tauris, T. and Savonije, G. (1999), Formation of millisecond pulsars, *Astronomy and Astrophysics*, **350**, pp. 928–944.

**APPENDIX A: APPENDIX**

For ease of reference, we reproduce Figure 1 and its caption from the pre-arXiv contribution of Kluźniak, Czerny and Ray (1992).

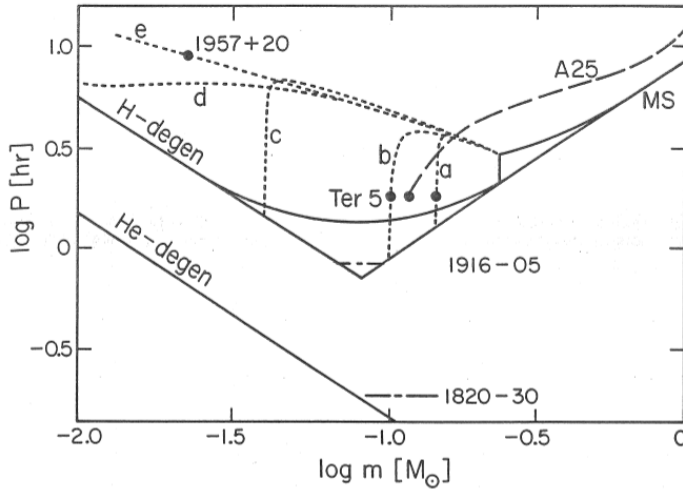


**Figure A1.** ‘Figure 1. Possible evolutionary tracks of systems with “evaporative” mass loss. The decimal logarithm of the orbital period in hours is plotted versus the decimal logarithm of the mass of the companion in units of Solar mass. Likely location of the eclipsing pulsars (filled circles) as well as possible positions of the X-ray binaries 4U 1916-05 and 4U 1820-30 are also indicated (dash-dot-dash lines). The thick straight line segments correspond to systems with a main-sequence or a cold degenerate dwarf companion in Roche-lobe contact. According to the standard theory of their evolution, cataclysmic variables follow the thin curve (in the direction of decreasing companion mass,  $m$ ). When this theory is applied to canonical LMXBs, the dotted tracks ensue, see Section 5 for details. The lines (a) through (e) differ only in the properties of the pulsar ablating its companion: in the strength of the magnetic dipole moment and in the initial value,  $P_0$ , of the rotational period of the neutron star. The values of  $P_0$  and  $\log(B/\text{Gauss})$ , where  $B \equiv \mu \times 10^{-18} \text{ cm}^{-3}$ , are respectively (a) 5.0 ms, 9.5; (b) 3.4 ms, 8.9; (c) 2.0 ms, 9.0; (d) 2.0 ms, 8.6; (e) 1.25 ms, 8.1. We assumed that 10% of the energy flux impinging on the companion is converted into kinetic energy of the evaporative plume, and we took  $\beta = 0.86$ .’

N.B. The parameter “ $\beta$ ” in the quoted caption corresponds to our  $\alpha$ .

# Frequency spectrum of axisymmetric horizontal oscillations in accretion disks

Luca Giussani<sup>1</sup>, Włodek Kluźniak<sup>2</sup> and Bhupendra Mishra<sup>2</sup>

<sup>1</sup>Centre des Etudes Supérieures Industrielle, 93 Boulevard de la Seine, 92000 Nanterre, France

<sup>2</sup>Nicolaus Copernicus Astronomical Center, Bartyccka 18, 00-716 Warsaw, Poland

## ABSTRACT

We present the spectrum of eigenfrequencies of axisymmetric acoustic-inertial oscillations of thin accretion disks for a Schwarzschild black hole modelled with a pseudo-potential. There are nine discrete frequencies, corresponding to trapped modes. Eigenmodes with nine or more radial nodes in the inner disk belong to the continuum, whose frequency range starts somewhat below the maximum value of the radial epicyclic frequency. The results are derived under the assumption that the oscillatory motion is parallel to the midplane of the disk.

**Keywords:** Relativistic stars: black holes – structure stability – oscillations – relativity – gravitation – accretion disks – hydrodynamics

## 1 ACOUSTIC-INERTIAL MODES

We consider acoustic-inertial modes of oscillation in the inner part of an accretion disk, closely following the formalism of Nowak and Wagoner (1991, 1992). Trapping of the fundamental axisymmetric mode with no nodes in the vertical ( $z$ ) direction was first demonstrated by Kato and Fukue (1980) in the Schwarzschild geometry. Nowak and Wagoner (1991) derive the equations of motion in a Lagrangian pseudo-Newtonian formalism and specialize to purely horizontal perturbed motions of the disk deriving eigenmodes and eigenfrequencies for the  $m = 0$  (axisymmetric) and  $m = 2$  (quadrupole) modes. Khanna et al. (2014) computed in an improved pseudo-potential the lowest radial modes (with up to three radial nodes) for azimuthal numbers  $m = 0$  through  $m = 4$ . Here, we present the complete spectrum of horizontal axisymmetric acoustic-inertial disk modes in a pseudopotential which reproduces the properties of the Schwarzschild-metric epicyclic frequency (Kluźniak and Lee, 2002; Khanna et al., 2014). The eigenfrequencies could be related to the quasi-coherent frequencies (QPOs) observed in the X-ray flux from black hole and neutron star systems (for a review see van der Klis M., 2000), as well as in cataclysmic variables (Woudt and Warner, 2002, and references therein).

## 2 EQUATION OF MOTION AND THE BOUNDARY CONDITION

We model the Schwarzschild metric with a Newtonian pseudo-potential that reproduces the Schwarzschild ratio of  $\kappa^2(r)/\Omega^2(r) = 1 - 6GM/(rc^2)$ :

$$\Phi_{\text{KL}}(r) = -(c^2/6) \exp\left(\frac{6GM}{rc^2} - 1\right). \quad (1)$$

We have dropped an additive constant and renormalized the original Kluźniak and Lee (2002) potential by a factor of  $1/e$  to guarantee the correct Schwarzschild value of  $\Omega(r_{\text{ms}})$ . The orbital frequency can be obtained from  $\Omega^2(r) = r^{-1}\partial\Phi_{\text{KL}}/\partial r$ , the radial epicyclic frequency from  $\kappa^2 = (2\Omega/r)d(r^2\Omega)/dr$  and the marginally stable orbit is at the zero of  $\kappa$ , at  $r_{\text{ms}} = 6GM/(rc^2)$ . Figure 1 compares our  $\kappa^2(r)$  with the Schwarzschild form and two other well-known pseudo-Newtonian models (Paczyński and Wiita, 1980; Nowak and Wagoner, 1991).

In this contribution we assume axisymmetric ( $m = 0$ ) horizontal modes, with the perturbation vector in cylindrical coordinates  $(\xi_*^r, \xi_*^\phi, \xi_*^z) = (\xi^r, \xi^\phi, 0) \exp(i\sigma t)$ . We use the equation of motion for  $\Psi(r) \equiv \sqrt{\gamma Pr} \xi^r(r)$  derived in the Lagrangian formalism of Friedman and Schutz (1978) by Nowak and Wagoner (1991)

$$c_s^2 d^2\Psi/dr^2 + (\sigma^2 - \kappa^2)\Psi = 0,$$

who also show that in the WKB approximation the azimuthal component of the equation of perturbed motion for thin disks reduces to  $\xi^\phi = 2i(\Omega/\sigma)\xi^r$ .

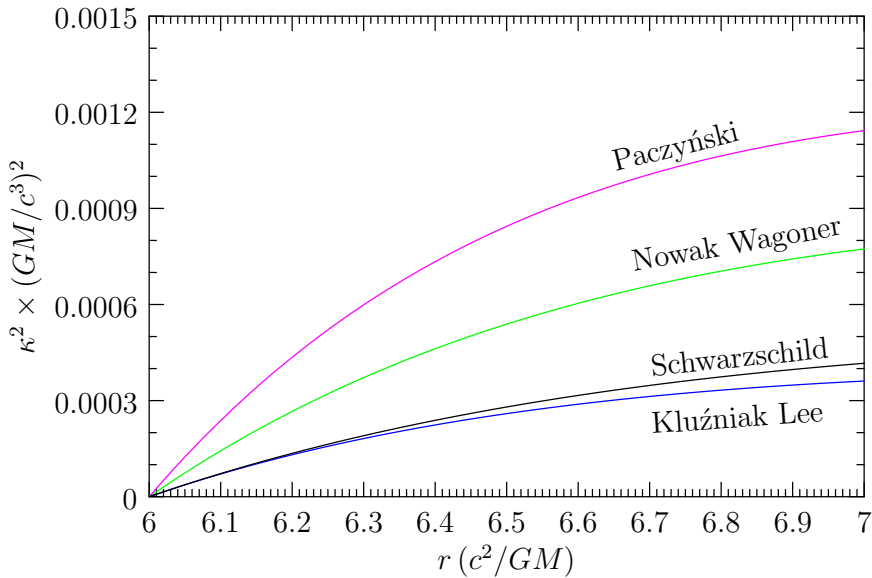


**Figure 1.** The Schwarzschild epicyclic frequency (squared) and its Newtonian models, from top to bottom: Paczyński and Wiita (1980); Nowak and Wagoner (1991), our Eq. (1).

Following Khanna et al. (2014) we rewrite the equation of motion, and the boundary condition that the Lagrangian perturbation of pressure vanishes at the unperturbed boundary, in dimensionless form as

$$\frac{d^2\Psi}{dx^2} + \left(\frac{a}{H}\right)^2 (\tilde{\sigma}^2 - \tilde{\kappa}^2) \Psi = 0, \quad (2)$$

with the boundary condition at  $x = 0$

$$\frac{d\Psi}{dx} = -\frac{\Psi}{2}, \quad (3)$$

where  $H$  is the half-thickness of the disk,  $a = r_{\text{ms}}$ , and the dimensionless variables are given by  $r = a(1 + x)$ ,  $\tilde{\sigma} = \sigma/\Omega(a)$ ,  $\tilde{\kappa}(x) = \kappa(r)/\Omega(a)$ . The speed of sound  $c_s = \sqrt{\gamma P/\rho}$  was eliminated with the condition of vertical hydrostatic equilibrium.

### 3 THE EIGENFREQUENCY SPECTRUM

We have numerically solved the eigenvalue problem given by Eqs. (2) and (3), for a thin disk of  $H/a = 10^{-3}$ , and present in Table 1 the eigenfrequencies for modes with  $\mu = 0, 1, \dots, 9$  radial nodes in the inner disk. The lowest nine eigenfrequencies ( $\mu = 0$  through 8), exhausting the discrete spectrum, correspond to oscillations which are trapped in the inner disk. As already noted by Kato and Fukue (1980), for eigenfrequencies exceeding the maximum of the epicyclic frequency,  $\sigma^2 > \kappa_{\text{max}}^2$ , the acoustic wave ranges throughout the disk (see also Kato et al., 1998), these frequencies belong to the continuum spectrum. The tenth entry in Table 1, with  $\mu = 9$  radial nodes in the inner disk, also belongs to the continuum, although it has a frequency below the maximum of the epicyclic frequency  $\sigma^2 < \kappa_{\text{max}}^2$  (Figs. 2, 3).

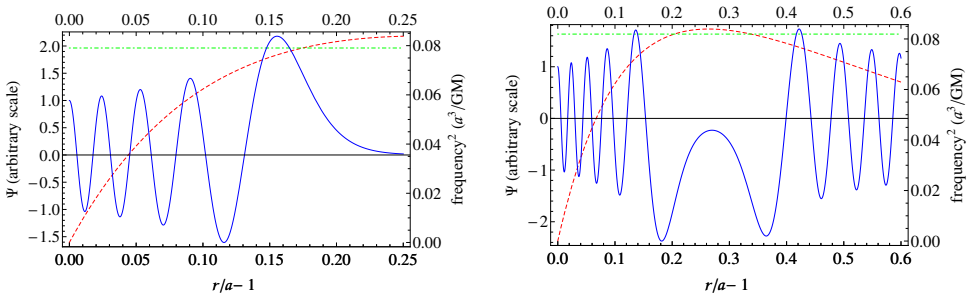


**Figure 2.** Two radial overtones for  $m = 0$  horizontal oscillations of a thin ( $H/a = 10^{-3}$ ) accretion disk. *Left Panel:* A trapped oscillation with  $\mu = 8$  radial nodes. *Right Panel:* An oscillation penetrating the epicyclic barrier (with  $\mu = 9$  radial nodes in the inner accretion disk and an unlimited number of radial nodes in the outer disk). Plotted are the radial wavefunction  $\Psi \propto r^{1/2}\xi^r$ : solid blue line (left scale); eigenfrequency (squared): dashed-dotted green line,  $\kappa^2(r)/\Omega^2(r_{\text{ms}})$ : dashed red line (right scale).

**Table 1.** Spectrum of eigenfrequencies for horizontal modes

mode	radial nodes	eigenfrequency	mode	
$m$	$\mu$	$\sigma \times \sqrt{(a^3/GM)}$	status	ref.
0	0	0.0988290000	trapped	Khanna et al. (2014)
0	1	0.1721372560	trapped	Khanna et al. (2014)
0	2	0.2049091375	trapped	Khanna et al. (2014)
0	3	0.2269122200	trapped	Khanna et al. (2014)
0	4	0.2433069000	trapped	this work
0	5	0.2561130000	trapped	this work
0	6	0.2663460000	trapped	this work
0	7	0.2745830000	trapped	this work
0	8	0.2811589000	trapped	this work
0	9	0.2862229000	not trapped	this work

In the Figure 2 we present the two eigenmodes corresponding to the last two entries in Table 1. The equations being linear in  $\Psi$ , we normalize the wavefunction to unity at the inner edge of the disk:  $\Psi(r_{\text{ms}}) = 1$  for illustration purposes. The left panel shows the highest-frequency eigenmode in the discrete portion of the spectrum of axisymmetric ( $m = 0$ ) horizontal disk oscillations, the wavefunction of this mode has  $\mu = 8$  radial nodes. Note that the wave becomes evanescent for  $\sigma^2 < \kappa^2$ , thus trapping the  $\mu = 8$  mode to the left of  $\kappa_{\text{max}}$ . Some of the lower overtones have been illustrated in Khanna et al. (2014).

The right panel of Fig. 2 illustrates one of the lowest frequency modes in the continuum. Here,  $\sigma < \kappa_{\text{max}}$  and is so close in value to  $\kappa_{\text{max}}$  that the wave is transmitted through the epicyclic barrier to the outer disk, where it has an unlimited number of radial nodes in addition to the  $\mu = 9$  radial nodes in the inner disk. As far as we are aware, this is a new finding, which has never been reported before. It may have an interesting astrophysical consequence. If the oscillations arise close to the marginally stable orbit, as suggested by Paczyński (1987), the ones transmitted to the outer disk are likely to be more easily observable, in that they may modulate the emission from large parts of the disk.

#### 4 DISCUSSION

We consider accretion disk oscillations in a Newtonian model of the Schwarzschild metric, Eq. (1), which accurately models the radial epicyclic frequency, at least close to the marginally stable orbit, see Fig. 1. No model is perfect, so although we correctly reproduce the ratio of epicyclic to orbital frequency  $\kappa(r)/\Omega(r) = \sqrt{1 - 6GM/(rc^2)}$ , and the correct value of orbital frequency at the marginally stable orbit,  $\Omega(r_{\text{ms}}) = c^3/(\sqrt{216}GM)$ , the maximum of  $\kappa$  occurs at  $r = (3 + \sqrt{21})(GM/c^2) \approx 7.58(GM/c^2)$  instead of the Schwarzschild value  $r = 8(GM/c^2)$ . Further, the equations of motion for the oscillation of the disk fluid were derived in a Newtonian formalism, not in full GR. These departures from GR may limit the quantitative accuracy of the presented results when applied to real

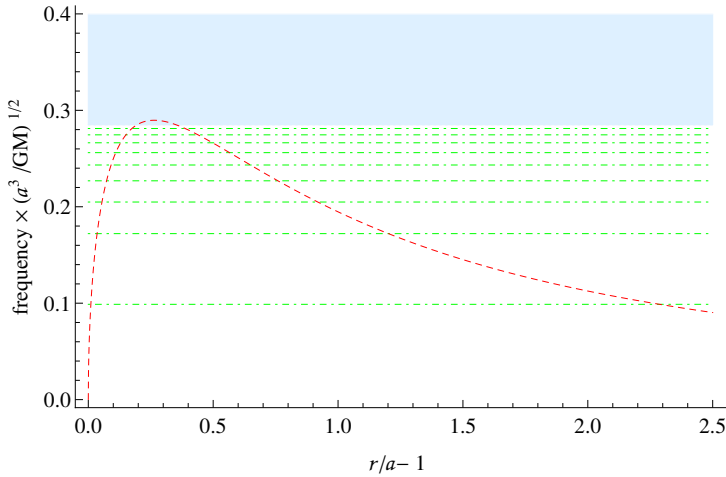


**Figure 3.** The spectrum of  $m = 0$  (axially symmetric) horizontal oscillations of a thin ( $H/a = 10^{-3}$ ) accretion disk for the potential of Eq. (1). Plotted are the epicyclic frequency (*dashed red curve*), and the eigenfrequencies  $\sigma$  in the discrete set (*dashed-dotted green lines*) and in the continuum (*shaded blue region*). All frequencies were scaled with  $(GM/a^3)^{1/2}$ . Here, and throughout the paper,  $a = r_{\text{ms}}$ .

black hole (or neutron star) accretion disks. An additional assumption which may not be quite accurate is that the oscillations of the disk are strictly parallel to the midplane of the disk, i.e. that the perturbation vector has a zero vertical component,  $\xi^z = 0$ .

We find that the spectrum of horizontal oscillations is composed of nine discrete frequencies and a continuum (Fig. 3). For the discrete spectrum the wave propagation region corresponds to those regions where  $\sigma^2 > \kappa^2(r)$  and is separated into the inner region of trapped oscillations, from  $r = r_{\text{ms}}$  to  $r \approx (7/6)r_{\text{ms}}$ , and an outer region extending to  $r \gg r_{\text{ms}}$  (Kato et al., 1998). However, the lowest frequency modes in the continuum, which satisfy  $\sigma < \kappa_{\text{max}}$ , are transmitted through the epicyclic barrier, and thus fluctuations in the inner disk may be transmitted to the outer disk for frequencies close to the maximum of the epicyclic one,  $\sigma^2 \approx \kappa_{\text{max}}^2$ .

## ACKNOWLEDGEMENTS

This work was supported in part by Polish NCN grant 2013/08/A/ST9/00795.

## REFERENCES

- Friedman, J. L. and Schutz, B. F. (1978), Lagrangian perturbation theory of nonrelativistic fluids, *Astrophys. J.*, **221**, p. 937.
- Kato, S. and Fukue, J. (1980), Trapped radial oscillations of gaseous disks around a black hole, *Publ. Astronom. Soc. Japan*, **32**, p. 377.
- Kato, S., Fukue, J. and Mineshige, S. (1998), *Black-Hole Accretion Disks*, Kyoto University Press.

- Khanna, S., Strzelecka, Z., Mishra, B. and Kluźniak, W. (2014), Eigenmodes of trapped horizontal oscillations in accretion disks, in Z. Stuchlík, G. Török and T. Pecháček, editors, *Proceedings of RAGtime 14–16: Workshops on black holes and neutron stars, Opava, Prague, 18–22 September/15–18 July/11–19 October '12/'13/'14*, pp. 145–158, Silesian University in Opava, Opava, ISBN 978-80-7510-126-6.
- Kluźniak, W. and Lee, W. H. (2002), The swallowing of a quark star by a black hole, *Monthly Notices Roy. Astronom. Soc.*, **335**, p. L29.
- Nowak, M. A. and Wagoner, R. V. (1991), Diskoseismology: Probing accretion disks. I – Trapped adiabatic oscillations, *Astrophys. J.*, **378**, p. 656.
- Nowak, M. A. and Wagoner, R. V. (1992), Diskoseismology: Probing accretion disks. II – G-modes, gravitational radiation reaction, and viscosity, *Astrophys. J.*, **393**, p. 697.
- Paczyński, B. (1987), Possible relation between the X-ray QPO phenomenon and general relativity, *Nature*, **327**, p. 303.
- Paczyński, B. and Wiita, P. J. (1980), Thick accretion disks and superluminal luminosities, *Astronomy and Astrophysics*, **88**, p. 23.
- van der Klis M. (2000), Millisecond Oscillations in X-ray Binaries, *Annual Review of Astronomy and Astrophysics*, **38**, p. 717.
- Woudt, P. A. and Warner, B. (2002), Dwarf nova oscillations and quasi-periodic oscillations in cataclysmic variables – I. Observations of VW Hyi, *Monthly Notices Roy. Astronom. Soc.*, **333**, p. 411.

# Embedding diagrams of Bardeen geometry

Kateřina Goluchová and Zdeněk Stuchlík

Institute of Physics, Faculty of Philosophy & Science, Silesian University in Opava,  
Bezručovo nám. 13, CZ-746 01 Opava, Czech Republic.

## ABSTRACT

General relativity combined with a non-linear electrodynamics enables to find regular black hole solutions. The best known solution of this kind is described by the Bardeen spacetime with spacetime parameters giving gravitational mass  $m$  and magnetic charge  $g$ . For ratio  $g/m$  large enough, the Bardeen spacetime describes a no-horizon regular solution. Here we demonstrate properties of the Bardeen spacetimes by the embedding diagrams of the equatorial plane of the ordinary geometry, and the optical geometry enabling reflection of properties of test particle motion.

**Keywords:** Bardeen geometry – black hole – embedding diagram

## 1 INTRODUCTION

Black holes predicted by the general relativity contain a physical singularity with diverging Riemann tensor components. Regular black hole solutions of the Einstein gravity have been found that eliminate the physical singularity from the spacetimes having an event horizon, but these are not vacuum solutions of the Einstein equations, but contain necessarily a properly chosen additional field, or modified gravity.

The well known regular spherically symmetric black hole solution containing a magnetic charge as a source has been proposed by Bardeen (1968). The magnetic charge is related to a non-linear electrodynamics (Ayón-Beato and García, 2000). The solution is characterized by the mass parameter  $m$  and the charge parameter  $g$ . Their geodesic structure is governed by the dimensionless ratio  $g/m$ . For properly chosen charge parameter  $g/m$ , the Bardeen solution allows for existence of fully regular spacetime, without an event horizon. We call it Bardeen “no-horizon” spacetime.

A detailed discussion of the geodesic structure of the regular Bardeen black hole and no-horizon spacetimes and its implication to optical phenomena were presented in Stuchlík and Schee (2014a). It has been shown that the geodesic structure of the regular Bardeen black holes outside the horizon is similar to those of the Schwarzschild or Reissner–Nordström (RN) black hole spacetimes, but under the inner horizon, no circular geodesics can exist. The geodesic structure of the Bardeen no-horizon spacetimes is similar to those of the naked singularity spacetimes of the RN type, or the Kehagias–Sfetsos (KS) type (Kehagias and Sfetsos, 2009; Stuchlík and Schee, 2014b; Stuchlík et al., 2014) that is related to the solution of the modified Hořava quantum gravity (Hořava, 2009a,b). In all of these no-horizon and

naked singularity spacetimes, an “antigravity” sphere exists consisting of static particles located at stable equilibrium points at a given “static” radius that can be surrounded by a Keplerian disc Stuchlík and Schee (2014b).

The basic properties of the Bardeen black hole and no-horizon spacetimes can be reflected by the embedding diagrams that illustrate in a proper way the curvature of the spacelike (constant time) surfaces and give for the ordinary space geometry an overall insight into its nature – (see e.g. Kristiansson et al. (1998); Stuchlík and Hledík (1999, 2002)). In the case of the optical geometry, the embeddings can give an illustration of some hidden properties of the geodesic structure of the spacetime (Stuchlík et al., 2000). Here we present the embeddings for both the Bardeen black hole and no-horizon spacetimes.

## 2 BARDEEN SPACETIMES

The spherically symmetric geometry of the regular Bardeen black-hole or no-horizon spacetimes is characterized in the standard spherical coordinates and the geometric units ( $c=G=1$ ) by the line element

$$ds^2 = -f(r) dt^2 + \frac{1}{f(r)} dr^2 + r^2(d\theta^2 + \sin^2 \theta d\phi^2), \quad (1)$$

where the “lapse”  $f(r)$  function depends only on the radial coordinate, the gravitational mass parameter  $m$  and the charge parameter  $g$ . The Bardeen spacetimes are constructed to be regular everywhere, i.e. the components of the Riemann tensor, and the Ricci scalar are finite at all  $r \geq 0$  (Ayón-Beato and García, 1999).

The lapse function  $f(r)$  reads

$$f(r) = 1 - \frac{2mr^2}{(g^2 + r^2)^{3/2}}. \quad (2)$$

The event horizons of the Bardeen black hole spacetimes, determined by the condition  $f(r) = 0$ , are given by

$$g^6 + (3g^2 - 4m^2)r^4 + 3g^4r^2 + r^6 = 0. \quad (3)$$

The critical value of the dimensionless parameter  $g/m$  separating the black-hole and the “no-horizon” Bardeen spacetimes reads

$$(g/m)_{\text{NoH/B}} = 0.7698. \quad (4)$$

In the “no horizon” Bardeen spacetimes the metric is regular at all radii  $r \geq 0$ . We assume  $r = 0$  to be the site of the self-gravitating charged source of the spacetime.

The optical geometry of the Bardeen spacetimes is given by the line element (Kristiansson et al., 1998)

$$ds_{\text{opt}}^2 = -dt^2 + \frac{dr^2}{f(r)^2} + \frac{1}{f(r)} r^2 d\theta^2 + \frac{r^2}{f(r)} \sin^2 \theta d\phi^2. \quad (5)$$

### 3 THE EMBEDDING PROCEDURE

We make the embedding of the equatorial plane,  $\theta = \pi/2$ , of the  $t = \text{const}$  spacelike sections of the spacetime and its optical geometry. For the ordinary, simply projected space, the 2D equatorial plane can be cast in the form

$$dl_{\text{ord}}^2 = \frac{dr^2}{f(r)} + r^2 d\phi^2, \quad (6)$$

while for the optical geometry we find

$$dl_{\text{opt}}^2 = \frac{dr^2}{f(r)^2} + \frac{r^2}{f(r)} d\phi^2. \quad (7)$$

The plane has to be embedded into the 3D flat space with line element

$$dl_{\text{3D}}^2 = dR^2 + R^2 d\phi^2 + dz^2. \quad (8)$$

The 3D flat space is expressed in the standard cylindrical coordinates  $R, z, \phi$ . The embedding is realized by the function  $Z = Z(R)$  that implies the line element of the 2D embedding surface in the form

$$dl_{\text{2D}}^2 = dR^2 + R^2 d\phi^2 + \left(\frac{dz}{dR}\right)^2 dR^2. \quad (9)$$

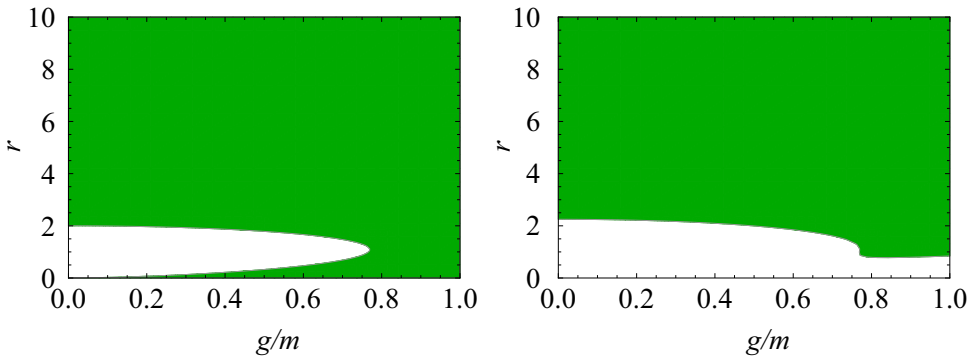


**Figure 1.** Embeddability limits of equatorial plane of directly projected (*left*) and optical (*right*) Bardeen geometry. *Green colour* indicates area that can be embedded.

### 4 EMBEDDING DIAGRAMS OF DIRECTLY PROJECTED GEOMETRY

In this case we can make the trivial identification

$$\phi = \varphi, \quad R = r \quad (10)$$

that implies the relation

$$\left(1 + \left(\frac{dz}{dr^2}\right)^2\right) = \frac{1}{f(r)}. \quad (11)$$

The embedding formula then takes a simple form

$$z = \int \sqrt{\frac{1}{f(r)} - 1} \, dr. \quad (12)$$

The embeddability conditions read

$$\frac{1}{f(r)} - 1 \geq 0, \quad f(r) \geq 0. \quad (13)$$

Clearly, the region between the horizons is not embeddable. The regions are given in dependence on the spacetime parameter  $g/m$  in Fig. 1. The embedding diagrams are for representative values of the parameter  $g/m$  given in Fig. 2.

## 5 EMBEDDING DIAGRAMS OF THE OPTICAL GEOMETRY

In the case of the optical geometry, the identification of the radial coordinate is not trivial, we have to define

$$\phi = \varphi, \quad R = \frac{r}{f^{1/2}(r)}. \quad (14)$$

Such an identification implies the relation

$$\left(\left(\frac{dR}{dr}\right)^2 + \left(\frac{dz}{dr^2}\right)^2\right) = \frac{1}{f^{1/2}(r)} \quad (15)$$

and the embedding formula takes the form

$$z = \int \sqrt{\frac{1}{f^2(r)} - \left(\frac{dR}{dr}\right)^2} \, dr. \quad (16)$$

The embeddability condition of the optical space reads

$$\frac{1}{f^2(r)} - \left(\frac{dR}{dr}\right)^2 \geq 0. \quad (17)$$

The limits on the embeddability are given in Fig. 1, while the typical embedding diagrams of the optical space are illustrated in Fig. 3.

Recall that the turning points of the embeddings of the optical space reflect an important information on the geodesic structure of the spacetime, namely they represent loci of the photon circular orbits (Stuchlík et al., 2000).

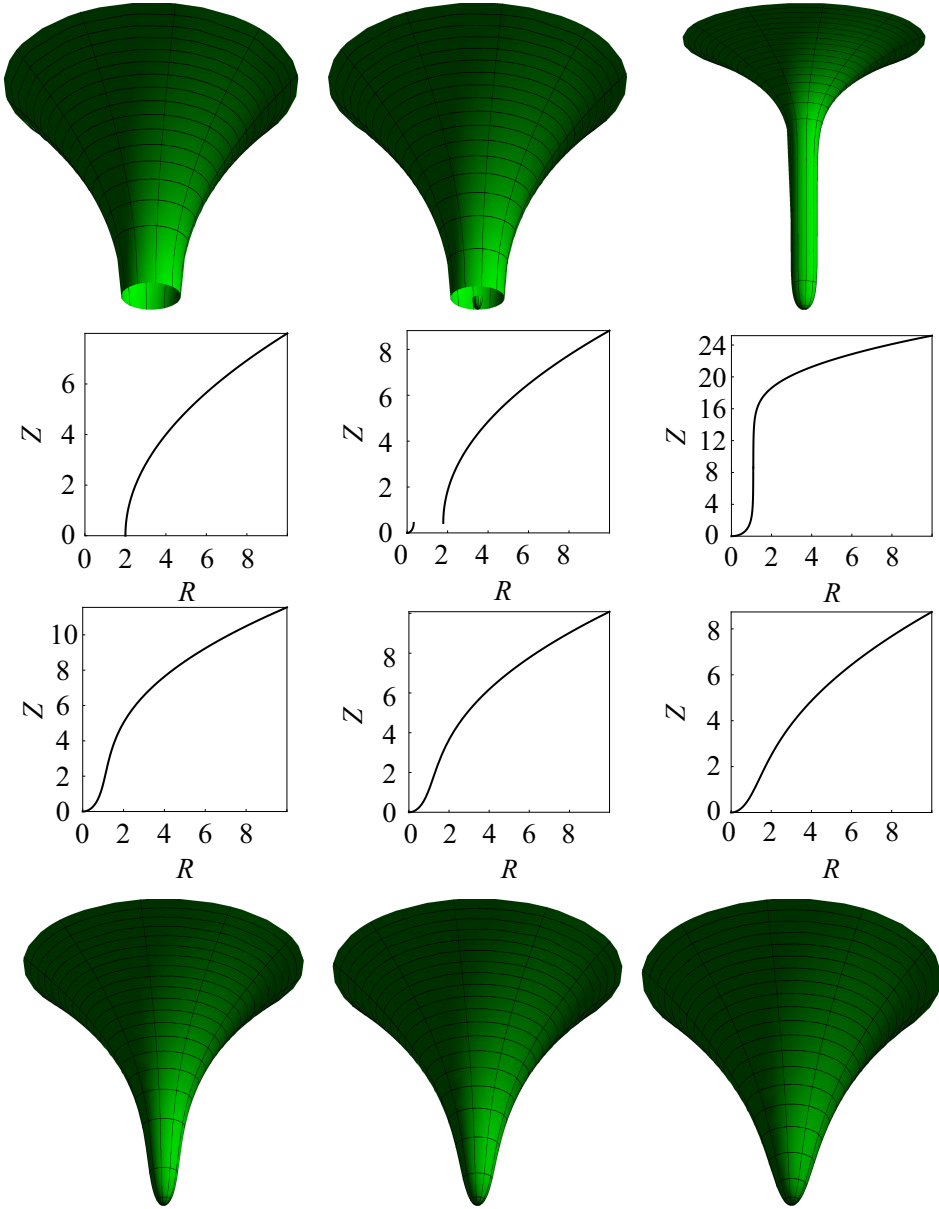


**Figure 2.** Embedding diagrams of directly projected geometry for different values of  $g/m$ . The integration in (12) ends slightly before horizons, because on the horizons there is  $dZ/dr = 0$ . Top part corresponds to  $g/m = 0$  (Schwarzschild geometry),  $g/m = 0.5$  (Bardeen black hole) and  $g/m = 0.7698$  (extreme Bardeen black hole). Bottom part corresponds to  $q/m = 0.8$  (there are two turning points in optical geometry, see Fig. 3),  $g/m = 0.858665$  (there is one turning point in optical geometry) and  $g/m = 1.0$  (there are no turning points in optical geometry).

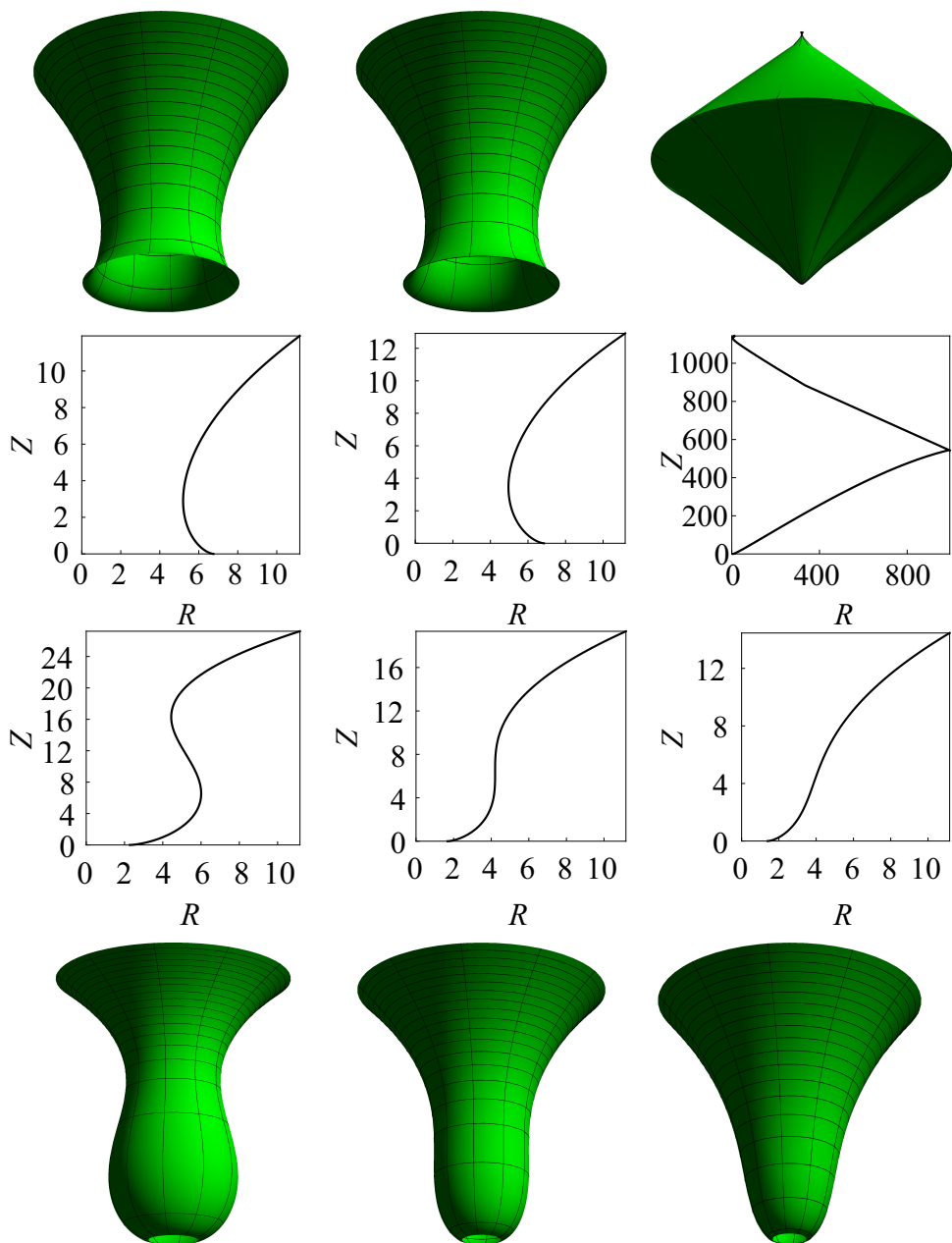


**Figure 3.** Embedding diagrams of optical geometry for different values of  $g/m$ . The integration in (16) ends slightly before embeddability limits for the same reason as in the normal case. The  $g/m$  values are exactly the same as on Figure 3.

## 6 CONCLUSIONS

We have constructed the embedding diagrams of the equatorial plane of the spherically symmetric regular Bardeen black-hole and no-horizon spacetimes for both the ordinary projected space, and the optical space. We have found the limits of embeddability of these spaces. The embeddability limits appear to be more extended in the vicinity of the coordinate origin  $r = 0$  while compared to those related to the embeddings of the Kehagias–Sfetsos spacetimes that are spherically symmetric solutions of modified Hořava quantum gravity (Goluchová et al., 2014). This is rather surprising result, as the Kehagias–Sfetsos spacetimes are singular at  $r = 0$ , while the Bardeen spacetimes are regular there. The reason is related to different character of the “antigravity” region occurring near the origin of both Kehagias–Sfetsos and Bardeen spacetimes (Vieira et al., 2014; Stuchlík and Schee, 2014b,a). The gravitation repulsion in the Bardeen spacetimes occurring near the coordinate origin is of the de Sitter character, while in the case of the Kehagias–Sfetsos spacetimes, it is much weaker, being of a quintessential character Stuchlík and Schee (2014b,a).

## ACKNOWLEDGEMENTS

The authors would like to thank the internal student grant SGS/23/2013 of the Silesian University, the EU grant Synergy CZ.1.07/2.3.00/20.0071. ZS acknowledge the Albert Einstein Centre for gravitation and astrophysics supported by the Czech Science Foundation Grant No. 14-37086G.

## REFERENCES

- Ayón-Beato, E. and García, A. (1999), Non-singular charged black hole solution for non-linear source, *General Relativity and Gravitation*, **31**, p. 629.
- Ayón-Beato, E. and García, A. (2000), The Bardeen model as a nonlinear magnetic monopole, *Phys. Lett. B*, **493**, pp. 149–152.
- Bardeen, J. (1968), in *Proceedings of GR5*, Tbilisi, USSR.
- Goluchová, K., Kulczycki, K., Vieira, R. S. S., Stuchlík, Z., Kluźniak, W. and Abramowicz, M. (2014), Hořava’s quantum gravity illustrated by embedding diagrams of Kehagias–Sfetsos spacetimes.
- Hořava, P. (2009a), Quantum gravity at a lifshitz point, *Phys. Rev. D*, **79**(8), p. 084008.
- Hořava, P. (2009b), Spectral dimension of the universe in quantum gravity at a lifshitz point, *Phys. Rev. Lett.*, **102**(16), p. 161301.
- Kehagias, A. and Sfetsos, K. (2009), The black hole and FRW geometries of non-relativistic gravity, *Phys. Rev. B*, **678**, pp. 123–126.
- Kristiansson, S., Sonogo, S. and Abramowicz, M. A. (1998), Optical space of the Reissner–Nordström solutions, *General Relativity and Gravitation*, **30**, pp. 275–288.
- Stuchlík, Z. and Hledík, S. (1999), Some properties of the Schwarzschild-de Sitter and Schwarzschild-anti-de Sitter spacetimes, *Phys. Rev. D*, **60**(4), p. 044006.
- Stuchlík, Z. and Hledík, S. (2002), Properties of the Reissner–Nordström spacetimes with a nonzero cosmological constant, *Acta Physica Slovaca*, **52**.
- Stuchlík, Z., Hledík, S. and Juráň, J. (2000), Optical reference geometry of Kerr–Newman spacetimes, *Classical Quantum Gravity*, **17**, pp. 2691–2718.

- Stuchlík, Z. and Schee, H. (2014a), Geodesics of bardeen and Ayon-Beato-Garcia regular black-hole and no-horizon spacetimes, *Submitted*.
- Stuchlík, Z. and Schee, H. (2014b), Optical effects related to keplerian discs orbiting Kehagias–Sfetsos naked singularities, *Classical Quantum Gravity*, accepted.
- Stuchlík, Z., Schee, J. and Abdujabbarov, A. (2014), Ultra-high-energy collisions of particles in the field of near-extreme Kehagias–Sfetsos naked singularities and their appearance to distant observers, *Phys. Rev. D*, **89**(10), p. 104048, may.
- Vieira, R. S. S., Schee, J., Kluzniak, W., Stuchlík, S. and Abramowicz, M. (2014), Circular geodesics of naked singularities in the Kehagias–Sfetsos metric of Hořava’s gravity, *Phys. Rev. D*, **90**(2), p. 024035.

# Triggered oscillations and destruction of magnetized relativistic tori in 2D

Jaroslav Hamerský<sup>1,2,a</sup> and Vladimír Karas<sup>1</sup>

<sup>1</sup>Astronomical Institute, Academy of Sciences of the Czech Republic,  
Boční II 1401, CZ-141 00 Prague, Czech Republic

<sup>2</sup>Charles University in Prague, Faculty of Mathematics and Physics,  
V Holešovičkách 2, CZ-18000 Prague, Czech Republic

<sup>a</sup>jaroslav.hamersky@asu.cas.cz

## ABSTRACT

Runaway instability operates under certain conditions in fluid tori around black holes. When active, it affects systems close to the critical (cusp overflowing) configuration. Here we start from our previous discussion of the role of runaway instability within a framework of an axially symmetric model of perfect fluid endowed with a purely toroidal magnetic field. The gradual accretion of material over the cusp transfers the mass and angular momentum onto the black hole, thereby changing the intrinsic parameters of the Kerr metric. By contributing to the total pressure, the magnetic field causes small departures from the corresponding non-magnetic configuration in the early phases of accretion. We showed that the toroidal magnetic component inside an accretion torus does not change the frequency of its oscillations significantly. We identified these oscillations as the radial epicyclic mode in our example. Nevertheless, these weak effects can trigger the runaway instability even in situations when the purely hydrodynamical regime of the torus is stable. On the other hand, in most cases the stable configuration remains unaffected, and the initial deviations gradually decay after several orbital periods. We showed examples of the torus evolution depending on the initial magnetization  $\beta$ , the slope  $q$ , and the spin  $a$ .

Perturbations in the vertical direction may lead to vertical oscillations. Here we propose that these oscillations could be enhanced (especially for an intermediate-mass black hole) by an orbiting star with a trajectory crossing the torus. First the oscillation of the torus material is triggered. Then the mass of the torus is dragged high enough above the equatorial plane and gradually accelerated along spin axis.

**Keywords:** Accretion: accretion discs – black-hole physics

## 1 INTRODUCTION

Toroidal equilibria of perfect fluid in permanent rotation were introduced a long time ago as an initial step on the way towards an astrophysically realistic description of accretion of gaseous material onto a black hole in active galactic nuclei and black hole binaries (Fishbone and Moncrief, 1976; Abramowicz et al., 1978; Pugliese et al., 2013). These axially symmetric and stationary solutions are subject to various types of instability (e.g. Abramowicz and Fragile, 2013). Here we concentrate on a global type of instability caused

by an overflow of material over the cusp of a critical equipotential surface (Daigne and Mochkovitch, 1997; Abramowicz et al., 1998; Korobkin et al., 2013). It was suggested that this may lead to specific features that should be observable in the radiation emitted from such a system (Zanotti et al., 2003).

The effect of the mentioned instability can be catastrophic under certain conditions. In particular, a black-hole torus becomes runaway unstable if the angular momentum profile within the torus does not rise sufficiently fast with radius (Abramowicz et al., 1998; Lu et al., 2000). The role of general relativity effects on the runaway mechanism was studied in Font and Daigne (2002) in the context of gamma-ray burst sources. These authors found that by allowing the mass of the black hole to grow by accretion, the disc becomes unstable. However, the parameter space of the problem is much richer than what could be taken into account in early works. For example, the self-gravity of the fluid tends to act against the stability of non-accreting tori (Goodman and Narayan, 1988; Masuda et al., 1998; Montero et al., 2010; Korobkin et al., 2011). Furthermore, the spin parameter can play a role for accretion onto a rotating black hole. In astrophysically realistic models, an interplay of mutually competing effects have to be taken into account.

The role of magnetic fields is known to be essential for accretion. Even the Rayleigh-stable tori (Seguin, 1975) with a radially increasing profile,  $dl/dR > 0$ , become dynamically unstable because of turbulence in the presence of a weak magnetic field (Balbus and Hawley, 1991). Komissarov (2006) has developed a suitable analytical (toy) model of such a magnetized torus described by a polytropic equation of state in Kerr metric. In this model the magnetic field only enters the equilibrium solution for the torus as an additional pressure-like term. We employed this solution as an initial configuration, which we then perturbed and evolved numerically by using a two-dimensional numerical scheme (HARM; see Gammie et al., 2003).

From the mass estimates based on scaling relations that use high-frequency characteristic timescales, the mass of the black hole in M82 X-1, the bright X-ray source in the starburst galaxy M82, was estimated to be 400 solar masses (Pasham et al., 2014). Accretion tori of such intermediate-mass black holes could be perturbed by an orbiting star which could tear out considerable amount of mass above the equatorial plane and amplify the amplitude of vertical oscillations so that the overflow from an equipotential surface could occur. As the mass approaches the horizon, centrifugal forces decelerate the mass, which causes an increase of pressure, and consequently this gas pressure accelerates the mass to create an outflow. We simulated this process effectively in 2D approach, assuming that the size of the perturbing star is approximately one fourth of the radial extent of accretion torus.

## 2 OSCILLATIONS OF MAGNETIZED RELATIVISTIC TORI

### 2.1 Axisymmetric accretion of magnetized fluid tori

The magnetized ideal fluid can be described by the energy-momentum tensor (e.g. Anile, 1989)

$$T^{\mu\nu} = (w + b^2)u^\mu u^\nu + \left(P_g + \frac{1}{2}b^2\right)g^{\mu\nu} - b^\mu b^\nu, \quad (1)$$

where  $w$  is the specific enthalpy,  $P_g$  is the gas pressure, and  $b^\mu$  is the projection of the magnetic field vector ( $b^2 = b^\mu b_\mu$ ). From the energy-momentum tensor conservation,  $T^{\mu\nu}_{;\nu} = 0$ , it follows for a purely axially rotating fluid (Abramowicz et al. 1978; 2013)

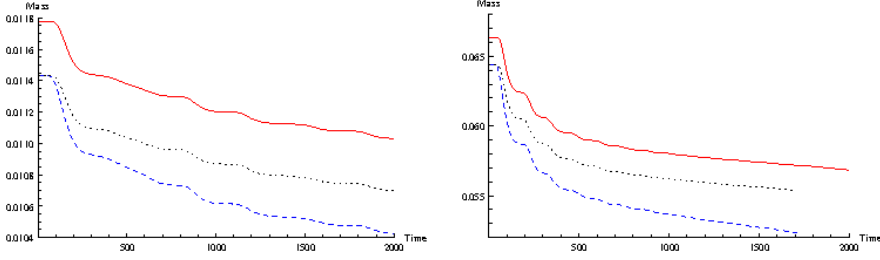
$$\ln |u_t| - \ln |u_{t_{\text{in}}}| + \int_0^{P_g} \frac{dP}{w} - \int_0^l \frac{\Omega dl}{1 - \Omega l} + \int_0^{\tilde{P}_m} \frac{d\tilde{P}}{\tilde{w}} = 0, \quad (2)$$

where  $u_t$  is the covariant component of the four-velocity (subscript “in” corresponds to the inner edge of the torus),  $\Omega = u^\varphi/u^t$  is the angular velocity and  $l = -u_\varphi/u_t$  is the angular momentum density. By assuming a suitable polytropic equation of state and the rotation law of the fluid, Eq. (2) can be integrated to obtain the structure of equipotential surfaces of the equilibrium configuration (Hamerský and Karas, 2013).

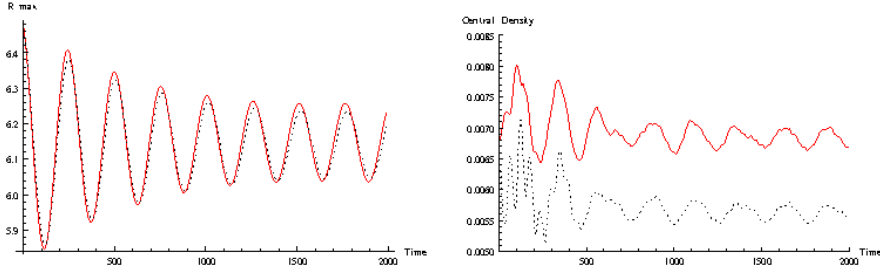
We assume that the above-described initial stationary state is pushed out of equilibrium. This leads to the capture of a small amount of material by the black hole, which increases the black-hole mass, and so the accretion occurs. Abramowicz et al. (1998) argued that tori with radially increasing specific angular momentum are more stable. The algorithm of the numerical experiment proceeds as follows. At the initial step the mass of the black hole was increased by a small amount, typically by about few percent of central object mass. After the time step  $\delta t$ , the elementary mass  $\delta M$  and angular momentum  $\delta L = l(R_{\text{in}}) \delta M$  are accreted across the horizon,  $r = r_+ \equiv [1 + \sqrt{1 - a^2}] GM/c^2$ . The mass increase  $\delta M$  is computed as a difference of the mass of torus  $M_d = \int_{\mathcal{V}} \rho d\mathcal{V}$  at  $t$  and  $t + \delta t$ , where  $d\mathcal{V} = u^t \sqrt{-g} d^3x$  is taken over the spatial volume occupied by the torus. The corresponding elementary spin increase is  $\delta a = l \delta M / (M + \delta M)$ . Therefore, at each step of the simulation we updated the model parameters by the corresponding low values of mass and angular momentum changes:  $M \rightarrow M + \delta M$ ,  $a \rightarrow a + \delta a$ . The inner cusp moves accordingly.

Figure 1 shows the dependence of the torus mass on time for different values  $\beta$  of the ratio between thermodynamical and magnetic pressure (plasma parameter),  $\beta \equiv P_g/P_m$ , for a torus with the radially increasing distribution of angular momentum,  $l(R) = l_{K, R=R_{\text{in}}} [1 + \epsilon(R - R_{\text{in}})]^q$  with  $q > 0$ ,  $0 < \epsilon \ll 1$ . This means that the reference level of the specific angular momentum is set to  $l = \text{const} = l_K(R_{\text{in}})$ , motivated by the standard theory of thick accretion discs, where the constant value is a limit for stability. A radially growing profile then helps to stabilise the configuration. From the graph we see that the amount of accreted mass is generally larger for smaller  $\beta$ . The plot also shows that the overall gradually decreasing trend is superposed with fast oscillations. After the initial drop of the torus mass (given by the magnitude of the initial perturbation,  $\delta M \simeq 0.01 M$ ) phases of enhanced accretion change with phases of diminished or zero accretion.

Figure 2 compares the magnetized vs. non-magnetized tori for the same spin ( $a = 0.3$ ). In the top panel we show the time dependence of the radial coordinate of the point with the highest mass density  $R = R_c$  (hence the highest pressure) of these two tori, and in the bottom panel the dependence of the highest mass density is captured as a function of time. In the limit of a non-magnetised slender torus ( $R_c \gg 1$ ) these oscillations correspond to the situation that has been treated previously by analytical methods (Blaes et al., 2006). Although the amplitude of  $R_c$  oscillations is quite small in these examples (because the oscillations were initiated by a weak perturbation and the torus centre is relatively far from the black hole), the outer layers of the torus are affected more significantly and can be accreted across the inner edge.



**Figure 1.** Torus mass,  $M_d(t)$ , relative to the black-hole mass as a function of time. The initial rapid accretion rate results in a drop of  $M_d$  that becomes partially stabilised during the subsequent evolution. Time is given in dimensionless units of  $GM/c^3$ . The orbital period is close to its Keplerian value near the inner edge, i.e. about  $\Delta t(R) \simeq 100$  for the material near  $R = R_{\text{in}}$ . *Left panel:* The case of spin  $a = 0.1$  is shown for different values of magnetisation parameters  $\beta = 3$  (*dashed*),  $\beta = 80$  (*dotted*), and  $\beta \rightarrow \infty$  (i.e. a non-magnetized case; *solid line*). *Right panel:* as above, but for  $a = 0.9$ . Figure adopted from (Hamerský and Karas, 2013).



**Figure 2.** Oscillation of the torus centre  $R = R_c$  (*left panel*; radius is expressed in geometrized units  $GM/c^2$  on the vertical axis), and of the central density  $\rho = \rho_c$  (*right panel*); density is relative to its peak value at the centre,  $\rho_c = \rho(R_c)$ . The *solid line* is for a non-magnetized case ( $\beta \gg 1$ ), the *dotted line* denotes the magnetized configuration ( $\beta = 3$ ). Figure adopted from (Hamerský and Karas, 2013).

## 2.2 Triggered oscillations and destruction of the torus

Vertical and radial oscillations of accretion tori may cause an overflow of matter onto the black hole because during these oscillations some parts of the torus occurs outside the equipotential surface for the initially stable torus. We assumed a following scenario of the periodically perturbed torus. At the beginning we perturb the distribution of mass inside the torus so that it would oscillate. Then we prescribe additional perturbations in the vertical direction which simulate the crossing of a star through the torus. This scenario is reasonable for intermediate-mass black holes since we can assume that the size of the torus and of the star are of the same order. This situation can be still treated without taking the self-gravity into account. During these crossings of the star mass is dragged up from the equatorial plane and consequently accreted. Before reaching the horizon the material is accelerated to create an outflow. Naturally, the interpretation of star-torus interaction is only tentative, because we use the 2D (azimuthally averaged) scheme.

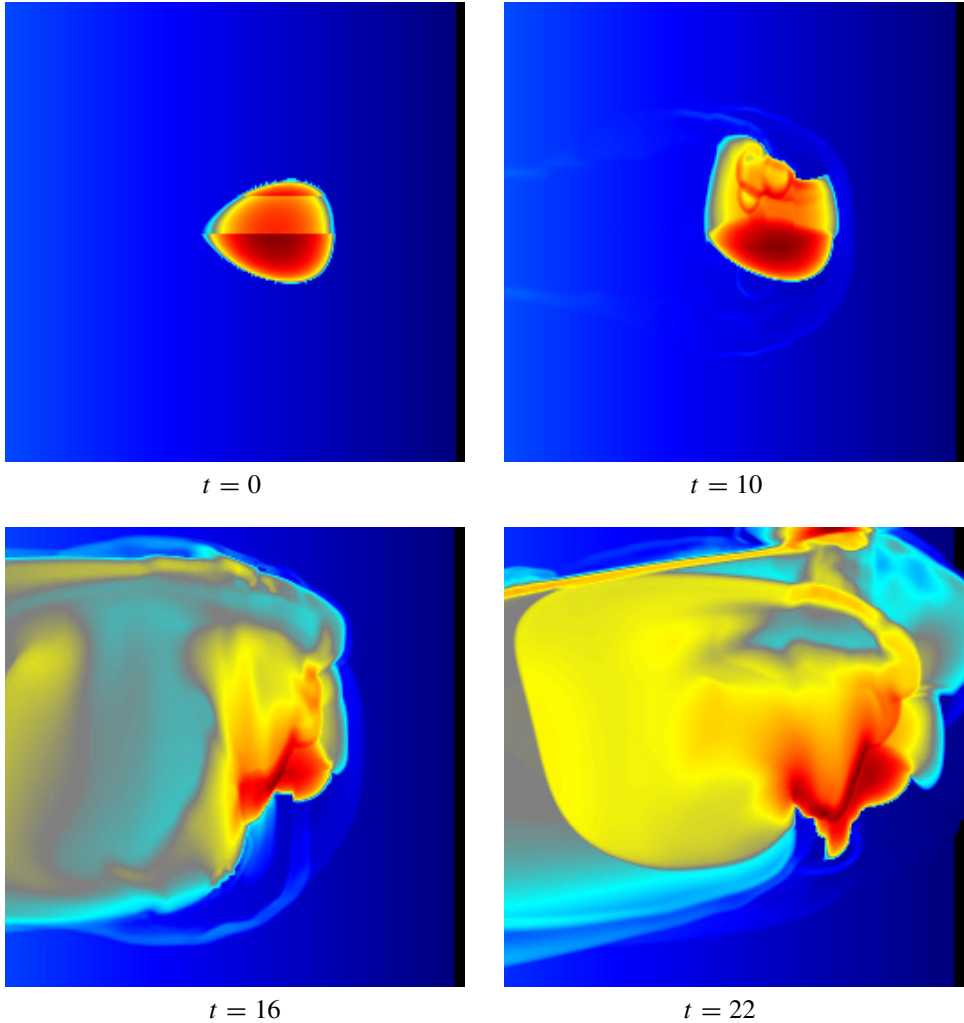


**Figure 3.** Distribution of mass density in various phases of the simulation (the colour scale in arbitrary units normalized to the maximum density). On the *left-top* panel there is a perturbed distribution of mass at time  $t = 0$ . *Next* panels show the profile of the torus after increasing the number of “star crossings”. Coordinates on the axes are identical to coordinates defined in HARM 2D numerical scheme (Gammie et al., 2003). Geometrical units are used, where time is scaled by  $GM/c^3$ .

Figure 3 shows the time evolution of the torus with additional perturbations. On these images the regions of constant radius correspond to vertical lines parallel to the vertical axis (HARM coordinates are used). The top and the bottom rim of the image correspond to rotation axis of the central Kerr black hole.

On the top part of the right-bottom panel in Fig. 3 one can see the outflow directed away from the horizon. This image is shown in Cartesian coordinates in Fig. 4 where the arrows express a direction and a magnitude of the velocity of the mass. The velocity of

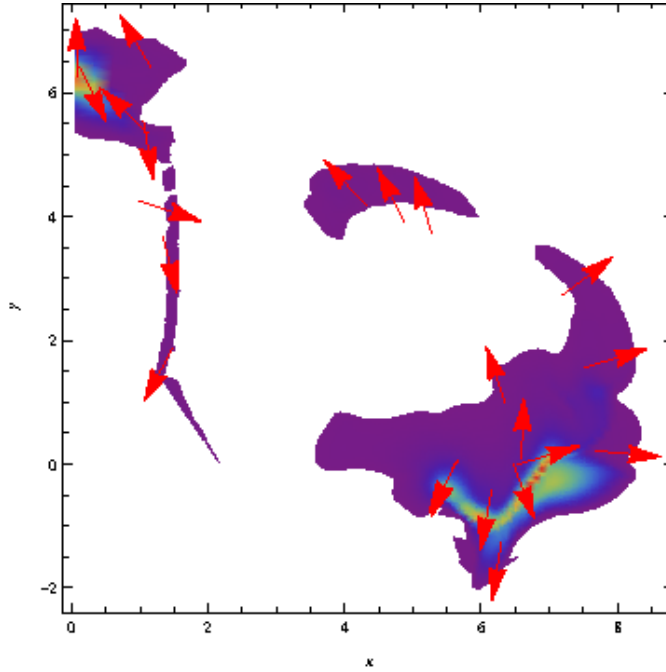


**Figure 4.** Distribution of mass (colour-coded in arbitrary units) with corresponding velocities indicated by red arrows. While the torus oscillates mainly in the vertical direction, some part of mass high above the equatorial plane has positive radial velocities.  $(X, Y)$  are Cartesian coordinates scaled with respect to  $R_g$ .

accelerated mass can reach values about  $0.3 c$ . We compared the non-magnetized case with the magnetized one. When we assumed the purely toroidal magnetic field present inside the torus according to the Komissarov solution (Komissarov, 2006) with the magnetization parameter  $\beta = 3$  there was more mass accreted compared to non-magnetized case and velocities of accelerated mass were higher approximately by 12%. We also tried to add a vertical component of the magnetic field to our simulations. However the strength of this field was not higher than 10% of the strength of the toroidal magnetic field because for stronger fields numerical problems in the code arise.

### 3 CONCLUSIONS

Within the framework of an axially symmetric magnetized fluid torus model we have extended the previous results on the onset of runaway instability of relativistic configurations near a rotating black hole. The numerical approach allows us to consider also large amplitude perturbations that can lead to significant outflows and even the torus destruction. We concentrated on systems with radially increasing specific angular momentum that are threaded by a purely toroidal magnetic field. We neglected self-gravity of the gaseous material (the mass of the torus was set to be at most several percent of the black-hole mass), nevertheless, we allowed for a gradual change of the Kerr metric mass and spin parameters by accretion over the inner edge. The angular momentum distribution within the torus was

also allowed to evolve, starting from the initial power-law profile. The mass transfer influences the location of the cusp of the critical configuration, which can lead to the runaway instability. The process of accretion is not perfectly monotonic, instead, there are changing phases of enhanced accretion rate and phases where the mass of torus remains almost constant. The overall gradual decrease of the torus mass is superposed with oscillations that can be seen by following the central density variations on the dynamical time-scale and the position of the centre of the torus. The oscillation amplitude is sensitive to the initial perturbation, but the frequency is not, namely, a small change of the metric coefficients does not affect the oscillation frequency. A large-amplitude perturbation leads to the torus complete destruction.

The toroidal magnetic field plays a more important role in the early phases of the accretion process until the perturbed configuration finds a new equilibrium or disappears because of the runaway instability. We showed that additional perturbations in the vertical direction can lead to relativistic outflows if the perturbations are strong enough so that the mass could get far from the equatorial plane. Otherwise the mass is accelerated dominantly in the radial direction and it moves back to the torus. We showed that the presence of magnetic field supports the acceleration of mass and consequently outflows can reach higher velocities. For further details see Hamerský and Karas (2014, in preparation).

## ACKNOWLEDGEMENTS

We acknowledge support from the student project of the Charles University (GAUK 139810; JH) and the collaboration project between the Czech Science Foundation and Deutsche Forschungsgemeinschaft (GACR-DFG 13-00070J; VK). The Astronomical Institute has been operated under the program RVO:67985815.

## REFERENCES

- Abramowicz, M., Jaroszynski, M. and Sikora, M. (1978), Relativistic, accreting disks, *Astronomy and Astrophysics*, **63**, pp. 221–224.
- Abramowicz, M. A. and Fragile, P. C. (2013), Foundations of Black Hole Accretion Disk Theory, *Living Reviews in Relativity*, **16**, p. 1, arXiv: 1104.5499.
- Abramowicz, M. A., Karas, V. and Lanza, A. (1998), On the runaway instability of relativistic tori, *Astronomy and Astrophysics*, **331**, pp. 1143–1146, arXiv: astro-ph/9712245.
- Anile, A. M. (1989), *Relativistic fluids and magneto-fluids: With applications in astrophysics and plasma physics*, Cambridge University Press, Cambridge and New York.
- Balbus, S. A. and Hawley, J. F. (1991), A powerful local shear instability in weakly magnetized disks. I - Linear analysis. II - Nonlinear evolution, *Astrophys. J.*, **376**, pp. 214–233.
- Blaes, O. M., Arras, P. and Fragile, P. C. (2006), Oscillation modes of relativistic slender tori, *Monthly Notices Roy. Astronom. Soc.*, **369**, pp. 1235–1252, arXiv: astro-ph/0601379.
- Daigne, F. and Mochkovitch, R. (1997), Gamma-ray bursts and the runaway instability of thick discs around black holes, *Monthly Notices Roy. Astronom. Soc.*, **285**, pp. L15–L19.
- Fishbone, L. G. and Moncrief, V. (1976), Relativistic fluid disks in orbit around Kerr black holes, *Astrophys. J.*, **207**, pp. 962–976.

- Font, J. A. and Daigne, F. (2002), On the Stability of Thick Accretion Disks around Black Holes, *Astrophys. J. Lett.*, **581**, pp. L23–L26, arXiv: astro-ph/0211102.
- Gammie, C. F., McKinney, J. C. and Tóth, G. (2003), HARM: A Numerical Scheme for General Relativistic Magnetohydrodynamics, *Astrophys. J.*, **589**, pp. 444–457, arXiv: astro-ph/0301509.
- Goodman, J. and Narayan, R. (1988), The stability of accretion tori. III - The effect of self-gravity, *Monthly Notices Roy. Astronom. Soc.*, **231**, pp. 97–114.
- Hamerský, J. and Karas, V. (2013), Effect of the toroidal magnetic field on the runaway instability of relativistic tori, *Astronomy and Astrophysics*, **555**, A32, arXiv: 1305.6515.
- Komissarov, S. S. (2006), Magnetized tori around Kerr black holes: analytic solutions with a toroidal magnetic field, *Monthly Notices Roy. Astronom. Soc.*, **368**, pp. 993–1000, arXiv: astro-ph/0601678.
- Korobkin, O., Abdikamalov, E., Stergioulas, N., Schnetter, E., Zink, B., Rosswog, S. and Ott, C. D. (2013), The runaway instability in general relativistic accretion discs, *Monthly Notices Roy. Astronom. Soc.*, **431**, pp. 349–354, arXiv: 1210.1214.
- Korobkin, O., Abdikamalov, E. B., Schnetter, E., Stergioulas, N. and Zink, B. (2011), Stability of general-relativistic accretion disks, *Phys. Rev. D*, **83**(4), 043007, arXiv: 1011.3010.
- Lu, Y., Cheng, K. S., Yang, L. T. and Zhang, L. (2000), A massive thick disc around a massive black hole and its runaway instability, *Monthly Notices Roy. Astronom. Soc.*, **314**, pp. 453–458.
- Masuda, N., Nishida, S. and Eriguchi, Y. (1998), The runaway instability of self-gravitating tori with non-constant specific angular momentum around black holes, *Monthly Notices Roy. Astronom. Soc.*, **297**, pp. 1139–1144.
- Montero, P. J., Font, J. A. and Shibata, M. (2010), Influence of Self-Gravity on the Runaway Instability of Black-Hole-Torus Systems, *Phys. Rev. Lett.*, **104**(19), 191101, arXiv: 1004.3102.
- Pasham, D. R., Strohmayer, T. E. and Mushotzky, R. F. (2014), A 400-solar-mass black hole in the galaxy M82, *Nature*, **513**, pp. 74–76, arXiv: 1501.03180.
- Pugliese, D., Montani, G. and Bernardini, M. G. (2013), On the Polish doughnut accretion disc via the effective potential approach, *Monthly Notices Roy. Astronom. Soc.*, **428**, pp. 952–982, arXiv: 1206.4009.
- Seguin, F. H. (1975), The stability of nonuniform rotation in relativistic stars, *Astrophys. J.*, **197**, pp. 745–765.
- Zanotti, O., Rezzolla, L. and Font, J. A. (2003), Quasi-periodic accretion and gravitational waves from oscillating ‘toroidal neutron stars’ around a Schwarzschild black hole, *Monthly Notices Roy. Astronom. Soc.*, **341**, pp. 832–848, arXiv: gr-qc/0210018.

# Regularity of pulsar glitches

Jakub Juryšek

Institute of Physics, Faculty of Philosophy and Science,  
Silesian University in Opava, Bezručovo nám. 13, Opava CZ-74601  
jakubjurysek@astronomie.cz

## ABSTRACT

Glitches are sudden changes (usually increases) of pulsars rotation rates, whose causes are still unknown. Study of glitches and their properties may lead to independent view to the physics of pulsars and to the properties and structure of neutron stars. In this contribution we present preliminary results of our analysis of the inter-glitch intervals. The studied data sample contains 30 pulsars with a number of detected glitches higher than four. Analysis of the data shows that there could exist linear correlation between glitch amplitudes and inter-glitch intervals in the case of 11 pulsars from studied data sample. These results alone may suggests that the global processes may be responsible for glitches.

**Keywords:** Pulsar – glitches – neutron stars

## 1 INTRODUCTION

Isolated pulsars are rotating neutron stars characterized by high rotational stability. Nowadays, we can obtain many important informations about astrophysical processes inside neutron stars and in their vicinity. Precise analysis of long-scale pulsar timing shows that rotational frequencies of the pulsars slowly decrease. Moreover, sometimes sudden change (usually increase) of rotational frequency  $\nu$  may occur and this phenomena is called *glitch*. Relative amplitudes of glitches  $\Delta\nu/\nu$  ranges  $10^{-11} \leq \Delta\nu/\nu \leq 10^{-5}$  (Espinoza et al., 2011). Since the first glitch detection at the end of 1970's (Vela pulsar, Radhakrishnan and Manchester (1969)), 439 glitches in 213 pulsars have been detected until today<sup>1</sup> (see online database of Jodrell Bank observatory<sup>2</sup> (Espinoza et al., 2011)). Glitches are detected in about one tenth of whole of 2302 discovered pulsars (Manchester et al., 2005).<sup>3</sup> Histogram of glitch amplitudes is shown in the left panel of Fig. 1. We can see two peaks at about  $\Delta\nu/\nu \approx 10^{-8}$  and  $\Delta\nu/\nu \approx 10^{-6}$ . The right panel of Fig. 1 shows all detected glitch amplitudes against characteristic age for all glitching pulsars. We can see that the glitches with large amplitude are occurring mostly in pulsars with characteristic age  $\tau \approx 10^4$  years.

<sup>1</sup> October 2013

<sup>2</sup> Actual version of Jodrell bank (JB) online database: <http://www.jb.man.ac.uk/pulsar/glitches.html>

<sup>3</sup> <http://www.atnf.csiro.au/research/pulsar/psrcat/>

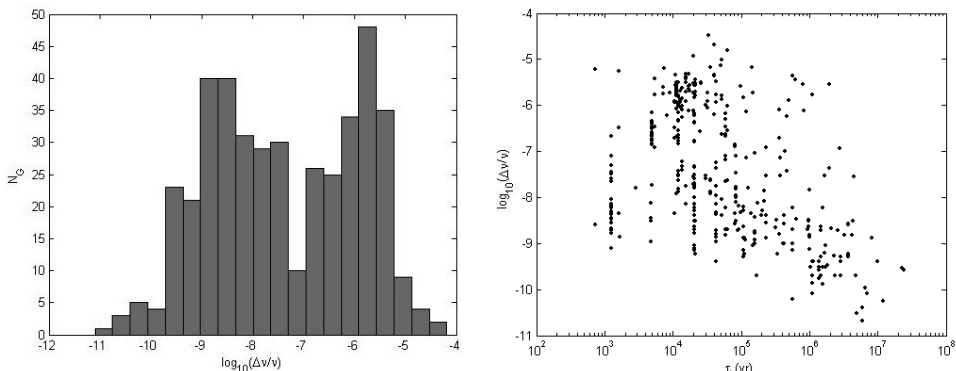


**Figure 1.** Statistical properties of glitch amplitudes. *Left:* Histogram of glitch amplitudes. *Right:* Relation between glitch amplitudes and characteristic ages of pulsars. The data were taken from on-line databases JB and ATNF.

On the other hand, glitches with amplitudes about  $\Delta\nu/\nu \approx 10^{-8}$  (left peak on the left panel of Fig. 1) are occurring at all glitching pulsars independently on their characteristic age.

During the glitch not only the rotational frequency  $\nu$  but also its time derivative (spin-down rate)  $\dot{\nu}$  is changed. Glitches are usually followed by slow relaxation of spin-down rate and frequency to their pre-glitch values. However in some cases, the post-glitch behaviour of  $\nu$  is more complicated. For example, the J0534+2200 (Crab) pulsar glitches were followed by persistent change of  $\dot{\nu}$  (Lyne et al., 1993). Moreover, some glitches of the J0358+5413 pulsar were followed by permanent change of rotational rate  $\nu$  (Lyne, 1987).

A physical mechanism of glitches is still under discussion (see e.g. a review of a contemporary theories of glitch mechanisms in the bachelor's thesis (Juryšek, 2014) and references there in). However, it is generally accepted that the glitches are caused by variable coupling between neutron star's crust and its superfluid interior (Gosh, 2007). Pulsar glitches are occurring sparsely and the inter-glitch intervals are long. The most glitching pulsars are J0537-6910, J0729-1448, J1740-3015 and J1341-6220 and their mean inter-glitch intervals range from  $\lambda \approx 138$  days to  $\lambda \approx 272$  days. That is the reason why the total amount of detected glitches increases very slowly and statistical relevance's of obtained results are relatively poor. Despite the weak statistics of glitch data it is very important to study glitches thoroughly, because the glitch behaviours can provide immensely valuable perspective on the properties of the pulsar and consequently on internal structure of neutron stars.

Based on generally accepted models of glitches it is possible to expect the existence of linear correlation between glitch amplitudes  $\Delta\nu/\nu$  and inter-glitch intervals (or glitch waiting times)  $\Delta t$ . Almost all previous analysis of glitch waiting times which have been carried out by many authors, see e.g. Wong et al. (2001); Yuan et al. (2010); Wang et al. (2000, 2012), have shown absence of any of the expected correlations, with the exception of two pulsars – J0537-6910 (Middleditch et al., 2006) and J1645-0317 (Shabanova, 2009). Furthermore, several authors (e.g. Wang et al. (2012) and Wong et al. (2001) in the case of the J0534+2200 pulsar or Melatos et al. (2008) using their sample of nine pulsars) have shown that the individual glitches are independent of each other. In the case of correlations

between  $\Delta v/v$  and  $\Delta t$  the global processes in the neutron star's crust would be responsible for glitches. On the other hand time independence of glitches may be result of local relaxations of mutually isolated momentum reservoirs.

In our own analysis, we focused on a glitch waiting times and our preliminary results are listed below in Section Data analysis and results, we finish our contribution with Summary and future work.

## 2 DATA ANALYSIS AND RESULTS

Since last studies of correlations between  $\Delta v/v$  and  $\Delta t$  were published, many new glitches were detected and that is why we repeated analysis of correlation on a large sample of pulsars and glitches. We have chosen 30 pulsars with four or more glitch detections ( $N_G \geq 4$ ) with an effort to use the largest possible sample of pulsars. We have used on-line JB database and the ATNF catalogue as the source of glitch amplitudes and times of arrival.

If origin of glitches is related to process of global character we can expect that larger glitch occurs after longer accumulation of momentum (e.g. in the crust of neutron star) and all accumulated momentum could be released. In this case correlation between glitch amplitudes  $\Delta v/v$  and time interval preceding the glitch  $\Delta t_P$  should exist. Basically, longer time of accumulation of momentum leads to larger glitch amplitude. Additionally, a glitch trigger mechanism may be completely independent on glitches themselves (e.g. accretion of matter or some other external processes). On the other hand, if there is some threshold value that accumulated momentum needs to overcome to trigger the glitch and if only part of the whole momentum reservoir is released during the glitch then correlation between glitch amplitude and waiting time after the glitch  $\Delta t_F$  should exist. This threshold value could be e.g. limit value of difference between rotation velocity of the crust and the interior superfluid. In this case the correlation is because the waiting time till next glitch is affected by the glitch amplitude of the preceding glitch (or equivalently by the amount of momentum from the reservoir that is released during the glitch).

In our study, we search for correlation between  $\Delta v/v$  and time intervals  $\Delta t_P$  and  $\Delta t_F$  on the whole sample of 30 pulsars. Correlations have been quantified using Pearson's correlation coefficients  $C_{\text{cor}}$ , which have been calculated using 'corrcoef' function implemented in MATLAB (2012) software. The resulting values of correlation coefficients are listed in the Table 1. The most significant correlations are marked using bold typeface. In some cases, high values of  $C_{\text{cor}} < 0$  are due to one outlying point in waiting time – glitch amplitude space and after we removed this point the correlation disappeared. Only those pulsars for which this case did not happened are marked in the Table 1. As we can see, there are 11 pulsars with significant correlations between amplitudes and glitch waiting times besides two previously published cases. There are both types of correlations between  $\Delta v/v$  and  $\Delta t_P/\Delta t_F$  in the cases of J1731-4744 and J1801-2451 pulsars. Moreover, both dependencies  $\Delta v/v$  on  $\Delta t_F$  are surprisingly giving the  $C_{\text{cor}} < 0$ . This contradicts the intuitive idea of gradual increase of stress in a global reservoir. Dependency of  $\Delta v/v$  on  $\Delta t_P$  at the J2301+5852 pulsar is also showing  $C_{\text{cor}} < 0$ .

## 3 SUMMARY AND FUTURE WORK

Based on our analysis of 30 pulsars with  $N_G \geq 4$  we can state that 13 of them show significant correlations between  $\Delta t_{P/F}$  and  $\Delta v/v$ . These results are surprising in comparison with

**Table 1.** Correlations between  $\Delta t_{P/F}$  and  $\Delta\nu/\nu$  at 30 pulsars with  $N_G \geq 4$ . The most significant correlations are marked using bold typeface.

PSR	$N_G$	$\Delta t_{P/F}$	$C_{\text{cor}}$	PSR	$N_G$	$\Delta t_{P/F}$	$C_{\text{cor}}$
<b>J0205+6449</b>	4	P	-0.3352	J1708-4009	6	P	-0.1101
		<b>F</b>	<b>0.9902</b>			F	0.5002
J0358+5413	6	P	-0.2719	<b>J1731-4744</b>	4	<b>P</b>	<b>0.9452</b>
		F	0.9907			<b>F</b>	<b>-0.9144</b>
<b>J0528+2200</b>	4	<b>P</b>	<b>0.9844</b>	J1740-3015	33	P	-0.027
		F	0.3780			F	0.4209
J0534+2200	25	P	0.0341	<b>J1801-2304</b>	11	P	0.6257
		F	0.0266			<b>F</b>	<b>0.7127</b>
<b>J0537-6910</b>	23	P	0.0431	<b>J1801-2451</b>	5	<b>P</b>	<b>0.8835</b>
		<b>F</b>	<b>0.9421</b>			<b>F</b>	<b>-0.9817</b>
J0631+1036	15	P	-0.0913	J1803-2137	5	P	0.1490
		F	0.7009			F	0.8901
J0729-1448	5	P	-0.3489	<b>J1814-1744</b>	7	P	-0.4347
		F	0.6838			<b>F</b>	<b>0.7564</b>
J0742-2822	7	P	0.1180	<b>J1833-1034</b>	4	<b>P</b>	<b>0.9874</b>
		F	-0.0818			F	0.1560
J0834-4511	17	P	0.4787	J1825-0935	6	P	-0.2448
		F	0.3724			F	-0.1525
J1048-5832	6	P	-0.4760	<b>J1826-1334</b>	5	P	-0.2183
		F	0.5806			<b>F</b>	<b>0.9606</b>
J1105-6107	5	P	-0.3693	J1902+0615	6	P	-0.3142
		F	0.8685			F	0.4899
J1341-6220	23	P	-0.0818	J1952+3252	6	P	0.8883
		F	0.2931			F	0.7052
<b>J1413-6141</b>	7	P	0.4147	J2225+6535	5	P	-0.3249
		<b>F</b>	<b>0.8433</b>			F	0.9983
J1420-6048	5	P	0.6533	<b>J2229+6114</b>	5	P	-0.2524
		F	0.2333			<b>F</b>	<b>0.9798</b>
<b>J1645-0317</b>	7	P	0.2863	<b>J2301+5852</b>	4	<b>P</b>	<b>-0.8873</b>
		<b>F</b>	<b>0.9888</b>			F	0.4054

previously published analyses. These results are in agreement with theories suggesting that a global processes in the neutron star's crust play the key role in the glitch mechanisms. In the case of a small number of detected glitches, the statistic reliability of obtained results is essential question and we will focus on this issue in the subsequent work (Juryšek and Urbanec, in prep.). There is need for further analysis in order to distinguish between local and global causes of glitches. At first, it is necessary to investigate mutual independence of individual glitches. We are working on more detailed analysis and we plan to include more significant results in the prepared paper.

## REFERENCES

- Espinoza, C. M., Lyne, A. G., Stappers, B. W. and Kramer, M. (2011), A study of 315 glitches in the rotation of 102 pulsars, *Monthly Notices Roy. Astronom. Soc.*, **414**, pp. 1679–1704, arXiv: 1102.1743.
- Gosh, P. (2007), *Rotation and Accretion Powered Pulsars*, World Scientific Publishing Co. Pte. Ltd., Singapore, ISBN 978-981-02-4744-7.
- Juryšek, J. (2014), *Glitche pulsaru*, Bachelor's thesis, Slezská univerzita v Opavě, Opava, Czech Republic.
- Juryšek, J. and Urbanec, M. (in prep.), Pulsar glitches: Quasiperiodicity and regularity.
- Lyne, A. G. (1987), A massive glitch in an old pulsar, *Nature*, **326**, pp. 569–571.
- Lyne, A. G., Pritchard, R. S. and Graham-Smith, F. (1993), Twenty-Three Years of Crab Pulsar Rotational History, *Monthly Notices Roy. Astronom. Soc.*, **265**, p. 1003.
- Manchester, R. N., Hobbs, G. B., Teoh, A. and Hobbs, M. (2005), The Australia Telescope National Facility Pulsar Catalogue, *Astronom. J.*, **129**, pp. 1993–2006, arXiv: astro-ph/0412641.
- MATLAB (2012), *version 7.14.0.739 (R2012a)*, The MathWorks Inc., Natick, Massachusetts.
- Melatos, A., Peralta, C. and Wyithe, J. S. B. (2008), Avalanche Dynamics of Radio Pulsar Glitches, *Astrophys. J.*, **672**, pp. 1103–1118, arXiv: 0710.1021.
- Middleditch, J., Marshall, F. E., Wang, Q. D., Gotthelf, E. V. and Zhang, W. (2006), Predicting the Starquakes in PSR J0537-6910, *Astrophys. J.*, **652**, pp. 1531–1546, arXiv: astro-ph/0605007.
- Radhakrishnan, V. and Manchester, R. N. (1969), Detection of a Change of State in the Pulsar PSR 0833-45, *Nature*, **222**, pp. 228–229.
- Shabanova, T. V. (2009), Nature of Cyclical Changes in the Timing Residuals from the Pulsar B1642 - 03, *Astrophys. J.*, **700**, pp. 1009–1016, arXiv: 0906.3641.
- Wang, J., Wang, N., Tong, H. and Yuan, J. (2012), Recent glitches detected in the Crab pulsar, *Astrophys. Space Sci.*, **340**, pp. 307–315, arXiv: 1203.4291.
- Wang, N., Manchester, R. N., Pace, R. T., Bailes, M., Kaspi, V. M., Stappers, B. W. and Lyne, A. G. (2000), Glitches in southern pulsars, *Monthly Notices Roy. Astronom. Soc.*, **317**, pp. 843–860, arXiv: astro-ph/0005561.
- Wong, T., Backer, D. C. and Lyne, A. G. (2001), Observations of a Series of Six Recent Glitches in the Crab Pulsar, *Astrophys. J.*, **548**, pp. 447–459, arXiv: astro-ph/0010010.
- Yuan, J. P., Wang, N., Manchester, R. N. and Liu, Z. Y. (2010), 29 glitches detected at Urumqi Observatory, *Monthly Notices Roy. Astronom. Soc.*, **404**, pp. 289–304, arXiv: 1001.1471.



# Modified Newtonian potentials for particles and fluids in permanent rotation around black holes

Vladimír Karas<sup>1,a</sup> and Marek A. Abramowicz<sup>2</sup>

<sup>1</sup>Astronomical Institute, Academy of Sciences of the Czech Republic,  
Boční II 1401, CZ-141 00 Prague, Czech Republic

<sup>2</sup>Copernicus Astronomical Center, Polish Academy of Sciences,  
ul. Bartycka 18, P-00 716 Warsaw, Poland

<sup>a</sup>vladimir.karas@cuni.cz

## ABSTRACT

Modified Newtonian potentials have been proposed for the description of relativistic effects acting on particles and fluids in permanent orbital motion around black holes. Here we further discuss spherically symmetric potentials like the one proposed by Artemova, Björnson & Novikov (1996, *Astrophysical Journal*, 461, 565), and we illustrate their virtues by studying the acceleration along circular trajectories. We compare the results with exact expressions in the spacetime of a rotating (Kerr) black hole.

**Keywords:** Accretion: accretion discs – black-hole physics

## 1 INTRODUCTION

The motion of material around black holes, both particles and fluids, is of particular importance for the present-day models of some astronomical objects, such as galactic X-ray sources and active galactic nuclei. In these systems, matter may be found rather close to the black-hole horizon, at a few gravitational radii ( $r_g = 2GM/c^2$ ; where  $M$  is the mass of the central black hole), and the effects of general relativity on the motion must be taken into account. (We will here set  $c = G = 1$ ; in addition, we will measure lengths in units of  $M$ , so that  $r_g = 2$  hereafter.) The relevant framework for discussing such fluids is then the Kerr spacetime of a rotating black hole (we consider here only test particles and fluids around the black hole, as is often done for astrophysical situations; however, for exact solutions of the Einstein equations with rotating bodies, see e.g. Islam (1985), and for more astrophysically realistic numerical solutions with self-gravitating material, see Lanza (1992); Nishida and Eriguchi (1994)). The relativistic effects for this matter can be ascribed mainly to two characteristic properties of motion around black holes: (i) presence of the marginally stable orbit ( $r = r_{ms}$ ) and the marginally bound orbit ( $r = r_{mb}$ ) which determine the regions of stable and energetically bound motion (their location determines also the inner edge of the toroidal fluid configurations; the exact location of  $r_{mb}$  and  $r_{ms}$  can be found by studying the effective potential; see Bardeen et al. (1972)); (ii) the frame

dragging of non-equatorial orbits (Lense–Thirring precession, often called the Wilkins (1972) effect in the case of motion close to a Kerr black hole). In order to incorporate these effects within the Newtonian framework (which is of course technically easier than a fully relativistic self-consistent approach), numerous authors have adopted the original idea of Paczyński and Wiita (1980) and employed modifications of the Newtonian potential (Nowak and Wagoner, 1991; Artemova et al., 1996; Crispino et al., 2011).<sup>1</sup>

In this Note we want to discuss simple (spherically symmetric) potentials appropriate for the description of matter in purely rotational motion, neglecting frame-dragging effects. This simplifies our discussion; see Semerák and Karas (1999) for detailed discussion and references concerning how to modify the Newtonian potential for including the effects of dragging. In previous studies, the main concern was about how to reproduce correctly the marginally bound and marginally stable orbits, since the properties of fluid tori are sensitive to the location of *both* of these orbits (cf. Muchotrzeb and Paczyński, 1982; Abramowicz et al., 1988; Kato et al., 1988; Chakrabarti, 1990). See also Tejeda and Rosswog (2013) and Barausse and Lehner (2013) for a recent discussion and new developments.

The Paczyński–Wiita potential,  $\Phi_{\text{PW}} = -1/(r - r_{\text{g}})$ , reproduces the correct location of  $r_{\text{mb}}$  and  $r_{\text{ms}}$  for a non-rotating black hole. Another form of the modified potential around a non-rotating black hole was used by Nowak and Wagoner (1991) to study relativistic wave-modes in accretion discs:  $\Phi_{\text{NW}} = -r^{-1} + 3r^{-2} - 12r^{-3}$  reproduces  $r_{\text{ms}}$  and the epicyclic frequency of radial oscillations  $\kappa$ . These two potentials  $\Phi_{\text{PW}}$  and  $\Phi_{\text{NW}}$  are not however applicable in the case of a rotating black hole. This situation has been treated by several authors, most recently and successfully by Artemova et al. (1996). Here we will further discuss the form of the potential which appears most convenient for modelling tori around rotating black holes. Note that tori rotate with non-Keplerian orbital velocity and they may extend well out of equatorial plane (Frank et al., 1992). One thus needs to consider also accelerated motion, though still in permanent rotation about the common axis of the black hole.

## 2 MODIFIED NEWTONIAN POTENTIAL FOR ROTATING BLACK HOLES

### 2.1 Motivation

The need for a practical and accurate modified potential leads to constraining its form according to the following conditions:

- (i) The modified potential should be a *simple* scalar function of the spherical radius  $r$ ;
- (ii) The potential should reduce to  $\Phi_{\text{PW}}$  in the limit of zero rotation (black-hole angular momentum parameter  $a = 0$ );
- (iii) The locations of  $r_{\text{ms}}$  and  $r_{\text{mb}}$  should be correctly reproduced *both* for the non-rotating case ( $a = 0$ ,  $r_{\text{ms}} = 6$ ,  $r_{\text{mb}} = 4$ ) and for the extreme rotating case ( $a = 1$ ,  $r_{\text{mb}} = r_{\text{ms}} = 1$ ).

<sup>1</sup> A different approach was adopted in Keres (1967); Israel (1970); de Felice (1980), where some properties of the Kerr metric are described in terms of an axially symmetric (non-spherical) potential which reflects the asymptotic properties of test particle motion.

These requirements are satisfied by the function

$$\Phi = -\frac{1}{(r - r_+)^{\bar{\beta}} r^{1-\bar{\beta}}}, \quad (1)$$

where  $r_+ = 1 + \sqrt{1 - a^2}$  is the black hole outer horizon, and the parameter  $\bar{\beta}(a)$  is a free function. The choice for this is constrained by imposing that the values of  $r_{\text{mb}}$  and  $r_{\text{ms}}$  should be exact in the Schwarzschild case and in the extreme Kerr case. We then adopt the simplest linear form:  $\bar{\beta} = 1 - a$ . Although, for  $\bar{\beta} = 0$ , Eq. (1) reduces to the Newtonian potential which does not have marginally bound and marginally stable orbits, the correct location of  $r_{\text{mb}} = r_{\text{ms}} = 1$  is nevertheless obtained in the limit of  $a \rightarrow 1$  (the extreme Kerr case).

One can verify that the properties of the potential (1) are almost identical with those of the potential  $\Phi_{\text{ABN}}$  of Frank et al. (1992) which corresponds to their Eq. (13) for the force:

$$F_5 = -\frac{1}{r^{2-\beta} (r - r_+)^{\beta}}, \quad (2)$$

with  $\beta = (r_{\text{ms}}/r_+) - 1$ . Expression (2) follows from the following conditions:

- (i) The free-fall acceleration has a similar form to that for a Schwarzschild black hole;
- (ii) The free-fall acceleration diverges to infinity near  $r = r_+$ .
- (iii) The marginally stable orbit is reproduced *exactly for all* values of  $a$  ( $0 \leq a \leq 1$ ).

Although the position of the important orbit  $r = r_{\text{mb}}$  is not mentioned in the derivation of  $F_5$ , one can verify that the correct sequence is maintained for all  $a$ :  $r_+ \leq r_{\text{mb}} \leq r_{\text{ms}} \leq 6$  (indeed, the accuracy is very good as we will see in the next paragraph). The potential corresponding to  $F_5$  is

$$\Phi_{\text{ABN}} = \frac{1}{(1 - \beta)r_+} \left(1 - \frac{r_+}{r}\right)^{1-\beta} - \Phi_{\infty}, \quad (3)$$

with  $\Phi_{\infty} = (1 - \beta)^{-1}r_+^{-1}$ .

## 2.2 Acceleration along circular orbits

We will now argue that the results for purely rotational motion of fluids in potentials (1) and (3) should be extremely similar and close to the exact relativistic treatment in the Kerr metric. This conjecture can be illustrated in two steps: first we will see that  $r_{\text{ms}}$  and  $r_{\text{mb}}$  are well reproduced (for both  $\Phi$  and  $\Phi_{\text{ABN}}$ ), and then we will study acceleration along non-Keplerian circular orbits (relevant for modelling tori).

We now illustrate the differences in the marginally bound radius as a function of the marginally stable radius. Figure 1 compares our modified Newtonian ratios  $y = r_{\text{mb}}/r_+$  and  $x = r_{\text{ms}}/r_+$  (evaluated by using Eq. 1) with the corresponding values of the Boyer–Lindquist radial coordinate in the Kerr metric. In both cases  $1 \leq x(a) \leq 3$  and  $1 \leq y(a) \leq 2$  when the angular-momentum parameter varies in the range  $1 \geq a \geq 0$ . Figure 1a shows that the two curves of  $y(x)$  (i.e. the modified Newtonian and Kerr cases) are practically

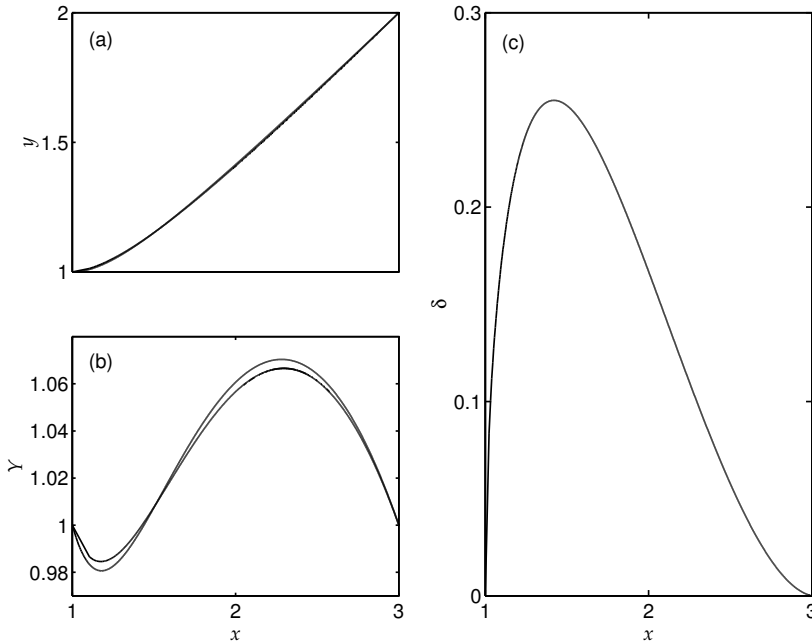


**Figure 1.** Radii of important orbits in the modified Newtonian potential  $\Phi$  compared with the Kerr case: (a) the radius of the marginally bound orbit  $y$  plotted as a function of the radius of the marginally stable orbit  $x$ , both measured in units of the black hole outer horizon radius  $r_+$ ; (b) the normalized marginally bound radius  $Y(x) = fy$ ; (c) the relative difference  $\delta(x)$  between the modified Newtonian and Kerr cases (see text for definitions).

indistinguishable. In order to amplify the tiny difference, we introduce  $Y = f \cdot y$  where the normalization factor is given by  $f = 1 - (x - 1)/4$ . The curves of  $Y(x)$  are plotted in Fig. 1b. We complement these graphs by showing (Fig. 1c)  $\delta = \sqrt{[\delta x]^2 + [\delta y]^2}$  where  $\delta x(a)$ ,  $\delta y(a)$  are the differences in  $x$  and  $y$  between the modified Newtonian and Kerr cases. It can be seen that  $\delta \lesssim 0.25$ , which indicates an accuracy of  $x$  and  $y$  better than about 20%. The error is a maximum at  $x \approx 1.4$  and it goes sharply to zero for *both*  $x = 1$  ( $a = 1$ ) and  $x = 3$  ( $a = 0$ ). One can construct analogous graphs for  $\Phi_{\text{ABN}}$  but the results are very similar to those for  $\Phi$ . It is therefore a matter of taste which potential to choose for studying toroids in modified Newtonian potentials, but  $\Phi_{\text{ABN}}$  is perhaps more practical as it has already been used by other authors (Miwa et al., 1998).

The structure of relativistic tori is determined by the radial acceleration along circular trajectories, and of course by the pressure gradient which, however, depends on the equation of state. We will therefore now discuss the radial acceleration for different  $r = \text{const}$  and different angular velocity  $\omega$ , and again we will compare the case of the modified Newtonian potential with that of the Kerr metric (free circular orbits in the equatorial plane have  $\omega = 1/(r^{3/2} + a)$  and acceleration magnitude  $A = 0$ , but we do not restrict only to such

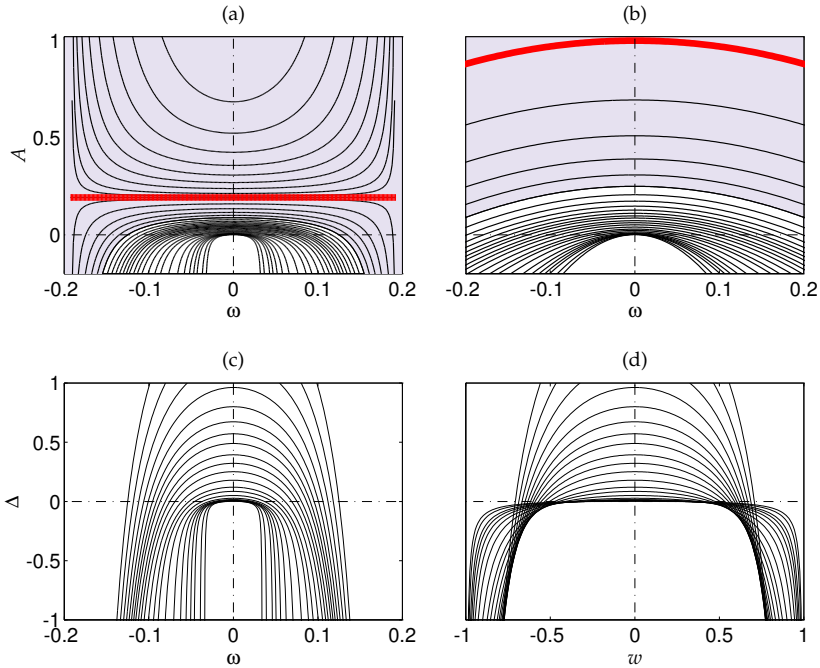


**Figure 2.** The acceleration magnitude  $A$  is plotted as a function of the angular velocity  $\omega$  along circular orbits with different radii: (a) the Schwarzschild case; (b) the modified Newtonian case  $\Phi_{\text{pw}}$  (the two plots are clearly different in the shaded area corresponding to  $r < r_{\text{mb}}$  but they are quite similar outside that region, i.e. in the bottom part of the plots); (c) and (d) show the relative difference  $\Delta$  between the two cases for radii in the range  $r_{\text{mb}} \leq r \leq 15 \rho$ . Acceptable accuracy of  $|\Delta| \lesssim 0.1$  corresponds to  $|w| \lesssim 0.5$  and  $r \gtrsim 1.9 r_{\text{mb}}$ .

cases). First, to explain how the graphs are constructed, we compare the acceleration for  $\Phi_{\text{pw}}$  and for the Schwarzschild metric in Fig. 2. Each curve gives the magnitude of the acceleration  $A$  along  $r = \text{const}$  orbits in the equatorial plane ( $\theta = 90^\circ$ ) of the Schwarzschild metric. (Only the radial component contributes to the acceleration in the equatorial plane; a general expression valid also outside of the equatorial plane in Kerr spacetime was given explicitly by Semerák (1994)). The radius progressively increases for the individual curves going from top to bottom of the plot. It has been widely discussed in the literature (Abramowicz and Prasanna, 1990) that  $A(\omega) = \text{const}$  at the photon orbit; this is indicated by a thick horizontal line in Fig. 2a. In fact, for applications to tori, we are mainly interested in orbits with radii greater than that of the marginally bound orbit, and therefore the whole portion of the graph corresponding to  $r < r_{\text{mb}}$  is covered by shading. (In this region the modified Newtonian potential approach is not accurate.) One can compare the shape of the curves in the Schwarzschild case to the modified Newtonian case of  $\Phi_{\text{pw}}$  in Fig. 2b. The relative difference  $\Delta$  between corresponding  $A$ 's from graphs 2a and 2b is plotted in the next two graphs, 2c–d, showing  $\Delta(\omega)$  and  $\Delta(w)$  ( $w$  denotes the speed in the local frame of

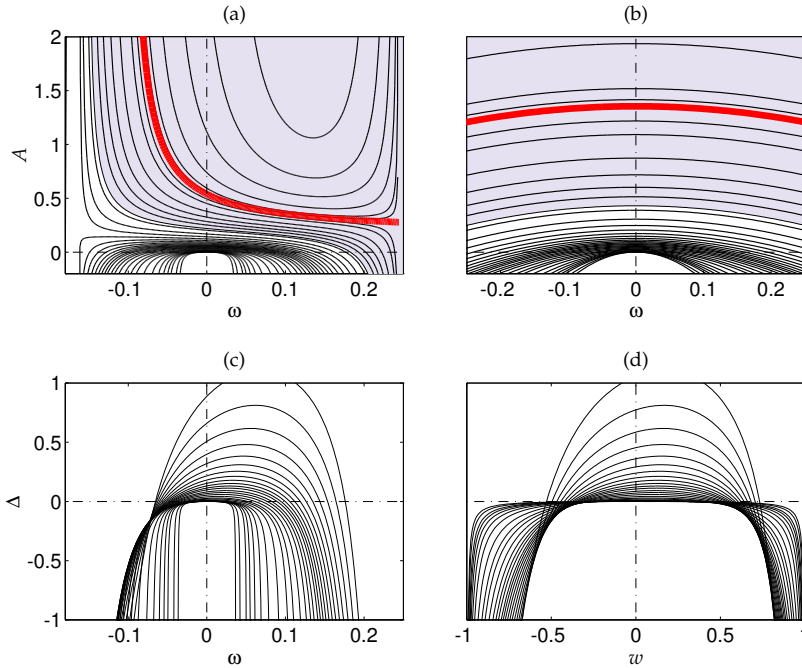


**Figure 3.** As in Fig. 2 but for the Kerr  $a = 0.5$  case (a), and for the equivalent  $\Phi_{\text{ABN}}$  case (b). Quite naturally,  $|\Delta|$  is on average large for the orbits with small radius. Comparing with analogous graphs for  $\Phi_{\text{PW}}$ , potential  $\Phi_{\text{ABN}}$  diminishes  $|\Delta|$  to smaller values, and is thus more accurate when  $a$  is nonzero. The graph here is not symmetrical about  $\omega = 0$  (due to frame-dragging in the Kerr metric); accuracy is maintained to higher  $|w|$  for corotating motion. Here, an acceptable accuracy of  $|\Delta| \lesssim 0.1$  corresponds to  $|w| \lesssim 0.5$  and  $r \gtrsim 1.6 r_{\text{mb}}$ .

a non-rotating observer, which corresponds to angular velocity  $\omega$ ;  $-1 < w < 1$ ;  $r > r_{\text{mb}}$ ). Here, the dimensionless quantity  $\Delta$  is defined as

$$\Delta = \frac{A_{\text{Exact}}(\omega) - A_{\text{Modified Newtonian}}(\omega)}{A_{\text{Exact}}(\omega = 0)} \quad (4)$$

which is to be evaluated for fixed  $r$ ,  $\theta$  and  $a$ . The outermost curve in Fig. 2c (with the largest magnitudes of  $\Delta$ ) corresponds to  $r = r_{\text{mb}}$ , while the innermost one (passing close to  $\omega = 0$ ,  $\Delta = 0$ ) corresponds to  $r = 15 r_{+}$ .

Figure 3 is constructed in the same way as Fig. 2, but now it compares the Kerr  $a = 0.5$  case with the equivalent modified Newtonian  $\Phi_{\text{ABN}}$  case. By inspecting graphs with different  $a$  we checked that the accuracy of the modified Newtonian potentials  $\Phi_{\text{PW}}$  and  $\Phi_{\text{ABN}}$  (as measured by  $\Delta$ ) is comparable in the non-rotating case but  $\Phi_{\text{ABN}}$  is better as soon as  $a$  is non-negligible. A similar conclusion can be drawn for  $\Phi$  from Eq. (1), and also for circular orbits outside the equatorial plane. Analogous plots to those in Figs. 2–3 have been constructed with other sets of parameters. We find that acceptable accuracy of about 10% in terms of  $\Delta$  is guaranteed whenever  $r \gtrsim 1.5 r_{\text{mb}}$ .

### 3 CONCLUSIONS

We have systematically checked and briefly illustrated that general relativistic effects on purely circular orbits can be imitated in a modified Newtonian potential. We have verified the accuracy of such models for the potentials  $\Phi$  (Eq. 1) and  $\Phi_{\text{ABN}}$  (Eq. 3), finding that these two are comparable and that both offer higher accuracy than the usual Paczyński and Wiita (1980) potential when the angular-momentum parameter  $a$  is nonzero. By using our criterion concerning the relative accuracy of the acceleration along circular orbits,  $|\Delta| \lesssim 0.1$ , we see that one can use the potential  $\Phi_{\text{ABN}}$  of Artemova et al. (1996) satisfactorily for modelling tori in permanent orbital motion around a rotating black hole. The error increases very close to  $r_{\text{mb}}$ . The same conclusion holds for analogous potentials (such as the one proposed in this note, Eq. 1) which reproduce the important orbits and accelerations for motion around a rotating black hole with an acceptable accuracy.

### ACKNOWLEDGEMENTS

We greatly appreciate comments by an unknown referee; his/her advice helped us to improve presentation of our paper. We acknowledge continued support from the project MŠMT – Kontakt II (LH14049), titled “Spectral and Timing Properties of Cosmic Black Holes”, and the Czech Science Foundation grant (GAČR 14-37086G), entitled “Albert Einstein Center for Gravitation and Astrophysics” in Prague. The Astronomical Institute of the Academy of Sciences has been operated under the project RVO:6798815.

### REFERENCES

- Abramowicz, M. A., Czerny, B., Lasota, J. P. and Szuszkiewicz, E. (1988), Slim accretion disks, *Astrophys. J.*, **332**, pp. 646–658.
- Abramowicz, M. A. and Prasanna, A. R. (1990), Centrifugal Force Reversal Near a Schwarzschild Black-Hole, *Monthly Notices Roy. Astronom. Soc.*, **245**, p. 720.
- Artemova, I. V., Bjoernsson, G. and Novikov, I. D. (1996), Modified Newtonian Potentials for the Description of Relativistic Effects in Accretion Disks around Black Holes, *Astrophys. J.*, **461**, p. 565.
- Barausse, E. and Lehner, L. (2013), Post-Newtonian approach to black hole-fluid systems, *Phys. Rev. D*, **88**(2), 024029, arXiv: 1306.5564.
- Bardeen, J. M., Press, W. H. and Teukolsky, S. A. (1972), Rotating Black Holes: Locally Nonrotating Frames, Energy Extraction, and Scalar Synchrotron Radiation, *Astrophys. J.*, **178**, pp. 347–370.
- Chakrabarti, S. K. (1990), *Theory of transonic astrophysical flows*, World Scientific Publication, Singapore.
- Crispino, L. C. B., da Cruz Filho, J. L. C. and Letelier, P. S. (2011), Pseudo-Newtonian potentials and the radiation emitted by a source swirling around a stellar object, *Phys. Rev. B*, **697**, pp. 506–511.
- de Felice, F. (1980), Angular momentum and separation constant in the Kerr metric, *Journal of Physics A: Mathematical and General*, **13**(5), p. 1701, URL <http://stacks.iop.org/0305-4470/13/i=5/a=027>.
- Frank, J., King, A. and Raine, D. (1992), *Accretion power in astrophysics.*, Cambridge University, Cambridge, Astrophys. Ser., Vol. 21.

- Islam, J. N. (1985), *Rotating fields in general relativity.*, Cambridge University Press, Cambridge, ISBN 0-521-26082-5.
- Israel, W. (1970), Source of the Kerr Metric, *Phys. Rev. D*, **2**, pp. 641–646.
- Kato, S., Honma, F. and Matsumoto, R. (1988), Pulsational instability of transonic regions of accretion disks with conventional alpha-viscosity, *Publ. Astronom. Soc. Japan*, **40**, pp. 709–727.
- Keres, H. (1967), Physical Interpretation of Solutions of the Einstein Equations, *Soviet Journal of Experimental and Theoretical Physics*, **25**, p. 504.
- Lanza, A. (1992), Self-gravitating thin disks around rapidly rotating black holes, *Astrophys. J.*, **389**, pp. 141–156.
- Miwa, T., Fukue, J., Watanabe, Y. and Katayama, M. (1998), Accretion Corona Immersed in Disk Radiation Fields, *Publ. Astronom. Soc. Japan*, **50**, pp. 325–331.
- Muchotrzeb, B. and Paczyński, B. (1982), Transonic accretion flow in a thin disk around a black hole, *acta*, **32**, pp. 1–11.
- Nishida, S. and Eriguchi, Y. (1994), A general relativistic toroid around a black hole, *Astrophys. J.*, **427**, pp. 429–437.
- Nowak, M. A. and Wagoner, R. V. (1991), Diskoseismology: Probing accretion disks. I - Trapped adiabatic oscillations, *Astrophys. J.*, **378**, pp. 656–664.
- Paczynski, B. and Wiita, P. J. (1980), Thick accretion disks and supercritical luminosities, *Astronomy and Astrophysics*, **88**, pp. 23–31.
- Semerák, O. (1994), On the competition of forces in the Kerr field, *Astronomy and Astrophysics*, **291**, pp. 679–686.
- Semerák, O. and Karas, V. (1999), Pseudo-Newtonian models of a rotating black hole field, *Astronomy and Astrophysics*, **343**, pp. 325–332, arXiv: astro-ph/9901289.
- Tejeda, E. and Rosswog, S. (2013), An accurate Newtonian description of particle motion around a Schwarzschild black hole, *Monthly Notices Roy. Astronom. Soc.*, **433**, pp. 1930–1940, arXiv: 1303.4068.
- Wilkins, D. C. (1972), Bound Geodesics in the Kerr Metric, *Phys. Rev. D*, **5**, pp. 814–822.

# Tidal disruption events from a nuclear star cluster as possible origin of transient relativistic spectral lines near SMBH

Vladimír Karas<sup>1,a</sup>, Michal Dovčiak<sup>1</sup>, Devaky Kunneriath<sup>1</sup>,  
Wenfei Yu<sup>2,b</sup> and Wenda Zhang<sup>2</sup>

<sup>1</sup>Astronomical Institute, Academy of Sciences of the Czech Republic,  
Boční II 1401, CZ-141 00 Prague, Czech Republic

<sup>2</sup>Shanghai Astronomical Observatory and Key Laboratory for Research in Galaxies  
and Cosmology, Chinese Academy of Sciences, 80 Nandan Road, Shanghai, 200030, China

<sup>a</sup>vladimir.karas@cuni.cz

<sup>b</sup>wenfei@shao.ac.cn

## ABSTRACT

We discuss a possibility that a tidal disruption event near a dormant supermassive black hole (SMBH) can give rise to spectral features of iron in 6–7 keV X-ray signal: a relativistic line profile emerges from debris illuminated and ionised by an intense flash produced from the destroyed star. This could provide a unique way to determine parameters of the system.

We consider a model where the nuclear stellar population acquires an oblate shape (i.e. a flattened distribution) in the inner region near a supermassive black hole, and also the primary irradiation flare is expected to occur more likely near the equatorial plane, co-planar with the infalling material. This suggests that the reprocessing of primary X-rays results in a transient profile that should be relevant for tidal-disruption events (TDE) in otherwise under-luminous (inactive) galactic nuclei, i.e. with no prior accretion disc.

Resonance mechanisms of the stellar motion can increase the orbital eccentricity for some stars in the nuclear cluster and help to bring them close to the tidal radius, where they can give rise to TDEs. The proposed scenario appears to be distinguishably different from the standard scheme of lamp-post model for the origin of the relativistic line in active galaxies, where the source is thought to be located predominantly near the symmetry axis.

**Keywords:** accretion: accretion discs – black-hole physics – galaxies: nuclei – tidal disruption events

## 1 INTRODUCTION

Near a supermassive black hole (SMBH) tidal disruptions occur during close encounters when a plunging star on an eccentric orbit reaches the critical (tidal) radius  $R = R_t \sim 10^{11} (M_\bullet/M_*)^{1/3} (R_*/R_\odot)$  cm, where  $M_*$  and  $R_*$  denote the mass and the radius of the satellite star,  $M_\bullet$  is the SMBH mass (Evans and Kochanek, 1989; Luminet and Marck,

1985; Rees, 1988). Stars approach the event horizon, and at a certain moment they become disrupted by tidal forces of the SMBH, producing a bright flash of intense radiation that illuminates the surrounding interstellar medium and a temporary accretion disc or a ring formed by the debris (Cannizzo et al., 1990). According to the standard picture of galactic nuclei, we can imagine a nuclear cluster around a galactic core as a system consisting of a central SMBH, an accretion disc and a dense stellar cluster, possibly of a flattened shape in its inner region (Kunneriath et al., 2014; Schödel et al., 2014). The fall-back rate of the remnant debris onto SMBH is expected to be influenced by relativistic effects (Cheng and Bogdanović, 2014).

The authors of ref. (Clausen et al., 2012) demonstrate that the photoionised debris of a tidally disrupted star can account for the emission lines observed in some optical spectra. In their case, the super-Eddington phase lasts about one to two hundred years; reproducing the line ratios requires an intermediate-mass black hole of  $M_{\bullet} \lesssim 200 M_{\odot}$ . Various characteristics of TDEs depend strongly on the stellar type (MacLeod et al., 2012), although the gradual decay of the light curve adopts a generic profile that is determined by the viscous processes. The emission of an X-ray irradiated flow, known as the reflection spectrum, can be expected, including a superposition of the continuum emission and spectral lines, including the prominent fluorescent emission lines of iron that have the rest energy around 6–7 keV (Karas, 2006; Karas et al., 2000, 2001; Ross and Fabian, 1993). In another context of X-ray emission lines, a method for O stars to determine the shock-heating rate by instabilities in their radiation-driven winds has been recently developed (Cohen et al., 2014). For this paper, we just remind the reader that the relativistically smeared spectral line emission from a black-hole accretion disc in a few keV band may be intrinsically narrow and unresolved in energy; it is the observed profile that becomes broadened and skewed (by a combination of Doppler and light-bending effects) when integrated over the azimuthal extent of accretion rings, and generally red-shifted by strong gravity of the central black hole.

One of the most constraining X-ray spectral information on a tidal disruption event (TDE) has resulted from the campaign on a quiescent galaxy SDSS1201+30 (Saxton et al., 2012). This is most likely an object without a prior accretion disc. The X-ray spectra are very soft, and can hardly be explained with standard accretion disk models. The strong variability was seen in the light curve and related to clumpy accretion with a combination of flaring and absorption events.

X-ray photons from TDE can illuminate, ionise and perturb the gaseous material infalling from the fresh accretion flow. In reference Zhang et al. (2014) we propose that the relativistic iron line from the TDE irradiated inflow can provide a unique way to determine parameters of the system, namely, the dimensionless black-hole spin  $a$  ( $-1 \leq a \leq 1$ ), the angle of the observer  $i$  (inclination,  $0 \leq i \leq 90$  deg;  $i = 0$  corresponds to pole-on view along the rotation axis), and the expansion velocity  $v_{\text{exp}}$  of ionisation front, which propagates outwards at velocity close to the speed of light and modulates the ionisation parameter of the medium. Hence, it affects also the iron-line emissivity.

According to the model, the line emission is triggered and modulated by the same, virtually instant TDE event. Unlike the case of continuously variable X-ray spectrum of active galactic nuclei (Esquej et al., 2012; Saxton et al., 2012), a quiescent source would be preferred, so that the transient relativistic line can be revealed.

## 2 HYPOTHESIS OF A RELATIVISTIC SPECTRAL LINE FROM TDE-IRRADIATED REMNANT ACCRETION DISC

In reference Šubr et al. (2004) we modelled the structure of the nuclear star cluster that is expected to arise as a result of the mutual interaction of main components of the galactic nucleus, i.e. a supermassive black hole, stars, and a gaseous/dusty torus that helps to bring stars towards the tidal disruption. An interesting conclusion from that paper concerns the formation of a flattened (oblate) stellar subsystem in the inner region surrounding the central SMBH (Just et al., 2012; Vilkoviskij and Czerny, 2002), which is a reminiscence on much smaller scales of the structure originally reported on the kiloparsec scale of the bulge of the Milky Way (Launhardt et al., 2002). In the other words, TDE from such a stellar population can be expected to occur predominantly in the equatorial plane of the system. Therefore, also the irradiation flash should arise with a higher chance within the plane, i.e. at large inclination angle with respect to a distant observer.

In our scenario for TDE, the flattened stellar system is associated with the effect of hydrodynamical dissipation of the stellar orbits by the dusty/gaseous torus. Further down, at very small radii near the horizon, also gravitational radiation can play a role. Moreover, a subset of stars on eccentric orbits is brought close to the central black hole where they plunge quickly below the tidal radius. Studying such a TDE would shed light on the accretion physics and the stellar dynamics in galactic nuclei, as well as the role of tidal disruptions for feeding and growth of SMBHs.

We put forward a possibility that the source of intense energy deposition occurs near the inner edge of the accretion disc, which resembles a radially narrow ring that gradually spreads by viscous forces and eventually disappears once the fraction of captured material is accreted. Basic form of the relativistic line from a narrow ring were investigated in ref. (Sochora et al., 2011). Following TDE, the spectral line is modulated via changing ionisation state of a remnant accretion disc that is created from the debris. This remnant accretion ring can be identified with a structure that has been proposed to arise around the circularisation radius at transient accretion events with low (sub-Keplerian) angular momentum (Bu and Yuan, 2014; Czerny et al., 2013; Hayasaki et al., 2013).

A non-negligible radial infall velocity of the accreted material is likely, and so the ionisation front moves radially outward through the material of the remnant disc at  $v = v_{\text{exp}}(r)$  that is not exceeding the speed of light (although it should be very close to it). We can set  $v_{\text{exp}} \simeq \text{const}$  as one of free model parameters. The corresponding mass fallback rate (denoted by the subscript ‘fb’ hereafter) proceeds as a characteristic power-law profile (Rees, 1988),  $\dot{M}(t) \propto K t^{-5/3}$  ( $K \equiv M_{\star}/t_{\text{fb}} = \text{const}$ ), which can significantly exceed the Eddington accretion rate for a period of weeks to years for the black hole mass  $M_{\bullet} \lesssim 10^7 M_{\odot}$  (Strubbe and Quataert, 2009).

The hypothesis about an enhanced capture rate and tidal disruptions of stars in the equatorial plane is supported also by simulations of the structure flattening in the inner regions of the nuclear cluster. In reference Šubr and Karas (2005b) a scenario was discussed based on a combination of simultaneous gravitational and hydrodynamical effects of the gaseous environment on orbiting stars, which are assumed to lead to an oblate, disc-like configuration. While the direct star-disc hydrodynamical interaction causes a continuous dissipation of the stellar orbital energy (and it is anyway very small in the Milky Way’s

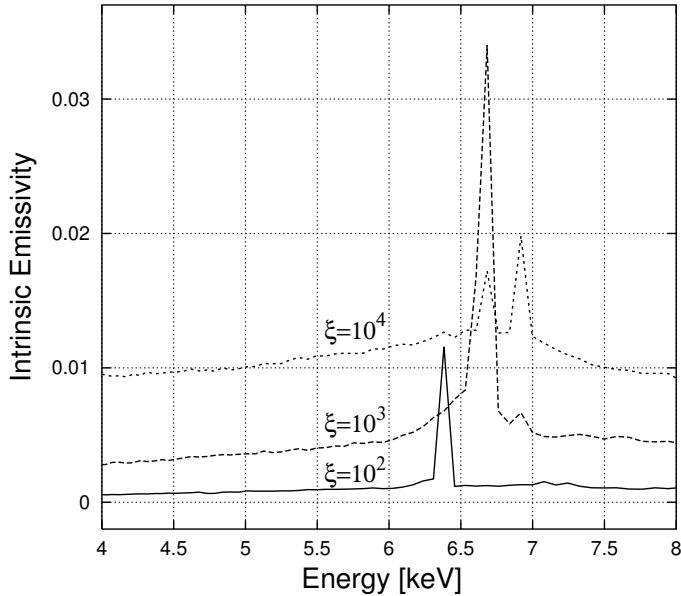


**Figure 1.** The intrinsic emissivity profile (arbitrary units) around the 6–7 keV spectral feature, as predicted by the model for hot parts of the ionisation front (Karas et al., 2000). The three curves correspond to different values of the ionisation parameter  $\xi$ . As the ionisation front expands through the infalling remnant disc, the changing ionisation state is revealed by the corresponding change of the iron line rest energy and intensity, until the emission feature disappears when the complete ionisation is reached.

central regions), gravity of the stellar ring, a self-gravitating accretion torus, or a flattened nuclear star-cluster all can lead to recurring variations of the orbital elements. An example of this evolution is plotted in Fig. 2, where we show the long-term orbital changes due to both the hydrodynamical and gravitational influence of the disc. As an example, parameters of that simulation were set to be consistent with the values reported for S2 star in the Galactic center (in this scheme it is the orbital trajectory of the star which defines the relevant plane). Alternatively, tidal disruption of stars by supermassive central black holes from dense star clusters has been modelled by high-accuracy direct N-body simulations (Zhong et al., 2014).

We note that in the X-ray and optical/UV bands, almost two dozens candidate TDEs have been already reported (Gezari et al., 2012; Greiner et al., 2000; Komossa and Greiner, 1999). These events are characterized by the thermal emission with temperature of  $\sim 10^4$ – $10^5$  K, and the peak bolometric luminosity about  $10^{43}$ – $10^{45}$   $\text{erg} \cdot \text{s}^{-1}$ . For the events with good coverage during the decay, the flux decline was found consistent with a power-law (index  $-5/3$ ), as predicted for canonical TDEs. Compared with the quiescence state, the flux can increase by a factor of  $\gtrsim 150$  during outbursts.

Detections of the fluorescent iron line from TDE are only tentative so far (Evans and Kochanek, 1989), however, finding this spectral signature should provide very valuable information. The expected properties of the reflection line depend sensitively on the ionisation state of the irradiated material (Ross and Fabian, 1993). Since in TDEs the continuum

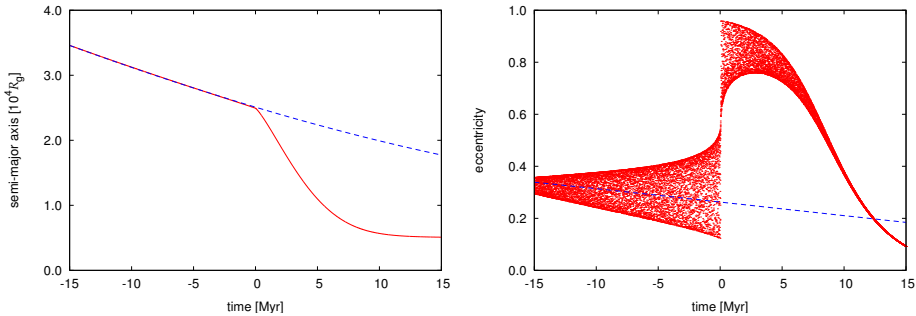


**Figure 2.** Temporal evolution of semi-major axis and eccentricity of the orbit of a star from a nuclear star cluster interacting with a disc (Šubr and Karas, 2005a). Dashed line corresponds to the case when the effect of disc gravity is neglected. Solid line (in the left panel) and dots (in the right panel) represent a simulation where both the hydrodynamical and gravitational interaction were considered. According to this scheme, TDE event is triggered at the moment of close encounter (zero time on the horizontal axis) between the star and SMBH ( $M_{\bullet} \simeq 4 \times 10^6 M_{\odot}$ ).

flux can vary by a large amplitude, we need to take also the variation of the ionisation parameter  $\xi(t)$  into consideration (see Fig. 1). For  $M_{\bullet} \approx 10^6 M_{\odot}$  SMBH, the peak mass fall-back rate can reach  $\sim 1.5 M_{\odot} \text{ yr}^{-1}$ , corresponding to luminosity of  $8.5 \times 10^{45} \text{ erg} \cdot \text{s}^{-1}$  (assuming the radiation efficiency of  $\eta \simeq 0.1$ ). Therefore, the rise of the illumination is significant by orders of magnitude compared to the quiescent state of a dormant nucleus.

### 3 DISCUSSION AND CONCLUSIONS

Gravitational effects act on the spectral features from the remnant TDE accretion disc by smearing the spectral features and moving the observed energy centroid across energy bins. In this way gravity exerts the influence on the ultimate form of the spectrum (Karas, 2006). The reprocessed radiation reaches the observer from different regions of the system. Furthermore, as strong-gravity plays a crucial role, photons may even follow multiple separate paths, joining each other at the observer at different moments. Individual rays experience unequal time lags for purely geometrical reasons and for relativistic time-dilation.

Time delay from a TDE flare to the moment of arrival of the observed iron line signal consists of two components: the expansion time  $t_{\text{exp}} = r/v_{\text{exp}}$ , and the time interval from the disc to the observer,  $t_{\text{delay}}$ . At large radius where the spacetime is flat to a good precision,  $t_{\text{delay}} \simeq -r \sin \phi + \text{const}$ , where  $\phi$  is the azimuthal angle on the disc plane (Karas et al., 2001). As  $v_{\text{exp}}$  is of order unity (i.e. comparable to the speed of light), the two quantities become comparable, and the delay interval is dominated by the longer one. At large inclination angles, the photons from the disc located in front of the black hole reach the observer first, then those from disc near the inner edge, and at last those from disc behind black hole.

In the cases of high expansion velocity combined with high inclination angle, a “nose” occurs ahead of the rings main signal (Zhang et al., 2014). The length of the nose increases with the inclination angle and with the expansion velocity. The line emission ceases once the accretion flow becomes highly ionised to a larger distance. On a phenomenological level of our model, the intrinsic emissivity of the remnant accretion ring and the expansion

velocity of the ionisation front are two degrees of freedom that allow us to capture the lamp-post scheme as well as the TDE-induced illumination in a common scenario. We note that the remnant accretion rings resulting from a TDE event are likely lacking axial symmetry. Therefore, as a next step to explore more realistic situations, spectral line profiles from elliptically shaped and tilted structures need to be taken into account (Chang and Choi, 2002; Eracleous et al., 1995; Fragile et al., 2005).

We conclude by stating that the proposed idea poses an observational challenge (because the iron line flux is expected to be only a weak and variable components of the X-ray signal from tidal-disruption events), nevertheless, it suggests a promising opportunity to verify the parameters of central black holes by an independent method. Moreover, it offers an interesting complement to the standard scenario for the origin of relativistically broadened spectral lines.

In the context of Galactic centre, let us remark that the 6–7 keV emission of iron has been extensively studied (Ponti et al., 2010; Wang et al., 2006) and the light-echo effect reported. However, the detection concerns a wider region (molecular clouds within the Central Molecular Zone surrounding the SMBH) than the immediate vicinity of the black-hole horizon, which we imagine here.

While in the lamp-post model the irradiating source is (usually) considered to be (almost) axially symmetric and located around the rotation axis, in the present scheme the primary excitation is more likely to occur from the equatorial region near the innermost stable circular orbit, commonly denoted as ISCO, which is about the minimum radius to which the accretion discs can extend. A convincing case of such a transient relativistic spectral feature from TDE is still to be found in X-rays.

## ACKNOWLEDGEMENTS

The authors highly appreciate the hospitality of Conference organisers in Prague. VK and DK thank the Czech Ministry of Education, Youth and Sports project LH14049, titled “Spectral and Timing Properties of Cosmic Black Holes”, that has been aimed to support the international collaboration in astrophysics. VK and MD acknowledge also the European Union 7th Framework Programme No. 312789 “StrongGravity”. The research of WY and WZ is supported in part by the National Natural Science Foundation of China under grants No. 11073043 and No. 11333005.

## REFERENCES

- Bu, D.-F. and Yuan, F. (2014), Does the circularization radius exist or not for low-angular-momentum accretion?, *Monthly Notices Roy. Astronom. Soc.*, **442**, pp. 917–920, arXiv: 1405.1489.
- Cannizzo, J. K., Lee, H. M. and Goodman, J. (1990), The disk accretion of a tidally disrupted star onto a massive black hole, *Astrophys. J.*, **351**, pp. 38–46.
- Chang, H.-Y. and Choi, C.-S. (2002), Iron Line Profiles from Relativistic Elliptical Accretion Disks, *Journal of Korean Astronomical Society*, **35**, pp. 123–130.
- Cheng, R. M. and Bogdanović, T. (2014), Tidal disruption of a star in the Schwarzschild spacetime: Relativistic effects in the return rate of debris, *Phys. Rev. D*, **90**(6), 064020, arXiv: 1407.3266.
- Clausen, D., Sigurdsson, S., Eracleous, M. and Irwin, J. A. (2012), Luminous [O III] and [N II] from tidally disrupted horizontal branch stars, *Monthly Notices Roy. Astronom. Soc.*, **424**, pp. 1268–1274, arXiv: 1205.3053.

- Cohen, D. H., Li, Z., Gayley, K. G., Owocki, S. P., Sundqvist, J. O., Petit, V. and Leutenegger, M. A. (2014), Measuring the shock-heating rate in the winds of O stars using X-ray line spectra, *Monthly Notices Roy. Astronom. Soc.*, **444**, pp. 3729–3737, arXiv: 1409.0856.
- Czerny, B., Kunneriath, D., Karas, V. and Das, T. K. (2013), Multiple accretion events as a trigger for Sagittarius A\* activity, *Astronomy and Astrophysics*, **555**, A97, arXiv: 1306.0900.
- Eracleous, M., Livio, M., Halpern, J. P. and Storchi-Bergmann, T. (1995), Elliptical accretion disks in active galactic nuclei, *Astrophys. J.*, **438**, pp. 610–622.
- Esquej, P., Saxton, R. D., Komossa, S. and Read, A. M. (2012), Tidal disruption events from the first XMM-Newton slew survey, in *European Physical Journal Web of Conferences*, volume 39 of *European Physical Journal Web of Conferences*, p. 2004.
- Evans, C. R. and Kochanek, C. S. (1989), The tidal disruption of a star by a massive black hole, *Astrophys. J. Lett.*, **346**, pp. L13–L16.
- Fragile, P. C., Miller, W. A. and Vandernoot, E. (2005), Iron-Line Emission as a Probe of Bardeen-Petterson Accretion Disks, *Astrophys. J.*, **635**, pp. 157–166, arXiv: astro-ph/0507309.
- Gezari, S., Chornock, R., Rest, A., Huber, M. E., Forster, K., Berger, E., Challis, P. J., Neill, J. D., Martin, D. C., Heckman, T., Lawrence, A., Norman, C., Narayan, G., Foley, R. J., Marion, G. H., Scolnic, D., Chomiuk, L., Soderberg, A., Smith, K., Kirshner, R. P., Riess, A. G., Smartt, S. J., Stubbs, C. W., Tonry, J. L., Wood-Vasey, W. M., Burgett, W. S., Chambers, K. C., Grav, T., Heasley, J. N., Kaiser, N., Kudritzki, R.-P., Magnier, E. A., Morgan, J. S. and Price, P. A. (2012), An ultraviolet-optical flare from the tidal disruption of a helium-rich stellar core, *Nature*, **485**, pp. 217–220, arXiv: 1205.0252.
- Greiner, J., Schwarz, R., Zharikov, S. and Orio, M. (2000), RX J1420.4+5334 - another tidal disruption event?, *Astronomy and Astrophysics*, **362**, pp. L25–L28, arXiv: astro-ph/0009430.
- Hayasaki, K., Stone, N. and Loeb, A. (2013), Finite, intense accretion bursts from tidal disruption of stars on bound orbits, *Monthly Notices Roy. Astronom. Soc.*, **434**, pp. 909–924, arXiv: 1210.1333.
- Just, A., Yurin, D., Makukov, M., Berczik, P., Omarov, C., Spurzem, R. and Vilkoviskij, E. Y. (2012), Enhanced Accretion Rates of Stars on Supermassive Black Holes by Star-Disk Interactions in Galactic Nuclei, *Astrophys. J.*, **758**, 51, arXiv: 1208.4954.
- Karas, V. (2006), Theoretical aspects of relativistic spectral features, *Astronomische Nachrichten*, **327**, pp. 961–968, arXiv: astro-ph/0609645.
- Karas, V., Czerny, B., Abrassart, A. and Abramowicz, M. A. (2000), A cloud model of active galactic nuclei: the iron K $\alpha$  line diagnostics, *Monthly Notices Roy. Astronom. Soc.*, **318**, pp. 547–560, arXiv: astro-ph/0006187.
- Karas, V., Martocchia, A. and Subr, L. (2001), Variable Line Profiles Due to Non-Axisymmetric Patterns in an Accretion Disc around a Rotating Black Hole, *Publ. Astronom. Soc. Japan*, **53**, pp. 189–199, arXiv: astro-ph/0102460.
- Komossa, S. and Greiner, J. (1999), Discovery of a giant and luminous X-ray outburst from the optically inactive galaxy pair RX J1242.6-1119, *Astronomy and Astrophysics*, **349**, pp. L45–L48, arXiv: astro-ph/9908216.
- Kunneriath, D., Schödel, R., Stolovy, S. and Feldmeier, A. (2014), Structure of the nuclear stellar cluster of the Milky Way galaxy, in L. O. Sjouwerman, C. C. Lang and J. Ott, editors, *IAU Symposium*, volume 303 of *IAU Symposium*, pp. 228–229.
- Launhardt, R., Zylka, R. and Mezger, P. G. (2002), The nuclear bulge of the Galaxy. III. Large-scale physical characteristics of stars and interstellar matter, *Astronomy and Astrophysics*, **384**, pp. 112–139, arXiv: astro-ph/0201294.
- Luminet, J.-P. and Marck, J.-A. (1985), Tidal squeezing of stars by Schwarzschild black holes, *Monthly Notices Roy. Astronom. Soc.*, **212**, pp. 57–75.

- MacLeod, M., Guillochon, J. and Ramirez-Ruiz, E. (2012), The Tidal Disruption of Giant Stars and their Contribution to the Flaring Supermassive Black Hole Population, *Astrophys. J.*, **757**, 134, arXiv: 1206.2922.
- Ponti, G., Terrier, R., Goldwurm, A., Belanger, G. and Trap, G. (2010), Discovery of a Superluminal Fe K Echo at the Galactic Center: The Glorious Past of Sgr A\* Preserved by Molecular Clouds, *Astrophys. J.*, **714**, pp. 732–747, arXiv: 1003.2001.
- Rees, M. J. (1988), Tidal disruption of stars by black holes of 10 to the 6th–10 to the 8th solar masses in nearby galaxies, *Nature*, **333**, pp. 523–528.
- Ross, R. R. and Fabian, A. C. (1993), The effects of photoionization on X-ray reflection spectra in active galactic nuclei, *Monthly Notices Roy. Astronom. Soc.*, **261**, pp. 74–82.
- Saxton, R. D., Read, A. M., Esquej, P., Komossa, S., Dougherty, S., Rodriguez-Pascual, P. and Barrado, D. (2012), A tidal disruption-like X-ray flare from the quiescent galaxy SDSS J120136.02+300305.5, *Astronomy and Astrophysics*, **541**, A106, arXiv: 1202.5900.
- Schödel, R., Feldmeier, A., Kunneriath, D., Stolovy, S., Neumayer, N., Amaro-Seoane, P. and Nishiyama, S. (2014), Surface brightness profile of the Milky Way’s nuclear star cluster, *Astronomy and Astrophysics*, **566**, A47, arXiv: 1403.6657.
- Sochora, V., Karas, V., Svoboda, J. and Dovčiak, M. (2011), Black hole accretion rings revealed by future X-ray spectroscopy, *Monthly Notices Roy. Astronom. Soc.*, **418**, pp. 276–283, arXiv: 1108.0545.
- Strubbe, L. E. and Quataert, E. (2009), Optical flares from the tidal disruption of stars by massive black holes, *Monthly Notices Roy. Astronom. Soc.*, **400**, pp. 2070–2084, arXiv: 0905.3735.
- Šubr, L. and Karas, V. (2005a), A manifestation of the Kozai mechanism in the galactic nuclei, in S. Hledík and Z. Stuchlík, editors, *RAGtime 6/7: Workshops on black holes and neutron stars*, pp. 281–293.
- Šubr, L. and Karas, V. (2005b), On highly eccentric stellar trajectories interacting with a self-gravitating disc in Sgr A\*, *Astronomy and Astrophysics*, **433**, pp. 405–413, arXiv: astro-ph/0501203.
- Šubr, L., Karas, V. and Huré, J.-M. (2004), Star-disc interactions in a galactic centre and oblateness of the inner stellar cluster, *Monthly Notices Roy. Astronom. Soc.*, **354**, pp. 1177–1188, arXiv: astro-ph/0408053.
- Vilkoviskij, E. Y. and Czerny, B. (2002), The role of the central stellar cluster in active galactic nuclei. I. Semi-analytical model, *Astronomy and Astrophysics*, **387**, pp. 804–817, arXiv: astro-ph/0203226.
- Wang, Q. D., Dong, H. and Lang, C. (2006), The interplay between star formation and the nuclear environment of our Galaxy: deep X-ray observations of the Galactic centre Arches and Quintuplet clusters, *Monthly Notices Roy. Astronom. Soc.*, **371**, pp. 38–54, arXiv: astro-ph/0606282.
- Zhang, W. et al. (2014), to be submitted.
- Zhong, S., Berczik, P. and Spurzem, R. (2014), Super Massive Black Hole in Galactic Nuclei with Tidal Disruption of Stars, *Astrophys. J.*, **792**, 137, arXiv: 1407.3537.

# Effects of environmental drag onto a fast-moving magnetic compact star near a supermassive black hole

Vladimír Karas,<sup>1,a</sup> Ladislav Šubr,<sup>2</sup> Devaky Kunneriath<sup>1</sup>  
and Michal Zajaček<sup>1,2</sup>

<sup>1</sup>Astronomical Institute, Academy of Sciences of the Czech Republic,  
Boční II 1401, CZ-141 00 Prague, Czech Republic

<sup>2</sup>Charles University, Faculty of Mathematics and Physics, Astronomical Institute,  
V Holešovičkách 2, CZ-18000 Prague, Czech Republic

<sup>a</sup>vladimir.karas@cuni.cz

## ABSTRACT

The hydrodynamical drag by interstellar gaseous environment can influence the orbital motion of stars near a supermassive black hole on long time-scales, even if the medium is diluted. This effect is generally more important for bodies with a large geometrical cross-sectional area, such as supergiants interacting with a relatively dense accretion disc in active galactic nuclei, whereas it is entirely negligible for compact stars embedded in a rarefied accretion flow in low-luminosity galactic nuclei.

We discuss whether a strong magnetic field of a neutron star can significantly enhance the drag effect by increasing the effective cross-sectional area for the mutual interaction, especially in the case of the hypersonic motion. We find that the increase due to magnetic forces is still far too small to be important, e.g. for the long term orbital evolution of the putative population of neutron stars in the Galactic centre, where the environment density is very low.

**Keywords:** Accretion: accretion discs – black-hole physics

## 1 INTRODUCTION

The problem of accretion onto a star or a black hole in the presence of magnetic fields has been investigated since many years: for the original account and basic ideas relevant to our present discussion, see e.g. Bisnovaty-Kogan and Ruzmaikin (1974, 1976); Ghosh and Lamb (1978); Kluźniak and Rappaport (2007). Most attention has been focused towards the accretion fed via an accretion disk. It has been recognized that the accretion process can proceed in various modes, depending mainly on the star compactness and rotation period, the accretion rate, and the magnetic field strength and orientation. In the past, somewhat less attention has been focused towards the magnetic version of the Bondi–Hoyle–Lyttleton problem of accretion onto isolated stars moving rapidly through the interstellar medium (e.g. Toropina et al., 2001, 2006).

The hydrodynamical drag can be safely ignored in late stages of a compact star inspiraling in a standard disc; see Karas and Šubr (2001). In that paper we considered also giant stars for which the drag is more important simply because of much larger geometrical cross-sectional area for the direct interaction with the disc material. Neutron stars and stellar-mass black holes were suspected to be too tiny and very weakly interacting in this respect (Narayan, 2000).

However, the effective cross section of a *magnetized* neutron star can be significantly larger and it can lead to an increased drag. We thus summarize formulae describing the interaction of a rotating magnetic star with accretion plasma (for a textbook account of the subject, see Lipunov (1987); also Romanova et al. (2005)).

## 2 BASIC ESTIMATES BASED ON CRITICAL RADII

Accretion of material by a star or a compact object has been studied since the late 1930s. First, astrophysicists investigated axially symmetric accretion onto a star moving through a cloud of interstellar medium (see “The evolution of stars” by Hoyle and Lyttleton (1939) and “On the effect of interstellar matter on the motion of a star” by Dodd and McCrea (1952)). A possibility was proposed of terrestrial climatic effects being due to density variations of the medium in the solar neighbourhood. Next, in the 1950s, the theory of spherical accretion of gas was developed (Bondi, 1952, “On spherically symmetric accretion”). This line of research has continued with more complicated studies of gas transport between individual components in binary systems, and led to the idea of accretion disks in the late 1960s.

A trivial order-of-magnitude estimate of the gravitational potential energy which can in principle be released in the course of accretion of a test mass  $m$  onto a spherical body with mass  $M$  and radius  $R_*$  gives

$$\Delta E_{\text{acc}} = \frac{GMm}{R_*} \begin{cases} \overset{\dagger}{\approx} 10^{20} \frac{M}{M_\odot} \frac{m}{1 \text{ g}} \frac{10 \text{ km}}{R_*} & [\text{erg}], \\ \overset{\ddagger}{\approx} 10^{53} \frac{M}{10^8 M_\odot} \frac{m}{M_\odot} \frac{10^{-4} \text{ pc}}{R_*} & [\text{erg}]. \end{cases} \quad (1)$$

Typical values for a neutron star ( $\dagger$ ) and for a super-massive black hole ( $\ddagger$ ) have been used in numerical estimates. Let us compare  $\Delta E_{\text{acc}}$  with the energy which could be extracted from the same mass  $m$  by nuclear fusion reactions. Hydrogen-to-helium burning, the most important case from the astrophysical viewpoint, gives

$$\Delta E_{\text{nuc}} = \Delta mc^2 \begin{cases} \approx 5 \times 10^{18} \frac{m}{1 \text{ g}} & [\text{erg}] \overset{\dagger}{\approx} 0.1 \Delta E_{\text{acc}}, \\ \approx 10^{52} \frac{m}{M_\odot} & [\text{erg}] \overset{\ddagger}{\approx} 0.1 \Delta E_{\text{acc}}. \end{cases} \quad (2)$$

Energy potentially releasable by accretion is very sensitive to a dimension-less *compactness parameter*,

$$\varepsilon \equiv \frac{2GM}{R_*c^2}. \quad (3)$$

Order-of-magnitude estimates of parameter  $\varepsilon$ : (i) Neutron stars –  $R_* \approx 10 \text{ km}$ ,  $\varepsilon \approx 0.1$ ; (ii) White dwarfs –  $R_* \approx 10^4 \text{ km}$ ,  $\varepsilon \approx 10^{-4}$  (as an example we mention binary systems

consisting of a white dwarf which accretes matter from a close, usually main sequence companion; these are cataclysmic variables); (iii) Solar-type stars –  $R_* \approx 10^6$  km,  $\varepsilon \approx 10^{-6}$ ; for example standard main-sequence stars in a binary system (symbiotic stars) belong to this category; (iv) Black holes –  $R_* \approx R_g \equiv 2GM/c^2 \approx 3(M/M_\odot)$  km,  $\varepsilon \gtrsim 0.1$  (black holes have no rigid surface. Under suitable conditions,  $R_*$  coincides with the last, innermost stable orbit below which material falls freely into the black hole. In the case of a non-rotating, Schwarzschild black hole,  $R_* = 3 R_g$ ,  $\varepsilon = 1/3$ .)

Another dimensionless quantity is also frequently designated as the compactness parameter in the theory of accretion onto compact objects. It takes into account the radiation luminosity  $L$  of the object:

$$\tilde{\varepsilon} \equiv \frac{L \Xi_T}{R_* m_e c^3}. \quad (4)$$

(The Thomson cross-section for electrons is  $\Xi_T = 6.65\,246 \times 10^{-25}$  cm<sup>2</sup>.)

In many situations, the accreted matter has apparently a non-negligible value of angular momentum which invalidates the basic assumption of the spherical approximation. Non-spherical accretion was originally investigated in the case of an interstellar medium captured by a moving object, e.g. a star in a nebula (Bondi and Hoyle, 1944).

Let us consider a *magnetic* star moving as a “bullet” along an inclined trajectory across the accretion disc plane. In the case of supersonic motion, the relevant interaction radius is called the Shvartsman radius (e.g. Lipunov, 1987; Romanova et al., 2001),

$$R_{\text{Sh}} \simeq 9.4 \times 10^{15} B_{12} P_1^{-2} v_7^{-1} n^{-1/2} \text{ [cm]}. \quad (5)$$

Notation for relevant variables follows the standard practice (e.g. Lipunov, 1987), in particular,  $B_{12}$  denotes the magnetic intensity scaled to the units of  $10^{12}$  Gauss.

Here one assumes that two conditions,  $R_{\text{Sh}} > R_{\text{acc}}$  and  $R_{\text{Sh}} > R_{\text{lc}}$ , are both satisfied, where the light cylinder is

$$R_{\text{lc}} = c/\Omega_* \simeq 4.8 \times 10^{12} P_3 \text{ [cm]}, \quad (6)$$

and the Bondi–Hoyle radius (Edgar 2004) is

$$R_{\text{acc}} = \frac{2GM}{w^2} = 9.4 \times 10^{11} \frac{M_{1.4}}{w_{200}^2} \text{ [cm]}, \quad (7)$$

$$w_{200} = \frac{\sqrt{c_s^2 + v^2}}{200 \text{ km/s}} \quad (8)$$

( $c_s$  is the sound speed,  $v$  is relative velocity).

The above given formula for  $R_{\text{Sh}}$  follows from the equality between the magnetic pressure  $P_m$  (due to a rotating dipole luminosity  $L_m$ ),

$$P_m = \frac{L_m}{4\pi R^2 c} = \frac{\kappa_t \mu^2}{4\pi R_{\text{lc}}^4 R^2} \quad (9)$$

( $\kappa_t \sim 1/2$ ), and the ram pressure

$$P_{\text{ram}} = \rho v^2 \simeq \frac{\dot{M} v^5}{G^2 M^2}. \quad (10)$$

Alternatively, one can write

$$R_{\text{Sh}}^2 = \frac{\kappa_t \mu^2 \Omega_*^4 G^2 M^2}{2 \dot{M} v^5 c^4}. \quad (11)$$

In these circumstances the accretion rate is small (much less than what would correspond to the direct accretion onto  $R_{\text{Sh}} > R_{\text{lc}} \gg R_*$  sphere), but the momentum exchange can still be significantly large, causing possibly a non-negligible drag.

On the other hand, in case of a star embedded in the disc plane, the relative velocity is small with respect to the surrounding medium, and so the characteristic cross-section is now given by the Alfvén (stopping) radius,  $R_A$ . For the latter one can derive different formulae depending on the exact situation:

Furthermore,

$$R_{\text{Ag}} = \left( \frac{\kappa_g \mu^2}{\dot{M}_{\text{BHL}}} \right)^{2/7}, \quad (12)$$

where  $\kappa_g \sim (2GM)^{-1/2}/2$  is a constant,  $\mu = B_* R_*^3/2$  is the magnetic moment. The asterisk denotes quantities that correspond to the star surface (in case of a dipole field one finds  $B_*$  at the pole =  $2B_*$  at equator; the numerical factor is somewhat uncertain in  $\kappa_g$ ).

The Bondi–Hoyle–Lyttleton accretion rate (BHL, assumed in the above-given relation) is

$$\dot{M}_{\text{BHL}} = \frac{\sigma \pi G^2 M^2 \rho_\infty}{w^3} = \pi R_{\text{acc}}^2 w \rho_\infty / 2, \quad (13)$$

$\sigma \sim 4$ . The equation for  $R_{\text{Ag}}$  is relevant in the situation when  $R_{\text{Ag}} < R_{\text{acc}}$  and  $R_{\text{Ag}} < R_{\text{lc}}$  both hold.

Finally,

$$R_{\text{Ap}} = \left( \frac{\kappa_p \mu^2 G^2 M^2}{\dot{M}_{\text{BHL}} w^5} \right)^{1/6}, \quad (14)$$

$\kappa_p \sim 1$  or  $2$ . The latter relation for  $R_{\text{Ap}}$  is relevant when  $R_{\text{Ap}} > R_{\text{acc}}$  and  $R_{\text{Ap}} < R_{\text{lc}}$ . In this case one can expect the accretion rate to be given roughly by  $\dot{M}_{\text{BH}}$ , but the momentum exchange is smaller than it was in the previous case (however, it takes continuously, while the star is embedded with the disc medium).

The above given derivation contains various parameters evaluated at the star surface – apart from the magnetic intensity  $B_*$  (or the magnetic dipole moment  $\mu$ ), it is the linear velocity of the star motion  $v$ , radius of the star  $R_*$ , the mass  $M$ , and the period of rotation  $P$ . It also contains the density of the environment  $\rho$  (resp.  $n$ ), and the corresponding velocity of sound,  $c_s$ .

In order to derive specific conclusions about the drag efficiency, one has to fix several parameters at their typical values or to set the typical values expected in the accretion disk. Only then one is prepared to investigate the dependency on  $B_*$ , which is the relevant information that we seek.

The magnetic field depends on the rotation period, so it is interesting to examine also the time dependence  $\Omega_*(t)$ . The most prominent deceleration effect of this kind is expected to occur in case of magnetars (e.g. Toropina et al., 2006) – they slow down on the time-scale of  $10^3$ – $10^4$  yrs. One can involve the power-law deceleration according to Mori and Ruderman (2003):

$$I\dot{\Omega} = -\kappa\mu^{n_1}\rho^{n_2}v^{n_3}\Omega^n, \quad (15)$$

where  $n_1 = (3 + n)/3$ ,  $n_2 = (3 - n)/6$ ,  $n_3 = (3 - 4n)/3$ ,  $\kappa = \text{const}$ ,  $n = \text{const}$  ( $-1 < n < 2$ ).

We can thus conclude that the magnetic star effective radius can be much larger than the geometrical one. However, the characteristic radii do not capture the entire reality; they only partly reflect the basic operation of the drag, which needs to be confirmed by computations carried out under more realistic assumptions. Obviously, the astrophysically realistic modelling needs MHD numerical simulations, such as those described by, e.g. Romanova et al. (2003); Spitkovsky (2006); Toropina et al. (2008), where the complex structure of the magnetosphere can be properly modelled.

### 3 CONCLUSIONS

The drag force is exerted on a moving star by the ambient medium. We can roughly estimate the effect by the cross-sectional area for the mutual interaction between the moving body and the surrounding interstellar gas. Compared with the geometrical radius, the magnetic “stand-off” radius (given by the equilibrium between the magnetic pressure and the hydrodynamic pressure) is significantly larger; it is the greatest one of several characteristic radii. One can expect that the stand-off radius determines the magnitude of the total drag force. To see this more clearly we listed different characteristic radii of the problem; these depend on the type of drag force that one takes into account (due to the thermal pressure versus the ram pressure acting against the star linear motion), and how quickly the magnetic effects decay with the distance from the star (dipole field versus the radiation field of a fast rotator).

Under realistic conditions of the supermassive black hole in the Galactic centre and similar low-luminosity (highly sub-Eddington) nuclei, however, the order-of-magnitude estimation of the characteristic radii for the interaction as well as numerical experiments show that the magnetic field of a compact star does not enhance the drag force significantly (Karas and Šubr, 2001), and so the orbital mechanics of magnetic compact stars comes out only slightly altered in comparison with the non-magnetised case. This conclusion ensures that the drag forces on compact stars can be safely neglected in calculations of orbital evolution of the neutron-star population near the Galactic centre.

Nonetheless, the interaction is still relevant in the context of creation of bow-shock structures (van Marle et al., 2011; Meyer et al., 2014). These have been revealed in several cases also in the Galactic centre (Mužić et al., 2010), where a dense cluster of fast-moving stars on close orbits exists and should include the tentative population of compact magnetized objects close to the supermassive black hole (Zajaček et al., 2014).

## ACKNOWLEDGEMENTS

We acknowledge continued support from the project MŠMT – Kontakt II (LH14049), titled “Spectral and Timing Properties of Cosmic Black Holes”, and the Czech Science Foundation grant (GAČR 13-00070J) supporting the international scientific collaboration in the Astronomical Institute of the Academy of Sciences.

## REFERENCES

- Bisnovatyi-Kogan, G. S. and Ruzmaikin, A. A. (1974), The Accretion of Matter by a Collapsing Star in the Presence of a Magnetic Field, *apss*, **28**, pp. 45–59.
- Bisnovatyi-Kogan, G. S. and Ruzmaikin, A. A. (1976), The accretion of matter by a collapsing star in the presence of a magnetic field. II - Selfconsistent stationary picture, *apss*, **42**, pp. 401–424.
- Bondi, H. (1952), On spherically symmetrical accretion, *Monthly Notices Roy. Astronom. Soc.*, **112**, p. 195.
- Bondi, H. and Hoyle, F. (1944), On the mechanism of accretion by stars, *Monthly Notices Roy. Astronom. Soc.*, **104**, p. 273.
- Dodd, K. N. and McCrea, W. J. (1952), On the effect of interstellar matter on the motion of a star, *Monthly Notices Roy. Astronom. Soc.*, **112**, p. 205.
- Ghosh, P. and Lamb, F. K. (1978), Disk accretion by magnetic neutron stars, *Astrophys. J. Lett.*, **223**, pp. L83–L87.
- Hoyle, F. and Lyttleton, R. A. (1939), The evolution of the stars, *Proceedings of the Cambridge Philosophical Society*, **35**, p. 592.
- Karas, V. and Šubr, L. (2001), Orbital decay of satellites crossing an accretion disc, *Astronomy and Astrophysics*, **376**, pp. 686–696, arXiv: astro-ph/0107232.
- Kluźniak, W. and Rappaport, S. (2007), Magnetically Torqued Thin Accretion Disks, *Astrophys. J.*, **671**, pp. 1990–2005, arXiv: 0709.2361.
- Lipunov, V. M. (1987), *The astrophysics of neutron stars*.
- Meyer, D. M.-A., Mackey, J., Langer, N., Gvaramadze, V. V., Mignone, A., Izzard, R. G. and Kaper, L. (2014), Models of the circumstellar medium of evolving, massive runaway stars moving through the Galactic plane, *Monthly Notices Roy. Astronom. Soc.*, **444**, pp. 2754–2775, arXiv: 1408.2828.
- Mori, K. and Ruderman, M. A. (2003), Isolated Magnetar Spin-Down, Soft X-Ray Emission, and RX J1856.5-3754, *Astrophys. J. Lett.*, **592**, pp. L75–L78, arXiv: astro-ph/0306516.
- Mužić, K., Eckart, A., Schödel, R., Buchholz, R., Zamaninasab, M. and Witzel, G. (2010), Comet-shaped sources at the Galactic center. Evidence of a wind from the central 0.2 pc, *Astronomy and Astrophysics*, **521**, A13, arXiv: 1006.0909.
- Narayan, R. (2000), Hydrodynamic Drag on a Compact Star Orbiting a Supermassive Black Hole, *Astrophys. J. Lett.*, **536**, pp. 663–667, arXiv: astro-ph/9907328.
- Romanova, M. M., Chulsky, G. A. and Lovelace, R. V. E. (2005), Winds, B-Fields, and Magnetotails of Pulsars, *Astrophys. J.*, **630**, pp. 1020–1028, arXiv: astro-ph/0505296.
- Romanova, M. M., Toropina, O. D., Toropin, Y. M. and Lovelace, R. V. E. (2001), Interaction of evolved pulsars and magnetars with the ISM, in J. C. Wheeler and H. Martel, editors, *20th Texas Symposium on relativistic astrophysics*, volume 586 of *American Institute of Physics Conference Series*, pp. 519–525.
- Romanova, M. M., Toropina, O. D., Toropin, Y. M. and Lovelace, R. V. E. (2003), Magnetohydrodynamic Simulations of Accretion onto a Star in the “Propeller” Regime, *Astrophys. J.*, **588**, pp. 400–407, arXiv: astro-ph/0209548.

- Spitkovsky, A. (2006), Time-dependent Force-free Pulsar Magnetospheres: Axisymmetric and Oblique Rotators, *Astrophys. J. Lett.*, **648**, pp. L51–L54, arXiv: astro-ph/0603147.
- Toropina, O. D., Romanova, M. M. and Lovelace, R. V. E. (2006), Spinning-down of moving magnetars in the propeller regime, *Monthly Notices Roy. Astronom. Soc.*, **371**, pp. 569–576, arXiv: astro-ph/0606254.
- Toropina, O. D., Romanova, M. M. and Lovelace, R. V. E. (2008), MHD Simulations of Accretion onto a Magnetized Neutron Star in the “propeller” Regime, *International Journal of Modern Physics D*, **17**, pp. 1723–1729.
- Toropina, O. D., Romanova, M. M., Toropin, Y. M. and Lovelace, R. V. E. (2001), Propagation of Magnetized Neutron Stars through the Interstellar Medium, *Astrophys. J.*, **561**, pp. 964–979, arXiv: astro-ph/0105422.
- van Marle, A. J., Meliani, Z., Keppens, R. and Decin, L. (2011), Computing the Dust Distribution in the Bow Shock of a Fast-moving, Evolved Star, *Astrophys. J. Lett.*, **734**, L26, arXiv: 1105.2387.
- Zajaček, M., Karas, V. and Kunneriath, D. (2014), submitted.



# Eigenmodes of trapped horizontal oscillations in accretion disks

Sourya Khanna<sup>1</sup>, Zofia Strzelecka<sup>2</sup>, Bhupendra Mishra<sup>3</sup>  
and Włodek Kluźniak<sup>3</sup>

<sup>1</sup>Leiden Observatory, Leiden University, PO Box 9513, 2300 RA Leiden, The Netherlands

<sup>2</sup>Imperial College London, Department of Physics, Blackett Laboratory,

Prince Consort Road, London SW7 2BB, United Kingdom

<sup>3</sup>Nicolaus Copernicus Astronomical Center, Bartycka 18, 00-716 Warsaw, Poland

## ABSTRACT

We present eigenfrequencies and eigenfunctions of trapped acoustic-inertial oscillations of thin accretion disks for a Schwarzschild black hole and a rapidly rotating Newtonian star (a Maclaurin spheroid). The results are derived in the formalism of Nowak and Wagoner (1991) with the assumption that the oscillatory motion is parallel to the midplane of the disk. The first four radial modes for each of five azimuthal modes ( $m = 0$  through  $m = 4$ ) are presented. The frequencies and wavefunctions of the lowest modes may be accurately approximated by Airy's function.

**Keywords:** Relativistic stars: black holes – structure stability – oscillations – relativity – gravitation – accretion disks – hydrodynamics

## 1 TRAPPED MODES

Kato and Fukue (1980) showed that acoustic-inertial modes may be trapped in the inner parts of an accretion disk. This occurs when the (radial) epicyclic frequency  $\kappa$  has a maximum, as is the case in the Schwarzschild metric of general relativity (GR) considered by the authors. Okazaki et al. (1987); Kato (1989) and Nowak and Wagoner (1991, 1992) consider a model of a black hole accretion disk in hydrostatic equilibrium, and derive a dispersion relation for modes with  $n = 0, 1, 2, 3, \dots$  nodes along the  $z$ -axis (the symmetry axis of the disk). The trapping occurs for oscillation frequencies below the maximum of the epicyclic frequency  $\omega < \kappa_{\max}$ . Here  $\omega(r) = m\Omega(r) + \sigma$  is the frequency in the frame co-rotating with the fluid (at angular frequency  $\Omega$ ),  $m$  is the azimuthal mode number,  $\sigma$  is the eigenfrequency of the mode, and  $\kappa^2 = (2\Omega/r)d(r^2\Omega)/dr$ . The  $n = 0$  modes will be trapped between the inner edge of the disk, close to the ISCO at  $\kappa(r_{\text{ms}}) = 0$ , and the lowest radius  $r$  satisfying  $\omega(r) = \kappa(r)$ , while for  $n = 1$  trapping occurs close to the maximum of  $\kappa$ , between those two radii at which  $\omega = \kappa$ . Further discussion can be found in the textbook by Kato et al. (1998). In this contribution we only consider the  $n = 0$  trapped modes.

Currently, the main interest in disk oscillations is related to the observed frequencies in the X-ray flux from black hole and neutron star systems (for a review see van der Klis M., 2000). For black hole disks the modes thought to be offering the most promising explanation (Wagoner et al., 2001) of the highest observed frequencies are the  $g$ -modes and

$c$ -modes, investigated in full GR by Perez et al. (1997); Silbergleit et al. (2001), although a different explanation seems to be required for the observed 3:2 ratio of the highest frequencies in the microquasars (Abramowicz and Kluźniak, 2001; Kluźniak et al., 2004; Török et al., 2005). Thus, the modes investigated here are not prime candidates for a theoretical counterpart to the observed high frequency QPOs (quasi-periodic oscillations) in black hole systems. However, similar phenomena are observed in white dwarf systems (Woudt and Warner, 2002), and while their harmonic content may be explained by a resonance (Kluźniak et al., 2005), the origin of the observed frequencies remains obscure. For this reason we would like to discuss disk oscillations in a framework valid equally in a GR and non-GR context.

## 2 EQUATION OF MOTION AND THE BOUNDARY CONDITION

We will be closely following the approach of Nowak and Wagoner (1991) who describe perturbations with a Lagrangian displacement vector in cylindrical coordinates  $(\xi_r^r, \xi_r^\phi, \xi_r^z) = (\xi^r, \xi^\phi, \xi^z) \exp[i(m\phi + \sigma t)]$  in the formalism of Friedman and Schutz (1978), and show

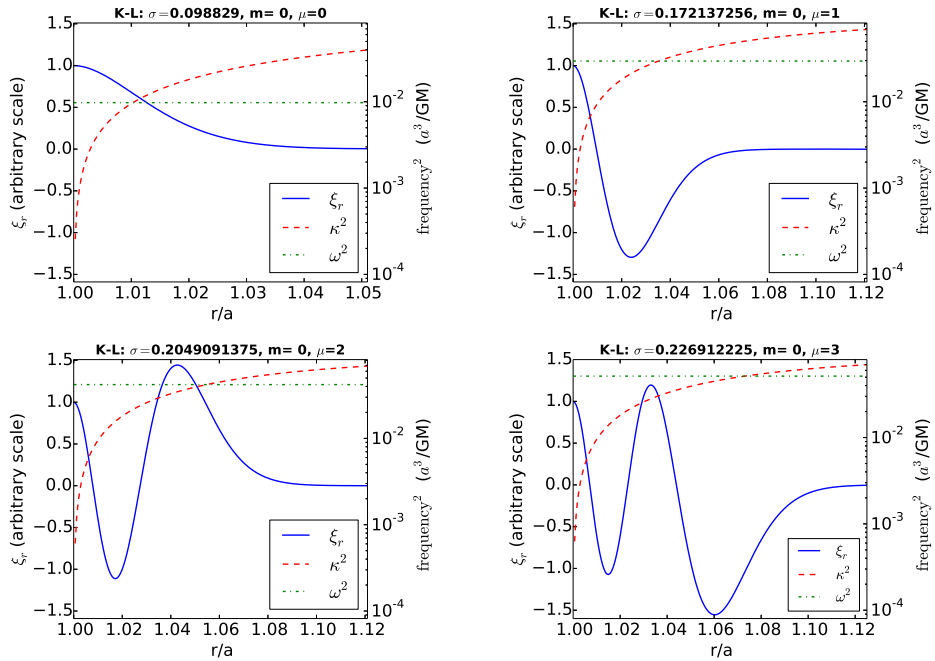


**Figure 1.** The fundamental and the first three radial overtones for  $m = 0$  trapped horizontal oscillations of a thin ( $H/a = 10^{-3}$ ) accretion disk for the potential of Eq. (4). Plotted are the wavefunction: solid (blue) line (arbitrary normalization, left scale);  $\omega^2(r)/\Omega^2(r_{\text{ms}})$ : dashed-dotted (green) line and  $\kappa^2(r)/\Omega^2(r_{\text{ms}})$ : dashed (red) line (logarithmic scale, right).

that in the WKB approximation the azimuthal component of the equation of perturbed motion for thin disks reduces to  $\xi^\phi = 2i(\Omega/\omega)\xi^r$ . In this contribution we assume horizontal motion, implying that  $\xi_*^z \equiv 0$  and  $\partial\xi_*^r/\partial z \equiv 0$ . In terms of  $\Psi(r) \equiv \sqrt{\gamma P r} \xi^r(r)$  the remaining component of the equation of motion then gives

$$\frac{d^2\Psi}{dr^2} + \frac{(\omega^2 - \kappa^2)}{c_s^2}\Psi = 0, \quad (1)$$

where  $c_s^2 = \gamma P/\rho$  is the speed of sound squared; the boundary condition is that the Lagrangian perturbation of pressure vanishes at the unperturbed boundary,  $\Delta P \equiv \gamma P \nabla \xi_* = 0$ , which reduces to

$$\frac{1}{r} \frac{\partial}{\partial r}(r\xi_*^r) + \frac{1}{r} \frac{\partial}{\partial \phi}(\xi_*^\phi) = 0$$

assuming that  $P \neq 0$  (Nowak and Wagoner, 1991). Neglecting derivatives of  $P$  this gives our final boundary condition at the inner edge, at  $r = a$ , which we will take to be at the marginally stable orbit (ISCO) at  $a = r_{\text{ms}}$ ,

$$\frac{d\Psi}{dr} = -\frac{\Psi}{2r}(1 - 4m\Omega/\omega).$$

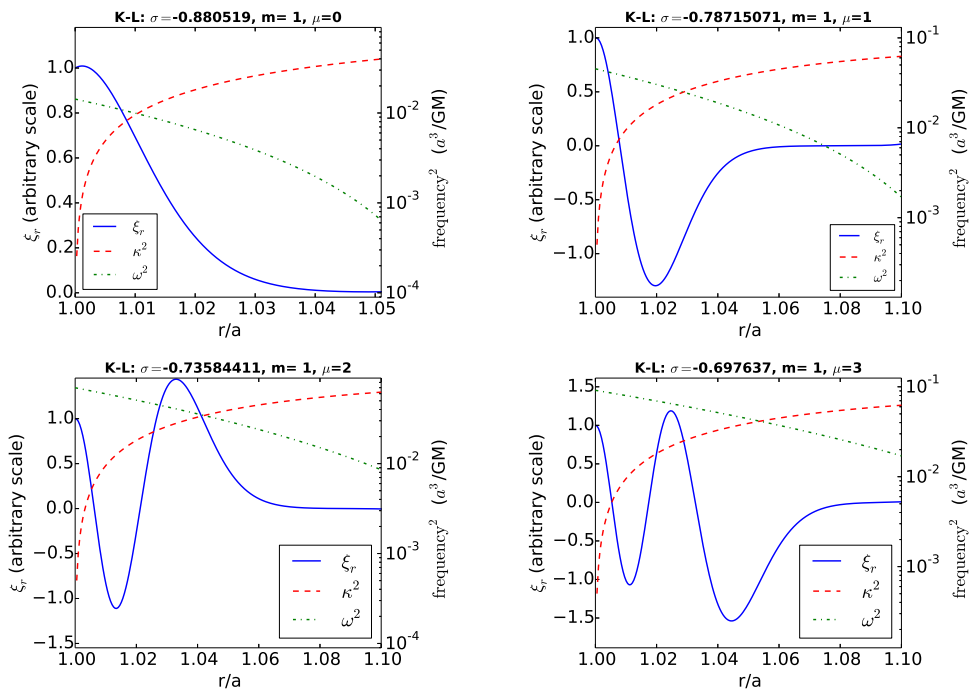


Figure 2. Same as Figure 1, but for  $m = 1$ .

In dimensionless form, with  $r = a(1 + x)$ ,  $\tilde{\omega}(x) = \omega(r)/\Omega(a)$ ,  $\tilde{\kappa}(x) = \kappa(r)/\Omega(a)$ ,  $\tilde{\sigma} = \sigma/\Omega(a)$ , and  $c_s = H\Omega(a)$ , the perturbation (wave) equation takes the form

$$\frac{d^2\Psi}{dx^2} + \left(\frac{a}{H}\right)^2 (\tilde{\omega}^2 - \tilde{\kappa}^2) \Psi = 0, \quad (2)$$

with the boundary condition at  $x = 0$

$$\frac{d\Psi}{dx} = -\frac{\Psi}{2}(1 - 4m/\tilde{\omega}). \quad (3)$$

In the last equation  $\tilde{\omega} = \tilde{\sigma} + m$ . Recall that in general  $\tilde{\omega}(x) = \tilde{\sigma} + m\Omega(r)/\Omega(a)$ .

In this contribution we are providing an atlas of eigenfrequencies and eigenfunctions for the fundamentals and the first three radial overtones of horizontal disk oscillations (labelled with the number of radial nodes,  $\mu = 0, 1, 2, 3$ ) for  $m = 0, 1, 2, 3, 4$ .

### 3 MODELS OF A SCHWARZSCHILD BLACK HOLE

Bohdan Paczyński showed that it is possible to capture essential qualitative features of motion in the Schwarzschild metric in a Newtonian model with a simple pseudo-potential  $\Phi(r) = -GM/(r - 2r_g)$  (Paczyński and Wiita, 1980), with  $r_g = GM/c^2$ . Nowak and

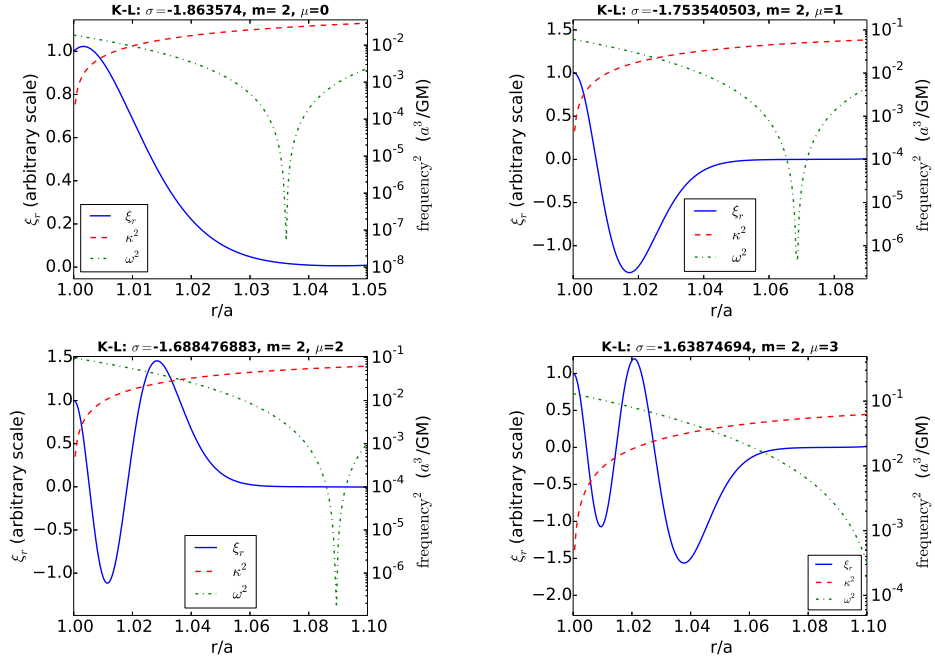


**Figure 3.** Same as Figure 1, but for  $m = 2$ .

Wagoner (1991) found the eigenfrequencies and eigenfunctions of Eq. (1) for the fundamental oscillations with  $m = 0$ , and  $m = 2$ , using values of  $\kappa^2(r)$  following from their own pseudo-potential  $\Phi(r) = -(GM/r)[1 - 6r_g/r + 12(r_g/r)^2]$ .

Here, we model the Schwarzschild metric with a Newtonian pseudo-potential designed expressly to reproduce the Schwarzschild ratio of  $\kappa^2(r)/\Omega^2(r) = 1 - 6r_g/r$ :

$$\Phi_{\text{KL}}(r) = -(c^2/6) \exp(6r_g/r - 1). \quad (4)$$

As we are only interested in the inner parts of an accretion disk, we have dropped an additive constant. We have also renormalized the original form of the potential (Kluźniak and Lee, 2002) by a factor of  $1/e$  to guarantee the correct value of  $\Omega(r_{\text{ms}})$ . The angular frequency of orbital motion follows from  $\Omega^2(r) = r^{-1}\partial\Phi_{\text{KL}}/\partial r$  and, as for the other two potentials, the marginally stable orbit comes out to be at  $r_{\text{ms}} = 6GM/c^2$ . We have numerically solved the eigenvalue problem given by Eqs. (2) and (3), for  $H/a = 10^{-3}$ . The equations being linear in  $\Psi$ , we normalize the wavefunction to unity at the inner edge of the disk:  $\Psi(r_{\text{ms}}) = 1$ . Figure 1 presents the eigenfrequencies  $\sigma$  and the eigenfunctions  $\Psi(r)$  for  $m = 0$  and  $\mu = 0, 1, 2, 3$ , while Figs. 2, 3, 4 and 5 present the same quantities, as well as  $\tilde{\omega}^2$ , for  $m = 1, 2, 3, 4$ , respectively.

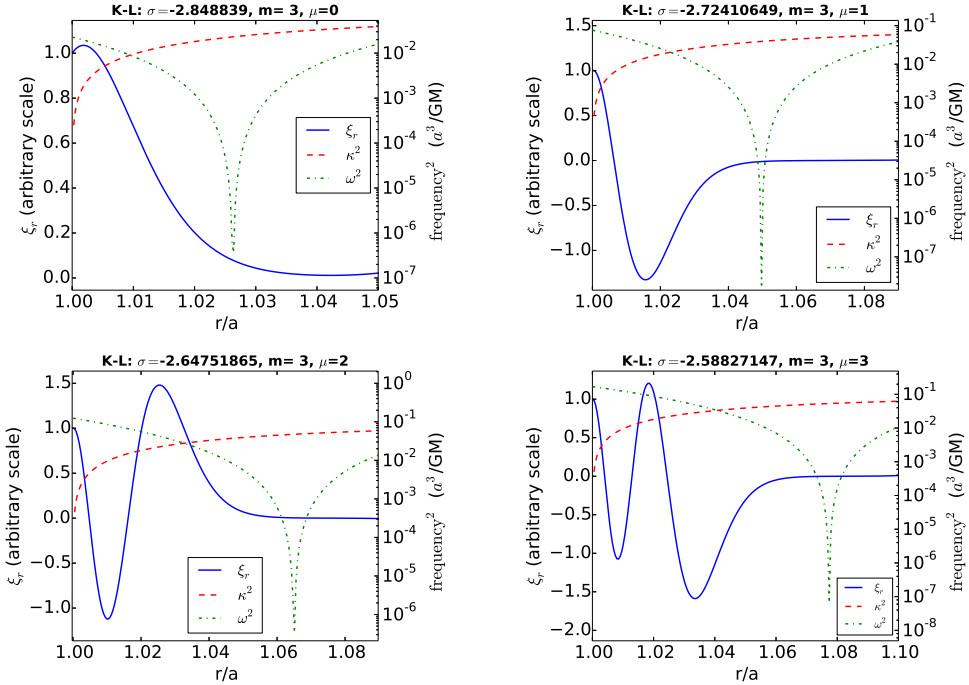


Figure 4. Same as Figure 1, but for  $m = 3$ .

## 4 ESSENTIALS OF ACOUSTIC-INERTIAL OSCILLATIONS

### 4.1 Wave equation

Dust orbiting an axially symmetric gravitating body in its equatorial plane ( $z = 0$ ) would settle in stable circular orbits. The orbit of each dust particle being stable, it corresponds to “rest” (we are only concerned with radial motion in this section) at a fixed radial distance from the center of the body in the minimum of the effective potential,  $V(r, z) = \Phi(r, z) + l^2/(2r^2)$ ,  $l \equiv r^2\Omega(r)$  being the conserved angular momentum of a given particle, and  $\Phi$  the gravitational potential of the body, both per unit mass. Consider small radial perturbations  $\delta r$  of motion of a dust disk (such as the rings of Saturn). Neglecting particle collisions, the perturbed dust would be executing radial harmonic (epicyclic) motion with respect of the stable orbits. The square of the frequency of this radial motion,  $\kappa^2 = \partial^2 V/\partial^2 r$  corresponds to the strength of the restoring force per unit mass:  $-\kappa^2\psi_*$  (if we denote the radial displacement  $\delta r = \psi_*$ ). If the dust disk is replaced by a fluid, there will be an additional restoring force corresponding to pressure perturbations.

It is well known that sound waves in a homogeneous medium can be described by a harmonic function both in space and in time, with a constant and uniform amplitude if attenuation is neglected. Thus, the acoustic displacement of the fluid satisfies both a wave

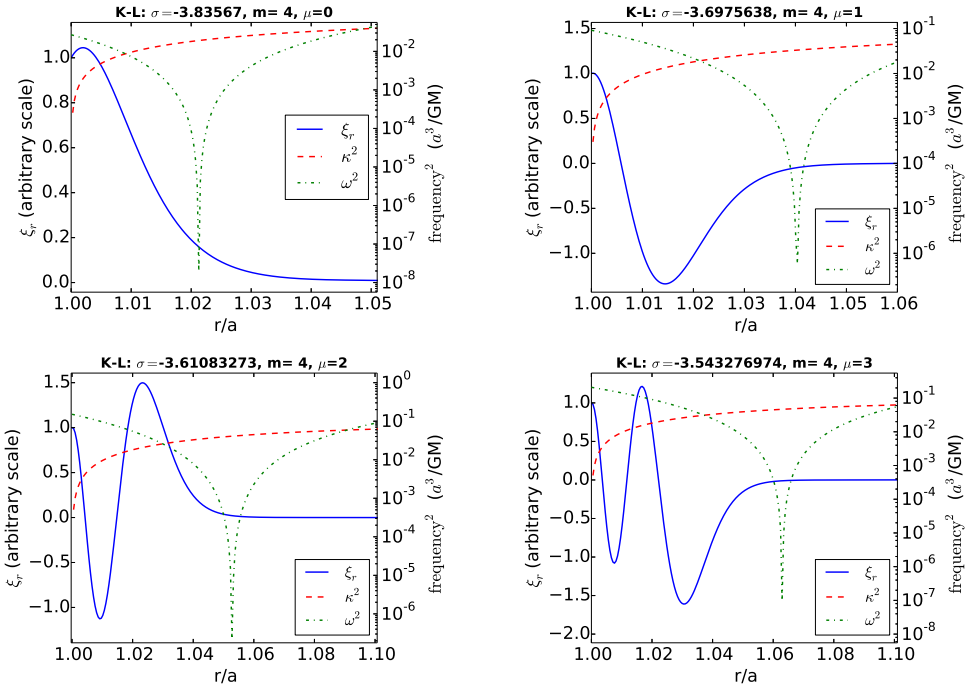


**Figure 5.** Same as Figure 1, but for  $m = 4$ .

equation

$$\frac{\partial^2 \psi_*}{\partial y^2} + k_s^2 \psi_* = 0, \quad (5)$$

and an oscillator equation

$$\frac{\partial^2 \psi_*}{\partial t^2} + \omega_s^2 \psi_* = 0, \quad (6)$$

corresponding to a restoring force  $-\omega_s^2 \psi_*$ . The frequency of the sound wave is related to the wave vector through the linear dispersion relation

$$k_s^2 = \omega_s^2 / c_s^2. \quad (7)$$

Clearly, taking into account in the oscillator equation both the ‘‘inertial’’ (epicyclic) and the acoustic restoring forces, and neglecting for the moment the difference between the cylindrical co-ordinate  $r$  and the Cartesian co-ordinate  $y$ , the acoustic-inertial displacement of the fluid can be described by a displacement  $\psi_*(y, t) = \psi(y) \exp(i\omega t)$ , with  $\omega^2 =$

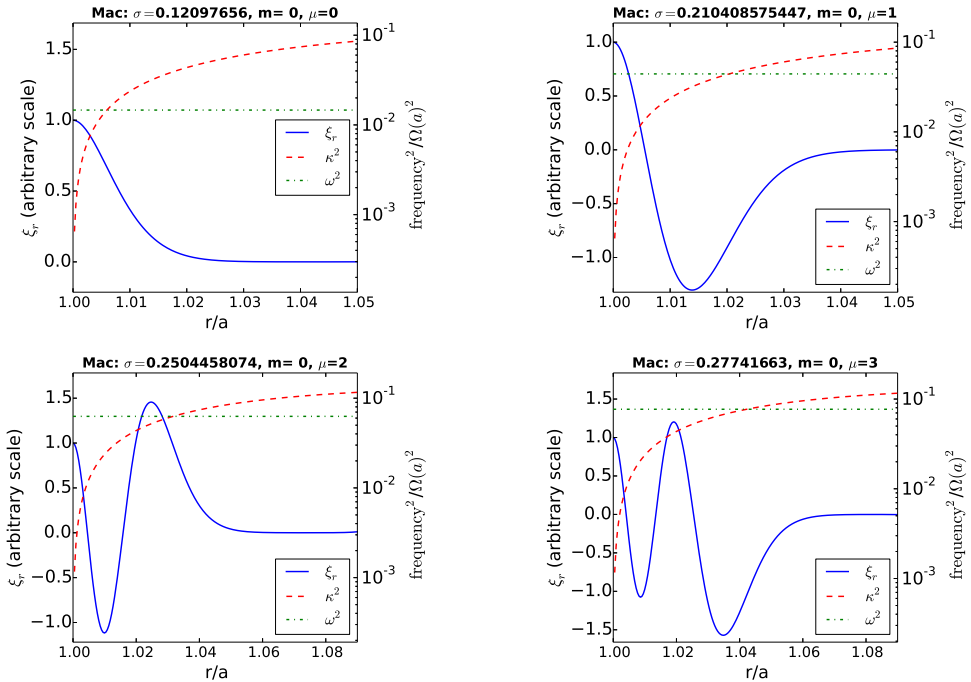


**Figure 6.** Same as Figure 1, but for the potential of a Maclaurin spheroid with ellipticity  $e = 0.834583178$ .

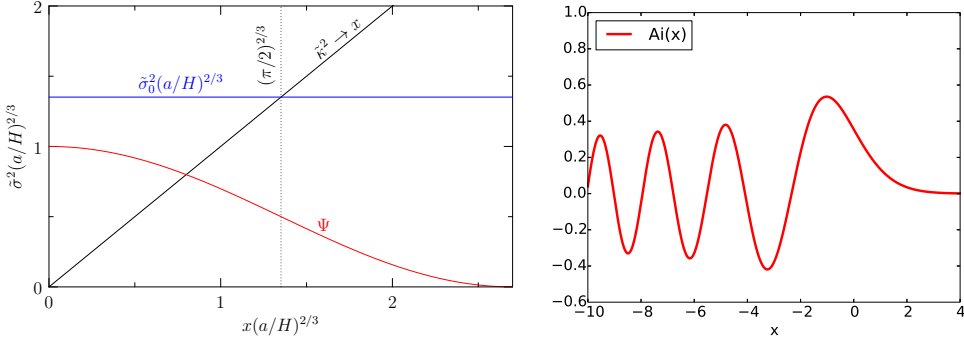


**Figure 7.** *Left Panel:* A simple approximation to the eigenfrequency  $\tilde{\sigma}_0$  of the axisymmetric fundamental mode ( $m = 0, \mu = 0$ ): a quarter wavelength fits in the inner region of the disk ( $\tilde{\sigma}_0^2 \geq \tilde{\kappa}^2$ ) before the wave becomes evanescent. The vertical dotted line indicates the value of  $x$  at which  $\tilde{\sigma}_0^2$  and  $x$  must intersect for this condition to be met:  $\tilde{\sigma}_0^2 = \tilde{\kappa}^2(x_0) \approx x_0$ , with  $x_0 = (\pi/2)^{2/3} \cdot (H/a)^{2/3}$ . The diagonal solid (black) line corresponds to the linear approximation  $\tilde{\kappa}^2(x) = x + \mathcal{O}(x^2)$ , which is valid for the potential of Eq. (4). See Equation (9) and Section 4.2 for details

*Right Panel:* A better approximation is obtained from the location of the extrema of Airy's function  $\text{Ai}(X)$ . Note that the shape of  $\text{Ai}(X)$  closely resembles the shape of the numerically found  $\Psi(x)$ .

$\kappa^2 + \omega_s^2$  (or, in the form written down by Binney and Tremaine, 1987,  $\omega^2 = \kappa^2 + k_s^2 c_s^2$ ). Substituting this new dispersion relation into Eq. (7), we see that Eq. (5) takes the form

$$\frac{d^2 \psi}{dy^2} + \frac{\omega^2 - \kappa^2}{c_s^2} \psi = 0. \quad (8)$$

Remarkably, this is the same equation that was rigorously derived by Nowak and Wagoner (1991), i.e. Eq. (1). In the remainder of this paper we will be discussing numerical solutions of its dimensionless version, Eq. (2), subject to the boundary condition Eq. (3), for a thin disk ( $H/a = 0.001$ ) in two different models of the gravitating body, i.e. for two different epicyclic frequencies  $\kappa(r)$ .

## 4.2 Estimates of the eigenfrequencies

It is possible to understand the values of the eigenfrequencies  $\sigma$  and the shape of the wavefunctions in a simple model of Eq. (2). For axially symmetric modes,  $m = 0$  and hence  $\omega = \sigma$ . The wave equation has oscillatory solutions for  $\omega^2 > \kappa^2$ , while the wave is evanescent for  $\omega^2 < \kappa^2$ . Thus the mode is trapped between  $a = r_{\text{ms}}$  (i.e.  $x = 0$ ) and  $r = r_0$  such that  $\sigma^2 = \kappa^2(r_0)$  (Fig. 7).

As  $\sigma^2 \ll \kappa_{\text{max}}^2$  for the fundamental mode and  $\kappa^2(r_{\text{ms}}) = 0$  we can model  $\kappa^2$  with a linear approximation (Nowak and Wagoner, 1991), which for the potential of Eq. (2) has the simple form  $\tilde{\kappa}^2 = x$ . Thus, the wave becomes evanescent at  $r_0/a - 1 = x_0 \approx \tilde{\sigma}^2$ . We can take the boundary condition on the wave to correspond to that of a banner flapping in the wind, with a crest at the edge [of the disk ( $x = 0$ )] and a node close to  $x_0$ . Perhaps a quarter wavelength of a sinusoid between  $x = 0$  and  $x = x_0$  is a fair approximation (Kato and Fukue, 1980).

With the above approximations, we have  $ax_0 = \lambda/4$ , and  $\tilde{\sigma}^2 = x_0$ . Now,  $k = 2\pi/\lambda \approx \sigma/c_s$  so  $\lambda/4 \approx \pi c_s/(2\sigma) = \pi H\Omega/(2\sigma)$ . Recall that  $\tilde{\sigma} = \sigma/\Omega(a)$ . Finally, we obtain  $\tilde{\sigma}^3 \approx \pi H/(2a)$ , yielding

$$\tilde{\sigma} \approx \left(\frac{\pi H}{2a}\right)^{1/3} \approx 1.16 \left(\frac{H}{a}\right)^{1/3}. \quad (9)$$

For  $H/a = 10^{-3}$  this yields  $\tilde{\sigma} \approx 0.116$ , while the numerically obtained value for the correct functional form of  $\kappa^2$  is  $\tilde{\sigma}_0 \approx 0.0988$ . Thus, this crude estimate of the eigenfrequency is off by less than 20%. However, as we will see directly below, we have obtained the correct scaling of the eigenfrequency with the dimensionless thickness of the disk (Kato and Fukue, 1980).

A more accurate estimate of the eigenfrequency can be obtained by noting that in the linear approximation to  $\kappa^2$  (which for the potential of Eq. (4) is simply  $\tilde{\kappa}^2 = x$ ), Eq. (2) corresponds to Airy's equation (Nowak and Wagoner, 1991). Indeed, with the substitution  $X = (x - \tilde{\sigma}^2)(a/H)^{2/3}$ , Eq. (2) becomes  $d^2\Psi/dX^2 = X\Psi$ , with the Airy function as the solution:  $\Psi(X) = \text{Ai}(X)$ . In the exact waveforms of Fig. 1, one can recognize the shape of Airy's function, to a good accuracy. The (implicit) eigenvalues  $\tilde{\sigma}$  can now be found directly

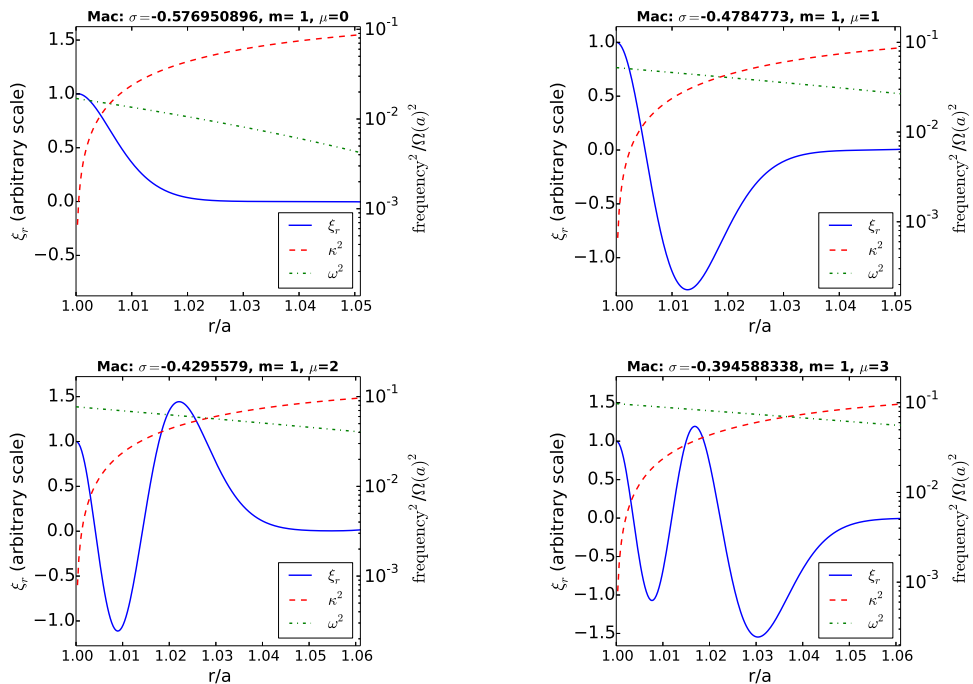


Figure 8. Same as Figure 6, but for  $m = 1$ .

from the boundary condition, Eq. (3), in the form

$$\frac{1}{\Psi} \frac{d\Psi}{dX} = \left(\frac{H}{a}\right)^{2/3} \frac{1}{2}(4m/\tilde{\omega} - 1).$$

Now, for  $H \ll a$ , the boundary condition (at  $x = 0$ ) becomes  $d \log \Psi / dX \ll 1$ , i.e. it is approximately that  $X$  corresponds to one of those  $X_\mu$  for which  $\text{Ai}(X_\mu)$  has an extremum,  $d\text{Ai}/dX|_{X_\mu} = 0$ . Thus,  $\tilde{\sigma}_\mu^2 \approx -(H/a)^{2/3} X_\mu$ ,  $\mu = 0, 1, 2, 3, \dots$ . We can compare these approximate eigenfrequencies (Table 1) with the numerically found eigenvalues for the correct form of  $\kappa^2$ . For the fundamental the agreement is quite good, but the accuracy of the Airy approximation gradually degrades as  $\sigma_\mu$  approaches the value  $\kappa_{\max}$ .

Table 1: Exact and approximate eigenvalues of Eqs. (2) and (3)

$m = 0, \quad H/a = 0.001$	$\mu = 0$	$\mu = 1$	$\mu = 2$	$\mu = 3$
$\tilde{\sigma}_\mu$ for $\kappa^2$ of Eq. (4)	0.0988...	0.172...	0.205...	0.227...
Airy approx.: $\sqrt{-0.01 X_\mu}$	0.101...	0.180...	0.229...	0.248...
Accuracy of approximation	2%	5%	7%	9%

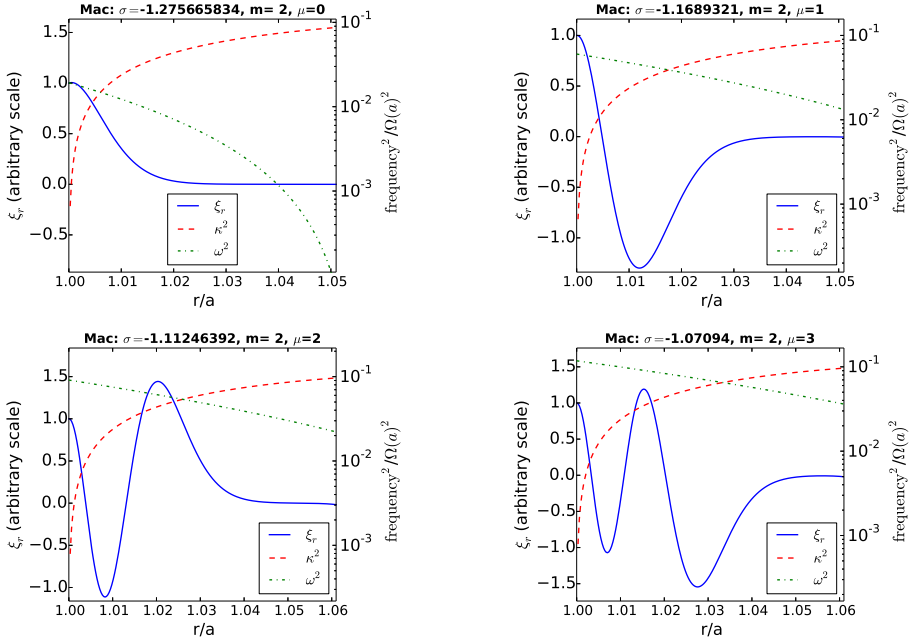
We thank Mr. Luca Giussani for providing us with the values of Airy’s extrema.

Table 2: Eigenvalues of Eqs. (2) and (3)

$H/a = 0.001$	$\mu = 0$	$\mu = 1$	$\mu = 2$	$\mu = 3$
KL Eq. (4), $m = 0$ . $\tilde{\sigma}_\mu =$	0.098829	0.172137	0.204909	0.226912
Maclaurin, $m = 0$ . $\tilde{\sigma}_\mu =$	0.120977	0.210409	0.250446	0.277417
KL Eq. (4), $m = 1$ . $\tilde{\sigma}_\mu =$	-0.880519	-0.787151	-0.735844	-0.697637
Maclaurin, $m = 1$ . $\tilde{\sigma}_\mu =$	-0.576951	-0.478477	-0.429558	-0.394588
KL Eq. (4), $m = 2$ . $\tilde{\sigma}_\mu =$	-1.86357	-1.753541	-1.688477	-1.638747
Maclaurin, $m = 2$ . $\tilde{\sigma}_\mu =$	-1.275666	-1.168932	-1.112464	-1.07094
KL Eq. (4), $m = 3$ . $\tilde{\sigma}_\mu =$	-2.848839	-2.724106	-2.647519	-2.588271
Maclaurin, $m = 3$ . $\tilde{\sigma}_\mu =$	-1.974981	-1.860566	-1.797395	-1.750153
KL Eq. (4), $m = 4$ . $\tilde{\sigma}_\mu =$	-3.83567	-3.697564	-3.610833	-3.543277
Maclaurin, $m = 4$ . $\tilde{\sigma}_\mu =$	-2.674776	-2.553138	-2.483865	-2.431476

## 5 TRAPPED OSCILLATIONS IN AN ACCRETION DISK AROUND A MACLAURIN SPHEROID

In previous sections, following Nowak and Wagoner (1991) we were discussing the trapped acoustic-inertial oscillations of a pseudo-Newtonian model of an accretion disk around



**Figure 9.** Same as Figure 6, but for  $m = 2$ .

a Schwarzschild black hole. Interestingly, the same trapping phenomenon occurs in strictly Newtonian gravity, for disks orbiting sufficiently oblate bodies. Kluźniak et al. (2001), and Zduńik and Gourgoulhon (2001) pointed out that oblateness of a gravitating body can destabilize orbits close to it, while Amsterdamski et al. (2002) showed that the marginally stable orbit exists in the Newtonian potential of classic Maclaurin spheroids for a sufficiently large ellipticity of the spheroid, i.e. a sufficiently large rotation rate of the spheroid. Kluźniak and Rosińska (2013) give explicit expressions for the angular velocity in circular orbits and for the corresponding epicyclic frequencies as a function of orbital radius and the ellipticity of the Maclaurin spheroid. Gondek-Rosińska et al. (2014) compare these analytic expressions with exact numerical solutions (in GR) of rapidly rotating quark stars, while Mishra and Vaidya (2014) give accretion disk solutions in the gravitational field of Maclaurin spheroids, which are reminiscent of the Shakura and Sunyaev (1973) black hole accretion disks.

Without further ado, we are presenting the eigenfrequencies and eigenvalues of trapped acoustic-inertial modes for an accretion disk around a Maclaurin spheroid of ellipticity  $e = 0.834583178$ . We are using the same equation and boundary conditions as before, Eqs. (2) and (3), with the functional form of  $\kappa^2(r)$  and  $\Omega^2(r)$  appropriate for the chosen Maclaurin spheroid. The only other change is that we need to reinterpret  $H$ : the condition of hydrostatic equilibrium is  $c_s = h\Omega_\perp$ , with  $h$  being the half-thickness of the disk, and  $\Omega_\perp$  the vertical epicyclic frequency which we absorb into an effective half-thickness  $H = h\Omega_\perp(a)/\Omega(a)$ . The results are summarized in Figs. 6, 8, 9, 10, 11 for modes with  $m = 0, 1, 2, 3, 4$ , respectively. The frequencies are compared in Table (2) with those obtained in

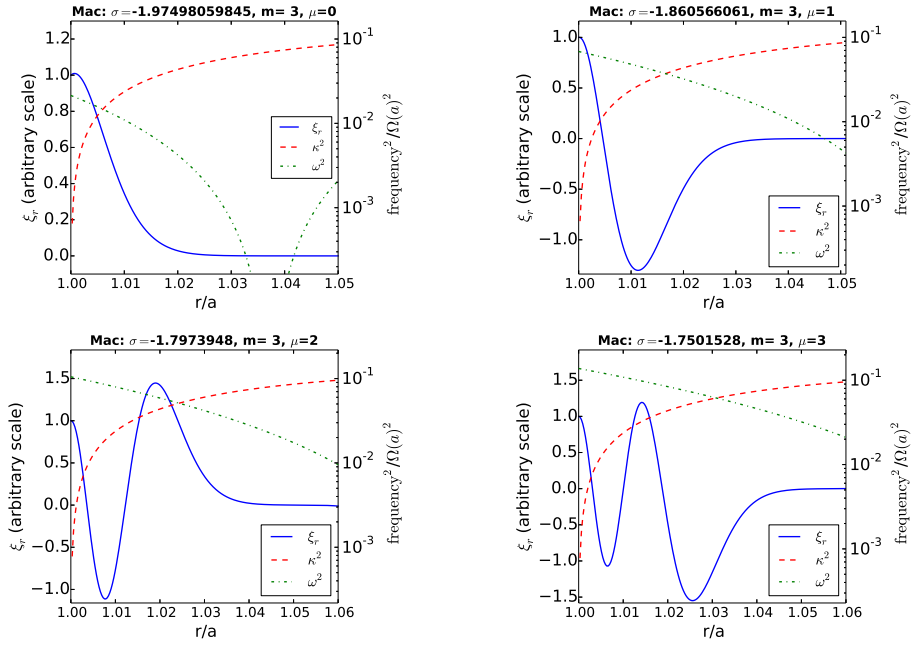


**Figure 10.** Same as Figure 6, but for  $m = 3$ .

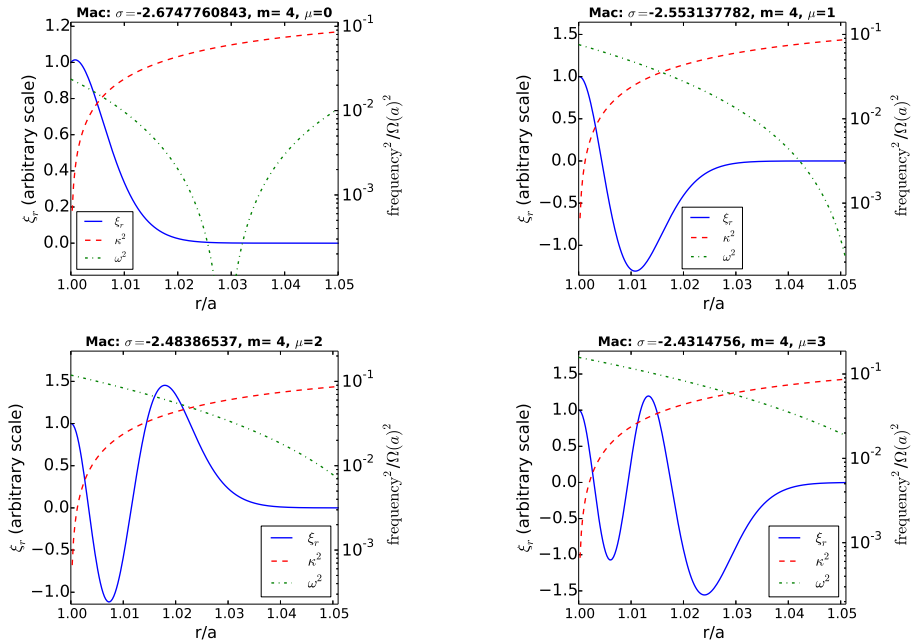


**Figure 11.** Same as Figure 6, but for  $m = 4$ .

the previous sections for the black-hole disk. For both the GR (“KL”) and the Newtonian (Maclaurin)  $m = 0$  model the ratio of the  $\mu = 2$  frequency to the fundamental is very close to 2:1.

## ACKNOWLEDGEMENTS

This work was supported in part by Polish NCN grant 2013/08/A/ST9/00795.

## REFERENCES

- Abramowicz, M. A. and Kluźniak, W. (2001), A precise determination of black hole spin in GRO J1655-40, *Astronomy and Astrophysics*, **374**, pp. L19–L20, arXiv: astro-ph/0105077.
- Amsterdamski, P., Bulik, T., Gondek-Rosińska, D. and Kluźniak, W. (2002), Marginally stable orbits around Maclaurin spheroids and low-mass quark stars, *Astronomy and Astrophysics*, **381**, p. L21.
- Binney, J. and Tremaine, S. (1987), *Galactic Dynamics*, Princeton University Press.
- Friedman, J. L. and Schutz, B. F. (1978), Lagrangian perturbation theory of nonrelativistic fluids, *Astrophys. J.*, **221**, p. 937.
- Gondek-Rosińska, D., Kluźniak, W., Stergioulas, N. and Wiśniewicz, M. (2014), Epicyclic frequencies for rotating strange quark stars: Importance of stellar oblateness, *Phys. Rev. D*, **89**, p. j4001.
- Kato, S. (1989), Low-frequency, one-armed corrugation waves in relativistic accretion disks, *Publ. Astronom. Soc. Japan*, **41**, p. 745.
- Kato, S. and Fukue, J. (1980), Trapped radial oscillations of gaseous disks around a black hole, *Publ. Astronom. Soc. Japan*, **32**, p. 377.
- Kato, S., Fukue, J. and Mineshige, S. (1998), *Black-Hole Accretion Disks*, Kyoto University Press.
- Kluźniak, W., Abramowicz, M. A. and Lee, W. H. (2004), High-frequency QPOs as a problem in physics: non-linear resonance, in P. Kaaret, F. K. Lamb and J. H. Swank, editors, *X-ray Timing 2003: Rossi and Beyond*, volume 714 of *American Institute of Physics Conference Series*, pp. 379–382, arXiv: astro-ph/0402013.
- Kluźniak, W., Bulik, T. and Gondek-Rosińska, D. (2001), Quark stars in low-mass x-ray binaries: for and against, *Proceedings of the Fourth INTEGRAL Workshop, Ed: B. Battrick*, **ESASP 459**, p. 301.
- Kluźniak, W., Lasota, J.-P., Abramowicz, M. A. and Warner, B. (2005), QPOs in cataclysmic variables and in X-ray binaries, *Astronomy and Astrophysics*, **440**, pp. L25–L28, arXiv: astro-ph/0503151.
- Kluźniak, W. and Lee, W. H. (2002), The swallowing of a quark star by a black hole, *Monthly Notices Roy. Astronom. Soc.*, **335**, p. L29.
- Kluźniak, W. and Rosińska, D. (2013), Orbital and epicyclic frequencies of Maclaurin spheroids, *Monthly Notices Roy. Astronom. Soc.*, **434**, p. 2825.
- Mishra, B. and Vaidya, B. (2014), Geometrically thin accretion disk around Maclaurin spheroid, *Astronomy and Astrophysics*, p. submitted.
- Nowak, M. A. and Wagoner, R. V. (1991), Diskoseismology: Probing accretion disks. I - Trapped adiabatic oscillations, *Astrophys. J.*, **378**, p. 656.
- Nowak, M. A. and Wagoner, R. V. (1992), Diskoseismology: Probing accretion disks. II - G-modes, gravitational radiation reaction, and viscosity, *Astrophys. J.*, **393**, p. 697.

- Okazaki, A. T., Kato, S. and Fukue, J. (1987), Global trapped oscillations of relativistic accretion disks, *Publ. Astronom. Soc. Japan*, **39**, p. 457.
- Paczynski, B. and Wiita, P. J. (1980), Thick accretion disks and superluminal luminosities, *Astronomy and Astrophysics*, **88**, p. 23.
- Perez, C., Silbergleit, A., Wagoner, R. and Lehr, D. (1997), Relativistic Diskoseismology. I. Analytical Results for “Gravity Modes”, *Astrophys. J.*, **476**, p. 589.
- Shakura, N. I. and Sunyaev, R. A. (1973), Black holes in binary systems. Observational appearance, *Astronomy and Astrophysics*, **24**, p. 337.
- Silbergleit, A., Wagoner, R. and Ortega-Rodríguez, M. (2001), Relativistic Diskoseismology. II. Analytical Results for C-modes, *Astrophys. J.*, **548**, p. 335.
- Török, G., Abramowicz, M. A., Kluźniak, W. and Stuchlík, Z. (2005), The orbital resonance model for twin peak kHz quasi periodic oscillations in microquasars, *Astronomy and Astrophysics*, **436**, pp. 1–8.
- van der Klis M. (2000), Millisecond Oscillations in X-ray Binaries, *AnnRevA&A*, **38**, p. 717.
- Wagoner, R., Silbergleit, A. and Ortega-Rodríguez, M. (2001), “Stable” Quasi-periodic Oscillations and Black Hole Properties from Diskoseismology, *Astrophys. J.*, **559**, p. L25.
- Woudt, P. A. and Warner, B. (2002), Dwarf nova oscillations and quasi-periodic oscillations in cataclysmic variables - I. Observations of VW Hya, *Monthly Notices Roy. Astronom. Soc.*, **333**, p. 411.
- Zdunik, J. L. and Gourgoulhon, E. (2001), Small strange stars and marginally stable orbit in Newtonian theory, *Phys. Rev. D*.

# Oscillations of electric current-carrying string loop near a Schwarzschild black hole immersed in an asymptotically uniform magnetic field

Martin Kološ<sup>a</sup>, Zdeněk Stuchlík<sup>b</sup> and Arman Tursunov<sup>c</sup>

Institute of Physics, Faculty of Philosophy & Science, Silesian University in Opava,  
Bezručovo nám. 13, CZ-746 01 Opava, Czech Republic

<sup>a</sup>[martin.kolos@fpf.slu.cz](mailto:martin.kolos@fpf.slu.cz)

<sup>b</sup>[zdenek.stuchlik@fpf.slu.cz](mailto:zdenek.stuchlik@fpf.slu.cz)

<sup>c</sup>[arman.tursunov@fpf.slu.cz](mailto:arman.tursunov@fpf.slu.cz)

## ABSTRACT

We study oscillations of an electric current-carrying and axially-symmetric string loop in the vicinity of a Schwarzschild black hole embedded in an asymptotically uniform magnetic field. The radial profiles of frequencies of small oscillations of the string loop around stable equilibrium points are given for the radial and vertical harmonic modes that are relevant also in the quasi-periodic stages of the oscillations. Their properties in dependence on the uniform magnetic field intensity and angular momentum parameters of the string loops are determined. We examine the relevance of resonant phenomena of the radial and vertical string-loop oscillations at their frequency ratio 3:2. The oscillatory frequencies of the string loops are compared with the frequencies of high-frequency quasi-periodic oscillations (HF QPOs) observed in the microquasars GRS 1915+105, XTE 1550-564, GRO 1655-40 containing a black hole. We have demonstrated that the influence of the uniform magnetic field does not allow us to explain all the observed data for non-rotating black holes. Clearly, rotation of the black hole is necessary to explain all the observed frequencies in the microquasars by the string loop oscillations.

**Keywords:** string loop oscillations – X-ray variability – HF QPO observations

## 1 INTRODUCTION

Relativistic current-carrying string loops moving axisymmetrically along the symmetry axis of the Kerr or Schwarzschild–de Sitter black holes have been recently studied extensively (Jacobson and Sotiriou, 2009; Kološ and Stuchlík, 2010, 2013). Such a configuration was also studied in (Larsen, 1994; Frolov and Larsen, 1999). Tension of such string loops prevents their expansion beyond some radius, while their worldsheet current introduces an angular momentum barrier preventing them from collapsing into the black hole. There is an important possible astrophysical relevance of the current-carrying string loops (Jacobson and Sotiriou, 2009), as they could in a simplified way represent plasma that exhibits

associated string-like behaviour via dynamics of the magnetic field lines in the plasma (Christensson and Hindmarsh, 1999; Semenov et al., 2004), or due to thin isolated flux tubes of magnetized plasma that could be described by an one-dimensional string (Spruit, 1981; Semenov and Bernikov, 1991; Cremaschini and Stuchlík, 2013). Motion of electrically charged string loops in combined external gravitational and electromagnetic fields has been recently studied for a Schwarzschild black hole immersed in a homogeneous magnetic field (Tursunov et al., 2013, 2014).

Understanding of the dynamics of charged particles in the combined electromagnetic and gravitational fields is necessary for the modelling of the MHD processes. The single-particle dynamics is relevant also for collective processes modelled in the framework of kinetic theory (Cremaschini and Stuchlík, 2013; Cremaschini et al., 2013; Cremaschini and Stuchlík, 2014). The oscillatory motion of charged particles around equatorial and off-equatorial circular orbits could be relevant in formation of magnetized string loops (Cremaschini and Stuchlík, 2013; Kovář, 2013). The string-like configurations of magnetized plasmas could occur in the accretion discs due to an instability or irradiation creating an ansamble of charged particles in epicyclic motion giving rise to the stringy structure due to kinetic dynamo effect. A nearly uniform and stable magnetic field can be naturally generated by a distant magnetar Kovář et al. (2014) a strongly magnetized star.

The astrophysical applications of the current carrying string loops have been focused on the problem of acceleration of string loops due to the transmutation process (Jacobson and Sotiriou, 2009). Since the string loops can be accelerated to ultra-relativistic velocities in the deep gravitational potential of compact objects (Stuchlík and Kološ, 2012a,b), the string loop transmutation can be well considered as a process of formation of ultra-relativistic jets, along with the standard model based on the Blandford–Znajek process (Blandford and Znajek, 1977). Here we concentrate our attention on the inverse situation of small oscillations of string loops in the vicinity of stable equilibrium points at the equatorial plane of black holes that was proposed as a possible model of HF QPOs observed in black hole and neutron star binary systems (Stuchlík and Kološ, 2012b).

In the black hole systems observed in both Galactic and extragalactic sources, strong gravity effects have a crucial role in three phenomena related to the accretion disc that is the emitting source: the spectral continuum, spectral profiled lines, and oscillations of the disc; clearly, strong gravity has an important role also in the binary systems containing neutron (quark) stars. HF QPOs of X-ray brightness had been observed in many Galactic Low Mass X-Ray Binaries (LMXB) containing neutron stars (see e.g. van der Klis, 2000; Barret et al., 2005; Belloni et al., 2007) or black holes (see e.g. McClintock and Remillard, 2006; Remillard, 2005; Remillard and McClintock, 2006). Some of the HF QPOs are in the kHz range and often come in pairs of the upper and lower frequencies ( $\nu_U$ ,  $\nu_L$ ) of *twin peaks* in the Fourier power spectra. Since the peaks of high frequencies are close to the orbital frequency of the marginally stable circular orbit representing the inner edge of Keplerian discs orbiting black holes (or neutron stars), the strong gravity effects must be relevant in explaining of HF QPOs (Török et al., 2005).

It has been shown in (Stuchlík and Kološ, 2014) that the frequencies of the twin peak oscillations observed in spectra of three different microquasars can be explained by the oscillations of string loop in the field of a Kerr black hole. Here we aim to extend previous research to the case of Schwarzschild black hole immersed in external uniform magnetic

field. Assuming small oscillations of a string loop near an equilibrium position corresponding to a minimum of the effective potential, the Hamiltonian of string loop motion can be perturbed with the first order term corresponding to linear harmonic oscillators in two uncoupled radial and vertical orthogonal modes (Stuchlík and Kološ, 2014). The higher order terms correspond to the non-linear phenomena causing coupling of the radial and vertical oscillatory modes and determine transition to chaotic motion through quasi-periodic stages of the oscillatory motion. The frequencies of the radial and vertical harmonic oscillations are relevant also in the quasi-periodic stages of the oscillatory motion (Kološ and Stuchlík, 2013).

## 2 MODEL OF STRING LOOP OSCILLATIONS

We study a string loop motion in the field of a black hole described by the Schwarzschild metric, characterized by the gravitational mass  $M$ ,

$$ds^2 = -A(r) dt^2 + A^{-1}(r) dr^2 + r^2(d\theta^2 + \sin^2\theta d\phi^2), \quad A(r) = 1 - \frac{2M}{r}. \quad (1)$$

We use the geometric units with  $c = G = 1$  and the Schwarzschild coordinates. In order to properly describe the string loop motion, it is useful to use the Cartesian coordinates

$$x = r \sin(\theta), \quad y = r \cos(\theta). \quad (2)$$

The string loop is threaded onto an axis of the black hole chosen to be the  $y$ -axis. Due to the assumed axisymmetry of the string loop motion, one point path can represent whole movement of the string. Trajectory of the string can be represented by a curve in the 2D  $x$ - $y$  plane. The string loop can oscillate, changing its radius in the  $x$ - $z$  plane, while propagating in the  $y$  direction.

We assume static, axisymmetric and asymptotically uniform magnetic field. Since the Schwarzschild spacetime is flat at spatial infinity only nonzero covariant component of the potential of the electromagnetic field takes the form (Wald, 1974)

$$A_\phi = \frac{B}{2} r^2 \sin^2\theta = \frac{B}{2} x^2. \quad (3)$$

The symmetries of the considered background gravitational and magnetic fields, corresponding to the  $t$  and  $\phi$  components of the Killing vector, imply the existence of two constants of the motion, namely the string loop energy  $E$  and the string loop angular momentum  $L$  (Tursunov et al., 2013, 2014).

Dynamics of an axisymmetric current-carrying string loop in a given axially symmetric and stationary Kerr spacetime in the absence of electromagnetic fields has been discussed in detail in (Jacobson and Sotiriou, 2009; Kološ and Stuchlík, 2013; Stuchlík and Kološ, 2014). In the spherically symmetric spacetime (1) immersed in external magnetic field the Hamiltonian governing the string loop dynamics can be expressed in the form (Tursunov et al., 2013)

$$H = \frac{1}{2} f(r) P_r^2 + \frac{1}{2r^2} P_\theta^2 - \frac{E^2}{2f(r)} + \frac{V_{\text{eff}}}{2f(r)}, \quad (4)$$

with an effective potential for the string loop motion in the combined gravitational and magnetic fields

$$V_{\text{eff}} = f(r) \left\{ \frac{B^2 x^3}{8} + \left( \frac{\Omega J B}{\sqrt{2}} + \mu \right) x + \frac{J^2}{x} \right\}^2. \quad (5)$$

In accordance with (Jacobson and Sotiriou, 2009), we have introduced new parameters that are conserved during the motion of string loop in the Schwarzschild spacetime combined with the uniform magnetic field,

$$J^2 \equiv \frac{j_\sigma^2 + j_\tau^2}{2}, \quad \omega \equiv -\frac{j_\sigma}{j_\tau}, \quad \Omega \equiv \frac{-\omega}{\sqrt{1 + \omega^2}}, \quad (6)$$

where the parameters  $j_\tau$ ,  $j_\sigma$  determines current of the string. The parameter  $J$  is always positive,  $J > 0$ , the dimensionless parameter  $\omega$  runs in the interval  $-\infty < \omega < \infty$ , and the dimensionless parameter  $\Omega$  varies in the range  $-1 < \Omega < 1$  (Tursunov et al., 2013, 2014).

We shall use for simplicity the dimensionless radial coordinate  $r/M \rightarrow r$ , dimensionless time coordinate  $t/M \rightarrow t$ , and we make the rescaling  $E/\mu \rightarrow E$  and  $J/\sqrt{\mu} \rightarrow J$ .

The equations of motion for  $\mu \in \{r, \theta\}$  are given by the Hamilton equations relating the position 4-vector and 4-momentum of the string loop

$$\frac{dX^\mu}{d\zeta} = \frac{\partial H}{\partial P_\mu}, \quad \frac{dP_\mu}{d\zeta} = -\frac{\partial H}{\partial X^\mu}. \quad (7)$$

The properties of the effective potential  $V_{\text{eff}}(r, \theta)$ , (5) were discussed in great details in (Tursunov et al., 2013, 2014), here we give a short overview. The local extrema of the effective potential cannot be located out of the equatorial plane corresponding to  $y = 0$ . Then the extrema of the angular momentum parameter of the string loop correspond to

$$J = J_{E\pm}(x; B, \Omega) \equiv \frac{B\Omega x^2(x-1) \mp \sqrt{G}}{2\sqrt{2}(x-3)} \quad (8)$$

where

$$G(x; \Omega, B) = B^2(x-1)^2 x^2 \Omega^2 + B^2(x-3)(3x-5)x^2 + 8(x-3)(x-1). \quad (9)$$

The behaviour of the functions  $J_{E\mp}(x; B, \Omega)$  is discussed in detail in (Tursunov et al., 2013).

There are four different types of the boundaries for string loop motion given by the condition

$$V_{\text{eff}}(x, y) = E^2 = \text{const.}, \quad (10)$$

for the string loop dynamics in the background constituted by a Schwarzschild BH immersed in an uniform magnetic field. We can distinguish them according to two properties: possibility of the string loop to escape to infinity in the  $y$ -direction, and possibility to collapse to the black hole. A detailed discussion can be found in (Kološ and Stuchlík, 2010; Tursunov

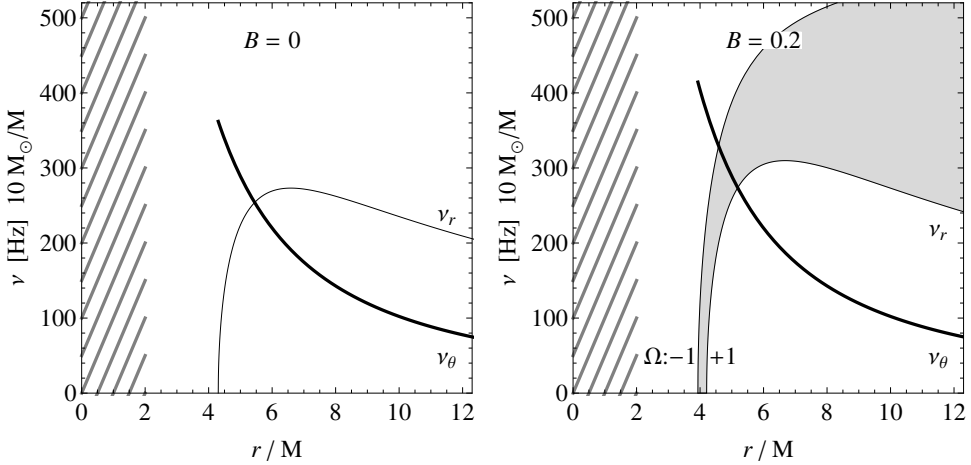


**Figure 1.** String-loop oscillatory frequencies  $\nu_r$  (thin curves) and  $\nu_\theta$  (thick curves), calculated in case of the Schwarzschild black hole with mass  $M = 10M_\odot$  for the absence (left plot) and the presence (right plot) of external magnetic field. We demonstrate extension of the frequency radial profiles for the complete range of the string loop parameter  $\Omega \in (-1, 1)$  for  $B = 0.2$  case (greyed area). The  $B = 0$  case is independent of the string loop parameter  $\Omega$ . Due to the symmetry of the uniform magnetic field, the vertical frequency  $\nu_\theta$  is independent of the parameter  $B$ . The area inside the horizon is dashed.

et al., 2013). The first case corresponds to no inner and outer boundary – the string loop can be captured by the black hole or escape to infinity. The second case corresponds to the situation with an outer boundary – the string loop must be captured by the black hole. The third case corresponds to the situation when both inner and outer boundary exist – the string loop is trapped in some region forming a potential “lake” around the black hole. The fourth case corresponds to an inner boundary – the string loop cannot fall into the black hole but it must escape to infinity. For our following discussion only the third case, corresponding to the possibility of the string loop to be trapped in some region, will be relevant.

## 2.1 Frequency of the radial and vertical harmonic oscillatory modes

The Hamiltonian (4) can be written as a sum of the dynamic and potential parts

$$H = H_D + H_P = \frac{1}{2}g^{rr}P_r^2 + \frac{1}{2}g^{\theta\theta}P_\theta^2 + H_P(r, \theta). \quad (11)$$

The string loop harmonic oscillations around a stable equilibrium position with fixed coordinates  $r_0$  and  $\theta_0 = \pi/2$  have the locally measured angular frequencies of the radial and vertical oscillatory motion given by (Stuchlík and Kološ, 2014)

$$\omega_r^2 = \frac{1}{g_{rr}} \frac{\partial^2 H_P}{\partial r^2}, \quad \omega_\theta^2 = \frac{1}{g_{\theta\theta}} \frac{\partial^2 H_P}{\partial \theta^2}. \quad (12)$$

The partial derivatives of the potential part of the Hamiltonian are calculated at the local minimum of the energy boundary function (effective potential) at  $r_0$  and  $\theta_0 = \pi/2$  which is governed by the angular momentum parameter  $J$  of the string loop.

The locally measured angular frequencies are connected with the angular frequencies measured by a distant observer,  $\Omega_{(r,\theta)}$ , by the gravitational redshift transformation (Stuchlík and Kološ, 2014) has the form

$$\Omega_{(r,\theta)} = \frac{\omega_{(r,\theta)}}{P^t}. \quad (13)$$

If the angular frequencies  $\Omega_{(r,\theta)}$ , or frequencies  $\nu_{(r,\theta)}$ , are expressed in the physical units, their dimensionless form has to be extended by the factor  $c^3/GM$ . Then the frequencies of the string loop oscillations measured by the distant observers are given by

$$\nu_{(r,\theta)} = \frac{1}{2\pi} \frac{c^3}{GM} \Omega_{(r,\theta)}. \quad (14)$$

This is the same factor as the one occurring in the case of the orbital and epicyclic frequencies of the geodesic motion in the Kerr spacetime (Aliev and Galtsov, 1981; Török and Stuchlík, 2005; Stuchlík and Schee, 2012). The order of magnitude and the mass-scaling of the frequencies of the radial and vertical oscillations are the same for both the current-carrying string loops and test particles and one can expect that the string loop oscillations could serve as an explanation of the HF QPOs observed in the strong gravity regions of black holes and neutron stars. The angular frequencies of the string loop oscillations related to a distant observer take the following dimensionless form

$$\begin{aligned} \Omega_{\Gamma}^2(r; \Omega, B) = & \frac{1}{r^4 (B^2 r^4 + 4\sqrt{2} B J_E r^2 \Omega + 8J_E^2 + 8r^2)^2} \\ & \times \left[ 16J_E^2 r^3 (B^2 r (r^2 - 6r + 4)(2\Omega^2 + 1) - 16) + 256r^4 \right. \\ & + 16\sqrt{2} B J_E r^4 \Omega (3B^2 r^4 - 13B^2 r^3 + 4(3B^2 + 1)r^2 - 24r + 16) \\ & + r^4 (15B^4 r^6 - 62B^4 r^5 + 12B^2 (5B^2 + 8)r^4 - 416B^2 r^3 - 384r) \\ & \left. + 64r^6 (6B^2 + 1) - 128\sqrt{2} B J_E^3 r^3 \Omega + 64J_E^4 (3r^2 - 14r + 12) \right], \end{aligned} \quad (15)$$

$$\Omega_{\theta}^2(r) = \frac{1}{r^3}, \quad (16)$$

where the function  $J_E(r; \Omega, B)$  is given by (8). Due to the symmetry of the uniform magnetic field (3), the horizontal frequency  $\Omega_{\theta}^2$  is independent of the effect of magnetic field given by the magnetic intensity parameter  $B$  and hence also independent of the string parameter  $\Omega$ .

In the Schwarzschild spacetime without magnetic field, the harmonic oscillations have frequencies (15–16) relative to distant observers given by expressions relatively very simple for both string loops and test particles. In the case of string loops they read (in dimensional form)

$$\Omega_{\Gamma}^2(r) = \frac{3M^2 - 5Mr + r^2}{r^4}, \quad \Omega_{\theta}^2(r) = \frac{M}{r^3}, \quad (17)$$

while for the epicyclic motion of test particles there is

$$\Omega_{r(\text{geo})}^2(r) = \frac{M(r - 6M)}{r^4}, \quad \Omega_{\theta(\text{geo})}^2(r) = \frac{M}{r^3}. \quad (18)$$

It is quite interesting that the latitudinal frequency of the string loop oscillations in the Schwarzschild or other spherically symmetric spacetimes equals to the latitudinal frequency of the epicyclic geodetical motion as observed by distant observers – for details see (Stuchlík and Kološ, 2012b). Therefore, only gravity is responsible for this frequency in both cases.

Dependencies of the radial and vertical frequencies of the string loop harmonic oscillations on the distance from the black hole are illustrated in Fig. 1 for the characteristic values of the magnetic field intensity  $B = 0, 0.2$ . In the Schwarzschild spacetime without magnetic field both the frequencies are independent on the parameter  $\Omega$ , see Fig. 1 (left). In the Schwarzschild spacetime with magnetic field  $B$ , the range of the radial and vertical frequencies depends on the string-loop parameter  $\Omega$ , and the parameter  $B$  of the magnetic field. Clearly, the range of allowed frequencies increases with increasing the strength of magnetic field  $B$  for the full range of the angular momentum parameter  $\Omega$ , see Fig. 1 (right).

### 3 TWIN HF QPOS IN BLACK HOLE SOURCES

The quasi-periodic character of the motion of string loops trapped in a toroidal space around the equatorial plane of a Schwarzschild black hole suggests interesting astrophysical application related to the HF QPOs observed in binary systems containing a black hole or a neutron star, or in active galactic nuclei. Some of the HF QPOs come in pairs of the upper and lower frequencies ( $\nu_U, \nu_L$ ) of *twin peaks* in the Fourier power spectra. Since the peaks of high frequencies are close to the orbital frequency of the marginally stable circular orbit representing the inner edge of Keplerian discs orbiting black holes (or neutron stars), the strong gravity effects must be relevant in explaining HF QPOs (Török et al., 2005). Usually, the Keplerian orbital and epicyclic (radial and latitudinal) frequencies of geodetical circular motion (Török and Stuchlík, 2005; Kotrllová et al., 2008; Stuchlík and Kotrllová, 2009) are assumed in models explaining the HF QPOs in both black hole and neutron star systems.

Before the twin peak HF QPOs have been discovered in microquasars (first by Strohmayer, 2001), and the 3:2 ratio pointed out, (Kluźniak and Abramowicz, 2001) suggested on theoretical grounds that these QPOs should have rational ratios, because of the resonances in oscillations of nearly Keplerian accretion disks; see also (Aliev and Galtsov, 1981). It seems that the resonance hypothesis is now well supported by observations, and the 3:2 ratio ( $2\nu_U = 3\nu_L$ ) is seen most often in twin peak QPOs in the LMXB containing black holes (microquasars). Here we concentrate on the case of 3:2 frequency ratio oscillations observed in three microquasars, GRO 1655-40, XTE 1550-564 and GRS 1915+105, that were discussed in recent literature (Török et al., 2011).

Unfortunately, neither of the recently discussed models based on geodesic oscillatory motion is able to explain the HF QPOs in all the microquasars (Török et al., 2011). Therefore, it is of some relevance to let the string loop oscillations, characterized by their radial and vertical (latitudinal) frequencies, to enter the play, as these frequencies

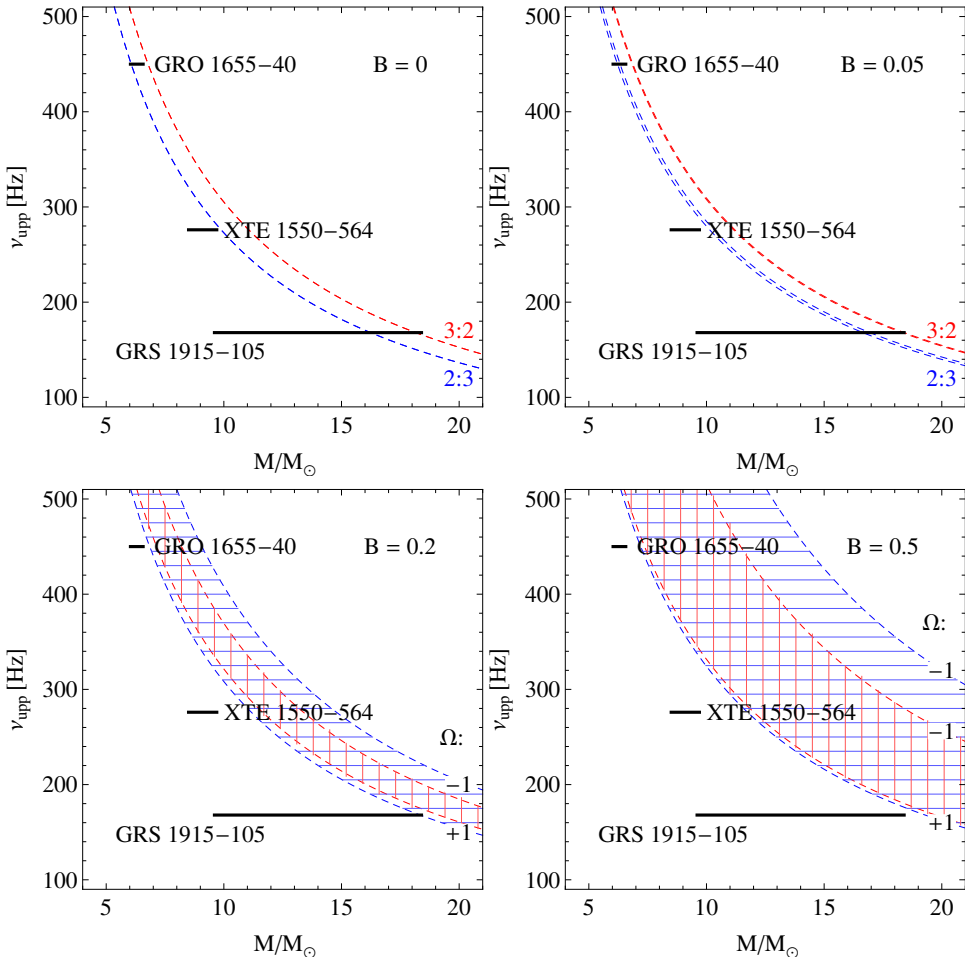


**Figure 2.** The upper string-loop oscillation frequency  $\nu_{\text{U}}$  at the 3:2 or 2:3 resonance radii, calculated in the framework of the string-loop model with maximal range of the string-loop parameter  $\Omega$  as a function of the black hole mass for typical values of magnetic field  $B = 0, 0.05, 0.2, 0.5$ , and compared to the mass-limits obtained from observations of the three microquasars GRO 1655-40, XTE 1550-564, GRG 1915-105 independent of HF QPO observation and depicted by the horizontal thick lines. Hatched areas cover the whole interval of  $\Omega \in (-1, 1)$ . The vertical red hatch corresponds to the 3:2 frequency ratio  $\nu_{\theta}/\nu_{\text{r}}$ , while the horizontal blue hatch corresponds to the 2:3 frequency ratio. The frequency  $\nu_{\text{U}}$  can appear in both 3:2 or 2:3 resonance radii.

are comparable to the epicyclic geodetical frequencies, but slightly different, enabling thus some relevant corrections to the predictions of the models based on the geodetical epicyclic frequencies  $\nu_{\theta}$ ,  $\nu_{\text{r}}$ . We again keep the assumption of the resonance phenomena occurring in the oscillatory motion. The resonant phenomena (parametric or forced) are discussed in standard textbooks (Landau and Lifshitz, 1969; Nayfeh and Mook, 1979), discussion of their relevance to the accretion phenomena can be found, e.g. in (Stuchlík et al., 2013).

We can assume applicability of the parametric resonance, discussed in (Landau and Lifshitz, 1969), focusing attention to the case of the frequency ratios  $\nu_\theta : \nu_r = 3:2$  or  $\nu_\theta : \nu_r = 2:3$ , as the observed values of the twin HF QPO frequencies for GRO 1655-40, XTE 1550-564 and GRS 1915+105 sources show clear ratio

$$\nu_U : \nu_L = 3 : 2 \tag{19}$$

for the upper  $\nu_U$  and lower  $\nu_L$  frequencies. We identify directly the frequencies  $\nu_U, \nu_L$  with  $\nu_\theta, \nu_r$  or  $\nu_r, \nu_\theta$  frequencies. In contrast to the resonance epicyclic model, the string loop oscillation model allows both frequency ratios

$$\nu_\theta : \nu_r = 3 : 2, \quad \nu_\theta : \nu_r = 2 : 3. \tag{20}$$

Since  $r_{3:2} < r_{2:3}$ , we call the first resonance radius, where  $\nu_\theta : \nu_r = 3:2$ , the inner one, and the second resonance radius, where  $\nu_\theta : \nu_r = 2:3$ , the outer one.

For the fixed magnetic field  $B$  and fixed string loop parameter  $\omega$  the upper frequency of the twin HF QPOs can be given as a function of the black hole mass  $M$ . If the black hole mass is restricted by independent observations, as is usually the case, we can obtain some restrictions on the string-loop resonant oscillations model, as illustrated in Fig. 2, where the situation is demonstrated for some values of magnetic field  $B = 0, 0.05, 0.2, 0.5$ . One can see from these plots that the string loop model can well fit the HF QPOs in GRO 1655-40 and GRS 1915-105 sources and gives the limitation on the magnetic field strength. However the observed frequencies for given mass are always lower then the frequencies given by the string loop model. Despite the fact that the parameter  $\Omega$  widens the frequency range of vertical oscillations, increasing of the magnetic field  $B$  implies again increasing frequencies. In other words, for any set of parameters of the model there is no possibility to decrease the frequencies of the string loop oscillations by the parameter of magnetic field  $B$  which leads to opposite result than required. In particular the results show that in order to fit all the sources with one model, it is not enough to consider the spherically symmetric black holes with the uniform magnetic field, i.e. a mechanism of decreasing of string loop frequencies is necessary. The role of such a mechanism can play, e.g. the rotation of the black hole, which has been already tested in our previous papers. Other possibility, is to consider more complex configuration of the magnetic field. Preliminary results with the dipole magnetic field configuration shows that the string loop model can explain the observed HF QPOs and allows us to predict the magnetic field intensities in the vicinity of testing sources. More detailed discussion about the oscillations of the string loop near the black hole embedded in an external dipole magnetic field will be given in a future work.

#### 4 CONCLUSIONS

We have calculated the frequencies of the radial and vertical string-loop oscillations in the field of a Schwarzschild black hole immersed in an uniform magnetic field. Unfortunately, it turns out that the effect of the magnetic field is opposite to our expectations and the frequencies obtained by our model in given configuration cannot explain the observed data for all the microquasars GRS 1915+105, XTE 1550-564, GRO 1655-40, see Fig. 2. Clearly, rotation of the black hole is necessary to explain all the observed frequencies in the microquasars by the string loop oscillations (Stuchlík and Kološ, 2014).

**ACKNOWLEDGEMENTS**

The authors would like to thank the EU grant Synergy CZ.1.07/2.3.00/20.0071, and the internal student grant SGS/23/2013 of the Silesian University. ZS and MK thank the Albert Einstein Centre for gravitation and astrophysics supported by the Czech Science Foundation No. 14-37086G.

**REFERENCES**

- Aliev, A. N. and Galtsov, D. V. (1981), Radiation from relativistic particles in nongeodesic motion in a strong gravitational field, *General Relativity and Gravitation*, **13**, pp. 899–912.
- Barret, D., Olive, J.-F. and Miller, M. C. (2005), An abrupt drop in the coherence of the lower kHz quasi-periodic oscillations in 4U 1636-536, *Monthly Notices of the Royal Astronomical Society*, **361**, pp. 855–860, arXiv: astro-ph/0505402.
- Belloni, T., Méndez, M. and Homan, J. (2007), On the kHz QPO frequency correlations in bright neutron star X-ray binaries, *Monthly Notices of the Royal Astronomical Society*, **376**, pp. 1133–1138, arXiv: astro-ph/0702157.
- Blandford, R. D. and Znajek, R. L. (1977), Electromagnetic extraction of energy from Kerr black holes, *Monthly Notices of the Royal Astronomical Society*, **179**, pp. 433–456.
- Christensson, M. and Hindmarsh, M. (1999), Magnetic fields in the early universe in the string approach to MHD, *Phys. Rev. D*, **60**(6), 063001, arXiv: astro-ph/9904358.
- Cremaschini, C. and Stuchlík, Z. (2013), Magnetic loop generation by collisionless gravitationally bound plasmas in axisymmetric tori, *Phys. Rev. E*, **87**(4), 043113.
- Cremaschini, C. and Stuchlík, Z. (2014), Transition from gas to plasma kinetic equilibria in gravitating axisymmetric structures, *Physics of Plasmas*, **21**(4), 042902.
- Cremaschini, C., Stuchlík, Z. and Tessarotto, M. (2013), Kinetic theory of quasi-stationary collisionless axisymmetric plasmas in the presence of strong rotation phenomena, *Physics of Plasmas*, **20**(5), p. 052905.
- Frolov, A. V. and Larsen, A. L. (1999), Chaotic scattering and capture of strings by a black hole, *Classical and Quantum Gravity*, **16**, pp. 3717–3724, arXiv: gr-qc/9908039.
- Jacobson, T. and Sotiriou, T. P. (2009), String dynamics and ejection along the axis of a spinning black hole, *Phys. Rev. D*, **79**(6), 065029, arXiv: 0812.3996.
- Kluzniak, W. and Abramowicz, M. A. (2001), The physics of kHz QPOs—strong gravity’s coupled anharmonic oscillators, *ArXiv Astrophysics e-prints*, arXiv: astro-ph/0105057.
- Kološ, M. and Stuchlík, Z. (2010), Current-carrying string loops in black-hole spacetimes with a repulsive cosmological constant, *Phys. Rev. D*, **82**(12), 125012, arXiv: 1103.4005.
- Kološ, M. and Stuchlík, Z. (2013), Dynamics of current-carrying string loops in the Kerr naked-singularity and black-hole spacetimes, *Phys. Rev. D*, **88**(6), 065004, arXiv: 1309.7357.
- Kotrlová, A., Stuchlík, Z. and Török, G. (2008), Quasiperiodic oscillations in a strong gravitational field around neutron stars testing braneworld models, *Classical and Quantum Gravity*, **25**(22), 225016, arXiv: 0812.0720.
- Kovář, J. (2013), Spiral motion formation in astrophysics, *European Physical Journal Plus*, **128**, p. 142.
- Kovář, J., Slaný, P., Cremaschini, C., Stuchlík, Z., Karas, V. and Trova, A. (2014), Electrically charged matter in rigid rotation around magnetized black hole, *Phys. Rev. D*, **90**(4), 044029, arXiv: 1409.0418.
- Landau, L. D. and Lifshitz, E. M. (1969), *Mechanics*, Oxford: Pergamon Press.

- Larsen, A. L. (1994), Chaotic string-capture by black hole, *Classical and Quantum Gravity*, **11**, pp. 1201–1210, arXiv: hep-th/9309086.
- McClintock, J. E. and Remillard, R. A. (2006), Black hole binaries, in W. H. G. Lewin and M. van der Klis, editors, *Compact stellar X-ray sources*, pp. 157–213, Cambridge University Press.
- Nayfeh, A. H. and Mook, D. T. (1979), Nonlinear oscillations, in *Nonlinear oscillations*, by Nayfeh, Ali Hasan; Mook, Dean T. New York : Wiley, c1979., Wiley, New York.
- Remillard, R. A. (2005), X-ray spectral states and high-frequency QPOs in black hole binaries, *Astronomische Nachrichten*, **326**, pp. 804–807, arXiv: astro-ph/0510699.
- Remillard, R. A. and McClintock, J. E. (2006), Active X-ray States of Black Hole Binaries: Current Overview, in *American Astronomical Society Meeting Abstracts*, volume 38 of *Bulletin of the American Astronomical Society*, p. 903.
- Semenov, V., Dyadechkin, S. and Punsly, B. (2004), Simulations of Jets Driven by Black Hole Rotation, *Science*, **305**, pp. 978–980, arXiv: astro-ph/0408371.
- Semenov, V. S. and Bernikov, L. V. (1991), Magnetic flux tubes - Nonlinear strings in relativistic magnetohydrodynamics, *Astrophysics and Space Science*, **184**, pp. 157–166.
- Spruit, H. C. (1981), Equations for thin flux tubes in ideal MHD, *Astronomy and Astrophysics*, **102**, pp. 129–133.
- Strohmayer, T. E. (2001), Discovery of a 450 Hz QPO from the Microquasar GRO J1655-40 with RXTE, *ArXiv Astrophysics e-prints*, arXiv: astro-ph/0104487.
- Stuchlík, Z. and Kološ, M. (2012a), Acceleration of string loops in the Schwarzschild-de Sitter geometry, *Phys. Rev. D*, **85**(6), 065022, arXiv: 1206.5658.
- Stuchlík, Z. and Kološ, M. (2012b), String loops in the field of braneworld spherically symmetric black holes and naked singularities, *Journal of Cosmology and Astroparticle Physics*, **10**, 008, arXiv: 1309.6879.
- Stuchlík, Z. and Kološ, M. (2014), String loops oscillating in the field of Kerr black holes as a possible explanation of twin high-frequency quasiperiodic oscillations observed in microquasars, *Phys. Rev. D*, **89**(6), 065007, arXiv: 1403.2748.
- Stuchlík, Z. and Kotrlová, A. (2009), Orbital resonances in discs around braneworld Kerr black holes, *General Relativity and Gravitation*, **41**, pp. 1305–1343, arXiv: 0812.5066.
- Stuchlík, Z., Kotrlová, A. and Török, G. (2013), Multi-resonance orbital model of high-frequency quasi-periodic oscillations: possible high-precision determination of black hole and neutron star spin, *Astronomy and Astrophysics*, **552**, A10, arXiv: 1305.3552.
- Stuchlík, Z. and Schee, J. (2012), Observational phenomena related to primordial Kerr superspinars, *Classical and Quantum Gravity*, **29**(6), 065002.
- Török, G., Abramowicz, M. A., Kluźniak, W. and Stuchlík, Z. (2005), The orbital resonance model for twin peak kHz quasi periodic oscillations in microquasars, *Astronomy and Astrophysics*, **436**, pp. 1–8.
- Török, G., Kotrlová, A., Šrámková, E. and Stuchlík, Z. (2011), Confronting the models of 3:2 quasiperiodic oscillations with the rapid spin of the microquasar GRS 1915+105, *Astronomy and Astrophysics*, **531**, A59, arXiv: 1103.2438.
- Török, G. and Stuchlík, Z. (2005), Radial and vertical epicyclic frequencies of Keplerian motion in the field of Kerr naked singularities. Comparison with the black hole case and possible instability of naked-singularity accretion discs, *Astronomy and Astrophysics*, **437**, pp. 775–788, arXiv: astro-ph/0502127.
- Tursunov, A., Kološ, M., Ahmedov, B. and Stuchlík, Z. (2013), Dynamics of an electric current-carrying string loop near a Schwarzschild black hole embedded in an external magnetic field, *Phys. Rev. D*, **87**(12), 125003.

- Tursunov, A., Kološ, M., Stuchlík, Z. and Ahmedov, B. (2014), Acceleration of electric current-carrying string loop near a Schwarzschild black hole immersed in an asymptotically uniform magnetic field, *Phys. Rev. D*, **90**(8), 085009, arXiv: 1409.4536.
- van der Klis, M. (2000), Millisecond Oscillations in X-ray Binaries, *Annual Review of Astronomy and Astrophysics*, **38**, pp. 717–760, arXiv: astro-ph/0001167.
- Wald, R. M. (1974), Black hole in a uniform magnetic field, *Phys. Rev. D*, **10**, pp. 1680–1685.

# Centaurus A as a source of ultra high energy cosmic rays

Volodymyr Marchenko,<sup>1,a</sup> Oleh Kobzar,<sup>2</sup> Oleksandr Sushchov<sup>2</sup>  
and Bohdan Hnatyk<sup>3</sup>

<sup>1</sup>Astronomical Observatory, Jagiellonian University, 171 Orła Str., 30-244 Krakow, Poland

<sup>2</sup>T. G. Shevchenko Chernihiv National Pedagogical University,  
53 Hetman Polubotok Str., 14013 Chernihiv, Ukraine

<sup>3</sup>Astronomical Observatory, Taras Shevchenko Kyiv National University, 3 Observatorna Str.,  
04053 Kyiv, Ukraine

<sup>a</sup>marchenko@oa.uj.edu.pl

## ABSTRACT

The propagation of ultra high energy cosmic rays in Galactic and extragalactic magnetic fields is investigated in the present paper. The motion of charged particles of different energies and chemical composition is simulated using different Galactic magnetic field models. Positions for the real sources of events registered at the Auger Observatory are calculated taking into account the influence of both Galactic and extragalactic turbulent fields. The possibility of their correlation with the Centaurus A radio galaxy is analysed.

**Keywords:** Ultra-high energy cosmic rays – cosmic magnetic fields – propagation of UHECRs

## 1 INTRODUCTION

Cosmic rays (CR) are known as fluxes of high-energy subatomic particles, photons or neutrino generating extended atmospheric showers of secondary particles that interact with molecules of nitrogen and oxygen which are prevalent in the Earth atmosphere's upper strata. CR possessing the energy  $E > 10^{19}$  eV arrive at the Earth with the interval of less than one event per year over  $1 \text{ km}^2$  in  $\pi$  steradian (i.e. with the energy flux of  $30 \text{ eV/cm}^2/\text{sec}$ ) (Greisen, 1966).

Ultra high energy cosmic rays (UHECR) are believed to be of extra-galactic origin due to the absence of sources powerful enough to provide their sufficient acceleration within our Galaxy as well as due to almost isotropic large-scale distribution of CR along the lines of their entering the atmosphere (The Pierre Auger Collaboration: J. Abraham et al., 2009). The hypothesis concerning UHECR's astrophysical nature is also supported by registering the Greisen–Zatsepin–Kuzmin (GZK) effect (Greisen, 1966) in the HiRes experiment (Abbasi et al., 2008), as well as in observations carried out at the Auger observatory (Abraham et al., 2008).

The correlation between CR and galaxies from the active galactic nuclei (AGN) Veron-Cetti-Veron (VCV) catalogue (Véron-Cetty and Véron, 2010) can be accepted as a possible explanation of UHECR's nature, provided their origin is extragalactic while their horizon is energy dependent which agrees with the data on GZK-cutoff.

According to the analysis of the refreshed data from the Auger observatory (Abreu et al., 2010), the registered UHECR's correlation with the galaxies from the VCV catalogue has diminished from level  $3\sigma$  to  $2\sigma$  compared to the previous version of data update. As the result only 30 % of UHECR potentially correlate with the directions towards AGN whereas the rest manifest the signs of isotropic distribution. The only exception is the neighbourhood of the closest to the Earth active galaxy Centaurus A where the registered set of ultra energy events appeared to be a lot more volumetric than it could be statistically correct to expect.

In this paper we verify the possibility of the observed in the area of Centaurus A events being UHECR accelerated in this galaxy. Therefore we solve the reversed task by modelling CR's trajectory on the basis of present data from Auger observatory. The model takes into account the influence of Galactic and extragalactic magnetic fields as well as the CR chemical composition.

## 2 MODELING

Magnetic field distorts the CR's charged particles trajectory via Lorentz force. If the field is static it does not affect the particle's energy. Considering the fact that typical values of CR energy far exceed the particles' rest energy we assume that they spread with velocity close to the speed of light. In this case the equations describing the motion of ultra-relativistic particles in the magnetic field  $B(r)$  are:

$$\frac{dv}{dt} = \frac{qc^2}{E}[v \times B], \quad \frac{dr}{dt} = v, \quad (1)$$

where  $q$  is particle's charge,  $E$  – its energy, provided the Lorentz factor  $\gamma \gg 1$  and velocity  $v$ .

## 3 MAGNETIC FIELDS

Modelling the motion of UHECR we considered influence of Galactic as well as extragalactic magnetic fields. Galactic magnetic field consists of regular and random components. The regular component's structure is believed to generally follow the matter's distribution in the Galaxy (Han, 2009). Nowadays the source and structure of extragalactic magnetic field are not exactly clear. Thus while solving specific tasks it is defined as having random structure (Beck, 2001).

### 3.1 Galactic magnetic field

*Regular component.* There are several models describing regular Galactic magnetic field (Sutherland et al., 2010). They differ in both parameters' numeric values and presence and structure of the field's components. The regular component of Galactic magnetic field is rather conveniently described via the spiral structure of  $2\pi$ -symmetry (axisymmetric spiral

(ASS)) or  $\pi$ -symmetry (bisymmetric spiral (BSS)) (Stanev, 1997). In our research we have applied the most recent models (Prouza and Šmída, 2003), (Kachelrieß et al., 2007) and (Pshirkov et al., 2011). They present the magnetic field as a superposition of the disc component and the field of Galactic halo. In (Prouza and Šmída, 2003) and (Kachelrieß et al., 2007) BSS symmetry is used for describing the disc field whereas in (Pshirkov et al., 2011) both ASS and BSS disc field's symmetry types are considered (henceforth we treat them off as different models).

The disc field comprises radial and azimuth components which are set in cylindrical coordinates in the disc's area by expressions

$$B_r = B(r, \theta) \sin(p), \quad B_\theta = B(r, \theta) \cos(p), \quad (2)$$

where pitch angle  $p$  is the angle between the magnetic vector at a certain point and the normal to radius-vector  $\mathbf{r}$  in this point.

The function  $B(r, \theta)$  is set by the equation of logarithm spiral:

$$B(r, \theta) = B(r) \cos \left[ \theta - \frac{1}{\tan p} \ln \left( \frac{r}{\xi_0} \right) \right], \quad (3)$$

or

$$B(r, \theta) = B(r) \cos \left[ \theta - \frac{1}{\tan p} \ln \left( \frac{r}{R_8} \right) + \varphi \right]. \quad (4)$$

Parameters in formulae (3) and (4) are set by expressions

$$\varphi = \frac{1}{\tan p} \ln \left( 1 + \frac{d}{R_8} \right) - \frac{\pi}{2}, \quad \xi_0 = (R_8 + d) \exp \left( -\frac{\pi}{2} \tan p \right), \quad (5)$$

where  $R_8 = 8.5$  kpc is the distance from the Galactic center to the Solar system,  $d$  is the distance from the Solar system to the closest field's inversion point.

The function of the radial profile  $B(r)$  is set by

$$B(r) = \begin{cases} B_8 \frac{R_8}{r \cos \varphi} = B_0 \frac{R_8}{r} & r > R_C, \\ B_8 \frac{R_8}{R_C \cos \varphi} = B_0 \frac{R_8}{R_C} & r < R_C, \end{cases} \quad (6)$$

where  $R_8$  is local field near the Solar system.

The vertical profile of the disc field above the Galactic plane and under it is considered exponentially decreasing:

$$B(r, \theta, z) = B(r, \theta) \exp \left( -\frac{|z|}{z_0} \right). \quad (7)$$

In models (Prouza and Šmída, 2003) and (Kachelrieß et al., 2007) the field of Galactic halo comprises poloidal and toroidal components while model (Pshirkov et al., 2011) contains the toroidal component only. For the description of the toroidal field we use the model of

discs located above and under the Galactic plane. The toroidal field's parameters are set by expressions

$$B_x = -B_T \operatorname{sign}(z) \left[ 1 + \left( \frac{|z| - h}{w} \right)^2 \right]^{-1} \cos \theta, \quad (8)$$

$$B_y = B_T \operatorname{sign}(z) \left[ 1 + \left( \frac{|z| - h}{w} \right)^2 \right]^{-1} \sin \theta, \quad (9)$$

where  $h$  is the height of discs above and under the Galactic plane,  $w$  is half-width of Lorenz distribution.

The function  $B_T$  in model (Prouza and Šmída, 2003) is given by the following expression

$$B_T = B_{T\max} \left[ \Theta(R_T - r) + \Theta(r - R_T) \exp\left(-\frac{r}{R_T}\right) \right], \quad (10)$$

while in model (Kachelrieß et al., 2007)

$$B_T = B_{T\max} \left[ \Theta(R_T - r) + \Theta(r - R_T) \exp\left(-\frac{R_T - r}{R_T}\right) \right], \quad (11)$$

where  $\Theta$  is Heaviside function,  $R_T$  is toroid's characteristic radius.

In model (Pshirkov et al., 2011)

$$B_T = B_{T\max} \frac{r}{R_T} \exp\left(\frac{R_T - r}{R_T}\right). \quad (12)$$

The field's dipole component is described by standard equations:

$$B_x = -3\mu_G \cos \phi \sin \phi \sin \theta / \rho^3, \quad (13)$$

$$B_y = -3\mu_G \cos \phi \sin \phi \cos \theta / \rho^3, \quad (14)$$

$$B_z = \mu_G (1 - \cos^2 \phi) / \rho^3, \quad (15)$$

where  $\rho = \sqrt{r^2 + z^2}$ ,  $\cos \phi = z/\rho$ ,  $\sin \phi = r/\rho$ ,  $\mu_G$  is the magnetic dipole momentum.

*Random component.* It is assumed (Pierre Auger Collaboration et al., 2012) that Galactic magnetic field's random component's impact primarily results into widening the range of UHECR's possible arrival directions relative to the direction defined by the deflection of the trajectory in the regular field. In this case the real location of CR's source is not explicated. Furthermore, under certain conditions the so called "lensing effect" in the magnetic field may occur and generate several images of CR's source (Giacinti et al., 2011a). Yet studying this kind of impact may be fruitful for exploring the properties of Galactic magnetic field and CR's propagation.

CR's ultra high energy is marked by the value of Larmor radius that by far exceeds the length of field's coherence  $l_0$ , the latter understood as the distance at which the field's random re-orientation occurs. Thus to estimate the effect caused by the random magnetic

field it is sufficient to consider two parameters:  $l_0$  and field's magnitude  $B_{\text{rms}}$  (Giacinti et al., 2010). The field  $B_{\text{rms}}$  is characterized by exponentially decreasing vertical profile  $R_{\text{rms}} = B_0 \exp(-|z|/z_0)$  (Giacinti et al., 2011b).

According to the observation data Galactic magnetic field's random component is commensurable to the regular one (Prouza and Šmída, 2003). In this paper we employ the values  $l_0 = 50$  pc,  $B_0 = 4 \mu\text{G}$ ,  $z_0 = 3$  kpc (Giacinti et al., 2011a).

CR deflection  $\vartheta$  in the random magnetic field on the covered distance  $L$  is set by the following expression (Berezinsky et al., 2004)

$$\langle \vartheta^2 \rangle = \frac{2}{9} \left( \frac{Ze}{E} c \right)^2 \langle B^2 \rangle L l_0, \quad (16)$$

where  $Ze$  is particle's charge,  $E$  is its energy.

The distance covered by UHECR (those registered by the Earth-located detectors) in the Galactic turbulent field can be estimated as

$$L_{\text{gal}} = \min \left( \frac{z_0}{\sin b_G}; L_{\text{max}} = 20 \text{ kpc} \right), \quad (17)$$

where  $b_G$  is Galactic latitude of CR's arrival direction. Thus we acquire the value of CR's final deflection

$$\vartheta = 22^\circ Z \left( \frac{L_{\text{gal}}}{1 \text{ kpc}} \right)^{1/2} \left( \frac{E}{10^{18} \text{ eV}} \right)^{-1}. \quad (18)$$

### 3.2 Extragalactic magnetic field

There are structures in the Universe comprising clusters of galaxies, filaments, layers of increased density and voids with low density. It is assumed that in entities of this kind magnetic field is boosted due to the formation of large scale structures. Diverse numeric modelling of the said process demonstrates correspondence extragalactic magnetic field's distribution with that of matter (Sigl et al., 2004). Astrophysical objects, UHECR's sources in particular, are normally located within the structured areas. Thus these magnetic structures as well as the Galactic magnetic field necessarily impact the propagation of CR. The structured extragalactic magnetic field influences both CR's deflection and the time of their reaching the observer.

According to the recent research of the gamma-ray range, extragalactic magnetic field possesses the value of approximately  $10^{-15}$  G in the voids (Ando and Kusenko, 2010). Although this estimation is rather contradictory; the prior estimation of magnetic field's lower limit being  $10^{-17}$ – $10^{-15}$  G (Taylor et al., 2011). In the suggested calculations we employ the simplest model in which space is divided into cubic cells of size  $l_c$ . The field is considered uniform within one cell while its direction varies randomly in between the cells. To limit the size of field  $B$  we used the value resulting from observation data concerning distant objects polarization plane's Faraday's rotation (Kronberg, 1994)  $\langle B \rangle \sqrt{l_0} \leq 10^{-9}$  G Mpc<sup>1/2</sup>, where  $l_0$  is magnetic field's coherence length. Generally  $l_0$  does not equal  $l_c$  strictly, though this difference is not significant for estimating UHECR's propagation in extragalactic magnetic field. For random extragalactic magnetic field like in the case of Galactic magnetic field's random component, CR's deflection is calculated through formula (16).

**Table 1.** “CR – Cen A” correlation. Magnetic field components: RG – regular Galactic, RRG – regular + random Galactic, RRGE – regular + random Galactic + extragalactic.

Energy, EeV	CR’s chemical composition for different models					
	(Prouza and Šmída, 2003)			(Kachelrieß et al., 2007)		
	RG	RRG	RRGE	RG	RRG	RRGE
142	Mg	Mg-Ar	Ne-Ca	–	Ca-Fe	S-Fe
79	He	He-Li	p-Be	He-Li	He-C	He-N
77	N-O	C-Ne	B-Ne	–	Mg-Ar	Ne-Ar
68	p	p	p-He	p	p-He	p-He
66	–	p	p	p	p	p
61	–	–	–	Ne-Mg	O-S	N-S
Energy, EeV	CR’s chemical composition for different models					
	(Pshirkov et al., 2011) – ASS			(Pshirkov et al., 2011) – BSS		
	RG	RRG	RRGE	RG	RRG	RRGE
68	p	p	p	–	–	p
66	p	p	p	–	–	p

Considering the limitations over the value of extragalactic magnetic field we acquire numeric values of deflection for CR with energy  $E$  and charge  $Z$ , located at the distance  $L_0$  from random sources:

$$\vartheta = 25^\circ Z \left( \frac{L_0}{1 \text{ Mpc}} \right)^{1/2} \left( \frac{E}{10^{18} \text{ eV}} \right)^{-1}. \quad (19)$$

#### 4 CENTAURUS A

The Auger observatory registered a set of UHECR in the region of Centaurus A galaxy which is the closest to the Solar system active one. The origin of the registered CR is most likely affiliated with the said galaxy (Abreu et al., 2010). We have modelled the CR’s motion in the magnetic field using the above-described methodology.

Figure 1 demonstrates the results of calculations carried out on the basis of various models of the regular Galactic magnetic field. Circles with figures denote the set of events registered by the Auger facility. Circles with the chemical elements symbols correspond to the calculated locations of UHECR’s sources for the indicated particle types. Radii of all circles reflect the Auger detectors’ experiment error within the confidence interval of  $1 \sigma$ . Results depicted in Fig. 1a were obtained via the use of model (Prouza and Šmída, 2003); those in Fig. 1b were achieved as the result of using model (Kachelrieß et al., 2007). The figures also demonstrate the outline of Centaurus A radiation areas. These areas are known to have conditions for accelerating CR up to ultra high energies (Rieger and Aharonian, 2009). Overlapping of the circles corresponding to the calculated sources’ location and the image of Centaurus A was chosen as the criterion for defining the correlation of the analysed events and the said galaxy.

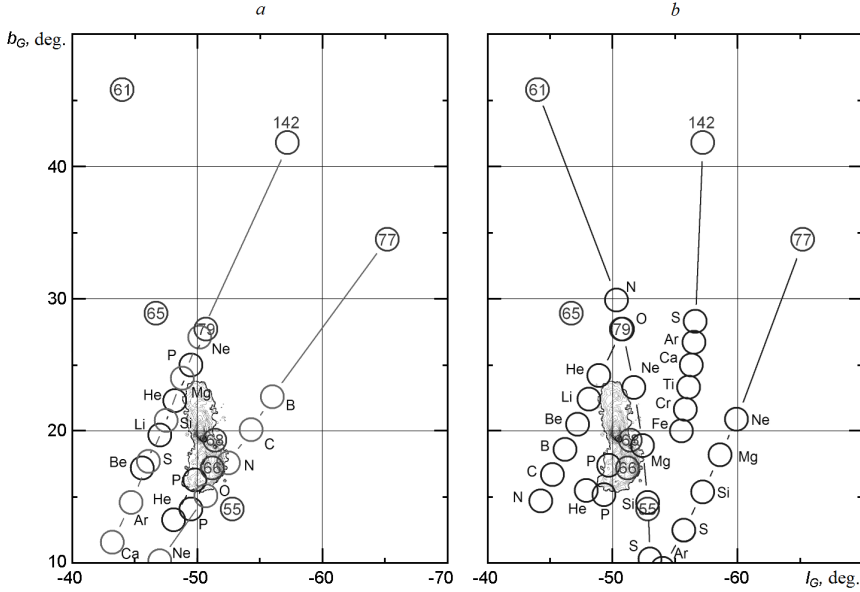


**Figure 1.** Source positions for different models of regular Galactic magnetic field: a – (Prouza and Šmída, 2003), b – (Kronberg, 1994).

Considering the Galactic field's random component as well as the extragalactic field, Eqs. (18) and (19) can lead to widening the area of the source's possible localization from few degrees (for light elements) up to  $10^{\circ}$ – $15^{\circ}$  (for heavy elements), but without actually changing its location.

We have found out that out of all CR coming from Centaurus A area only six can in fact originate in this galaxy – those with the energy of 61, 66, 68, 77, 79 and 142 EeV. Table 1 demonstrates chemical composition of the particles with the indicated energy. These particles correlate with Centaurus A following the two chosen models of the Galactic field and considering the impact of the magnetic field's various components.

## 5 CONCLUSIONS

Centaurus A may be the source of the events in its nearby region registered by the Auger observatory. Models (Prouza and Šmída, 2003) and (Kachelrieß et al., 2007) provide similar results. According to the calculations carried out on the basis of model (Prouza and Šmída, 2003) five events correlate with Centaurus A. When model (Kachelrieß et al., 2007) is employed six such events correlate with Centaurus A. The common tendency of shifting CR's chemical composition towards heavier nuclei at the boost of energy of the corresponding event is noted in all cases of possible correlation with the object under investigation. It is relevant for both models.

## REFERENCES

- Abbasi, R. U., Abu-Zayyad, T., Allen, M., Amman, J. F., Archbold, G., Belov, K., Belz, J. W., Ben Zvi, S. Y., Bergman, D. R., Blake, S. A., Brusova, O. A., Burt, G. W., Cannon, C., Cao, Z., Connolly, B. C., Deng, W., Fedorova, Y., Finley, C. B., Gray, R. C., Hanlon, W. F., Hoffman, C. M., Holzschneider, M. H., Hughes, G., Hütemeyer, P., Jones, B. F., Jui, C. C. H., Kim, K., Kirm, M. A., Loh, E. C., Maestas, M. M., Manago, N., Marek, L. J., Martens, K., Matthews, J. A. J., Matthews, J. N., Moore, S. A., O'Neill, A., Painter, C. A., Perera, L., Reil, K., Riehle, R., Roberts, M., Rodriguez, D., Sasaki, N., Schnetzer, S. R., Scott, L. M., Sinnis, G., Smith, J. D., Sokolsky, P., Song, C., Springer, R. W., Stokes, B. T., Thomas, S. B., Thomas, J. R., Thomson, G. B., Tupa, D., Westerhoff, S., Wiencke, L. R., Zhang, X. and Zech, A. (2008), First Observation of the Greisen-Zatsepin-Kuzmin Suppression, *Phys. Rev. Lett.*, **100**(10), 101101, arXiv: astro-ph/0703099.
- Abraham, J., Abreu, P., Aglietta, M., Aguirre, C., Allard, D., Allekotte, I., Allen, J., Allison, P., Alvarez-Muñiz, J., Ambrosio, M. and et al. (2008), Observation of the Suppression of the Flux of Cosmic Rays above  $4 \times 10^{19}$  eV, *Phys. Rev. Lett.*, **101**(6), 061101, arXiv: 0806.4302.
- Abreu, P., Aglietta, M., Ahn, E. J., Allard, D., Allekotte, I., Allen, J., Alvarez Castillo, J., Alvarez-Muñiz, J., Ambrosio, M., Aminaei, A. and et al. (2010), Update on the correlation of the highest energy cosmic rays with nearby extragalactic matter, *Astroparticle Physics*, **34**, pp. 314–326, arXiv: 1009.1855.
- Ando, S. and Kusenko, A. (2010), Evidence for Gamma-ray Halos Around Active Galactic Nuclei and the First Measurement of Intergalactic Magnetic Fields, *Astrophys. J. Lett.*, **722**, pp. L39–L44, arXiv: 1005.1924.
- Beck, R. (2001), Galactic and Extragalactic Magnetic Fields, *Space Science Reviews*, **99**, pp. 243–260, arXiv: astro-ph/0012402.
- Berezinsky, V. S., Grigorieva, S. I. and Hnatyk, B. I. (2004), Extragalactic UHE proton spectrum and prediction for iron-nuclei flux at  $10^8$ - $10^9$  GeV, *Astroparticle Physics*, **21**, pp. 617–625, arXiv: astro-ph/0403477.
- Giacinti, G., Derks, X. and Semikoz, D. V. (2010), Search for single sources of ultra high energy cosmic rays on the sky, *Journal of Cosmology and Astroparticle Physics*, **3**, 022, arXiv: 0907.1035.
- Giacinti, G., Kachelrieß, M., Semikoz, D. V. and Sigl, G. (2011a), Propagation of Ultrahigh Energy Nuclei in the Magnetic Field of our Galaxy, *International Cosmic Ray Conference*, **2**, p. 43.
- Giacinti, G., Kachelrieß, M., Semikoz, D. V. and Sigl, G. (2011b), Ultrahigh energy nuclei in the turbulent Galactic magnetic field, *Astroparticle Physics*, **35**, pp. 192–200, arXiv: 1104.1141.
- Greisen, K. (1966), End to the Cosmic-Ray Spectrum?, *Phys. Rev. Lett.*, **16**, pp. 748–750.
- Han, J. (2009), The magnetic structure of our Galaxy: a review of observations, in K. G. Strassmeier, A. G. Kosovichev and J. E. Beckman, editors, *IAU Symposium*, volume 259 of *IAU Symposium*, pp. 455–466, arXiv: 0901.1165.
- Kachelrieß, M., Serpico, P. D. and Teshima, M. (2007), The Galactic magnetic field as spectrograph for ultra-high energy cosmic rays, *Astroparticle Physics*, **26**, pp. 378–386, arXiv: astro-ph/0510444.
- Kronberg, P. P. (1994), Extragalactic magnetic fields, *Reports on Progress in Physics*, **57**, pp. 325–382.
- Pierre Auger Collaboration, Abreu, P., Aglietta, M., Ahn, E. J., Albuquerque, I. F. M., Allard, D., Allekotte, I., Allen, J., Allison, P., Alvarez Castillo, J. and et al. (2012), Search for signatures of magnetically-induced alignment in the arrival directions measured by the Pierre Auger Observatory, *Astroparticle Physics*, **35**, pp. 354–361, arXiv: 1111.2472.
- Prouza, M. and Šmída, R. (2003), The Galactic magnetic field and propagation of ultra-high energy cosmic rays, *Astronomy and Astrophysics*, **410**, pp. 1–10, arXiv: astro-ph/0307165.

- Pshirkov, M. S., Tinyakov, P. G., Kronberg, P. P. and Newton-McGee, K. J. (2011), Deriving the Global Structure of the Galactic Magnetic Field from Faraday Rotation Measures of Extragalactic Sources, *Astrophys. J.*, **738**, 192, arXiv: 1103.0814.
- Rieger, F. M. and Aharonian, F. A. (2009), Centaurus A as TeV  $\gamma$ -ray and possible UHE cosmic-ray source, *Astronomy and Astrophysics*, **506**, pp. L41–L44, arXiv: 0910.2327.
- Sigl, G., Miniati, F. and EnBlin, T. A. (2004), Ultrahigh energy cosmic ray probes of large scale structure and magnetic fields, *Phys. Rev. D*, **70**(4), 043007, arXiv: astro-ph/0401084.
- Stanev, T. (1997), Ultra-high-energy Cosmic Rays and the Large-scale Structure of the Galactic Magnetic Field, *Astrophys. J.*, **479**, pp. 290–295, arXiv: astro-ph/9607086.
- Sutherland, M. S., Baughman, B. M. and Beatty, J. J. (2010), CRT: A numerical tool for propagating ultra-high energy cosmic rays through Galactic magnetic field models, *Astroparticle Physics*, **34**, pp. 198–204, arXiv: 1010.3172.
- Taylor, A. M., Vovk, I. and Neronov, A. (2011), Extragalactic magnetic fields constraints from simultaneous GeV-TeV observations of blazars, *Astronomy and Astrophysics*, **529**, A144, arXiv: 1101.0932.
- The Pierre Auger Collaboration: J. Abraham, Abreu, P., Aglietta, M., Aguirre, C., Ahn, E. J., Allard, D., Allekotte, I., Allen, J., Alvarez-Muñiz, J., Ambrosio, M. and et al. (2009), Astrophysical Sources of Cosmic Rays and Related Measurements with the Pierre Auger Observatory, *ArXiv e-prints*, arXiv: 0906.2347.
- Véron-Cetty, M.-P. and Véron, P. (2010), A catalogue of quasars and active nuclei: 13th edition, *Astronomy and Astrophysics*, **518**, A10.



# Causal horizons and some topics concerning structure formation

John Miller<sup>1,2,a</sup> and Ilia Musco<sup>3,4</sup>

<sup>1</sup>SISSA, International School for Advanced Studies, Via Bonomea 265, I-34136 Trieste, Italy

<sup>2</sup>Department of Physics (Astrophysics), University of Oxford, Keble Road, Oxford OX1 3RH, UK

<sup>3</sup>Centre of Mathematics for Applications, Department of Mathematics, University of Oslo,  
PO Box 1053 Blindern, NO-0316 Oslo, Norway

<sup>4</sup>Laboratoire Univers et Théories, UMR 8102 CNRS, Observatoire de Paris,  
Université Paris Diderot, 5 Place Jules Janssen, F-92190 Meudon, France

<sup>a</sup>[jcm@astro.ox.ac.uk](mailto:jcm@astro.ox.ac.uk)

## ABSTRACT

This is a write-up of a talk given at the Opava RAGtime meeting in 2011, but it has been updated to include some subsequent related developments. The talk focused on discussion of some aspects of black hole and cosmological horizons under rather general circumstances, and on two different topics related to formation of cosmological structures at different epochs of the universe: virialization of cold dark matter during standard structure formation in the matter-dominated era, and primordial black hole formation during the radiative era.

**Keywords:** black hole physics – early universe – large-scale structure of the universe

## 1 INTRODUCTION

This presentation focuses firstly on two different types of causal horizon: those for black holes (where no causal signal can get *out* from inside), and that for the universe (where no causal signal can get *in* from outside). Also, we discuss some topics connected with formation of structure in the universe in the matter-dominated and radiative eras. We follow the convention of using units for which  $c = G = 1$  except in Section 3.1, where the treatment is entirely Newtonian and it is convenient to retain  $G$ .

In all of these discussions, we will make the (major) simplification of considering just spherical symmetry but, apart from that, we will remain rather general. We start from the Friedman–Robertson–Walker metric for describing a homogeneous and isotropic background universe and we use the spatially-flat form of it, in line with current observations:

$$ds^2 = -dt^2 + S^2(t) \left[ dr^2 + r^2(d\theta^2 + \sin^2\theta d\varphi^2) \right], \quad (1)$$

where  $r$  is a co-moving radial coordinate and  $S(t)$  is the scale factor. This can be written in the alternative form

$$ds^2 = -dt^2 + S^2(t) dr^2 + R^2 (d\theta^2 + \sin^2 \theta d\phi^2), \quad (2)$$

where  $R = S(t)r$  is a circumference coordinate (invariantly defined as being the proper circumference of a circle, centred on the origin, divided by  $2\pi$ ). This is the same quantity as used for the radial coordinate in the standard form of the Schwarzschild metric.

The above description is for a uniform medium; when we have a (spherically symmetric) deviation away from this, the metric can then be written in the generalised form

$$ds^2 = -a^2 dt^2 + b^2 dr^2 + R^2 (d\theta^2 + \sin^2 \theta d\phi^2), \quad (3)$$

with  $a$ ,  $b$  and  $R$  all being functions of  $r$  and  $t$ . Using a diagonal form of the metric like this (with no cross terms involving  $dr dt$ , etc.) implies a particular choice of time slicing, and the time coordinate here is often called “cosmic time”. The form of metric (3) can be used in principle for any spherically-symmetric space-time, although it is often more convenient in practice to use other kinds of slicing.

## 2 CAUSAL HORIZONS

In this section, we discuss how the concepts of black-hole and cosmological horizons emerge from a general treatment of outgoing and ingoing null rays. We continue to assume spherical symmetry and take the medium to be a perfect fluid, but our discussion is general in the sense that it is independent of the equation of state used for the matter and we make no assumptions of homogeneity (with reference to the cosmological case), or of stationarity, asymptotic flatness and the presence of vacuum exteriors (with reference to the black holes). It can be interesting to see how well-known results emerge in this approach.

First, we consider the general treatment of radial null rays, using the cosmic time form of the metric (3) introduced above. Along the path of any radial null ray, we have  $ds = d\theta = d\phi = 0$  and so

$$dr = \pm \frac{a}{b} dt, \quad (4)$$

with the plus corresponding to an outgoing ray and the minus to an ingoing one. Note that here “outgoing” and “ingoing” are defined with respect to the comoving frame of local matter. This convention is used throughout the present section.

The general expression for changes in  $R$  along a radial worldline is

$$dR = \frac{\partial R}{\partial t} dt + \frac{\partial R}{\partial r} dr, \quad (5)$$

and so along a radial *null ray*

$$dR = \left( \frac{\partial R}{\partial t} \pm \frac{a}{b} \frac{\partial R}{\partial r} \right) dt. \quad (6)$$

Following the classic paper of Misner (1969), we now introduce the operators

$$D_t \equiv \frac{1}{a} \frac{\partial}{\partial t} \quad \text{and} \quad D_r \equiv \frac{1}{b} \frac{\partial}{\partial r}. \quad (7)$$

Applying these to the circumference coordinate  $R$ , one then defines the quantities

$$U \equiv D_t R \quad \text{and} \quad \Gamma \equiv D_r R, \quad (8)$$

where  $U$  is the radial component of four-velocity in the ‘‘Eulerian’’ frame, with respect to which the fluid is moving, and  $\Gamma$  is a generalized Lorentz factor (which reduces to the standard one in the special relativistic limit). In terms of these,

$$\frac{\partial R}{\partial t} = aU \quad \text{and} \quad \frac{\partial R}{\partial r} = b\Gamma. \quad (9)$$

Inserting these into Eq. (6) gives the expression for how  $R$  changes with time along a radial null ray:

$$\frac{dR}{dt} = a(U \pm \Gamma), \quad (10)$$

where the plus is again for a ray which is outgoing (with respect to the matter) while the minus is for an ingoing one.

To find an expression for  $\Gamma$ , we need to use the Einstein field equation. As usual, we approximate the matter to behave as a perfect fluid with the stress-energy tensor

$$T^{\mu\nu} = (e + p)u^\mu u^\nu + pg^{\mu\nu}, \quad (11)$$

where  $e$  is the energy density,  $p$  is the pressure and  $u^\mu$  is the four-velocity. The  $G_0^0$  and  $G_1^1$  components of the Einstein equation then give

$$4\pi R^2 e R_{,r} = \frac{1}{2} (R + RU^2 - R\Gamma^2)_{,r}, \quad (12)$$

and

$$4\pi R^2 apU = -\frac{1}{2} (R + RU^2 - R\Gamma^2)_{,t}, \quad (13)$$

with the commas representing partial derivatives. It is convenient to make the definition

$$m \equiv \frac{1}{2} (R + RU^2 - R\Gamma^2). \quad (14)$$

Integrating equation (12) then gives

$$m = \int 4\pi R^2 e dR, \quad (15)$$

(corresponding to the interpretation of  $m$  as the mass contained within radius  $R$ ), while Eq. (13) gives

$$D_t m = -4\pi R^2 pU, \quad (16)$$

(representing the change of energy resulting from work done against pressure during expansion or contraction). Rearranging the terms in (14) then gives

$$\Gamma^2 = 1 + U^2 - \frac{2m}{R}. \quad (17)$$

Returning now to Eq. (10), the limiting surface at which an outgoing radial light ray cannot move to larger  $R$ , is given by

$$\left(\frac{dR}{dt}\right)_{\text{out}} = a(U + \Gamma) = 0, \quad (18)$$

implying

$$\Gamma = -U. \quad (19)$$

This corresponds to the so-called ‘‘apparent horizon’’ of a black hole. Similarly, the limiting surface at which an ingoing radial light ray cannot move to smaller  $R$  is given by

$$\left(\frac{dR}{dt}\right)_{\text{in}} = a(U - \Gamma) = 0, \quad (20)$$

implying

$$\Gamma = U. \quad (21)$$

This corresponds to the cosmological (Hubble) horizon. Note that the surfaces for which (19) and (21) hold are *marginally trapped surfaces* and so are representations of a concept (Penrose, 1965) which plays a fundamental role in general relativity.

Conditions (19) and (21) are different, of course, but for both of them

$$\Gamma^2 = U^2, \quad (22)$$

and so, using (17), they both correspond to the condition

$$R = 2m, \quad (23)$$

which is a familiar result! Although we have used cosmic-time slicing in this derivation, the final result is actually independent of the slicing used. We stress again that our derivation here does not depend on any assumptions of homogeneity (with reference to the cosmological case), or of stationarity, asymptotic flatness and the presence of vacuum exteriors (with reference to black holes).

### 3 COSMOLOGICAL STRUCTURE FORMATION

In this section, we discuss some topics concerning cosmological structure formation at two different stages in the history of the universe: in the matter-dominated and radiative eras. The main interest is in the consequences of perturbations which started as small quantum fluctuations in the very early universe and were then inflated onto supra-horizon scales,

eventually re-entering the horizon as the universe continued to expand, and becoming causally connected again. (“Horizon” here refers to the *cosmological* horizon.) We focus on the case of an over-density surrounded by a compensating under-density. Once the over-density has re-entered the horizon, there is a possibility that it could then evolve into a persisting condensed structure. A perturbation originating at a very early time, such as those mentioned above, may have begun with a mixture of growing and decaying components, but any decaying part would soon have faded away so that by the time of horizon re-entry, only the growing part would remain. Growing-modes are special; they have a particular combination of density and velocity perturbation which makes them “hold together” as they evolve.

We discuss below the re-entry of perturbations during the *matter-dominated era*, when the matter is commonly described as pressureless, with  $p = 0$  (although we will have more to say about that), and during those parts of the *radiative era* (defined as being when only relativistic zero-rest-mass particles are important) in which  $p = e/3$  is a good approximation. The first case can lead to formation of galactic or pre-galactic equilibrium structures, whereas in the second case primordial black holes (on a much smaller scale) are the only condensed structures that can be formed.

### 3.1 Virialization in the matter-dominated era

Cosmologists like to use equations of state of the form  $p = we$ , where  $w$  is a constant. The cases  $p = e/3$  and  $p = 0$  do fit with this, of course, but it is questionable whether taking  $p = 0$  actually makes sense in general for the matter-dominated era. For calculating the evolution of a uniform background universe, it is indeed satisfactory, but it becomes problematic when dealing with structure formation beyond the regime of linear perturbations. For cold dark matter (CDM) particles, it is frequently said that they must be pressureless because of being effectively collisionless, but this misses the point that pressure comes from the random motion of particles and is only indirectly influenced by collisions between them. If CDM particles have a non-zero velocity dispersion, then they automatically have a non-zero pressure and this is generally not irrelevant even if it may be small. The role of collisions is in assisting the particle distribution function to relax towards an isotropic Maxwellian, not directly in producing the pressure. A completely collisionless medium can certainly have a finite pressure (although that will generally not be isotropic).

In this subsection, we investigate the phenomenology of the “turn-round radius” and the “virialization radius” for perturbations when they re-enter the cosmological horizon and begin to feel their self-gravity. Initially, the over-density is continuing to expand along with the rest of the universe (although slightly more slowly because of the velocity perturbation in a growing mode) but, as it progressively begins to feel its self-gravity more, it slows down further and eventually reverses its expansion into a contraction. Its radius when that happens is called the turn-round radius. We will follow here just the subsequent behaviour of the dark matter component, which is more or less collisionless. As the contraction proceeds, the random velocities of the constituent particles progressively increase until eventually the effect of their random motions is sufficient to balance gravity (possibly aided by rotation) and the configuration settles into an equilibrium state. Its radius then is called the virialization radius (we explain this more below). In numerical simulations, it is often found that this virialization radius is roughly half of the turn-round radius.

Clearly, structure formation is in general a three-dimensional problem, but could one get a reasonable approximate picture for the above process by using a simple spherically-symmetric toy model? If so, that could be useful for trial inclusion of further effects (dynamical scalar fields, etc.). Our idea is to include the random motions of the CDM particles in terms of an effective temperature  $T$  and insert that into a model equation of state, giving a pressure  $p$ . We proceed as follows. CDM particles are non-relativistic and so the thermal energy per particle is given by

$$u = \frac{3}{2} k_B T, \quad (24)$$

(assuming local isotropy;  $k_B$  is Boltzmann's constant). The thermal energy density is then

$$\rho \varepsilon = \frac{3}{2} n k_B T, \quad (25)$$

(where  $\rho$  is the rest-mass density,  $\varepsilon$  is the specific internal energy, and  $n$  is the particle number density). The ideal gas law  $p = n k_B T$  then gives

$$p = \frac{2}{3} \rho \varepsilon, \quad (26)$$

which leads to

$$p = K(s) \rho^{5/3}, \quad (27)$$

using the first law of thermodynamics. This is the well-known polytropic relation for a monatomic non-relativistic gas (here  $K(s)$  is a function of the specific entropy  $s$  and goes to a constant for adiabatic processes).

Next, we recall the considerations leading to a simple form of the virial theorem, following Taylor (1970). (Note that the treatment in this subsection is entirely Newtonian and it is convenient to retain the  $G$  in the equations for this part; also  $r$  is here the standard classical radial coordinate.) The equation of hydrostatic equilibrium

$$\frac{dp}{dr} = -\frac{Gm\rho}{r^2}, \quad (28)$$

where  $m$  is the mass contained within radius  $r$ , can be rearranged to give

$$4\pi r^3 dp = -\left(\frac{Gm}{r}\right) 4\pi r^2 \rho dr. \quad (29)$$

We now integrate Eq. (29) over the volume of the spherical object:

$$\int 3V dp = \int \Phi dm, \quad (30)$$

where  $V$  is the volume contained within radius  $r$  and  $\Phi = -(Gm/r)$  is the gravitational potential at radius  $r$ . Integrating the left-hand side by parts then gives

$$3[pV] - 3 \int p dV = \Omega, \quad (31)$$

where  $\Omega$  is the gravitational potential energy of the object. Taking the pressure at the surface to be zero and inserting the equation of state expression (26) for  $p$ , one obtains

$$-3 \int \frac{2}{3} \rho \varepsilon dV = -2U = \Omega, \quad (32)$$

where  $U$  is the total internal energy of the object. The overall total energy is then

$$E = U + \Omega = \frac{1}{2} \Omega, \quad (33)$$

which is negative, as it must be for a gravitationally-bound object. When Equation (33) is satisfied, the configuration is said to be virialized.

We will now use these ideas for studying the issue of the turn-round radius and virialization radius within our simple toy model. We will use the subscripts tr and v to denote “turn-round” and “virial” respectively. The configuration starts off (at the turn-round radius  $R_{\text{tr}}$ ) out of hydrostatic equilibrium and not satisfying Eq. (33). As the contraction proceeds, the pressure plays an increasing role in counteracting gravity until eventually equilibrium is reached and the virial condition (33) is satisfied. The radius at which this happens is the virialization radius ( $R_{\text{v}}$ ) mentioned earlier.

Assuming conservation of the total energy during the contraction,

$$E = U_{\text{v}} + \Omega_{\text{v}} = U_{\text{tr}} + \Omega_{\text{tr}}. \quad (34)$$

At the turn-round radius, the energy in the random motions of the CDM particles is still going to be small (it grows later as the contraction proceeds) and so it seems safe to assume that the initial total internal energy term  $U_{\text{tr}}$  can be neglected. Doing this, and using expression (33) at the virial radius, we have

$$E = \frac{1}{2} \Omega_{\text{v}} = \Omega_{\text{tr}}. \quad (35)$$

If we now make the (rough) assumptions that the total mass  $M$  does not change during the contraction and that, throughout, we can write

$$\Omega = -\frac{GM^2}{R} \times \text{constant}, \quad (36)$$

then  $\Omega_{\text{v}}/2 = \Omega_{\text{tr}}$  gives

$$\frac{GM^2}{2R_{\text{v}}} = \frac{GM^2}{R_{\text{tr}}}, \quad (37)$$

and so

$$R_{\text{v}} = \frac{1}{2} R_{\text{tr}}, \quad (38)$$

in agreement with the numerical results.

Our purpose here has been to suggest that this type of “fluid” treatment of cold dark matter might be a useful approach in some circumstances. Clearly, implementations could be made much more detailed than the one which we have sketched above.

### 3.2 The radiative era and primordial black holes

Objects composed of matter for which  $p = e/3$  have an adiabatic index of  $4/3$  and are fundamentally unstable. Because of this, collapsing perturbations in the radiative era do not produce equilibrium condensed structures, but either form black holes (if the perturbation amplitude  $\delta$  is greater than a certain critical threshold value  $\delta_c$ ) or bounce and return back into the roughly uniform medium from which they came. Black holes formed then could have lower masses than ones formed today by the collapse of stars. Since this type of matter has no intrinsic scale, the question arises of whether the phenomenon known as “critical collapse” (Choptuik, 1993) might occur under these circumstances despite the background being that of the expanding universe. The standard form of critical collapse is characterised by the property that, for values of  $(\delta - \delta_c)$  which are positive but sufficiently small, the mass of the black hole formed,  $M_{\text{BH}}$ , is related to  $(\delta - \delta_c)$  by a scaling law, i.e.

$$M_{\text{BH}} \propto (\delta - \delta_c)^\gamma, \quad (39)$$

(with  $\gamma$  being a constant) when the nature of the unperturbed background is kept fixed and the perturbations introduced differ in amplitude but not in shape. This sort of behaviour has been seen in quite a wide range of numerical simulations treating idealised circumstances (see the review by Gundlach and Martín-García, 2007) but its occurrence under “real-world” circumstances is less clear. It seemed possible that the radiative era of the early universe might provide an arena for this, although a potential problem comes from the fact that the universe itself has an intrinsic scale (the cosmological horizon scale) which might or might not interfere with the scaling behaviour. Niemeyer and Jedamzik (1999) made calculations which demonstrated the presence of a scaling law under these circumstances over a restricted range of  $(\delta - \delta_c)$  but when more extensive calculations were made, going closer to the critical limit (Hawke and Stewart, 2002), it was found that the scaling law eventually broke as the behaviour became more extreme near to the critical limit. We then reinvestigated this ourselves (Musco et al., 2009), focusing particularly on the use of perturbations containing only a growing-mode component (following on from the discussion at the beginning of Section 3). For our calculations, we used a purpose-built numerical GR hydro code implementing an AMR technique within a null-slicing approach, and able to go down to extremely small values of  $(\delta - \delta_c)$ . Using growing-mode initial data, without any decaying component (following the methodology of Polnarev and Musco, 2007), we found that the scaling behaviour did go all the way down to the smallest values of  $(\delta - \delta_c)$  that we were able to treat, well beyond the breaking point found previously. Results are shown in Fig. 1. In our work, we define  $\delta$  as being the relative mass excess inside the over-dense region at the time when it re-enters the cosmological horizon, and measure  $M_{\text{BH}}$  in units of  $M_{\text{H}}$ , the cosmological horizon mass at that time, so that the results are independent of epoch within the radiative era. Note that black holes produced like this would have typically lower masses when formed earlier rather than later (related with the value of  $M_{\text{H}}$  at the time).

In the literature on critical collapse, a key feature is the occurrence of similarity solutions accompanying the scaling laws (Evans and Coleman, 1994). As  $(\delta - \delta_c) \rightarrow 0$ , a critical solution is approached where all of the matter in the original contracting region is progressively shed during the contraction which ends, with zero matter, at a time referred to as the critical time  $t_c$ . The later stages of this follow a similarity solution. For small positive

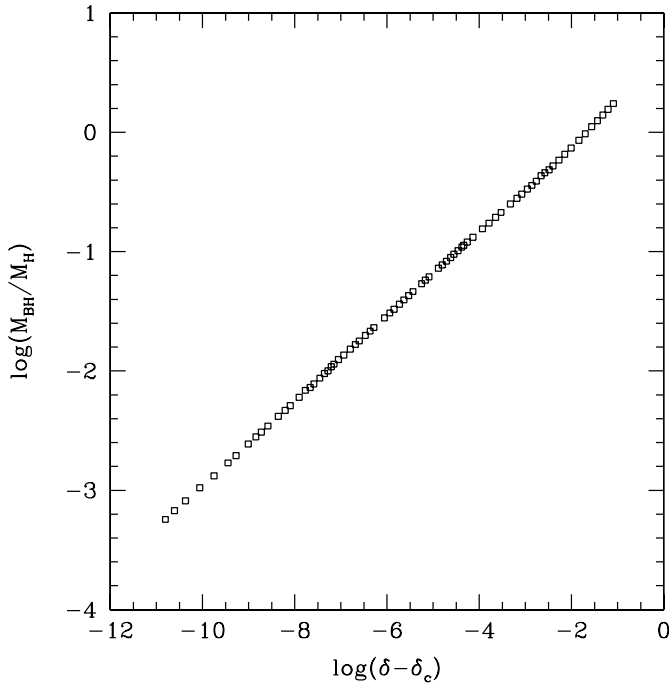


**Figure 1.** Scaling behaviour for  $M_{\text{BH}}$  as a function of  $(\delta - \delta_c)$ .  $M_{\text{BH}}$  is measured in units of  $M_{\text{H}}$ , the mass within the cosmological horizon when the perturbation re-enters it. For  $M_{\text{BH}} \lesssim M_{\text{H}}$ , the points are well fitted by a scaling law with  $\gamma = 0.357$ , which matches well with the corresponding result obtained semi-analytically by Maison (1996) for standard critical collapse with this type of matter.

values of  $(\delta - \delta_c)$ , the similarity solution is closely approached but eventually there is a divergence away from it, with the remaining material then collapsing to form a black hole. It is interesting to see how this plays out in our case, where the collapse occurs within the background of an expanding universe. We have investigated this in some detail (Musco and Miller, 2013). Figure 2 shows our results from a run with  $\delta - \delta_c \sim 10^{-9}$ , which is rather close to the critical limit; the four-velocity  $U$  is plotted as a function of the similarity coordinate  $\xi = R/(t_c - t)$  at a succession of times (solid curves), with the higher peaks corresponding to the later times. Note the shedding of material occurring via a relativistic wind. One can see the progressive approach of the simulation results towards the similarity solution (dashed curve), with the range of the zone of agreement increasing with time. At the last time shown, the similarity solution is being closely approximated over all of the contracting region, where  $U$  is negative (although it is quite hard to see this as being negative in the figure because of the scale), and also over the part of the surrounding region out to the maximum of  $U$ ; beyond this, the simulation results diverge completely away from the similarity solution and eventually merge into the surrounding Friedmann–Robertson–Walker universe. The similarity behaviour breaks soon after the last time shown here, with the start of the final collapse leading to black hole formation. We should stress that the use of a logarithmic coordinate in Fig. 2 has the effect of making features appear much more

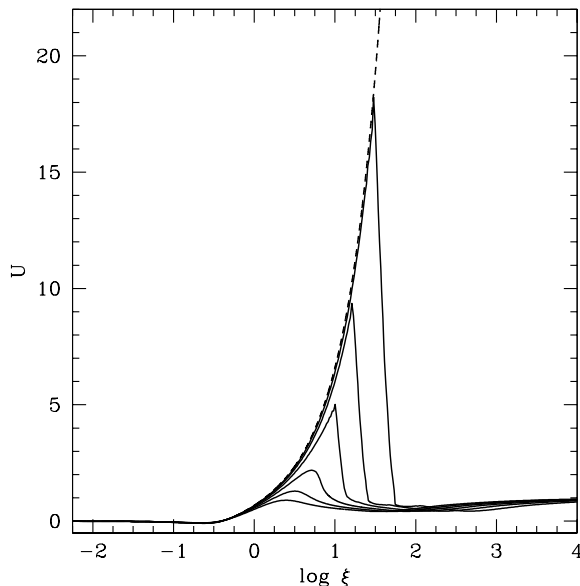


**Figure 2.** Simulation results for the velocity  $U$  (from a run with  $\delta - \delta_c \sim 10^{-9}$ ) plotted against the similarity coordinate  $\xi = R/(t_c - t)$ . The plot shows curves for a succession of times during the close approach to the similarity solution, with the higher peaks corresponding to the later times. The precise similarity solution for the collapsing matter is marked with the dashed curve, which is partly covered by the solid curves.

abrupt than they would do with a standard linear coordinate. The almost vertical parts of the curves are nowhere near to being shocks and correspond to smoothly varying features when viewed on a linear scale.

#### 4 CONCLUSIONS

We have touched here on a number of topics. Firstly, a unified treatment has been given of black-hole and cosmological horizons in terms of co-moving trapped surfaces. This does not depend on any assumptions of homogeneity (in the cosmological case), or of stationarity, asymptotic flatness and the presence of vacuum exteriors (for the black holes). We then went on to discuss two topics concerned with cosmological structure formation: virialization of cold dark matter during standard structure formation in the matter-dominated era, and primordial black hole formation during the radiative era. In the first case, we presented a simple toy model which serves as an analytic demonstration of phenomena observed in numerical simulations; in the second case, we presented results showing that black-hole formation by collapse of cosmological perturbations in the radiative era completely follows the well-known phenomenology of critical collapse, as long as the perturbations are of the growing-mode type when they re-enter the cosmological horizon.

## ACKNOWLEDGEMENTS

The research of Ilia Musco is currently being supported by postdoctoral funding from ERC-StG EDECS contract no. 279954.

## REFERENCES

- Choptuik, M. W. (1993), Universality and scaling in gravitational collapse of a massless scalar field, *Phys. Rev. Lett.*, **70**, pp. 9–12.
- Evans, C. R. and Coleman, J. S. (1994), Critical phenomena and self-similarity in the gravitational collapse of radiation fluid, *Phys. Rev. Lett.*, **72**, pp. 1782–1785, arXiv: [gr-qc/9402041](https://arxiv.org/abs/gr-qc/9402041).
- Gundlach, C. and Martín-García, J. M. (2007), Critical Phenomena in Gravitational Collapse, *Living Reviews in Relativity*, **10**, p. 5, arXiv: [0711.4620](https://arxiv.org/abs/0711.4620).
- Hawke, I. and Stewart, J. M. (2002), The dynamics of primordial black-hole formation, **19**, pp. 3687–3707.
- Maison, D. (1996), Non-universality of critical behaviour in spherically symmetric gravitational collapse, *Phys. Rev. B*, **366**, pp. 82–84, arXiv: [gr-qc/9504008](https://arxiv.org/abs/gr-qc/9504008).
- Misner, C. W. (1969), Gravitational Collapse, in M. Chrétien, S. Deser and J. Goldstein, editors, *Astrophysics and General Relativity, Volume 1*, p. 113.
- Musco, I. and Miller, J. C. (2013), Primordial black hole formation in the early universe: critical behaviour and self-similarity, **30**(14), 145009, arXiv: [1201.2379](https://arxiv.org/abs/1201.2379).
- Musco, I., Miller, J. C. and Polnarev, A. G. (2009), Primordial black hole formation in the radiative era: investigation of the critical nature of the collapse, **26**(23), 235001, arXiv: [0811.1452](https://arxiv.org/abs/0811.1452).
- Niemeyer, J. C. and Jedamzik, K. (1999), Dynamics of primordial black hole formation, *Phys. Rev. D*, **59**(12), 124013, arXiv: [astro-ph/9901292](https://arxiv.org/abs/astro-ph/9901292).
- Penrose, R. (1965), Gravitational collapse and space-time singularities, *Phys. Rev. Lett.*, **14**, pp. 57–59, URL <http://link.aps.org/doi/10.1103/PhysRevLett.14.57>.
- Polnarev, A. G. and Musco, I. (2007), Curvature profiles as initial conditions for primordial black hole formation, **24**, pp. 1405–1431, arXiv: [gr-qc/0605122](https://arxiv.org/abs/gr-qc/0605122).
- Tayler, R. J. (1970), *The stars: Their structure and evolution*.



# Geometrically thin accretion disk around Maclaurin spheroids

Bhupendra Mishra<sup>1</sup> and Bhargav Vaidya<sup>2</sup>

<sup>1</sup>Nicolaus Copernicus Astronomical Center, Bartycka 18, 00-716 Warsaw, Poland

<sup>2</sup>Dipartimento di Fisica ‘Amedeo Avogadro’ Università degli Studi di Torino  
Via Pietro Giuria 1, 10125 Torino, Italy

## ABSTRACT

We studied a semi-analytic and numerical model of geometrically thin disk around Maclaurin spheroid. We are mainly interested in the inner region of the so called alpha-disk, alpha being the viscosity parameter. We found minor changes in the emitted spectra from the disk for a change in eccentricity of Maclaurin spheroid. We also found that change in eccentricity of Maclaurin spheroid changes various disk parameters like disk thickness, surface density and central temperature. Numerical work has been carried out to see the viscous time evolution of the non-stationary accretion disk around Maclaurin spheroid. In numerical model we showed that if the eccentricity of the Maclaurin spheroid is high the matter will diffuse slowly during the disk evolution.

**Keywords:** accretion – accretion disk – hydrodynamics – stars: neutron

## 1 INTRODUCTION

Geometrically thin accretion disks have been studied intensively in last few decades using some very robust models. The best known analytic models for describing the accretion disk were proposed by Shakura and Sunyaev (1973), Novikov and Thorne (1973) and Lynden-Bell and Pringle (1974). Shakura and Sunyaev (1973) considered Newtonian potential around spherically symmetric body (black hole). To investigate relativistic effects due to strong gravity in the accretion process a different choice of potential or metric is required. Novikov and Thorne (1973) considered thin accretion disk around rotating black holes using Kerr space-time. Novikov and Thorne (1973) solutions are extension of Newtonian results by Shakura and Sunyaev (1973) to relativistic regime.

Using relativistic approach Kovács et al. (2009) solved the non-stationary thin accretion disk around quark stars. Gondek-Rosińska et al. (2014) calculated the effect of eccentricity of quark-star on the orbital frequencies to investigate the quasi periodic oscillations (QPOs). Recently Khanna et al. (2014) computed trapped horizontal modes in accretion disk around Maclaurin spheroids. Bisnovatyi-Kogan (1993) studied the correlation between mass accretion rate and eccentricity of the rapidly rotating star. In the same trend we performed a semi-analytic and numerical study of viscous (constant ‘alpha’) accretion disk around

a Maclaurin spheroid. We used Maclaurin spheroid potential for a constant density and mass central object. This model describes that how the Maclaurin spheroid potential will affect the dynamics of accreting matter. We are focused only close to Maclaurin spheroid to have the effects of multipoles in our calculations. As a first attempt we assumed constant  $\alpha$  viscosity prescription to proceed with analytic and numerical work.

In Maclaurin spheroid potential there occurs an innermost stable circular orbit (ISCO) even in Newtonian dynamics (Amsterdamski et al., 2002; Kluźniak and Rosińska, 2013). We chose a constant density and mass Maclaurin spheroid and assumed that it is rotating rapidly. Rapid rotation of Maclaurin spheroid can change its eccentricity and so semi-major axis. In Kluźniak and Rosińska (2013), it has been shown that if the eccentricity is less than a critical value of  $e_c = 0.8345$ , the ISCO will lie on the equator of the accreting source but if it is higher than this value it will be detached from the surface of the star. Keeping this change in mind we investigated the cases where eccentricity is less than critical limit. We see a change in inner radius of the accretion disk with change in eccentricity because the semi-major axis of the accreting Maclaurin spheroid is changing. We also simulated the non-stationary accretion disk around Maclaurin spheroid by solving the diffusion equation for the accreting matter. We again assumed the Maclaurin spheroid potential to proceed with the study of non-stationary disk.

The article is organized in the following manner. In Section 2 we describe physical model of accretion disk which covers steady thin disk and also numerical study of the time evolution of the accretion disk. Section 3 is devoted for describing all the results we obtained analytically and numerically. In Section 4 we discuss all the results described in Section 3 and we conclude in Section A with future applications of our accretion disk model around Maclaurin spheroids. A more general and detailed description of this article can be found in Mishra and Vaidya (2015).

## 2 PHYSICAL MODEL

### 2.1 Maclaurin Spheroid

We considered Maclaurin spheroid potential and followed Shakura and Sunyaev (1973) alpha disk model. We assumed ideal gas equation of state for computing the gas pressure. The semi-major axis  $a$  of the Maclaurin spheroid changes with eccentricity because we assume constant density and mass Maclaurin spheroid. We also assumed that the disk terminates at the surface of the Maclaurin spheroid. This assumption causes a change in semi-major axis and so inner radius of the accretion disk due to change in eccentricity. The semi-major axis of the Maclaurin spheroid is defined as a function of its radius for  $e = 0.0$ ,

$$a = R_0 / (1 - e^2)^{1/6}, \quad (1)$$

where  $a$  is the semi-major axis of the Maclaurin spheroid and  $R_0$  is the semi-major axis of Maclaurin spheroid for eccentricity,  $e = 0.0$ . The maximum value of eccentricity we chose in this paper is  $e = 0.8345$ . There is a reason behind choosing this limit, in case of potential for Maclaurin spheroid the radial epicyclic frequency has maximum at  $r = \sqrt{2}ae$  for

spheroid eccentricities  $e > 1/\sqrt{2}$  but it vanishes for  $e_c = 0.83458318$  at the equator of the star (Kluźniak and Rosińska, 2013). With further increase in the eccentricity  $e > e_c$ , the innermost stable circular orbit (ISCO) will be separated from the equator of star and it will be at  $r_{\text{ms}} = 1.198203 ae$  (Kluźniak and Rosińska, 2013). Following this assumption we always kept the inner radius at no-torque boundary (the radius at which the viscosity is zero) which coincides with the variable semi-major axis of Maclaurin spheroid. One can increase the eccentricity further to investigate the accretion disk for which the inner radius does not lie at the surface of Maclaurin spheroid but in this paper we shall not discuss it. The angular velocity (orbital frequency) in case of Maclaurin spheroid potential is given by

$$\Omega^2(e, r) = 2\pi G\rho_*(1 - e^2)^{1/2}e^{-3}[\gamma_r - \cos\gamma_r \sin\gamma_r], \quad (2)$$

where  $\gamma_r = \arcsin(ae/r)$ ,  $a$  is the semi-major axis of Maclaurin spheroid and  $\rho_*$  is constant density of the Maclaurin spheroid (Kluźniak and Rosińska, 2013). Now we have angular velocity of the matter for Maclaurin spheroid potential, next goal is to follow Shakura and Sunyaev (1973) alpha disk model and do the calculations for angular velocity calculated from Eq. (2). This analytic approach gave us various disk parameters like, half-thickness, surface density, temperature and radial velocity in the inner, middle and outer region of the accretion disk.

## 2.2 Steady thin accretion disk

We considered a thin accretion disk (height of disk is much smaller than its radial width) around Maclaurin spheroid. Calculations are done in cylindrical coordinate system  $(r, \phi, z)$ , assuming azimuthal symmetry. The goal of this model is to study the steady-state disk and see the behaviour of disk parameters and emitted spectra of the stationary accretion disk. To proceed the calculations for steady-state disk we used Eqs. (2) and (3) to analytically calculate disk parameters in inner region of the accretion disk. The angular momentum equation in terms of angular velocity of accreting matter is given by

$$-v_r \Sigma \frac{d\Omega r^2}{dr} = \frac{1}{r} \frac{d}{dr} W_{r\phi} r^2, \quad (3)$$

where  $v_r$  is the radial velocity,  $W_{r\phi}$  is the stress between adjacent layers (Shakura and Sunyaev, 1973), which is assumed to be a function of sound speed  $v_s$  and surface density  $\Sigma$ .

$$\Sigma = 2 \int_0^{z_0} \rho dz, \quad (4)$$

$$W_{r\phi} = -\alpha \Sigma v_s^2, \quad (5)$$

where  $\alpha$  is constant viscosity coefficient. In stationary disk model  $\dot{M} = -2\pi \Sigma v_r r = \text{const}$  and  $v_r < 0$ . Integrating Eq. (3) gives

$$\dot{M} \Omega r^2 = -2\pi W_{r\phi} r^2 + C, \quad (6)$$

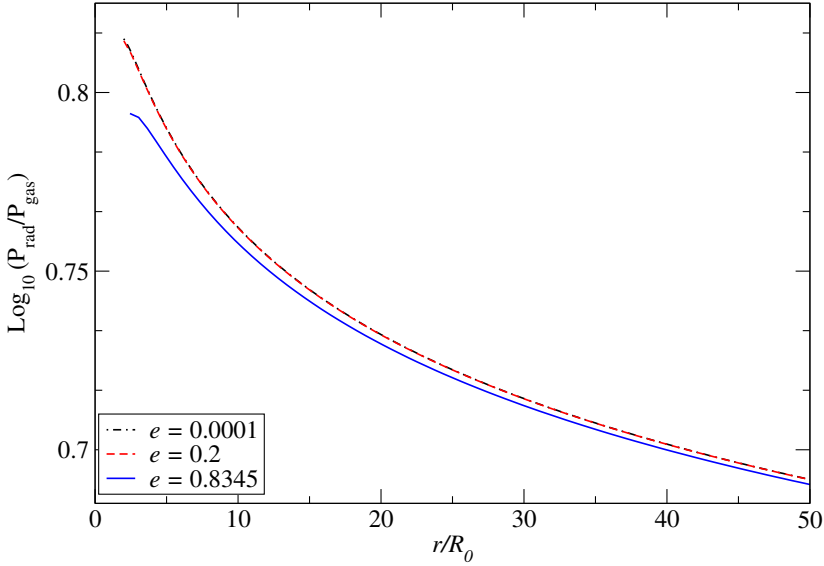


**Figure 1.** Plot shows the region of interest (*inner region*). The vertical axis shows the ratio of radiation pressure  $P_{\text{rad}}$  to gas pressure  $P_{\text{gas}}$ . The horizontal axis corresponds to radial distance from the center of the star. Three different eccentricities  $e = 10^{-4}$  (*black dotted-dashed curve*),  $e = 0.2$  (*red dashed curve*) and  $e = 0.8345$  (*solid blue curve*) have been shown in the plot.

where  $C$  is constant which we calculated by using no-torque boundary condition (Shakura and Sunyaev, 1973). Finally we get the equation to calculate disk parameters in all three regions of the accretion disk.

$$\dot{M} \left( \Omega r^2 - \Omega(a)a^2 \right) = 2\pi\alpha \Sigma v_s^2 r^2. \quad (7)$$

Now the energy flux radiated from the surface unit as function of  $\Omega(e, r)$  is given by

$$Q = - \frac{\dot{M} \left( \Omega r^2 - \Omega(a)a^2 \right) d\Omega}{4\pi r dr}. \quad (8)$$

using Eq. (7) and Eq. (8) together with assumption of radiation pressure dominated region we calculated disk thickness, surface density, temperature and radial velocity in the inner (radiation pressure dominated) region of the accretion disk.

### 2.2.1 Radiation pressure dominated region

In the same fashion like Shakura and Sunyaev (1973), we formulated three different regions in the accretion disk, the inner one is radiation pressure dominated where in the interaction of matter and radiation electron scattering on free electrons has dominating contribution. Figure 1 verifies our claim that we are studying the inner radiation pressure dominated region. We substituted  $\Omega(e, r)$  in Eq. (7) and Eq. (8) from Eq. (2) to calculate the disk

parameters like disk half thickness  $z_0(r)$ , surface density  $\Sigma(r)$ , central temperature  $T(r)$  and radial velocity  $v_r(r)$  of the matter. We expressed the analytic expression in terms of defined parameters  $\gamma_r$ ,  $\gamma_a$ ,  $p_r$ ,  $p_a$  and  $k_1$  to abbreviate the complicated expressions.

$$z_0(r) = \sigma \dot{M} \sin^2 \gamma_r \tan \gamma_r (8\pi p_r c)^{-1} \left( 1 - \left( \frac{p_a}{p_r} \right)^{1/2} \left( \frac{a}{r} \right)^2 \right), \quad (9)$$

$$\Sigma(r) = 32\pi c^2 p_r^{3/2} \tan^2 \gamma_r \left( \alpha \sigma^2 k_1^{1/2} \dot{M} \right)^{-1} \left( 1 - \left( \frac{p_a}{p_r} \right)^{1/2} \left( \frac{a}{r} \right)^2 \right)^{-1}, \quad (10)$$

$$\varepsilon(r) = 6cp_r^{3/2} k_1^{1/2} \left( \alpha \sigma \sin^2 \gamma_r \tan \gamma_r \right)^{-1}, \quad (11)$$

$$T(r) = (\varepsilon(r)/b)^{1/4}, \quad (12)$$

$$\tau(r) = \sqrt{0.11\sigma_T T(r)^{-7/2} n(r) \Sigma(r)}, \quad (13)$$

$$n(r) = \Sigma(r)/2mpz_0(r), \quad (14)$$

$$v_r(r) = -\dot{M}/2\pi \Sigma(r)r, \quad (15)$$

where,

$$k_1 = 2\pi G\rho_*(1 - e^2)^{1/2} e^{-3}, \quad (16)$$

$$\gamma_r = \arcsin(ae/r), \quad (17)$$

$$\gamma_a = \arcsin(e), \quad (18)$$

$$p_r = (\gamma_r - \sin \gamma_r \cos \gamma_r), \quad (19)$$

$$p_a = (\gamma_a - \sin \gamma_a \cos \gamma_a). \quad (20)$$

$\dot{M}$  is mass accretion rate,  $\sigma$  is opacity,  $b = 3\sigma_b/c$  where  $\sigma_b$  is Stefan Boltzmann constant,  $\sigma_T$  is Thomson cross-section of electron,  $z_0(r)$  is half-thickness of the disk,  $\Sigma(r)$  is the radial distribution of surface density,  $\varepsilon(r)$  is radial distribution of energy density,  $T(r)$  is radial distribution of the central temperature,  $\tau(r)$  is optical thickness,  $n(r)$  is the number density and  $v_r(r)$  is the radial velocity of the matter in the steady thin accretion disk.

### 2.3 Non-stationary accretion disk

In this model we numerically solved the time evolution of the geometrically thin accretion disk around Maclaurin spheroid. The viscous friction causes a transport of angular momentum outwards and matter accretion on to the Maclaurin spheroid. We numerically integrated the diffusion equation Eq. (21) with constant viscosity  $\nu$  as a first approximation. We used Crank–Nicolson method which is described in Birnstiel et al. (2010) to solve the diffusion-advection equation in code units. The equation we present here can be used to solve the time evolution of accretion disk around different potentials or orbital frequency.

$$\frac{\partial \Sigma}{\partial t} = -\frac{1}{r} \frac{\partial}{\partial r} \left[ \frac{1}{2\pi (r^2 \Omega)'} \frac{\partial G}{\partial r} \right], \quad (21)$$

$$v_r = \frac{1}{2\pi r \Sigma (r^2 \Omega)'} \frac{\partial G}{\partial r}, \quad (22)$$

where,

$$G(r, t) = 2\pi r \nu \Sigma r^2 \Omega' \quad (23)$$

is the torque exerted by two adjacent rings to each other in the accreting matter. Now if we choose the Keplerian angular velocity the above equations reduce to diffusion equation used for study of accretion disk evolution by various models based on Newtonian potential of a spherically symmetric body (Lynden-Bell and Pringle, 1974).

$$\frac{\partial \Sigma}{\partial t} = \frac{3}{r} \frac{\partial}{\partial r} \left[ r^{1/2} \frac{\partial}{\partial r} \left( \nu \Sigma r^{1/2} \right) \right], \quad (24)$$

$$v_r = -\frac{3}{\Sigma r^{1/2}} \frac{\partial}{\partial r} \left( \nu \Sigma r^{1/2} \right), \quad (25)$$

where  $\Sigma$  is the surface density,  $\nu$  is kinematic viscosity and  $v_r$  is the radial velocity. Now using Eqs. (2), (21) and (22) we shall compute the time evolution of the accretion disk for different eccentricities  $e$  of the Maclaurin spheroid. Depending on eccentricity  $e$ , matter can be diffused either rapidly or slowly.

### 3 RESULTS

#### 3.1 Steady state disk

In our calculations the radius of Maclaurin spheroid for  $e = 0.0$  is  $R_0 = 10^6$  cm. This radius will also work for our scaling of radial distance. The constant density of Maclaurin spheroid is  $\rho_* = 10^{15}$  g·cm<sup>-3</sup>. In this article we kept accretion rate fixed at  $\dot{M} = 10^{17}$  g·s<sup>-1</sup> and changed the eccentricity  $e$  of the central object to see the effect on the disk thickness, surface density, temperature and radial velocity of accreting matter in the inner region of accretion disk. We chose three values of eccentricity which are  $e = 10^{-4}$ ,  $e = 0.8345$  with an intermediate value of  $e = 0.2$ . Figure 2 presents the radial variation of the half-thickness  $z_0(r)$ , surface density  $\Sigma(r)$ , central temperature  $T(r)$  and radial velocity  $v_r(r)$ . In this figure the inner grid point of the plot for all the parameters is  $2R_0$  to avoid singularities at the inner boundary of the disk. We see from upper left panel a difference in the half thickness of the accretion disk for different eccentricities  $e = 10^{-4}$  (black dashed-dotted curve),  $e = 0.2$  (red dashed curve) and  $e = 0.8345$  (solid blue curve). Higher eccentricity  $e$  of the star corresponds to lower disk thickness at a particular radial distance from the center of Maclaurin spheroid. The upper right panel shows the logarithmic variation of the surface density distribution in the inner region of the accretion disk. We see that for higher eccentricities the surface density is higher than for the lower eccentricities. The surface density  $\Sigma(r)$  also increases with radial distance in the inner region of the accretion disk. The lower left panel shows the radial variation of central temperature  $T(r)$  in the accretion disk. The lower right panel shows the radial velocity profile  $v_r(r)$  in the accretion disk. We see a very small difference in radial velocity for different eccentricities  $e$ .

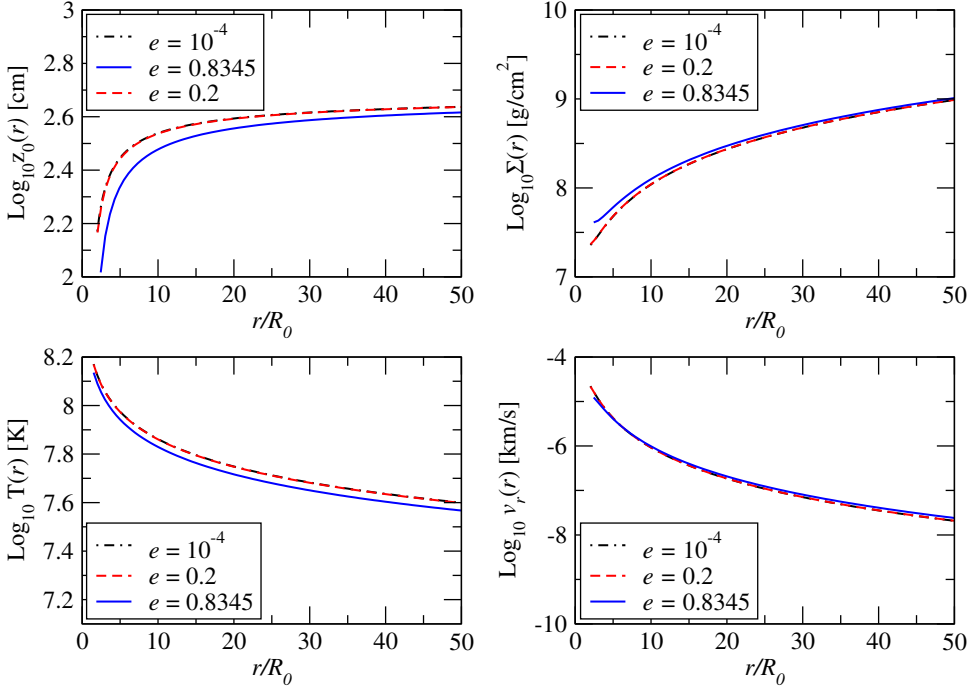


**Figure 2.** Multiplot shows radial variation of height  $z_0(r)$ , surface density  $\Sigma(r)$ , central temperature  $T(r)$  and radial velocity  $v_r(r)$ . The different chosen eccentricities are shown by  $e = 10^{-4}$  (black dotted-dashed curve),  $e = 0.2$  (red dashed curve) and  $e = 0.8345$  (solid blue curve). This color convention for chosen eccentricities is same throughout the article. The right upper panel shows the logarithmic radial variation of the surface density  $\Sigma(r)$ . The left lower panel shows the logarithmic radial variation of the central temperature  $T(r)$ . The lower right panel shows the logarithmic radial variation of the radial velocity  $v_r(r)$  of the accreting matter.

### 3.2 Emitted Spectra from the disk

A very useful quantity for observational interest is emitted spectra from the accretion disk. Emitted spectra also corresponds to the size of accretion disk. We computed spectra using surface temperature of the disk. We chose a fixed outer radius of the accretion disk to see the behaviour of the emitted spectra with change in eccentricity. The accretion disk we assumed here is optically thick in the  $z$  direction therefore we can assume that each element of the disk emits as black body with surface temperature  $T_s(r)$ . Using angular velocity from Eq. (2) and equating the dissipation rate per unit area to the black body flux we computed surface temperature  $T_s(r)$  of the accretion disk. Using the calculated temperature we can calculate intensity and with intensity emitted spectra of the accretion disk.

$$T_s(r) = \left[ \frac{\dot{M} r \Omega T_1(r) d\Omega}{4\pi\sigma dr} \right]^{1/4} \quad (26)$$

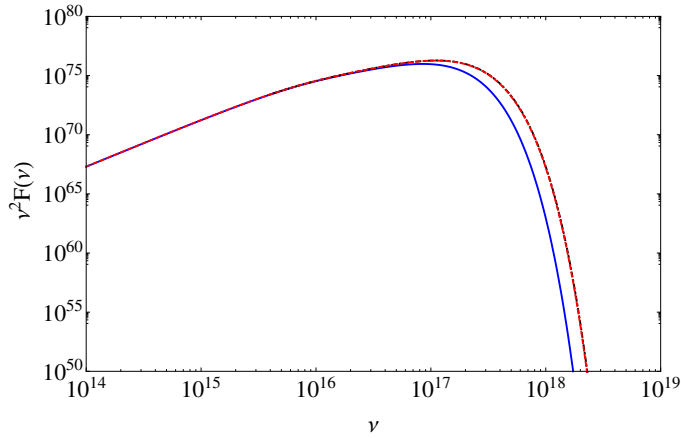


**Figure 3.** Logarithmic plot shows the emitted spectra from the accretion disk. *Black dotted dashed* curve corresponds to  $e = 10^{-4}$ , *red dashed* curve corresponds to  $e = 0.2$  and *blue solid* curve correspond to  $e = 0.8345$ .

where  $T_1(r)$  is defined as

$$T_1(r) = 1 - \frac{\Omega(a)a^2}{\Omega(r)r^2} \quad (27)$$

approximating the disk emitted spectra with black body we have

$$I(\nu) = B_\nu[T_s(r)] = \frac{2h\nu^3}{c^2(e^{h\nu/kT_s(r)} - 1)}, \quad (28)$$

using Eq. (27) we computed flux emitted from accretion disk by integration over the whole disk.

$$F(\nu) = 2\pi \int_{a(e)}^{R_{\text{out}}} I(\nu)r \, dr \quad (29)$$

the integration of Eq. (29) gives emitted spectra from the disk. Figure 3 shows the logarithmic variation of emitted spectra from the accretion disk for eccentricities  $e = 10^{-4}$  (black dashed curve)  $e = 0.2$  (red dashed curve) and  $e = 0.8345$  (solid blue curve). We found difference in emitted spectra at low frequencies. At high frequencies the difference is very small for changes in eccentricity of Maclaurin spheroid.

### 3.3 Evolution of surface density

We studied the non-stationary accretion disk using model described in Section 2.3. We assumed an initial Gaussian density distribution of matter at a radial distance of  $r = 1.5a$  as the initial condition to solve the diffusion equation (Eq. 21). In all the results of non-stationary disk the time is in viscous time scale,  $t_{\text{visc}} = a^2/\nu$ ,  $a$  being the semi-major axis

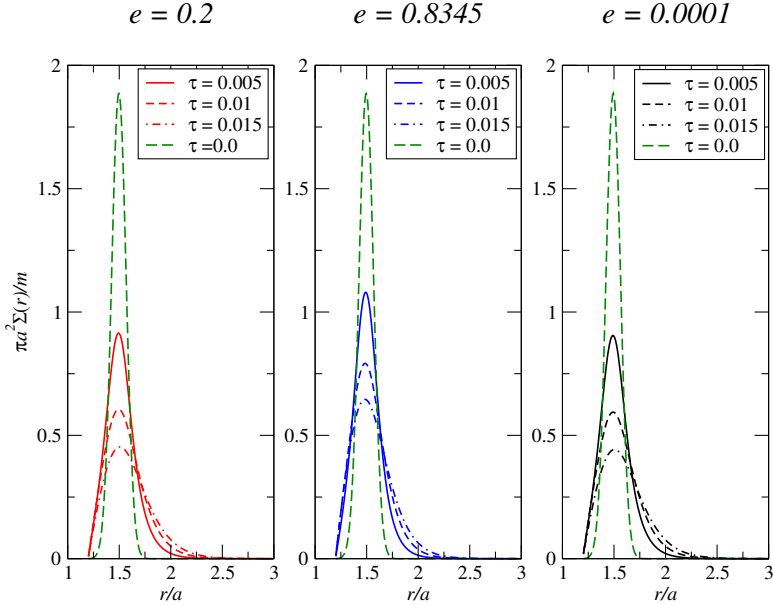


**Figure 4.** Time evolution of the ring of matter at a radial distance of  $r = 1.5a$ . The vertical axis shows the surface density scaled with initial surface density of ring of matter with mass  $m$ . The horizontal axis corresponds to radial distance from the center of star.

of the star. In our model we are interested for constant viscosity prescription therefore the kinematic viscosity coefficient  $\nu = 0.01$  (in code units) is constant throughout our numerical computation. In Figure 4 we plotted the time evolution of surface density for the ring of matter at  $r = 1.5a$  for  $e = 10^{-4}$ ,  $e = 0.2$  and  $e = 0.8345$ . The vertical axis shows the surface density  $\Sigma(r)$  scaled with initial surface density. The horizontal axis corresponds to radial distance from the center of star scaled with semi-major axis  $a$  of the Maclaurin spheroid.

We also tested our numerical code by reducing the code parameters to the limiting case of spherically symmetric potential. In the appendix various code parameters are defined in which we chose parameter  $D$  (Eq. A2) which corresponds to the diffusion of matter. Figure 5 shows the variation of  $D$  with radial distance for eccentricities  $e = 10^{-4}$  (black dotted-dashed curve),  $e = 0.2$  (red dashed curve) and  $e = 0.8345$  (solid blue curve). The limiting value in case of Keplerian angular velocity or  $e = 0.0$  is  $D = -3.0$ . We see from Fig. 5 that as we decrease the eccentricity, parameter  $D$  is converging to  $D = -3.0$ . Also for larger radial distance the parameter  $D$  converges to the limit of spherically symmetric potential ( $D = -3.0$ ).

#### 4 DISCUSSION AND CONCLUSIONS

We conclude that our implementation of Maclaurin spheroid potential causes changes in the steady state disk parameters like half thickness of the disk. We also see that the change in eccentricity of the Maclaurin spheroid gives small change in central temperature of the

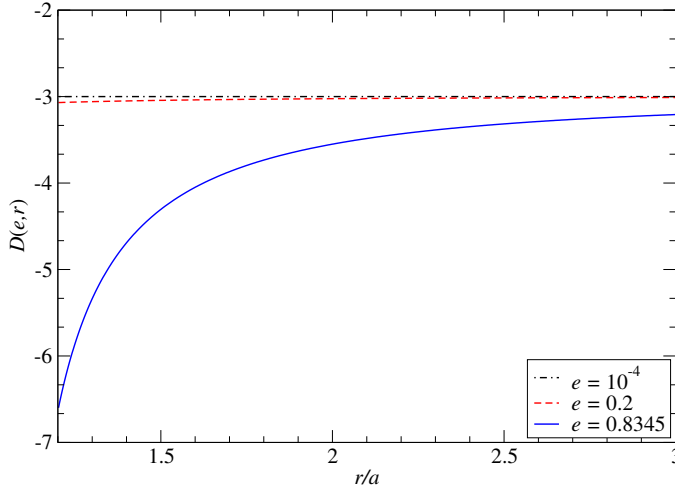


**Figure 5.** Plot shows the test of our code in the limiting case when  $e \rightarrow 0$  (spherically symmetric object). The vertical axis shows the variation of the parameter  $D$  defined in Eq. (A2). The horizontal axis shows the radial distance from the center of star. Three different eccentricities  $e = 10^{-4}$  (black dotted-dashed curve),  $e = 0.2$  (red dashed curve) and upper limit in our model  $e = 0.8345$  are plotted.

accretion disk. The radial velocity in case of steady state disk is inversely proportional to the corresponding surface density profile. This gives a very minor change in radial velocity profile for different eccentricities.

We computed the disk spectra for three values of eccentricity  $e = 10^{-4}$ ,  $e = 0.2$  and  $e = 0.8345$ . We know from the existing results that a change in the disk area changes the emitted spectra. In this paper the only parameter we changed is the eccentricity and a change in the eccentricity of the Maclaurin spheroid is changing the semi-major axis of the star as well as surface temperature  $T_s(r)$ . This small change in inner radius of the disk due to change in semi-major axis and change in surface temperature  $T_s(r)$  causes a change in emitted spectra from the inner region of the accretion disk. The emitted spectra is affected only at high frequency region because this is emitted from inner parts of the accretion disk where Maclaurin spheroid potential dominates.

The results of non-stationary accretion disk are also dependent on eccentricity of Maclaurin spheroid. We found that if the eccentricity of the central object is lower the viscous evolution of the accretion disk will be more rapid as compare to high eccentricity. The choice of initial location of Gaussian distribution of matter is also important in our numerical model. We kept initial distribution of matter at  $r = 1.5a$ , which is very close to the Maclaurin spheroid. If we start at large radial distance as we can see from Fig. 5, the effect of eccentricity change will not be significant. From this result we can also explain that a spin-up or spin-down of the rapidly rotating Maclaurin spheroid can change the viscous evolution of the accretion disk. Maclaurin spheroid potential can also affect observed variability in the accretion disks around quark stars or white dwarfs. Change in viscous evolution and emitted spectra from disk can also observationally help in discriminating the neutron stars from quark stars, which is open astrophysics problem in scientific community.

## ACKNOWLEDGEMENTS

We thank to Włodek Kluźniak for proposing this project. We also thank to F. H. Vincent and A. Manousakis for discussions. Research was supported by Polish NCN grant UMO-34 2011/01/B/ST9/05439 and 2013/08/A/ST9/00795.

## REFERENCES

- Amsterdamski, P., Bulik, T., Gondek-Rosińska, D. and Kluźniak, W. (2002), Marginally stable orbits around Maclaurin spheroids and low-mass quark stars, *Astronomy and Astrophysics*, **381**, pp. L21–L24, arXiv: astro-ph/0012547.
- Birnstiel, T., Dullemond, C. P. and Brauer, F. (2010), Gas- and dust evolution in protoplanetary disks, *Astronomy and Astrophysics*, **513**, A79, arXiv: 1002.0335.
- Bisnovatyi-Kogan, G. S. (1993), A self-consistent solution for an accretion disc structure around a rapidly rotating non-magnetized star, *Astronomy and Astrophysics*, **274**, p. 796.
- Gondek-Rosińska, D., Kluźniak, W., Stergioulas, N. and Wiśniewicz, M. (2014), Epicyclic frequencies for rotating strange quark stars: Importance of stellar oblateness, *Phys. Rev. D*, **89**(10), 104001, arXiv: 1403.1129.
- Khanna, S., Strzelecka, Z., Mishra, B. and Kluźniak, W. (2014), Eigenmodes of trapped horizontal oscillations in accretion disks, in Z. Stuchlík, G. Török and T. Pecháček, editors, *Proceedings of RAGtime 14–16: Workshops on black holes and neutron stars, Opava, Prague, 18–22 September/15–18 July/11–19 October '12/'13/'14*, pp. 145–158, Silesian University in Opava, Opava, ISBN 978-80-7510-126-6, in this proceedings.
- Kluźniak, W. and Rosińska, D. (2013), Orbital and epicyclic frequencies of Maclaurin spheroids, *Monthly Notices Roy. Astronom. Soc.*, **434**, pp. 2825–2829.
- Kovács, Z., Cheng, K. S. and Harko, T. (2009), Thin accretion discs around neutron and quark stars, *Astronomy and Astrophysics*, **500**, pp. 621–631.
- Lynden-Bell, D. and Pringle, J. E. (1974), The evolution of viscous discs and the origin of the nebular variables., *Monthly Notices Roy. Astronom. Soc.*, **168**, pp. 603–637.
- Mishra, B. and Vaidya, B. (2015), A geometrically thin accretion disc around a Maclaurin spheroid, *Monthly Notices Roy. Astronom. Soc.*, **447**, pp. 1154–1163, arXiv: 1411.6054.
- Novikov, I. D. and Thorne, K. S. (1973), Astrophysics of black holes., in C. Dewitt and B. S. Dewitt, editors, *Black Holes (Les Astres Occlus)*, pp. 343–450.
- Shakura, N. I. and Sunyaev, R. A. (1973), Black holes in binary systems. Observational appearance., *Astronomy and Astrophysics*, **24**, pp. 337–355.

**APPENDIX A: NON-STATIONARY ACCRETION DISK**

In this section we shall describe the different terms which we calculated for our model to fit with Eq. (A1)

$$\frac{\partial \Sigma}{\partial t} + \frac{\partial}{\partial r}(\Sigma u) - \frac{\partial}{\partial r} \left[ h D \frac{\partial}{\partial r} \left( v \frac{\Sigma}{h} \right) \right] = L \Sigma, \quad (\text{A1})$$

where

$$D = r\Omega' / (2\Omega + r\Omega'), \quad (\text{A2})$$

$$u = v\Omega' / (2\Omega + r\Omega'), \quad (\text{A3})$$

$$h = 1/r^3\Omega', \quad (\text{A4})$$

$$L = -vr^3\Omega' \left[ \frac{3}{r^4 l_1} + \frac{3\Omega' + r\Omega''}{r^3 l_1^2} \right], \quad (\text{A5})$$

where again,

$$l_1 = (2\Omega + r\Omega'). \quad (\text{A6})$$

# Numerical simulations of thin accretion discs with PLUTO

Varadarajan Parthasarathy<sup>a</sup> and Włodek Kluźniak

Copernicus Astronomical Center, ul. Bartycka 18, 00-716 Warszawa, Poland

<sup>a</sup>varada@camk.edu.pl

## ABSTRACT

Our goal is to perform global simulations of thin accretion discs around compact bodies like neutron stars with dipolar magnetic profile and black holes by exploiting the facilities provided by state-of-the-art grid-based, high resolution shock capturing (HRSC) and finite volume codes. We have used the Godunov-type code PLUTO to simulate a thin disc around a compact object prescribed with a pseudo-Newtonian potential in a purely hydrodynamical (HD) regime, with numerical viscosity as a first step towards achieving our goal as mentioned above.

**Keywords:** Accretion discs – pseudo-Newtonian – PLUTO – hydrodynamics – compact objects – black holes

## 1 INTRODUCTION

Disc like structures are ubiquitous as known from several astronomical observations. It is now understood that these are the result of accretion flows, which have been studied by the astrophysical community since 1968. The first analytic solution was obtained by Shakura and Sunyaev (1973), hereafter SS, preceded by a numerical solution obtained by Prendergast and Burbidge (1968). The model of SS was geometrically thin steady accretion discs and since 1973, their approach has become a standard framework, which assumes that irrespective of the physics involved in the production of stress, the result scales with the pressure. The main features of the SS model are the  $\alpha$  viscosity prescription and the assumption of vertical extent of the disc being smaller than its radial scale. This gives rise to a small parameter or disc-aspect ratio  $\epsilon \equiv c_s/\Omega r$ , where  $c_s$  is the sound speed and  $\Omega$  is the Keplerian angular velocity, which allows detailed solutions for the flow (Kluźniak and Kita, 2000; Regev and Gitelman, 2002). The origin of viscosity in accretion discs and the exact mechanism of angular momentum transport is still not understood with clarity, since  $\alpha$  prescription is valid for vertically averaged thin discs, however it is worth noting that Balbus and Hawley (1991) have proposed the magneto-rotational instability (MRI) as the origin of MHD turbulence, which is efficient in transporting angular momentum. There is a consensus that MRI is the origin of viscosity in accretion discs.

Our motivation to perform numerical simulations is to determine an appropriate model in three dimensional time-evolution scenario, which incorporates known physical ideas along with a robust numerical scheme.

## 2 NUMERICAL CODE: PLUTO

PLUTO (Mignone et al., 2007) is a Godunov-type shock-capturing code, constructed to integrate system of conservation laws given as

$$\frac{\partial \mathbf{U}}{\partial t} = -\nabla \cdot \mathbf{T}(\mathbf{U}) + \mathbf{S}(\mathbf{U}), \quad (1)$$

where  $\mathbf{U}$  represents a state vector of conserved quantities,  $\mathbf{T}(\mathbf{U})$  represents fluxes of each component of state vector and  $\mathbf{S}(\mathbf{U})$  defines the source terms. PLUTO provides a modular environment capable of simulating hypersonic flows in presence of discontinuities in multi-dimensional Cartesian and curvilinear coordinates. The code in its current version (v4.0) is equipped with four independent physics modules, namely hydrodynamics (HD), magnetohydrodynamics (MHD), relativistic hydrodynamics (RHD) and relativistic magnetohydrodynamics (MHD), which perform numerical integration of the Euler/Navier–Stokes equations, ideal/resistive MHD equations, energy-momentum conservation laws of special relativistic perfect gas, and equations of special relativistic magnetized ideal plasma.

In the HD module we numerically solve the following equations:

$$\frac{\partial \rho}{\partial t} + \nabla \cdot (\rho \mathbf{v}) = 0, \quad (2)$$

$$\frac{\partial \rho \mathbf{v}}{\partial t} + \nabla \cdot (\rho \mathbf{v} \mathbf{v} + p \mathbf{I}) = -\rho \nabla \Phi, \quad (3)$$

$$\frac{\partial E}{\partial t} + \nabla \cdot [(E + p) \mathbf{v}] = \rho \mathbf{v} \cdot \mathbf{g}, \quad (4)$$

where the conservative variables, fluxes and source terms are

$$\mathbf{U} = \begin{pmatrix} \rho \\ \mathbf{m} \\ E \end{pmatrix}, \quad \mathbf{T}(\mathbf{U}) = \begin{pmatrix} \rho \mathbf{v}^T \\ \rho \mathbf{v} \mathbf{v} + p \mathbf{I} \\ (E + p) \mathbf{v}^T \end{pmatrix}, \quad \mathbf{S}(\mathbf{U}) = \begin{pmatrix} 0 \\ -\rho \nabla \Phi \\ \rho \mathbf{v} \cdot \mathbf{g} \end{pmatrix}. \quad (5)$$

The mass density is  $\rho$ , momentum density is  $\mathbf{m} = \rho \mathbf{v}$ , pressure is  $p$ , acceleration vector is  $\mathbf{g}$  and the total energy density  $E$  is

$$E = \rho \epsilon + \frac{\mathbf{m}^2}{2\rho}, \quad (6)$$

where an equation of state provides the closure  $p = p(\rho, \epsilon)$ . For a polytrope<sup>1</sup>, with  $\gamma = 5/3$ , the total energy density is

$$E = \frac{p}{\gamma - 1} + \frac{\mathbf{m}^2}{2\rho}. \quad (7)$$

In PLUTO, the numerical integration of Eq. (1) is performed with high-resolution shock-capturing scheme (HRSC), where the algorithm employed will capture the discontinuities

<sup>1</sup> In this code adiabatic index is same as polytropic index, hence  $\gamma = \Gamma$ .

in the solution and smear them over few grid cells, without producing spurious oscillations near the discontinuities, using finite volume methods in which discrete data is represented as averages over a control volume on structured grids. Generically, the paradigm of HRSC was developed by merging Godunov-type methods with advanced numerical methods, capable of obtaining higher order accuracy in smooth parts of the solution and provide higher resolution of discontinuities without large smearing over grids.

### 3 NUMERICAL SIMULATIONS

#### 3.1 Initial Conditions

We perform simulations in spherical coordinates  $(R, \theta)$ , in 2.5 dimensions (2.5D) assuming axisymmetry around the rotation axis of the disc. The 2.5D considers two spatially independent coordinates, but all three components of velocities (also magnetic fields if present). The setup (Zanni and Ferreira, 2009) consists of a thin disc, a corona and a compact body at the center whose gravitational potential (Kluźniak and Lee, 2002) we take to be

$$\Phi(R) = -\frac{1}{6} \exp\left(\frac{6r_g}{R} - 1\right), \quad (8)$$

where gravitational radius  $r_g = 1$ . The initial density and thermal pressure of the disc are determined by the vertical hydrostatic equilibrium

$$\rho_d = \left(\frac{2}{5\epsilon^2} \left[\frac{1}{R} - \left(1 - \frac{5\epsilon^2}{2}\right) \frac{1}{r}\right]\right)^{3/2}, \quad (9)$$

$$p_d = \epsilon^2 \rho_d^{5/3}, \quad (10)$$

where cylindrical radius is given as  $r = R \sin(\theta)$ ,  $\gamma = 5/3$ ,  $\epsilon = 0.1$ . The azimuthal velocity is obtained from the radial equilibrium

$$v_{\phi d} = \sqrt{\frac{\exp\left(\frac{6}{r} - 1\right)}{r}} \quad (11)$$

and the meridional flow is given as

$$v_{Rd} = -\alpha\epsilon^2 \left[10 - \frac{32}{3} \Lambda\alpha^2 - \Lambda \left(5 - \frac{1}{\epsilon^2 \tan^2 \theta}\right)\right] \sqrt{\frac{1}{R \sin^3 \theta}}, \quad (12)$$

with  $\alpha = 0.01$  and  $\Lambda = 11/5 (1 + 64\alpha^2/25)$ . The corona is a non-rotating polytrope, with density and pressure given as

$$\rho_c = \rho_a \left(\frac{1}{R}\right)^{\frac{1}{\gamma-1}}, \quad p_c = \frac{\gamma-1}{\gamma} \left(\frac{1}{R}\right)^{\frac{\gamma}{\gamma-1}}. \quad (13)$$

The density contrast between corona and disc is set by the parameter  $\rho_a = 0.01$ .

### 3.2 Computational Domain and Boundary Conditions

The computational domain is a two dimensional box in  $(R, \theta)$ , angular coordinate spanning the sector  $[0, \pi/2]$  and delimited by the radial coordinate extending over  $[3, 20]$ . Both the radial and angular coordinates are discretized with 127 points on a uniform grid. As we perform 2.5D simulation there is axisymmetry about the rotation axis and planar symmetry with respect to the disc mid-plane. At the inner edge of the disc, we employ outflow (zero gradient) boundary condition and at the outer edge of the disc we prescribe a numerical condition, such that the flow from the inner boundary is fed back to the outer boundary, which aids in conserving the mass by preventing the disc from being drained.

### 3.3 A Note On Viscosity

In the simulation reported here we have not employed a physical prescription for viscosity, which in PLUTO is achieved by adding viscous stress tensor to Eq. (1)

$$\frac{\partial \mathbf{U}}{\partial t} + \nabla \cdot \mathbf{T} = \nabla \cdot \mathbf{\Pi} + \mathbf{S}, \quad (14)$$

where  $\mathbf{\Pi}$  is the viscous stress tensor, with components

$$(\mathbf{\Pi})_{ij} = 2 \frac{\eta}{h_i h_j} \left( \frac{v_{i;j} + v_{j;i}}{2} \right) + \left( \eta_b - \frac{2}{3} \eta \right) \nabla \cdot \mathbf{v} \delta_{ij}, \quad (15)$$

where  $\eta$ ,  $\eta_b$  are shear and bulk coefficient of viscosity,  $v_{i;j}$ ,  $v_{j;i}$  are covariant derivatives, and  $h_i$ ,  $h_j$  are geometrical elements in the corresponding directions respectively.

The most conspicuous phenomenon while performing numerical simulations of the equations of fluid dynamics is shock waves, which physically is a transition zone across which ram pressure is converted into thermal pressure and kinetic energy into enthalpy. Numerical treatment of shocks<sup>2</sup> is a complicated issue, which was dealt with by adding large but non-physical value of viscosity to the algorithms such that the narrow transition zones got thickened and it was possible to handle shocks computationally. This is known as artificial viscosity, introduced for numerical purposes for ease in computational treatment of physical processes. It is to be noted that artificial viscosity is different from numerical viscosity which is a result of smoothing effect.

Convective flux exchanges momentum between neighbouring elements and the resultant in a given element is then added to the existing momentum in order to get an average for that element. As the time step advances the previously calculated average value is passed to the next element and consecutive steps of such smoothing effect will create a diffusion of momentum along the flow. However such a numerical diffusion which depends only on fluid convection, does not work like viscous stress as shown in Eq. (15) which satisfies well known physical laws. We still exploit numerical viscosity for our simulation by simply trusting the robustness of the approximate numerical schemes in PLUTO, that has been tested against several benchmark test problems.

<sup>2</sup> Personal communication with numerical experts.

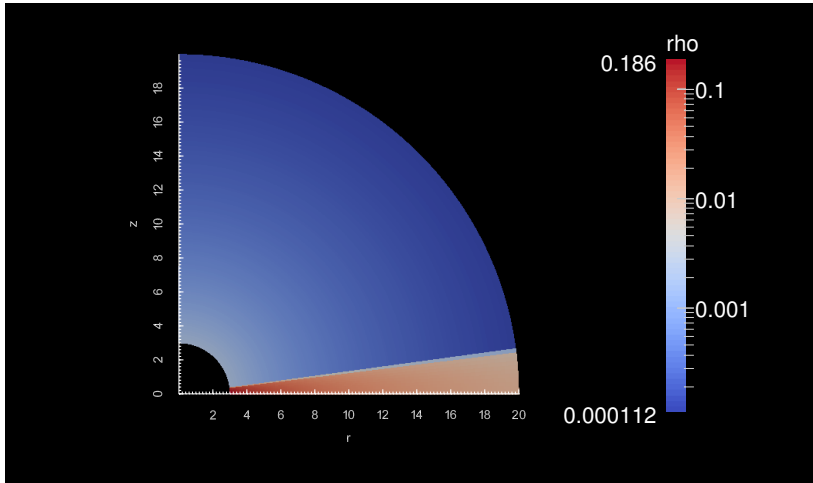


**Figure 1.** The initial appearance of disc and corona. Colours represent logarithmic density.

### 3.4 Discussion of Simulations

Our simulation is intended to be a substrate on which we plan to work further and not a scientific result at present. We perform the simulation for about 100 orbital periods corresponding to the innermost stable circular orbit. We observed that the part of the disc within the innermost stable circular orbit was not stable and in a few rotations the disc relaxed by shedding some of its mass, which through our boundary condition was fed back to the disc, thereby preventing the disc from being drained. As expected the disc finally reaches stationary state with the inner edge at the innermost stable circular orbit ( $r = 6$ ). As mentioned previously we have used numerical viscosity, which is responsible for transporting angular momentum outwards. We have delimited the angular sector such that the radial grid starts three units from the origin due to numerical reasons. While testing our routines further, we are able to overcome this issue by physical prescription of viscosity, however due to constraints in time we are yet to perform simulations with physical viscosity.

We present the results obtained from our simulation as follows. Figure 1 shows the initial appearance of the disc and corona described by Eqs. (9) and (13). The evolution of the disc into a steady state following a relaxation process is shown in Figs. 2 and 3 and the distribution of density at the midplane of the disc is plotted in Figs. 4 and 5 respectively. The profiles of the azimuthal velocity at the midplane of the disc are plotted in Figs. 6 and 7, comparison of these two figures shows the stability of the velocity profile at  $t \geq 10$ .

## 4 CONCLUSIONS

We have performed numerical simulations using the hydrodynamical module in PLUTO to obtain steady thin discs around a compact object prescribed with a pseudo-Newtonian potential. The disc relaxes in few rotations and reaches a steady state with its inner edge

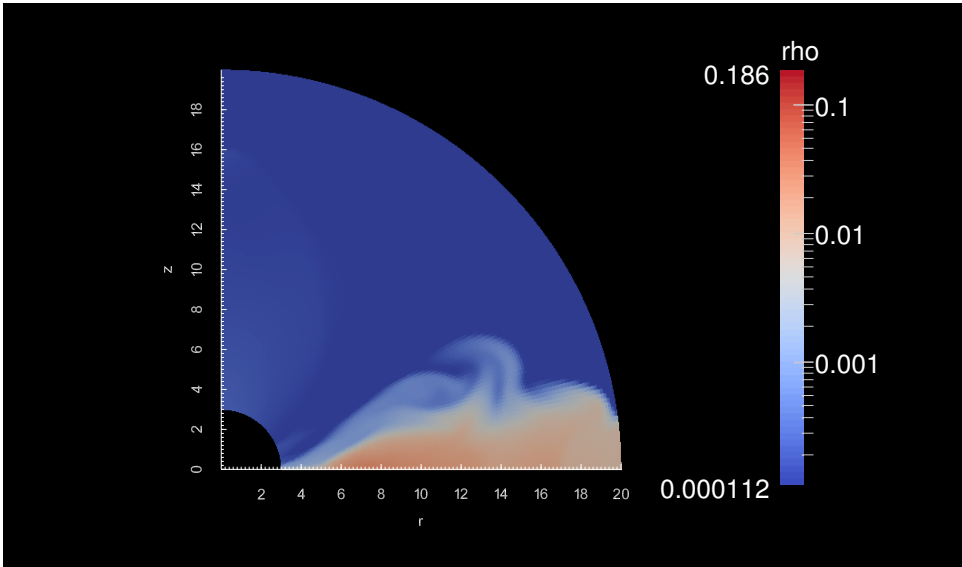


**Figure 2.** Logarithmic plot of density at  $t = 10.0$ .

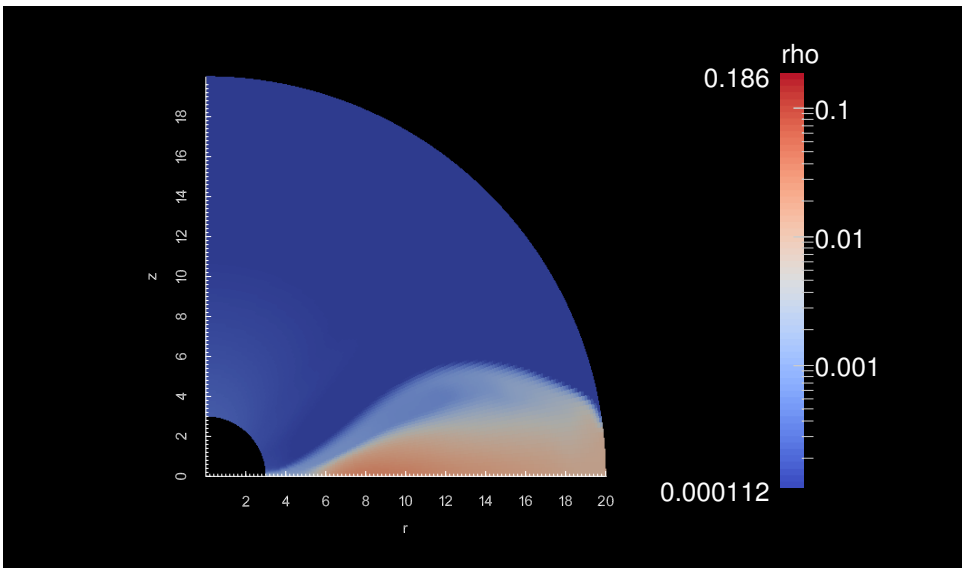


**Figure 3.** Logarithmic plot of density at  $t = 70.0$ .

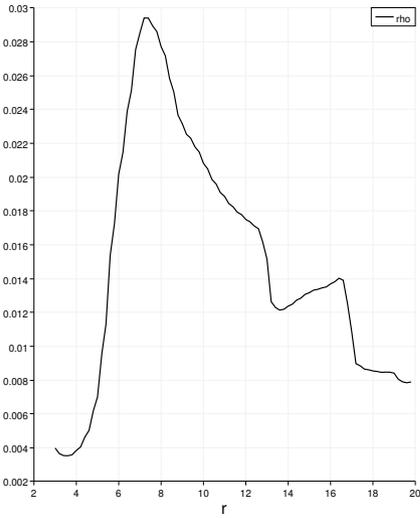


**Figure 4.** Density in the midplane of disc at  $t = 10.0$ .

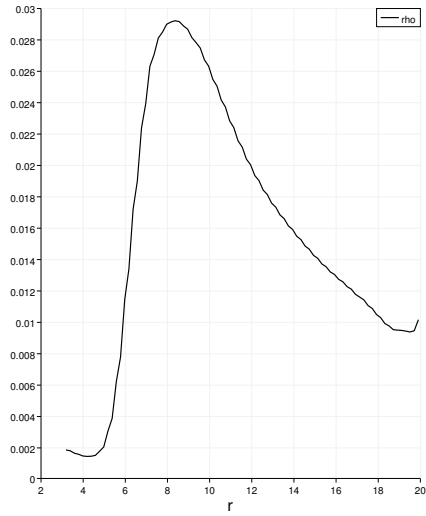


**Figure 5.** Density in the midplane of disc at  $t = 70.0$ .

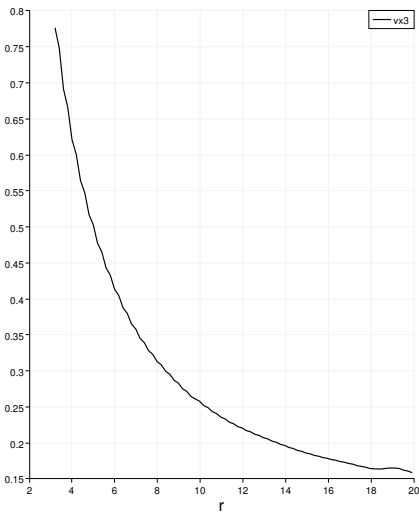


**Figure 6.** Keplerian profile of azimuthal velocity in the midplane of disc at  $t = 10.0$ .

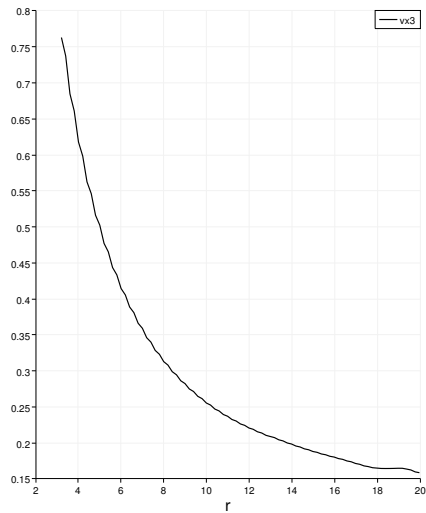


**Figure 7.** Keplerian profile of azimuthal velocity in the midplane of disc at  $t = 70.0$ .

at innermost stable circular orbit. The profile of the azimuthal velocity remains Keplerian throughout. We plan to improve our routines in the code and successfully perform global simulations of thin discs around neutron stars with dipolar magnetic field.

## ACKNOWLEDGEMENTS

We would like to acknowledge Dr. Miljenko Čemeljić for his crucial guidance and interesting discussions with nuances of the code. This work was supported by NCN grant 2013/08/A/ST9/00795.

## REFERENCES

- Balbus, S. A. and Hawley, J. F. (1991), A powerful local shear instability in weakly magnetized disks. I - Linear analysis. II - Nonlinear evolution, *Astrophys. J.*, **376**, pp. 214–233.
- Kluźniak, W. and Kita, D. (2000), Three-dimensional structure of an alpha accretion disk, *ArXiv Astrophysics e-prints*, arXiv: astro-ph/0006266.
- Kluźniak, W. and Lee, W. H. (2002), The swallowing of a quark star by a black hole, *Monthly Notices Roy. Astronom. Soc.*, **335**, pp. L29–L32, arXiv: astro-ph/0206511.
- Mignone, A., Bodo, G., Massaglia, S., Matsakos, T., Tesileanu, O., Zanni, C. and Ferrari, A. (2007), PLUTO: A Numerical Code for Computational Astrophysics, *Astrophys. J. Suppl.*, **170**, pp. 228–242, arXiv: astro-ph/0701854.
- Prendergast, K. H. and Burbidge, G. R. (1968), On the Nature of Some Galactic X-Ray Sources, *Astrophys. J. Lett.*, **151**, p. L83.
- Regev, O. and Gitelman, L. (2002), Asymptotic models of meridional flows in thin viscous accretion disks, *Astronomy and Astrophysics*, **396**, pp. 623–628, arXiv: astro-ph/0210293.
- Shakura, N. I. and Sunyaev, R. A. (1973), Black holes in binary systems. Observational appearance., *Astronomy and Astrophysics*, **24**, pp. 337–355.
- Zanni, C. and Ferreira, J. (2009), MHD simulations of accretion onto a dipolar magnetosphere. I. Accretion curtains and the disk-locking paradigm, *Astronomy and Astrophysics*, **508**, pp. 1117–1133.

# Radiating perfect fluid tori in static braneworld spacetime: frequency shift map of torus image

Jan Schee, Pavlína Adámková and Zdeněk Stuchlík

Institute of Physics, Faculty of Philosophy & Science, Silesian University in Opava,  
Bezručovo nám. 13, CZ-746 01 Opava, Czech Republic

## ABSTRACT

The imprints of the tidal-charge parameter  $b$  are determined for the spectral line profiles generated by radiation from the surface of optically thick perfect-fluid tori orbiting a spherically symmetric braneworld black holes. We assume that each point on the surface radiates isotropically at a fixed spectral line frequency. We give the direct and indirect image of a torus and the spectral line profile in dependence on the impact parameter for a large inclination angle to the distant observer when the relativistic effects are strongest. We give the map of the frequency shift across the surface and dependence of the maximal and minimal frequency shift of the radiation from the tori surface, giving thus a relevant information on the tidal charge parameter  $b$ .

## INTRODUCTION

The quantum gravity effects take place in the Planck energy scale where the classical Einstein theory of gravity breaks down. The classical black hole and big bang physical singularities are assumed to be removed by the quantum gravity. However, traces of the quantum gravity effects can be expected even on the energy scales substantially below the Planck scale making the quantum gravity potentially testable. Among many candidates to quantum gravity there are two leading theories, namely the M-theory and the loop quantum gravity. In this paper we consider some effects predicted by the Randall–Sundrum (RS) model that arises from the M-theory (Randall and Sundrum, 1999). The RS model assumes a large scale hidden dimension and can be considered as a practical framework to study possible imprints of the string theory in astrophysical phenomena, using the simple modifications of the standard models of self-gravitating objects like black holes or naked singularities. In the case of the so called braneworld models of black holes the effect of gravity in the hidden dimension is reflected by a single parameter, called tidal charge due to the formal analogy with the electromagnetic effects (Dadhich et al., 2000; Aliev and Gümrukçuoğlu, 2005; Schee and Stuchlík, 2009a,b; Stuchlík and Kotrlová, 2009). The astrophysical phenomena can then put restrictions on the parameters of the braneworld models of black holes.

## 1 STATIC AND SPHERICALLY SYMMETRIC BRANEWORLD BLACK HOLE

In the framework of M-theory (string theory), gravitation is truly higher-dimensional interaction that becomes effectively 4D at energies low enough,  $E < E_{\text{pl}}$ . In the braneworld models, the observable universe is a 3-brane to which the electromagnetic, weak and strong forces (non-gravitational matter fields), described by the standard model, are confined while gravity can enter the extra spatial dimension. The size of such dimension can be much larger than  $l_{\text{pl}} \simeq 10^{-33}$  cm.

Randall and Sundrum (1999) have shown that gravity can be localized near the brane at low energies even in the case of non-compact, infinite size extra spatial dimensions. The corresponding warped spacetimes satisfy 5D Einstein field equations which induce braneworld field equations. The braneworld constrained equations can be given in the form of modified Einstein equations containing additional terms which reflect the bulk effects onto the brane. The vacuum, spherically symmetric solution of the constrained braneworld equations, in the standard Schwarzschild coordinates, reads (Dadhich et al., 2000)

$$ds^2 = -f(r) dt^2 + \frac{1}{f(r)} dr^2 + r^2 d\theta^2 + r^2 \sin^2 \theta d\phi^2, \quad (1)$$

where the lapse function takes the form

$$f(r) = 1 - \frac{2M}{r} + \frac{\tilde{b}}{r^2} = 1 - \frac{2}{r} + \frac{b}{r^2}. \quad (2)$$

Parameter  $\tilde{b} \equiv bM^2$  is the braneworld parameter called tidal charge that is reflecting the back reaction of the bulk gravity on the brane. Usually,  $b < 0$  is assumed, but  $b > 0$  is also considered (see Schee and Stuchlík, 2009a).

The loci of event horizons are given by the condition

$$f(r) = 0, \quad (3)$$

which yields

- two horizon black hole

$$r_{\text{H}\pm} = 1 \pm \sqrt{1 - b} \quad \text{for } b < 1, \quad (4)$$

- one horizon black hole

$$r_{\text{H}} = 2 \quad \text{for } b = 1, \quad (5)$$

- naked singularity for  $b > 1$ .

## 2 MOTION OF PHOTONS

The test particle and photon equations of motion are given by the geodesics of the spacetime and in the metric (1) they are separable by Hamilton–Jacobi method. In the case of massless

particles (photons) they read

$$\frac{dr}{dw} = \pm \sqrt{1 - f(r) \frac{\lambda^2 + q}{r^2}}, \quad (6)$$

$$\frac{d\theta}{dw} = \pm \frac{1}{r^2} \sqrt{q - \lambda^2 \cot^2 \theta}, \quad (7)$$

$$\frac{dt}{dw} = \frac{1}{f(r)}, \quad (8)$$

$$\frac{d\phi}{dw} = \frac{\lambda}{r^2 \sin^2 \theta}, \quad (9)$$

where we have introduced constants of motion  $\lambda = -p_\phi/p_t$  and  $q$  reflecting the components of the angular momentum of the particle. In the spherically symmetric spacetimes, the motion occurs always in a central plane of the geometry.

The turning points of the radial motion, if they exists for given constants of motion  $\lambda$  and  $q$ , are represented by the roots of the polynomial equation

$$r^2 - f(r)\mathcal{L} = r^4 + \mathcal{L}r^2 - 2\mathcal{L}r + \mathcal{L}b = 0. \quad (10)$$

$\mathcal{L} = \lambda^2 + q$  represents the total angular momentum of the particle.

In the case of the latitudinal motion, the turning points occur at

$$\theta = \tan^{-1} \sqrt{\frac{q}{\lambda^2}}. \quad (11)$$

### 3 TEST PERFECT FLUID TORI

The structure and shape of test perfect fluid tori is determined by the relativistic Euler equation. It can be obtained by the following procedure (Kozłowski et al., 1978; Stuchlík et al., 2000):

- The perfect fluid energy-momentum tensor components  $T_{\mu\nu}$  relative to coordinate basis read

$$T_{\mu\nu} = (p + \rho)U_\mu U_\nu - pg_{\mu\nu}, \quad (12)$$

where  $p$  ( $\rho$ ) is the perfect fluid pressure (energy density) and  $g_{\mu\nu}$  are the metric components.

- The elements of the perfect fluid move along circular trajectories, i.e. their four-velocity components read

$$U^\mu = (U^t, 0, 0, U^\phi). \quad (13)$$

- The Euler equation can be cast as

$$\frac{\nabla_\mu p}{p + \rho} = -\nabla_\mu \ln(U_t) + \frac{\Omega \nabla_\mu l}{1 - \Omega l}, \quad (14)$$

where  $\Omega(l)$  is the angular velocity (angular momentum) of the fluid element, being defined by

$$\Omega = \frac{U^\phi}{U^t}, \quad l = -\frac{U_\phi}{U_t}. \quad (15)$$

For barotropic fluid ( $p = p(\rho)$ ) it follows from Eq. (14) that there exists an invariant function  $\Omega = \Omega(l)$  and surfaces of constant pressure are given by Boyer's condition

$$\int_0^p \frac{dp}{p + \rho} = W(p) - W(0) = -\ln \frac{U_t}{(U_t)_{\text{in}}} + \int_{l_{\text{in}}}^l \frac{\Omega dl}{1 - \Omega l}. \quad (16)$$

• To obtain a particular structure, one has to specify the functions  $\Omega = \Omega(l)$  and  $l = l(r, \theta)$ . In the case of a marginally stable torus, the specific angular momentum of the fluid element remains constant across the toroid,  $l = l_0 = \text{const}$ . The angular velocity of the fluid then reads

$$\Omega = -\frac{g_{tt}}{g_{\phi\phi}} l_0 = \frac{f(r)}{r^2 \sin^2 \theta} l_0. \quad (17)$$

Under these assumptions, the function  $W = W(r, \theta)$  takes the simple form

$$W(r, \theta) = \ln U_t, \quad (18)$$

where  $U_t$  follows from normalization of the four-velocity  $U^\mu$ ,  $-1 = U_\mu U^\mu$ , and reads

$$(U_t)^{-2} = \frac{g_{\phi\phi} + l_0^2 g_{tt}}{g_{tt} g_{\phi\phi}} = \frac{r^2 \sin^2 \theta - f(r) l_0^2}{f(r) r^2 \sin^2 \theta}. \quad (19)$$

The final form of the potential given by Eq.(18) reads

$$W(r, \theta) = \frac{1}{2} \ln U_t^2 = \frac{1}{2} \ln \left[ \frac{f(r) r^2 \sin^2 \theta}{r^2 \sin^2 \theta - f(r) l_0^2} \right]. \quad (20)$$

#### 4 FREQUENCY SHIFT MAP ON THE TORUS IMAGE

In order to illustrate imprints of the braneworld tidal charge parameter  $b$  in radiation emitted from the surface of toroidal configurations orbiting the braneworld spherically symmetric black hole, we use several assumptions that simplify the situation to give clear signatures of the tidal charge. We assume the torus to be marginally stable, having  $l = \text{const}$ , being optically thick, and radiating from the surface where the elements of orbiting torus radiate isotropically and at a frequency fixed across the whole surface. We give the shape and frequency shift map of the radiation from the surface of the torus. Since the frequency of the surface radiation is assumed to be constant, we can construct the profiled spectral lines related to such toroidal configuration. We give also the map of the maximal and minimal frequency shift from the torus surface in dependence on the tidal charge parameter. In our

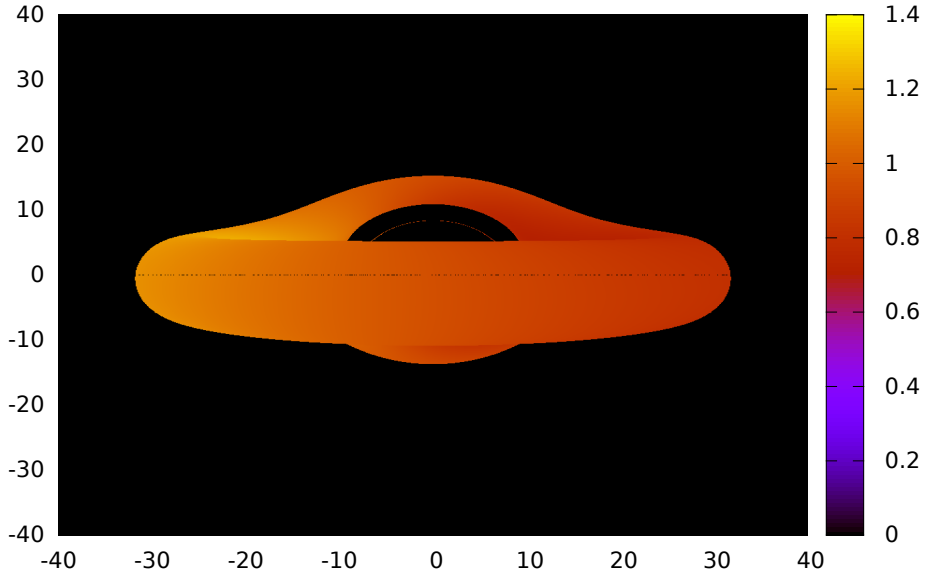


**Figure 1.** Illustrative example of the torus image and the frequency-shift map. The braneworld parameter is put to  $b = -6$  and the observer inclination angle is  $\theta_o = 85^\circ$ . The colour of the torus depicts the frequency shift labeled by the colour code covering the frequency-shift range  $g \in (0, 1.4)$ .

calculations we use the techniques developed for the braneworld black hole spacetimes in our previous works (Schee and Stuchlík, 2009a,b; Stuchlík and Kotrllová, 2009).

The frequency shift of the radiation is determined by the formula

$$g = \frac{(k_\mu U^\mu)_{\text{obs}}}{(k_\mu U^\mu)_{\text{em}}} = \frac{[f(r) - \Omega r^2 \sin^2 \theta]^{1/2}}{1 - \lambda \Omega}, \quad (21)$$

where  $\lambda$  is the impact parameter of the received photon and  $\Omega$  is the angular velocity of the radiating element relative to distant observer.

For a series of braneworld parameter  $b$ , we have constructed corresponding series of the perfect fluid tori using the following procedure:

- for given braneworld parameter  $b$  the Keplerian marginally bound orbit of radius  $r_{\text{mb}}$  is determined,
- the corresponding angular momentum of the fluid element in the torus is calculated,  $l_{\text{torus}} = l_{\text{K}}(r_{\text{mb}}, b)$  where  $l_{\text{K}}$  is angular momentum of the Keplerian orbit and is given by the formula (Stuchlík and Kotrllová, 2009)

$$l_{\text{K}} = \frac{r^2}{f(r)} \Omega_{\text{K}}, \quad \Omega_{\text{K}} = \sqrt{\frac{r-b}{r^4}}, \quad (22)$$

- the value of  $l_{\text{torus}}$  is used to specify value of the potential  $W$  at the torus surface

$$W_{\text{surf}} = hW(r_{\text{AtMin}}, \pi/2; l_{\text{torus}}), \quad (23)$$

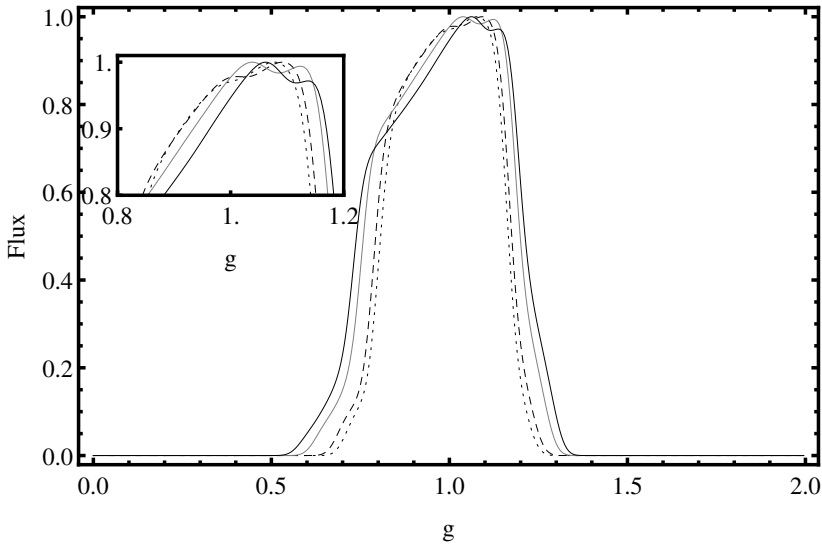


**Figure 2.** Spectral line profile of radiation from thick tori as detected by observer with inclination  $\theta_o = 85^\circ$  generated for four representative values of braneworld parameter  $b = -6$  (dotted),  $-4$  (dashed),  $-1$  (thin), and  $0$  (thick).

where we have chosen  $h = 0.9$  and  $r_{\text{AtMin}}$  is the location of the minimum of the potential  $W$ , determined from the condition

$$\frac{dW}{dr} = 0 \Rightarrow l_{\text{torus}}^2 [b + (r - 2)r]^2 + (b - r)r^4 = 0. \quad (24)$$

Having determined the surface of the marginally stable torus for particular brane-world parameter  $b$ , we integrate the equations of motions of photon having impact parameters  $(\lambda, q)$  corresponding to  $(\alpha, \beta)$  detector plane coordinates and look for intersection of such null geodesic with the torus surface,  $(r_i, \theta_i)$ ; the corresponding frequency shift  $g = g(r_i, \theta_i)$  has been calculated from (21) – for details see (Schee and Stuchlík, 2009a,b).

## 5 RESULTS

As an illustrative example the image of the marginally stable ( $l = \text{const}$ ) torus seen by a distant observer having inclination  $\theta_o = 85^\circ$  is shown in Fig. 1. The frequency-shift map is given by the colour varied across the surface of the torus.

Using the methods presented in (Schee and Stuchlík, 2009b), the profiled spectral lines of radiation from whole the torus surface are given in Fig. 2 for some characteristic values of the tidal charge parameter  $b$ . We can see that the imprint of the tidal charge is quantitative only, but it is well measurable in principle.

There are minimal,  $g_{\text{min}}$ , and maximal,  $g_{\text{max}}$ , values of the frequency shift of radiation from the torus surface having a fixed frequency. The qualitative and quantitative effect of braneworld parameter is reflected in the plots of the  $g_{\text{min}}$  ( $g_{\text{max}}$ ) values for series values of braneworld parameter  $b$  given in Fig. 3.

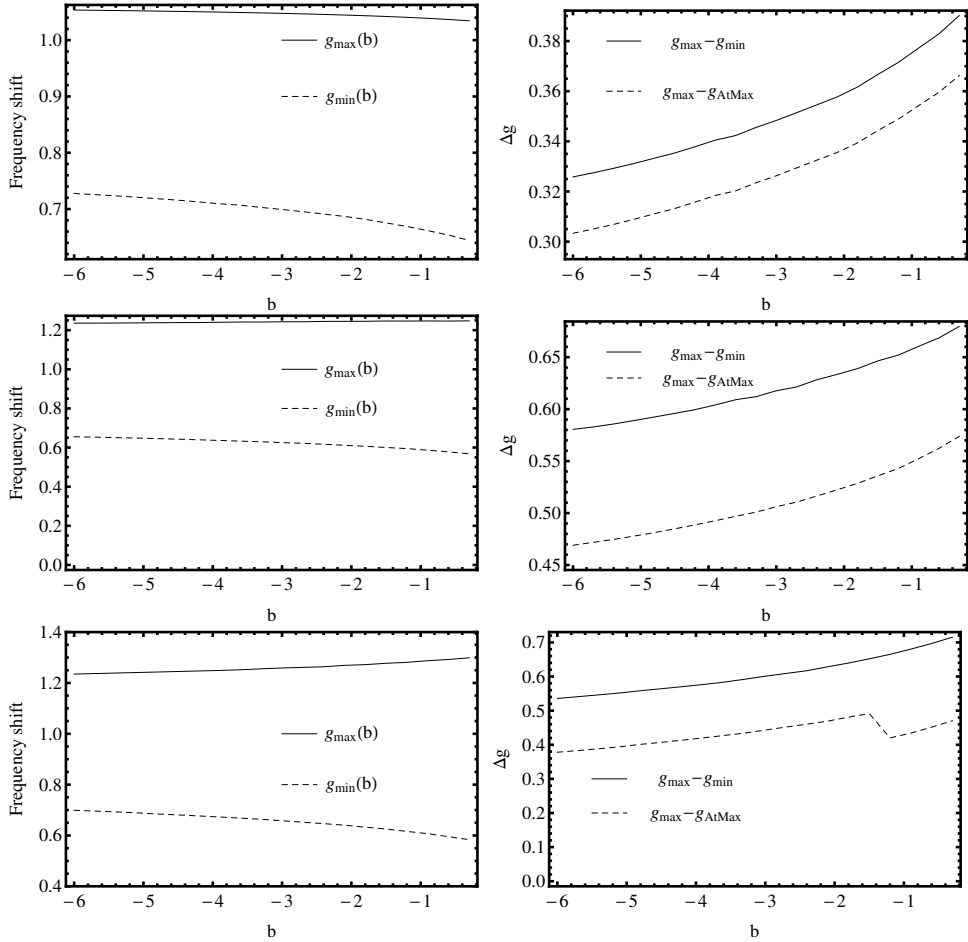


**Figure 3.** The frequency minimal (maximal) shift  $g_{\min}$  ( $g_{\max}$ ) plotted in the *left* figure and the frequency shift differences  $\Delta g(b) = g_{\max}(b) - g_{\min}(b)$  and  $\tilde{\Delta g} = g_{\max}(b) - g_{\text{AtMax}}(b)$  plotted in the figure on the *right*. The parameter  $g_{\text{AtMax}}$  is the frequency shift corresponding to maximal specific flux of the profiled line. The observer inclination is  $\theta_o = 30^\circ$  (*top*),  $60^\circ$  (*middle*) and  $85^\circ$  (*bottom*).

The values of  $g_{\min}$  and  $g_{\max}$  determine the width of the profile of spectral line  $\Delta g$ . From the Figure 2 (left column plots and solid lines in the plots in right column), one can conclude that the value of  $\Delta g$  increase with increasing value of braneworld parameter  $b$ . So for the case of  $b = 0$  the width  $\Delta g$  is largest while for  $b = -6$  it reaches the smallest value.

We have defined also a new parameter

$$\tilde{\Delta g} = g_{\max}(b) - g_{\text{AtMax}}(b) \quad (25)$$

reflecting more subtle character of profiled spectral line. One can see that for small and intermediate inclination angles its behaviour is similar to  $\Delta g$ . However in the case of high inclination angle,  $\theta_o = 85^\circ$ , there is discontinuity in  $\tilde{\Delta g}$  reflecting the change of position

of the flux maximum, as we vary the value of braneworld parameter. The maximum moves from the right for  $b = -6$  to middle for  $b = 0$  as one can see also in Fig. 2. To determine how much the choice of the tori sequence influence this effect we shall run another sequences which we postpone to a future work.

## 6 CONCLUSIONS

We can conclude that the toroidal configuration orbiting in the field of the braneworld black holes can give clear signatures of the influence of the tidal charge parameter of the braneworld. The most useful seem to be the maps of the frequency shift. However, the profiled spectral lines can give a relevant information too.

## ACKNOWLEDGEMENTS

The authors would like to thank the internal student grant SGS/23/2013 of the Silesian University, the EU grant Synergy CZ.1.07/2.3.00/20.0071. JS and ZS acknowledge the Albert Einstein Centre for gravitation and astrophysics supported by the Czech Science Foundation Grant No. 14-37086G.

## REFERENCES

- Aliev, A. N. and Gümrukçüoğlu, A. E. (2005), Charged rotating black holes on a 3-brane, *Phys. Rev. D*, **71**, p. 104027.
- Dadhich, N., Maartens, R., Papadopoulos, P. and Rezanian, V. (2000), Black holes on the brane, *Phys. Rev. B*, **487**, p. 1.
- Kozłowski, M., Jaroszynski, M. and Abramowicz, M. A. (1978), The analytic theory of fluid disks orbiting the kerr black hole, *Astronomy and Astrophysics*, **63**, pp. 209–220.
- Randall, L. and Sundrum, R. (1999), An alternative to compactification, *Phys. Rev. Lett.*, **83(23)**, pp. 4690–4693.
- Schee, J. and Stuchlík, Z. (2009a), Optical phenomena in the field of braneworld kerr black holes, *Internat. J. Modern Phys. A*, **18**, pp. 983–1024.
- Schee, J. and Stuchlík, Z. (2009b), Profiles of emission lines generated by rings orbiting braneworld kerr black holes, *General Relativity and Gravitation*, **41**, pp. 1795–1818.
- Stuchlík, Z. and Kotrlová, A. (2009), Orbital resonances in discs around braneworld kerr black holes, *General Relativity and Gravitation*, **41**, pp. 1305–1343.
- Stuchlík, Z., Slaný, P. and Hledík, S. (2000), Equilibrium configurations of perfect fluid orbiting schwarzschild-de sitter black holes, *Astronomy and Astrophysics*, **363**, pp. 425–439.

# Equilibria of charged dust tori in a dipole magnetic field: hydrodynamic approach

Petr Slaný<sup>1,a</sup>, Jiří Kovář<sup>1</sup>, Zdeněk Stuchlík<sup>1</sup> and Vladimír Karas<sup>2</sup>

<sup>1</sup>Institute of Physics, Faculty of Philosophy & Science, Silesian University in Opava,  
Bezručovo nám. 13, CZ-746 01 Opava, Czech Republic

<sup>2</sup>Astronomical Institute, Academy of Sciences, Boční II, CZ-141 31 Prague, Czech Republic

<sup>a</sup>[petr.slany@fpf.slu.cz](mailto:petr.slany@fpf.slu.cz)

## ABSTRACT

We present Newtonian model of non-conductive charged perfect fluid tori orbiting in combined spherical gravitational and dipolar magnetic fields, focusing on stationary, axisymmetric toroidal structures. Matter in such tori exhibits a purely circulatory motion and the resulting convection carries charges into permanent rotation around the symmetry axis. As a main result we demonstrate possible existence of off-equatorial charged tori and equatorial tori with cusps enabling outflows of matter from the torus also in Newtonian regime. From astrophysical point of view, our investigation can provide an insight into processes determining vertical structure of dusty tori surrounding accretion discs.

**Keywords:** dust tori – electric charge – magnetic field – equilibrium – outflows

## 1 INTRODUCTION

Supermassive black holes of typical masses  $M_{\bullet} \simeq 10^6\text{--}10^8 M_{\odot}$  are frequently present in nuclei of galaxies, being surrounded by a torus of obscuring material (dust). Moreover, different types of active galactic nuclei in Seyfert galaxies can be unified by introducing some form of obscuring tori, which are believed to encircle the central black hole (Antonucci and Miller, 1985; Urry and Padovani, 1995). The presence of a geometrically and optically thick dusty structure is an essential component of the unification scheme (Hönig and Kishimoto, 2010). The torus structure is thought to be inhomogeneous, in the form of molecular/dusty clumps (clouds).

Equilibrium figures of gaseous tori have been studied in great detail, e.g. in Kozłowski et al. (1978); Abramowicz et al. (1978); Kato et al. (2008), however, the vertical component of the pressure gradient, required to maintain the equilibrium, does not seem to be sufficient in dusty tori (e.g. Murphy and Yaqoob, 2009 and references cited therein). Despite of the fact that signatures of obscuration (especially those seen in X-ray spectra) and variability properties strongly indicate the need for a significant vertical extent of obscuring tori in many Seyfert type 2 galaxies, the physical model for the tori remains uncertain and the vertical structure of dusty tori needs further discussion. For example, it has been proposed by Czerny and Hryniewicz (2011) that vertical motions of the dust clumps play an important role.

Due to complex electromagnetic processes like photoionisation or plasma electron and ion currents entering the grain surface, the dust particles should possess some net electric charge. In this case, the electrostatic charge is one of the essential parameters that control the dynamics of dust grains embedded in the surrounding cosmic plasma. It was shown, that when electromagnetic forces are taken into account, electrically charged matter can establish vertically extended structures that “levitate” above and under the equatorial plane. The Newtonian study of charged dust grains orbiting in planetary magnetospheres and forming halo orbits were published, e.g. in Howard et al. (1999); Dullin et al. (2002), while the question, if such halo orbits can survive also in strong gravitational fields near compact objects, was successfully answered in Kovář et al. (2008); Stuchlík et al. (2009); Kovář et al. (2010), using both pseudo-Newtonian and general relativistic studies. Of course, in many astrophysical scenarios such simple test-particle approaches fail because of higher densities of charged matter in reality. Then possible approaches follow from the kinetic theory (suitable for lower density matter) or from hydrodynamics (suitable for higher densities).

In this overview we present Newtonian hydrodynamic model of perfect fluid tori with electric charge spread through the fluid of infinite resistivity, which is an opposite limit to the well known ideal magnetohydrodynamics with zero resistivity commonly used to model many astrophysical plasmas (e.g. Punsly, 2001). In more details, the topic presented here is treated in Slaný et al. (2013). General relativistic version of our approach was published in Kovář et al. (2011, 2014) where the charged perfect-fluid tori of infinite resistivity encircling the Reissner–Nordström black hole (without any magnetic field) and Schwarzschild black hole embedded in a homogeneous magnetic field, respectively, were analysed. The kinetic approach suitable for modelling toroidal structures is outlined in Cremaschini et al. (2013).

## 2 NEWTONIAN MODEL FOR INCOMPRESSIBLE FLUID

The Euler equation for a perfect fluid orbiting in gravitational and electromagnetic fields has the form:

$$\varrho_m(\partial_t v_i + v^j \nabla_j v_i) = -\nabla_i P - \varrho_m \nabla_i \Phi + \varrho_e (E_i + \epsilon_{ijk} v^j B^k), \quad (1)$$

where  $\varrho_m$  and  $\varrho_e$  are mass-density and charge-density, respectively,  $P$  denotes pressure,  $\mathbf{v}$  is velocity field in the fluid, and  $\Phi$  corresponds to the gravitational potential. The electromagnetic field is described by its electric part  $\mathbf{E}$  and magnetic part  $\mathbf{B}$ .

Here, we assume stationary, axisymmetric flow of test charged perfect fluid in external spherical gravitational and dipolar magnetic fields. In spherical polar coordinates  $(r, \theta, \varphi)$

$$\Phi = -\frac{GM}{r}, \quad (2)$$

$$E_i = 0, \quad i = (r, \theta, \varphi), \quad (3)$$

$$B_r = 2\mu \frac{\cos \theta}{r^3}, \quad B_\theta = \mu \frac{\sin \theta}{r^3}, \quad (4)$$

where  $M$  is the mass of central object and  $\mu > 0$  corresponds to magnetic dipole moment of external magnetic field. For stationary, axisymmetric flow

$$v_r = v_\theta = 0, \quad v_\varphi = v_\varphi(r, \theta). \quad (5)$$

The condition of hydrostatic equilibrium is described by two partial differential equations, following from Euler's equation:

$$\frac{\partial P}{\partial r} = -\varrho_m \frac{GM}{r^2} + \varrho_m \frac{v_\varphi^2}{r} - \varrho_e v_\varphi \mu \frac{\sin \theta}{r^3}, \quad (6)$$

$$\frac{1}{r} \frac{\partial P}{\partial \theta} = \varrho_m \frac{v_\varphi^2}{r} \cot \theta + 2\varrho_e v_\varphi \mu \frac{\cos \theta}{r^3}. \quad (7)$$

In order to solve this set of equations, it is useful to assume charge density in the form

$$\varrho_e = \varrho_m q(r, \theta), \quad (8)$$

where  $q(r, \theta)$  describes specific charge distribution in the fluid. Further we need an equation of state.

The simplest and also very illustrative is the case of incompressible fluid characterized by condition

$$\varrho_m = \text{const}. \quad (9)$$

Analysis of integrability conditions for the set of PDEs (6) and (7) reveals that the orbital velocity  $v_\varphi$  could be of the same form as in the uncharged case, i.e.

$$v_\varphi(r, \theta) = K_2 (r \sin \theta)^{K_1}, \quad (10)$$

where  $K_1$  and  $K_2$  are constants which have to be specified. Assuming that the specific charge can be written in a separated form  $q(r, \theta) = q_1(r) q_2(\theta)$ , we obtain 4 families of specific charge distribution:

- (1)  $q(r, \theta) = C r^{-3(K_1-1)/2}$ ,
- (2)  $q(r, \theta) = C r^{3/2} (\sin \theta)^{-3K_1}$ ,
- (3)  $q(r, \theta) = C r^{-3K_1/2} \sin^3 \theta$ ,
- (4)  $q(r, \theta) = C (\sin \theta)^{3(1-K_1)}$ ,

where  $C$  is another constant.

In the centre of the torus, the pressure is expected to be maximal, descending monotonically to zero value at the torus surface. Analysis of the condition  $\nabla P = 0$  reveals that in the case of charged tori there are two possibilities for torus location: (i) *equatorial torus* with its centre in the equatorial plane ( $\theta = \pi/2$ ), (ii) *off-equatorial torus* with the centre at  $\theta \neq \pi/2$ .

## 2.1 Equatorial tori

Uncharged perfect-fluid tori are presented in many classical textbooks on accretion discs, see, e.g. Frank et al. (2002) where also their Newtonian version is presented. These structures are characterized by their equipotential surfaces of "gravito-centrifugal" potential governing the motion of a barotropic fluid in prescribed gravitational field. The equipotential surfaces coincide with isobaric surfaces,  $P = \text{const}$ . In Newtonian regime, there are closed toroidal surfaces around the circle corresponding to the centre of the torus.

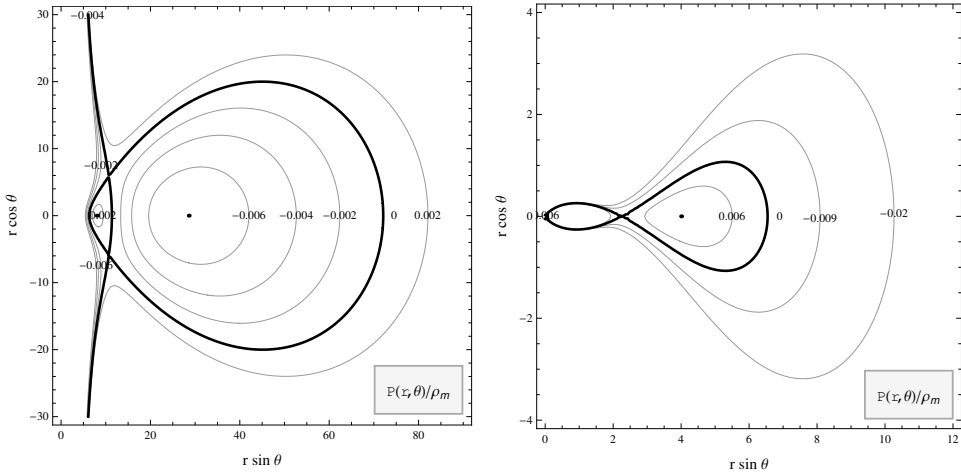


**Figure 1.** Charged Newtonian tori with cusps. The left panel shows negatively charged torus with cusps out of the equator (physically relevant torus is the small one on the *left*), while the *right* panel shows positively charged torus with the cusp in the equator.

Abramowicz and co-workers showed (Abramowicz et al., 1978; Kozłowski et al., 1978) that in relativistic regime, one of equipotential surfaces can be marginally closed containing the critical point, so-called *cusp*, in the inner edge in the equatorial plane, which enables outflow of matter from the torus and, in fact, accretion onto central compact object. Next, Stuchlík and co-workers showed, see e.g. (Stuchlík et al., 2000; Slaný and Stuchlík, 2005) that cosmic repulsion, represented by the cosmological term in Einstein equations, leads to the existence of another cusp in the structure of equipotential surfaces, now being located at the outer edge in the equatorial plane. For current value of the cosmological constant, however, the outer cusp could be relevant only for very huge toroidal structures of galactic dimensions around supermassive black holes.

In the case of charged tori, we have shown that the cusps can exist also in Newtonian regime and, moreover, that their location is not bound to the equatorial plane only. Structure of isobaric surfaces for cases with cusps is presented in Fig. 1. The left panel describes negatively charged 1<sup>st</sup>-family torus<sup>1</sup> with uniform distribution of the specific angular momentum  $\ell(r, \theta) = K_2 = \text{const}$ <sup>2</sup> and spherical distribution of the specific charge. The right panel presents positively charged 4<sup>th</sup>-family torus with uniform distribution of the specific angular momentum and radial distribution of the specific charge.

## 2.2 Off-equatorial tori

For negatively charged fluid of the 2<sup>nd</sup>, 3<sup>rd</sup> and 4<sup>th</sup> family-type there exists the possibility of stable off-equatorial tori located symmetrically above and under the equatorial plane. The situation for tori with uniform distribution of the specific angular momentum ( $K_1 = -1$ )

<sup>1</sup> In all presented situations we will expect positive rotation of the torus, i.e.  $v_\varphi > 0$  for all fluid elements. In the case of negative rotation, the electric charge of the torus would be opposite.

<sup>2</sup> Tori with constant specific angular momentum correspond to the choice  $K_1 = -1$ .

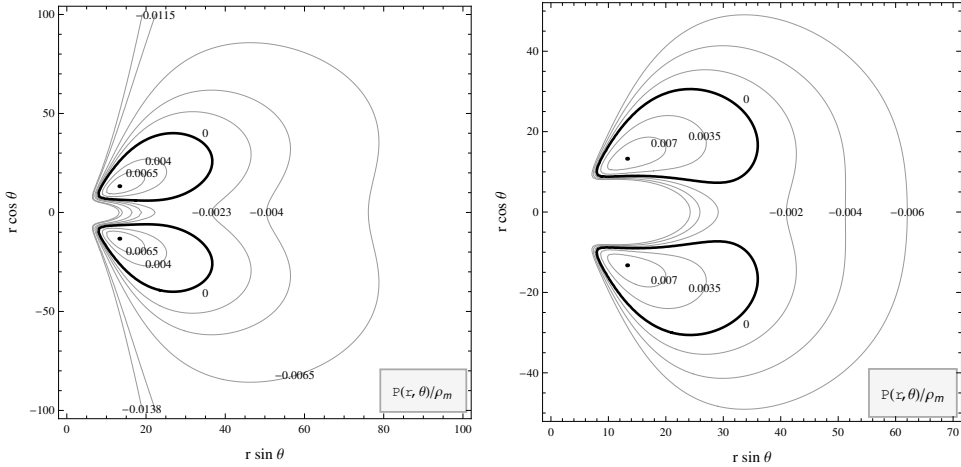


**Figure 2.** Off-equatorial negatively charged tori with cylindrical (*left panel*) and radial (*right panel*) distribution of the specific charge.

is presented in Fig. 2 where the left panel shows tori with cylindrical distribution of the specific charge (2<sup>nd</sup>-family) while the right panel shows tori with radial distribution of the specific charge (4<sup>th</sup>-family).

### 3 COMMENTS

For any perfect fluid, the basic set of partial differential equations (PDEs) (6) and (7) has the form

$$\frac{1}{\varrho_m} \frac{\partial P}{\partial r} = \mathcal{A}(r, \theta), \quad (11)$$

$$\frac{1}{\varrho_m} \frac{\partial P}{\partial \theta} = \mathcal{B}(r, \theta). \quad (12)$$

If we define a new function

$$h(r, \theta) = \frac{P}{\varrho_m}, \quad (13)$$

the above set of PDEs can be written for incompressible fluid in the form

$$\frac{\partial h}{\partial r} = \mathcal{A}(r, \theta), \quad (14)$$

$$\frac{\partial h}{\partial \theta} = \mathcal{B}(r, \theta). \quad (15)$$

Now we can think about more general fluid described by polytropic equation of state,  $P = K \varrho_m^\gamma$ . Since surfaces  $P(r, \theta) = \text{const}$  coincide with surfaces  $\varrho_m(r, \theta) = \text{const}$ , due to which they coincide also with surfaces  $h(r, \theta) = \text{const}$ , we can use the function  $h$  instead of

pressure  $P$  in the analysis of stationary configurations also for the polytropic fluid. In this case the set (11) and (12) takes the form

$$\frac{\partial h}{\partial r} = \frac{\gamma - 1}{\gamma} \mathcal{A}(r, \theta), \quad (16)$$

$$\frac{\partial h}{\partial \theta} = \frac{\gamma - 1}{\gamma} \mathcal{B}(r, \theta), \quad (17)$$

being just rescaled version of analogical set (14) and (15) for incompressible fluid. We conclude, therefore, that the results obtained for incompressible fluid are fully relevant also for the polytropic fluid.

## ACKNOWLEDGEMENTS

The present work was supported by the EU project Synergy CZ.1.07/2.3.00/20.0071. The authors also greatly appreciate support from the Czech Science Foundation (GAČR) through the project 14-37086G.

## REFERENCES

- Abramowicz, M., Jaroszynski, M. and Sikora, M. (1978), Relativistic, accreting disks, *Astronomy and Astrophysics*, **63**, pp. 221–224.
- Antonucci, R. R. J. and Miller, J. S. (1985), Spectropolarimetry and the nature of NGC 1068, *Astrophys. J.*, **297**, pp. 621–632.
- Cremaschini, C., Kovář, J., Slaný, P., Stuchlík, Z. and Karas, V. (2013), Kinetic Theory of Equilibrium Axisymmetric Collisionless Plasmas in Off-equatorial Tori around Compact Objects, *Astrophys. J. Suppl.*, **209**, 15, arXiv: 1309.3979.
- Czerny, B. and Hryniewicz, K. (2011), The origin of the broad line region in active galactic nuclei, *Astronomy and Astrophysics*, **525**, L8, arXiv: 1010.6201.
- Dullin, H. R., Horányi, M. and Howard, J. E. (2002), Generalizations of the Störmer problem for dust grain orbits, *Physica D Nonlinear Phenomena*, **171**, pp. 178–195, arXiv: nlin/0104057.
- Frank, J., King, A. and Raine, D. J. (2002), *Accretion Power in Astrophysics*, Cambridge University Press, Cambridge, third edition.
- Hönig, S. F. and Kishimoto, M. (2010), The dusty heart of nearby active galaxies. II. From clumpy torus models to physical properties of dust around AGN, *Astronomy and Astrophysics*, **523**, A27, arXiv: 0909.4539.
- Howard, J. E., Horányi, M. and Stewart, G. R. (1999), Global Dynamics of Charged Dust Particles in Planetary Magnetospheres, *Phys. Rev. Lett.*, **83**, pp. 3993–3996.
- Kato, S., Fukue, J. and Mineshige, S. (2008), *Black-Hole Accretion Disks — Towards a New Paradigm*, Kyoto University Press, Kyoto, Japan, ISBN 978-4-87698-740-5.
- Kovář, J., Kopáček, O., Karas, V. and Stuchlík, Z. (2010), Off-equatorial orbits in strong gravitational fields near compact objects – II: halo motion around magnetic compact stars and magnetized black holes, **27**(13), 135006, arXiv: 1005.3270.
- Kovář, J., Slaný, P., Cremaschini, C., Stuchlík, Z., Karas, V. and Trova, A. (2014), Electrically charged matter in rigid rotation around magnetized black hole, *Phys. Rev. D*, **90**(4), 044029, arXiv: 1409.0418.

- Kovář, J., Slaný, P., Stuchlík, Z., Karas, V., Cremaschini, C. and Miller, J. C. (2011), Role of electric charge in shaping equilibrium configurations of fluid tori encircling black holes, *Phys. Rev. D*, **84**(8), 084002, arXiv: 1110.4843.
- Kovář, J., Stuchlík, Z. and Karas, V. (2008), Off-equatorial orbits in strong gravitational fields near compact objects, *Classical and Quantum Gravity*, **25**(9), 095011, arXiv: 0803.3155.
- Kozłowski, M., Jaroszynski, M. and Abramowicz, M. A. (1978), The analytic theory of fluid disks orbiting the Kerr black hole, *Astronomy and Astrophysics*, **63**, pp. 209–220.
- Murphy, K. D. and Yaqoob, T. (2009), An X-ray spectral model for Compton-thick toroidal reprocessors, *Monthly Notices Roy. Astronom. Soc.*, **397**, pp. 1549–1562, arXiv: 0905.3188.
- Punsly, B. (2001), *Black hole gravitohydrodynamics*, Springer, New York.
- Slaný, P., Kovář, J., Stuchlík, Z. and Karas, V. (2013), Charged Tori in Spherical Gravitational and Dipolar Magnetic Fields, *Astrophys. J. Suppl.*, **205**, 3, arXiv: 1302.2356.
- Slaný, P. and Stuchlík, Z. (2005), Relativistic thick discs in the Kerr de Sitter backgrounds, **22**, pp. 3623–3651.
- Stuchlík, Z., Kovář, J. and Karas, V. (2009), Off-equatorial circular orbits in magnetic fields of compact objects, in K. G. Strassmeier, A. G. Kosovichev and J. E. Beckman, editors, *IAU Symposium*, volume 259 of *IAU Symposium*, pp. 125–126.
- Stuchlík, Z., Slaný, P. and Hledík, S. (2000), Equilibrium configurations of perfect fluid orbiting Schwarzschild-de Sitter black holes, *Astronomy and Astrophysics*, **363**, pp. 425–439.
- Urry, C. M. and Padovani, P. (1995), Unified Schemes for Radio-Loud Active Galactic Nuclei, *Publications of the Astronomical Society of the Pacific*, **107**, p. 803, arXiv: astro-ph/9506063.



# Black hole spin inferred from disc oscillation models of high-frequency quasi-periodic oscillations

Eva Šrámková and Gabriel Török

Institute of Physics, Faculty of Philosophy & Science, Silesian University in Opava,  
Bezručovo nám. 13, CZ-746 01 Opava, Czech Republic

**Keywords:** X-Rays: Binaries – Black Hole Physics – Accretion, Accretion Discs

## ABSTRACT

In the past several years, estimations of black hole spin in the three Galactic microquasars GRS 1915+105, GRO J1655–40, and XTE J1550–564 have been carried out based on several models of 3:2 high-frequency quasi-periodic oscillations (HF QPOs). When compared to spin predictions obtained by spectral fitting methods, the different approaches fail to provide consistent results. Most of the so far calculated QPO estimates are implied by models that deal with geodesic accretion flow. In the present work, we assume a non-geodesic flow defined by the model of a pressure-supported perfect fluid torus. We consider several QPO models and explore influence of the consideration of presence of the pressure forces on the predicted QPO frequencies and spin predictions. Our results indicate that in some cases the influence can be quite significant. This is in particular true for the so-called “vertical precession resonance” model and the warped disc resonance model. In other cases, on the other hand, the model predictions do not much vary from those corresponding to geodesic calculations. This applies namely for the model assuming  $m = -1$  radial and  $m = -2$  vertical disc-oscillation modes. The same is true for the epicyclic resonance (Er) model, but only providing that  $a \lesssim 0.9$ . When it is  $a \gtrsim 0.9$ , the situation changes and the influence of pressure forces becomes stronger. Such behaviour leads to very interesting conclusions. Within the Er model framework, individual sources with a moderate spin should exhibit a smaller spread of the measured 3:2 QPO frequencies than sources with a near-extreme spin. This should be further examined using the data available through the proposed Large Observatory for X-ray Timing (LOFT).

## 1 INTRODUCTION

Studying the X-ray spectra and variability provides a useful tool for putting constraints on the properties of compact objects like is the mass or spin of a black hole. One of the standard ways to measure the spin is through fitting the X-ray spectral continuum or the relativistically broadened Fe K alpha lines (see e.g. McClintock et al., 2006, 2007; Middleton et al., 2006;

**Table 1.** Properties of the three microquasars GRO 1655-40, GRS 1915+105, and XTE 1550-564. The individual columns display the frequencies of the lower and upper QPO peaks (Strohmayer, 2001; Remillard et al., 2002, 2003), the mass estimates (Greene et al., 2001; Greiner et al., 2001; Orosz et al., 2002; McClintock and Remillard, 2003), and the spin predictions carried out by the spectral fitting methods.

Source	$\nu_L$ [Hz]	$\nu_U$ [Hz]	Mass [ $M_\odot$ ]	$a$
GRO 1655-40	300	450	6.0–6.6	0.65–0.80* 0.97–0.99 <sup>†</sup>
GRS 1915+105	113	168	10.0–18.0	0.98–1.00 <sup>Δ</sup> $\sim 0.7^\nabla$
XTE 1550-564	184	276	8.4–10.8	0.75–0.77 <sup>⊖</sup>

\*From McClintock et al. (2007). <sup>†</sup>From Miller et al. (2009). <sup>Δ</sup>From McClintock et al. (2006).

<sup>∇</sup> From Middleton et al. (2006). <sup>⊖</sup>From Miller et al. (2009).

Done et al., 2007; Miller, 2007; Shafee et al., 2008; McClintock et al., 2010, 2011, 2014). Within the recent years, another approach has been gaining popularity – the determination of their properties through the theory of high-frequency quasi-periodic oscillations (HF QPOs).

The quasiperiodic modulation of the X-ray flux, which occurs at frequencies comparable to frequencies of orbital motion, has been observed in the X-ray power density spectra of the low-mass X-ray binaries for several decades (see, e.g. van der Klis, 2006; Belloni and Stella, 2014, for a review). In the black hole systems, the HF QPOs appear at frequencies that often form rational ratios with a preferred ratio of 3:2 (Abramowicz and Kluźniak, 2001; McClintock and Remillard, 2003, see Table 1). A significant amount of models proposed to explain the 3:2 HF QPOs deal with orbital motion and some oscillatory modes of the accretion disc. Such models relate the observed QPO frequencies to the corresponding orbital and disc-oscillation frequencies that are often defined by certain combination of the orbital Keplerian frequency and the radial and vertical epicyclic frequencies. In Kerr geometry, these frequencies depend on mass and spin of the black hole, and it is therefore possible to determine the black hole mass or spin from the observed 3:2 QPO frequencies and the specific QPO model. Such spin estimations have been carried out by several authors in the past (Wagoner et al., 2001; Abramowicz and Kluźniak, 2001; Kato, 2004; Török et al., 2005, 2011).

Most of the so-far obtained black hole spin estimations based on the QPO models have been obtained considering a geodesic accretion flow. In the case of more general flows, non-geodesic effects connected to, e.g. pressure gradients, magnetic fields or other forces may have potentially significant impact on the spin predictions implied by these models. Here we aim to quantify such impact in the particular case of non-geodesic influence introduced by pressure forces that are present in a specific type of accretion flow modelled

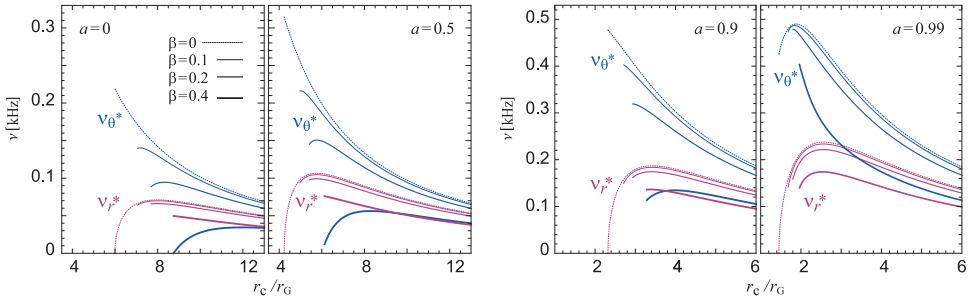


**Figure 1.** After Šrámková et al. (2015a). Frequencies  $\nu_r^*$  and  $\nu_\theta^*$  of  $m = 0$  radial and vertical disc-oscillation modes calculated at the centre of the torus,  $r = r_c$ , plotted for various torus thickness ( $\beta$ ) and black hole spin  $a$ . The calculated frequency values tend to decrease with increasing torus size.

by a pressure-supported, perfect fluid torus. The properties of epicyclic modes of torus oscillations, e.g. modifications to their frequencies due to pressure gradients present in the torus, were calculated by Blaes et al. (2007) in the pseudo-Newtonian approximation and later generalised by Straub and Šrámková (2009) for Kerr geometry.

We assume here several QPO models that were discussed by Török et al. (2011) who calculated spin values predicted by the models dealing with purely geodesic flow for three Galactic microquasars displaying the 3:2 twin-peak HF QPOs – GRS 1915+105, GRO J1655-40, and XTE J1550-564. Using the results of Straub and Šrámková (2009), we carry out the estimates of black hole spin based on the several previously assumed QPO models considering non-geodesic accretion flow of the pressure-supported torus. In this paper, we provide a short summary of the current findings explored by Šrámková et al. (2015a,b).

## 2 MODEL OF EQUILIBRIUM PRESSURE-SUPPORTED TORUS

The slightly non-geodesic accretion flow considered in this work is modelled by an equilibrium, slightly non-slender pressure-supported perfect fluid torus, which orbits a rotating Kerr black hole and has a constant specific angular momentum distribution. A detailed description of such model of torus is given in Straub and Šrámková (2009). In this accretion flow, the radial and vertical epicyclic oscillations of the fluid are modified by the pressure forces. These modifications were explored by Straub and Šrámková who calculated explicit formulae for the pressure corrections to epicyclic frequencies in a slightly non-slender constant specific angular momentum torus orbiting a Kerr black hole. In Figure 1, we illustrate how the pressure effects modify the frequencies of the axisymmetric  $m = 0$  oscillation modes.

## 3 DISC-OSCILLATION QPO MODELS

We focus our attention on the so-called ‘disc-oscillation’ QPO models that involve various oscillatory modes of accretion disc oscillations. The list of the considered models and their corresponding frequency relations of the lower and upper QPO is summarised in

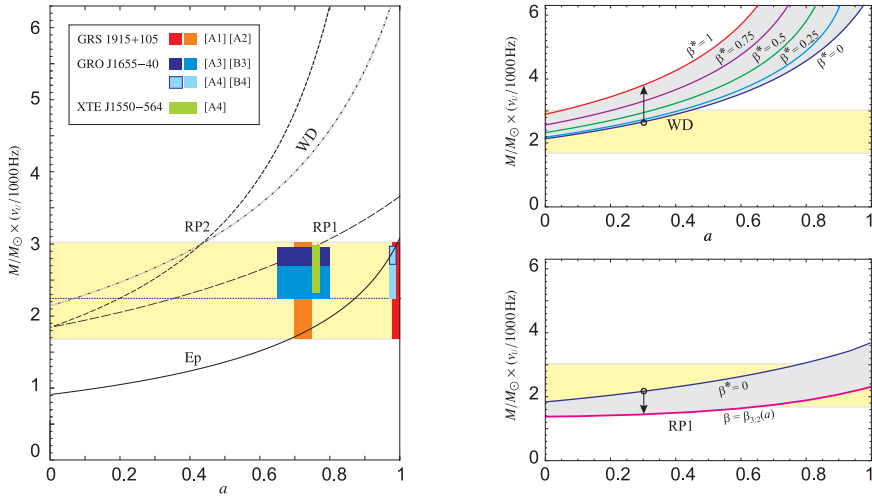


**Figure 2.** *Left:* After Török et al. (2011). Curves  $M(a)$  implied by the individual geodesic models. The light yellow rectangle indicates the observationally determined interval of  $\nu_U \times M$  including each of the individual microquasars. The colour boxes are drawn for the QPO independent mass and spin estimates given by different authors. *Right:* Pressure corrections implied for the RP1 and WD model. The geodesic case is marked by the blue line. In the case of WD model, the corrections grow with increasing torus thickness (the value  $\beta^*$  corresponds to the maximal allowed thickness). For the RP1 model, the situation is more complicated. For each value of  $a$ , there is a specific limit value of the torus thickness that does not allow the required frequency ratio. The resulting estimates indicated by the shadow area are then carried out numerically.

Table 2. It comprehends the “warped disc” (WD) model (Kato, 2004) that in general assumes oscillation modes in a warped accretion disc. Then there is the “3:2 epicyclic resonance” model of Abramowicz and Kluźniak that attributes the twin-peak HF QPOs to a non-linear resonance between two axisymmetric epicyclic accretion disc oscillation modes. Furthermore, there are another two resonance models that we denote as the “RP1” model (Bursa, 2005) and the “RP2” model (Török et al., 2011). Both of these models deal with a certain combination of non-axisymmetric disc-oscillations modes. More details on these models can be found in Török et al. (2011).

#### 4 SPIN ESTIMATES IMPLIED BY THE NON-GEODESIC QPO MODELS

We use here the formulae for pressure corrections to epicyclic frequencies calculated by Straub and Šrámková. From the 3:2 observed QPO frequencies and estimated ranges of mass of the three microquasars, we infer the spin predicted by the QPO models. For our calculations, we take into account relevant properties of the three microquasars summarized in Table 1. Outputs of these calculations are illustrated in Figs. 2 and 3. The intervals of spin predicted by the individual QPO models carried out for the non-geodesic case are listed in Table 2 and compared to spin predictions calculated by Török et al. (2011).

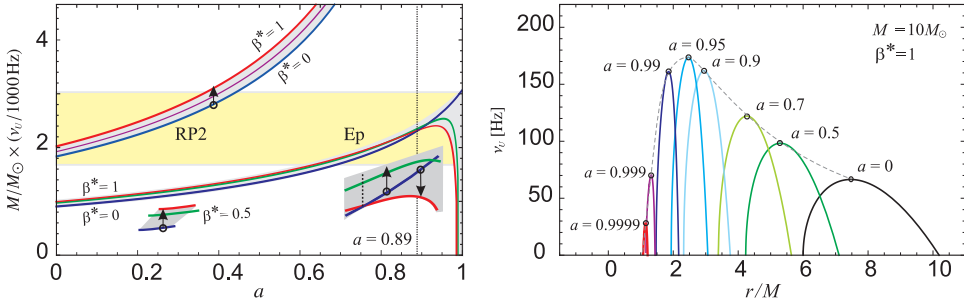


**Figure 3.** *Left:* Pressure corrections implied for the Ep and the RP2 model. The geodesic case is marked by the blue line. The corrections are rather small except for the case of the Ep model when considering high spin values. *Right:* Frequencies of the  $m = 0$  radial epicyclic mode calculated for tori with cusp tend to increase with increasing spin up to  $a \sim 0.95$ . For high values of  $a$ , they rapidly decrease with increasing  $a$ .

## 5 DISCUSSION AND CONCLUSIONS

Several groups of authors have applied different spectral fitting methods to measure the black hole spin in the three microquasars. We display the intervals of mass and spin of these sources implied by the spectral methods in the mass-spin diagram in the left panel of Fig. 2. The intervals are illustrated in the figure using the several coloured boxes. It is clear from the Figure that the spin predictions carried out by different authors are somewhat inconsistent.

Comparing the spin measurements obtained by the spectral methods to those predicted by theoretical QPO models may help to shed some light on the present puzzling situation. We present such comparison within the mass-spin diagrams displayed in Figs. 2 and 3. The individual curves in the Figures correspond to spin values predicted by the several QPO models given in Table 2. In the left panel of Fig. 2, we show curves corresponding to geodesic-flow estimates calculated by Török et al. (2011), while in the right panel of Fig. 2 and left panel of Fig. 3 we compare these estimates to estimates predicted by QPO models that involve non-geodesic flow described by the equilibrium, pressure-supported fluid torus. Different curves correspond to different torus thickness, which is marked using parameter  $\beta^*$ . Within the adopted notation, the curves marked by  $\beta^* = 0$  correspond to the case of a slender torus limit for which the epicyclic frequencies are equal to those of free test particles of geodesic motion. The curves marked by  $\beta^* = 1$  then correspond to the case of a torus with cusp.<sup>1</sup>

It is apparent from the Figures that presence of the pressure forces in the accretion flow may imply relatively large modifications to the QPO frequencies and consequently also to spin intervals previously predicted for the geodesic flow. This holds namely for the case of the WD and the RP1 model, both of which are shown in the right panel of Fig. 2.

<sup>1</sup> In the right panel of Fig. 3, we illustrate behaviour of the frequencies of  $m = 0$  radial epicyclic mode calculated for  $\beta^* = 1$ .

**Table 2.** Frequency relations corresponding to individual QPO models and the spin of the three microquasars implied by these models for the geodesic ( $a$ ) and non-geodesic ( $a^*$ ) case. The relations are expressed in terms of three fundamental frequencies of the perturbed circular geodesic motion. These are the Keplerian frequency, and the radial and vertical epicyclic frequencies, which are denoted by  $\nu_K$ ,  $\nu_r$  and  $\nu_\theta$ , respectively.

Model	Frequency Relations		$a \sim$	$a^* \sim$
<b>WD</b>	$\nu_L = 2(\nu_K - \nu_r)$	$\nu_U = 2\nu_K - \nu_r$	$<0.45$	$<0.45$
<b>Ep</b>	$\nu_L = \nu_r$	$\nu_U = \nu_\theta$	$0.7 - 1$	$0.6 - 1$
<b>RP1</b>	$\nu_L = \nu_K - \nu_r$	$\nu_U = \nu_\theta$	$<0.80$	$0 - 1$
<b>RP2</b>	$\nu_L = \nu_K - \nu_r$	$\nu_U = 2\nu_K - \nu_\theta$	$<0.45$	$<0.45$

The behaviour of curves illustrated in Fig. 3 shows that for the RP2 model assuming  $m = -1$  radial and  $m = -2$  vertical disc-oscillation modes the non-geodesic effects related to pressure do not cause any significant impact. For the Ep model, the results are similar when it is  $a \lesssim 0.9$ . The situation becomes different for  $a \gtrsim 0.9$ , in which case the predicted QPO frequency rapidly decreases as the torus thickness rises. This leads to an interesting conclusion for the Ep model. Within the model framework, individual sources with a moderate spin ( $a \lesssim 0.9$ ) should exhibit a smaller spread of the measured 3:2 QPO frequencies than sources with a near-extreme spin, such as GRS-1915+105 ( $a \sim 1$ ). Clearly, this could be further examined using the large amount of high-resolution data available through the proposed Large Observatory for X-ray Timing (LOFT; Feroci et al., 2012).

## ACKNOWLEDGEMENTS

The authors would like to acknowledge the support of the Czech grant GAČR 209/12/P740 and the project CZ.1.07/2.3.00/20.0071 “Synergy” aimed to support international collaboration of the Institute of Physics of SU Opava. We also acknowledge financial support from the internal grant of SU Opava, SGS/11/2013.

## REFERENCES

- Abramowicz, M. A. and Kluźniak, W. (2001), A precise determination of black hole spin in GRO J1655-40, *Astronomy and Astrophysics*, **374**, pp. L19–L20, arXiv: astro-ph/0105077.
- Belloni, T. M. and Stella, L. (2014), Fast Variability from Black-Hole Binaries, *Space Science Reviews*, **183**, pp. 43–60, arXiv: 1407.7373.
- Blaes, O. M., Šrámková, E., Abramowicz, M. A., Kluźniak, W. and Torkelsson, U. (2007), Epicyclic Oscillations of Fluid Bodies: Newtonian Nonslender Torus, *Astrophys. J.*, **665**, pp. 642–653, arXiv: 0706.4483.
- Bursa, M. (2005), High-frequency QPOs in GRO J1655-40: Constraints on resonance models by spectral fits, in S. Hledík and Z. Stuchlík, editors, *RAGtime 6/7: Workshops on black holes and neutron stars*, pp. 39–45.

- Done, C., Gierliński, M. and Kubota, A. (2007), Modelling the behaviour of accretion flows in X-ray binaries. Everything you always wanted to know about accretion but were afraid to ask, *Astronom. and Astrophys. Rev.*, **15**, pp. 1–66, arXiv: 0708.0148.
- Feroci, M. et al. (2012), The Large Observatory for X-ray Timing (LOFT), *Experimental Astronomy*, **34**, pp. 415–444, arXiv: 1107.0436.
- Greene, J., Bailyn, C. D. and Orosz, J. A. (2001), Optical and Infrared Photometry of the Microquasar GRO J1655-40 in Quiescence, *Astrophys. J.*, **554**, pp. 1290–1297, arXiv: astro-ph/0101337.
- Greiner, J., Cuby, J. G. and McCaughrean, M. J. (2001), An unusually massive stellar black hole in the Galaxy, *Nature*, **414**, pp. 522–525, arXiv: astro-ph/0111538.
- Kato, S. (2004), Wave-Warp Resonant Interactions in Relativistic Disks and kHz QPOs, *Publ. Astronom. Soc. Japan*, **56**, pp. 559–567.
- McClintock, J. E., Narayan, R., and Shafee, R. (2007), Estimating the Spins of Stellar-Mass Black Holes, in *Black Holes*, pp. 252–260, Cambridge University Press, ISBN 978-1-107-00553-2 hardback, arXiv: astro-ph/0707.4492.
- McClintock, J. E., Narayan, R., Davis, S. W., Gou, L., Kulkarni, A., Orosz, J. A., Penna, R. F., Remillard, R. A. and Steiner, J. F. (2011), Measuring the spins of accreting black holes, *Classical Quantum Gravity*, **28**(11), 114009, arXiv: 1101.0811.
- McClintock, J. E., Narayan, R., Gou, L., Liu, J., Penna, R. F. and Steiner, J. F. (2010), Measuring the Spins of Stellar Black Holes: A Progress Report, *X-ray Astronomy 2009; Present Status, Multi-Wavelength Approach and Future Perspectives*, **1248**, pp. 101–106, arXiv: 0911.5408.
- McClintock, J. E., Narayan, R. and Steiner, J. F. (2014), Black Hole Spin via Continuum Fitting and the Role of Spin in Powering Transient Jets, *Space Science Reviews*, **183**, pp. 295–322.
- McClintock, J. E. and Remillard, R. A. (2003), Black hole binaries, arXiv: astro-ph/0306213.
- McClintock, J. E., Shafee, R., Narayan, R., Remillard, R. A., Davis, S. W. and Li, L.-X. (2006), The Spin of the Near-Extreme Kerr Black Hole GRS 1915+105, *Astrophys. J.*, **652**, pp. 518–539, arXiv: astro-ph/0606076.
- Middleton, M., Done, C., Gierliński, M. and Davis, S. W. (2006), Black hole spin in GRS 1915+105, *Monthly Notices Roy. Astronom. Soc.*, **373**, pp. 1004–1012, arXiv: astro-ph/0601540.
- Miller, J. M. (2007), Relativistic X-Ray Lines from the Inner Accretion Disks Around Black Holes, *Annual Review of Astronomy and Astrophysics*, **45**, pp. 441–479, arXiv: 0705.0540.
- Miller, J. M., Reynolds, C. S., Fabian, A. C., Miniutti, G. and Gallo, L. C. (2009), Stellar-Mass Black Hole Spin Constraints from Disk Reflection and Continuum Modeling, *Astrophys. J.*, **697**, pp. 900–912, arXiv: 0902.2840.
- Orosz, J. A., Groot, P. J., van der Klis, M., McClintock, J. E., Garcia, M. R., Zhao, P., Jain, R. K., Bailyn, C. D. and Remillard, R. A. (2002), Dynamical Evidence for a Black Hole in the Microquasar XTE J1550-564, *Astrophys. J.*, **568**, pp. 845–861, arXiv: astro-ph/0112101.
- Remillard, R. A., Muno, M. P., McClintock, J. E. and Orosz, J. A. (2002), Evidence for Harmonic Relationships in the High-Frequency Quasi-periodic Oscillations of XTE J1550-564 and GRO J1655-40, *Astrophys. J.*, **580**, pp. 1030–1042, arXiv: astro-ph/0202305.
- Remillard, R. A., Muno, M. P., McClintock, J. E. and Orosz, J. A. (2003), “Voice-prints” within the unstable light curves of GRS 1915+105: QPOs at 165 and 113 Hz, in *AAS/High Energy Astrophysics Division #7*, volume 35 of *Bulletin of the American Astronomical Society*, p. 648.
- Shafee, R., McKinney, J. C., Narayan, R., Tchekhovskoy, A., Gammie, C. F. and McClintock, J. E. (2008), Three-Dimensional Simulations of Magnetized Thin Accretion Disks around Black Holes: Stress in the Plunging Region, *Astrophys. J. Lett.*, **687**, pp. L25–L28, arXiv: 0808.2860.
- Šrámková, E., Török, G., Kotrlová, A., Bakala, P., Abramowicz, M. A., Stuchlík, Z., Goluchová, K. and Kluźniak, W. (2015a), astronomy and Astrophysics submitted.

- Šrámková, E., Török, G., Kotrlová, A., Bakala, P., Abramowicz, M. A., Stuchlík, Z., Goluchová, K. and Kluźniak, W. (2015b), in preparation.
- Straub, O. and Šrámková, E. (2009), Epicyclic oscillations of non-slender fluid tori around Kerr black holes, *Classical Quantum Gravity*, **26**(5), 055011, arXiv: 0901.1635.
- Strohmayer, T. E. (2001), Discovery of a 450 HZ Quasi-periodic Oscillation from the Microquasar GRO J1655-40 with the Rossi X-Ray Timing Explorer, *Astrophys. J. Lett.*, **552**, pp. L49–L53.
- Török, G., Abramowicz, M. A., Kluźniak, W. and Stuchlík, Z. (2005), The orbital resonance model for twin peak kHz quasi periodic oscillations in microquasars, *Astronomy and Astrophysics*, **436**, pp. 1–8.
- Török, G., Kotrlová, A., Šrámková, E. and Stuchlík, Z. (2011), Confronting the models of 3:2 quasiperiodic oscillations with the rapid spin of the microquasar GRS 1915+105, *Astronomy and Astrophysics*, **531**, A59, arXiv: 1103.2438.
- van der Klis, M. (2006), *Rapid X-ray Variability*, Cambridge Univ. Press, Cambridge.
- Wagoner, R. V., Silbergleit, A. S. and Ortega-Rodríguez, M. (2001), “Stable” Quasi-periodic Oscillations and Black Hole Properties from Diskoseismology, *Astrophys. J. Lett.*, **559**, pp. L25–L28, arXiv: astro-ph/0107168.

# Braneworld naked singularities

Zdeněk Stuchlík<sup>a</sup> and Martin Blaschke<sup>b</sup>

Institute of Physics, Faculty of Philosophy & Science, Silesian University in Opava,  
Bezručovo nám. 13, CZ-746 01 Opava, Czech Republic

<sup>a</sup>[zdenek.stuchlik@fpf.slu.cz](mailto:zdenek.stuchlik@fpf.slu.cz)

<sup>b</sup>[martin.blaschke@fpf.slu.cz](mailto:martin.blaschke@fpf.slu.cz)

## ABSTRACT

We are investigating singularity structure of the rotating black hole and naked singularity spacetimes in the Randall–Sundrum second type (RSII) of the brane-world scenario. We will show that structure of this singularity is very similar to its classical counterpart, even in the cases of negative tidal charge, which is equivalent to the Kerr–Newman black hole with the complex charge  $Q$  (with zero real part). We also study behaviour of the ergosphere and will show that this region can exist under specific situation.

**Keywords:** Randall Sundrum – Brane-world

## 1 INTRODUCTION

In recent years, one of the promising approaches to the higher-dimensional gravity theories seems to be the string theory and particularly the M-theory (Hořava and Witten, 1996; Hořava and Witten, 1996). This new idea is describing gravity as a truly higher-dimensional interaction becoming effectively 4D at low enough energies. These theories inspired so called braneworld models, in which the observable universe is a 3-brane on which the standard-model fields are confined, while gravity enters the extra spatial dimensions, the size of which may be much larger than the Planck length scales  $\ell_P \sim 10^{-33}$  cm, (Arkani-Hamed et al., 1998). The braneworld models could therefore provide an elegant solution to the hierarchy problem of the electroweak and quantum gravity scales, as these scales become to be of the same order (TeV) due to large scale extra dimensions, (Arkani-Hamed et al., 1998). Therefore, future collider experiments can test the braneworld models quite well, including the hypothetical mini black hole production on the TeV-energy scales, (Dimopoulos and Landsberg, 2001). On the other hand, the braneworld models could be observationally tested since they influence astrophysically important properties of the black holes. Gravity can be localized near the brane at low energies even with a non-compact, infinite size extra dimension with the warped spacetime satisfying the 5D Einstein equations with negative cosmological constant as shown by, (Randall and Sundrum, 1999). In this paper we investigate the influence of the (RSII) brane-world effects on the singularity structure in a Kerr black hole. We also study extension of the ergosphere.

## 2 GEOMETRY

Using standard Boyer–Lindquist coordinates  $(t, r, \theta, \varphi)$  and geometric units ( $c = G = 1$ ), we can write the line element of the rotating (Kerr) black hole on the 3D-brane in the form

$$ds^2 = - \left( 1 - \frac{2Mr - b}{\Sigma} \right) dt^2 - \frac{2a(2Mr - b)}{\Sigma} \sin^2\theta dt d\varphi + \frac{\Sigma}{\Delta} dr^2 + \Sigma d\theta^2 + \left( r^2 + a^2 + \frac{2Mr - b}{\Sigma} a^2 \sin^2\theta \right) \sin^2\theta d\varphi^2, \quad (1)$$

where

$$\Delta = r^2 - 2Mr + a^2 + b, \quad (2)$$

$$\Sigma = r^2 + a^2 \cos^2\theta, \quad (3)$$

$M$  and  $a = J/M$  are the mass parameter and the specific angular momentum of the background, while the braneworld parameter  $b$ , called “tidal charge”, represents the imprint of non-local (tidal) gravitational effects of the bulk space, (Aliiev and Gümrukçüoğlu, 2005).

## 3 SINGULARITY

Our goal is to find out whether the brane parameter  $b$  has strong influence onto the structure of the Kerr-like ring singularity at  $r = 0, \theta = \pi/2$ . The Kretschmann’s scalar  $K = R_{\alpha\beta\gamma\delta} R^{\alpha\beta\gamma\delta}$  is a good tool to probe the structure of spacetimes singularities. Using Eq. (1) we get

$$K = \frac{8}{(r^2 + a^2 t^2)^6} \left( r^4 A - 2a^2 r^2 B t^2 + a^4 C t^4 - 6a^6 M^2 t^6 \right), \quad (4)$$

where<sup>1</sup>

$$t = \cos\theta, \quad (5)$$

$$A = (7b^2 - 12bMr + 6M^2 r^2), \quad (6)$$

$$B = (17b^2 - 60bMr + 45M^2 r^2), \quad (7)$$

$$C = (7b^2 - 60bMr + 90M^2 r^2). \quad (8)$$

The Kretschmann scalar is formally same as in the case of the Kerr–Newmann metric with  $Q^2 \rightarrow b$  (Henry, 2000). Naturally, the negative values of brane parameter would have some effect onto  $K$ , but we can see from the denominator of Eq. (4), that it has no effect onto position of the physical singularity. As an example there is a plot of  $K$  with  $(M = 1, a = 0.8, b = -0.8)$  at Fig. 1.

<sup>1</sup> Substitution  $t = \cos\theta$  is used here just to tremendously fasten computation of the Kretschmann scalar by program Mathematica v8.0.

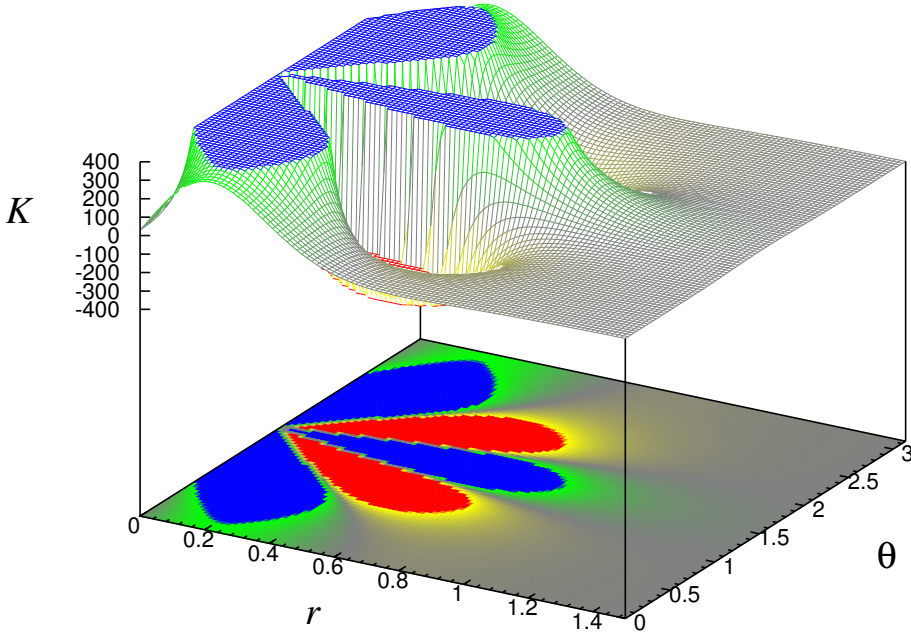


**Figure 1.** Example of the Kretschmann's scalar  $K$  for  $M = 1$ ,  $a = 0.8$ ,  $b = -0.8$  to illustrate its similarity to the Kerr–Newmann case.

Discussion about singularity can be more effectively done if we transform our metric into the so called Kerr–Schild form

$$g_{\mu\nu} = \eta_{\mu\nu} + l_{\mu}l_{\nu}, \quad (9)$$

where  $\eta_{\mu\nu}$  is a flat metric and  $l_{\mu}$  is a null vector with respect to  $\eta_{\mu\nu}$ . Using substitution

$$dt = dx^0 + \left( \frac{r^2 + a^2}{\Delta} - 1 \right) dr, \quad (10)$$

$$d\varphi = d\tilde{\varphi} + \frac{a}{\Delta} dr, \quad (11)$$

$$x = (r \cos(\tilde{\varphi}) + a \sin(\tilde{\varphi})) \sin \theta, \quad (12)$$

$$y = (r \sin(\tilde{\varphi}) - a \cos(\tilde{\varphi})) \sin \theta, \quad (13)$$

$$z = r \cos \theta, \quad (14)$$

and after burdensome calculation we end up with metric in a form:

$$ds^2 = -(dx^0)^2 + (dx)^2 + (dy)^2 + (dz)^2 + \frac{(2Mr - b)r^2}{r^4 + a^2z^2} \times \left\{ dx^0 - \frac{1}{r^2 + a^2} \left[ r(x dx + y dy) + a(x dy - y dx) - \frac{1}{r} z dz \right] \right\}^2, \quad (15)$$

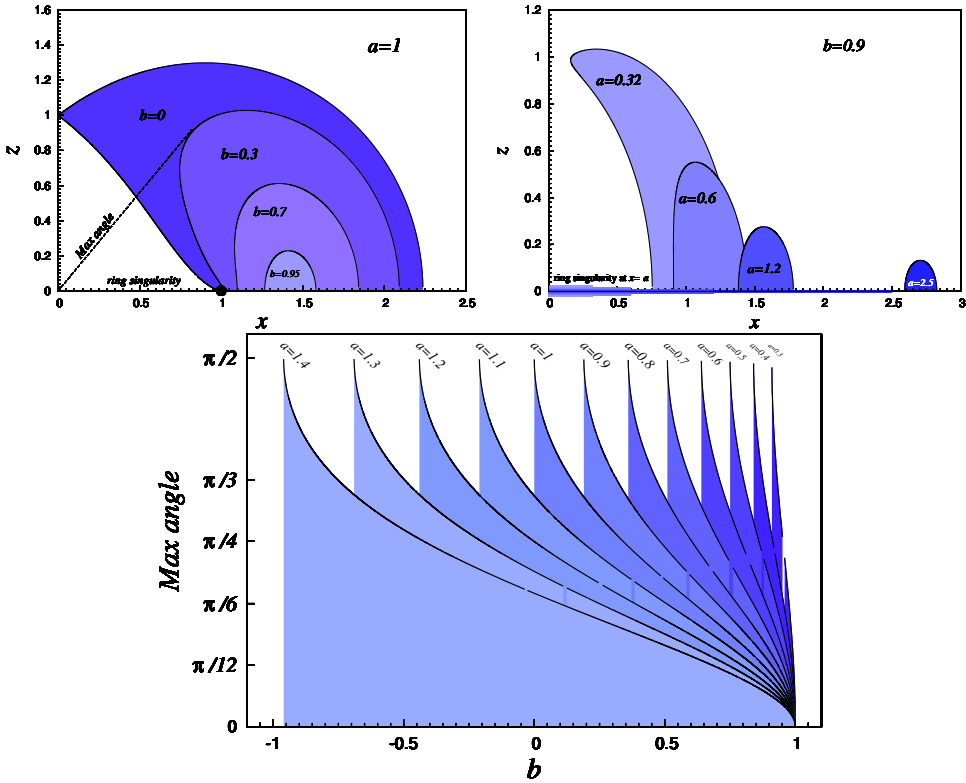


**Figure 2.** *Upper Left:* Polar slice through the brany Kerr spacetime in Cartesian Kerr–Schild coordinates. Spin parameter  $a$  is fixed to value 1 and brany parameter  $b$  is appropriately chosen to demonstrate its influence on ergosphere. *Upper Right:* Polar slice through the brany Kerr spacetime in Cartesian Kerr–Schild coordinates. Brany parameter  $b$  is fixed to value 0.9 and spin parameter  $a$  is appropriately chosen to demonstrate its influence on ergosphere. *Middle:* Maximal possible angle  $\alpha = \arctan(z/x)$  for a particular ergosphere.

where  $r$  is defined, implicitly, by

$$r^4 - r^2(x^2 + y^2 + z^2 - a^2) - a^2z^2 = 0. \tag{16}$$

The metric (15) is analytic everywhere except at

$$x^2 + y^2 + z^2 = a^2 \quad \text{and} \quad z = 0. \tag{17}$$

This condition is same as in the case of the standard Kerr black hole so we clearly can see that brany parameter  $b$  has no influence to singularity of the space-time what so ever. The physical “ring” singularity of the braneworld rotating black holes (and naked singularities) is located at  $r = 0$  and  $\theta = \pi/2$ , as in the Kerr spacetimes. For completeness we also enlist components of Ricci tensor. Ricci scalar is exactly zero, but the braneworld black hole spacetime is not Ricci flat.

Components of Ricci tensor are:

$$R_{tt} = 4b \frac{a^2 + 2\Delta - a^2 \cos(2\theta)}{(a^2 + 2r^2 + a^2 \cos(2\theta))^3}, \quad (18)$$

$$R_{t\varphi} = -8ab \frac{(a^2 + \Delta) \sin^2 \theta}{(a^2 + 2r^2 + a^2 \cos(2\theta))^3}, \quad (19)$$

$$R_{\varphi t} = R_{t\varphi}, \quad (20)$$

$$R_{rr} = -\frac{R_{\theta\theta}}{\Delta}, \quad (21)$$

$$R_{\theta\theta} = \frac{2b}{a^2 + 2r^2 + a^2 \cos(2\theta)}, \quad (22)$$

$$R_{\varphi\varphi} = 4b \sin^2(\theta) \frac{3a^4 + 2r^4 + a^2(b - 2Mr + 5r^2) - a^2 \Delta \cos(2\theta)}{(a^2 + 2r^2 + a^2 \cos(2\theta))^3}. \quad (23)$$

#### 4 ERGOSPHERE

The ergosphere of Kerr black hole and naked singularities plays a crucial role in astrophysical phenomena related, e.g. to the Penrose process (Penrose and Floyd, 1971), or the ultra high-energy particle collisions. A specially interesting phenomena occur in the case of the naked-singularity spacetimes, (Stuchlík, 1980; Stuchlík and Schee, 2013). Here we explore how the ergosphere extension depends on the tidal charge  $b$  and spin  $a$ . Ergosphere is a closed area of space with border defined by the condition:

$$g_{tt} = 0. \quad (24)$$

It is more convenient to investigate ergosphere in the Kerr–Schild coordinates (15). We can use spacetime symmetry and focus only on polar slice with  $y = 0$ . In this case the condition for border of ergosphere is simply given by (see for example Visser, 2007)

$$\begin{aligned} x^2 &= \frac{(a^2 + r^2) \Delta}{a^2}, \\ z^2 &= \frac{(2Mr - b)r^2 - r^4}{a^2}. \end{aligned} \quad (25)$$

In the Figure 2 we give some examples of the ergosphere's shape. Figures illustrate the influence of the brany parameter  $b$  on the ergosphere. From expression for  $z^2$  we see that existence of ergosphere is conditioned by (in  $M = 1$  units)

$$b < 1. \quad (26)$$

We can also infer that ergosphere is getting larger as brane parameter is getting smaller.

The ergosphere completely surrounds the ring singularity in the black hole cases only. To illustrate this phenomenon we have defined maximal possible angle of ergosphere viewed from the origin of coordinate system:

$$\alpha = \text{Max} : \arctan \frac{z}{x}, \quad (27)$$

where  $z, x$  are coordinates of point which belongs to ergosphere (see Fig. 2).

For every positive spin  $a > 0$  there always exists an ergosphere, but as spin increases, the volume of the ergosphere and the maximal angle  $\alpha$  decreases. The ergosphere is in a sense pushed away from the ring singularity by increasing spin.

## 5 CONCLUSIONS

We have shown that tidal charge  $b$  representing influence of the bulk space on the brane-world has no effect on the effective structure of singularity of the rotating Kerr black hole existing on the brane. Also we have shown how this parameter influences the ergosphere.

## ACKNOWLEDGEMENTS

This work was supported by EU grant Synergy CZ.1.07./2.3.00/20.0071, the internal student grant SGS/23/2013 of the Silesian University, and the Albert Einstein Centre for gravitation and astrophysics supported by the Czech Science Foundation Grant No. 14-37086G.

## REFERENCES

- Aliev, A. N. and Gümrukçüoğlu, A. E. (2005), Charged rotating black holes on a 3-brane, *Phys. Rev. D*, **71**(10), p. 104027, arXiv: hep-th/0502223.
- Arkani-Hamed, N., Dimopoulos, S. and Dvali, G. (1998), The hierarchy problem and new dimensions at a millimeter, *Physics Letters B*, **429**, pp. 263–272, arXiv: hep-ph/9803315.
- Dimopoulos, S. and Landsberg, G. (2001), Black Holes at the Large Hadron Collider, *Physical Review Letters*, **87**(16), 161602, arXiv: hep-ph/0106295.
- Henry, R. C. (2000), Kretschmann Scalar for a Kerr-Newman Black Hole, *Astrophys. J.*, **535**, pp. 350–353, arXiv: arXiv:astro-ph/9912320.
- Hořava, P. and Witten, E. (1996), Eleven-dimensional supergravity on a manifold with boundary, *Nuclear Physics B*, **475**, pp. 94–114, arXiv: hep-th/9603142.
- Hořava, P. and Witten, E. (1996), Heterotic and Type I string dynamics from eleven dimensions, *Nuclear Physics B*, **460**, pp. 506–524, arXiv: hep-th/9510209.
- Penrose, R. and Floyd, R. M. (1971), Extraction of Rotational Energy from a Black Hole, *Nature Physical Science*, **229**, pp. 177–179.
- Randall, L. and Sundrum, R. (1999), An Alternative to Compactification, *Physical Review Letters*, **83**, pp. 4690–4693, arXiv: hep-th/9906064.
- Stuchlík, Z. (1980), Equatorial circular orbits and the motion of the shell of dust in the field of a rotating naked singularity, *Bulletin of the Astronomical Institutes of Czechoslovakia*, **31**, pp. 129–144.
- Stuchlík, Z. and Schee, J. (2013), Ultra-high-energy collisions in the superspinning Kerr geometry, *Classical and Quantum Gravity*, **30**(7), 075012.
- Visser, M. (2007), The Kerr spacetime: A brief introduction, *ArXiv e-prints*, arXiv: 0706.0622.

# HF QPOs in the neutron star binary system XTE J1701-462 fitted by the model of oscillating string loops

Zdeněk Stuchlík<sup>a</sup> and Martin Kološ<sup>b</sup>

Institute of Physics, Faculty of Philosophy & Science, Silesian University in Opava,  
Bezručovo nám. 13, CZ-746 01 Opava, Czech Republic

<sup>a</sup>zdenek.stuchlik@fpf.slu.cz

<sup>b</sup>martin.kolos@fpf.slu.cz

## ABSTRACT

Axisymmetric string loops oscillating around a stable equilibrium position in the Kerr background are applied to explain the special set of frequencies related to the high-frequency quasiperiodic oscillations observed in the low mass X-ray binary XTE J1701-462 containing a neutron star. Frequencies of the radial and vertical string loop oscillations are determined by the mass  $M$  and dimensionless spin  $a$  of the neutron star, and by dimensionless parameter  $\omega$  describing combined effects of the string loop tension and its angular momentum. Equilibrium position of the string loop is given by its angular momentum and energy. The string-loop oscillation model can explain the observed kHz frequencies, but the stringy parameter  $\omega$  cannot be the same for all the three HF QPO observations in the XTE J1701-462 source; the limits on the acceptable values of  $\omega$  are given in dependence on the spacetime parameters  $M$  and  $a$ . However, the model implies restriction  $M > 3.3M_{\odot}$  on the neutron star mass that is too high to be compatible with the standard theory of neutron stars. A proper correction on the mass-limit can be generally introduced due to the electromagnetic interaction of an electrically charged string loop with magnetic field of the neutron star.

**Keywords:** string loops – quasiperiodic oscillations – XTE J1701-462 – X-ray binary

## 1 INTRODUCTION

The axisymmetric current-carrying string loops are governed by their tension and angular momentum. Tension prevents their expansion beyond some radius, current introduces an angular momentum preventing them from collapse. First, cosmic strings were introduced as remnants of some phase transitions in the very early universe – see (Vilenkin and Shellard, 1995) for a review. Later strings represented as superconducting vortices were introduced by (Witten, 1985). However, the current-carrying string loops could represent also plasma exhibiting a string-like behaviour due to dynamics of the magnetic field lines (Semenov

et al., 2004; Christensson and Hindmarsh, 1999), or due to the thin flux tubes of magnetized plasma simply described as 1D strings (Semenov and Bernikov, 1991; Cremaschini and Stuchlík, 2013; Cremaschini et al., 2013; Cremaschini and Stuchlík, 2014; Kovář, 2013).

It has been demonstrated that the current-carrying string loops moving axisymmetrically along the symmetry axis of the Kerr or Schwarzschild–de Sitter black holes have significant astrophysical applications (Jacobson and Sotiriou, 2009; Kološ and Stuchlík, 2010; Stuchlík and Kološ, 2012a; Kološ and Stuchlík, 2013; Stuchlík and Kološ, 2014b,a). Transmission of their oscillatory internal energy into energy of the translational motion causes an outward-directed acceleration of the string loops in the strong gravity of stars or compact objects, as neutron stars, black holes, or naked singularities (Jacobson and Sotiriou, 2009; Stuchlík and Kološ, 2012a,b; Kološ and Stuchlík, 2013). Such an effect can be important also for the electrically charged string loops moving in combined gravitational and electromagnetic fields (Tursunov et al., 2013). Since the resulting translational motion can be ultra-relativistic, the transmutation of the string loop energy can serve as an alternative explanation of relativistic jets.

Quite recently, it has been demonstrated that small oscillations of a string loop around stable equilibrium positions in the equatorial plane of the Kerr geometry can be considered in the lowest approximation as two uncoupled linear harmonic oscillators governing the radial and vertical oscillations of the string loop (Kološ and Stuchlík, 2013). The frequencies of the radial and vertical harmonic oscillations of the string loops were given and discussed in (Stuchlík and Kološ, 2014b). It has been shown that the string loop harmonic or quasi-harmonic oscillations can explain frequencies of the twin high-frequency quasiperiodic oscillations (HF QPO) observed in the three Galactic microquasars GRS 1915+105, XTE 1550-564, GRO 1655-40, i.e. low-mass X-ray binary (LMXB) systems containing a black hole (Stuchlík and Kološ, 2014b). Moreover, they can explain also the special frequency set of kHz QPOs observed in the peculiar source XTE J170-407 containing a neutron star, where a single HF QPO and two twin HF QPOs with the frequency ratio 3:2 were observed (Pawar et al., 2013; Stuchlík and Kološ, 2014a). Here we apply the string loop oscillation model for an analogical data set observed in the source XTE J1701-462 containing a neutron star.

The radial profiles of the string loop oscillations qualitatively differ from those related to the radial and vertical oscillations of the geodesic, epicyclic motion of test particle in the Kerr geometry. Especially, there is a crossing point of the radial and vertical frequencies in the Kerr black hole spacetimes for the string loop oscillation allowing for creation of single-frequency peaks to be observed in the field of black holes or neutron stars, while for the test particle oscillations such a crossing is possible only in the Kerr naked singularity spacetimes (Török and Stuchlík, 2005; Stuchlík and Schee, 2012).

## 2 HF QPOS IN XTE J1701-462

A detailed analysis of the HF QPOs in the source XTE J1701-462 has been reported in (Homan et al., 2007). The results are rather unexpected and very interesting, since a very special set of frequencies has been discovered in this study. In one of the three observational events a single HF QPO has been detected at a characteristic frequency

$$f_{(A)L} = f_{(A)U} = 800 \text{ Hz}. \quad (1)$$

In the other two observations, twin HF QPOs has been detected at characteristic frequencies

$$f_{(B)L} = 600 \text{ Hz}, \quad f_{(B)U} = 900 \text{ Hz}, \quad (2)$$

$$f_{(C)L} = 450 \text{ Hz}, \quad f_{(C)U} = 750 \text{ Hz}, \quad (3)$$

where we use the index U for the upper and the index L for the lower of the twin frequencies observed simultaneously. The first one of the twin peaks demonstrates precisely the frequency ratio 3:2, while the second one has the frequency ratio 5:3.

We shall use the special character of the radial profiles of the frequencies of the harmonic radial and vertical oscillations of axially symmetric string loops in order to explain the frequency set observed in the source XTE J1701-462 containing a neutron star. We shall assume that the exterior of the neutron star can be well described by the standard Kerr spacetime. Such an assumption is correct for massive neutron stars having mass  $M > 2M_{\odot}$  (Urbanec et al., 2013).

### 3 DYNAMICS OF STRING LOOPS

Dynamics of an axisymmetric current-carrying string loop in a given axially symmetric and stationary, Kerr, spacetime with metric  $g_{\alpha\beta}$  has been studied in detail in (Jacobson and Sotiriou, 2009; Kološ and Stuchlík, 2013). Harmonic or quasiharmonic oscillations of string loops in the Kerr spacetimes have been studied in (Stuchlík and Kološ, 2014b). Here we give a short overview.

The string loop motion is governed by barriers due to the tension and the angular momentum that are modified by the gravitational field. Dynamics of the string loop is determined by the action

$$S = \int d^2\sigma \sqrt{-h} (\mu + h^{ab} \varphi_{,a} \varphi_{,b}), \quad (4)$$

where  $\varphi_{,a} = j_a$  determines current of the string loop,  $\mu > 0$  reflects the string tension, and  $h^{ab}$  represents the metric induced on the string worldsheet. The worldsheet stress-energy tensor density  $\tilde{\Sigma}^{ab}$  can be expressed in the form (Jacobson and Sotiriou, 2009; Kološ and Stuchlík, 2013),

$$\tilde{\Sigma}^{\tau\tau} = \frac{J^2}{g_{\phi\phi}} + \mu, \quad \tilde{\Sigma}^{\sigma\sigma} = \frac{J^2}{g_{\phi\phi}} - \mu, \quad \tilde{\Sigma}^{\sigma\tau} = \frac{-2j_{\tau} j_{\sigma}}{g_{\phi\phi}}, \quad J^2 \equiv j_{\sigma}^2 + j_{\tau}^2. \quad (5)$$

The parameters  $J^2 = j_{\tau}^2 + j_{\sigma}^2$  and  $\omega = -j_{\tau}/j_{\sigma}$  describe the angular momentum of the string loop (Kološ and Stuchlík, 2010; Stuchlík and Kološ, 2012b)

As demonstrated in (Larsen, 1993), the string loop motion can be described by the Hamilton equations related to the 4-momentum  $P_{\mu}$  with the Hamiltonian

$$H = \frac{1}{2} g^{rr} P_r^2 + \frac{1}{2} g^{\theta\theta} P_{\theta}^2 + \frac{1}{2} g_{\phi\phi} (\Sigma^{\tau\tau})^2 + \frac{g_{\phi\phi} (E + g_{t\phi} \Sigma^{\sigma\tau})^2}{2(g_{tt} g_{\phi\phi} - g_{t\phi}^2)}. \quad (6)$$

The Hamiltonian can be written as a sum of dynamic and potential parts

$$H = H_D + H_P = \frac{1}{2}g^{rr}P_r^2 + \frac{1}{2}g^{\theta\theta}P_\theta^2 + H_P(r, \theta). \quad (7)$$

Using the conserved energy  $E = -p_t$  and the angular momentum parameters  $J$  and  $\omega$  (5), the potential part of the Hamiltonian reads

$$H_P = \frac{1}{2}g_{\phi\phi} \left( \frac{J^2}{g_{\phi\phi}} + 1 \right)^2 + \frac{1}{2} \frac{g_{\phi\phi}}{g_{tt}g_{\phi\phi} - g_{t\phi}^2} \left( E + \frac{g_{t\phi}}{g_{\phi\phi}} \frac{2J^2\omega}{\omega^2 + 1} \right)^2. \quad (8)$$

The boundary of the string loop motion is given by the condition  $H_P = 0$  that implies the energy boundary function  $E_b(r, \theta)$  in the form (Kološ and Stuchlík, 2013; Stuchlík and Kološ, 2014b),

$$E = E_b(r, \theta) = \sqrt{g_{t\phi}^2 - g_{tt}g_{\phi\phi}} \tilde{\Sigma}^{\tau\tau} - g_{t\phi} \tilde{\Sigma}^{\sigma\tau}. \quad (9)$$

The energy boundary function  $E_b(r, \theta)$  governs the dynamics of the string loops, serving as an effective potential of their motion. The rescaling  $E/\mu \rightarrow E$  and  $J/\sqrt{\mu} \rightarrow J$  implies that the energy boundary function in the standard Boyer–Lindquist  $r, \theta$  coordinates (Carter, 1973) takes the form

$$E_b(r, \theta; a, J, \omega) = \frac{4a\omega J^2 r}{(\omega^2 + 1)G} + \sqrt{\Delta} \left( \frac{J^2 R^2}{G \sin(\theta)} + \sin(\theta) \right), \quad (10)$$

where

$$G(r, \theta; a) = (a^2 + r^2) R^2 + 2a^2 r \sin^2(\theta). \quad (11)$$

In the Kerr metric

$$R^2 = r^2 + a^2 \cos^2 \theta, \quad \Delta = r^2 - 2Mr + a^2, \quad (12)$$

where  $a$  denotes spin and  $M$  mass parameters of the Kerr spacetimes. Of course, for the exterior of neutron stars we have to consider only the part of the Kerr spacetime limited by the condition  $r \geq R_{\text{surface}} > r_+$ .

In the following, we shall use for simplicity the dimensionless radial coordinate  $r \rightarrow r/M$ , dimensionless time coordinate  $t \rightarrow t/M$  and dimensionless spin  $a \rightarrow a/M$ ; this is equivalent to using of  $M = 1$  in the metric tensor. We will return to the dimensional quantities in the Section 5.

Detailed discussion of the properties of the energy boundary function  $E_b(r, \theta)$  is presented in (Kološ and Stuchlík, 2013) for both the Kerr black hole and naked singularity spacetimes. Here we focus on the properties in the black hole spacetimes that can be relevant for rotating neutron stars as demonstrated in (Urbanec et al., 2013; Török et al., 2008) – in this case the local extrema of the energy boundary function can be located in the equatorial plane only.

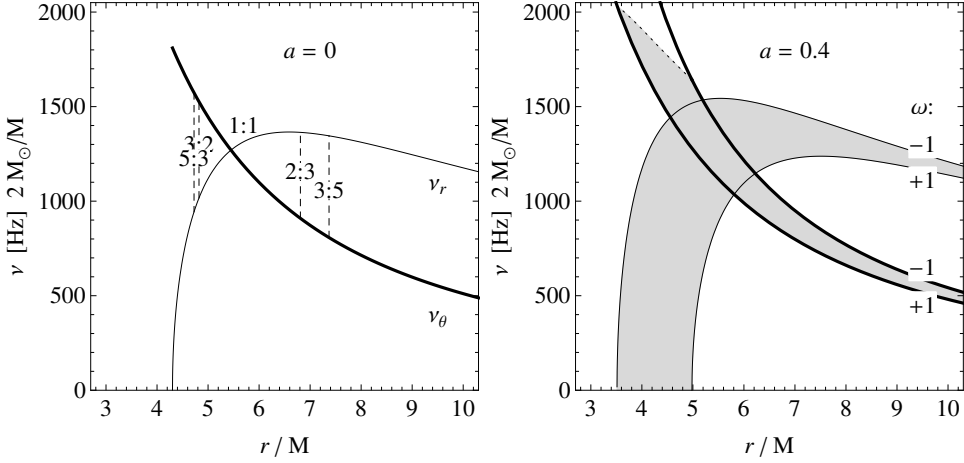


**Figure 1.** String-loop oscillatory frequencies  $\nu_r$  (*thin curves*) and  $\nu_\theta$  (*thick curves*), calculated for the Kerr metrics with  $M = 2M_\odot$ . Their radial profiles are illustrated for values of dimensionless spin  $a = 0, 0.4$  that are characteristic of our study of neutron star system. We demonstrate extension of the frequency radial profiles for the complete range of the string loop parameter  $\omega \in (-1, 1)$ . The vertical frequency curves are restricted to the region of existence (zero point) of the corresponding radial frequency curves – the relevant region is greyed.

The local extrema of the energy boundary function  $E_b(r; a, J, \omega)$ , governing the equilibrium positions of the string loops in the equatorial plane ( $\theta = \pi/2$ ), are determined by the function  $J_E^2(r; a, \omega)$  defined by (Kološ and Stuchlík, 2013; Stuchlík and Kološ, 2014b)

$$J_E^2(r; a, \omega) = \frac{(r-1)(\omega^2+1)H^2}{4a\omega\sqrt{\Delta}(a^2+3r^2) + (\omega^2+1)F}, \quad (13)$$

where

$$H(r; a) = r^3 + a^2(2+r), \quad F(r; a) = (r-3)r^4 - 2a^4 + a^2r(r^2 - 3r + 6). \quad (14)$$

A detailed discussion of the properties of the energy boundary function  $E_b(r; a, J, \omega)$  and the string loop motion can be found in (Kološ and Stuchlík, 2013; Stuchlík and Kološ, 2014b). We have to concentrate on the situations when for a string loop with fixed values of the angular momentum parameters  $J$  and  $\omega$  a stable equilibrium position of the string loop exists being given by the equation

$$J^2 = J_E^2(r; a, \omega). \quad (15)$$

Around such stable equilibrium positions, small oscillations of string loops occur, if their energy slightly exceeds the minimal value of the effective potential at the stable equilibrium positions.

#### 4 RADIAL AND VERTICAL OSCILLATIONS OF CURRENT-CARRYING STRING LOOPS AND THEIR FREQUENCIES

The analysis of the oscillatory motion of string loops around their stable equilibrium positions, based on the perturbative treatment of the Hamiltonian, can be found in (Kološ and Stuchlík, 2013; Stuchlík and Kološ, 2014b). The generally chaotic motion of the string loops can be in the first approximation of the motion around the stable equilibrium position considered as a regular motion – the corresponding part of the perturbative Hamiltonian represents two uncoupled linear harmonic oscillatory modes for the motion in the radial and vertical directions.

For string loop harmonic oscillations around a stable equilibrium position the variations of the radial and latitudinal coordinates are governed by the equations

$$\ddot{\delta r} + \omega_r^2 \delta r = 0, \quad \ddot{\delta \theta} + \omega_\theta^2 \delta \theta = 0. \quad (16)$$

The locally measured angular frequencies are given by (Stuchlík and Kološ, 2014b) and read

$$\omega_r^2 = \frac{1}{g_{rr}} \frac{\partial^2 H_P}{\partial r^2}, \quad \omega_\theta^2 = \frac{1}{g_{\theta\theta}} \frac{\partial^2 H_P}{\partial \theta^2}, \quad (17)$$

where the partial derivatives of the potential part of the Hamiltonian are calculated at the local minimum of the energy boundary function. The locally measured angular frequencies are connected to the angular frequencies related to distant observers,  $\Omega_{(r,\theta)}$ , by the gravitational redshift transformation (Stuchlík and Kološ, 2014b),

$$\Omega_{(r,\theta)} = \frac{df_{(r,\theta)}}{dt} = \frac{\omega_{(r,\theta)}}{P^t}. \quad (18)$$

If the angular frequencies  $\Omega_{(r,\theta)}$ , or frequencies  $\nu_{(r,\theta)}$ , of the string loop oscillation are expressed in the physical units, their dimensionless form has to be extended by the factor  $c^3/GM$ . Then the frequencies of the string loop oscillations measured by the distant observers are given by

$$\nu_{(r,\theta)} = \frac{1}{2\pi} \frac{c^3}{GM} \Omega_{(r,\theta)}. \quad (19)$$

This is the same factor as the one occurring in the case of the orbital and epicyclic frequencies of the geodesic motion in the Kerr spacetime (Aliev and Galtsov, 1981; Török and Stuchlík, 2005; Stuchlík and Schee, 2012). The order of magnitude and the mass-scaling of the frequencies of the radial and vertical oscillations is the same for both the current-carrying string loops and test particles, therefore the string loop oscillations could serve as an alternate explanation of the HF QPOs observed in the strong gravity regions of black holes and neutron stars.

The angular frequencies of the string loop oscillations related to distant observers take the dimensionless form

$$\Omega_r^2(r; a, \omega) = \frac{J_{E(\text{ex})} \left( 2a\omega\sqrt{\Delta} (a^2 + 3r^2) + (\omega^2 + 1) F_1 \right)}{2r (a^2(r+2) + r^3)^2 F_3^2}, \quad (20)$$

$$\Omega_{\theta}^2(r; a, \omega) = \frac{\sqrt{\Delta} \left( 2a\omega\sqrt{\Delta} (2a^2 - 3a^2r - 3r^3) + (\omega^2 + 1) F_2 \right)}{r^2 (a^2(r+2) + r^3) F_3}, \quad (21)$$

where

$$F_1(r, a) = a^2r^3 - a^2\Delta + r^5 - 2r^4, \quad (22)$$

$$F_2(r; a) = a^4(3r - 2) + 2a^2(2r - 3)r^2 + r^5, \quad (23)$$

$$F_3(r; a, \omega) = 2a\omega(a^2 + 3r^2) + \sqrt{\Delta}(\omega^2 + 1)(r^3 - a^2), \quad (24)$$

$$\begin{aligned} J_{\text{E(ex)}}(r; a, \omega) = & (\omega^2 + 1)H(r - 1) \left( 6a^2r - 3a^2r^2 - 6a^2 - 5r^4 + 12r^3 \right) \\ & + 4a\omega H \Delta^{-1/2} \left[ (a^2 + 3r^2)(\Delta - (r - 1)^2) - 6\Delta r(r - 1) \right] \\ & - (\omega^2 + 1) \left[ FH + 2F(a^2 + 3r^2)(r - 1) \right] \\ & + 8a\omega\sqrt{\Delta}(a^2 + 3r^2)^2(r - 1). \end{aligned} \quad (25)$$

The function  $J_{\text{E(ex)}}(r; a, \omega)$  governs the local extrema of the function  $J_{\text{E}}(r; a, \omega)$ . Its zero points determine the marginally stable equilibrium positions of the string loops. The conditions

$$J_{\text{E(ex)}} = 0 \quad \text{and} \quad J_{\text{E}}^2 \geq 0, \quad (26)$$

satisfied simultaneously, put the limit on validity of the formulae giving the angular frequencies of the radial and vertical oscillations – for details see (Stuchlík and Kološ, 2014b).

The radial profiles of the frequencies of the radial and vertical string loop harmonic oscillations are demonstrated in Fig. 1 for two characteristic values of the Kerr spin parameter  $a = 0, 0.4$ . In the Schwarzschild spacetime ( $a = 0$ ), both the frequencies are independent of the parameter  $\omega$ . In the Kerr spacetimes, the range of the radial and vertical frequencies depends on the string-loop parameter  $\omega$ , and the spin parameter  $a$  of the spacetime. Extension of the range of allowed frequencies increases with increasing spin. For all values of the spin and at each radius where the two oscillatory modes can occur, the vertical frequency has its maximum (minimum) for string loops with  $\omega = -1$  ( $\omega = +1$ ), while the radial frequency has its maximum (minimum) for string loops with  $\omega = +1$  ( $\omega = -1$ ); see Fig. 1.

## 5 STRING-LOOP OSCILLATIONS AS A MODEL OF HF QPOS IN THE XTE J1701-462 SOURCE

The rotating neutron stars can be conveniently described by the Hartle–Thorne geometry. Recently it has been demonstrated that agreement of the external Hartle–Thorne and Kerr geometries is sufficiently high for neutron stars with the mass  $M > 2M_{\odot}$ , the dimensionless spin  $a < 0.5$ , and the relative quadrupole moment  $q/a^2 < 2$  (Urbanec et al., 2013). Here we assume that the XTE J1701-462 neutron star is at a state enabling description of its exterior

**Table 1.** Four possible combinations of HF QPOs observed in the XTE J1701-462 source.

		$f_{(A)}$	$f_{(B)}$	$f_{(C)}$
case 1	$\nu_r : \nu_\theta$	1:1	3:2	5:3
case 2	$\nu_r : \nu_\theta$	1:1	3:2	3:5
case 3	$\nu_r : \nu_\theta$	1:1	2:3	5:3
case 4	$\nu_r : \nu_\theta$	1:1	2:3	3:5

by the Kerr geometry – we shall see that the predictions of the string loop oscillation model put high limits on the mass and dimensionless spin of the neutron star, in agreement with this assumption.

The upper theoretical constraint on the neutron star mass based on realistic equations of state of the subnuclear matter reads

$$M < M_{\max\text{NS}} = 2.8 M_\odot, \quad a < 0.5 \quad (27)$$

(see e.g. Akmal and Pandharipande, 1997; Akmal et al., 1998; Chamel et al., 2013). The upper theoretical limit on the neutron star spin reads  $a_{\max\text{NS}} \sim 0.7$ , (Lo and Lin, 2011).

For a given twin HF QPOs observed in a given source, we have to consider fixed values of the string parameter  $\omega$  and the spacetime parameters  $M$  and  $a$ . If several twin HF QPOs are observed in the source, the spin and mass parameters have to be fixed, but the string loop parameter  $\omega$  can be varied, as different twin frequency observations could be generated by different string loops that could be created and decayed successively with different parameter  $\omega$  reflecting locally different conditions in the source. Therefore, the string-loop oscillation model naturally introduces a possibility of significant scatter in distribution of frequencies of the twin HF QPOs. The range of the scatter increases with increasing spin of the Kerr geometry.

Here we assume relevance of resonant phenomena, e.g. a parametric resonance (Landau and Lifshitz, 1969), at all of the three HF QPO events observed in the XTE J1701-462 source. We consider the rational frequency ratios  $\nu_\theta : \nu_r = 3:2$  or  $\nu_\theta : \nu_r = 5:3$  for the twin HF QPOs, and  $\nu_\theta : \nu_r = 1:1$  for the single HF QPO, to be directly related to the observed values of the QPO frequencies in the XTE J1701-462 source. We identify the frequencies  $\nu_U, \nu_L$  with  $\nu_\theta, \nu_r$  or  $\nu_r, \nu_\theta$  frequencies. There are four possible combinations of this identification, enabled by the properties of the string loop oscillation model. The resonant phenomena between the radial and vertical oscillatory modes can occur at resonant radii  $r_{1:1}, r_{3:2}, r_{2:3}, r_{5:3}, r_{3:5}$ . The four possible cases of their combination are presented in Table 2.

The fitting of the string loop oscillation frequencies to the observed frequencies is presented in Fig. 2. for all the four cases of possible combinations of the resonant radii of the string loop oscillations. At each of the three observed events, and each of the resonant radii, the fitting is related to the upper of the observed frequencies (or the common frequency at  $r_{1:1}$ ); the precision of the frequency measurement is also taken into account. The fitting procedure determines for each of the observed events a region of the  $M - a$  parameter space, determined by the limiting values of the string loop parameter  $\omega \in (-1, 1)$ . Due to the degeneracy of the radial profiles of the string loop oscillation frequencies in the Schwarzschild

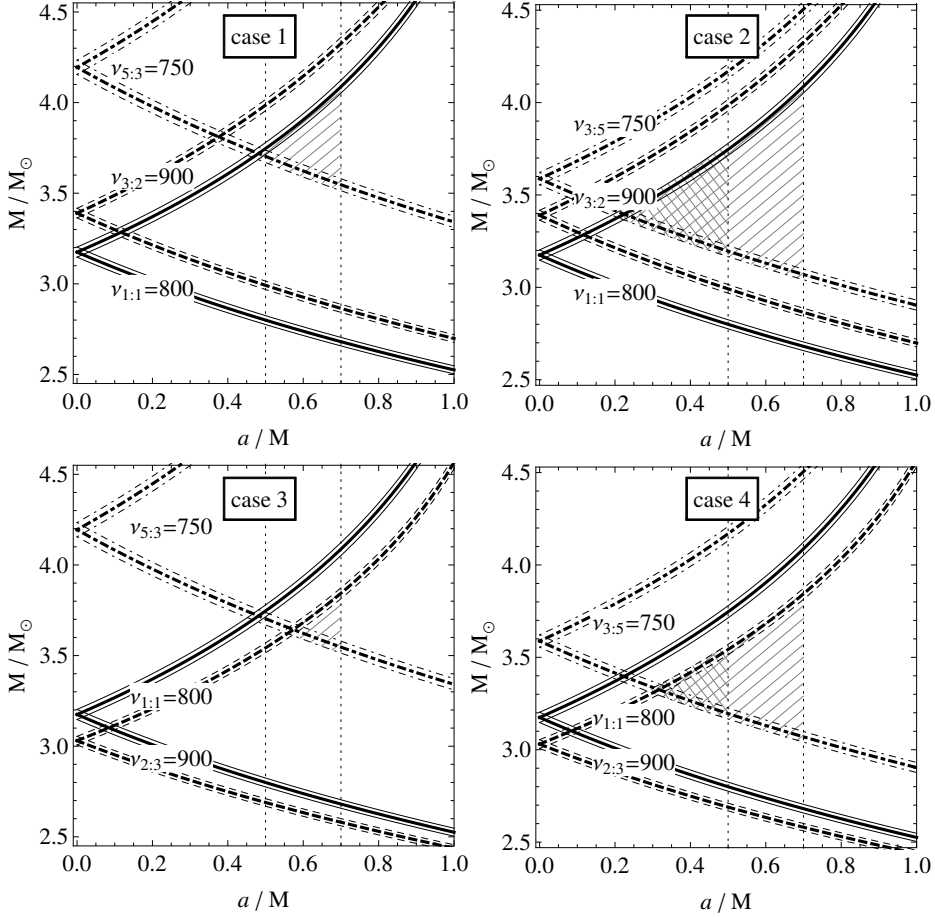


**Figure 2.** Restrictions on the mass  $M$  and spin  $a$  parameters of the neutron star in the XTE J1701-462 source implied by the string loop oscillation model applied to the three observational events of HF QPOs at the source. We assume that the three observational events occur at the resonant points of the radial and vertical string loop oscillations. Four different cases of the combinations of the resonant points related to the three observational events are possible – see Table 1. The upper branches are for parameter  $\omega = +1$  and the lower branches for parameter  $\omega = -1$ , allowed regions of the spacetime parameters  $M, a$  are hatched. The most promising is the second case, where we consider the 1:1 resonance with frequency  $\nu_{1:1} = 800$  Hz combined with 3:5 and 3:2 resonances with frequencies  $\nu_{3:5} = 750$  Hz and  $\nu_{3:2} = 900$  Hz.

spacetimes ( $a = 0$ ), the fitting predicts only one value of the mass parameter  $M$  for the spin  $a = 0$  at each observational event. Extension of the allowed region related to the whole interval of string loop parameter  $\omega \in (-1, 1)$  (the interval of allowed values of  $M$ ) increases with increasing spin  $a$ . The string loop oscillation model thus implies a “triangular” limit on the spacetime parameters  $M, a$  for each of the observed events of HF QPOs, as shown in Fig. 2. The limits have to be satisfied simultaneously, and we thus directly obtain the

**Table 2.** Restriction on the parameters of the neutron star in the XTE J1701-462 source implied by the string loop oscillation model of HF QPOs. Presented values correspond to the hatched regions from Fig. 2.

case 1:				case 2:			
	$a = 0.48$	$a = 0.5$	$a = 0.7$		$a = 0.22$	$a = 0.5$	$a = 0.7$
$M/M_{\odot}$	3.72	3.70–3.75	3.55–4.09	$M/M_{\odot}$	3.40	3.20–3.75	3.07–4.09
$\omega_{1:1}$	1	0.69–1	0.27–1	$\omega_{1:1}$	1	0.03–1	-0.08–1
$\omega_{3:2}$	0.33	0.29–0.34	0.09–0.44	$\omega_{3:2}$	0.01	-0.24–0.34	-0.31–0.44
$\omega_{5:3}$	-1	-1–-0.61	-1–-0.08	$\omega_{3:5}$	-1	-1–-0.19	-1–-0.39
case 3:				case 4:			
	$a = 0.57$	$a = 0.5$	$a = 0.7$		$a = 0.32$	$a = 0.5$	$a = 0.7$
$M/M_{\odot}$	3.64	#	3.55–3.84	$M/M_{\odot}$	3.32	3.20–3.54	3.07–3.84
$\omega_{1:1}$	0.44	#	0.27–0.49	$\omega_{1:1}$	0.26	0.03–0.40	-0.08–0.49
$\omega_{2:3}$	1	#	0.45–1	$\omega_{2:3}$	1	0.22–1	0.06–1
$\omega_{5:3}$	-1	#	-1–-0.27	$\omega_{3:5}$	-1	-1–-0.03	-1–-0.22

region of allowed values of the spacetime parameters, if the theoretical restrictions on the spin ( $a < 0.5$  related to the Hartle–Thorne model of neutron stars) are also taken into account. (We demonstrate in Fig. 2. also the limit related to the fully general-relativistic restriction on the neutron star spin,  $a < 0.7$ ). Along with the restrictions on the spacetime parameters  $M$  and  $a$ , restrictions on the stringy parameter  $\omega$  are obtained simultaneously. The results representing the limits on the spacetime and string loop parameters  $M$ ,  $\omega$  are presented in Table 2 for the characteristic limiting values of the spin parameter  $a$ . Of course, the restrictions on the radii where the resonant oscillations occur have to be also taken into the account, if we test the Hartle–Thorne models of the neutron star for concrete equations of state.

Our results indicate that only the cases 2 and 4, with both the resonant radii related to  $r_{3:5}$ , are physically realistic, as the other two cases, where the radius  $r_{5:3}$  enters the play, give unrealistic values of the neutron star spin. Using the results obtained in the case 2, we can see that for the lowest value of the spin,  $a = 0.2$ , we obtain the unique value of the neutron star mass,  $M = 3.4 M_{\odot}$ . In the edge of the allowed range of spin ( $a = 0.5$ ), we can obtain the mass  $M = 3.2 M_{\odot}$ . This is above the range of neutron star mass applied by realistic equations of state, being on the theoretical limit given by general restrictions on the neutron star mass as discussed in (Ruffini, 1973). Note that a similar situation, with one single and two twin HF QPOs, occurs for the neutron star source XTE J1701-407, but in this case the restrictions implied by the string loop oscillation model on the spin and mass of the neutron star are in accord with realistic equations of state, as shown in (Stuchlík and Kološ, 2014a). The resonant radii are depicted along with the radial profiles of the radial and vertical frequencies in Fig. 3 for some characteristic allowed values of the spacetime parameters  $M$  and  $a$ .

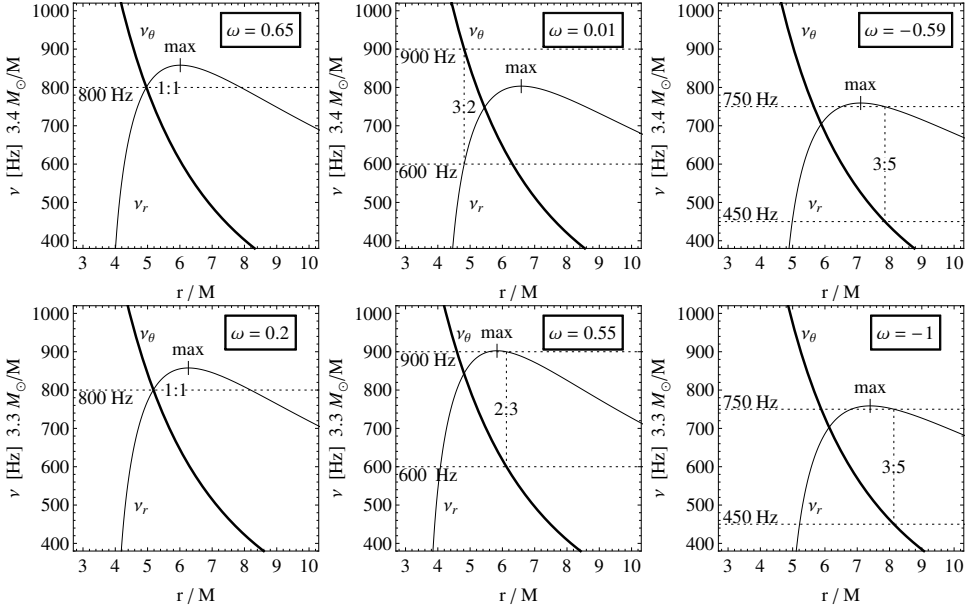


**Figure 3.** Examples of the radial profiles of the string-loop oscillatory frequencies  $\nu_r$  (thin curves) and  $\nu_\theta$  (thick curves) as related to the three observational events are given for two representative situations allowed by the combination of the resonant points in the case 2 and 4. The parameters of the Kerr metric are mass  $M = 3.4 M_\odot$  and spin  $a = 0.25$  for the first row (case 2),  $M = 3.3 M_\odot$  and spin  $a = 0.35$  for the second row (case 4). The related values of the parameter  $\omega$  are depicted in all the subfigures. Relevant resonant frequencies are also given.

## 6 CONCLUSIONS

We have demonstrated that the three HF QPOs observed in the XTE J1701-462 LMXB source containing a neutron star can be formally explained by the string loop oscillating model introduced in (Stuchlík and Kološ, 2014b) for the oscillations in the Kerr spacetime. This model, reflecting oscillations of string loops governed by interplay of tension and angular momentum, gives relevant restrictions on the spacetime parameters  $M$ ,  $a$  and the string loop parameter  $\omega$  that must be varied for the three observational events. We cannot fit the observed data assuming only one string loop having a fixed value of the parameter  $\omega$  reflecting locally different conditions in the source.

The string-loop oscillation model implies that the neutron star spacetime parameters are restricted to the intervals  $0.2 < a < 0.4$  and  $3.3 < M/M_\odot < 3.6$  predicting thus a very massive and fast rotating neutron star. Since the neutron star has to be very massive, we can conclude that the application for the Kerr geometry in the fitting procedure could be justified, as for the near-maximum-mass neutron stars the exterior Hartle–Thorne geometry has to be close to the exterior Kerr geometry, giving close predictions of the physical phenomena occurring in their vicinity. However, the predicted mass is too high to be acceptable for realistic equations of state. Therefore, our results indicate that if the string loop oscillation model has to be relevant for the HF QPOs observed in the XTE J1701-462 source,

an electrically charged string loop interacting with the neutron star magnetic field has to be invoked in order to allow for mass acceptable due to the Hartle-Thorne model using realistic equations of state (Tursunov et al., 2014; Stuchlík and Kološ, 2014a).

## ACKNOWLEDGEMENTS

The authors would like to thank the EU grant Synergy CZ.1.07./2.3.00/20.0071, the internal student grant SGS/23/2013 of the Silesian University, and the Albert Einstein Centre for gravitation and astrophysics supported by the Czech Science Foundation Grant No. 14-37086G.

## REFERENCES

- Akmal, A. and Pandharipande, V. R. (1997), Spin-isospin structure and pion condensation in nucleon matter, *Phys. Rev. C*, **56**, pp. 2261–2279, arXiv: [nucl-th/9705013](#).
- Akmal, A., Pandharipande, V. R. and Ravenhall, D. G. (1998), The equation of state for nucleon matter and neutron star structure, *ArXiv Nuclear Theory e-prints*, arXiv: [nucl-th/9804027](#).
- Aliev, A. N. and Galtsov, D. V. (1981), Radiation from relativistic particles in nongeodesic motion in a strong gravitational field, *General Relativity and Gravitation*, **13**, pp. 899–912.
- Carter, B. (1973), Black hole equilibrium states., in C. Dewitt and B. S. Dewitt, editors, *Black Holes (Les Astres Occlus)*, pp. 57–214.
- Chamel, N., Haensel, P., Zdunik, J. L. and Fantina, A. F. (2013), On the Maximum Mass of Neutron Stars, *Internat. J. Modern Phys. A*, **22**, 1330018, arXiv: [1307.3995](#).
- Christensson, M. and Hindmarsh, M. (1999), Magnetic fields in the early universe in the string approach to MHD, *Phys. Rev. D*, **60**(6), 063001, arXiv: [astro-ph/9904358](#).
- Cremaschini, C. and Stuchlík, Z. (2013), Magnetic loop generation by collisionless gravitationally bound plasmas in axisymmetric tori, *Phys. Rev. E*, **87**(4), 043113.
- Cremaschini, C. and Stuchlík, Z. (2014), Transition from gas to plasma kinetic equilibria in gravitating axisymmetric structures, *Phys. Plasmas*, **21**(4), 042902.
- Cremaschini, C., Stuchlík, Z. and Tessarotto, M. (2013), Kinetic theory of quasi-stationary collisionless axisymmetric plasmas in the presence of strong rotation phenomena, *Phys. Plasmas*, **20**(5), p. 052905.
- Homan, J. et al. (2007), Rossi X-Ray Timing Explorer Observations of the First Transient Z Source XTE J1701-462: Shedding New Light on Mass Accretion in Luminous Neutron Star X-Ray Binaries, *Astrophys. J.*, **656**, pp. 420–430, arXiv: [astro-ph/0610803](#).
- Jacobson, T. and Sotiriou, T. P. (2009), String dynamics and ejection along the axis of a spinning black hole, *Phys. Rev. D*, **79**(6), 065029, arXiv: [0812.3996](#).
- Kološ, M. and Stuchlík, Z. (2010), Current-carrying string loops in black-hole spacetimes with a repulsive cosmological constant, *Phys. Rev. D*, **82**(12), 125012, arXiv: [1103.4005](#).
- Kološ, M. and Stuchlík, Z. (2013), Dynamics of current-carrying string loops in the Kerr naked-singularity and black-hole spacetimes, *Phys. Rev. D*, **88**(6), 065004, arXiv: [1309.7357](#).
- Kovář, J. (2013), Spiral motion formation in astrophysics, *European Physical Journal Plus*, **128**, p. 142.
- Landau, L. D. and Lifshitz, E. M. (1969), *Mechanics*, Oxford: Pergamon Press.
- Larsen, A. L. (1993), Dynamics of cosmic strings and springs; a covariant formulation, *Classical and Quantum Gravity*, **10**, pp. 1541–1548, arXiv: [hep-th/9304086](#).

- Lo, K.-W. and Lin, L.-M. (2011), The Spin Parameter of Uniformly Rotating Compact Stars, *Astrophys. J.*, **728**, 12, arXiv: 1011.3563.
- Pawar, D. D., Kalamkar, M., Altamirano, D., Linares, M., Shanthi, K., Strohmayer, T., Bhattacharya, D. and van der Klis, M. (2013), Discovery of twin kHz quasi-periodic oscillations in the low-mass X-ray binary XTE J1701-407, *Monthly Notices Roy. Astronom. Soc.*, **433**, pp. 2436–2444, arXiv: 1306.0168.
- Ruffini, R. (1973), On the energetics of black holes., in C. Dewitt and B. S. Dewitt, editors, *Black Holes (Les Astres Occlus)*, pp. 451–546.
- Semenov, V., Dyadechkin, S. and Punsly, B. (2004), Simulations of Jets Driven by Black Hole Rotation, *Science*, **305**, pp. 978–980, arXiv: astro-ph/0408371.
- Semenov, V. S. and Bernikov, L. V. (1991), Magnetic flux tubes - Nonlinear strings in relativistic magnetohydrodynamics, *Astrophys. and Space Sci.*, **184**, pp. 157–166.
- Stuchlík, Z. and Kološ, M. (2012a), Acceleration of string loops in the Schwarzschild-de Sitter geometry, *Phys. Rev. D*, **85**(6), 065022, arXiv: 1206.5658.
- Stuchlík, Z. and Kološ, M. (2012b), String loops in the field of braneworld spherically symmetric black holes and naked singularities, *Journal of Cosmology and Astroparticle Physics*, **10**, 008, arXiv: 1309.6879.
- Stuchlík, Z. and Kološ, M. (2014a), String loop oscillation model fitting frequency of kHz quasiperiodic oscillations in the low-mass X-ray binary XTE J1701-407, *submitted to Classical and Quantum Gravity*.
- Stuchlík, Z. and Kološ, M. (2014b), String loops oscillating in the field of Kerr black holes as a possible explanation of twin high-frequency quasiperiodic oscillations observed in microquasars, *Phys. Rev. D*, **89**(6), 065007, arXiv: 1403.2748.
- Stuchlík, Z. and Schee, J. (2012), Observational phenomena related to primordial Kerr superspinars, *Classical and Quantum Gravity*, **29**(6), 065002.
- Török, G., Bakala, P., Stuchlík, Z. and Čech, P. (2008), Modeling the Twin Peak QPO Distribution in the Atoll Source 4U 1636-53, *Acta Astronomica*, **58**, pp. 1–14.
- Török, G. and Stuchlík, Z. (2005), Radial and vertical epicyclic frequencies of Keplerian motion in the field of Kerr naked singularities. Comparison with the black hole case and possible instability of naked-singularity accretion discs, *Astronomy and Astrophysics*, **437**, pp. 775–788, arXiv: astro-ph/0502127.
- Tursunov, A., Kološ, M., Ahmedov, B. and Stuchlík, Z. (2013), Dynamics of an electric current-carrying string loop near a Schwarzschild black hole embedded in an external magnetic field, *Phys. Rev. D*, **87**(12), 125003.
- Tursunov, A., Kološ, M., Ahmedov, B. and Stuchlík, Z. (2014), Acceleration of electric current-carrying string loop near a Schwarzschild black hole immersed in an asymptotically uniform magnetic field, *submitted into Phys. Rev. D*.
- Urbanec, M., Miller, J. C. and Stuchlík, Z. (2013), Quadrupole moments of rotating neutron stars and strange stars, *Monthly Notices Roy. Astronom. Soc.*, **433**, pp. 1903–1909, arXiv: 1301.5925.
- Vilenkin, A. and Shellard, E. P. S. (1995), *Cosmic Strings and Other Topological Defects*, Cambridge University Press.
- Witten, E. (1985), Superconducting strings, *Nuclear Physics B*, **249**, pp. 557–592.



# Determination of Characteristics of Eclipsing Binaries with Spots: Phenomenological vs Physical Models

Mariia G. Tkachenko<sup>a</sup> and Ivan L. Andronov<sup>b</sup>

Odessa National Maritime University, Mechnikov st. 23, UA-65029 Odessa, Ukraine

<sup>a</sup>masha.vodn@yandex.ua

<sup>b</sup>tt\_ari@ukr.net

## ABSTRACT

We discuss methods for modelling eclipsing binary stars using the “physical”, “simplified”, and “phenomenological” models. There are few realizations of the “physical” Wilson–Devinney (1971) code and its improvements, e.g. Binary Maker, Phoebe. A parameter search using the Monte-Carlo method was realized by Zola et al. (2010), which is efficient in expense of too many evaluations of the test function. We compare existing algorithms of minimization of multi-parametric functions and propose to use a “combined” algorithm, depending on if the Hessian matrix is positively determined. To study methods, a simply fast-computed function resembling the “complete” test function for the physical model. Also we adopt a simplified model of an eclipsing binary at a circular orbit assuming spherical components with an uniform brightness distribution. This model resembles more advanced models in a sense of correlated parameter estimates due to a similar topology of the test function. Such a model may be applied to detached Algol-type systems, where the tidal distortion of components is negligible.

**Keywords:** variable stars – eclipsing binaries – algols – data analysis – time series analysis – parameter determination

## 1 INTRODUCTION

Determination of the model parameters of various astrophysical objects, comparison with observations and, if needed, further improvement of the model, is one of the main directions of science, particularly, of the study of variable stars. And so we try to find the best method for the determination of the parameters of eclipsing binary stars. For this purpose, we have used observations of one eclipsing binary system, which was analysed by (Zola et al., 2010). This star is AM Leonis, which was observed using 3 filters (B, V, R). For the analysis, we used the computer code written by Professor Stanisław Zoła (Zola et al., 1997). In the program, the Monte-Carlo method is implemented. As a result, the parameters were determined and the corresponding light curves are presented in the paper (Andronov and Tkachenko, 2013)

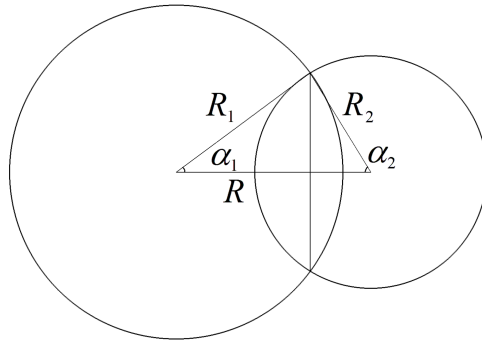


**Figure 1.** Scheme of eclipsing binary system with spherical components. Number 1 corresponds to a larger star, which eclipses the smaller star at phases close to 0.

With an increasing number of evaluations, the points are being concentrated to smaller and smaller regions. And, finally, the “cloud” should converge to a single point. Practically this process is very slow. This is why we try to find more effective algorithms. At the “potential – potential” diagram (Andronov and Tkachenko, 2013), we see that the best solution corresponds to an “over-contact” system, which makes an addition link of equal potentials  $\Omega_1 = \Omega_2$  and corresponding decrease of the number of unknown parameters.

Such a method needs a lot of computation time. We had made fitting using a hundred thousands sets of model parameters. The best 1500 (user defined) points are stored in the file and one may plot the “parameter – parameter diagrams”. Of course, the number of parameters is large, so one may choose many pairs of parameters. However, some parameters are suggested to be fixed, and thus a smaller number of parameters is to be determined.

Looking for the “parameter–parameter” diagrams, we see that there are strong correlations between the parameters, e.g. the temperature in our computations is fixed for one star. If not, the temperature difference is only slightly dependent on temperature, thus both temperatures may not be determined accurately from modelling. So the best solution may not be unique; it may fill some sub-space in the space of parameters.

This is a common problem: the parameter estimates are dependent. Our tests were made on another function, which is similar in behaviour to a test function used for modelling of eclipsing binaries.

To determine the statistically best sets of the parameters, there are some methods for optimization of the test function which is dependent on these parameters (Cherepashchuk, 1993; Kallrath and Milone, 2009). As for the majority of binary stars the observations are not sufficient to determine all parameters, for smoothing the light curves may be used “phenomenological fits”. Often were used trigonometric polynomials (=“restricted Fourier series”), following a pioneer work of (Pickering, 1881) and other authors, see (Parenago and Kukarkin, 1936) for a detailed historical review. Andronov (2010, 2012) proposed a method of phenomenological modelling of eclipsing variables (most effective for algols, but also applicable for EB and EW – type stars).

Below we discuss the “simplified” and “phenomenological” models.

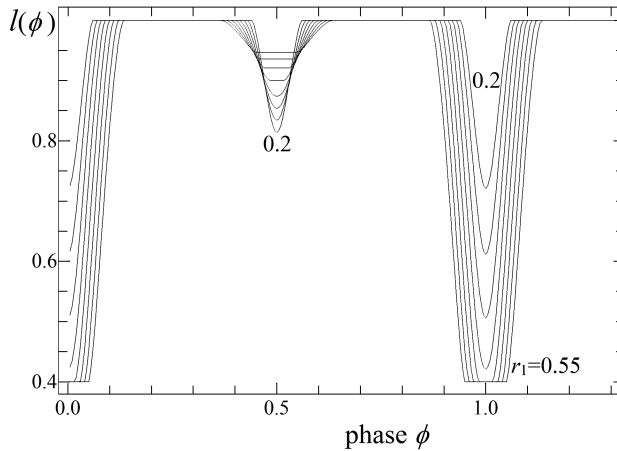


**Figure 2.** A set of theoretical light curves for the “simplified” model generated for  $R_1$  in a range from 0.2 to 0.55 with a step of 0.05 for fixed values of other parameters listed in the text.

## 2 “SIMPLIFIED” MODEL

The simplest model is based on the following main assumptions: the stars are spherically symmetric (this is physically reliable for detached stars with components being deeply inside their Roche lobes); the surface brightness distribution is uniform. This challenges the limb darkening law, but is often used for teaching students because of simplicity of the mathematical expressions, e.g. (Andronov, 1991). Similar simplified model of an eclipsing binary star is also presented by Dan Bruton (<http://www.physics.sfasu.edu/astro/ebstar/ebstar.html>). The scheme is shown in Fig. 1. The parameters are  $L_1$ ,  $L_2$  (proportional to luminosities), radii  $R_1$ ,  $R_2$ , distance  $R$  between the projections of centres to the celestial sphere.

The square of the eclipsed segment is  $S = S_1 + S_2$

$$S_1 = R_1^2(\alpha_1 - \sin \alpha_1 \cos \alpha_1), \quad (1)$$

$$S_2 = R_2^2(\alpha_2 - \sin \alpha_2 \cos \alpha_2), \quad (2)$$

where the angles  $\alpha_1$ ,  $\alpha_2$  may be determined from the cosine theorem:

$$\cos \alpha_1 = \frac{R^2 + R_1^2 - R_2^2}{2R_1R} = \frac{R^2 + \eta}{2R_1R}, \quad (3)$$

$$\cos \alpha_2 = \frac{R^2 + R_2^2 - R_1^2}{2R_2R} = \frac{R^2 - \eta}{2R_2R}, \quad (4)$$

where obviously  $\eta = R_1^2 - R_2^2$  and  $|R_1 - R_2| \leq R \leq |R_1 + R_2|$ . The total flux is  $L = L_1 + L_2$ , if  $R \geq R_1 + R_2$  (i.e. both stars are visible,  $S = 0$ ). For  $R \leq R_1 + R_2$ ,  $S = \pi R_2^2$  (assuming that  $R_2 \leq R_1$ ). Generally,  $L = L_1 + L_2 - L_j S / \pi R_j^2$ , where  $j$  is the number of star

which is behind another, i.e.  $j = 1$ , if  $\cos 2\pi\phi \leq 0$ , and  $j = 2$ , if  $\cos 2\pi\phi \geq 0$ . Here  $\phi$  is phase ( $\phi = 0$ ) corresponds to a full eclipse, independently on which star has larger brightness). For scaling purposes, a dimensionless variable  $l(\phi) = L(\phi)/(L_1 + L_2)$  is usually introduced. For tests, we used a light curve generated for the following parameters:  $R_1 = 0.3$ ,  $R_2 = 0.2$ ,  $L_1 = 0.4$ ,  $L_2 = 0.6$  and  $i = 80^\circ$ . The phases were computed with a step of 0.02. This light curve as well as other generated for a set of values of  $R_1$  is shown in Fig. 2. As a test function we have used:

$$F = \sum_{i=1}^n \frac{(x_i - \alpha x_c(\phi_i))^2}{\sigma_i^2}, \quad (5)$$

where  $x_i$  (or  $l_i$ ) are values of the signal at phases  $\phi_i$  with a corresponding accuracy estimate  $\sigma_i$ , and  $x_c$  are theoretical values computed for a given trial set of  $m$  parameters. For normally distributed errors and absence of systematic differences between the observations and theoretical values, the parameter  $F$  is a random variable with  $\chi_{n-m}^2$  a statistical distribution (Anderson, 1984; Cherepashchuk, 1993). For the analysis carried out in this work, we used a simplified model with  $\sigma_i = 1$ . This assumption does not challenge the basic properties of the test function. The scaling parameter is sometimes determined as  $x(0.75)/x_c(0.75)$ , i.e. at a phase where both components are visible, and the flux (intensity) has its theoretical maximum (in the “no spots” model). To improve statistical accuracy, it may be recommended to use a scaling parameter computed for all real observations:

$$\alpha = \frac{\sum_{i=1}^n \frac{x_i}{\sigma_i^2}}{\sum_{i=1}^n \frac{x_c(\phi_i)}{\sigma_i^2}}, \quad (6)$$

This corresponds to a least squares estimate of a scaling parameter, i.e. the model value of the out-of-eclipse intensity  $L = L_1 + L_2$  may be theoretically an any positive number, and these parameters may be “independent”. By introducing  $l_1 = L_1/L$  and  $l_2 = L_2/L$ , we get an obvious relation  $l_2 = 1 - l_1$ , i.e. one parameter. For  $L$  sometimes are used values at the observed light curve at the phase 0.75 (i.e. when both stars are to be visible so maximal light). We prefer instead to use all the data with scaling as in Eq. (6). Even in our simplified model, the number of parameters is still large (4). At Figure 4, the lines of equal levels of  $F$  are shown. One may see that the zones of small values are elongated and inclined showing a high correlation between estimates of 2 parameters. In fact this correlation is present for other pairs of parameters. This means that there may be relatively large regions in the multi-parameter space which produce theoretical light curves of nearly equal coincidence with observations.

In the software by Zola et al. (2010), the Monte-Carlo method is used, and at each trial computation of the light curve, the random parameters  $C_k$ ,  $k = 1, 2, 3, 4$  are used in a corresponding range:  $C_k = C_{k,\min} + (C_{k,\max} - C_{k,\min}) \text{rand}$ , where  $\text{rand}$  is a uniformly distributed random value. Then one may plot “parameter – parameter” diagrams for “best” points after a number of  $N$  trial computations. The “best” means sorting of sets of the parameters according to the values of the test function  $F$ . Initially, the points are distributed

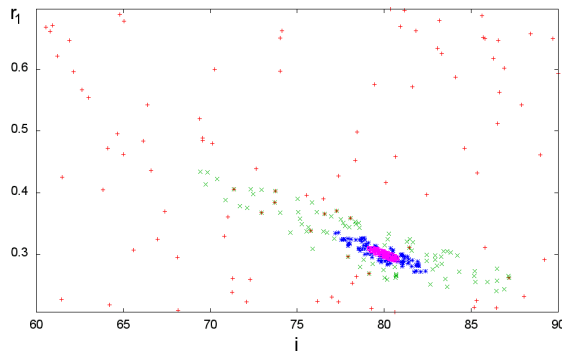


**Figure 3.** The “parameter–parameter” diagram. The best (according to the value of the test function) 100 points after  $10^2$ ,  $10^3$ ,  $10^4$ ,  $10^5$  trial computations, respectively.

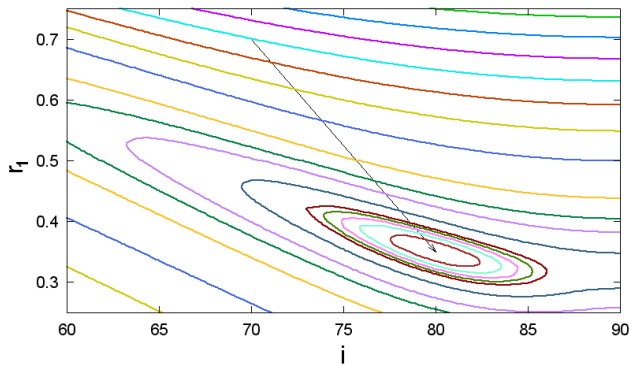


**Figure 4.** Lines of equal values of the test function  $F$  for fixed values of other parameters. The arrow shows position of the “true” parameters used to generate the signal.

uniformly. With an increasing  $N$ , “better” (with smaller  $F$ ) points concentrate to a minimum. There may be some local minima, if the number of parameters will be larger (e.g. spot(s) present in the atmosphere(s) of component(s)). We had made computations for an artificial function of  $m (= 1, 2, 3)$  variables (Andronov and Tkachenko, 2013). The minimal value  $\delta$  (as a true value was set to zero), which was obtained using  $N$  trial computations in the Monte-Carlo method is statistically proportional to

$$\delta \propto N^{-2/m}, \tag{7}$$

i.e. the number of computations  $N \propto \delta^{-m/2}$  drastically increases with both an increasing accuracy and number of parameters. For our simplified model, the numerical experiments statistically support this relation. Also, the distance between the “successful computations” (when the test function becomes smaller than all previous ones)  $\Delta N \propto N$ . Obviously, it is not realistic to make computations of the test function for billions of times to get a set of statistically optimal parameters. In the “brute force” method, the test functions are

computed using a grid in the  $m$  – dimensional space, so the interval of each parameter is divided by  $n_i$  points. The number of computations is  $N = n_1 n_2 \dots n_m$  should be still large. Either the Monte Carlo method, or the “brute force” one allow to determine positions of the possible local extrema in an addition to the global one. However, if the preliminary position is determined, one should use faster methods to reach the minimum. Classically, there may be used the method of the “steepest descent” (also called the “gradient descent”), where the new set of parameters may be determined as

$$C_{k+1,i} = C_{k,i} - \lambda h_{k,i}, \quad (8)$$

where  $C_{k,i}$  is the estimated value of the coefficient  $C_i$  at  $k$ -th iteration,  $h_{k,i}$  – proposed vector of direction for the coefficient  $C_i$ , and  $\lambda$  is a parameter. Typically one may use one of the methods for one-dimensional minimization (Press et al., 2007; Korn and Korn, 1968), determine a next set of the parameters  $C_{k,i}$ , recompute a new vector  $h_{k,i}$  and again minimize  $\lambda$ . In the method of the steepest descent, one may use a  $h_{k,i} = \partial F / \partial C_i$  gradient as a simplest approximation to this vector. Another approach (Newton–Raphson) is to redefine a function  $F(\lambda) = F(C_i, i = 1 \dots m)$ , compute the root of equation  $\partial F / \partial \lambda = 0$ , and then to use a parabolic approximation to this function. Thus

$$\lambda = \left( \partial F / \partial \lambda \right) / \left( \partial^2 F / \partial \lambda^2 \right). \quad (9)$$

There may be some modifications of the method based on a decrease of  $\lambda$ , which may be recommended, if the shape of the function significantly differs from a parabola. In the method of “conjugated gradients”, the function is approximated by a second-order polynomial. Finally it is usually recommended to use the (Marquardt, 1963) algorithm. We tested this algorithm with a combination of the “steepest descent” (when the determinant of the Hessian matrix is negative) and “conjugated gradients” (if positive), which both are efficient for a complex behaviour of the test function.

### 3 PHENOMENOLOGICAL MODELLING

Besides physical modelling of binary stars, there are methods, which could be introduced as “phenomenological” ones. In other words, we apply approximations with some phenomenological parameters, which have no direct relation to physical parameters – masses, luminosities, radii etc. The most often used are algebraic polynomial approximations, included in the majority of computer programs (e.g. electronic tables like Microsoft Office Excel, Libre/Open Office Calc, GNUMERIC etc.). For periodic processes, one can use a trigonometric polynomial (also called “restricted sum of Fourier series”)

$$\begin{aligned} x_c(\phi, s) &= C_1 + \sum_{j=1}^s (C_{2j} \cos(2j\pi\phi) + C_{2j+1} \sin(2j\pi\phi)) \\ &= C_1 + \sum_{j=1}^s R_j \cos(2j\pi(\phi - \phi_j)). \end{aligned} \quad (10)$$

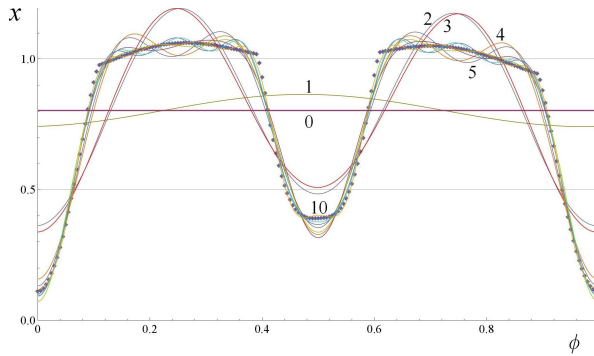


**Figure 5.** Trigonometrical polynomial approximations of the phenomenological light curve. The degree  $s$  is shown by numbers near corresponding curves.

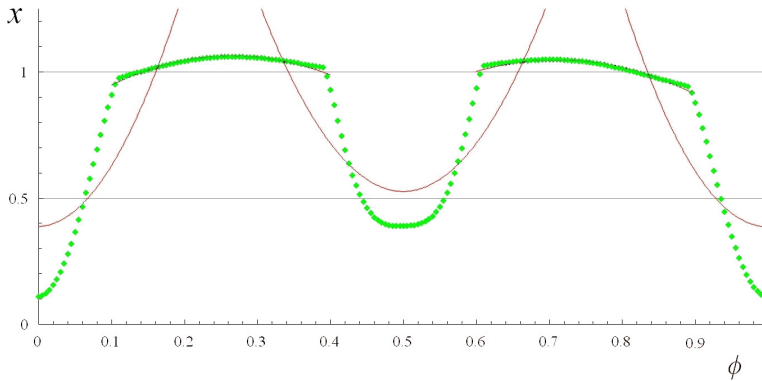


**Figure 6.** The model light curve and its approximation by parabola at the intervals of phases centered on mainima and maxima, as proposed by (Papageorgiou et al., 2014)

The upper Equation is used for determination (using the Least Squares method) of the parameters  $C_\alpha$ ,  $\alpha = 1 \dots m$ , where the number of parameters is  $m = 1 + 2s$ , where the lower converts the pairs of the coefficients  $C_{2j+1}$ ,  $C_{2j+1}$  for each  $(j - 1)$ -th harmonic according to usual relations

$$\begin{aligned}
 C_{2j} &= R_j \cos(2j\pi\phi_0) , \\
 C_{2j+1} &= R_j \sin(2j\pi\phi_0) , \\
 R_j &= (C_{2j}^2 + C_{2j+1}^2)^{1/2} , \\
 \phi_j &= \text{atan}(C_{2j+1}/C_{2j})/2\pi + 0.25(1 - \text{sign}(C_{2j})) .
 \end{aligned}
 \tag{11}$$

Here  $j = 1 \dots j_{\max}$ ,  $j_{\max} = n/2$  for even  $n$  and  $j_{\max} = (n - 1)/2$  for odd  $n$ . Using the Least Squares algorithm, it is possible to determine parameters  $C_\alpha$  even for irregularly spaced data e.g. (Andronov, 1994). Only under strong conditions  $\phi_k = \phi_0 + k/n$ , where

$k = 0 \dots n - 1$ ,  $n$  is the number of observations, one may obtain simplified expressions for the “Discrete Fourier Transform” (DFT) as an extension of the original Fourier (1822) method:

$$\begin{aligned} C_0 &= \frac{1}{n} \sum_{k=0}^{n-1} x_k, \\ C_{2j} &= \frac{2}{n} \sum_{k=0}^{n-1} x_k \cos(2j\pi k/n), \\ C_{2j+1} &= \frac{2}{n} \sum_{k=0}^{n-1} x_k \sin(2j\pi k/n). \end{aligned} \tag{12}$$

If  $j = n/2$ , then

$$\begin{aligned} C_n &= \frac{1}{n} \sum_{k=0}^{n-1} (-1)^k x_k, \\ C_{n+1} &= 0. \end{aligned} \tag{13}$$

For irregularly spaced data, there are at least 6 different modifications of the method, which are called themselves as “Fourier Transform”, and give same correct results only under assumptions listed above for the DFT. For irregularly spaced data The links may be found in (Andronov, 2003).

Theoretically, the degree of the trigonometric polynomial  $s$  is infinite for continuous case (number of data  $n \rightarrow \infty$ ) and should be  $s = j_{\max} = \text{int}(n/2)$ , i.e. may be a large number. For this case, one will get an interpolating function. For lower degree  $s < j_{\max}$ , the function is smoothing, and one may use different criteria for choosing the statistically optimal value, e.g. the Fischer’s criterion (or equivalent one based on the Beta-type distribution), the criterion of minimum of r.m.s. error estimate of the smoothing function (at the moments of observations; integrated over all interval; or at some specific value of the argument), or the maximum of the “signal-to-noise” ratio.

However, these sums may show apparent waves (so called Gibbs phenomenon). It may be illustrated in Fig. (5) for a sample function. One may see different approximations. With an increasing  $s$ , the approximation  $x_c(\phi, s)$  becomes closer (in a sense of the Least Squares), but the apparent waves are well pronounced at  $m \ll n$ .

To decrease the number of parameters, (Andronov, 2010, 2012) proposed an approximation combined from a second-degree trigonometric polynomial and a local function modelling the shape of the eclipses:

$$\begin{aligned} x_c(\phi) &= C_1 + C_2 \cos(2\pi\phi) + C_3 \sin(2\pi\phi) + \\ &+ C_4 \cos(4\pi\phi) + C_5 \sin(4\pi\phi) + \\ &+ C_6 H(\phi - \phi_0, C_8, \beta_1) + C_7 H(\phi - \phi_0 + 0.5, C_8, \beta_2). \end{aligned} \tag{14}$$

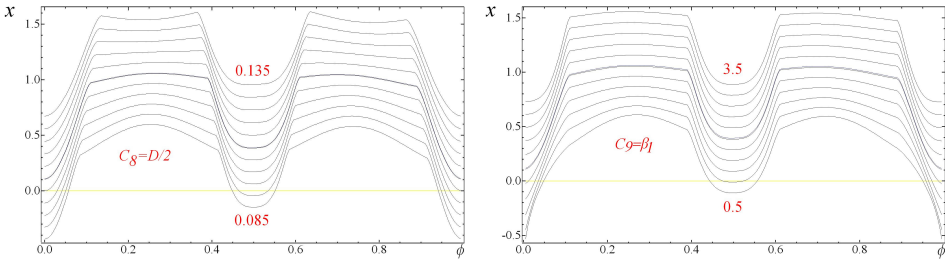


**Figure 7.** Dependencies of the light curves (intensity vs. phase) on the parameters  $C_8 = D/2$  (left) and  $C_9 = \beta_1$  (right). The relative shift in intensity between subsequent curves is 0.1. The thick line shows a best fit curve

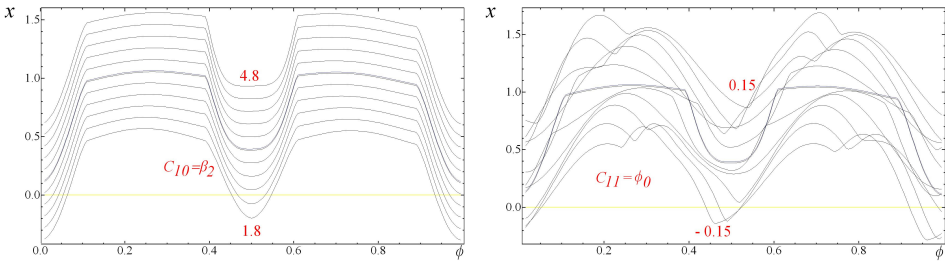


**Figure 8.** Dependencies of the light curves on the parameters  $C_{10} = \beta_2$  (left) and  $C_{11} = \phi_0$  (right).

$$H(\phi, C_8, \beta) = \begin{cases} V(z) = (1 - |z|^\beta)^{3/2} & \text{if } |z| < 1, \\ 0 & \text{if } |z| \geq 1, \end{cases} \quad (15)$$

where  $z = 2\phi/D$ ,  $\phi = E - \text{int}(E + 0, 5) - \text{phase}$ ,  $E = (t - T_0)/P$  – (non-integer) cycle number,  $t$  – time,  $T_0$  – initial epoch,  $P$  – period,  $D$  – full duration of minimum in units of  $P$ .

Papageorgiou et al. (2014) made a statistical study of a sample of eclipsing binaries. They have used an oversimplified approximations of the light curves, approximating the my a parabolic fit over overlapping intervals  $[-0.2, +0.2]$ ,  $[0.1, 0.4]$ ,  $[0.3, 0.7]$ ,  $[0.6, 0.9]$ ,  $[0.8, 1.2]$ . Obviously, the first and last interval correspond to the same observations. In Figure 6 we show their fit to our sample light curve. One may see a relatively good approximation of the out-of-eclipse part of the light curve, and a bad approximation of the zone of minimum. A better coincidence of the fit near minima may be expected for EW-type stars, whereas for EA-type stars our NAV algorithm produces significantly better approximation for all phases.

To illustrate the dependence of the “best fit” light curves on the “non-linear” parameters  $C_8 \dots C_{11}$ , we show corresponding approximations in Fig. 7 and Fig. 8. The thick line in the middle of each figures corresponds to the curve for the sample parameters 1,  $-0.04$ ,  $0.01$ ,  $-0.05$ ,  $0.01$ ,  $-0.8$ ,  $-0.6$ ,  $0.11$ ,  $2$ ,  $3.3$ ,  $0$  for  $C_1 \dots C_{11}$ , respectively.

One may see the significant variations of the shape of the curve and, for each real observations, the best fit solution is expected to be unique. As in previous cases, the solution may be determined using different methods.

#### 4 CONCLUSIONS

The “simplified” and “phenomenological” models are discussed. The behaviour of the test functions resembles that of the test-function for the “physical” model based on the Wilson and Devinney (1971) code and its improvements. Few algorithms for the statistically optimal determination of the parameters have been tested on these test functions, and we prefer to use a “combined” algorithm, where the best method for an estimate of the next set of the parameters is chosen at each step, making the convergence of the numerical solution as fast as possible.

The specified shapes – either for the “simplified” model, or the “phenomenological” one – are much more effective for the EA-type stars with narrow minima, but also can be applied to EB-type and EW-type stars with smooth variations.

We developed the software realizing various methods for study of variable stars. The results of this study will be used in the frame of the projects “Ukrainian Virtual Observatory” (UkrVO) (Vavilova et al., 2012) and “Inter-Longitude Astronomy” (Andronov et al., 2010).

#### REFERENCES

- Anderson, T. W. (1984), *An Introduction to Multivariate Statistical Analysis*, Wiley Series in Probability and Mathematical Statistics, Wiley, ISBN 9780471521600, URL <http://books.google.com.pe/books?id=9dA0AAAACAAJ>.
- Andronov, I. L. (1991), Structure and evolution of stars, Odessa Inst. Adv. Teachers.
- Andronov, I. L. (1994), (Multi-) Frequency Variations of Stars. Some Methods and Results, *Odessa Astronomical Publications*, **7**, p. 49.
- Andronov, I. L. (2003), Multiperiodic versus noise variations: mathematical methods, in C. Sterken, editor, *Interplay of Periodic, Cyclic and Stochastic Variability in Selected Areas of the H-R Diagram*, volume 292 of *Astronomical Society of the Pacific Conference Series*, p. 391.
- Andronov, I. L. (2010), Mathematical modeling of the light curves using the “new algol variables” (nav) algorithm, Int. Conf. KOLOS-2010 Abstract Booklet.
- Andronov, I. L. (2012), Phenomenological modeling of the light curves of algol-type eclipsing binary stars, *Astrophysics*, **55**, pp. 536–550, arXiv: 1208.3655.
- Andronov, I. L., Antoniuk, K. A., Baklanov, A. V., Breus, V. V., Burwitz, V., Chinarova, L. L., Chochol, D., Dubovsky, P. A., Han, W., Hegedus, T., Henden, A., Hric, L., Chun-Hwey, K., Yonggi, K., Kolesnikov, S. V., Kudzej, I., Liakos, A., Niarchos, P. G., Oksanen, A., Patkos, L., Petrik, K., Pit', N. V., Shakhovskoy, N. M., Virnina, N. A., Yoon, J. and Zola, S. (2010), Inter-Longitude Astronomy (ILA) Project: Current Highlights And Perspectives. I. Magnetic vs. Non-Magnetic Interacting Binary Stars, *Odessa Astronomical Publications*, **23**, p. 8.
- Andronov, I. L. and Tkachenko, M. G. (2013), Comparative Analysis of Numerical Methods for Parameter Determination, *Czestochowski Kalendarz Astronomiczny 2014*, pp. 173–180, arXiv: 1310.1967.

- Cherepashchuk, A. M. (1993), Parametric Models in Inverse Problems of Astrophysics, *Astronomicheskii Zhurnal*, **70**, p. 1157.
- Kallrath, J. and Milone, E. F. (2009), *Eclipsing Binary Stars: Modeling and Analysis*, Springer-Verlag, New York, ISBN 978-1-4419-0698-4.
- Korn, G. A. and Korn, T. M. (1968), *Definitions, theorems, and formulas for reference and review*, McGraw-Hill, New York.
- Marquardt, D. (1963), A Method for the Solution of Certain Problems in Least Squares, *J. Soc. Indust. Appl. Math.*, **11**(2), pp. 431–441.
- Papageorgiou, A., Klefogiannis, G. and Christopoulou, P.-E. (2014), An automated search of O'Connell effect from surveys of eclipsing binaries, *Contributions of the Astronomical Observatory Skalnaté Pleso*, **43**, pp. 470–472.
- Parento, P. P. and Kukarkin, B. W. (1936), The Shapes of Light Curves of Long Period Cepheids. Mit 12 Abbildungen., *Zeitschrift für Astrophysik*, **11**, p. 337.
- Pickering, E. (1881), Variable Stars of Short Period., *Proc. Amer. Acad. Arts and Sciences*, **16**, pp. 257–278.
- Press, W. H., Teukolsky, S. A., Vetterling, W. T. and Flannery, B. P. (2007), *Numerical Recipes 3rd Edition: The Art of Scientific Computing*, Cambridge University Press, New York, NY, USA, 3 edition, ISBN 0521880688, 9780521880688.
- Vavilova, I. B., Pakulyak, L. K., Shlyapnikov, A. A., Protsyuk, Y. I., Savanevich, V. E., Andronov, I. L., Andruk, V. N., Kondrashova, N. N., Baklanov, A. V., Golovin, A. V., Fedorov, P. N., Akhmetov, V. S., Isak, I. I., Mazhaev, A. E., Golovnya, V. V., Virun, N. V., Zolotukhina, A. V., Kazantseva, L. V., Virnina, N. A., Breus, V. V., Kashuba, S. G., Chinarova, L. L., Kudashkina, L. S. and Epishev, V. P. (2012), Astroinformation resource of the Ukrainian virtual observatory: Joint observational data archive, scientific tasks, and software, *Kinematics and Physics of Celestial Bodies*, **28**, pp. 85–102.
- Wilson, R. E. and Devinney, E. J. (1971), Realization of Accurate Close-Binary Light Curves: Application to MR Cygni, *Astrophys. J.*, **166**, p. 605.
- Zola, S., Gazeas, K., Kreiner, J. M., Ogloza, W., Siwak, M., Koziel-Wierzbowska, D. and Winiarski, M. (2010), Physical parameters of components in close binary systems - VII, *Monthly Notices Roy. Astronom. Soc.*, **408**, pp. 464–474.
- Zola, S., Kolonko, M. and Szczech, M. (1997), Analysis of a photoelectric light curve of the WUMa-type binary ST Ind., *Astronomy and Astrophysics*, **324**, pp. 1010–1012.



# Confronting models of twin peak quasi-periodic oscillations: Mass and spin estimates fixed by neutron star equation of state

Gabriel Török<sup>1</sup>, Kateřina Goluchová<sup>1</sup>, Martin Urbanec<sup>1</sup>,  
Eva Šrámková<sup>1</sup>, Karel Adámek<sup>1</sup>, Gabriela Urbancová<sup>1</sup>,  
Tomáš Pecháček<sup>2</sup>, Pavel Bakala<sup>1</sup>, Zdeněk Stuchlík<sup>1</sup>,  
Jiří Horák<sup>2</sup> and Jakub Juryšek<sup>1</sup>

<sup>1</sup>Institute of Physics, Faculty of Philosophy & Science, Silesian University in Opava,  
Bezručovo nám. 13, CZ-746 01 Opava, Czech Republic

<sup>2</sup>Astronomical Institute, Boční II 1401/2a, CZ-14131 Praha 4 – Spořilov, Czech Republic

## ABSTRACT

Twin-peak quasiperiodic oscillations (QPOs) are observed in the X-ray power-density spectra of several accreting low-mass neutron star (NS) binaries. In our work we consider several QPO models and focus especially on the atoll source 4U 1636-53 with its large set of QPO measurements. We find that the considered models require the QPO excitation radii in 4U 1636-53 to be close to the inner-most stable circular orbit of the accretion disc. We explore and summarize mass-angular-momentum relations and limits on NS compactness implied by individual QPO models. We confront these relations with NS parameters given by various NS equations of state (EoS). The application of concrete EoS removes the degeneracy in the mass and angular momentum determined from the QPO models when the spin frequency is known. Moreover, the applied NS EoS are compatible only with some of the considered QPO models. In our work we compare simplified calculations that assume Kerr background geometry to the detailed calculations considering NS oblateness influence in Hartle–Thorne spacetimes.

**Keywords:** X-rays: binaries – Accretion, accretion disks – Stars: neutron – Equation of state

## 1 INTRODUCTION

Accreting neutron stars (NSs) are believed to be the compact component in more than 20 low mass X-ray binaries (LMXBs). In these systems, the mass is transferred from the companion by overflowing the Roche lobe and forming an accretion disk that surrounds the NS. The disk contributes significantly to high X-ray luminosity of these objects while the most of the radiation comes from its inner parts and disk-NS boundary layer. According to their X-ray spectral and timing properties, the NS LMXBs were further classified into Z and atoll sources, whose names were inspired by the shapes of tracks they trace in the color-color

diagram (e.g. van der Klis, 2005). While the Z sources are generally more stable and brighter, the atoll sources are weaker and shows significant changes in X-ray luminosity. Both classes exhibit a variability over a large range of frequencies. Apart of irregular changes, their power spectra contain also relatively coherent features known as quasiperiodic oscillations (QPOs).

So called low frequency QPOs have frequencies in the range of 1–100 Hz. In the case of Z-sources they have been further classified into horizontal, flaring, and normal branch oscillations (HBO, FBO and NBO, respectively) according to the position of the source in the color-color diagram. Oscillations of similar properties to HBOs were observed also in several atoll sources (see van der Klis, 2006 for a review). Much attention among theorists is however attracted to the kilohertz QPOs (100–1000 Hz) because their high frequencies are comparable to the orbital timescale in a vicinity of a NS. It is believed that this coincidence represents a strong indication that the corresponding signal originates in the innermost parts of the accretion disks or close to the surface of the NS itself. This believe was also supported by means of Fourier-resolved spectroscopy (e.g. Gilfanov et al., 2000).

The kHz QPOs have similar properties in both Z and atoll sources. They are frequently observed in pairs often called twin peak QPOs. Their ‘upper’ and ‘lower’ QPO frequencies ( $\nu_u$  and  $\nu_l$ , respectively) exhibit a strong and remarkably stable positive correlation and clustering around the rational ratios. These ratios are emphasized either due to the intrinsic source clustering or weakness of the two QPOs outside the limited frequency range (suggesting possible resonant energy exchange between two physical oscillators Abramowicz et al., 2003a; Belloni et al., 2005, 2007; Török et al., 2008a,b,c; Barret and Boutelier, 2008; Horák et al., 2009; Boutelier et al., 2010). The other properties of each oscillation (e.g. the rms-amplitude and the quality factor) seem to depend mostly on its frequency, and the way how they vary is different between the upper or lower oscillation. These differences often help to identify the type of kHz QPO in cases when only one peak is present in power spectra (Barret et al., 2005, 2006; Méndez, 2006; Török, 2009).

Many models have been proposed to explain the rich phenomenology of twin peak QPOs (Alpar and Shaham, 1985; Lamb et al., 1985; Miller et al., 1998; Psaltis et al., 1999; Wagoner, 1999; Wagoner et al., 2001; Abramowicz and Kluźniak, 2001; Kluźniak and Abramowicz, 2001; Kato, 2001; Titarchuk and Wood, 2002; Abramowicz et al., 2003b,c; Rezzolla et al., 2003; Kluźniak et al., 2004; Pétri, 2005; Zhang, 2005; Bursa, 2005; Török et al., 2007; Kato, 2007, 2008; Stuchlík et al., 2008; Čadež et al., 2008; Kostić et al., 2009; Germanà et al., 2009; Mukhopadhyay, 2009 and several others). While any acceptable model should address both the excitation mechanism and subsequent modulation of the resulting X-ray signal as well as their overall observational properties, most of the theoretical effort has been so far devoted to the observed frequencies. Clearly, their correlations serve as a first test of the model viability.

Comparison between the observed and expected frequencies can reveal the mass and angular momentum of the NS. These can be confronted with models of rotating NS based on a modern equation of state (EoS, e.g. Urbanec et al., 2010b). Here we extend the work started by Török et al. (2010, 2012). We explore and summarize findings on mass-angular-momentum relations and limits on NS compactness implied by several QPO models. We confront these findings with NS parameters given by various EoS. Our paper briefly sketch some results from the prepared publication of Török et al. (2015).

## 2 TWIN PEAK QPO MODELS AND THEIR APPROXIMATION IN KERR SPACETIMES

Within the framework of many QPO models, the observable frequencies can be expressed directly in terms of epicyclic frequencies. Formulae for the Keplerian, radial and vertical epicyclic frequency in Kerr spacetimes were first derived by Aliev and Galtsov (1981). In a commonly used form (e.g. Török and Stuchlík, 2005) they read

$$\Omega_K = \frac{\mathcal{F}}{j + x^{3/2}}, \quad \nu_r = \Gamma \Omega_K, \quad \nu_\theta = \Delta \Omega_K, \quad (1)$$

where

$$\Gamma = \sqrt{\frac{-3j^2 + 8j\sqrt{x} + (-6+x)x}{x^2}}, \quad \Delta = \sqrt{1 + \frac{j(3j - 4\sqrt{x})}{x^2}}, \quad (2)$$

$x \equiv r/M$ , and the “relativistic factor”  $\mathcal{F}$  reads  $\mathcal{F} \equiv c^3/(2\pi GM)$ . We note that Kerr geometry represents an applicable approximation of NS spacetimes when the compact object mass is high (Török et al., 2010; Urbanec et al., 2013).

### 2.1 Twin peak QPO Models

Here we investigate a subset of models which have been previously considered in studies of Török et al. (2011, 2012). Below we briefly outline the list of these models.

*RP model.* The relativistic precession model explains the kHz QPOs as a direct manifestation of modes of relativistic epicyclic motion of blobs at various radii  $r$  in the inner parts of the accretion disc (Stella and Vietri, 1999). For the RP model, one can easily solve relations defining the upper and lower QPO frequencies in terms of the orbital frequencies to arrive at an explicit formula which relates the upper and lower QPO frequencies in units of Hertz as (Török et al., 2010, 2012)

$$\nu_L = \nu_U \left\{ 1 - \left[ 1 + \frac{8j\nu_U}{\mathcal{F} - j\nu_U} - 6 \left( \frac{\nu_U}{\mathcal{F} - j\nu_U} \right)^{2/3} - 3j^2 \left( \frac{\nu_U}{\mathcal{F} - j\nu_U} \right)^{4/3} \right]^{1/2} \right\}. \quad (3)$$

*TD model.* Concept similar to RP model where QPOs are generated by a tidal disruption of large accreting inhomogeneities (Germanà et al., 2009). The evaluation of the explicit relation between the two observed QPO frequencies is possible in a way similar to the RP model (Török et al., 2012),

$$\nu_U = \nu_L \left\{ 1 + \left[ 1 + \frac{8j\nu_L}{\mathcal{F} - j\nu_L} - 6 \left( \frac{\nu_L}{\mathcal{F} - j\nu_L} \right)^{2/3} - 3j^2 \left( \frac{\nu_L}{\mathcal{F} - j\nu_L} \right)^{4/3} \right]^{1/2} \right\}. \quad (4)$$

*WD model.* Oscillation model that assumes non-axisymmetric modes (Kato, 2001). The upper and lower QPO frequencies for the WD model can be expressed as

$$\nu_U = 2(1 - \Gamma) \Omega_K, \quad \nu_L = (2 - \Gamma) \Omega_K. \quad (5)$$

*RP1 and RP2 models.* Models dealing with non-axisymmetric disc-oscillation modes whose frequencies almost coincide with the frequencies predicted by the RP model (Bursa, 2005; Török et al., 2010). For the RP1 model they can be written as

$$\nu_U = \Omega_K \Delta, \quad \nu_L = (1 - \Gamma) \Omega_K, \quad (6)$$

and for the RP2 model as

$$\nu_U = (2 - \Delta) \Omega_K, \quad \nu_L = (1 - \Gamma) \Omega_K. \quad (7)$$

### 3 MASS AND SPIN OF NS IN ATOLL SOURCE 4U 1636-53 (ESTIMATES ASSUMING HIGH NS COMPACTNESS)

Observations of the peculiar Z-source Circinus X-1 display unusually low QPO frequencies. On the contrary, the atoll source 4U 1636-53 displays the twin-peak QPOs at very high frequencies (see the left panel of Fig. 1). In Török et al. (2011, 2012) we have assumed high mass (Kerr) approximation of NS spacetimes and demonstrated that

- For each twin-peak QPO model and source, the model consideration results in a specific relation between the NS mass  $M$  and angular-momentum  $j$  rather than in their single preferred combination.
- The data of sources displaying high QPO frequencies (or low frequency ratios, e.g. 4U 1636-53) are much more useful for testing the orbital QPO models than the data of sources displaying low QPO frequencies (or high frequency ratios, e.g. Circinus X-1).
- The considered QPO models require the QPO excitation radii in 4U 1636-53 to be close to the inner-most stable circular orbit of the accretion disc (ISCO).
- The inferred mass of NS in 4U 1636-53 is rather high, above  $1.8 M_\odot$ , when geodesic models are assumed.

For the atoll source 4U 1636-53 there is a good evidence on the NS spin frequency based on the X-ray burst measurements. Depending on the (two- or one-) hot spot model consideration, the NS spin frequency equals either 291 Hz or 582 Hz (Strohmayer and Markwardt, 2002). Thus, one can in principle infer the angular momentum  $j$  and remove the  $M$ - $j$  degeneracies related to the individual twin-peak QPO models.

#### 3.1 Twin Peak QPO Models vs. NS EoS

Following Török et al. (2012) we calculate  $\chi^2$  maps resulting from fitting of the 4U 1636-53 data for various twin-peak QPO models. These maps are compared to the  $M$ - $j$  relations calculated from several NS EoS assuming that the spin frequency is either 290 Hz or 580 Hz (depending on the consideration of one or two hot-spot model for X-ray bursts). In our calculations we follow the approach of Hartle (1967); Hartle and Thorne (1968); Chandrasekhar and Miller (1974); Miller (1977); Urbanec et al. (2010a). We assume the following set of EoS:

- SLy 4 (Řípková Stone et al., 2003).
- APR (Akmal et al., 1998).
- AU-WFF1, UU-WFF2 and WS-WFF3 (Wiringa et al., 1988; Stergioulas and Friedman, 1995).

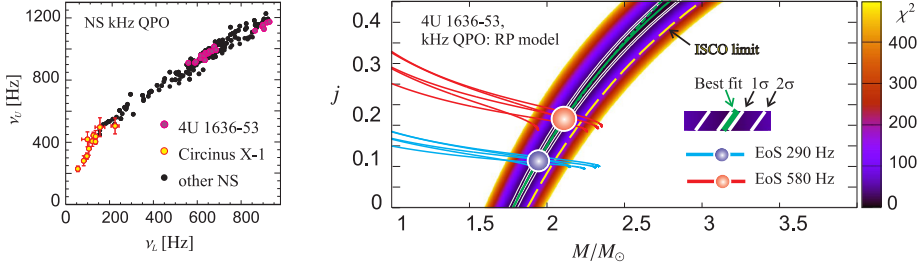


**Figure 1.** After Török et al. (2012). *Left:* Frequencies of kHz QPOs in various NS sources. *Right:* The  $\chi^2$  map of RP model vs. mass-angular momentum relations predicted by NS EoS. The  $\chi^2$  map results from the fits of RP model to the kHz QPO data of 4U 1636-53. The green line indicates the best  $\chi^2$  for a fixed  $M$  while the dashed green line denotes its quadratic approximation. The white lines indicate corresponding  $1\sigma$  and  $2\sigma$  confidence levels. The dashed-yellow line indicates a simplified estimate on the upper limits on  $M$  and  $j$  assuming that the highest observed upper QPO frequency in 4U 1636-53 is associated to the ISCO. The NS EoS are assumed for the rotational frequency inferred from the X-ray burst measurements. The blue spot roughly indicates the combination of mass and spin resulting from the consideration of the spin frequency 290 Hz, several concrete equations of state and given QPO model. The red spot indicates the same but for the spin frequency 580 Hz.

In the right panel of Fig. 1 we illustrate the potential of such approach in the case of the relativistic precession QPO model while other models are considered in Fig. 2. Related indicative estimates of NS parameters are summarized in Table 1.

#### 4 CALCULATIONS IN HARTLE–THORNE SPACETIMES CONSIDERING NS OBLATENESS

So far we have neglected influence of NS oblateness assuming that the star is very compact having thus oblateness factor  $\tilde{q} \equiv q/j^2$  close to the Kerr limit, i.e. it has been assumed that  $\tilde{q} \sim 1$ . In a more general case of  $\tilde{q} > 1$ , one can assume NS spacetime approximated by Hartle–Thorne geometry (Hartle, 1967; Hartle and Thorne, 1968).

Based on this approximation, the Keplerian orbital frequency can be expressed as (Abramowicz et al., 2003a)

$$\Omega_{\text{K}} = \frac{\mathcal{F}}{x^{3/2}} \left[ 1 - \frac{j}{x^{3/2}} + j^2 F_1(x) + q F_2(x) \right], \quad (8)$$

where

$$\begin{aligned} F_1(x) &= [48 - 80x + 4x^2 - 18x^3 + 40x^4 + 10x^5 + 15x^6 - 15x^7] \\ &\quad (16(x-2)x^4)^{-1} + A(x), \\ F_2(x) &= \frac{5(6 - 8x - 2x^2 - 3x^3 + 3x^4)}{16(x-2)x} - A(x), \\ A(x) &= \frac{15(x^3 - 2)}{32} \ln \left( \frac{x}{x-2} \right). \end{aligned}$$

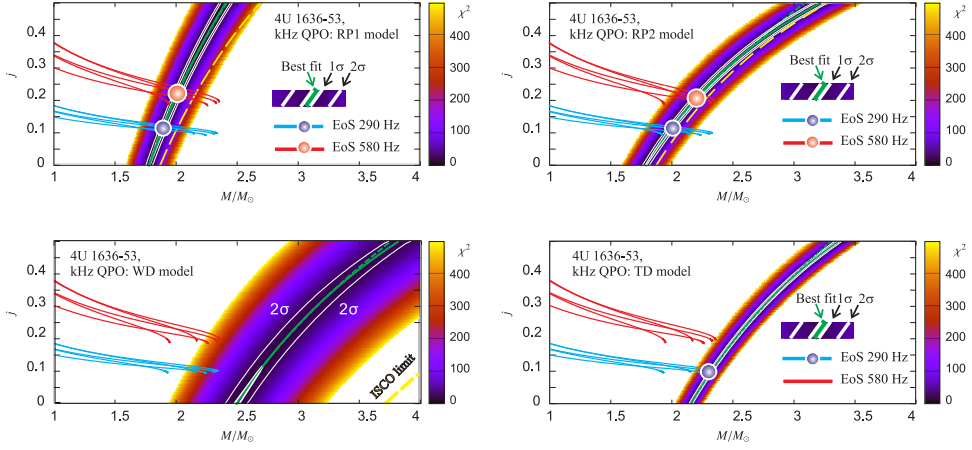


**Figure 2.** The  $\chi^2$  map of RP model vs. mass-angular momentum relations predicted by NS EoS. The *green* line indicates the best  $\chi^2$  for a fixed  $M$  while the *dashed green* line denotes its quadratic approximation. The *white* lines indicate corresponding  $1\sigma$  and  $2\sigma$  confidence levels. The *dashed-yellow* lines indicate simplified estimates on the upper limits on  $M$  and  $j$  assuming that the highest observed upper QPO frequency in 4U 1636-53 is associated to the ISCO. The NS EoS are assumed for the rotational frequency inferred from the X-ray burst measurements. The *blue* spot roughly indicates the combination of mass and spin resulting from the consideration of the spin frequency 290 Hz, several concrete equations of state and given QPO model. The *red* spot indicates the same but for the spin frequency 580 Hz.

Radial and vertical epicyclic frequency are then described by the following terms

$$\nu_r^2 = \frac{\mathcal{F}^2(x-6)}{x^4} [1 + jF_1(x) - j^2F_2(x) - qF_3(x)], \quad (9)$$

$$\nu_\theta^2 = \frac{\mathcal{F}^2}{x^3} [1 - jG_1(x) + j^2G_2(x) + qG_3(x)], \quad (10)$$

where

$$F_1(x) = \frac{6(x+2)}{x^{3/2}(x-6)},$$

$$F_2(x) = [8x^4(x-2)(x-6)]^{-1} [384 - 720x - 112x^2 - 76x^3 - 138x^4 - 130x^5 + 635x^6 - 375x^7 + 60x^8] + A(x),$$

$$F_3(x) = \frac{5(48 + 30x + 26x^2 - 127x^3 + 75x^4 - 12x^5)}{8x(x-2)(x-6)} - A(x),$$

$$A(x) = \frac{15x(x-2)(2+13x-4x^2)}{16(x-6)} \ln\left(\frac{x}{x-2}\right), \quad (11)$$

**Table 1.** Neutron star parameters implied by consideration of twin peak QPO models in Kerr spacetimes. The displayed values result from the confrontation of these models with outcomes of NS modelling shown in Figs. 1 and 2.

<b>Model, frequencies</b>	<b>M(290 Hz)</b>	<b>j(290 Hz)</b>	<b>M(580 Hz)</b>	<b>j(580 Hz)</b>
<b>RP</b> $\nu_L = \nu_K - \nu_r,$ $\nu_U = \nu_K$	$1.9 M_\odot$	0.11	$2.1 M_\odot$	0.21
<b>TD</b> $\nu_L = \nu_K,$ $\nu_U = \nu_K + \nu_r$	$2.3 M_\odot$	0.10	–	–
<b>WD</b> $\nu_L = 2(\nu_K - \nu_r),$ $\nu_U = 2\nu_K - \nu_r$	–	–	–	–
<b>RP1</b> $\nu_L = \nu_K - \nu_r,$ $\nu_U = \nu_\theta$	$1.8 M_\odot$	0.11	$2.0 M_\odot$	0.21
<b>RP2</b> $\nu_L = \nu_K - \nu_r,$ $\nu_U = 2\nu_K - \nu_\theta$	$2.0 M_\odot$	0.11	$2.2 M_\odot$	0.20

$$G_1(x) = \frac{6}{x^{3/2}},$$

$$G_2(x) = [8x^4(x-2)]^{-1} [48 - 224x + 28x^2 + 6x^3 - 170x^4 + 295x^5 - 165x^6 + 30x^7] - B(x),$$

$$G_3(x) = \frac{5(6 + 34x - 59x^2 + 33x^3 - 6x^4)}{8x(x-2)} + B(x),$$

$$B(x) = \frac{15(2x-1)(x-2)^2}{16} \ln\left(\frac{x}{x-2}\right).$$

#### 4.1 Results for RP Model (Hartle–Thorne Spacetimes)

Assuming the formulae above we calculated 3D- $\chi^2$  maps for the RP model. In the left panel of Fig. 3 we show behaviour of the best  $\chi^2$  as a function of  $M$  and  $j$  for several color-coded values of  $\tilde{q}$ . For each value of  $\tilde{q}$  there is a preferred  $M$ - $j$  relation. We find that, although such a relation has a global minimum, the gradient of  $\chi^2$  is always much lower along the relation than the gradient in the perpendicular direction. In other words,  $\chi^2$  maps for a fixed  $\tilde{q}$  are of the same type as that calculated in Kerr spacetime. It follows then that there is a global  $M$ - $j$ - $\tilde{q}$  degeneracy in the sense discussed by Török et al. (2012).

As emphasized by Urbanec et al. (2010b), Török et al. (2010), Kluźniak and Rosińska (2013), Török et al. (2014), and Rosińska et al. (2014), newtonian effects following from the influence of quadrupole moment act on orbital frequencies in opposite way than relativistic

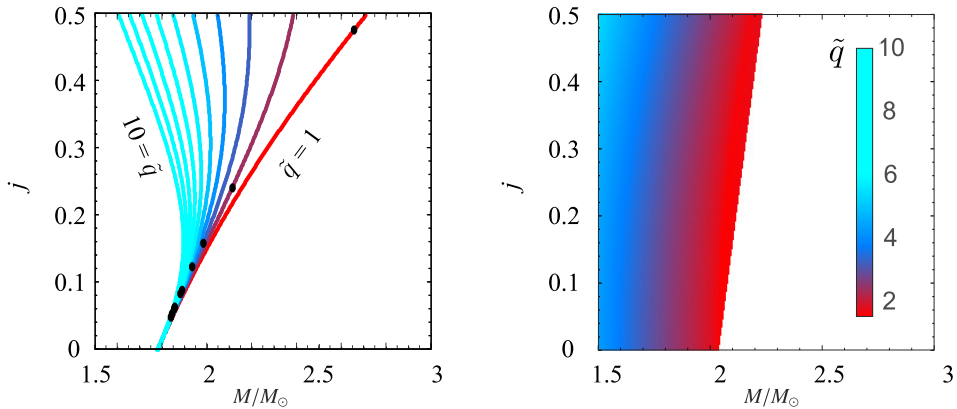


**Figure 3.** *Left:* Behaviour of the best  $\chi^2$  as a function of  $M$  and  $j$  for several values of  $\tilde{q}$ . *Dots* denote global minima for each value of  $\tilde{q}$  (see however the main text – Section 4.1, for a comment on this). *Right:* The 2D surface in the 3D  $M$ - $j$ - $\tilde{q}$  space given by SLy4 EoS.

effects when the angular momentum is increased. The behaviour of the relations shown in the left panel of Fig. 3 is determined by this interplay. Because of this, we can see that high NS oblateness can compensate the increase of the estimated mass due to high angular momentum.

## 5 CONSIDERATION OF CONCRETE EOS

The relations for RP model drawn in the left panel of Fig. 3 result from fitting of 4U 1636-53 datapoints considering the general Hartle–Thorne spacetime. The consideration does not include strong restrictions following from NS modelling. It can be shown that a concrete NS EoS covers only a 2D surface in the 3D  $M$ - $j$ - $\tilde{q}$  space. Thus, when a given EoS is assumed, only corresponding 2D surface is relevant for fitting of datapoints by a given QPO model. Following Urbanec et al. (2013), we illustrate such a surface in the right panel of Fig. 3 for SLy4 EoS. The color-coding of the plot is the same as that on the left panel of the same Figure. The corresponding final  $M$ - $j$ - $\chi^2$  map for the RP model is shown in the left panel of Fig. 4. The right panel of this Figure then shows equivalent  $\chi^2$  map drawn for the NS mass and spin frequency.

## 6 CONCLUSIONS

Using Kerr spacetime approximation valid for NS with high compactness (high mass) we find that fitting of twin peak QPO data results rather in mass-angular-momentum ( $M$ - $j$ ) relations rather than preferred combinations of  $M$  and  $j$  specific for a given model and source. We also demonstrate that the application of concrete EoS removes the degeneracy in the mass and angular momentum determined from the QPO models when the spin frequency is known. Moreover, the applied NS EoS seem to be compatible only with some of the considered QPO models.

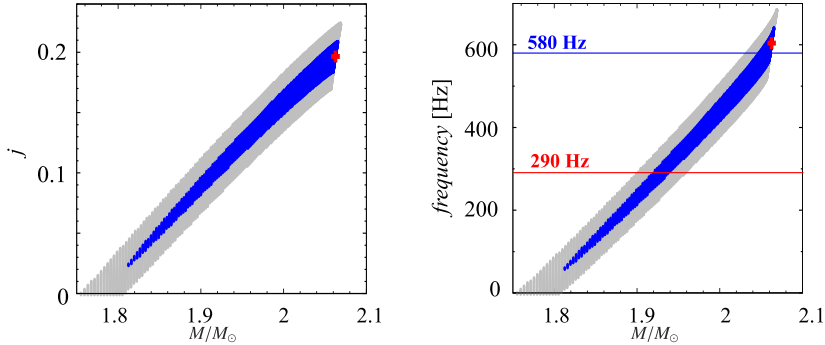


**Figure 4.** *Left:* The final  $M$ - $j$ - $\chi^2$  map for the RP model. Global minimum is denoted by *red* marker. The *dark* colour area denotes  $1\sigma$  confidence level, the *light* colour area denotes  $2\sigma$  confidence level. *Right:* The same map, but drawn for the NS spin frequency. The horizontal *blue* line denotes the higher possible spin frequency measured from X-ray bursts (i.e. 580 Hz). The horizontal *red* line denotes the lower possible spin frequency measured from X-ray bursts (i.e. 290 Hz).

Detailed consideration of rotating NS spacetimes including the influence of NS oblateness reveal  $M$ - $j$  relations similar to the case of Kerr approximation. Finally, inspecting the left panel of Fig. 4, we can see that the concrete EoS, SLy4, considered for RP model then implies a clear  $M$ - $j$  relation. This relation exhibits a shallow minimum. The right panel of the same Figure shows the equivalent relation between the NS mass and spin frequency as well as its shallow minimum. Taking into account the favoured spin frequency inferred from X-ray bursts, 580 Hz, we can see that the NS mass and angular momentum have to be around

$$M \sim 2.05 M_{\odot}, \quad j \sim 0.2. \quad (12)$$

These values are in good agreement with those inferred from the simplified consideration using Kerr spacetimes given in Table 1. Considering the shallow  $\chi^2$  minima denoted in Fig. 4, it can be interesting that its frequency value almost coincides with the measured spin frequency of 580 Hz.

In the Figure 5 we show several relations between the mass and spin frequency obtained for RP model and miscellaneous EoS. These relations are similar to the one discussed above. However, we can see that in several cases given EoS does not provide any match for the spin 580 Hz or even for the spin 290 Hz. This can rule out the considered QPO model and EoS combination. The selection effect comes from the limits on maximal mass allowed by individual EoS. Full discussion of these results will be presented in Török et al. (2015) along with an analogical consideration of the other models examined here in Section 3 and listed in Table 1.

## ACKNOWLEDGEMENTS

GT, ES and MU would like to acknowledge the Czech grant GAČR 209/12/P740. We also acknowledge the project CZ.1.07/2.3.00/20.0071 “Synergy”, aimed to foster international collaboration of the Institute of Physics of SU Opava. We also acknowledge financial support from the internal grants of SU Opava, SGS/11/2013 and SGS/23/2013.

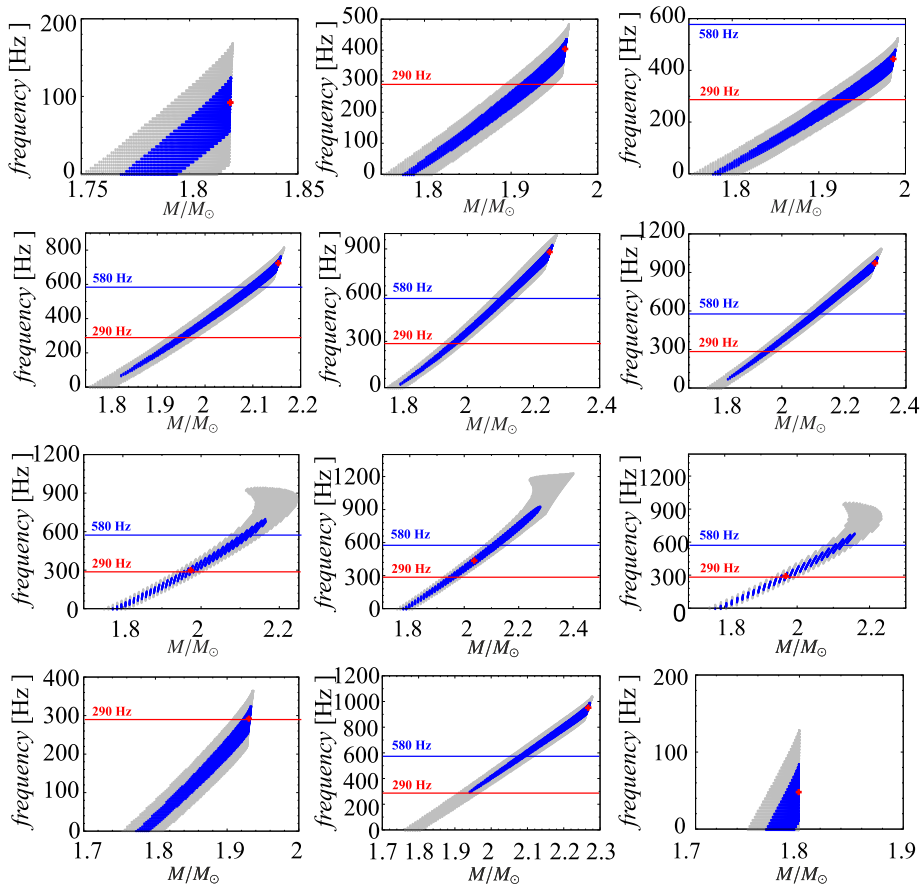


**Figure 5.** The mass-spin  $\chi^2$  maps for the RP model and 12 different EoS. Global minima are denoted by red marker. The dark colour areas denote  $1\sigma$  confidence levels, the light colour areas denote  $2\sigma$  confidence levels. The horizontal blue lines denote the higher possible spin frequency measured from X-ray bursts (i.e. 580 Hz). The horizontal red lines denote the lower possible spin frequency measured from X-ray bursts (i.e. 290 Hz).

## REFERENCES

- Abramowicz, M. A., Almergren, G. J. E., Kluźniak, W. and Thampan, A. V. (2003a), The Hartle–Thorne circular geodesics, *ArXiv General Relativity and Quantum Cosmology e-prints*, arXiv: gr-qc/0312070.
- Abramowicz, M. A., Bulik, T., Bursa, M. and Kluźniak, W. (2003b), Evidence for a 2:3 resonance in Sco X-1 kHz QPOs, *Astronomy and Astrophysics*, **404**, pp. L21–L24, arXiv: astro-ph/0206490.
- Abramowicz, M. A., Karas, V., Kluźniak, W., Lee, W. H. and Rebusco, P. (2003c), Non-Linear Resonance in Nearly Geodesic Motion in Low-Mass X-Ray Binaries, *Publ. Astronom. Soc. Japan*, **55**, pp. 467–466, arXiv: astro-ph/0302183.
- Abramowicz, M. A. and Kluźniak, W. (2001), A precise determination of black hole spin in GRO J1655-40, *Astronomy and Astrophysics*, **374**, pp. L19–L20, arXiv: astro-ph/0105077.

- Akmal, A., Pandharipande, V. R. and Ravenhall, D. G. (1998), Equation of state of nucleon matter and neutron star structure, *Phys. Rev. C*, **58**, pp. 1804–1828, arXiv: [nucl-th/9804027](#).
- Aliev, A. N. and Galtsov, D. V. (1981), Radiation from relativistic particles in nongeodesic motion in a strong gravitational field, *General Relativity and Gravitation*, **13**, pp. 899–912.
- Alpar, M. A. and Shaham, J. (1985), Is GX5 - 1 a millisecond pulsar?, *Nature*, **316**, pp. 239–241.
- Barret, D. and Boutelier, M. (2008), Frequency ratio of twin kHz quasi-periodic oscillations: The case of 4U1820-303, *New Astronomy Reviews*, **51**, pp. 835–840.
- Barret, D., Olive, J.-F. and Miller, M. C. (2005), An abrupt drop in the coherence of the lower kHz quasi-periodic oscillations in 4U 1636-536, *Monthly Notices Roy. Astronom. Soc.*, **361**, pp. 855–860, arXiv: [astro-ph/0505402](#).
- Barret, D., Olive, J.-F. and Miller, M. C. (2006), The coherence of kilohertz quasi-periodic oscillations in the X-rays from accreting neutron stars, *Monthly Notices Roy. Astronom. Soc.*, **370**, pp. 1140–1146, arXiv: [astro-ph/0605486](#).
- Belloni, T., Homan, J., Motta, S., Ratti, E. and Méndez, M. (2007), Rossi XTE monitoring of 4U1636-53 - I. Long-term evolution and kHz quasi-periodic oscillations, *Monthly Notices Roy. Astronom. Soc.*, **379**, pp. 247–252, arXiv: [0705.0793](#).
- Belloni, T., Méndez, M. and Homan, J. (2005), The distribution of kHz QPO frequencies in bright low mass X-ray binaries, *Astronomy and Astrophysics*, **437**, pp. 209–216, arXiv: [astro-ph/0501186](#).
- Boutelier, M., Barret, D., Lin, Y. and Török, G. (2010), On the distribution of frequency ratios of kHz quasi-periodic oscillations, *Monthly Notices Roy. Astronom. Soc.*, **401**, pp. 1290–1298, arXiv: [0909.2990](#).
- Bursa, M. (2005), High-frequency QPOs in GRO J1655-40: Constraints on resonance models by spectral fits, in S. Hledík and Z. Stuchlík, editors, *Proceedings of RAGtime 6/7: Workshops on black holes and neutron stars, Opava, 16–18/18–20 September 2004/2005*, pp. 39–45, Silesian University in Opava, Opava, ISBN 80-7248-334-X.
- Chandrasekhar, S. and Miller, J. C. (1974), On slowly rotating homogeneous masses in general relativity, *Monthly Notices Roy. Astronom. Soc.*, **167**, pp. 63–80.
- Germanà, C., Kostić, U., Čadež, A. and Calvani, M. (2009), Tidal Disruption of Small Satellites Orbiting Black Holes, in J. Rodriguez and P. Ferrando, editors, *American Institute of Physics Conference Series*, volume 1126 of *American Institute of Physics Conference Series*, pp. 367–369, arXiv: [0902.2134](#).
- Gilfanov, M., Churazov, E. and Revnivtsev, M. (2000), Frequency-resolved spectroscopy of Cyg X-1: fast variability of the reflected emission in the soft state, *Monthly Notices Roy. Astronom. Soc.*, **316**, pp. 923–928, arXiv: [astro-ph/0001450](#).
- Hartle, J. B. (1967), Slowly Rotating Relativistic Stars. I. Equations of Structure, *Astrophys. J.*, **150**, p. 1005.
- Hartle, J. B. and Thorne, K. S. (1968), Slowly Rotating Relativistic Stars. II. Models for Neutron Stars and Supermassive Stars, *Astrophys. J.*, **153**, p. 807.
- Horák, J., Abramowicz, M. A., Kluźniak, W., Rebusco, P. and Török, G. (2009), Internal resonance in nonlinear disk oscillations and the amplitude evolution of neutron-star kilohertz QPOs, *Astronomy and Astrophysics*, **499**, pp. 535–540, arXiv: [0901.3076](#).
- Kato, S. (2001), Basic Properties of Thin-Disk Oscillations, *Publ. Astronom. Soc. Japan*, **53**, pp. 1–24.
- Kato, S. (2007), Frequency Correlations of QPOs Based on a Disk Oscillation Model in Warped Disks, *Publ. Astronom. Soc. Japan*, **59**, pp. 451–455, arXiv: [astro-ph/0701085](#).
- Kato, S. (2008), Resonant Excitation of Disk Oscillations in Deformed Disks II: A Model of High-Frequency QPOs, *Publ. Astronom. Soc. Japan*, **60**, pp. 111–, arXiv: [0709.2467](#).

- Kluźniak, W. and Abramowicz, M. A. (2001), The physics of kHz QPOs—strong gravity’s coupled anharmonic oscillators, *ArXiv Astrophysics e-prints*, arXiv: [astro-ph/0105057](#).
- Kluźniak, W., Abramowicz, M. A., Kato, S., Lee, W. H. and Stergioulas, N. (2004), Nonlinear Resonance in the Accretion Disk of a Millisecond Pulsar, *Astrophys. J. Lett.*, **603**, pp. L89–L92, arXiv: [astro-ph/0308035](#).
- Kluźniak, W. and Rosińska, D. (2013), Orbital and epicyclic frequencies of Maclaurin spheroids, *Monthly Notices Roy. Astronom. Soc.*, **434**, pp. 2825–2829.
- Kostić, U., Čadež, A., Calvani, M. and Gomboc, A. (2009), Tidal effects on small bodies by massive black holes, *Astronomy and Astrophysics*, **496**, pp. 307–315, arXiv: [0901.3447](#).
- Lamb, F. K., Shibazaki, N., Alpar, M. A. and Shaham, J. (1985), Quasi-periodic oscillations in bright galactic-bulge X-ray sources, *Nature*, **317**, pp. 681–687.
- Méndez, M. (2006), On the maximum amplitude and coherence of the kilohertz quasi-periodic oscillations in low-mass X-ray binaries, *Monthly Notices Roy. Astronom. Soc.*, **371**, pp. 1925–1938, arXiv: [astro-ph/0607433](#).
- Miller, J. C. (1977), Quasi-stationary gravitational collapse of slowly rotating bodies in general relativity, *Monthly Notices of the Royal Astronomical Society*, **179**, pp. 483–498.
- Miller, M. C., Lamb, F. K. and Psaltis, D. (1998), Sonic-Point Model of Kilohertz Quasi-periodic Brightness Oscillations in Low-Mass X-Ray Binaries, *Astrophys. J.*, **508**, pp. 791–830, arXiv: [astro-ph/9609157](#).
- Mukhopadhyay, B. (2009), Higher-Order Nonlinearity in Accretion Disks: Quasi-Periodic Oscillations of Black Hole and Neutron Star Sources and Their Spin, *Astrophys. J.*, **694**, pp. 387–395, arXiv: [0811.2033](#).
- Pétri, J. (2005), An explanation for the kHz-QPO twin peaks separation in slow and fast rotators, *Astronomy and Astrophysics*, **439**, pp. L27–L30, arXiv: [astro-ph/0507167](#).
- Psaltis, D., Wijnands, R., Homan, J., Jonker, P. G., van der Klis, M., Miller, M. C., Lamb, F. K., Kuulkers, E., van Paradijs, J. and Lewin, W. H. G. (1999), On the Magnetospheric Beat-Frequency and Lense-Thirring Interpretations of the Horizontal-Branch Oscillation in the Z Sources, *Astrophys. J.*, **520**, pp. 763–775, arXiv: [astro-ph/9903105](#).
- Rezzolla, L., Yoshida, S. and Zanotti, O. (2003), Oscillations of vertically integrated relativistic tori - I. Axisymmetric modes in a Schwarzschild space-time, *Monthly Notices Roy. Astronom. Soc.*, **344**, pp. 978–992, arXiv: [astro-ph/0307488](#).
- Rosińska, D., Kluźniak, W., Stergioulas, N. and Wiśniewicz, M. (2014), Epicyclic frequencies for rotating strange quark stars: Importance of stellar oblateness, *Phys. Rev. D*, **89**(10), 104001, arXiv: [1403.1129](#).
- Stella, L. and Vietri, M. (1999), kHz Quasiperiodic Oscillations in Low-Mass X-Ray Binaries as Probes of General Relativity in the Strong-Field Regime, *Phys. Rev. Lett.*, **82**, pp. 17–20, arXiv: [astro-ph/9812124](#).
- Stergioulas, N. and Friedman, J. L. (1995), Comparing models of rapidly rotating relativistic stars constructed by two numerical methods, *Astrophys. J.*, **444**, pp. 306–311, arXiv: [astro-ph/9411032](#).
- Strohmayer, T. E. and Markwardt, C. B. (2002), Evidence for a Millisecond Pulsar in 4U 1636-53 during a Superburst, *Astrophys. J.*, **577**, pp. 337–345, arXiv: [astro-ph/0205435](#).
- Stuchlík, Z., Konar, S., Miller, J. C. and Hledík, S. (2008), Gravitational excitation of high frequency QPOs, *Astronomy and Astrophysics*, **489**, pp. 963–966, arXiv: [0808.3641](#).
- Titarchuk, L. and Wood, K. (2002), On the Low and High Frequency Correlation in Quasi-periodic Oscillations among White Dwarf, Neutron Star, and Black Hole Binaries, *Astrophys. J. Lett.*, **577**, pp. L23–L26, arXiv: [astro-ph/0208212](#).

- Török, G. (2009), Reversal of the amplitude difference of kHz QPOs in six atoll sources, *Astronomy and Astrophysics*, **497**, pp. 661–665, arXiv: 0812.4751.
- Török, G., Abramowicz, M. A., Bakala, P., Bursa, M., Horák, J., Kluzniak, W., Rebusco, P. and Stuchlík, Z. (2008a), Distribution of Kilohertz QPO Frequencies and Their Ratios in the Atoll Source 4U 1636-53, *Acta Astronomica*, **58**, pp. 15–21, arXiv: 0802.4070.
- Török, G., Abramowicz, M. A., Bakala, P., Bursa, M., Horák, J., Rebusco, P. and Stuchlík, Z. (2008b), On the Origin of Clustering of Frequency Ratios in the Atoll Source 4U 1636-53, *Acta Astronomica*, **58**, pp. 113–119, arXiv: 0802.4026.
- Török, G., Bakala, P., Stuchlík, Z. and Čech, P. (2008c), Modeling the Twin Peak QPO Distribution in the Atoll Source 4U 1636-53, *Acta Astronomica*, **58**, pp. 1–14.
- Török, G., Bakala, P., Šrámková, E., Stuchlík, Z. and Urbanec, M. (2010), On Mass Constraints Implied by the Relativistic Precession Model of Twin-peak Quasi-periodic Oscillations in Circinus X-1, *Astrophys. J.*, **714**, pp. 748–757, arXiv: 1008.0088.
- Török, G., Bakala, P., Šrámková, E., Stuchlík, Z., Urbanec, M. and Goluchová, K. (2012), Mass-Angular-momentum Relations Implied by Models of Twin Peak Quasi-periodic Oscillations, *Astrophys. J.*, **760**, 138, arXiv: 1408.4220.
- Török, G., Goluchová, K., Urbanec, M., Šrámková, E., Adámek, K., Urbancová, G., Bakala, P., Pecháček, T., Stuchlík, Z., Horák, J. and Juryšek, J. (2015), Confronting models of khz quasi-periodic oscillations with models of rotating neutron stars, *in prep.*
- Török, G., Kotrlová, A., Šrámková, E. and Stuchlík, Z. (2011), Confronting the models of 3:2 quasiperiodic oscillations with the rapid spin of the microquasar GRS 1915+105, *Astronomy and Astrophysics*, **531**, A59, arXiv: 1103.2438.
- Török, G. and Stuchlík, Z. (2005), Radial and vertical epicyclic frequencies of Keplerian motion in the field of Kerr naked singularities. Comparison with the black hole case and possible instability of naked-singularity accretion discs, *Astronomy and Astrophysics*, **437**, pp. 775–788, arXiv: astro-ph/0502127.
- Török, G., Stuchlík, Z. and Bakala, P. (2007), A remark about possible unity of the neutron star and black hole high frequency QPOs, *Central European J. Phys.*, **5**, pp. 457–462.
- Török, G., Urbanec, M., Adámek, K. and Urbancová, G. (2014), Appearance of innermost stable circular orbits of accretion discs around rotating neutron stars, *Astronomy and Astrophysics*, **564**, L5, arXiv: 1403.3728.
- Urbanec, M., Běťák, E. and Stuchlík, Z. (2010a), Observational Tests of Neutron Star Relativistic Mean Field Equations of State, *Acta Astronomica*, **60**, pp. 149–163, arXiv: 1007.3446.
- Urbanec, M., Miller, J. C. and Stuchlík, Z. (2013), Quadrupole moments of rotating neutron stars and strange stars, *Monthly Notices Roy. Astronom. Soc.*, **433**, pp. 1903–1909, arXiv: 1301.5925.
- Urbanec, M., Török, G., Šrámková, E., Čech, P., Stuchlík, Z. and Bakala, P. (2010b), Disc-oscillation resonance and neutron star QPOs: 3:2 epicyclic orbital model, *Astronomy and Astrophysics*, **522**, A72, arXiv: 1007.4961.
- Čadež, A., Calvani, M. and Kostić, U. (2008), On the tidal evolution of the orbits of low-mass satellites around black holes, *Astronomy and Astrophysics*, **487**, pp. 527–532, arXiv: 0809.1783.
- Řípkovská Stone, J., Miller, J. C., Konciewicz, R., Stevenson, P. D. and Strayer, M. R. (2003), Nuclear matter and neutron-star properties calculated with the Skyrme interaction, *Phys. Rev. C*, **68**(3), 034324.
- van der Klis, M. (2005), The QPO phenomenon, *Astronom. Nachr.*, **326**, pp. 798–803.
- van der Klis, M. (2006), *Rapid X-ray Variability*, pp. 39–112.
- Wagoner, R. V. (1999), Relativistic diskoseismology., *Physics Reports*, **311**, pp. 259–269, arXiv: astro-ph/9805028.

- Wagoner, R. V., Silbergleit, A. S. and Ortega-Rodríguez, M. (2001), “Stable” Quasi-periodic Oscillations and Black Hole Properties from Diskoseismology, *Astrophys. J.*, **559**, pp. L25–L28, arXiv: astro-ph/0107168.
- Wiringa, R. B., Fiks, V. and Fabrocini, A. (1988), Equation of state for dense nucleon matter, *Phys. Rev. C*, **38**, pp. 1010–1037.
- Zhang, C.-M. (2005), Some Conclusions on the MHD Alfvén Wave Oscillation Model of kHz QPO, *Chinese Journal of Astronomy and Astrophysics Supplement*, **5**, pp. 21–26.

# Twin peak quasi-periodic oscillations as signature of oscillating cusp torus

Gabriel Török,<sup>1</sup> Kateřina Goluchová,<sup>1</sup> Jiří Horák,<sup>2</sup>  
Eva Šrámková,<sup>1</sup> Martin Urbanec,<sup>1</sup> Tomáš Pecháček<sup>2</sup>  
and Pavel Bakala<sup>1</sup>

<sup>1</sup>Institute of Physics, Faculty of Philosophy & Science, Silesian University in Opava,  
Bezručovo nám. 13, CZ-746 01 Opava, Czech Republic

<sup>2</sup>Astronomical Institute, Boční II 1401/2a, CZ-14131 Praha 4, Czech Republic

## ABSTRACT

We propose a new model of twin-peak quasi-periodic oscillations. This model considers an oscillating torus with cusp that changes location of its centre around radii very close to innermost stable circular orbit. Preliminary results of analytically and computationally complex calculations indicate that the model can provide very good fits of data and matches several neutron star equations of state.

**Keywords:** X-rays: binaries – Accretion, accretion disks – Stars: neutron – Equation of state

## 1 INTRODUCTION

Many models have been proposed to explain a phenomenon of twin peak quasi-periodic oscillations observed in neutron-star low-mass X-ray binaries (QPOs in LMXBs). It is believed that QPOs are carrying signatures of strong gravity and dense matter composition. Serious theoretical effort has been devoted to explain the observed frequencies and their correlations. The brief introduction to twin peak QPOs and their models can be found in paper of Török et al. (2014) in this Volume.

One of the first QPO models, the so called relativistic-precession model (RP model) identifies the twin-peak kHz QPO frequencies  $\nu_U$  and  $\nu_L$  with two fundamental frequencies of a nearly circular geodesic motion: the Keplerian orbital frequency and the periastron-precession frequency,

$$\nu_U = \nu_K, \quad \nu_L = \nu_{\text{per}} = \nu_K - \nu_r, \quad (1)$$

where  $\nu_r$  denotes the radial epicyclic frequency. The correlations among them is then obtained by varying the radius of the underlying circular orbit in a reasonable range. Within this framework it is usually assumed that the variable component of the observed X-ray signal originates in a bright localized spot or blob orbiting the neutron star on a slightly eccentric

orbit. The observed radiation is then periodically modulated due to the relativistic effects. It has been shown that the model is roughly matching the observed  $\nu_U(\nu_L)$  correlations (Stella and Vietri, 1999; Belloni et al., 2007; Török et al., 2012). Nevertheless the RP model also suffers some theoretical difficulties. It is not clear whether the modulation of a radiation from a small localized spot can produce sufficiently strong signal modulation to explain a relatively large observed QPO amplitudes. It is then expected that larger spots (giving higher amount of modulated photons) can undergo a serious shearing due to the differential rotation in the surrounding accretion disk. This does not agree with a high coherence of the QPO signal which is often observed. The model also lacks an explanation of inferred existence of preferred orbits which should be responsible for appearance of QPO pairs and clustering of their frequencies.

Only slightly later, Abramowicz and Kluźniak (2001); Kluźniak and Abramowicz (2001) proposed concept of orbital resonance models. Within this concept, QPOs originate in resonances between oscillation modes of the accreted fluid. The most quoted, so called 3:2 epicyclic resonance model identifies the resonant eigenfrequencies with frequencies  $\nu_\theta$  and  $\nu_r$  of radial and vertical epicyclic axisymmetric modes of disc (or torus) oscillations. It is assumed that

$$\nu_U = \nu_\theta, \quad \nu_L = \nu_r \Leftrightarrow \nu_U/\nu_L = 3/2, \quad (2)$$

while the correlation  $\nu_U(\nu_L)$  arises from resonant corrections to the eigenfrequencies (Abramowicz et al., 2005a,b). We stress that the model deals with a collective motion of the accreted matter. Moreover, the oscillation modes of innermost region of the accretion flow can modulate the amount of matter transferred to NS surface through the boundary layer (Paczynski, 1987; Abramowicz et al., 2007; Horák, 2005). Therefore, it may naturally explain both high amplitudes and coherence of the kHz QPOs. Nevertheless, it is questionable whether the resonant corrections to the eigenfrequencies can be large enough to explain the whole observed range of  $\nu_U$  and  $\nu_L$ . Furthermore, it was shown that the model implies large range of NS masses and has difficulties when confronted to models of rotating NS based on up-to-date equations of state (EoS, see Urbanec et al., 2010; Török et al., 2012).

Motivated by partial success of above models and their complementary difficulties, we present a modified framework for interpreting twin peak QPOs. Our paper sketch results from the prepared publication of Török et al. (2015).

## 2 OSCILLATING TORI

Our model is largely based on the theoretical work of Straub and Šrámková (2009). Throughout this Section we adopt Kerr geometry as description of slowly rotating compact NS. We assume that the innermost region of accretion flow is hot enough to form a pressure supported torus of a moderate thickness. Assuming a non-relativistic polytropic equation of state and neglecting the poloidal components of the fluid velocity (so that the fluid follows circular orbits), the equilibrium torus shape and its structure are completely determined by the Lane–Emden function, which is given by a simple analytic formula (Straub and Šrámková, 2009; Abramowicz et al., 2006)

$$f = 1 - \frac{1}{nc_{s0}^2} \ln \frac{\mathcal{E}}{\mathcal{E}_0}. \quad (3)$$

In this equation,  $\mathcal{E} = (-g^{tt} + 2\ell g^{t\phi} - \ell^2 g^{\phi\phi})^{-1/2}$  denotes the energy of a particle on a (non-geodesic) circular orbit having the specific angular momentum  $\ell$ . We assume that the angular momentum is constant in the whole volume of the torus,  $\ell = \ell_0 = \text{const}$ . As we assume that the torus is located in the vicinity of the innermost stable circular orbit (ISCO) where also Keplerian angular momentum is nearly constant, we believe that it is a reasonable approximation. Meaning of other symbols in Eq. (3) is straightforward:  $n$  is the polytropic index ( $n = 3$  for a radiation pressure dominated fluid),  $g^{\mu\nu}$  are the contravariant component of Kerr metric (we employ the  $(-+++)$  signature) and  $c_{s0}$  is the sound speed at the center of the torus located at radius  $r_0$  in the equatorial plane, where the pressure gradient vanishes and where the energy  $\mathcal{E}$  takes the value  $\mathcal{E}_0$ . Vanishing of the pressure forces in the torus center implies that the streamline  $r = r_0, \theta = \pi/2$  is a geodesic line and therefore the fluid angular momentum takes the Keplerian value at that radius,  $\ell_0 = \ell_K(r_0)$ .

The surfaces of constant density and pressure coincide with those of constant  $f$  and their values can be calculated from  $f$  by  $\rho = \rho_0 f^n$  and  $p = p_0 f^{n+1}$ , where  $\rho_0$  and  $p_0$  refer to the values at the torus center that corresponds to  $f = 1$ . On the other hand, the surface of the torus, where both pressure and density vanishes is given by the condition  $f = 0$ . It is also worth to note that the position of the center  $r_0$  and a shape of these surfaces are entirely given by the value of  $\ell_0$  and the spacetime geometry, while the particular values of  $p$  and  $\rho$  and therefore also the location of the overall surface of the torus are set by the central value of the sound speed  $c_{s0}$ .

Straub and Šrámková (2009) introduce a dimensionless parameter  $\beta$  that characterizes a size of the torus,

$$\beta = \frac{\sqrt{2n}c_{s0}}{r_0\mathcal{E}_0(\ell_0 g_0^{\phi\phi} - g_0^{t\phi})}. \quad (4)$$

This parameter is roughly proportional to the Mach number of the flow at the torus center as can be seen from its Newtonian limit  $\beta = \sqrt{2n}(c_s/r\Omega)_0$  (compare with Blaes, 1985). In addition, it is also roughly proportional to the ratio of the radial (or vertical) extension of the torus to its central radius  $r_0$ . Hence, the sound-crossing time and the dynamical timescale of the torus are roughly similar.

## 2.1 Marginally overflowing tori (cusp tori)

The stationary solution does not exist for an arbitrary large value of  $\beta$  (Abramowicz et al., 1978). Apart of the obvious limit  $\beta \leq 1$ , there is much stronger constrain coming from general relativity. Large enough tori that extend below the ISCO radius, may be terminated there by a “cusp”, where the rotation of the flow becomes Keplerian again. This is a consequence of the fact that the Keplerian angular momentum close to a relativistic object reaches its minimum at ISCO and raises up again bellow.

The cusp corresponds to a saddle point of the Lane–Emden function and the corresponding self-crossing equipotential limits the surface of any stationary rotating fluid configuration with given angular momentum  $\ell_0$ . Fluid that appear outside this surface, is accreted onto the central star on the dynamical timescale driven by gravity and pressure forces without need of viscosity Paczynski (1977). Abramowicz et al. (1978) calculated

analytically the accretion rate from a slightly overflowing torus, his result agrees very well with numerical simulations.

The critical value of the  $\beta$ -parameter giving a marginally overflowing torus follows from Eqs. (3) and (4),

$$\beta_c(r_0) = \frac{\sqrt{2 \ln(\mathcal{E}_c/\mathcal{E}_0)}}{r_0 \mathcal{E}_0 (\ell_0 g_0^{\phi\phi} - g_0^{t\phi})}, \quad (5)$$

where  $\mathcal{E}_c = \mathcal{E}(r_c)$  is the particle energy at the cusp. Its location  $r = r_c$  can be found by equating the Keplerian angular momentum to the fluid angular momentum  $\ell_0$ . This procedure leads to the third-order algebraic equation (in  $\sqrt{r_c}$ ), giving the position of the cusp in terms of the location of the torus center,

$$r_c^{3/2} - \frac{(2r_0^{1/2} - jM^{1/2})(r_0^{1/2} - jM^{1/2})}{(r_0^{3/2} - 2Mr_0^{1/2} + jM^{3/2})M^{1/2}} (r_c - r_0^{1/2}r_c^{1/2}) + j \frac{r_0(r_0^{1/2} - j)}{r_0^{3/2} - 2Mr_0^{1/2} + jM^{3/2}} = 0, \quad (6)$$

where  $r_0 \geq r_{\text{ISCO}}(j)$ . If the stellar spin is neglected ( $j = 0$ ), this equation is reduced to the quadratic one and its solution can be expressed as

$$r_c = r_0 \left( \frac{M + \sqrt{(2r_0 - 3M)M}}{r_0 - 2M} \right)^2, \quad r_0 \geq 6M \quad (7)$$

and the critical  $\beta$ -parameter reads

$$\beta_c = \frac{(r_0 - r_c)(r_0 - 2M)^2 [r_0 r_c - 2M(r_0 + 2r_c)]^{1/2}}{r_c r_0 (r_c - 2M)^{1/2} (r_0 - 3M)^{1/2}}. \quad (8)$$

## 2.2 Frequencies of epicyclic oscillations

Abramowicz et al. (2006) pointed out the existence of the radial and vertical epicyclic modes that describes a global motion of the torus. They have found that, in the limit of infinitesimally slender tori  $\beta \rightarrow 0$ , frequencies of this modes  $\nu_R$  and  $\nu_V$  measured in the fluid reference frame coincide with the epicyclic frequencies of test particles,

$$\nu_r = \left( 1 - \frac{6M}{r} + \frac{8jM^{3/2}}{r^{3/2}} - \frac{3j^2M^2}{r^2} \right)^{1/2} \nu_K, \quad (9)$$

$$\nu_\theta = \left( 1 - \frac{4jM^{3/2}}{r^{3/2}} + \frac{3j^2M^2}{r^2} \right)^{1/2} \nu_K, \quad (10)$$

while at fixed azimuth their frequencies are given by  $\nu_{R,m} = \nu_r + m\nu_K$  and  $\nu_{V,m} = \nu_\theta + m\nu_K$  with  $m$  being the integer azimuthal wave number. In particular, the  $m = -1$  radial and

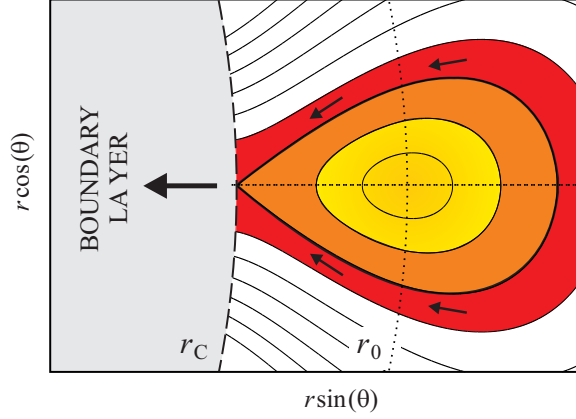


**Figure 1.** Illustration of the equipotential surfaces of an accretion torus. The yellow colour denotes a non-accreting equilibrium torus. The orange colour denotes the case of the cusp torus.

vertical modes give the frequencies of the periastron and nodal precession of a weakly eccentric and tilted torus. It is also worth to note that they now describe a collective motion of the fluid, rather than a motion of individual particles.

In a more realistic case, when  $\beta \geq 0$ , the pressure gradients start to contribute to the restoring force of the perturbed torus shifting their frequencies to new ‘corrected’ values,

$$\nu_{R,m}(r_0, \beta) = \nu_r(r_0) + m\nu_K(r_0) + \Delta\nu_{R,m}(r_0, \beta), \quad (11)$$

$$\nu_{V,m}(r_0, \beta) = \nu_\theta(r_0) + m\nu_K(r_0) + \Delta\nu_{V,m}(r_0, \beta). \quad (12)$$

The pressure corrections  $\Delta\nu_{R,m}$  and  $\Delta\nu_{V,m}$  have been calculated by Straub and Šrámková (2009) using perturbation expansion in  $\beta$ -parameter. They found that a first non-zero corrections are of the order of  $\beta^2$ .

### 3 FREQUENCY IDENTIFICATION

We identify the observed QPO frequencies with frequencies of the epicyclic modes of torus oscillations. We propose that the upper kilohertz QPO frequency is the Keplerian orbital frequency of the fluid at the center of the torus, where both pressure and density peaks and from which the most of torus radiation emerges. The lower kilohertz QPO corresponds to the frequency of the non-axisymmetric  $m = -1$  radial epicyclic mode. Overall, there is

$$\nu_U \equiv \nu_K(r_0), \quad \nu_L \equiv \nu_{R,-1}(r_0, \beta). \quad (13)$$

The QPO frequencies are then strong functions of the position of the center of the torus  $r_0$  and its thickness  $\beta$ . Obviously, a choice  $\beta = 0$  (slender tori) recovers the RP model frequencies completely, as the QPO frequencies would be now given entirely by the geodesic frequencies. In addition, in the case of a finite thickness  $\beta > 0$ , they also weakly depend on the value of the polytropic index  $n$ . In the following discussion, we fix  $n = 3$  as the inner parts of the accretion flow are believed to be radiation-pressure dominated.

We assume the cusp configuration

$$\beta(r_0) \doteq \beta_c(r_0). \quad (14)$$

In other words, we expect that for given  $r_0$  is the torus always close to its maximal possible size, just filling its ‘Roche-like’ lobe.

Thus, our model predicts that QPO frequencies are function of single parameter, the position of the center of the torus  $r_0$ ,

$$\nu_u \equiv \nu_K(r_0), \quad \nu_l \equiv \nu_{R,-1}[r_0, \beta_c(r_0)]. \quad (15)$$

Therefore, one obtains a unique correlation among them by changing this parameter in a reasonable range. In the next section we compare this predicted correlation with the data of the atoll source 4U 1636-53.

## 4 APPLICATION TO TWIN PEAK QPOS IN 4U 1636-53

Török et al. (2012, 2014) have confronted several QPO models to the data of atoll source 4U 1636-53. They have outlined a comparison between individual matches of the model to the data as well as quantitative estimates of inferred NS parameters. We apply the same fitting procedure to the discussed cusp torus model.

### 4.1 Non-rotating approximation

First, we investigate the case of a simple one parametric fit assuming non-rotating NS approximated by Schwarzschild geometry. In this way we can obtain a comparison to the RP model and a rough estimate of the NS mass implied by our cusp torus model.

In the left panel of Fig. 2 we plot the sequence of equipotential contours of cusp tori which provides the best match of 4U 1636-53 data. In the right panel of the same Figure we show this best fit. The RP model best fit is included for comparison. Clearly, the cusp torus model matches the observed trend better than the RP one. In more detail, the related  $\chi^2$  improvement is about  $\Delta\chi^2 \approx 80\%$ . The NS mass inferred from the cusp torus model is then

$$M_0 = 1.69 [\pm 0.01] M_\odot, \quad (16)$$

where the scatter in the estimated mass corresponds to the  $2\sigma$  confidence level. Considering results of Török et al. (2012, 2014), we can expect that the mass (16) belongs to a mass-angular momentum relation implied by the model.

### 4.2 Consideration of NS rotation

The results of the two-dimensional fitting of the parameters  $M$  and  $j$  are shown in the left panel of Fig. 3. The Figure illustrates  $\chi^2$  behaviour in the form of color-coded map. Remarkably, the best fits are reached when  $M$  and  $j$  are related through the specific relation denoted by the green line.

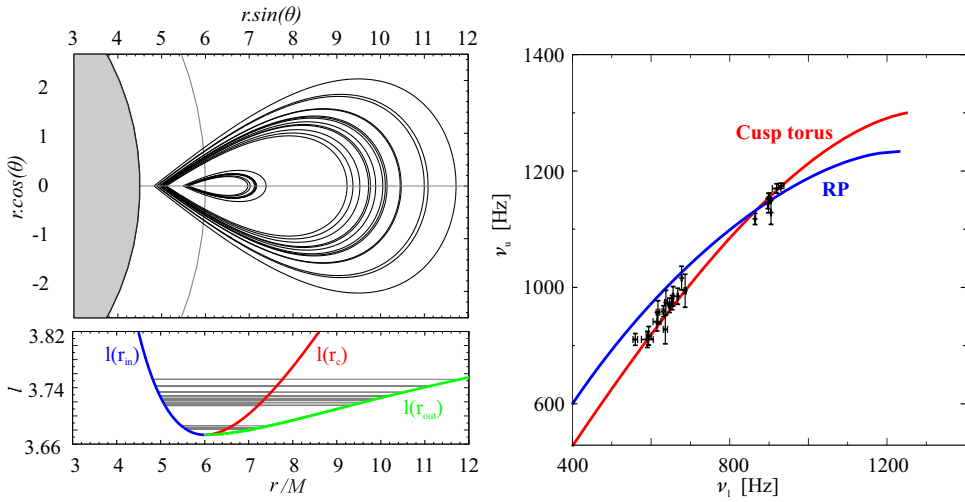


**Figure 2.** *Left:* Sequence of cusp tori corresponding to one-parametric fit of 4U 1636-53 data. *Bottom panel* indicates angular momentum behaviour. *Right:* Corresponding frequency relation (red curve) plotted together with the data. The blue curve indicating the best fit by RP model ( $j = 0$ ) is shown for a comparison.

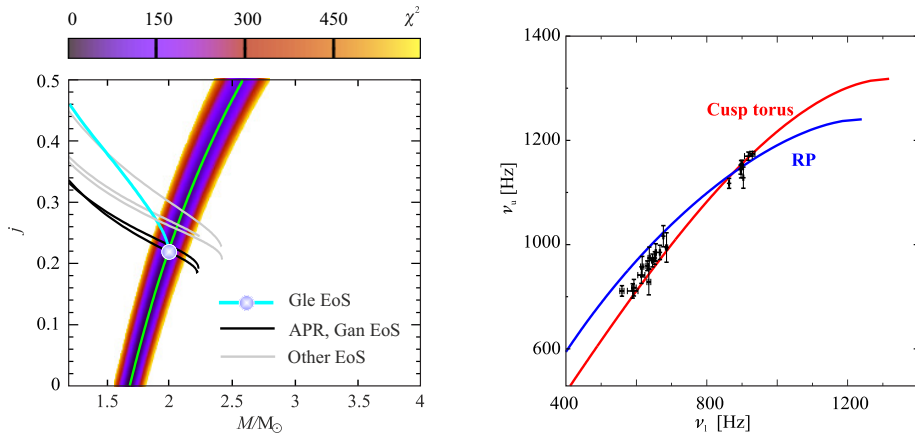


**Figure 3.** *Left:* Two-dimensional color-coded map of  $\chi^2$  behaviour resulting from fitting of data points by the cusp torus model. The green curve indicates the preferred mass-angular momentum relation. The other curves indicate mass-angular momentum relations predicted by models of rotating NS. These are drawn for several NS and spin (rotational frequency) 580 Hz inferred from the X-ray burst measurements. The spot roughly indicates combination of  $M \sim 2 M_\odot$  and  $\sim 0.2$ . *Right:* Consideration of  $j = 0.22$ . The red curve indicate the prediction of cusp torus model. The blue curve indicates the best fit by RP model for the same angular momentum,  $j = 0.22$ .

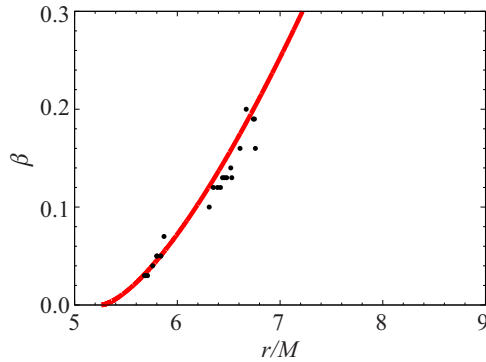


**Figure 4.** Combinations of  $\beta$  and  $r$  exactly matching individual data points vs. cusp torus relation.

## 5 DISCUSSION AND CONCLUSIONS

There is good evidence on the NS spin frequency of 4U 1636–53 based on X-ray burst measurements. Depending on the (two- or one-) hot-spot model consideration, the spin  $\nu_s$  reads either  $\nu_s \doteq 290$  Hz or  $\nu_s \doteq 580$  Hz (Strohmayer and Markwardt, 2002). The value of 580 Hz is usually preferred. In the left panel of Fig. 3 we include several mass-angular momentum relations expected from models of rotating NS (see Török et al., 2014 for details) assuming this spin. We can see that there are overlaps between these relations and the relation inferred from the cusp torus model.

In the right panel of Fig. 3 we show the best fit of the model to the data for  $j = 0.22$  corresponding to

$$M_0 = 2.00 [\pm 0.02] M_\odot, \quad (17)$$

where the scatter in the estimated mass corresponds to the  $2\sigma$  confidence level. We choose  $j = 0.22$  as a referential value since it roughly corresponds to three different EoS. Furthermore, as discussed by Urbanec et al. (2013), the NS oblateness factor is decreasing along the displayed EoS relation towards the low values close to the Kerr limit. Thus, the Kerr approximation adopted here should be well applicable. In the same panel, the RP model best fit drawn for  $j = 0.22$  is included for a comparison. In analogy to the non-rotating case, the cusp torus fit is better than a fit based on RP model. Having these results we also attempted to fit the data by the discussed torus frequencies but considering any torus thickness and fixed  $M = 2 M_\odot$  and  $j = 0.22$ . We searched for the combinations of  $\beta$  and  $r$  matching each individual data point. The result of this procedure is shown in Fig. 4. Clearly, the obtained values are distributed very close to the cusp relation.

Overall, there is a strong indication that twin peak QPOs can be identified with a particular non-axisymmetric  $m = -1$  radial epicyclic mode and Keplerian orbital motion associated to the cusp torus. These modes may naturally give strong modulation of both emerging radiation and the accretion rate. They are therefore very good candidates for explaining high amplitudes of QPO. In addition, their eigenfrequencies change only weakly on the spatial scale of the turbulent motion, therefore it may be expected that they may survive also in highly turbulent media typical for accretion flows.

Finally, we note that the presented concept has also potential to explain the observed low frequency QPOs. As noticed by Rosińska et al. (2014); Kluźniak and Rosińska (2013) the frequencies of vertical epicyclic modes seem to be very sensitive to the NS quadrupole moment. Their consideration thus rather exceeds the framework of Kerr spacetime approximation adopted here. Nevertheless, we roughly investigated also the frequencies of non-axisymmetric  $m = -1$  vertical epicyclic mode of cusp tori. Assuming the same mass, angular momentum and radii as those in Figs. 3 and 4 we obtained values of tens of Hertz. These are of the same order as the observed frequencies of low frequency QPOs. The  $m = -1$  vertical epicyclic mode may therefore play the same role in the framework of cusp torus model as the Lense–Thirring precession in the framework of RP model.

## ACKNOWLEDGEMENTS

GT, ES and MU would like to acknowledge the Czech grant GAČR 209/12/P740. We also acknowledge the project CZ.1.07/2.3.00/20.0071 “Synergy”, aimed to foster international collaboration of the Institute of Physics of SU Opava. We also acknowledge financial support from the internal grant of SU Opava, SGS/11/2013.

## REFERENCES

- Abramowicz, M., Jaroszynski, M. and Sikora, M. (1978), Relativistic, accreting disks, *Astronomy and Astrophysics*, **63**, pp. 221–224.
- Abramowicz, M. A., Barret, D., Bursa, M., Horák, J., Kluźniak, W., Rebusco, P. and Török, G. (2005a), A note on the slope-shift anticorrelation in the neutron star kHz QPOs data, in S. Hledík and Z. Stuchlík, editors, *RAGtime 6/7: Workshops on black holes and neutron stars*, pp. 1–9.
- Abramowicz, M. A., Barret, D., Bursa, M., Horák, J., Kluźniak, W., Rebusco, P. and Török, G. (2005b), The correlations and anticorrelations in QPO data, *Astronom. Nachr.*, **326**, pp. 864–866, arXiv: astro-ph/0510462.
- Abramowicz, M. A., Blaes, O. M., Horák, J., Kluźniak, W. and Rebusco, P. (2006), Epicyclic oscillations of fluid bodies: II. Strong gravity, *Classical Quantum Gravity*, **23**, pp. 1689–1696, arXiv: astro-ph/0511375.
- Abramowicz, M. A., Horák, J. and Kluźniak, W. (2007), Modulation of the Neutron Star Boundary Layer Luminosity by Disk Oscillations, *Acta Astronomica*, **57**, pp. 1–10.
- Abramowicz, M. A. and Kluźniak, W. (2001), A precise determination of black hole spin in GRO J1655-40, *Astronomy and Astrophysics*, **374**, pp. L19–L20, arXiv: astro-ph/0105077.
- Belloni, T., Méndez, M. and Homan, J. (2007), On the kHz QPO frequency correlations in bright neutron star X-ray binaries, *Monthly Notices Roy. Astronom. Soc.*, **376**, pp. 1133–1138, arXiv: astro-ph/0702157.
- Blaes, O. M. (1985), Oscillations of slender tori, *Monthly Notices Roy. Astronom. Soc.*, **216**, pp. 553–563.
- Horák, J. (2005), A possible mechanism for QPOs modulation in neutron star sources, *Astronom. Nachr.*, **326**, pp. 845–848, arXiv: astro-ph/0511569.
- Kluźniak, W. and Abramowicz, M. A. (2001), Strong-Field Gravity and Orbital Resonance in Black Holes and Neutron Stars — kHz Quasi-Periodic Oscillations (QPO), *Acta Physica Polonica B*, **32**, p. 3605.

- Kluźniak, W. and Rosińska, D. (2013), Orbital and epicyclic frequencies of Maclaurin spheroids, *Monthly Notices Roy. Astronom. Soc.*, **434**, pp. 2825–2829.
- Paczynski, B. (1977), A model of accretion disks in close binaries, *Astrophys. J.*, **216**, pp. 822–826.
- Paczynski, B. (1987), Possible relation between the X-ray QPO phenomenon and general relativity, *Nature*, **327**, p. 303.
- Rosińska, D., Kluźniak, W., Stergioulas, N. and Wiśniewicz, M. (2014), Epicyclic frequencies for rotating strange quark stars: Importance of stellar oblateness, *Phys. Rev. D*, **89**(10), 104001, arXiv: 1403.1129.
- Stella, L. and Vietri, M. (1999), kHz Quasiperiodic Oscillations in Low-Mass X-Ray Binaries as Probes of General Relativity in the Strong-Field Regime, *Phys. Rev. Lett.*, **82**, pp. 17–20, arXiv: astro-ph/9812124.
- Straub, O. and Šrámková, E. (2009), Epicyclic oscillations of non-slender fluid tori around Kerr black holes, *Classical Quantum Gravity*, **26**(5), 055011, arXiv: 0901.1635.
- Strohmayer, T. E. and Markwardt, C. B. (2002), Evidence for a Millisecond Pulsar in 4U 1636-53 during a Superburst, *Astrophys. J.*, **577**, pp. 337–345, arXiv: astro-ph/0205435.
- Török, G., Bakala, P., Šrámková, E., Stuchlík, Z., Urbanec, M. and Goluchová, K. (2012), Mass-Angular-momentum Relations Implied by Models of Twin Peak Quasi-periodic Oscillations, *Astrophys. J.*, **760**, 138, arXiv: 1408.4220.
- Török, G., Goluchová, K., Horák, J., Šrámková, E., Urbanec, M., Pecháček, T. and Bakala, P. (2015), Twin peak quasi-periodic oscillations as signature of oscillating cusp torus, *in prep.*
- Török, G., Goluchová, K., Urbanec, M., Šrámková, E., Adámek, K., Urbanecová, G., Pecháček, T., Bakala, P., Stuchlík, Z., Horák, J. and Jurýšek, J. (2014), Confronting models of twin peak quasi-periodic oscillations: Mass and spin estimates fixed by neutron star equation of state, in Z. Stuchlík, G. Török and T. Pecháček, editors, *Proceedings of RAGtime 14–16: Workshops on black holes and neutron stars, Opava, Prague, 18–22 September/15–18 July/11–19 October '12/'13/'14*, pp. 269–282, Silesian University in Opava, Opava, ISBN 978-80-7510-126-6, in this proceedings.
- Urbanec, M., Miller, J. C. and Stuchlík, Z. (2013), Quadrupole moments of rotating neutron stars and strange stars, *Monthly Notices Roy. Astronom. Soc.*, **433**, pp. 1903–1909, arXiv: 1301.5925.
- Urbanec, M., Török, G., Šrámková, E., Čech, P., Stuchlík, Z. and Bakala, P. (2010), Disc-oscillation resonance and neutron star QPOs: 3:2 epicyclic orbital model, *Astronomy and Astrophysics*, **522**, A72, arXiv: 1007.4961.

# Stress-energy tensor of a radiating sphere inclosing black hole

Maciek Wielgus<sup>1,2,a</sup> and Marek Abramowicz<sup>1,3,4,b</sup>

<sup>1</sup>Nicolaus Copernicus Astronomical Center, Polish Academy of Sciences,  
ul. Bartycka 18, 00-716 Warszawa, Poland

<sup>2</sup>Institute of Micromechanics and Photonics, ul. A. Boboli 8, 02-525 Warszawa, Poland

<sup>3</sup>Institute of Physics, Faculty of Philosophy and Science, Silesian University in Opava,  
Bezručovo nám. 13, 746 01 Opava, Czech Republic

<sup>4</sup>Physics Department, Gothenburg University, 412-96 Göteborg, Sweden

<sup>a</sup>maciek.wielgus@gmail.com

<sup>b</sup>marek.abramowicz@physics.gu.se

## ABSTRACT

We consider a uniformly luminous radiating sphere and a static black hole located in the center of that sphere. We give analytic formulas for radiation stress-energy tensor components in such a configuration, for the observer located at an arbitrary distance from the static black hole horizon.

**Keywords:** black hole – radiation in general relativity – stress-energy tensor

## 1 INTRODUCTION

In Abramowicz et al. (1990) an analytic formula for the stress-energy tensor of uniformly radiating static relativistic star was found, for ZAMO (zero angular momentum observer) at the arbitrary distance from the star surface. The result is very useful for investigations of the test particle motion in a curved spacetime, under the radiation four-force influence and several groups pursue this branch of research in recent years, see e.g. Bini and Geralico (2010); Sok Oh et al. (2011); Stahl et al. (2012); Wielgus et al. (2012); Stahl et al. (2013). Here we consider the extended problem, i.e. the observer may be located inside the uniformly radiating luminous sphere of radius  $R$ . In that way we complete the solution of Abramowicz et al. (1990), allowing for any ratio of the radiating sphere's and observer's radii in the Schwarzschild spacetime (it is assumed that the radiating sphere does not contribute to the spacetime curvature). But the problem is not only interesting for the reason of the mathematical completeness of this solution. Such a solution is particularly well suited to describe the interactions between black hole and the Cosmic Background Radiation, which corresponds to the uniformly luminous sphere located at infinity. The extended solution is also physically relevant when we consider the radiation from numerous, randomly spread sources, that can be approximated by a homogeneous luminosity. That can be the case of a black hole located in the center of a spherical galaxy, for instance, or the radiatively efficient spherical accretion on the black hole.

## 2 CASE OF THE LUMINOUS INNER SPHERE

Let us first review the solution for an observer located above the static luminous sphere in Schwarzschild spacetime, given by Abramowicz et al. (1990). We follow a slightly different approach, giving some more general formulas, in order to make a very smooth extension to the case of  $r < R$  (observer located at radius  $r$  inside the luminous sphere of radius  $R$ ) in the next section. Assuming homogeneous, isotropic radiation flux in the emitter's rest frame we conclude that the luminosity observed by any static observer located at a given radial location is constant over the observed sphere surface. Thus, the problem of calculating the radiation stress-energy tensor components in the static ZAMO frame reduces to the calculation of the constant specific intensity moments. Hence, radial dependence of the following two quantities need to be established

- (1) specific intensity  $I(r)$  (value to be integrated over the observer's local sky),
- (2) sphere viewing angle  $\alpha_0$  (boundary for the specific intensity integration).

Specific intensity as seen by the observer located at radial distance  $r$  corresponds to the surface intensity  $I(R)$  of the radiation source, gravitationally redshifted by the presence of the central mass. The quantities that are conserved along the particular light ray travelling through the curved spacetime are the *photon energy*

$$E = p^\alpha \eta_\alpha = 0 = \text{const.}, \quad (1)$$

for the photon four-momentum  $p^\alpha$  and Killing vector  $\eta^\alpha = \delta_t^\alpha$ , and the *redshifted intensity*

$$I_0 = \frac{I(r)}{(p^\alpha v_\alpha)^4} = \text{const.}, \quad (2)$$

for the stationary observer's four-velocity  $v^\alpha = \eta^\alpha (|g_{tt}|)^{-1/2}$ , see Misner et al. (1973) section 4.22 for some more details. Hence, we find

$$I(r) = I(R) \left( \frac{1 - 2M/R}{1 - 2M/r} \right)^2, \quad (3)$$

so clearly  $I(r) < I(R)$  for  $r > R$ . Viewing angle  $\alpha_0$  corresponds to the largest possible value of angle  $\alpha$  in the Fig. 1, which occurs for the largest possible emission angle  $\delta_0$  for which the photon can be observed. For  $R \geq 3M$   $\delta_0 = \pi/2$ , i.e. all emitted photons are able to escape from the star vicinity. This is not true for  $2M < R < 3M$ , where

$$\sin^2 \delta_0 = 27(1 - 2M/R)/R^2. \quad (4)$$

This result will be explained a little further. The relevant angles can be defined using the photon four-velocity in the local orthonormal frame  $u^{(\alpha)}$ , i.e.

$$\tan \alpha = \left[ \frac{u^{(\varphi)}}{u^{(r)}} \right]_{\text{OB}} = \left[ \frac{g_{\varphi\varphi} (u^\varphi)^2}{g_{rr} (u^r)^2} \right]_{\text{OB}}^{1/2}; \quad \tan \delta = \left[ \frac{u^{(\varphi)}}{u^{(r)}} \right]_{\text{EM}} = \left[ \frac{g_{\varphi\varphi} (u^\varphi)^2}{g_{rr} (u^r)^2} \right]_{\text{EM}}^{1/2}, \quad (5)$$

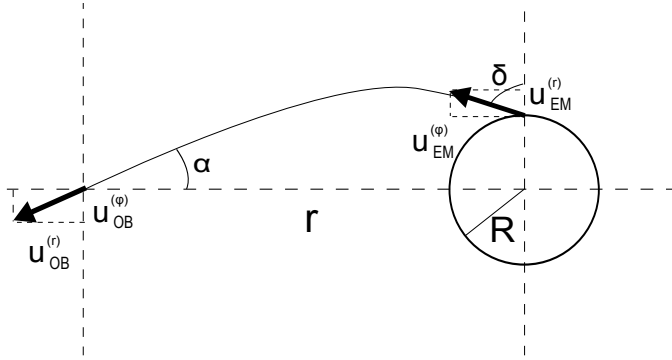


Figure 1. Photon emitted from the star surface \$R\$ with the emission angle \$\delta\$.

lower subscripts OB and EM denoting the location of the photon emission and observation, respectively. Using the normalization \$u^\alpha u\_\alpha = 0\$ it is easy to show that the following equation *always* holds

$$\frac{r^2 \sin^2 \gamma}{1 - 2M/r} = -\frac{u_\phi}{u_t} = \ell = \text{const.}, \tag{6}$$

where \$\tan \gamma = u^{(\phi)}/u^{(r)}\$, \$\gamma\_{OB} = \alpha\$ and \$\gamma\_{EM} = \delta\$, from which we find that

$$\sin^2 \alpha_0 = \left(\frac{R}{r}\right)^2 \left(\frac{1 - 2M/r}{1 - 2M/R}\right) \sin^2 \delta_0 \tag{7}$$

and since \$\alpha\_0(r)\$ must decrease with radius, the *only* solution is

$$\alpha_0(r) = \begin{cases} \arcsin \left[ \frac{R}{r} \left( \frac{1-2M/r}{1-2M/R} \right)^{1/2} \right] & \text{for } 3M \leq R \leq r \\ \arcsin \left[ \frac{3\sqrt{3}M(1-2M/r)^{1/2}}{r} \right] & \text{for } R < 3M < r \\ \pi - \arcsin \left[ \frac{3\sqrt{3}M(1-2M/r)^{1/2}}{r} \right] & \text{for } R < r < 3M \end{cases} \tag{8}$$

Finally, having calculated the \$I(r)\$ and \$\alpha\_0(r)\$ distributions, the stress-energy tensor ZAMO components are found by the integration over the observer's local sky

$$T^{(\alpha)(\beta)}(r) = I(r) \int n^{(\alpha)} n^{(\beta)} d\Omega; \quad n^{(\alpha)} = p^{(\alpha)}/p^{(t)} \tag{9}$$

to give

$$T^{(t)(t)} = 2\pi I(r)(1 - \cos \alpha_0), \tag{10}$$

$$T^{(t)(r)} = \pi I(r) \sin^2 \alpha_0, \tag{11}$$

$$T^{(r)(r)} = \frac{2}{3}\pi I(r)(1 - \cos^3 \alpha_0), \tag{12}$$

$$T^{(\theta)(\theta)} = T^{(\varphi)(\varphi)} = \frac{1}{3}\pi I(r)(2 - 3 \cos \alpha_0 + \cos^3 \alpha_0). \tag{13}$$

All other components are simply equal to zero.

### 3 LUMINOUS OUTER SPHERE

The case of the observer located inside the luminous sphere is similar to certain extent, since in the static spacetime photons may travel along the same null geodesic trajectory in both directions. Hence, the relation (3) holds all the same, only difference being that  $I(r) > I(R)$  for  $R > r$ , i.e. radiation is now *blueshifted* in the static observer's frame. Equation (3) also ensures that the observer's local sky is uniformly bright with exception of the part occluded by the black hole. Hence, the remaining part is to calculate the angular diameter of the black hole as a function of radius. For the analogy with the previous case, we denote this quantity with  $2\alpha_0$ , see Fig. 2. Note that it follows from the Eq. (6) that photons *always* cross the horizon  $r = 2M$  with angle  $\gamma = 0$ , i.e. perpendicularly to the horizon surface. Let us now investigate the relation (6) in more details. One may notice that for a photon trajectory to extend from  $r_0 \gg 2M$  to the black hole horizon it is necessary that we are able to define a meaningful photon radial four-velocity component for every  $r_0 > r > 2M$ , i.e. if

$$u^r u_r > 0 \implies u_\varphi u^\varphi + u_t u^t < 0 \implies \ell^2 \leq -\frac{g_{\varphi\varphi}}{g_{tt}} \leq 27. \tag{14}$$

The number 27 is a value of a global maximum of  $-g_{\varphi\varphi}/g_{tt}$  that occurs for  $r = 3M$ . This means that only photons with  $\ell < 3\sqrt{3}$  fall into the black hole and putting the maximum value of  $\ell$  into Eq. (6), we find Eq. (4) (remember that the outgoing trajectory in the case of inner luminous sphere corresponds to the ingoing trajectory in the outer luminous sphere case). Considering that  $\alpha_0$  must decrease monotonously with  $r$ , the *only* solution for  $\alpha_0(r)$

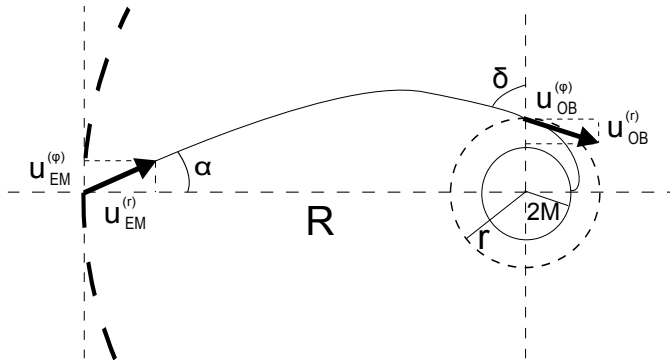


**Figure 2.** Photon emitted from the outer sphere surface  $R$  with the emission angle  $\alpha$ .

that satisfies Eq. (6) is

$$\alpha_0(r) = \begin{cases} \arcsin \left[ \frac{3\sqrt{3}M(1-2M/r)^{1/2}}{r} \right] & \text{for } r \geq 3M, \\ \pi - \arcsin \left[ \frac{3\sqrt{3}M(1-2M/r)^{1/2}}{r} \right] & \text{for } r < 3M, \end{cases} \quad (15)$$

which is the same as the Eq. (8) in the case of inner radiating sphere radius  $R < 3M$ . Note that the formula for  $\alpha(r)$  does not depend on luminous sphere radius  $R$ . Finally, after the local sky integration, we find

$$T^{(t)(t)} = 2\pi I(r)(1 + \cos \alpha_0), \quad (16)$$

$$T^{(t)(r)} = -\pi I(r) \sin^2 \alpha_0, \quad (17)$$

$$T^{(r)(r)} = \frac{2}{3}\pi I(r)(1 + \cos^3 \alpha_0), \quad (18)$$

$$T^{(\theta)(\theta)} = T^{(\phi)(\phi)} = \frac{1}{3}\pi I(r)(2 + 3 \cos \alpha_0 - \cos^3 \alpha_0). \quad (19)$$

This system is quite similar to the result of Abramowicz et al. (1990), yet the flux is of a different sign, and the angle is substituted  $\alpha_0 \rightarrow \pi - \alpha_0$ . It is interesting to observe, that  $\alpha_0 \rightarrow \pi$  as  $r \rightarrow 2M$ , so the area of integration (bright sky region) goes to zero as the observer approaches the horizon. On the other hand,  $I(r)$  given by Eq. (3) diverges in such a limit. So does the result of integration, the stress-energy tensor components, vanish in the limit of the horizon, diverge or have some finite limit? The answer to this question and its implications are discussed in details by Wielgus et al. (2014).

## 4 CONCLUSIONS

We presented the extension of the classic analytic calculation of a static luminous star radiation stress-energy tensor to the case of a luminous sphere observed from the inside. We found out that because of the symmetries involved, such a problem has a very similar solution. Analysis of the Cosmic Background Radiation field properties close to the black hole horizon is one example of application of the presented formulas.

## ACKNOWLEDGEMENTS

This work was supported by the Czech Grant CZ.1.07/2.3.00/20.0071 (“Synergy”, Opava) as well as the Polish NCN grant UMO-2011/01/B/ST9/05439. We thank George F. R. Ellis and Frederic Vincent for many illuminating discussions about the subject of radiation treatment in general relativity.

## REFERENCES

- Abramowicz, M. A., Ellis, G. F. R. and Lanza, A. (1990), Relativistic effects in superluminal jets and neutron star winds, *Astrophys. J.*, **361**, pp. 470–482.
- Bini, D. and Geralico, A. (2010), Spinning bodies and the Poynting-Robertson effect in the Schwarzschild spacetime, *Classical Quantum Gravity*, **27**(18), 185014, arXiv: 1107.2793.

- Misner, C. W., Thorne, K. S. and Wheeler, J. A. (1973), *Gravitation*, Freeman, San Francisco.
- Sok Oh, J., Kim, H. and Mok Lee, H. (2011), Finite size effects on the Poynting-Robertson effect: A fully general relativistic treatment, *New Astronomy*, **16**, pp. 183–186, arXiv: 1011.3104.
- Stahl, A., Kluźniak, W., Wielgus, M. and Abramowicz, M. (2013), Escape, capture, and levitation of matter in Eddington outbursts, *Astronomy and Astrophysics*, **555**, A114, arXiv: 1306.6556.
- Stahl, A., Wielgus, M., Abramowicz, M., Kluźniak, W. and Yu, W. (2012), Eddington capture sphere around luminous stars, *Astronomy and Astrophysics*, **546**, A54, arXiv: 1208.2231.
- Wielgus, M., Ellis, G. F. R., Vincent, F. H. and Abramowicz, M. A. (2014), Cosmic background radiation in the vicinity of a Schwarzschild black hole: No classic firewall, *Phys. Rev. D*, **90**(12), 124024, arXiv: 1406.6551.
- Wielgus, M., Stahl, A., Abramowicz, M. and Kluźniak, W. (2012), Oscillations of the Eddington capture sphere, *Astronomy and Astrophysics*, **545**, A123, arXiv: 1208.2939.

# Unusual behaviour of epicyclic frequencies around rapidly rotating compact stars

Mateusz Wiśniewicz,<sup>1,a</sup> Dorota Gondek-Rosińska,<sup>1</sup>  
Włodek Kluźniak<sup>2</sup> and Nikolaos Stergioulas<sup>3</sup>

<sup>1</sup>Institute of Astronomy, Faculty of Physics & Astronomy, University of Zielona Góra,  
Szafrana 2, 65-001 Zielona Góra, Poland

<sup>2</sup>Nicolaus Copernicus Astronomical Center, Bartycka 18, 00-716 Warszawa, Poland

<sup>3</sup>Aristotle University of Thessaloniki, Thessaloniki, Greece

<sup>a</sup>mateusz@astro.ia.uz.zgora.pl

## ABSTRACT

We report on numerical calculations of orbital and epicyclic frequencies in nearly circular orbits around rotating neutron stars and strange quark stars. The FPS equation of state was used to describe the neutron star structure while the MIT bag model was used to model the equation of state of strange quark stars. The uniformly rotating stellar configurations were computed in full general relativity. We find that the vertical epicyclic frequency is very sensitive to the oblateness of the rotating star. For models of rotating neutron stars of moderate mass, as well as for strange quark star models, the sense of the nodal precession of test particle orbits close to the star changes at a certain stellar rotation rate. These findings may have implications for models of kHz QPOs.

**Keywords:** epicyclic frequencies – neutron star – strange star – quark star – general relativity – numerical relativity – quasi-periodic oscillations

## 1 INTRODUCTION

The discovery of kHz Quasi-periodic oscillations (QPOs) is among the most important scientific result of Rossi X-ray Timing Explorer (RXTE). To date, kHz QPOs have been discovered in about 20 neutron star low-mass X-ray binaries (LMXBs), which typically exhibit two high frequency peaks in the power spectra of the X-ray flux. The QPO phenomenon promises to be a probe of the innermost regions of accretion disks around compact objects such as white dwarfs, neutron stars and black holes, although the promise has not yet been fully realized (see van der Klis, 2000, for a review). Most models of kHz QPOs involve orbital and epicyclic frequencies (Kato and Fukue, 1980; Nowak and Wagoner, 1991, 1992; Perez et al., 1997; Stella et al., 1999; Wagoner, 1999; Abramowicz and Kluźniak, 2001; Silbergleit et al., 2001; Kluźniak, 2005; Stuchlík et al., 2012, 2013).

In the case of Newtonian gravity of a spherically symmetric body the three basic frequencies associated with nearly circular motion, i.e. the orbital ( $\Omega_K$ ), radial epicyclic ( $\omega_r$ ), and vertical epicyclic ( $\omega_z$ ) frequencies are equal to each other. In the case of black holes,

the radial epicyclic frequency is lower than the orbital one, both in the Schwarzschild and the Kerr metrics. For prograde orbits of the Kerr black hole, the vertical epicyclic frequency is lower than the orbital frequency, but higher than the radial epicyclic one, while for retrograde orbits the vertical epicyclic is larger than the orbital frequency (Perez et al., 1997).

However, in Newtonian gravity the degeneracy between the three frequencies can be broken by rotation. It has been shown that for extremely oblate bodies in strictly Newtonian gravity the radial epicyclic frequency may even go to zero at a certain distance from the body (and be imaginary closer to it), so that no stable orbits will exist close to a very rapidly rotating fluid configuration (Kluźniak et al., 2001; Zdunik and Gourgoulhon, 2001). In particular, no stable circular orbits exist right outside Maclaurin spheroids of ellipticity  $e > 0.834583178$  (Amsterdamski et al., 2002). Further, it has been shown that in Newton's gravity, the ordering of the frequencies around an oblate body such as a Maclaurin spheroid is  $\omega_r < \Omega_K < \omega_z$  (Kluźniak and Rosińska, 2013). In summary, the Newtonian effects of oblateness are the opposite of those of frame-dragging in Kerr geometry for prograde orbits: the innermost stable circular orbit is pushed away from the gravitating body and the vertical epicyclic frequency is increased.

For rotating bodies in general relativity (GR) there is a competition between frame-dragging and effects of oblateness (Stergioulas et al., 1999). Effects of oblateness of the gravitating rotating body have also been noted in GR in the context of the “relativistic precession model” of neutron star kHz QPOs, which relies on the differences between the orbital and epicyclic frequencies (Morsink and Stella, 1999). In the case of rapidly rotating strange quark stars Gondek-Rosińska et al. (2014), computed the frequencies for two stellar masses ( $M = 1.4 M_\odot$  and  $M = 1.96 M_\odot$ ), and showed that the vertical epicyclic frequency and the related nodal precession rate of inclined orbits are very sensitive to the oblateness of the rotating star. In particular, for rotating stellar models of moderate and high-mass strange quark stars, the sense of the nodal precession (given by the sign of  $\Omega_K - \omega_z$ ) changes at a certain rotation rate. We defer a discussion of the potential astrophysical implications of this finding till Section 3.

We report on numerical calculations of orbital and epicyclic frequencies for rotating strange quark stars and neutron stars for a wide range of masses and two rotation rates. We have used the RNS code for our calculations (Stergioulas and Friedman, 1995). In this contribution we are discussing the similarities between the behaviour of epicyclic frequencies in strange stars and in neutron stars modelled with the FPS equation of state.

## 2 PROPERTIES OF CIRCULAR ORBITS IN THE METRIC OF ROTATING NEUTRON STARS AND QUARK STARS

We have performed all of our numerical calculations of strange quark stars in the framework of the MIT bag model (Farhi and Jaffe, 1984). In this model quark matter is composed of massless up and down quarks, massive strange quarks and electrons. We use the simplest MIT bag model with massless strange quarks, with the equation of state given by  $P = a(\rho - \rho_0)c^2$ , where  $P$  is the pressure,  $\rho$  is mass-energy density, and  $c$  is the speed of light. We take  $a = 1/3$  and  $\rho_0 = 4.2785 \times 10^{14} \text{ g/cm}^3$ .

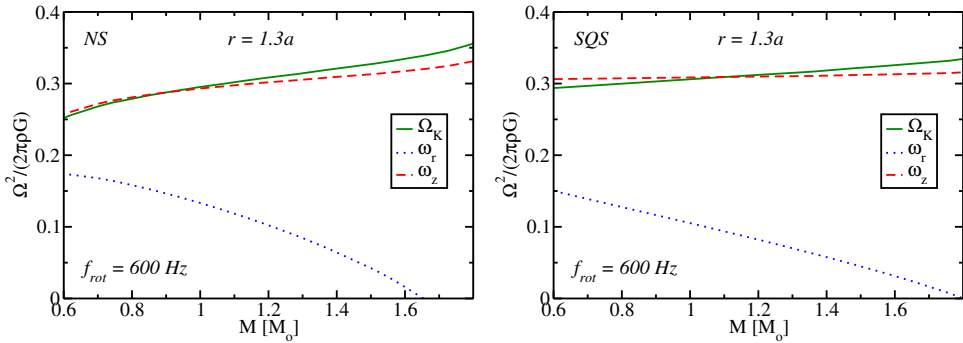


**Figure 1.** Squares of the orbital and epicyclic frequencies (scaled with  $2\pi G\rho$ ) at  $r = 1.3a$  versus gravitational mass for uniformly rotating neutron stars (*left panel*), and strange quark stars (*right panel*), rotating at a fixed frequency  $f_{\text{rot}} = 600 \text{ Hz}$ . The solid (*green*) line corresponds to orbital frequency, the dashed (*red*) line to vertical epicyclic frequency and the dotted (*blue*) line to radial epicyclic frequency.

For computing neutron star models we have used a modern version of FPS equation of state (see Cook et al., 1994, for a review) proposed by Friedman and Pandharipande (1981).

The orbital and epicyclic frequencies are exhibited for a wide range of masses of strange stars and neutron stars, for two stellar rotation rates, 600 Hz and 900 Hz. In the former case (Fig. 1) we present the frequencies squared for orbits at some distance from the star (at  $r = 1.3a$ ), while in the latter (Fig. 2) the same quantities are displayed for orbits grazing the stellar equator ( $r = a$ ).

The effects of oblateness on the epicyclic frequencies in numerical solutions for a neutron star rotating at 400 Hz has been clearly seen in the unusually small difference  $\Omega_K - \omega_z > 0$  between the orbital frequency and the vertical epicyclic one (Kluźniak et al., 2004). It had been expected that frame-dragging effects dominate those of oblateness (Kluźniak, 1998; Morsink and Stella, 1999). However, we now show for the first time that the vertical epicyclic frequency in prograde circular orbits around a neutron star may be even larger than the orbital frequency ( $\omega_z - \Omega_K > 0$ ). As this occurs for astrophysically interesting masses, the effect could have important consequences for models of QPOs (see Section 3), some of which have already been studied for quark stars (Gondek-Rosińska et al., 2014).

Figure 1 shows the scaled orbital and epicyclic frequencies versus gravitational mass (in units of mass of the Sun) at  $r = 1.3a$  for uniformly rotating neutron stars (left panel) and strange quark stars (right panel) rotating at a fixed frequency  $f_{\text{rot}} = 600 \text{ Hz}$ . While at the astrophysically expected masses of  $M > M_\odot$  the vertical epicyclic frequency is less than the orbital one ( $\omega_z < \Omega_K$ ) for the neutron star modelled with the FPS equation of state (as expected for a metric close to the Kerr one), for lower masses the opposite relation holds,  $\omega_z > \Omega_K$ , as a result of stellar oblateness. However, for higher masses effects of strong gravity, such as frame dragging, dominate the qualitative behaviour of the frequency curves. For the quark star model, the results are qualitatively similar, except that the change in sign of  $\omega_z - \Omega_K$  takes place at a higher mass value ( $M \approx 1.1 M_\odot$  for the quark star versus  $M \approx 0.9 M_\odot$  for the FPS neutron star).

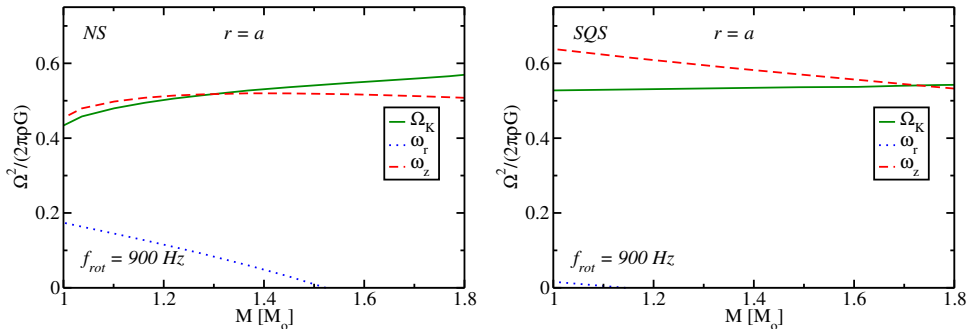


**Figure 2.** Squares of the orbital and epicyclic frequencies (scaled with  $2\pi G\rho$ ) at the stellar equator ( $r = a$ ) versus gravitational mass for uniformly rotating neutron stars (*left panel*), and strange quark stars (*right panel*), rotating at a fixed frequency  $f_{\text{rot}} = 900$  Hz. The solid (*green*) line corresponds to orbital frequency, the dashed (*red*) line to vertical epicyclic frequency and the dotted (*blue*) line to radial epicyclic frequency.

Figure 2 shows the same effects for more rapidly rotating stars ( $f_{\text{rot}} = 900$  Hz). The frequencies are presented for  $r = a$ , i.e. at the stellar equator. Interestingly, the effects of oblateness on the epicyclic frequencies are now seen to qualitatively affect the ordering of the frequencies at typical pulsar masses ( $\omega_z > \Omega_K$  for the FPS neutron stars with values of  $M$  up to the canonical mass of  $1.4 M_\odot$ , while for quark stars this is true up to  $1.7 M_\odot$ ). In part this is because of the higher rotation rate for these models, i.e. their larger oblateness, and in part because the orbits are closer to the star in Fig. 2 than in Fig. 1 – the higher multipoles decay rapidly with the radial distance, so their effect is more pronounced near the star.

### 3 DISCUSSION AND CONCLUSIONS

The purpose of this work is to study in GR the influence of oblateness on the orbital and epicyclic frequencies for rapidly rotating neutron stars and to compare the results to analogous results for strange quark stars (Gondek-Rosińska et al., 2014). Surprisingly, we have found that effects of oblateness familiar from Newtonian studies (Kluźniak and Rosińska, 2013), such as decreasing of the radial epicyclic frequency with the stellar rotation rate and the vertical epicyclic frequency exceeding the orbital one ( $\omega_z > \Omega_K$ ), are present for realistic models of rotating neutron stars in general relativity.

Epicyclic frequencies determine the properties of oscillation modes of thin accretion disks (Kato and Fukue, 1980; Wagoner, 1999). One of the most promising modes that may correspond to the observed QPOs, the *c*-mode, is described by a corrugation of the disk precessing at a frequency close to  $\Omega_K - \omega_z$ , and it may be present only if  $\omega_z < \Omega_K$  (Silbergleit et al., 2001). Our results indicate that for some neutron stars (at least for the FPS equation of state) the latter condition may not hold throughout the inner accretion disk. This could indicate the necessity of revisiting the QPO models. In another class of models (e.g. Kluźniak, 2008), one of the kHz QPOs could correspond directly to motion with the frequency  $\omega_z$ . One possibility that could now be taken into account is that the higher of the twin kHz QPO frequencies may have a value larger than the orbital frequency ( $\omega_z > \Omega_K$ ).

## ACKNOWLEDGEMENTS

This work was supported in part by the POMOST/2012-6/11 Program of Foundation for Polish Science and by NCN grant 2013/08/A/ST9/00795.

## REFERENCES

- Abramowicz, M. A. and Kluźniak, W. (2001), A precise determination of black hole spin in GRO J1655-40, *Astronomy and Astrophysics*, **374**, pp. L19–L20.
- Amsterdamski, P., Bulik, T., Gondek-Rosińska, D. and Kluźniak, W. (2002), Marginally stable orbits around Maclaurin spheroids and low-mass quark stars, *Astronomy and Astrophysics*, **381**, pp. L21–L24.
- Cook, G. B., Shapiro, S. L. and Teukolsky, S. A. (1994), Rapidly rotating polytropes in general relativity, *Astrophys. J.*, **422**, pp. 227–242.
- Farhi, E. and Jaffe, R. L. (1984), Strange matter, *Phys. Rev. D*, **30**, pp. 2379–2390.
- Friedman, B. and Pandharipande, V. R. (1981), Hot and cold, nuclear and neutron matter, *Nuclear Phys. A*, **361**, pp. 502–520.
- Gondek-Rosińska, D., Kluźniak, W., Stergioulas, N. and Wiśniewicz, M. (2014), Epicyclic frequencies for rotating strange quark stars: Importance of stellar oblateness, *Phys. Rev. D*, **89**(10), 104001.
- Kato, S. and Fukue, J. (1980), Trapped Radial Oscillations of Gaseous Disks around a Black Hole, *Publ. Astronom. Soc. Japan*, **32**, p. 377.
- Kluźniak, W. (1998), General Relativistic Constraints on the Equation of State of Dense Matter Implied by Kilohertz Quasi-periodic Oscillations in Neutron-Star X-Ray Binaries, *Astrophys. J. Lett.*, **509**, pp. L37–L40.
- Kluźniak, W. (2005), High frequency QPOs, nonlinear oscillations in strong gravity, *Astronom. Nachr.*, **326**, pp. 820–823.
- Kluźniak, W. (2008), Resonance model for high-frequency QPOs in white dwarfs, neutron stars and black holes, *New Astronomy*, **51**, pp. 841–845.
- Kluźniak, W., Abramowicz, M. A., Kato, S., Lee, W. H. and Stergioulas, N. (2004), Nonlinear Resonance in the Accretion Disk of a Millisecond Pulsar, *Astrophys. J. Lett.*, **603**, pp. L89–L92.
- Kluźniak, W., Bulik, T. and Gondek-Rosińska, D. (2001), Quark stars in low-mass X-ray binaries: for and against, in A. Gimenez, V. Reglero and C. Winkler, editors, *Exploring the Gamma-Ray Universe*, volume 459 of *ESA Special Publication*, pp. 301–304.
- Kluźniak, W. and Rosińska, D. (2013), Orbital and epicyclic frequencies of Maclaurin spheroids, *Monthly Notices Roy. Astronom. Soc.*, **434**, pp. 2825–2829.
- Morsink, S. M. and Stella, L. (1999), Relativistic Precession around Rotating Neutron Stars: Effects Due to Frame Dragging and Stellar Oblateness, *Astrophys. J.*, **513**, pp. 827–844.
- Nowak, M. A. and Wagoner, R. V. (1991), Diskoseismology: Probing accretion disks. I - Trapped adiabatic oscillations, *Astrophys. J.*, **378**, pp. 656–664.
- Nowak, M. A. and Wagoner, R. V. (1992), Diskoseismology: Probing accretion disks. II - G-modes, gravitational radiation reaction, and viscosity, *Astrophys. J.*, **393**, pp. 697–707.
- Perez, C. A., Silbergleit, A. S., Wagoner, R. V. and Lehr, D. E. (1997), Relativistic Diskoseismology. I. Analytical Results for “Gravity Modes”, *Astrophys. J.*, **476**, pp. 589–604.
- Silbergleit, A. S., Wagoner, R. V. and Ortega-Rodríguez, M. (2001), Relativistic Diskoseismology. II. Analytical Results for C-modes, *Astrophys. J.*, **548**, pp. 335–347.
- Stella, L., Vietri, M. and Morsink, S. (1999), General Relativistic Effects in QPOs, *Astrophysical Letters and Communications*, **38**, p. 57.

- Stergioulas, N. and Friedman, J. L. (1995), Comparing models of rapidly rotating relativistic stars constructed by two numerical methods, *Astrophys. J.*, **444**, pp. 306–311.
- Stergioulas, N., Kluźniak, W. and Bulik, T. (1999), Keplerian frequencies and innermost stable circular orbits of rapidly rotating strange stars, *Astronomy and Astrophysics*, **352**, pp. L116–L120.
- Stuchlík, Z., Kotrlová, A. and Török, G. (2012), Resonant Switch Model of Twin Peak HF QPOs Applied to the Source 4U 1636-53, *Acta Astronom.*, **62**, pp. 389–407.
- Stuchlík, Z., Kotrlová, A. and Török, G. (2013), Multi-resonance orbital model of high-frequency quasi-periodic oscillations: possible high-precision determination of black hole and neutron star spin, *Astronomy and Astrophysics*, **552**, A10.
- van der Klis, M. (2000), Millisecond Oscillations in X-ray Binaries, *Annual Review of Astronomy and Astrophysics*, **38**, pp. 717–760.
- Wagoner, R. V. (1999), Relativistic diskoseismology., *Phys. Rep.*, **311**, pp. 259–269.
- Zdunik, J. L. and Gourgoulhon, E. (2001), Small strange stars and marginally stable orbit in Newtonian theory, *Phys. Rev. D*, **63**(8), 087501.

# High frequency oscillations of a slim disk undergoing a limit-cycle outburst

Li Xue,<sup>1,2,a</sup> Włodek Kluźniak,<sup>2</sup> Aleksander Sądowski<sup>4</sup>  
Ju-Fu Lu<sup>1</sup> and Marek Abramowicz<sup>2,3,5</sup>

<sup>1</sup>Department of Astronomy and Institute of Theoretical Physics and Astrophysics,  
Xiamen University, Xiamen, Fujian 361005, China

<sup>2</sup>Copernicus Astronomical Center, ul. Bartycka 18, PL-00-716 Warszawa, Poland

<sup>3</sup>Institute of Physics, Faculty of Philosophy & Science, Silesian University in Opava,  
Bezručovo nám. 13, CZ-746 01 Opava, Czech Republic

<sup>4</sup>MIT Kavli Institute for Astrophysics and Space Research, 70 Vassar St., Cambridge,  
MA 02134, USA

<sup>5</sup>Physics Department, Gothenburg University, SE-412-96 Göteborg, Sweden

<sup>a</sup>lixue@xmu.edu.cn

## ABSTRACT

We numerically investigate thermally unstable accretion discs around non-spinning and fast-spinning black holes. We adopt an additional evolutionary viscosity equation, based on the results of recent MHD simulations, which replaces the standard  $\alpha$ -prescription. We find oscillations which arise from the sonic point and propagate outwards. By directly integrating the cooling flux on each radius we obtain light-curves, calculate their PSD, and find a series of harmonics with base frequency very close to the predicted frequency of a p-mode in QPO theory.

**Keywords:** accretion, accretion disks – gravitation – relativistic processes – stars: black holes – X-rays: bursts

## 1 INTRODUCTION

High-frequency quasi-periodic oscillations (HFQPOs) have been observed in some black hole (BH) X-ray binaries. They appear only in the “steep power law” state at high luminosities ( $L > 0.1 L_{\text{Edd}}$ ) and are in range of 40 to 450 Hz. These frequencies are comparable to the orbital frequency of the innermost stable circular orbit (ISCO) of a stellar-mass BH. It is believed that the mechanism behind them are closely related to the dynamics of inner regions of BH accretion disks (see Remillard and McClintock, 2006; Kato et al., 2008; Belloni et al., 2012, for reviews).

In order to study oscillations of thermally unstable accretion disks, we solve their evolution using a non-stationary, 1+1 dimensional, general relativistic spectral code, and implement a new prescription for viscosity, motivated by recent MHD simulations. Our work is similar to Chen and Taam (1995), who used the standard  $\alpha$ -prescription, and a comparison between our model and theirs will be given in Section 3.

## 2 EVOLUTIONARY VISCOSITY

In our previous paper (Xue et al., 2011), we have described a code and relevant equations for the axisymmetric relativistic accretion flows around spinning black holes. The viscosity in that code is described by the standard  $\alpha$ -prescription (Shakura and Sunyaev, 1973). The viscous stress (only  $r\phi$ -component is non-vanishing) can be written as (The asterisk denotes the standard  $\alpha$ -prescription)

$$S_{r\phi}^* = -\frac{v\Sigma A^{3/2}\gamma^3}{2r^3\Delta^{1/2}}\frac{\partial\Omega}{\partial r}, \quad (1)$$

$$v = \frac{2}{3}\alpha H\sqrt{\frac{p}{\rho}}, \quad (2)$$

where  $\Sigma$ ,  $p$ ,  $\rho$  and  $\Omega$  are the mass surface density, total pressure, mass density and rotational angular velocity of accreted gas respectively, and  $\gamma$ ,  $A$  and  $\Delta$  are the relativistic factors whose detailed definitions can be found in Xue et al. (2011). This famous prescription has been used extensively since 1973. It is perfectly simple but may not closely accord with actual accretion flows. The MHD shearing box simulation of Hirose et al. (2009) implied that there is certain time-delay between the viscous stress and total pressure. Penna et al. (2013), relying on several relativistic MHD global simulations, pointed out that the parameter  $\alpha$  is a function of radius, and is not constant in the inner disk region. Therefore, following Hirose et al. (2009) and Penna et al. (2013), we update the code by adopting an additional time-dependent stress equation instead of the  $\alpha$ -prescription. This time-dependent equation can be written as

$$n\tilde{\tau}\frac{\partial S_{r\phi}}{\partial t} = S_{r\phi}^* - S_{r\phi}, \quad (3)$$

$$\tilde{\tau} = -\left(\frac{\gamma^2 A \Omega}{r^4} \frac{\partial \ln \Omega}{\partial \ln r}\right)^{-1}, \quad (4)$$

where  $\tilde{\tau}$  is the typical time-delay (in practice, we scale it up with the  $n$  factor in Eq. (3)). When  $n \rightarrow 0$ , Eq. (3) implies  $S_{r\phi} = S_{r\phi}^*$ , which is equivalent to Eq. (1). It means that the  $\alpha$ -prescription is a trivial case of Eq. (3).

To mimic the radial dependence of the parameter  $\alpha$  observed by Penna et al. (2013), we apply the following  $\alpha$ -profile:

$$\alpha = \alpha_0 \left( \frac{1 - 2Mr^{-1} + a^2r^{-2}}{1 - 3Mr^{-1} + 2aM^{1/2}r^{-3/2}} \right)^6, \quad (5)$$

where  $M$  and  $a$  are the mass and spin of black hole, respectively. The radial factor, including the exponent 6, was suggested by Penna et al. (2013). Under this profile,  $\alpha$  is almost a constant  $\alpha_0$  in outer disc region with large  $r$  and increases to higher value radially inwards. We set  $\alpha_0 = 0.1$  and fix the mass supplying rate  $\dot{M}_S = 0.06 \dot{M}_{\text{Edd}}$  at the outer boundary in this work. These settings are sufficient to make the disc thermally unstable since we observe the limit-cycle outbursts from running code. The impact of viscous time-delay on the thermal instability may be unremarkable since we always observe the similar outbursts

on the models with different time-delay parameters  $n$  in the range 0 to 4. This confirms the analysis of Lin et al. (2011) and Ciesielski et al. (2012) on this kind of delay. However, we find that this time-delay may determine the appearance of the oscillation in the discs (detailed paper in preparation).

### 3 RESULTS AND DISCUSSION

In Figure 1 we show the power spectral densities (PSDs) of oscillating light-curves for two typical models (around non-spinning and fast-spinning  $\sim 10 M_{\odot}$  black holes). The fundamental frequency (the lowest frequency of harmonics) is  $\sim 74.9$  Hz for the non-spinning model and  $\sim 285.6$  Hz for the fast-spinning model, which are both close to 71.3 Hz and 300 Hz predicted by the p-mode theory (see below).

The spectrum shows harmonics with frequencies in a regular integer series 1:2:3, . . . The relative strength between harmonics for the fast-spinning model looks much more irregular than the non-spinning one. If there were some background noise in those spectrum of Fig. 1, one might see the losing of some harmonics. For example, in the right panel of Fig. 1, the peak C would be easier to be overwhelmed by noise than peak D. These interesting features are potentially useful for explain the observational QPO pairs. However, direct comparison would require more careful treatment. One should carefully consider the gravitational redshift and ray-bending of the emitted photons. However, for convenience, we only construct the lightcurves by directly integrating the radiation cooling flux at each radius in this work. In order to roughly demonstrate the effects of gravitational red-shift or other blocking effects on radiation emitted from the inner disk region, we show, in Fig. 2, four PSDs made from the light-curves without the radiation contribution from a certain inner cutting region. It is remarkable that the fundamental harmonic (inside the rectangle in all four panels) can not be easily removed from PSDs because of the outward propagation of the oscillation from ISCO. It implies that the measurement of black hole spin with QPO will be very robust even in a case when modulation of the innermost disk is not visible.

Similar oscillations were observed by Chen and Taam (1995) who used the regular viscosity prescription with  $S_{r\phi} \propto \alpha p_{\text{gas}}$ . Perhaps this difference in the treatment of viscosity leads to the different PSDs of our models and theirs. In our models multiple harmonics of the base frequency are observed.

We argue that the oscillations observed in our models could be the trapped p-modes, which are excited by the sonic-point instability in a transonic accretion flow across ISCO (Kato, 1978; Kato et al., 2008). Kato (1978) and Kato et al. (2008) point out that the sonic-point instability requires large  $\alpha$ . The  $\alpha$ -profile implemented in our code implies that the effective  $\alpha$  in the inner disk region is large enough to trigger the sonic-point instability.

We directly inspect the numerical light-curves and their PSDs obtained from our code. We observe oscillations only in the limit-cycle outburst state ( $L \gtrsim 0.2 L_{\text{Edd}}$ ) when the inner disk region has switched to slim disk mode. On the contrary, there are no oscillations observed in the limit-cycle quiet state ( $L \sim 0.01 L_{\text{Edd}}$ ). This is consistent with the QPO observations (Kato et al., 2008), but not with the sonic-point instability theory which does not discriminate between accretion rates. Recently, the shearing box simulation of Hirose et al. (2014) implied that the effective  $\alpha$  is enhanced by the vertical convection during the

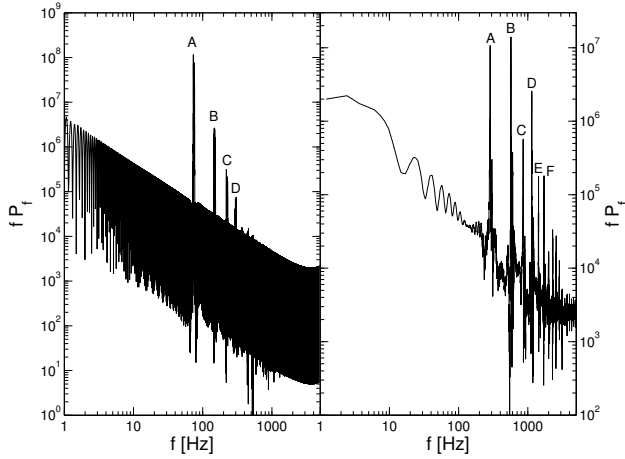


**Figure 1.** PSDs of light-curves. The left panel is for the disk around a non-spinning black hole ( $a_* = 0$ ,  $M = 10 M_\odot$ ,  $n = 1$ ). The right panel is for the disk around a fast-spinning black hole ( $a_* = 0.947$ ,  $M = 7.02 M_\odot$ ,  $n = 4$ ). In left panel, the frequencies of peaks A to D are 74.9 Hz, 149.5 Hz, 224.0 Hz, and 299.2 Hz respectively. In the right panel, the frequencies of peaks A to F are 285.6 Hz, 570.1 Hz, 855.7 Hz, 1140 Hz, 1427 Hz, and 1711 Hz respectively.

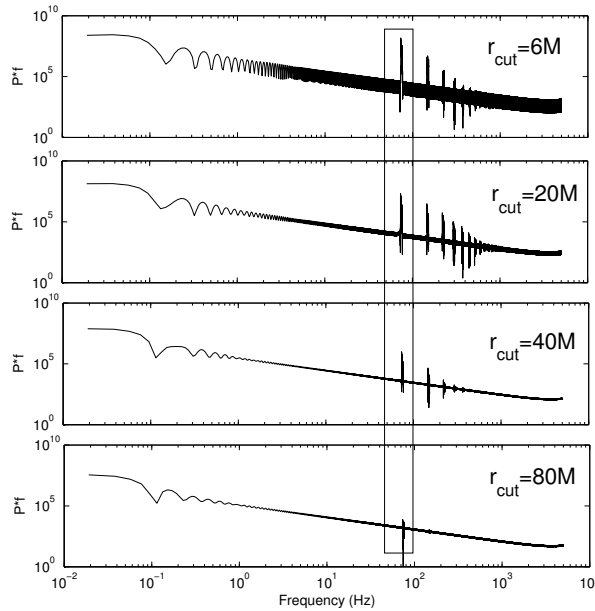


**Figure 2.** PSDs of light-curves. From upper to lower, the radius  $r_{\text{cut}}$  of the cut out region increases from  $6 M$  to  $80 M$  for the same non-spinning model.

outburst, which is similar to the conception of Milsom et al. (1994). Thus, large  $\alpha$  required by the HFQPO may be caused by the outburst, explaining why HFQPOs are observed only in high luminosity state.

## ACKNOWLEDGEMENTS

This work was supported by the National Natural Science Foundation of China under grants 11233006 and 11373002, Polish NCN grants UMO-2011/01/B/ST9/05439, 2013/08/A/ST9/00795, and Czech ASCRM100031242 CZ.1.07/2.3.00/20.0071 Synergy (Opava) project.

## REFERENCES

- Belloni, T. M., Sanna, A. and Méndez, M. (2012), High-frequency quasi-periodic oscillations in black hole binaries, *Monthly Notices Roy. Astronom. Soc.*, **426**, pp. 1701–1709, arXiv: 1207.2311.
- Chen, X. and Taam, R. E. (1995), Variability of accretion disks surrounding black holes: The role of inertial-acoustic mode instabilities, *Astrophys. J.*, **441**, pp. 354–360, arXiv: astro-ph/9409019.
- Ciesielski, A., Wielgus, M., Kluźniak, W., Sądowski, A., Abramowicz, M., Lasota, J.-P. and Rebusco, P. (2012), Stability of radiation-pressure dominated disks. I. The dispersion relation for a delayed heating  $\alpha$ -viscosity prescription, *Astronomy and Astrophysics*, **538**, A148, arXiv: 1106.2335.
- Hirose, S., Blaes, O., Krolik, J. H., Coleman, M. S. B. and Sano, T. (2014), Convection Causes Enhanced Magnetic Turbulence in Accretion Disks in Outburst, *Astrophys. J.*, **787**, 1, arXiv: 1403.3096.
- Hirose, S., Krolik, J. H. and Blaes, O. (2009), Radiation-Dominated Disks are Thermally Stable, *Astrophys. J.*, **691**, pp. 16–31, arXiv: 0809.1708.
- Kato, S. (1978), Pulsational instability of accretion disks to axially symmetric oscillations, *Monthly Notices Roy. Astronom. Soc.*, **185**, pp. 629–642.
- Kato, S., Fukue, J. and Mineshige, S. (2008), *Towards a New Paradigm*, Kyoto University Press, Kyoto, Japan, ISBN 978-4-87698-740-5.
- Lin, D.-B., Gu, W.-M. and Lu, J.-F. (2011), Effects of the stress evolution process on the thermal stability of thin accretion discs, *Monthly Notices Roy. Astronom. Soc.*, **415**, pp. 2319–2322, arXiv: 1104.0859.
- Milsom, J. A., Chen, X. and Taam, R. E. (1994), The vertical structure and stability of accretion disks surrounding black holes and neutron stars, *Astrophys. J.*, **421**, pp. 668–676.
- Penna, R. F., Sądowski, A., Kulkarni, A. K. and Narayan, R. (2013), The Shakura-Sunyaev viscosity prescription with variable  $\alpha$  ( $r$ ), *Monthly Notices Roy. Astronom. Soc.*, **428**, pp. 2255–2274, arXiv: 1211.0526.
- Remillard, R. A. and McClintock, J. E. (2006), X-Ray Properties of Black-Hole Binaries, *Annual Review of Astronomy and Astrophysics*, **44**, pp. 49–92, arXiv: astro-ph/0606352.
- Shakura, N. I. and Sunyaev, R. A. (1973), Black holes in binary systems. Observational appearance., *Astronomy and Astrophysics*, **24**, pp. 337–355.
- Xue, L., Sądowski, A., Abramowicz, M. A. and Lu, J.-F. (2011), Studies of Thermally Unstable Accretion Disks Around Black Holes with Adaptive Pseudospectral Domain Decomposition Method. II. Limit-cycle Behavior in Accretion Disks around Kerr Black Holes, *Astrophys. J. Suppl.*, **195**, 7, arXiv: 1105.4534.



# The Komissarov Model of Sgr A\*

Wenchi Yan,<sup>1,a</sup> Frederic H. Vincent,<sup>1</sup> Marek A. Abramowicz,<sup>1,2,3</sup>  
Andrzej A. Zdziarski<sup>1</sup> and Odele Straub<sup>4</sup>

<sup>1</sup>Nicolaus Copernicus Astronomical Centre, ul. Bartycka 18, PL-00-716 Warsaw, Poland

<sup>2</sup>Physics Department, Gothenburg University, SE-412-96 Göteborg, Sweden

<sup>3</sup>Institute of Physics, Faculty of Philosophy & Science, Silesian University in Opava,  
Bezručovo nám. 13, CZ-746 01 Opava, Czech Republic

<sup>4</sup>LUTH, Observatoire de Paris, CNRS, Université Paris Diderot,

5 place Jules Janssen, 92190 Meudon, France

<sup>a</sup>wyan@camk.edu.pl

## ABSTRACT

Astrophysical black holes observed from Earth have a very small apparent size in the sky. The largest of all is the supermassive black hole, Sagittarius A\*, in the centre of our Galaxy with an apparent diameter of  $53 \mu\text{as}$  (micro-arcseconds). We construct a model of magnetized accretion torus surrounding the central black hole in Sgr A\* in two different geometries of the magnetic field. For the toroidal one (“the Komissarov model”) we assume stationarity, axial symmetry, constant specific angular momentum, polytropic equation of state and small optical depth. The last assumption allows one to use the ray-tracing technique to calculate the transfer of radiation. For the mass and spin of the Sgr A\* black hole we adopt  $M = 4 \times 10^6 M_{\odot}$  and  $a = 0.5$ .

**Keywords:** Galaxy: centre – Accretion, accretion discs – Black hole physics – Relativistic processes

## 1 INTRODUCTION

Sagittarius A\* was first observed in the radio band (Balick and Brown, 1974), but its observed emission ranges from radio to X-ray energies. The most remarkable feature of Sgr A\* is its complex variability at all observable wavelengths. The luminosity fluctuations increase with increasing wave energy, from a factor of a few at radio to a few orders of magnitude in the X-ray band (see e.g. Genzel et al., 2010, for a review). The spectral peak lies in the millimetre radio band and brings forth a peak luminosity of  $\lesssim 10^{36} \text{ erg}\cdot\text{s}^{-1}$ . The accretion structure around Sgr A\* is thus extremely dim given its enormous mass. Therefore, adequate disc models describe a radiatively inefficient emitter like an advection dominated accretion flow (ADAF, Narayan and Yi 1995) or an ion torus (see Straub et al., 2012, and references therein). The term *advection* means here that a large part of the gravitationally liberated thermal energy is not converted into radiation but carried inward with the ionised, hot accretion flow.

In the millimetre radio range, i.e. at wavelengths corresponding to the spectral peak of Sgr A\*, the Event Horizon Telescope (EHT), operational in 2015–2020, and the orbital telescope RadioAstron, launched in 2011, will be able to perform high resolution Very Large Baseline Interferometry (VLBI) observations. Like this, images of the immediate environment of the black hole will be obtained, in particular those of the accretion flow.

These new observational possibilities on Sgr A\* have stimulated a lot of recent research, reviewed, e.g. by Broderick et al. (2014). The hope is that a detailed knowledge of theoretically predicted observational appearance of the structure of the accretion flow in Sgr A\* will provide powerful and reliable tools to test Einstein's general relativity at its strong field limit. While eventually sophisticated numerical models (Global General Relativistic Radiation Magnetohydrodynamics – GGRRMHD etc.) of Sgr A\* will be used to make a meaningful comparison between theory and observations, in the foreseeable future simple *analytic* models will be invaluable as a secure guide in the vast parameter space that needs to be explored.

Following this idea, we have recently constructed an analytic optically thin Polish Doughnut model of Sgr A\* (Straub et al., 2012). It assumed that the magnetic field in Sgr A\* had no global structure, but instead was chaotic, i.e. locally isotropic. In this paper we make the next logical step by considering a model with a globally ordered (toroidal) magnetic field. We use the Komissarov (2006) analytic model of a magnetized optically thin Polish Doughnut and follow all its assumptions. In the Komissarov model, all general relativistic effects, and influence of the (toroidal) magnetic field are fully and exactly taken into account. They are calculated from the first principles with no approximation. The presence of a magnetic field is important in calculations of the synchrotron radiation emissivity, which is also done. We consider here a torus-shaped, barotropic, and *stationary* disk with axisymmetry and constant angular momentum around a Kerr black hole. The disk is fully ionized. These assumptions reflect the basic physics of the real object.

We summarize the basic features of the magnetized torus model and its synchrotron radiation in Sections 2 and 3, respectively. Section 4 presents conclusions and perspectives.

## 2 MAGNETIZED ACCRETION TORUS

### 2.1 Toroidal magnetic field (the Komissarov model)

We constructed a magnetized accretion torus at the Galactic centre using the model developed by Komissarov (2006), which describes analytically a polytropic accretion torus with toroidal magnetic field in the Kerr spacetime. The magnetized accretion flow is described by the conservation law that takes the form,

$$\nabla_{\alpha} T_{\beta}^{\alpha} = 0, \quad T_{\beta}^{\alpha} = (h + b^2) u^{\alpha} u_{\beta} + \left( p + \frac{b^2}{2} \right) \delta_{\beta}^{\alpha} - b^{\alpha} b_{\beta}, \quad (1)$$

where  $h = p + \rho$  is the enthalpy, with  $p$  and  $\rho$  being the pressure and energy density of the fluid, and  $b$  is the magnitude of the magnetic field. The induction equation is

$$\nabla_{\alpha} (*F^{\alpha\beta}) = 0, \quad *F^{\alpha\beta} = u^{\alpha} b^{\beta} - b^{\alpha} u^{\beta} \quad (2)$$

and the equation of continuity

$$\nabla_\alpha(nu^\alpha) = 0. \quad (3)$$

The fluid 4-velocity is assumed to be

$$\mathbf{u} = (u^t, 0, 0, u^\varphi), \quad (4)$$

using Boyer–Lindquist coordinates. We assume a constant specific angular momentum

$$\ell_0 \equiv -u_\varphi/u_t. \quad (5)$$

This quantity is expressed in terms of the dimensionless specific angular momentum

$$\lambda = \frac{\ell_0 - \ell_{\text{ms}}}{\ell_{\text{mb}} - \ell_{\text{ms}}}, \quad 0 \leq \lambda \leq 1, \quad (6)$$

where  $\ell_{\text{ms}}$  and  $\ell_{\text{mb}}$  are the specific angular momentum at the marginally stable and bound orbits respectively. These assumptions fully determine the 4-velocity.

The gas and magnetic pressures  $p$  and  $p_m$  are assumed to follow the polytropic prescription

$$p = \kappa h^k, \quad p_m = \kappa_m \mathcal{L}^{k-1} h^k, \quad (7)$$

where  $\kappa$  and  $\kappa_m$  are polytropic constants,  $k$  is the polytropic index (assumed identical for gas and magnetic pressures), and  $\mathcal{L} \equiv g_{t\varphi}^2 - g_{tt}g_{\varphi\varphi}$  where  $g_{\mu\nu}$  is the Kerr metric.

The conservation of stress-energy leads to

$$W_s - W + \frac{k}{k-1} (\kappa + \kappa_m \mathcal{L}^{k-1}) h^{k-1} = 0 \quad (8)$$

where the potential  $W = -\ln|u_t|$  is used. We assume that the torus fills its Roche lobe, which fixes the central radius of the torus and its surface, thus the values of the potential at the centre,  $W_c$ , and at the surface,  $W_s$ , of the torus. This immediately gives

$$h = h_c \left( \frac{\omega \kappa + \kappa_m \mathcal{L}_c^{k-1}}{\kappa + \kappa_m \mathcal{L}^{k-1}} \right)^{1/(k-1)}, \quad (9)$$

where  $\omega = (W - W_s)/(W_c - W_s)$  and  $\mathcal{L}_c$  is the value of  $\mathcal{L}$  at the centre of the torus.

The polytropic constants  $\kappa$  and  $\kappa_m$  can be expressed according to

$$\kappa = h_c^{1-k} (W_c - W_s) \frac{k-1}{k} \frac{\beta_c}{1+\beta_c}, \quad \kappa_m = \frac{\mathcal{L}_c^{1-k}}{\beta_c} \kappa, \quad (10)$$

where  $\beta_c$  is the central magnetic pressure ratio,  $\beta_c \equiv p_c/p_{m,c}$ . The electron number density

$$n_e = \frac{h - \kappa h^k}{\mu_e m_u} \quad (11)$$

is then known analytically.

The magnetic field in Boyer–Lindquist frame is assumed to be toroidal:  $b^\alpha = (b^t, 0, 0, b^\varphi)$ . Using the definition of the magnetic pressure,  $p_m = b^\alpha b_\alpha / 2$ , and assuming that  $b^\alpha u_\alpha = 0$  (i.e. the magnetic field 4-vector is in the rest space of the comoving observer), it is easy to get

$$b^\varphi = \sqrt{\frac{2p_m}{g_{\varphi\varphi} + 2\ell_0 g_{t\varphi} + \ell_0^2 g_{tt}}}, \quad b^t = \ell_0 b^\varphi, \quad (12)$$

which is fully known analytically.<sup>1</sup> The magnitude of the magnetic 3-vector field  $\mathbf{B}$  measured by an observer comoving with the fluid is then  $\|\mathbf{B}\| = \sqrt{b^\alpha b_\alpha}$ . Let us consider one synchrotron photon emitted at a given point of the torus. Let  $\mathbf{p}$  be the 4-vector tangent to the photon geodesic and  $\mathbf{l}$  be its projection orthogonal to  $\mathbf{u}$ . The angle  $\vartheta$  between the magnetic field  $\mathbf{B}$  and the direction of emission is given by  $\mathbf{l} \cdot \mathbf{B} = \|\mathbf{l}\| \|\mathbf{B}\| \cos \vartheta$ , it is known analytically as well.

We now note that such an accretion torus cannot be made of a perfect gas. If it were, then  $pm_u / (\rho k_B) = T / \mu_e$  where  $T$  is the electron temperature and  $k_B$  is the Boltzmann constant. However, it is easy to see that  $p/\rho$  is independent of the central value of the enthalpy  $h_c$ . Thus the temperature would be independent of  $h_c$  as well, and would be purely determined by the geometry of spacetime, which does not make sense. We will still assume that there exists a relation  $T = Cp/\rho$  where  $C$  is a constant, but does not take its perfect-gas value. Rather, we choose  $T_c$  at the centre of the torus and define the constant  $C$  by  $T_c = Cp_c/\rho_c$ . Then

$$T = T_c \left( \frac{\rho}{\rho_c} \right)^{k-1} \quad (13)$$

depends on the choice of  $T_c$ , and no longer only on spacetime geometry.

## 2.2 Isotropic magnetic field

An accretion torus with isotropic (i.e. chaotic) magnetic field has already been studied around Sgr A\* by Straub et al. (2012). This model is simply the limit of the Komissarov (2006) model with  $\kappa_m = 0$ . The section above thus directly applies to this simpler case. The magnetic field strength is obtained by assuming that the magnetic pressure is everywhere related to the gas pressure through

$$p_m = \frac{1}{\beta} p \quad (14)$$

thus, the  $\beta$  parameter is valid in the whole torus, not only at its centre. Then the magnetic field strength is given by

$$B^2 = 2p_m. \quad (15)$$

<sup>1</sup> Note that  $b^t$  is proportional to  $b^\varphi$  is a natural result of setting  $b^r = 0$ .

### 3 SYNCHROTRON RADIATION

Millimetre-wavelength emission coming from Sgr A\* has been attributed to a region close to the event horizon of the supermassive black hole and can be explained by thermal synchrotron radiation (see, e.g. Genzel et al., 2010).

#### 3.1 Toroidal magnetic field

Wardziński and Zdziarski (2000) show that for a mildly relativistic Maxwellian electron distribution,

$$n_e(\gamma) = \frac{n_e}{\theta_e} \frac{\gamma(\gamma^2 - 1)^{1/2}}{K_2(1/\theta_e)} \exp\left[-\frac{\gamma}{\theta_e}\right], \quad (16)$$

where  $\theta_e = k_B T / (m_e c^2)$ ,  $m_e$  being the electron mass,  $\gamma = (1 - v^2/c^2)^{-1/2}$  is the Lorentz factor and  $K_2$  is a modified Bessel function, the emission coefficient is

$$j_\nu^{\text{dir}} = \frac{\pi e^2}{2c} (\nu \nu_0)^{1/2} \mathcal{X}(\gamma_0) n_e(\gamma_0) \left(1 + 2 \frac{\cot^2 \vartheta}{\gamma_0^2}\right) \times \\ \times \left[1 - (1 - \gamma_0^{-2}) \cos^2 \vartheta\right]^{1/4} \mathcal{Z}(\vartheta, \gamma_0), \quad (17)$$

where  $\nu_0 \equiv eB / (2\pi m_e c)$  is the cyclotron frequency. The superscript dir means that this emission coefficient depends on the angle between the magnetic field and the direction of emission, no angle averaging has been performed. Then,

$$\gamma_0 = \begin{cases} \left[1 + \left(\frac{2\nu\theta_e}{\nu_0}\right) \left(1 + \frac{9\nu\theta_e \sin^2 \vartheta}{2\nu_0}\right)^{-\frac{1}{3}}\right]^{\frac{1}{2}} & \theta_e \lesssim 0.08, \\ \left[1 + \left(\frac{4\nu\theta_e}{3\nu_0 \sin \vartheta}\right)^{\frac{2}{3}}\right]^{\frac{1}{2}} & \theta_e \gtrsim 0.08 \end{cases} \quad (18)$$

is the Lorentz factor of those thermal electrons that contribute most to the emission at  $\nu$ , and

$$\mathcal{X}(\gamma) = \begin{cases} \left[\frac{2\theta_e(\gamma^2 - 1)}{\gamma(3\gamma^2 - 1)}\right]^{1/2}, & \theta_e \lesssim 0.08 \\ \left(\frac{2\theta_e}{3\gamma}\right)^{1/2}, & \theta_e \gtrsim 0.08 \end{cases} \quad (19)$$

$$t \equiv (\gamma^2 - 1)^{\frac{1}{2}} \sin \vartheta, \quad n \equiv \frac{\nu(1 + t^0(\gamma_0)^2)}{\nu_0 \gamma}, \quad \mathcal{Z}(\vartheta, \gamma) = \left\{ \frac{t \exp\left[(1 + t^2)^{-\frac{1}{2}}\right]}{1 + (1 + t^2)^{\frac{1}{2}}} \right\}^{2n}. \quad (20)$$

Synchrotron radiation becomes self-absorbed below a critical frequency  $\nu_c$  where the plasma becomes optically thick. The emitted spectrum below this frequency will follow the Rayleigh–Jeans emission law. Following Narayan and Yi (1995) we determine the self-absorption critical frequency by asking that at this frequency and at the current radius  $r$ , the synchrotron emission over the volume of the sphere with radius  $r$  equates the Rayleigh–Jeans emission from the surface of this sphere, i.e.

$$\frac{4}{3}\pi r^3 j_v^{\text{dir}}(\nu_c) = \pi B_\nu(\nu_c) 4\pi r^2, \quad (21)$$

where  $B_\nu = 2k_B T \nu^2 / c^2$  is the Rayleigh–Jeans emission law. The synchrotron emitted spectrum is then smoothly connected with a Rayleigh–Jeans spectrum below  $\nu_c$ .

### 3.2 Isotropic magnetic field

Wardziński and Zdziarski (2000) give the angle-averaged limit of the synchrotron emission

$$j_v^{\text{avg}} = \frac{2^{1/6} \pi^{3/2} e^2 n_e v}{3^{5/6} c K_2(1/\theta_e) v^{1/6}} \exp \left[ - \left( \frac{9v}{2} \right)^{1/3} \right], \quad (22)$$

where  $v = v/(v_0 \theta_e^2)$ . The superscript avg now refers to an emission coefficient after angle averaging. There is a multiplicative correction factor  $a$  in this expression in Wardziński and Zdziarski (2000), which is close to unity, and which we do not take into in this work as we are not interested in very precise values of synchrotron fluxes. We note that the equation above is only valid for a mildly relativistic plasma,  $\theta_e \lesssim 1$ . This condition is satisfied in our model.

The self-absorbed synchrotron is treated in the same way as for the toroidal magnetic field case.

Figure 1 illustrates the synchrotron images of a Komissarov torus at 1.3 mm and demonstrates that for some values of spin and inclination, the size of the emitting zone satisfies the VLBI constraints imposed by Doeleman et al. (2008).

## 4 CONCLUSION AND PERSPECTIVES

We have constructed a millimetre-wavelength synchrotron radiative model for Sgr A\* based on the fully general relativistic, analytical magnetized torus model of Komissarov (2006), who assumes a purely toroidal magnetic field. Our work presented here is only theoretical. It will be useful to construction of a multi-dimensional network of Komissarov’s models. For each model of the network one calculates the theoretical silhouette (in different wavelengths) and theoretical electromagnetic spectra of Sgr A\*, as could be found in another paper of the same authors (Vincent et al., 2014). This may be then compared with the observed silhouette and spectra. The best fit may give an estimate the black hole spin, and other parameters.

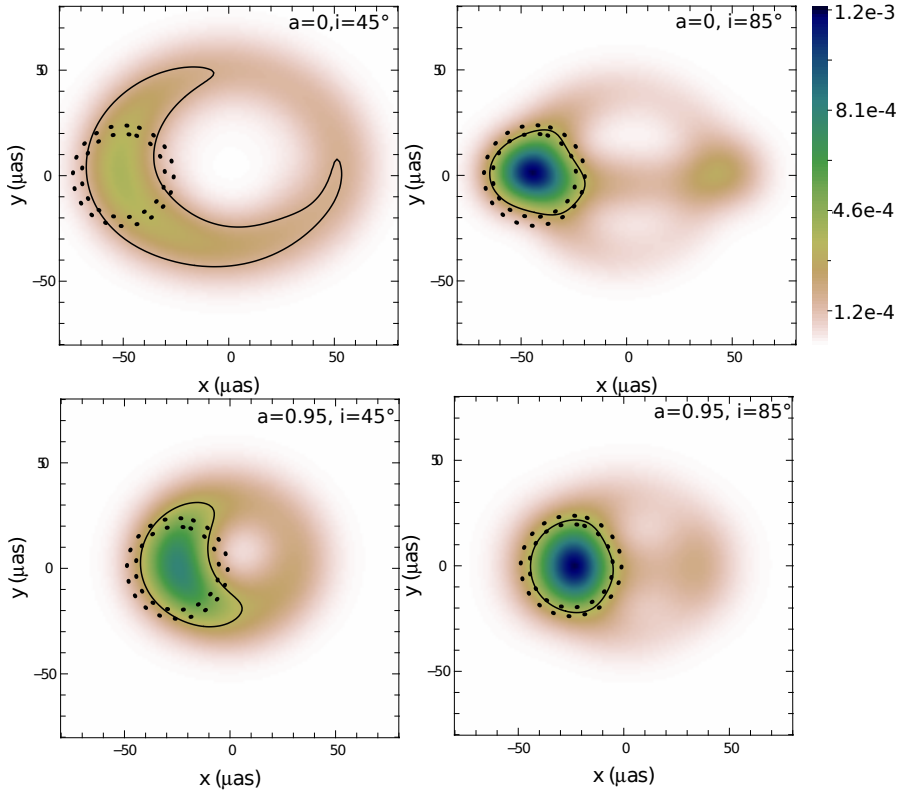


**Figure 1.** Images (maps of specific intensity) at 1.3 mm of a torus satisfying the millimetre spectral constraints for Sgr A\* (see Vincent et al., 2014, for details). The dotted circle show the  $1\sigma$  confidence domain from Doeleman et al. (2008). The thin solid curve encompass the region containing 50 % of the total flux. Here  $a$  and  $i$  are the black hole spin and inclination. The color bar is common to all panels, and graduated in cgs units ( $\text{erg} \cdot \text{s}^{-1} \text{cm}^2 \text{str}^{-1} \text{Hz}^{-1}$ ).

We believe that the Komissarov model for Sgr A\* as developed in this work may be of interest for the future data analysis linked with the EHT project. In particular, this model may be a suitable test bed for investigating the observational counterparts of compact objects alternative to the Kerr black hole.

In order to further test the possibility to constrain the magnetic field geometry in the vicinity of Sgr A\*, future work will be dedicated to investigating the polarization predictions of the Komissarov and chaotic models. Future work will also be dedicated to developing a full analysis of the parameter space of the Komissarov model in order to provide a robust fit to observed data.

## ACKNOWLEDGEMENTS

The present work was supported by the Polish NCN grants UMO-2013/08/A/ST9/00795, UMO-2011/01/B/ST9/05439 and Czech Grant MSM 4781305903.

**REFERENCES**

- Balick, B. and Brown, R. L. (1974), Intense sub-arcsecond structure in the galactic center, **194**, pp. 265–270.
- Broderick, A. E., Johannsen, T., Loeb, A. and Psaltis, D. (2014), Testing the No-hair Theorem with Event Horizon Telescope Observations of Sagittarius A\*, **784**, 7, arXiv: 1311.5564.
- Doeleman, S. S., Weintroub, J., Rogers, A. E. E., Plambeck, R., Freund, R., Tilanus, R. P. J., Friberg, P., Ziurys, L. M., Moran, J. M., Corey, B., Young, K. H., Smythe, D. L., Titus, M., Marrone, D. P., Cappallo, R. J., Bock, D. C.-J., Bower, G. C., Chamberlin, R., Davis, G. R., Krichbaum, T. P., Lamb, J., Maness, H., Niell, A. E., Roy, A., Strittmatter, P., Werthimer, D., Whitney, A. R. and Woody, D. (2008), Event-horizon-scale structure in the supermassive black hole candidate at the Galactic Centre, *Nature*, **455**, pp. 78–80, arXiv: 0809.2442.
- Genzel, R., Eisenhauer, F. and Gillessen, S. (2010), The Galactic Center massive black hole and nuclear star cluster, **82**, pp. 3121–3195, arXiv: 1006.0064.
- Komissarov, S. S. (2006), Magnetized tori around Kerr black holes: analytic solutions with a toroidal magnetic field, **368**, pp. 993–1000, arXiv: astro-ph/0601678.
- Narayan, R. and Yi, I. (1995), Advection-dominated Accretion: Underfed Black Holes and Neutron Stars, **452**, p. 710, arXiv: astro-ph/9411059.
- Straub, O., Vincent, F. H., Abramowicz, M. A., Gourgoulhon, E. and Paumard, T. (2012), Modelling the black hole silhouette in Sagittarius A\* with ion tori, **543**, A83, arXiv: 1203.2618.
- Vincent, F. H., Yan, W., Abramowicz, M. A., Zdziarski, A. A. and Straub, O. (2014), A magnetized torus for modeling Sgr A\* millimeter images and spectra, *ArXiv e-prints*, arXiv: 1406.0353.
- Wardziński, G. and Zdziarski, A. A. (2000), Thermal synchrotron radiation and its Comptonization in compact X-ray sources, **314**, pp. 183–198, arXiv: astro-ph/9911126.





Title: **Proceedings of RAGtime 14–16: Workshops on black holes and neutron stars, 18–22 Sept./15–18 July/11–19 Oct. '12/'13/'14, Opava, Prague, Czech Republic**

Published by: Silesian University in Opava  
Faculty of Philosophy and Science  
Institute of Physics  
Bezručovo nám. 13  
CZ-746 01 Opava, Prague  
Czech Republic

Editors: Z. Stuchlík, G. Török and T. Pecháček

Cover design: Otakar Karlas

Copyright © 2014 by Silesian University in Opava

All rights reserved. No part of this publication may be reproduced, stored in a retrieval system or transmitted in any form or by any means, electronic, mechanical, photocopying, recording or otherwise, without the prior permission of the Publisher.

1st edition

Printed by: Z + M Partner, s.r.o.  
Valchařska 3261/17  
CZ-702 00 Ostrava-Moravská Ostrava  
Czech Republic

Published in December 2014



INVESTMENTS IN EDUCATION DEVELOPMENT

The publication was prepared as the study material in the framework of the project “Supporting Integration with the International Theoretical and Observational Research Network in Relativistic Astrophysics of Compact Objects”, CZ.1.07/2.3.00/20.0071. The project is co-financed by European Social fund and state budget of the Czech Republic.

ISBN 978-80-7510-127-3

ISSN 2336-5668 (Print)

ISSN 2336-5676 (Online)

Typeset in L<sup>A</sup>T<sub>E</sub>X



Název: **Proceedings of RAGtime 14–16: Workshops on black holes and neutron stars, 18–22 Sept./15–18 July/11–19 Oct. '12/'13/'14, Opava, Prague, Czech Republic**

Nakladatel: Slezská univerzita v Opavě  
Filozoficko-přírodovědecká fakulta  
Ústav fyziky  
Bezručovo nám. 13  
CZ-746 01 Opava, Prague  
Česká republika

Editoři: Z. Stuchlík, G. Török and T. Pecháček

Obálka: Otakar Karlas

Copyright © 2014 by Slezská univerzita v Opavě

Všechna práva vyhrazena. Žádná část této publikace nesmí být reprodukována, přenášena jakoukoli formou, elektronicky, mechanicky, kopírováním, nahráváním nebo jakýmikoli systémy pro skladování informací bez předchozího souhlasu nakladatele.

První vydání

Tisk: Z + M Partner, s.r.o.  
Valchařska 3261/17  
CZ-702 00 Ostrava-Moravská Ostrava  
Czech Republic

Vydáno v prosinci 2014



INVESTMENTS IN EDUCATION DEVELOPMENT

The publication was prepared as the study material in the framework of the project “Supporting Integration with the International Theoretical and Observational Research Network in Relativistic Astrophysics of Compact Objects”, CZ.1.07/2.3.00/20.0071. The project is co-financed by European Social fund and state budget of the Czech Republic.

ISBN 978-80-7510-127-3  
ISSN 2336-5668 (Print)  
ISSN 2336-5676 (Online)

Vysázeno systémem L<sup>A</sup>T<sub>E</sub>X







## INVESTMENTS IN EDUCATION DEVELOPMENT

ISBN 978-80-7510-127-3

ISSN 2336-5676